Enhanced Bioethanol Production from Potato Peel Waste: Nano-Assisted Detoxification, Co-Fermentation with *Saccharomyces cerevisiae* and *Pichia stipitis*, and Process Scale-Up

By

ADENIYI PHILIP ADEBULE

Student number: 220112666

B.Sc. (*Hons*.) Microbiology

M.Sc. Microbiology

Submitted in fulfilment of the academic requirements for the degree of

Doctor of Philosophy in Microbiology

School of Biological Sciences

College of Agriculture, Engineering and Science

University of KwaZulu-Natal

Pietermaritzburg

South Africa

March 2026

PREFACE

The candidate (Adeniyi Philip Adebule) completed the research in this thesis while based in the Discipline of Biological Sciences (Microbiology), School of Agriculture and Science, College of Agriculture, Engineering and Science, University of KwaZulu-Natal, Pietermaritzburg, South Africa.

The contents of this work have not been submitted in any form to another university, and except where the work of others is acknowledged in the text, the results reported are due to investigations by the candidate.

....……...

Signed: Professor Gueguim E.B. Kana (Supervisor)

Date: 13 March 2026

....……...

Signed: Dr Isaac A. Sanusi (Co-supervisor)

Date: 13 March 2026

DECLARATION 1: PLAGIARISM

I, **Adeniyi Philip Adebule**, declare that:

1. the research reported in this thesis, except where otherwise indicated or acknowledged, is my original research,

2. this thesis has not been submitted for any degree or examination at any other university,

3. this thesis does not contain other persons' data, pictures, graphs or other information unless specifically acknowledged as being sourced from other persons,

4. this thesis does not contain other persons' writing unless specifically acknowledged as being sourced from other researchers. Where other written sources have been quoted, then:

    a) their words have been rewritten, but the general information attributed to them has been referenced,

    b) where their exact words have been used, then their writing has been placed in italics and inside quotation marks and referenced,

5. where I have used material for which publications followed, I have indicated in detail my role in the work,

6. this thesis is primarily a collection of material, prepared by me, published as journal articles or presented as a poster and oral presentations at conferences. In some cases, additional material has been included,

7. this thesis does not contain text, graphics or tables copied and pasted from the internet unless specifically acknowledged, and the source is detailed in the thesis and in the reference sections.

……..

Signed: Adeniyi Philip Adebule

DECLARATION 2: PUBLICATIONS AND MANUSCRIPTS

This thesis represents a compilation of manuscripts/ published work, where each chapter is an individual entity prepared as per the journals' specifications; thus, some repetition between chapters has been unavoidable. The first author (student) conducted all experimental work, data collection, and manuscript preparation under the guidance of the second and/or third author (supervisor). The * indicates the corresponding author.

Chapter 2

Adeniyi P. Adebule, Isaac A. Sanusi, E.B. Gueguim Kana*, 2024. Progress in the development of nanoparticle-based detoxification of pretreated lignocellulosic hydrolysate for bioethanol production: Literature survey and bibliometric review.

Chapter 3

Adeniyi P. Adebule, Isaac A. Sanusi, E.B. Gueguim Kana*, 2024. Nano-based surface adsorption detoxification of process inhibitors for improved bioethanol productivity, Bioresource Technology Reports, 25 (2024) 101783, https://doi.org/10.1016/j.biteb.2024.101783.

Chapter 4

Adeniyi P. Adebule, Isaac A. Sanusi, E.B. Gueguim Kana*, 2024. Adsorption kinetics and thermodynamics of Fe_3O_4-nanoparticle-based detoxification of process inhibitors in pretreated waste potato peel hydrolysate, Bioresource Technology Reports, 102185, https://doi.org/10.1016/j.biteb.2025.102185.

Chapter 5

Adeniyi P. Adebule, Isaac A. Sanusi, E.B. Gueguim Kana*, 2025. Growth-associated and Non-growth-associated Bioethanol Production Kinetics from Nanoadsorbent-Detoxified Pretreated Hydrolysate. *Catalysis Letters*, *155*(3): 96. https://doi.org/10.1007/s10562-024-04868-8.

Chapter 6

Adeniyi P. Adebule, Isaac A. Sanusi, E.B. Gueguim Kana*, 2024. Improved ethanol production via optimised co-fermentation of *Saccharomyces cerevisiae* and *Pichia stipitis* post-nanoparticle detoxification of pretreated waste potato peel hydrolysate.

Chapter 7

Adeniyi P. Adebule, Isaac A. Sanusi, E.B. Gueguim Kana*, 2024. Process scale-up and kinetic evaluation of co-fermentation of detoxified pretreated potato peel hydrolysate for sustainable bioethanol production.

CONFERENCE CONTRIBUTIONS

- **Adeniyi P. Adebule,** Isaac A. Sanusi, E.B. Gueguim Kana. Enhanced bioethanol fermentation of Nano-based detoxified pretreated potato peel waste (PPW) hydrolysate by co-culture of *Saccharomyces cerevisiae* and *Pichia stipitis. College of Agriculture, Engineering, and Science Postgraduate Research and innovation symposium* (PRIS), University of Kwazulu-Natal, South Africa. Nov. 2- 3, 2022. Flash presentation.

- **Adeniyi P. Adebule,** Isaac A. Sanusi, E.B. Gueguim Kana. Bioethanol production from two-forms of potato peels wastes: optimized hybrid pretreatment and fermentation condition on process kinetics. 5th National Global Change Conference (GCC5), University of the Free State, Bloemfontein, 30 January – 2 February 2023. Oral presentation.

- **Adeniyi P. Adebule,** Isaac A. Sanusi, E.B. Gueguim Kana. Nano-based process development for bioethanol production from pretreated waste potato peel: Improved detoxification, saccharification efficiency and reducing sugar recovery. *College of Agriculture, Engineering, and Science Postgraduate Research & innovation symposium* (PRIS), University of Kwazulu-Natal, South Africa. Dec. 8- 9, 2022. Flash presentation.

- **Adebule, A. P. and** Sanusi, A. I. Hybrid pretreatment Modelling and optimization for enhanced sugar recovery from fresh potato peel waste. The 3rd Nigerian Academy of Science (NAS) Scientific Conference, FCT, Abuja, Nigeria. *Science and Technology Innovation for National and Development*, Jan. 25-26, 2022 (Oral presentation).

- **Adebule, A. P.** Modelling and optimization of hybrid pretreatment for enhanced sugar recovery from potato peel waste. *College of Agriculture, Engineering, and Sciences Postgraduate Research and innovation symposium* (Virtual), University of Kwazulu-Natal, South Africa. Dec. 9- 10, 2021. Oral presentation.

……

Signed: Adeniyi Philip Adebule

Date: 13 March 2026

ABSTRACT

The environmental and climate impacts associated with fossil fuel consumption have led to the search for sustainable alternatives, including renewable, bio-based fuels and products from lignocellulosic biomasses. Lignocellulosic biomass, particularly agro-industrial residues like potato peels, has emerged as a promising feedstock for second-generation bioethanol production. However, the microbial conversion of lignocellulosic biomass into large-scale bioethanol production is challenged by several factors, including the formation of inhibitory compounds during biomass pretreatment, inefficient utilization of mixed sugars and low yield. Therefore, this study explored the co-fermentation of *S. cerevisiae* and *P. stipitis*, integrated with nanoparticle-based detoxification of inhibitory compounds, process kinetics and scale-up to enhance bioethanol production efficiency from potato peel waste (PPW) hydrolysates.

In this study, the pretreated PPW hydrolysate was subjected to a Fe_3O_4 nanoparticle-assisted detoxification process modelling and optimization using Response Surface Methodology (RSM) for the simultaneous removal of five key fermentation inhibitors: furfural, 5-hydroxymethylfurfural (HMF), phenol, acetic acid, and formaldehyde. An artificial neural network (ANN) was employed to model the removal of inhibitors and identify key process variables. The RSM and ANN strategies were complemented with sensitivity analysis, adsorption-desorption kinetics, and thermodynamic studies to further elucidate the underlying detoxification mechanisms. The detoxified PPW hydrolysate was employed for bioethanol production, comparatively using simultaneous saccharification and fermentation (SSF) and separate hydrolysis and fermentation (SHF) strategies to establish the most efficient fermentation strategy. This was followed by substrate utilization, growth and bioethanol production kinetic studies. Thereafter, the simultaneous saccharification and co-fermentation (SSCF) process with *S. cerevisiae* and *P. stipitis* was modelled and optimized using the RSM to maximize sugar bioconversion for improved bioethanol production. The optimised SSCF was evaluated for preliminary scale-up with specific consideration given to reactor geometry, rheological behaviour, and hydrodynamic parameters.

First, the pretreated PPW hydrolysate was subjected to optimized nanoparticle-assisted detoxification conditions, resulting in significant removal efficiencies for furfural (1.65-fold), 5-hydroxymethylfurfural (1.21-fold), phenol (1.95-fold), acetic acid (3.25-fold), and formaldehyde (1.55-fold), without sugar loss. Sensitivity analysis revealed that pH and initial inhibitor concentration were the critical influencing factors. The characteristic profile and

adsorption mechanism of Fe_3O_4 nanoparticles (NPs) were elucidated using scanning electron microscopy (SEM), transmission electron microscopy (TEM), Fourier-transform infrared spectroscopy (FTIR), UV spectrophotometry, X-ray diffraction (XRD), point of zero charge (PZC), and the Brunauer–Emmett–Teller (BET), suggesting surface adsorption and complexation as the primary detoxification mechanisms. The adsorption mechanisms were further substantiated through pseudo-first-order, pseudo-second-order, intra-particle diffusion, Elovich, Langmuir, Freundlich, Temkin and thermodynamic studies. The finding indicated chemisorptive interactions between Fe_3O_4 nanoparticles and inhibitors. Phenol and HMF adsorption best fitted the Langmuir model (R^2 = 0.997 and 0.966), respectively, suggesting monolayer adsorption on uniform surfaces. Acetic acid and formaldehyde followed the Freundlich model (R^2 = 0.985 and 0.980), respectively, indicating heterogeneous surface adsorption, while furfural fitted the Temkin model (R^2 = 0.970), reflecting moderate, energy-distributed adsorption. The Fe_3O_4 nanoadsorbent demonstrated a multi-site adsorption mechanism involving hydrogen bonding, π–π interactions, and electrostatic forces, consistent with chemisorption. Hence, the optimally detoxified hydrolysate was employed for bioethanol production.

The SSF bioethanol production strategies demonstrated improved performance over SHF, achieving a saccharification efficiency of 88.95% and a bioethanol yield of 26 g/L. Consequently, the logistic function, modified Gompertz, Luedeking-Piret, and modified Luedeking-Piret performed on the SSF process further revealed improved metabolic performance that was predominantly growth-associated (α = 3.515 g P/g X and γ = 6.543 g S/g X), with a low cell maintenance coefficient (δ) value (0.0019 g S/g X h). This data indicated that *S. cerevisiae* relies strongly on efficient substrate availability and processability for optimal ethanol biosynthesis under detoxified conditions. However, the inefficient bioconversion of fermentable sugars in the detoxified hydrolysate necessitated the adoption of a co-fermentation strategy to enable simultaneous utilization of glucose and xylose present in the hydrolysate. For the SSCF process optimization, the optimal co-fermentation conditions were determined to be a zero-hour co-inoculation time, an inoculation ratio of 1:4 (*S. cerevisiae* to *P. stipitis*), and a 10% solid loading. Under these conditions, improved bioethanol concentration of 48.7 g/L, maximum specific growth rate (μ_{max}) (0.752 h^{-1}), bioethanol productivity (4.06 g/L/h), yield (0.505 g/g) and fermentation efficiency of 99% were achieved.

Scaling the SSCF process from 1 L to 10 L while maintaining constant non-gassed power (0.012 W), impeller tip speed (0.35 m/s), temperature (35°C), and pH 5.78, ensured comparable

bioethanol production efficiencies with productivities of 3.653 and 3.635 g/L/h and bioethanol concentrations of 43.68 g/L at 1 L and 10 L, respectively. A desirable pumping capacity (V_P = 3.9 × 10^{-4} m^3/**s**) and a 10-fold reduction in Power-to-Volume ratio (P/V_L= 1.2 W/m^3) characterised the 10L scale, indicating a significant improvement in energy efficiency at pilot scale. The logistic model (R^2 >0.938) yielded maximum specific growth rate (μ_{max}) of 0.436 h^{-1} (1 L) and 0.415 h^{-1} (10 L), and maximum biomass concentration (X_{max}) of 16.40 g/L (1 L) and 16.88 g/L (10 L). The modified Gompertz model (R^2 >0.99) showed comparable maximum potential bioethanol concentration [P_m] (44.37 g/L for 1 L; 44.09 g/L for 10 L), maximum bioethanol production rate [$r_{p,m}$] (6.68 g/L/h for 1 L; 6.63 g/L/h for 10 L), and lag time [t_L] (2.94 h for 1 L; 2.69 h for 10 L). Interestingly, growth-associated product (α, 4.744 g P/g X) and substrate utilization (γ, 6.611 g S/g X) coefficients further aligned with experimental data (R^2 >0.90), confirming model fitness across scales.

This study presents a novel integrated strategy that combines dual optimisation of Fe_3O_4 nanoparticle-assisted detoxification of pretreated potato peel waste (PPW) hydrolysate and co-fermentation of detoxified PPW hydrolysate using *S. cerevisiae* and *P. stipitis* to enhance bioethanol production. The findings further demonstrated the efficiency and underlying mechanisms of Fe_3O_4 nanoparticles in improving the processability of hydrolysate, substrate affinity, substrate uptake as well as growth kinetics of *S. cerevisiae* and *P. stipitis*, thereby enhancing bioethanol productivity, yield and subsequent pilot scale-up. Underscoring the suitability of the developed process design for industrial implementation towards sustainable large-scale bioethanol production from agricultural residues.

Keywords: Bioethanol, co-fermentation, detoxification, inhibitors, nanoparticles, scale up

ACKNOWLEDGMENTS

With a heart full of gratitude, I first and foremost give all glory to God Almighty, the unfailing source of my wisdom, knowledge, understanding, and strength. His grace has carried me through every step of this research journey, making the successful completion of this research possible.

To my esteemed supervisor, Professor Evariste Bosco Gueguim Kana, I am profoundly grateful. Thank you for graciously accepting me as your PhD student and guiding me through an exciting and challenging interdisciplinary project. Your invaluable insights, unwavering support, and constructive criticism at every stage have been instrumental in shaping both this work and my growth as a researcher. It was an honour to work under your supervision.

My heartfelt thanks go to Dr Adeyemi Isaac Sanusi. Words cannot express my enduring gratitude for your moral, spiritual, mental, and financial support. Your presence was truly God-sent, and your immense assistance has been a cornerstone of my journey. Thank you for standing by me so selflessly, sir. To Ms Cynthia Matyumza, I am sincerely appreciative of your assistance in characterizing the synthesized nanoparticles using SEM and TEM, and to Dr LS Beukes for your moral support and encouragement. I also thank Dr Solomon Oloyede and Dr Abimbola Oluwalana for your expert guidance on FT-IR and UV studies. Your professional advice made a significant difference and lightened what could have been a burdensome task.

Special thanks to Ms Sithokozile P. Mtshatsha of the International Office for your support in visa processing and mediating with DHA at critical moments—you were a true blessing. To my ever-available family in PMB, Dr Stella Eregie and Emmanuel Ngerem, thank you for always being there. Your kindness will always have a special place in my heart. I am equally thankful to the past and present scholars in Lab 117, Rabie Saunders Building, UKZN, who supported me throughout this thesis journey, especially Nyasha, Caitlyn, Sine, Anthea, and Bishop. Our academic and social interactions made this journey richer and more fulfilling. I will treasure the memories we built together. I am deeply grateful to Dr Gabriel Aruwajoye, Dr Ayodeji, Dr Titi Agbaje-Adedoyin, Dr Inuwaye Nike, Dr Aanu Oyebamiji, Dr Fayomi Samuel and Prof. Omololu Fagbadebo for your constant encouragement, motivation, and advice. I am sincerely thankful to Dr Lawal of Grey's Hospital and Mrs Yewande Lawal (Pietermaritzburg) for your kind and timely medical support and guidance. Your care and concern were invaluable and provided much-needed comfort and strength for my family during trying times.

Pastor Selva, Pastor Lally, and friends at New City Church, your prayers, fellowship, and the moments of joy we shared brought much-needed balance to the intense seasons of research. I am especially grateful to the Bankole family for giving me a safe landing in PMB, and to Seffie Princen (Mumsee), thank you for being a mother to me while I lived in your home—you made it feel like family. I acknowledge the fatherly support of my academic mentors, including Prof. S.O. Adebule and Prof. O.R. Akinyeye. I am humbled and grateful for all the mothers who carried me with their love and support: Pastors (Mrs.) Owoseeni, Mrs Ogunfidodo, Mrs Deyin Adelola, Mrs Bolaji Fatoba, Mrs Kemi Familugba, Mrs Bose Akeju, and especially Mrs Olubusola Omotayo Fasheun (Mummy Fash)—thank you for embracing me as your son. Your kindness and constant concern are deeply treasured. I sincerely appreciate the Fasheun family (PMB) for offering me shelter and unwavering support during a critical period. Although the journey had its challenges, your generosity gave me a foothold and a way forward. The Adebule and Abegunde dynasties from Aisegba Ekiti, Nigeria, were pivotal to the overall success of this journey. To my siblings (Mrs Yemi Ogunjobi, Engr. Olusola, Dr Damilola, Engr. Ayomide, and Mr Toluwase Adebule), in-laws, and their families, your understanding, encouragement, and prayers have been a vital source of strength. I am blessed to have you.

My profound appreciation also goes to my parents-in-law, Mr and Mrs Babatunde Adeyemo, for your unwavering prayers, love, and constant encouragement. Your quiet faith in my journey has been a powerful source of strength. I reserve my heartfelt gratitude for my parents, Mr and Mrs Adeola and Olufunke Adebule. Your boundless love, sacrifices, prayers, and unwavering support have shaped who I am today. Sir and Ma, you are truly exceptional.

I wish to express my deepest gratitude to the love of my life, Tobi Elizabeth Adebule; thank you for believing in me, trusting me, and standing by me with unshakable support, even across the miles. You are a priceless gift from God, and I am endlessly grateful for you. Finally, to our beautiful daughter, Princess Emmanuella, and the wonderful siblings we look forward to welcoming in the future, your presence and promise give me renewed purpose and joy each day. I dedicate this achievement to God and everyone who contributed to the success of this journey.

TABLE OF CONTENTS

LIST OF TABLES

SECTION **PAGE NO.**

CHAPTER 2

CHAPTER 3

CHAPTER 4

CHAPTER 5

CHAPTER 6

CHAPTER 7

LIST OF FIGURES

SECTION **PAGE NO.**

CHAPTER 1

CHAPTER 2

CHAPTER 3

CHAPTER 5

CHAPTER 6

CHAPTER 1

General Introduction

1.1. Background

In response to the growing severity of environmental degradation and the global shift toward sustainable energy, the pursuit of lignocellulosic biofuels, especially bioethanol, has gained considerable momentum. As a renewable, low-carbon alternative to fossil fuels, lignocellulosic bioethanol offers a viable pathway to reduce greenhouse gas emissions, enhance energy resilience, and promote the valorisation of agricultural waste and residues. Agricultural residues, such as potato peels, which are rich in fermentable sugars, represent a sustainable and underutilised feedstock for bioethanol production. However, their bioconversion is hindered by inhibitory compounds, such as furfural, hydroxymethylfurfural (HMF), and phenolics, which are formed alongside fermentable sugars during the pretreatment process. These inhibitors limit fermentation efficiency and ethanol yield. Therefore, addressing these challenges is vital to unlocking the full potential of lignocellulosic bioethanol. The following section highlights the importance of sustainable biofuels, particularly bioethanol, alongside microbial fermentation strategies and detoxification approach essential for scalable, eco-friendly production.

1.1.1. Bioethanol as a sustainable and renewable fuel

The current global energy landscape is shifting away from conventional non-renewable fossil fuels, which are limited by finite reserves, environmental concerns, and their contribution to climate change, toward sustainable, renewable alternatives (Holechek et al., 2022; Dalei et al., 2024). Microbial biofuels such as hydrogen, methane, ethanol, and biodiesel have been shown to be valuable alternative energy sources. Bioethanol, a leading second-generation biofuel, is highly desirable due to its economic and environmental benefits, including a high-octane rating, compatibility with existing infrastructure, and lower greenhouse gas emissions, all of which drive substantial demand that necessitates large-scale production (Dandasena and Shahi, 2023). In 2023, global bioethanol production reached 116 billion litres (70% of liquid biofuels) and is projected to grow further as policy mandates for biofuel blending strengthen worldwide (World Bioenergy Association, 2024). The global effort towards bioethanol development is evident in major producing nations, such as the United States of America (USA), Brazil, India, China,

Canada, and several European Union (EU) member states (Fig. 1.1), actively engaging and implementing programs to reduce reliance on conventional fossil fuels (RFA, 2022). African nations, including South Africa, are also recognizing bioethanol's role in mitigating climate change caused by global warming resulting from fossil fuel dependence. In South Africa, the bioethanol industry is emerging, and the abundance of locally available biomass presents substantial potential for large-scale ethanol production (IEA Bioenergy, 2024; Mvelase and Ferrer, 2024). South Africa has committed to strategic greenhouse gas mitigation actions, aiming to reduce its emissions by 42% below its emission growth trajectory by 2025. This shift towards bioethanol production is not only a global initiative but a strategic response to the growing demand for sustainable fuels and biofuel development. In line with these national and global efforts, there is an increasing research and policy interest directed toward second-generation non-food-based feedstocks, particularly lignocellulosic biomass, due to their abundance, minimal competition with food resources, and capacity to support sustainable and economically viable bioethanol production systems.

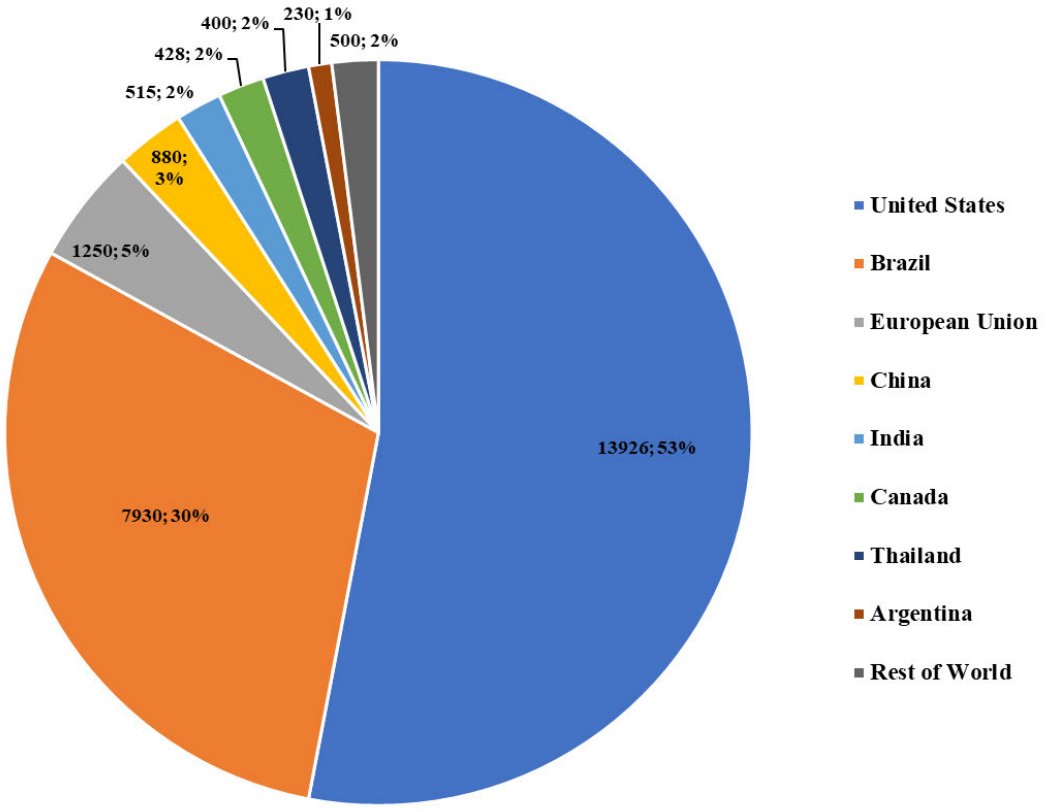

Figure 1.1. Global ethanol production by country by 2022 (RFA, 2022)

1.1.2. Lignocellulosic biomass for bioethanol production

Among the array of sustainable and renewable energy sources, lignocellulosic biomass (LB) possesses significant potential as a biofuel feedstock offering a pathway to valorising waste streams into fuels and chemicals without competing directly with food crops, thereby allowing for effective mitigation of the challenges associated with dependence on fossil fuels (El-Araby, 2024). Globally, LB generation is estimated at 181.5 billion tons and is primarily composed of cellulose (40–50%), hemicellulose, and lignin, forming a recalcitrant matrix that presents a challenge for bioconversion (Ashokkumar et al., 2022). In broader agricultural contexts, LB includes residues such as sugarcane bagasse, corn stover, wheat straw, potato peels, fruit peels, cassava peels, and yam peels are particularly valuable and promising due to their high carbohydrate (Chohan et al., 2020; Woźniak et al., 2025; Sanusi et al., 2021; Baur et al., 2025). Potato peel waste (PPW), a significant byproduct of the potato processing industry, represents a promising LB feedstock for bioethanol production due to its high starch and carbohydrate content (Awogbemi et al., 2022; Chakraborty et al., 2024). Globally, substantial quantities of PPW are generated annually, posing waste management challenges that can be addressed through valorization into biofuels (Singh et al., 2024). PPW typically consists of starch (25-55%), non-starch polysaccharides (30%), lignin (20%), protein (18%), and lipids (1%), making it a suitable substrate for fermentation subsequent to adequate pretreatment and hydrolysis to convert the starch and cellulose into fermentable sugars (Barampouti et al., 2023; Singh et al., 2024).

1.1.3. Bioethanol fermentation strategies

Typically, bioethanol fermentation is achieved through the conversion of fermentable sugars (glucose, xylose, and other simple sugars) derived from cellulose and hemicellulose into ethanol using microorganisms. Bioethanol can be produced by microbes, including *Saccharomyces cerevisiae*, non-*Saccharomyces* yeasts (such as *Candida, Kloeckera, Hanseniaspora, Brettanomyces, Pichia, Lachancea,* and *Kluyveromyces* spp.), thermophilic microorganisms (such as *Geobacillus thermoglucosidasius* and *Thermoanerobacterium saccharolyticum*), and bacteria (such as *Zymomonas mobilis* and other microorganisms, including *Clostridium* species, which metabolise fermentable sugars under microaerophilic or anaerobic conditions to produce ethanol (González-Gloria et al., 2024). *S. cerevisiae* produces ethanol through the Embden-Meyerhof-Parnas (EMP) pathway (glycolysis), where glucose is converted to pyruvate, then to ethanol with NAD+ regeneration.

Pichia stipitis, on the other hand, metabolizes xylose via the pentose phosphate pathway. First, xylose is reduced to xylitol by the enzyme xylose reductase; subsequently, xylulose-5-phosphate is converted to pyruvate, linking up with the glycolytic pathway for ethanol production (Bertels et al., 2021).

The batch, fed-batch, and continuous fermentation are the primary modes of fermentation; however, several different strategies have been developed, including separated hydrolysis and fermentation (SHF), simultaneous saccharification and fermentation (SSF), pre-saccharification and simultaneous saccharification and fermentation (PSSF), consolidated bioprocessing (CBP), and consolidated bio-saccharification (CBS) (Singh et al., 2022), and more still being explored. These strategies have the potential to yield various outputs derivable from lignocellulosic hydrolysates by separating or combining different steps of bioprocessing. Such differences further impact the performance and cost-effectiveness of downstream fermentation, which are important factors in designing downstream fermentation products and processes (Wang et al., 2024). SSF, in comparison with other strategies, simultaneously integrates the saccharification and fermentation phases in a bioreactor, thereby reducing overall operational costs while avoiding the accumulation of high sugar concentrations in the hydrolysate and related inhibitory effects. However, the overall efficiency of the SSF is usually hampered by the challenge of synchronising fermentation with saccharification, due to the difference in temperature and pH optimal conditions, especially when the temperature for saccharification is high enough to inhibit the fermentation microbes (except in the case of thermophilic microorganisms) (Chavan et al., 2023).

Furthermore, the inefficient utilization or retention of fermentative sugars, both pentoses and hexoses from the LB hydrolysate, is a common challenge in a closed system after saccharification. This often leads to carbon catabolite repression, which significantly reduces ethanol production (Policastro et al., 2021). Excess retention of sugar (in the form of pentoses) in the LB hydrolysates can be addressed by co-fermentation. Co-fermentation (also known as co-inoculation) strategy is a promising technique for enhancing bioethanol production by utilising multiple microbial strains or processes to convert biomass into ethanol more efficiently (Miah et al., 2022). Co-cultures of multiple microorganism strains are also often applied in SSF, a strategy called simultaneous saccharification and co-fermentation (SSCF) (Naseeruddin et al., 2021; Miah et al., 2022). This strategy has been developed to achieve effective xylose utilisation and less product inhibition (Miah et al., 2022). SSCF effectively

utilises both pentoses (from hemicellulose) and hexoses (from cellulose), thereby maximising the conversion of sugars from lignocellulosic biomass, which is crucial for achieving high ethanol yields (Moreno et al., 2013). This approach is beneficial for producing more complex metabolites and enhances strain growth and fermentation processes through the synergistic interactions between different strains (Sharma et al., 2020). Some studies have reported that the SSCF strategy can lead to reduced product yields, often due to factors such as nutrient competition and the accumulation of inhibitory metabolic by-products. However, targeted process optimisation has the potential to mitigate these challenges and enhance overall performance (Sharma et al., 2021; Derman et al., 2022).

1.1.4. Fermentation inhibitors

Fermentation of pretreated substrates, such as potato peel waste (PPW), holds substantial potential for high ethanol yields, particularly when using the simultaneous saccharification and co-fermentation (SSCF) strategy. However, the presence of inhibitory compounds generated during pretreatment alongside fermentable sugars significantly hampers process efficiency (Ashokkumar et al., 2022). Pretreatment processes, particularly acid hydrolysis, lead to the formation of compounds such as furfural and hydroxymethylfurfural (HMF) from the degradation of sugars, which can inhibit the growth and metabolic activity of fermenting microorganisms (Lei et al., 2024). Additionally, phenolic compounds derived from lignin in PPW act as fermentation inhibitors by disrupting enzymatic activity and destabilizing cellular electrochemical gradients. These effects compromise microbial membrane integrity, leading to inhibited cell growth, prolonged lag phases, and decreased ethanol productivity (Sjulander and Kikas, 2020). Furthermore, the presence of organic acids (such as acetic acid and formaldehyde), which are byproducts of the hydrolysis of the polysaccharide (cellulose and hemicellulose) components of potato peels (Mazzoli, 2021), can also inhibit fermentation and may require specific removal or detoxification steps (Vescovo et al., 2025). Although several detoxification methods have been explored (Sjulander and Kikas, 2020), many have shown limited efficacy and are often associated with significant loss of fermentable sugars (Sarawan et al., 2019). On the other hand, nanotechnology could offer efficient removal of inhibitory compounds due to its multifunctional potential (Sanusi et al., 2021). Harnessing the potential of nanoparticles for removing inhibitory compounds and subsequently catalysing enzymatic hydrolysis could enhance fermentation performance, ultimately facilitating industrial scalability.

1.1.5. Nanotechnology roles in inhibitor detoxification and fermentation

Nanotechnology is a novel approach for the detoxification of inhibitor compounds in LB hydrolysate, leveraging the unique properties of nanoparticles (NPs), such as size, surface charge, structural porosity, high adsorption capacity, high surface area to volume ratio, multi-surface functional potential, and recyclability (Meena et al., 2024). These characteristics enable NPs to adsorb and degrade inhibitors, enhancing biofuel production efficiency. The interaction between inhibitors and NPs occurs selectively or non-selectively, depending on the functional properties of the inhibitors and the NP surface. Overall, nano-adsorbents exhibit strong potential for removing process inhibitors through tailored chemical and physical interactions, such as ligand formation and complexation of Fe_3O_4 nanoparticles with volatile organic inhibitory compounds (VOICs) (Sanusi et al., 2021). Magnetic nanoparticles (MNPs) have predominantly been utilised in bioenergy production compared to other nanoparticle groups, owing to their versatility in binding to various target compounds, biodegradability, low cytotoxicity to biomass cells, ease of synthesis, and, significantly, their magnetic properties facilitating easy recoverability and recyclability (Chen et al., 2018).

Additionally, MNPs can contribute metallic supplements in bioprocessing to achieve various functions, such as enzyme activation and stabilization, enzyme cofactors, growth factors, and chelating of other compounds (Thanigaivel et al., 2023). Although nanoparticle inclusion has shown potential in bioprocesses, there is limited knowledge regarding the potential of NPs in removing inhibitory compounds from lignocellulosic hydrolysates, as well as the interactive effects of detoxification process conditions, such as nanoparticle dosage, pH, exposure time, and temperature. Furthermore, the influence of nano-detoxified hydrolysates on microbial viability, co-fermentation efficiency, and ethanol productivity remains underexplored. Bridging these knowledge gaps is essential for ensuring the process scalability toward industrial bioethanol production.

1.2. Problem statement and justification of study

Although potato peel waste holds significant promise as a feedstock for bioethanol production, its industrial-scale application remains limited due to the inherent complexities of biomass conversion, suboptimal fermentation efficiency, and the generation of inhibitory compounds during the pretreatment process. These challenges contribute to low concentrations of

fermentable sugars, reduced ethanol yields, and overall process inefficiency (Rorke and Gueguim Kana, 2017; Sanusi et al., 2020).

To address these drawbacks, the development of effective detoxification strategies to mitigate the adverse effects of inhibitory compounds on microbial fermentation is critical. A recent study by Sanusi et al. (2021) has demonstrated the potential of Fe_3O_4 nanoparticles for the removal of inhibitory compounds; however, the comprehensive understanding of the selective adsorption of fermentation inhibitors while preserving fermentable sugars, the nanoadsorbent-detoxification mechanism and the adsorption–desorption kinetics of Fe_3O_4 nanoparticles (NPs) for the simultaneous removal of fermentation inhibitors is currently limited. Addressing these knowledge gaps will advance understanding of nanobased detoxification mechanisms and inform the development of more efficient and scalable detoxification strategies, ultimately enhancing the fermentability of lignocellulosic hydrolysates (Malinowska et al., 2020; Xiao et al., 2021; Alzoubi et al., 2023). Moreover, the effects and interactions of key operational parameters on detoxification efficacy are insufficiently explored.

Furthermore, there is a dearth of knowledge on the individual and interactive effects of co-inoculation time, co-inoculation ratio, and solid loading on achieving optimal bioethanol concentration and conversion using waste potato peel as substrate. Identifying the most efficient process strategy in conjunction with co-fermentation (using separate hydrolysis and fermentation (SHF) or simultaneous saccharification and fermentation (SSF)) is essential for improving overall process performance.

The potential of nanoparticle-assisted detoxification and sequential co-fermentation for maximum process performance using pretreated PPW remains largely undeveloped. Likewise, there are significant knowledge gaps in implementing such an integrated process at a pilot scale using optimized detoxified potato peel waste (PPW) hydrolysates. Therefore, modelling and optimization of co-fermentation processes using nanoparticle-assisted detoxified PPW hydrolysate could potentially enhance substrate conversion efficiency and maximize bioethanol yield. The current study addresses these knowledge gaps by presenting a novel integrated approach that couples the dual optimization of Fe_3O_4 nanoparticle-assisted detoxification of pretreated potato peel waste (PPW) hydrolysate with co-fermentation by *S. cerevisiae* and *P. stipitis* to enhance bioethanol production. This integrated strategy provides insights into process optimization and offers a scalable framework for sustainable, industrial-scale bioethanol production from lignocellulosic feedstocks.

1.3 Aim and objectives

This study aimed to improve bioethanol production from potato peel waste by optimising a simultaneous saccharification and co-fermentation (SSCF) process using *S. cerevisiae* and *P. stipitis*, integrated with Fe_3O_4 nanoparticle-assisted detoxification of inhibitors in the pretreated hydrolysate.

To achieve this aim, the following specific objectives were undertaken:

i. To model and optimize Fe_3O_4 nanoparticle-assisted detoxification of pretreated potato peel hydrolysate, and to investigate adsorption–desorption kinetics to elucidate the underlying detoxification mechanisms.
ii. To perform a comparative assessment of separate hydrolysis and fermentation (SHF) and simultaneous saccharification and fermentation (SSF) strategies using optimized detoxified hydrolysate (ODH), evaluating ethanol yield, sugar conversion efficiency, and fermentation dynamics.
iii. To model and optimize the SSCF process using *S. cerevisiae* and *P. stipitis* with ODH to maximize sugar utilization and bioethanol yield.
iv. To conduct kinetic studies of the SSCF process, modelling microbial growth, ethanol production, and substrate consumption using ODH as the substrate
v. To perform a preliminary scale-up study of the optimized SSCF process, assessing its feasibility, efficiency, and potential for industrial application.

1.4. Outline of thesis structure

This thesis comprises eight chapters, presented in the research paper format as prescribed by the College of Agriculture, Engineering and Science (CAES) thesis template at the University of KwaZulu-Natal, South Africa. Each experimental chapter is self-contained, featuring an abstract, introduction, materials and methods, results and discussion, conclusion, and references. The central theme across all chapters is the enhancement of bioethanol production through the development of an optimized co-fermentation process integrated with nanoparticle-assisted detoxification of process inhibitors.

Chapter 1 provides the background and general outline of this research and states the aims and objectives.

Chapter 2 presents an extensive review of literature on the lignocellulosic biomass potential, pretreatment processes, inhibitor formation, and nanoparticle involvement in inhibitor detoxification for improved bioethanol production through co-fermentation.

Chapter 3 discusses substrate preparation, with a focus on the modelling and optimisation of nanoparticle-assisted detoxification of inhibitors from PPW hydrolysate to improve bioethanol productivity. Furthermore, nanoparticle recyclability and sensitivity analysis of detoxification parameters were conducted.

Chapter 4 examines the characteristic profile and adsorption mechanism of Fe_3O_4 nanoparticles (NPs), before and after detoxification using scanning electron microscopy (SEM), transmission electron microscopy (TEM), Fourier-transform infrared spectroscopy (FTIR), UV spectrophotometry, X-ray diffraction (XRD), point of zero charge (PZC), and the Brunauer–Emmett–Teller (BET) method of surface characterization. Subsequently, batch adsorption kinetics, isotherms, and thermodynamic study of Fe_3O_4-NP for the detoxification of fermentation process inhibitors from pretreated potato peels waste (PPW) hydrolysate.

Chapter 5 explores the comparative assessment of bioethanol production by SSF and SHF strategies. Additionally, kinetic modelling and validation were performed to characterize microbial cell growth, bioethanol production, and substrate utilization dynamics.

Chapter 6 models and optimizes simultaneous saccharification and co-fermentation (SSCF) by *S. cerevisiae* and *P. stipitis* for the enhancement of ethanol production using detoxified hydrolysate, employing response surface methodology. In addition, kinetic modelling of the bioethanol co-fermentation process was undertaken to determine the process dynamics (including cell growth, bioethanol formation, and substrate utilization) with the aim of determining the specific growth rate, affinity to the fermentation substrate, and maximum bioethanol production rate.

Chapter 7 examines the scale-up process design of SSCF using *S. cerevisiae* and *P. stipitis* (as developed in Chapter 6), scaling from 1 L to 10 L for bioethanol production using detoxified hydrolysate. In addition, the kinetics of the bioethanol fermentation process were investigated, and the fermentation effluent was analyzed for its potential valorisation.

Chapter 8 integrates the research findings from the experimental chapters into a cohesive scientific argument that addresses the aim, objectives, and problem statement of the study

Chapter 9 presents the major conclusions of this study and offers recommendations for future research.

References

Alzoubi, F., Noqta, O. A., AlZoubi, T., AlJabaly, H., Alkhateeb, H., Alqadi, M., Makhadmeh, G., 2023. Exploring the impact of pH on the properties of citric acid-coated iron oxide nanoparticles as high-performance T2 contrast agent for MRI applications. Results in Engineering, 18, 101206. https://doi.org/10.1016/j.rineng.2023.101206.

Ashokkumar, V., Flora, G., Venkatkarthick, R., SenthilKannan, K., Kuppam, C., Stephy, G.M., Kamyab, H., Chen, W.H., Thomas, J., Ngamcharussrivichai, C., 2022. Advanced technologies on the sustainable approaches for conversion of organic waste to valuable bioproducts: Emerging circular bioeconomy perspective. Fuel, 324, 124313. https://doi.org/10.1016/j.fuel.2022.124313.

Awogbemi, O., Kallon, D. V. V., Owoputi, A. O., 2022. Biofuel generation from potato peel waste: current state and prospects. Recycling, 7(2), 23. https://doi.org/10.3390/recycling7020023.

Barampouti, E. M., Christofi, A., Malamis, D., Mai, S., 2023. A sustainable approach to valorize potato peel waste towards biofuel production. Biomass Conversion and Biorefinery, 13(9), 8197-8208. https://doi.org/10.1007/s13399-021-01811-4.

Baur, R. T., Tuedic, S., Promploy, J., Kirasamutranon, K., 2025. Optimizing biomass pellet quality from sugarcane leaves and bamboo for sustainable biofuel production. Advances in Bamboo Science, 11, 100153. https://doi.org/10.1016/j.bamboo.2025.100153.

Bertels, L. K., Fernández Murillo, L., Heinisch, J. J., 2021. The pentose phosphate pathway in yeasts-more than a poor cousin of glycolysis. Biomolecules, 11(5), 725. https://doi.org/10.3390/biom11050725.

Chakraborty, P., Kumar, R., Chakrabortty, S., Saha, S., Chattaraj, S., Roy, S., Banerjee, A., Tripathy, S. K., Ghosh, A. K., Jeon, B. H., 2024. Technological advancements in the pretreatment of lignocellulosic biomass for effective valorization: A review of challenges and prospects. J. Ind. Eng. Chem. 137, 29-60. https://doi.org/10.1016/j.jiec.2024.03.025.

Chavan, S., Shete, A., Mirza, Y., Dharne, M.S., 2023. Investigation of Cold-Active and Mesophilic Cellulases: Opportunities Awaited. Biomass Conv. Bioref., 13, 8829-8852. https://doi.org/10.1007/s13399-021-02047-y.

Chen, Y., Zhang, Y., Kou, Q., Liu, Y., Han, D., Wang, D., Sun, Y., Zhang, Y., Wang, Y., Lu, Z., Chen, L., 2018. Enhanced catalytic reduction of 4-nitrophenol driven by Fe_3O_4-Au magnetic nanocomposite interface engineering: from facile preparation to recyclable application. Nanomaterials, 8(5), 353. https://doi.org/10.3390/nano8050353.

Chohan, N. A., Aruwajoye, G. S., Sewsynker-Sukai, Y., Kana, E. G., 2020. Valorisation of potato peel wastes for bioethanol production using simultaneous saccharification and fermentation: Process optimization and kinetic assessment. Renewable Energy, 146, 1031-1040. https://doi.org/10.1016/j.renene.2019.07.042.

Dalei, N. N., Gupta, A. 2024. Adoption of renewable energy to phase down fossil fuel energy consumption and mitigate territorial emissions: Evidence from BRICS group countries using panel FGLS and panel GEE models. Discover Sustainability, 5, 52. https://doi.org/10.1007/s43621-024-00237-y.

Dandasena, T. K., Shahi, S., 2023. A Renewable Biofuel-Bioethanol: A Review. Journal of Advanced Zoology, 44(S3), 1698-1706. https://doi.org/10.17762/jaz.v44iS3.2388.

Derman, E., Abdulla, R., Marbawi, H., Sabullah, M. K., Gansau, J. A., Ravindra, P., 2022. Simultaneous saccharification and fermentation of empty fruit bunches of palm for bioethanol production using a microbial consortium of *S. cerevisiae* and *T. harzianum*. Fermentation, 8(7), 295. https://doi.org/10.3390/fermentation8070295.

El-Araby, R. 2024. Biofuel production: exploring renewable energy solutions for a greener future. Biotechnol Biofuels 17, 129. https://doi.org/10.1186/s13068-024-02571-9.

González-Gloria, K. D., Tomás-Pejó, E., Amaya-Delgado, L., Rodríguez-Jasso, R. M., Loredo-Treviño, A., Singh, A., Hans, M., Martín, C., Kumar, S., Ruiz, H. A., 2024. Biochemical and biorefinery platform for second-generation bioethanol: fermentative strategies and microorganisms. Fermentation, 10(7), 361. https://doi.org/10.3390/fermentation10070361.

Holechek, J. L., Geli, H. M. E., Sawalhah, M. N., Valdez, R. 2022. A global assessment: Can renewable energy replace fossil fuels by 2050? Sustainability, 14(8), 4792. https://doi.org/10.3390/su14084792.

IEA Bioenergy. 2024. Country Report 2024: South Africa. Retrieved from (https://www.ieabioenergy.com/wpcontent/uploads/2024/12/CountryReport2024_SouthAfrica_final.pdf).

Lei, C., Guo, X., Zhang, M., Zhou, X., Ding, N., Ren, J., Liu, M., Jia, C., Wang, Y., Zhao, J., Dong, Z., 2024. Regulating the metabolic flux of pyruvate dehydrogenase bypass to enhance lipid production in *Saccharomyces cerevisiae*. Communications Biology, 7(1), 1399. https://doi.org/10.1038/s42003-024-07103-7.

Malinowska, I., Ryżyńska, Z., Mrotek, E., Klimczuk, T., Zielińska-Jurek, A., 2020. Synthesis of $CoFe_2O_4$ nanoparticles: the effect of ionic strength, concentration, and precursor type on morphology and magnetic properties. Journal of Nanomaterials, 2020(1), 9046219. https://doi.org/10.1155/2020/9046219.

Mazzoli, R., 2021. Current progress in production of building-block organic acids by consolidated bioprocessing of lignocellulose. Fermentation, 7(4), 248. https://doi.org/10.3390/fermentation7040248.

Meena, P. L., Saini, J. K., Surela, A. K., Poswal, K., Chhachhia, L. K., 2024. Fabrication of polyaniline-coated porous and fibrous nanocomposite with granular morphology using tea waste carbon for effective removal of rhodamine B dye from water samples. Biomass Conversion and Biorefinery, 14(2), 1711-1730. https://doi.org/10.1007/s13399-021-02267-2.

Miah, R., Siddiqa, A., Chakraborty, U., Tuli, J. F., Barman, N. K., Uddin, A., Aziz, T., Sharif, N., Dey, S. K., Yamada, M., Talukder, A. A., 2022. Development of high temperature simultaneous saccharification and fermentation by thermosensitive *Saccharomyces cerevisiae* and *Bacillus amyloliquefaciens*. Scientific Reports, 12(1), 3630. https://doi.org/10.1038/s41598-022-07589-3.

Moreno, A. D., Tomás-Pejó, E., Ibarra, D., Ballesteros, M., Olsson, L., 2013. Fed-batch SSCF using steam-exploded wheat straw at high dry matter consistencies and a xylose-fermenting *Saccharomyces cerevisiae* strain: effect of laccase supplementation. Biotechnology for biofuels, 6, 1-10. https://doi.org/10.1186/1754-6834-6-160.

Mvelase, L., Ferrer, S., 2024. The economy-wide impact of bioethanol production in South Africa. Energy Conversion and Management: X, 24, 100729. https://doi.org/10.1016/j.ecmx.2024.100729.

Naseeruddin, S., Desai, S., Venkateswar Rao, L., 2021. Co-culture of *Saccharomyces cerevisiae* (VS3) and *Pichia stipitis* (NCIM 3498) enhances bioethanol yield from concentrated Prosopis juliflora hydrolysate. 3 Biotech 11, 21. https://doi.org/10.1007/s13205-020-02595-6.

Policastro, G., Giugliano, M., Luongo, V., Napolitano, R., Fabbricino, M., 2021. Carbon catabolite repression occurrence in photo fermentation of ethanol-rich substrates. Journal of Environmental Management, 297, 113371. https://doi.org/10.1016/j.jenvman.2021.113371.

Renewable Fuels Association, 2022. Industry statistics, Renewable Fuels Association, Washington, DC., USA. ⟨http://ethanolrfa.org/resources/industry/statistics/#1454099788442-e48b2782-ea53⟩. Accessed 12th February 2024.

Rorke, D. C. S., Gueguim Kana, E. B., 2017. Kinetics of bioethanol production from waste sorghum leaves using *Saccharomyces cerevisiae* BY4743, Fermentation, 3, 19. http://dx.doi.org/10.3390/fermentation3020019.

Sanusi, I. A., Suinyuy, T. N., Lateef, A., Kana, G.E.B., 2020. Effect of nickel oxide nanoparticles on bioethanol production: Process optimization, kinetic and metabolic studies. Process Biochem, 92:386-400. https://doi.org/10.1016/j.procbio.2020.01.029.

Sanusi, A. I., Suinyuy, T. N., Kana, G. E. B., 2021. Impact of nanoparticle inclusion on bioethanol production process kinetics and inhibitor profile. Biotechnology Reports, 29, 1-12. https://doi.org/10.1016/j.btre.2021.e00585.

Sarawan, C., Suinyuy, T. N., Sewsynker-Sukai, Y., Gueguim Kana, E.B., 2019. Optimized activated charcoal detoxification of acid-pretreated lignocellulosic substrate and assessment for bioethanol production, Bioresource Technology, 286, 1-10. https://doi.org/10.1016/j.biortech.2019.121403.

Sharma, D., Saini, A., Sharma, D., Saini, A., 2020. Saccharification fermentation and process integration. Lignocellulosic ethanol production from a biorefinery perspective: sustainable valorization of waste, pp.111-158. https://doi.org/10.1007/978-981-15-4573-3_4.

Sharma, S., Jha, P. K., Panwar, A., 2021. Production of bioethanol from wheat straw via optimization of co-culture conditions of *Bacillus licheniformis* and *Saccharomyces cerevisiae*. Discover Energy, 1, 1-8. https://doi.org/10.1007/s43937-021-00004-4.

Singh, M., Sharma, V., Gupta, R., 2024. Biovalorization of potato peel waste: An overview. Roots, Tubers, and Bulb Crop Wastes: Management by Biorefinery Approaches, 19-41. https://doi.org/10.1007/978-981-99-8266-0_2.

Singh, N., Singhania, R. R., Nigam, P. S., Dong, C. D. Patel, A. K., Puri, M. 2022. Global Status of Lignocellulosic Biorefinery: Challenges and Perspectives. Bioresour. Technol., 344, 126415. https://doi.org/10.1016/j.biortech.2021.126415.

Sjulander, N., Kikas, T., 2020. Origin, Impact and Control of Lignocellulosic Inhibitors in Bioethanol Production: A Review. Energies. 13(18): 4751. https://doi.org/10.3390/en13184751.

Thanigaivel, S., Rajendran, S., Gnanasekaran, L., Chew, K. W., Tran, D. T., Tran, H. D., Nghia, N.K. and Show, P.L., 2023. Nanotechnology for improved production of algal biofuels: a review. Environmental Chemistry Letters, 21(2), 821-837. https://doi.org/10.1007/s10311-022-01529-3.

Vescovo, D., Manetti, C., Ruggieri, R., Spizzirri, U. G., Aiello, F., Martuscelli, M., Restuccia, D., 2025. The valorization of potato peels as a functional ingredient in the food industry: A comprehensive review. Foods, 14(8), 1333. https://doi.org/10.3390/foods14081333.

Wang, Y., Zhang, Y., Cui, Q., Feng, Y., Xuan, J., 2024. Composition of Lignocellulose Hydrolysate in Different Biorefinery Strategies: Nutrients and Inhibitors. Molecules, 29(10), 2275. https://doi.org/10.3390/molecules29102275.

World Bioenergy Association. 2024. Global Bioenergy Report 2024. (https://www.worldbioenergy.org/uploads/241023%20GBS%20Report%20Short%20Version.pdf). Accessed May 11, 2025.

Woźniak, A., Kuligowski, K., Świerczek, L., Cenian, A., 2025. Review of lignocellulosic biomass pretreatment using physical, thermal and chemical methods for higher yields in bioethanol production. Sustainability, 17(1), 287. https://doi.org/10.3390/su17010287.

Xiao, W., Su, Z., Zhao, Y. and Wang, C., 2021. Microwave-assisted polyol process for time-saving synthesis of superparamagnetic nanoparticles and application in artificial mimic enzyme. Nano Express, 2(2), 020001. https://doi.org/10.1088/2632-959X/abf2ce.

CHAPTER 2

Literature Review

Detoxification and fermentation strategies in lignocellulosic bioethanol production: a comprehensive review

Some part of this chapter has been published in Biomass and Bioenergy, 206 (2026) 108628 with the title: Progress in the development of detoxification strategies and the current use of nanoparticle-based detoxification in pretreated lignocellulosic hydrolysate for bioethanol production in a biorefinery scenario. (https://doi.org/10.1016/j.biombioe.2025.108628).

Abstract

The production of bioethanol from lignocellulosic biomass (LB) is a promising solution to reduce the dependency on fossil fuels consumption and mitigate the associated environmental challenges. However, the presence of inhibitory compounds in pretreated lignocellulosic hydrolysates poses significant challenges to efficient microbial fermentation, limiting industrial potential of bioethanol production. Hence, this review provides a comprehensive analysis on the detoxification of inhibitory compounds in pretreated lignocellulosic hydrolysate. Likewise, the emerging application of nanoparticle in pretreated lignocellulosic hydrolysate detoxification was discussed. By synthesising existing literature and identifying research gaps, this review also provides insights on potential future innovations in lignocellulosic biorefinery strategies to enhance the feasibility and sustainability of large-scale bioethanol production. Furthermore, a bibliometric analysis highlighting key research trends, influential publications, emerging collaborations and future potential in this field were provided.

Keywords: Bioethanol, fermentation, inhibitors, nanoparticle, pretreated hydrolysates

Corresponding author: Tel.: +27-616181662, E-mail address: Sanusi_isaac@yahoo.com

2.1. Introduction

The global energy landscape is increasingly shaped by rising energy demand, environmental degradation associated with continued dependence on fossil fuels, and persistent geopolitical instabilities. With continued population growth and expanding industrialization, energy consumption is intensifying, placing immense pressure on finite fossil fuel reserves. The combustion of fossil fuels for energy generation releases substantial quantities of greenhouse gases (GHGs), primarily carbon dioxide (CO_2), which are widely recognized as primary drivers of climate change and global warming (Roy et al., 2021). This critical environmental challenge, coupled with the inherent unsustainability of a fossil-dependent energy system, necessitates an urgent and large-scale transition towards renewable and sustainable energy alternatives. Lignocellulosic biomass (LB), derived from plant residues and agricultural waste, represents one of the most abundant clean energy sources and raw materials for the sustainable generation of renewable energy and a wide range of industrially significant chemicals (Baral et al., 2019), with a potential to meet nearly 40% of the world's energy demands (Alio et al., 2020).

Among the diverse renewable energy options, bioethanol has emerged as a particularly promising and strategically important liquid fuel. Bioethanol represents a viable alternative to conventional gasoline due to its compatibility with existing fuel infrastructure, enabling integration without requiring major modifications to vehicles or supply chains. Bioethanol derived from biomass is considered carbon-neutral in its lifecycle, as the CO_2 emitted during combustion is theoretically offset by the uptake during photosynthesis, thereby contributing to net CO_2 reduction and supporting climate mitigation goals (Onyeaka et al., 2025). Global demand for renewable liquid bioethanol has steadily increased across major producing and consuming regions (the United States, Brazil, the European Union, India, China, Canada, and Thailand), underscoring its growing integration into national energy strategies. Consistent with this trend, global annual biomass consumption is projected to rise significantly, from 72 gigatonnes (Gt) in 2020 to an anticipated 100 Gt by 2030, confirming the role of biomass in future energy systems (Ribeiro et al., 2023). This growing reliance on biomass as a renewable resource underscores the critical need for efficient and sustainable conversion technologies that prioritise the valorisation of waste streams.

In recent years, significant advances have been made in converting Lignocellulosic biomass (LB) into bioethanol and other valuable bioproducts. Lignocellulosic biomass is primarily composed of polymeric materials exhibiting both polar and non-polar characteristics, including

cellulose, hemicellulose, and lignin (Kommoji et al., 2021). These structural components contribute to the inherent recalcitrance of LB, posing challenges for chemical and biological deconstruction. To overcome this, process developments have focused on pretreatment methods aimed at disrupting the complex cell wall matrix, reducing cellulose crystallinity, and achieving effective delignification. Pretreatment is thus a critical step to enhance the accessibility of enzymes and microbes to fermentable sugars during downstream processing. Pretreatment techniques used for LB can be generally categorized into physical, chemical, biological, or combined approaches (Vijayalakshmi et al., 2021). The pretreatment processes generate fermentation-inhibitory compounds, such as furans (hydroxymethylfurfural and furfural), phenolic compounds, and organic acids, which remain a significant bottleneck in LB bioprocessing (Kumar et al., 2020). These inhibitors have been implicated in interfering with microbial growth and metabolic activities during fermentation, reducing bioethanol yield and process efficiency. Consequently, efficient detoxification strategies to remove the inhibitors from lignocellulosic hydrolysates are crucial in developing a viable biorefinery. Several conventional detoxification methods have demonstrated limited efficiency, high cost, or environmental drawbacks. Recently, nanoparticle-based technologies have emerged as effective alternatives for removing fermentation-inhibitory compounds due to their distinctive physicochemical properties, including catalytic activity, a high surface area-to-volume ratio, and adsorption functionality. Progress in the synthesis and functionalisation of nanoparticles has enabled the selective removal of specific inhibitors, paving the way for optimised fermentation processes and enhanced bioethanol production (Sanusi et al., 2021). Integrating nanoparticle-based detoxification methods into biorefineries aligns with the broader concept of a circular economy, where waste materials are converted into high-value products (Rajak et al., 2021). Additionally, the interplay between nanoparticle properties, LB hydrolysate composition, and microbial fermentation dynamics requires deeper exploration to optimise system performance, especially in biofuel production such as bioethanol. Following pretreatment and hydrolysate detoxification, fermentation plays a vital role in converting released sugars into bioethanol. Traditional single-strain fermentations are often limited in their ability to utilize the full spectrum of lignocellulosic sugars, particularly pentoses from hemicellulose. Co-fermentation strategies, employing mixed or engineered microorganisms, enable the simultaneous utilization of hexose and pentose sugars, thereby enhancing sugar conversion, ethanol yield, and inhibitor tolerance in pretreated biomass.

This review critically examines the detoxification and fermentation strategies integral to LB bioethanol production, with emphasis on the valorization of potato peel waste (PPW). Also, the review synthesizes current knowledge across several key stages of the bioethanol production process: detailed characterization of PPW as a lignocellulosic feedstock, various pretreatment technologies designed to enhance sugar accessibility, the formation and detrimental impact of inhibitory compounds generated during biomass deconstruction, and a thorough analysis of diverse detoxification strategies, including traditional methods and emerging nanoparticle-assisted techniques. Furthermore, the review explores microbial fermentation processes, with a focus on *S. cerevisiae* and *P. stipitis*, their sugar preferences, stress tolerance mechanisms, and different fermentation strategies, including the advanced co-fermentation approaches aimed at maximizing ethanol yields from mixed sugar streams. Additionally, the review explores process and kinetic modelling, optimization, and key scale-up considerations, including bioreactor design and mass-heat transfer challenges. It also highlights research gaps and prospects for enhancing PPW-based bioethanol production, improving fermentability and yields, and advancing integrated, sustainable biorefineries toward commercial viability.

2.2. Lignocellulosic biomass

Lignocellulosic biomass (LB) serves as a renewable feedstock for biorefinery bioprocesses due to its relative abundance, availability, and compositional heterogeneity (Ghodke et al., 2024). The annual global production of lignocellulosic biomass approximates 182 billion tons (Zytner et al., 2023). Current utilization, however, accounts for a mere 8.2 billion tons, with 7 billion from forestry, agriculture, and grasses, and 1.2 billion originating from agricultural residues (Ashokkumar et al., 2022). This disparity highlights a significant underutilization of available resources. Lignocellulosic biomass (second-generation biomass) provides a sustainable alternative to first-generation feedstocks, thereby mitigating the competition for arable land required for food crop cultivation. Lignocellulosic biomass is categorised into different groups based on its source, as shown in Fig. 2.1. These include (1) dedicated whole plants, (2) agricultural residues (such as corn stover; sugarcane leaves and bagasse; straws of rice, wheat, barley; cassava and potato peels), (3) agro-wastes (4) forest biomass (5) forest wastes (6) industrial wastes, and (7) municipal solid wastes. Lignocellulosic biomass, in its typical form, exhibits a complex matrix of organic constituents, including carbohydrate polymers (starch, cellulose, and hemicellulose), lignin, and a spectrum of other biomolecules such as fatty acids, lipids, and proteins. Structurally, lignocellulosic biomass is composed mainly of polymers,

including cellulose (20-60%), hemicellulose (15-40%), and lignin (5-30%), along with components such as extractives and ash. The aligned bundles of crystalline and amorphous cellulose microfibrils are embedded within a disordered matrix of hemicellulose and lignin, forming a complex, rigid structural network (Kommoji et al., 2021).

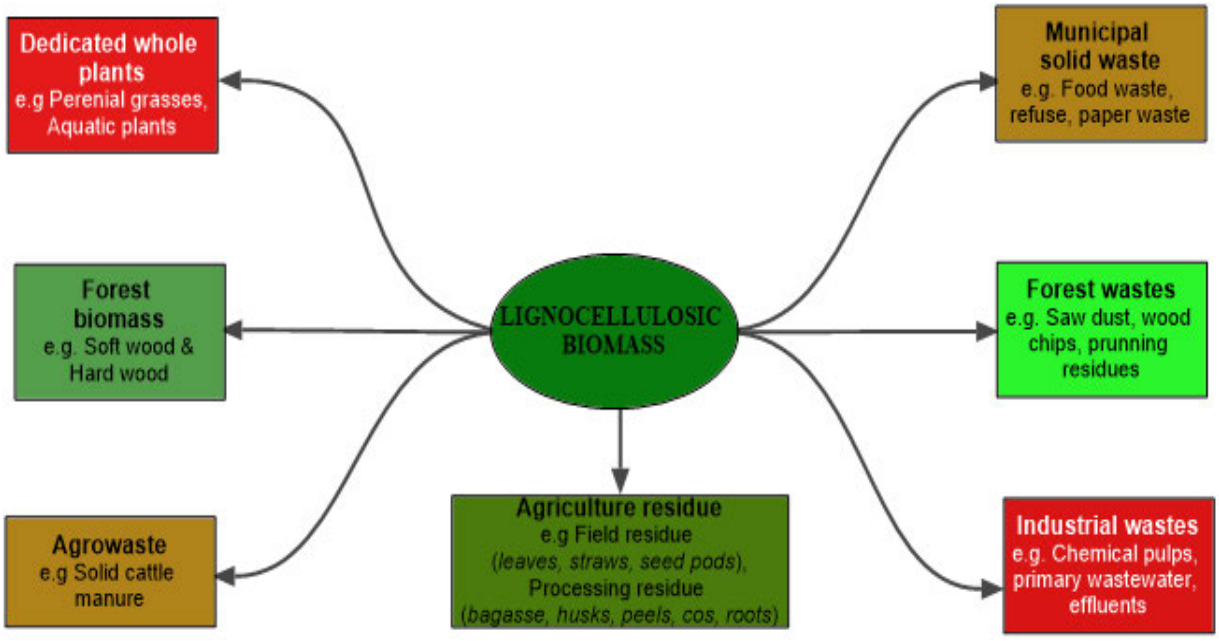

Figure 2.1. The main groups of lignocellulosic feedstocks.

The recalcitrant nature of lignocellulosic biomass to degradation is predicated upon cellulose's crystallinity, lignin's hydrophobicity, and cellulose encapsulation by the lignin-hemicellulose matrix (Singhvi and Gokhale, 2019).

2.2.1. Potato peel waste (PPW) as a suitable LB feedstock for biofuels production

Potato (*Solanum tuberosum L.*) is a major global crop with annual production of around 370–383 million tonnes, cultivated across most soil types, except those with high salinity or alkalinity (Subedi et al., 2019; FAO, 2024). China leads in production, followed by India, Russia, Ukraine, and the USA, with China and India accounting for approximately one-third of global output (FAO, 2024). Africa produced approximately 30 million metric tons of potatoes in 2023 (Fig. 2.2A), with South Africa producing just over 2.5 million tonnes in 2022 (Fig. 2.2A), approximately 8.5% of the continent's total, ranking third after Egypt and Algeria, with 6.9 million and 4.6 million metric tons of potato output, respectively.

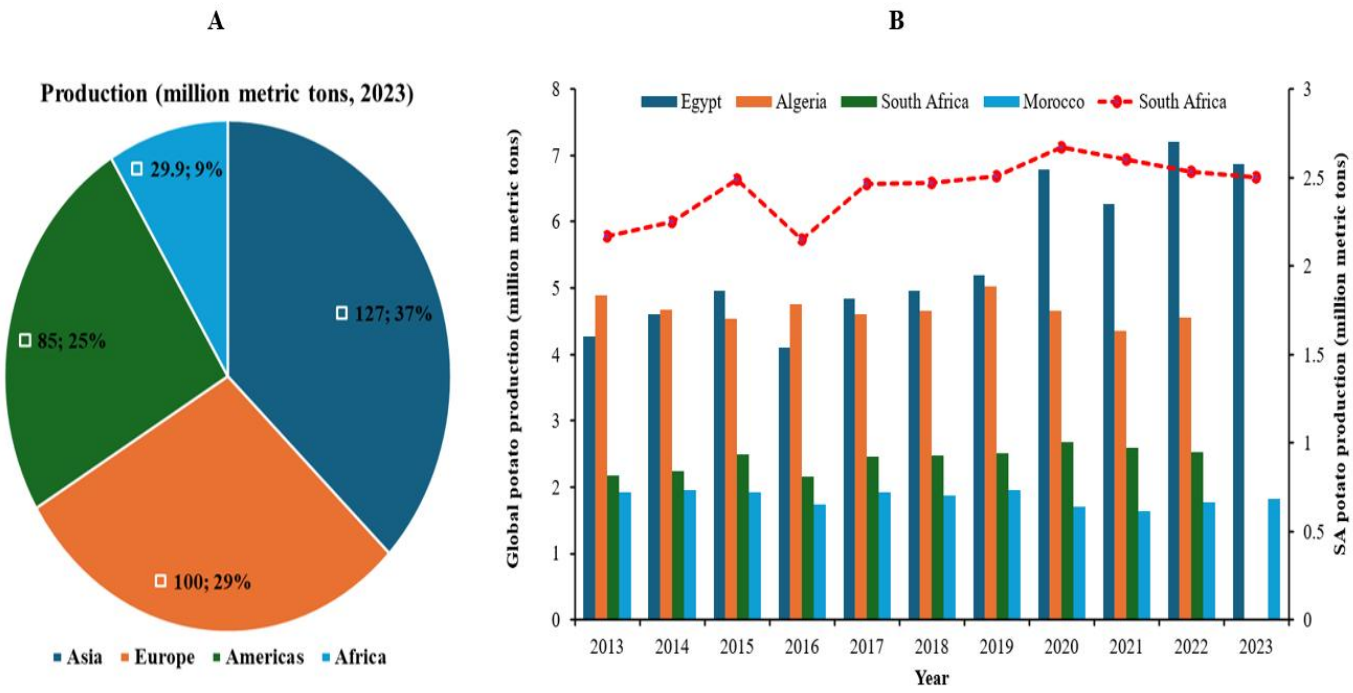

Figure 2.2. Continental potato production in 2023 (A) and potato production by the top 4 countries in Africa between 2013 and 2022 (B) (FAO, 2024).

Industrial potato processing for products such as chips, fries, and mashed potatoes generates substantial waste, including peels, pulp, and starch, which constitute valuable agro-industrial byproducts (Mushtaq et al., 2024). Potato peel waste (PPW) alone represents 15- 40% of tuber weight and is often discarded or used in animal feed, leading to environmental issues such as odour, leachate, and methane emissions (Soni et al., 2023). Valorizing PPW for bioethanol or other bioproducts mitigates disposal challenges and enhances economic sustainability (Chohan et al., 2020). PPW, a lignocellulosic feedstock, is generally rich in fermentable carbohydrates, including cellulose, hemicellulose, starch, and pectin, with variations in composition depending on cultivation regions. Other constituents of PPW include a range of nutritionally essential components such as dietary fibres, lipids, fatty acids, polyphenols, and phenolic acids (Pathak et al., 2017). According to Liang and McDonald (2014), potato peels typically contains starch (25%), non-starch polysaccharide (30%), protein (18%), acid-soluble and acid-insoluble lignin (20%), lipids (1%), and ash (6%), outlined in Table 2. 1. The lipid fraction includes long-chain fatty acids, alcohols, triglycerides, sterols, sterol esters, and phenolics. Lignin units are also integrated into the potato cell wall structure (Liang and McDonald, 2014).

Although potato peel (PP) contains a high starch content (52% dry weight), its fermentable reducing sugar concentration is low (0.6% dry weight), rendering direct fermentation unfeasible. Therefore, an initial hydrolysis step, either enzymatic or acidic, is required to depolymerize the carbohydrate matrix into fermentable sugars (Arapoglou et al., 2010). Moreso, elemental analysis of PP (dry weight) indicates carbon (43.78 ± 0.15%), hydrogen (5.96 ± 0.12%), nitrogen (4.06 ± 0.01%), and oxygen (46.21 ± 0.28%), corresponding to a C/N ratio of 10.7 and a pH of 6.5 (Pathak et al., 2017), with a calorific value of 17.37 ± 0.38 MJ/kg (Liang and McDonald, 2014). The relatively high carbohydrate content of PPW, primarily in the form of starch and other polysaccharides, underpins its potential as a substrate for enzymatic hydrolysis, producing fermentable sugars.

This potential has attracted significant attention in recent years, with several studies demonstrating the feasibility of PPW valorization for bioethanol and other bioproducts, as outlined in Table 2.2. For instance, Sanusi et al. (2019) studied the impact of nanoparticle (Fe_3O_4 NPs) inclusion on ethanol production from potato peel hydrolysate using *S. cerevisiae* BY4743, from which Fe_3O_4 NPs enhanced glucose utilization of 99.95%, and 51% fermentation efficiency, yielding 0.26 g/g ethanol equivalent to a maximum ethanol concentration of 5.24 g/L at the production rate of 0.72 g/L/h. Similarly, Zondi et al. (2025) reported a bioethanol concentration of 21.37 g/L during SSF of potato peel waste pretreated with black liquor (alkaline pretreatment), where the inclusion of CuO NPs enhanced fermentation performance by *Saccharomyces cerevisiae* BY4743.

Table 2.1. Composition of raw potato peel waste.

	Arapoglou et al., 2010	Liang et al., 2014	Hijosa-Valsero et al, 2018	Hossain et al., 2018	Javed et al., 2019
Parameter	Dry Weight (%)	Dry Weight (%)	Dry Weight (%)	Dry Weight (%)	Dry Weight (g per 100 g)
Moisture	85.06	nd	5.26	77.3	83.3–85.1
Protein (N_{tot}6.25)	8.0	17.1 ± 0.3	10.73	13.13	1.2–3.0
Lipids	nd	1.2 ± 0.0	nd	nd	0.1–0.4
Carbohydrates (total)	68.7	63.2 ± 4.2	43.2	70.3	8.7–12.4
Starch	52.14	34.3 ± 2.7	23.01	nd	7.8–12.4
Dietary fiber (total)	nd	nd	nd	nd	2.5
Reducing sugars	1.0	nd	nd	nd	nd
Ash	6.34	9.6 ± 0.1	7.45	5.9	0.9–1.6
Phenolic compounds	nd	nd	2.5 mg/g	nd	1.02–2.92
Flavonoids (total)	nd	nd	nd	nd	0.51–0.96

nd = not determined

(Adapted from Awogbemi et al., 2022).

Table 2.2. Bioproducts from potato peel waste under different process conditions.

Microorganism	Substrate Loading	Pretreatment strategy	Fermentation Method	Process Conditions	Bioproducts	Reference
Saccharomyces cerevisiae	2% w/w	NaOH (1% w/v) pretreatment	SHF	Enzymatic hydrolysis (NS22109 and NS22177), 30°C, 72h	71.37 g/L bioethanol	Barampouti et al., 2023
Saccharomyces cerevisiae	22.81% w/v	3% H_2SO_4 + steam	SHF	Multi-enzyme hydrolysis, supplement (0.1% w/v peptone, $(NH_4)(H_2PO_4)$ and ZnSO4 at 30°C, 72h	54.75 g/L bioethanol	Soni et al., 2023
Saccharomyces cerevisiae	20–24% w/v	3% H_2SO_4 + steam pretreatment	SHF	3% H_2SO_4 + steam pretreatment, multi-enzyme hydrolysis, 30°C, 72h	43.2 g/L bioethanol	Soni et al., 2023
Saccharomyces cerevisiae		Organosolv (75% ethanol plus 1% acid, 180 °C);	SHF	Enzymatic hydrolysis (Cellulase [Cellic® CTec2]); 32 °C, 48 h	18.1 g/L bioethanol	Soltaninejad et al., 2022
Saccharomyces cerevisiae	5% w/v	NaOH (1% w/v, 6 h at 50 °C) pretreatment	SSF	Fermentation (40 µL Spirizyme Excel XHS·g^{-1} starch, 175 µLNS87014·g^{-1} cellulose; 2% w/w *S. cerevisiae)*	9 g/L bioethanol	Felekis et al., 2023
Wickerhamomyces anomalus	5% w/v	0.1% w/v H_2SO_4 at 121°C, 1h, plus 0.1% w/v NaOH 80°C for 24h	SSF	commercial cellulase blend (CEL) (Cellic CTec2-CEL, 223 FPU/mL) + alpha-amylase from *Bacillus* sp. Gb67 (B.A.), 11 FAU/mL; pH 7.0, 30°C, 24h	0.49 g/g ethanol yield	Atitallah et al., 2019
Wickerhamomyces anomalus	5% w/v	0.1% w/v H2SO4 at 121°C, 1h, plus 0.1% w/v NaOH 80°C for 24h	SHF	Commercial cellulase blend (CEL) (Cellic CTec2-CEL, 223 FPU/mL) + alpha-amylase from *Bacillus* sp. Gb67 (B.A.), 11 FAU/mL; pH 4.8, 50°C, 24h	0.47 g/g ethanol yield	Atitallah et al., 2019
Rhizopus oryzae	8% w/v	Nil	Batch fermentation	Particle size 1–2 mm, 35°C, 150rpm, 96- 192h	18.83 (ethanol), 3.14 (lactic acid)	Ozer Uyar and Uyar (2023).
Bacillus subtilis QY4	5% solids	Acidic and acid-assisted autoclave treatment +1M NaOH @ 70°C neutralization	SSF	Acid hydrolysis, 2% inoculum fermentation (37 °C at 120 rpm for 72 h.	0.601 IU/mL/min Amylase, 1.269 IU/mL/min cellulase	Mushtaq et al., 2024
Microbial inoculum (Sludge)	10% w/v	Acid hydrolysis (0.9% [w/w] H_2SO_4 solution for 1 h)	Anaerobic co-digestion	60 PPW: 40, 10 g/L volatile solids (VS) added	Biogas yield (485 mL/g), Methane yield (283.4 mL/g)	Achinas et al., 2019
Saccharomyces cerevisiae BY4743.	12.25% w/v	3.68% (v/v) HCl, 69.62°C for 2.57 h; 121 °C, 5 min	SSF	15 Units/g Amyloglucosidase, 10% (v/v) inoculum, pH 5.78, 40°C, 24 h at 120 rpm.	22.54 g/L bioethanol	Chohan et al., 2020
Saccharomyces cerevisiae BY4743.	5 %w/v	3.68% (v/v) HCl, 69.62°C for 2.57 h; 121 °C, 5 min	SSF	0.01 wt% Fe_3O_4 nanoparticle, 15 Units/g Amyloglucosidase, 10% (v/v) inoculum, pH 5.78, 40°C, 24 h, 120 rpm.	0.22 g/g (5.21 g/L)	Sanusi et al., 2019
Saccharomyces cerevisiae BY4743.	11.52%w/v	Alkaline pretreatment (black liquor)	SSF	0.338 wt% CuO NP inclusion, enzymatic hydrolysis (Amylase), Saccharification (amyl glucosidase [0.058 mL/g], 42 °C, 24h	21.37 g/L bioethanol	Zondi et al., 2025

Chohan et al. (2020) achieved 22.54 g/L bioethanol and 0.32 g/g yield within 16 h from soaking-assisted thermal pretreated potato peel waste (PPW) hydrolysate using *S. cerevisiae* BY4743 at 40 °C, pH 5.78, and 12.25% w/v solids. Similarly, Atitallah et al. (2019) compared SHF and SSF strategies for PPW using *Wickerhamomyces anomalus*, applying sequential acid–alkali pretreatment (0.1% H_2SO_4 at 121 °C for 1 h, followed by 0.1% NaOH at 80 °C for 24 h) and enzymatic hydrolysis with α-amylase (*Bacillus* sp. Gb67) and Cellic® CTec2 (223 FPU/mL), which resulted in ethanol yields of 0.49 g/g (SSF) and 0.47 g/g (SHF). In another study, 1% NaOH-pretreated PPW fermented by *S. cerevisiae* yielded 9 ± 0.9 g/L ethanol (Felekis et al., 2023). Notably, Barampouti et al. (2023) achieved a substantially higher ethanol concentration of 71.37 g/L using similar pretreatment (1% NaOH for 6 h at 50 °C) combined with commercial enzymes (Spirizyme Excel XHS, 40 µL/g starch; NS87014, 175 µL/g cellulose) and 2% w/w *S. cerevisiae* under SSF conditions.

Soni et al. (2023) reported that SHF of PPW pretreated with 3% H_2SO_4 and steam pretreated PPW, followed by multi-enzyme hydrolysis at 30 °C for 72 h, yielded 43.2 g/L bioethanol, which increased to 54.75 g/L with nutrient supplementation (0.1% peptone, $(NH_4)(H_2PO_4)$, $ZnSO_4$), highlighting the role of nutrients in enhancing productivity. Similarly, organosolv-pretreated PPW (75% ethanol, 1% acid, 180 °C) hydrolyzed with Cellic® CTec2 at 32 °C for 48 h produced 18.1 g/L ethanol (Soltaninejad et al., 2022). Other value-added bioproducts (such as lactic acid, enzymes, biogas, methane, butanol, etc.) have been produced using PPW. Ozer Uyar and Uyar (2023) achieved simultaneous ethanol (18.83 g/L) and lactic acid (3.14 g/L) production using *Rhizopus oryzae*, Mushtaq et al. (2024) produced amylase (0.601 IU/mL/min) and cellulase (1.269 IU/mL/min) with *B. subtilis* QY4, and Achinas et al. (2019) reported biogas (485 mL/g) and methane (283.4 mL/g) yields via anaerobic co-digestion after acid hydrolysis of PPW. Collectively, these findings establish PPW as a highly adaptable feedstock for a wide array of bioprocesses within a circular bioeconomy. Despite these potentials, the direct utilization of PPW is constrained by the complex structure of its lignocellulosic matrix, which limits the immediate fermentability and necessitates pretreatment to achieve complete bioconversion (Awogbemi et al., 2022).

2.3. Pretreatment Strategies for Lignocellulosic Biomass

Lignocellulosic biomass (LB), such as potato peel waste (PPW), exhibits a highly complex and recalcitrant structure consisting mainly of cellulose, hemicellulose, and lignin. The strong lignin–carbohydrate linkages within this matrix restrict polysaccharide accessibility to

hydrolytic enzymes and microorganisms, thereby limiting efficient conversion into fermentable sugars. Consequently, pretreatment is essential to disrupt this rigid structure, facilitating the breakdown of lignin and hemicellulose that encase cellulose and enabling its effective release (Weng et al., 2021). Several factors, including the crystalline structure of cellulose, the degree of lignification, and the structural complexity and heterogeneity of cell-wall constituents, contribute to the recalcitrance of lignocellulosic biomass, which must be overcome for efficient valorisation in biorefinery processes (Olatunji et al., 2021). This intrinsic resistance remains the major barrier to cost-effective conversion of lignocellulosic feedstocks into bioethanol and other biochemicals. Pretreatment is therefore an indispensable preliminary step in the lignocellulosic bioethanol production process, as it disrupts the complex biomass matrix and enhances cellulose and hemicellulose accessibility for subsequent enzymatic or chemical hydrolysis and microbial fermentation. The choice of pretreatment depends on feedstock type and composition, and several strategies have been developed to fractionate, solubilize, and separate cellulose, hemicellulose, and lignin into fermentable forms (Osman et al., 2021). These approaches are broadly classified as physical, chemical, physicochemical, biological, or combined techniques (Fig. 2.3).

2.3.1. Physical pretreatment method

Physical pretreatment primarily alters substrate particle size, surface area, crystallinity index, and degree of polymerization (Kumar et al., 2020). This process significantly increases the exposed surface area of the biomass, which is crucial for improving the efficiency of enzymatic hydrolysis by providing more contact points for enzymes. The reduced particle size further promotes uniform heat transfer and improved mixing in bioreactors. Common physical pretreatments include mechanical operations, densification, torrefaction, ultrasonication, and irradiation methods such as microwave, electron beam, and gamma rays (Varella et al., 2024).

2.3.1.1. Mechanical pretreatment: The mechanical pretreatment methods, including milling, shredding, chipping, freezing, osmotic shocks, and extrusion, are widely employed to improve the digestibility of lignocellulosic biomass (LCB) (Dahunsi, 2019). Such operations facilitate the breakdown of structural components, reducing lag time during anaerobic digestion and increasing methane yield by up to 22% (Dahunsi, 2019). Extrusion, in particular, enhanced biogas production from forestry biomass by 190% (Karimipour-Fard et al., 2024). These processes decrease cellulose crystallinity, increase surface area and bulk density, and alter polymerization degree, thereby promoting lignin and hemicellulose removal and enhancing

digestibility. Despite their effectiveness and lower emissions, mechanical size reduction can be energy- and capital-intensive, increasing process costs.

2.3.1.2. Densification and torrefaction: Densification is a physical pretreatment technique that mitigates the low bulk density of lignocellulosic feedstocks through methods such as pelleting, briquetting, and screw extrusion, thereby increasing material density, reducing moisture content, lowering transportation costs, and enhancing the yields and composition of pyrolysis products (He et al., 2020). Torrefaction thermal pretreatment process (either dry or wet) is achieved at elevated temperatures, typically ranging from light (~200 °C) to severe (~290 °C). At these temperatures, the dry torrefaction process induces partial degradation of hemicellulose, cellulose, and lignin, producing a more uniform, hydrophobic biomass with improved susceptibility to downstream conversion and enhanced bio-oil quality (He et al., 2020). Meanwhile, wet torrefaction (hydrothermal carbonization) is performed in hot-compressed water or subcritical water at milder temperatures (180–260 °C) and pressures (around 47 bar). This process hydrates cellulose while solubilizing hemicellulose and portions of lignin, resulting in a solid fraction with superior conversion properties and a liquid phase enriched with phenolics, furfurals, hexoses, and other sugars, offering additional valorization potential (Kostyniuk and Likozar, 2024).

2.3.1.3. Microwave irradiation and ultrasonication: The microwave irradiation technique is increasingly applied in the physical pretreatment of lignocellulosic biomass (LB) due to its rapid volumetric heating, which efficiently disrupts biomass structure. Microwave fields induce electric fields that cleave hydrogen bonds and alter liquid-phase dynamics, with both thermal (bipolar heating) and non-thermal (dipole reorientation, bond cleavage, protein deconformation) effects contributing to enhanced bioenergy recovery. This technique has been shown to improve cellulose digestibility and sugar yields. For example, microwave-assisted pretreatment with power level, treatment time, solid-to-liquid ratio and dilute acid ratio of 700 W, 6.92 min, 1:18.26 w/v, and 3.67% for barley husk, 600 W, 6.96 min, 1:17.22 w/v, and 3.47% for oat husk, 600 W, 6.92 min, 1:16.69 w/v, and 1.85% for wheat bran, and 460 W, 6.15 min, 1:17.14 w/v, and 2.72% for rye bran. The maximum fermentable sugar recoveries were 37.21 (0.68 g/g), 38.84 (0.67 g/g), 49.65 (0.83 g/g), and 36.27 g/L (0.62 g/g) under optimum conditions, respectively (Germec et al., 2017). However, uneven power distribution, limited penetration in larger samples, and lack of uniformity constrain its industrial scalability (Aguilar-Reynosa et al., 2017). Similarly, ultrasonication employs high-intensity ultrasound to

generate shear forces that disrupt biomass network structures, thereby enhancing microbial accessibility and bioenergy production. While both methods improve biomass susceptibility, their high energy demands make them less sustainable when applied independently, necessitating integration with other pretreatment strategies for optimal impact.

2.3.2. Chemical pretreatment method

Chemical pretreatment methods are facilitated by chemical-mediation reactions capable of high-rate solubilisation of LB substrate under controlled conditions, targeting the breakdown of hemicelluloses and lignin, leading to a weakened lignin-holocellulose network and enhancing cellulose accessibility and microbial digestibility (Barampouti et al., 2023; Moodley et al., 2020). Commonly used chemical pretreatment methods include acids, alkalines, inorganic salts, ionic liquids, and organosolvents, depending on the structural composition of the biomass in question.

2.3.2.1. Acid pretreatment: This pretreatment method typically employs mineral acids (such as sulfuric acid (H_2SO_4), hydrochloric acid (HCl), phosphoric acid (H_3PO_4), nitric acid (HNO_3), and organic acids, often in dilute concentrations) to disrupt the rigid LB structure (Fatma et al., 2018). The primary mechanism involves hemicellulose hydrolysis, releasing pentose and hexose sugars (like xylose and arabinose, glucose) into the liquid hydrolysate (Aruwajoye et al., 2017). For instance, Sanusi et al. (2021) employed a low acid (0.92% v/v) pretreatment to hydrolyse potato peel waste in a soaking-assisted thermal pretreatment process. Conversely, highly concentrated acids are generally avoided due to their corrosive nature, toxicity, and hazardous handling requirements. A significant drawback of acid pretreatment, particularly under harsh conditions, is the formation of inhibitory compounds including furfural (from pentose dehydration), 5-hydroxymethylfurfural (HMF, from hexose dehydration), and phenolic or aldehydic derivatives. These inhibitors often necessitate subsequent detoxification to ensure efficient microbial fermentation (Hernández Beltrán et al., 2019).

2.3.2.2. Alkaline pretreatment: Alkaline pretreatment utilizes alkaline solutions, such as sodium hydroxide (NaOH), calcium hydroxide ($Ca(OH)_2$), or ammonium hydroxide (NH_4OH), often at high concentrations and low temperatures. The process acts through saponification of hemicellulose–lignin ester linkages and lignin dissolution, resulting in biomass swelling, increased porosity, and enhanced enzyme accessibility (Barampouti et al., 2023). Alkali pretreatments of LB using 3.0% KOH and 3.0% NaOH in the presence of urea have been

reported by Zahoor et al. (2021). Alkaline pretreatment is generally preferred for lignin-rich biomass and generally produces fewer inhibitory furans than acid pretreatment.

2.3.2.3. Inorganic salts: Pretreatment by inorganic salts, such as alkaline earth metal chlorides ($CaCl_2$ and $MgCl_2$), alkaline metal chlorides (KCl and NaCl), and transition metal chlorides ($CuCl_2$, and $FeCl_3$), is gaining attention due to their ability to increase cellulose and hemicellulose conversion rates and hydrolysis yields. Inorganic salts primarily function through the dissociation of Lewis acids in aqueous media, generating complex cations that cleave glycosidic linkages, while hydrated cations act as nucleophiles to depolymerize hemicellulose into monosaccharides (Moodley et al., 2020). Optimal salt type and concentration must be tailored to specific lignocellulosic feedstocks to maximize pretreatment efficiency.

2.3.2.4. Organosolv: This pretreatment method utilises organic solvents (such as methanol, ethanol, or acetone) or their aqueous mixtures, often in conjunction with acid or alkali catalysts, at elevated temperatures and pressures (Soltaninejad et al., 2022). The organosolv process selectively dissolves lignin and hemicellulose, leaving a relatively pure cellulose residue. A key advantage is the recovery of high-purity lignin for valorization, but efficient solvent recovery is essential to prevent microbial toxicity and ensure cost-effective scalability.

2.3.2.5. Ionic liquids (ILs): Ionic liquids are non-conventional solvents composed entirely of ions, characterized by low vapor pressure, high thermal stability, and tunable properties. ILs are highly effective in solubilizing and fractionating lignocellulose, hydrolyzing lignin and hemicellulose while enhancing cellulose digestibility (Ovejero-Pérez et al., 2024). ILs minimize toxic byproducts and can be recycled, but their industrial use is constrained by high cost and the need for efficient recovery strategies such as distillation, extraction, adsorption, or crystallization (Kucharska et al., 2018).

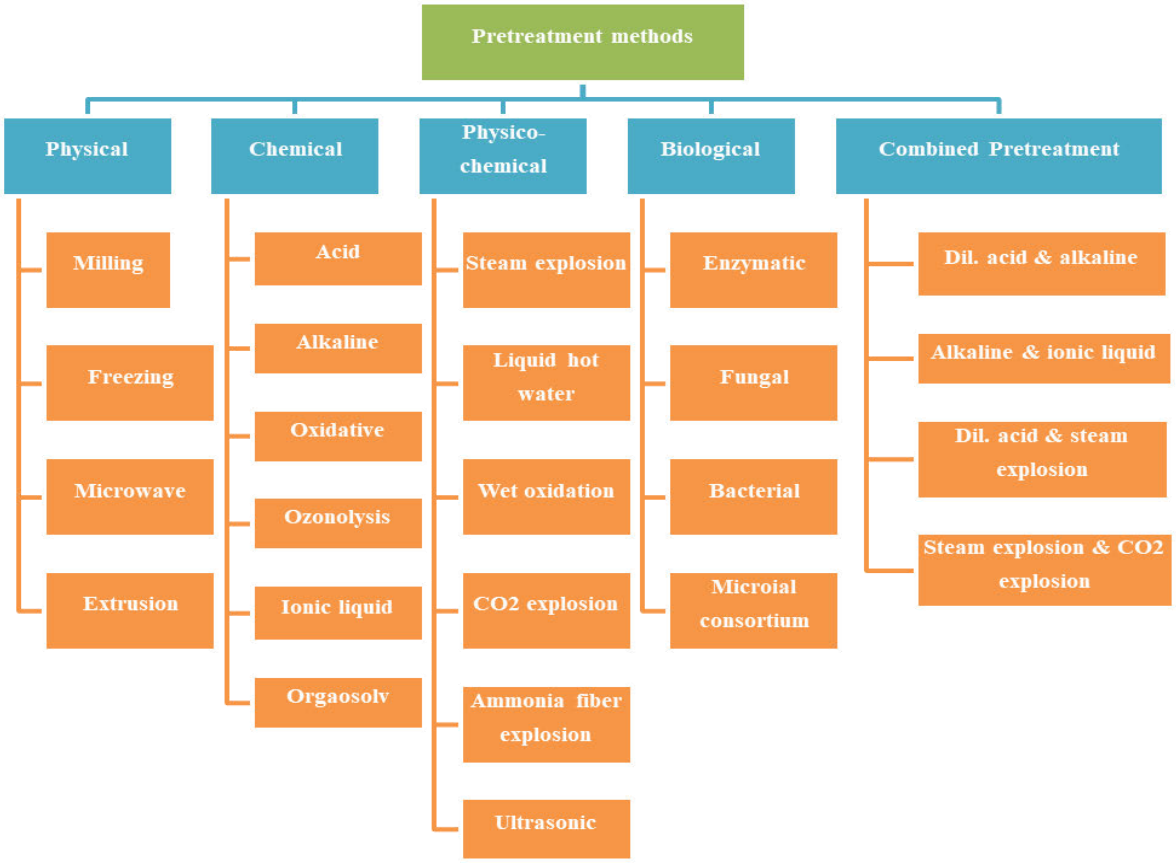

Figure 2.3. Pretreatment methods for LB.

2.3.3. Biological pretreatment methods

Biological pretreatment strategies utilize microorganisms or their enzymes to selectively degrade lignin and hemicellulose under mild conditions, providing an environmentally friendly alternative to chemical or thermochemical methods. This pretreatment exploits the ligninolytic, cellulolytic, and hemicellulolytic potential of microorganisms or their enzymatic systems (Anu et al., 2024). Moreso, these approaches generally require less energy and produce fewer inhibitory compounds.

2.3.3.1. Live microbes: A typical example is the use of live microbes (either bacteria or fungi) to degrade lignocellulosic structures. Bacterial consortia, such as *Bacillus subtilis* (Anu et al., 2021), *B. firmus* K-1 (Baramee et al., 2020), and *Ochrobactrum oryzae* BMP03 (Tsegaye et al., 2018), have been reported to be effective in modifying biomass. Fungal pretreatments are particularly effective due to their robust ligninolytic systems, which secrete extracellular enzymes (e.g., cellulases, xylanases) for biomass deconstruction (Anu et al., 2021). Examples include soft rot ascomycetes (*Trichoderma reesei*, *Aspergillus* sp., *Panusneo strigosus* I9 [Knežević et al., 2021]), white/brown rot basidiomycetes (*Phanerochaete chrysosporium*,

Pleurotus ostreatus, *P. sajor-caju*, *Pycnoporus cinnabarinus*, *Schizophyllum* sp.) (da Silva Machado and Ferraz, 2017), and anaerobic species, such as *Ceriporiopsis subvermispora*, *Orpinomyces* sp. (Huang et al., 2019).

Moreover, the usage of microbial consortia offers more efficient pretreatment than single strains, in terms of accelerated pretreatment time, higher stability, improved substrate digestibility and hydrolysis, and enhanced yields. For instance, the coculture of *Aspergillus niger* CBS 554.65 and *T. reesei* CBS 383.78, *P. chrysosporium* and *P. ostreatus* (Ming et al., 2019), and the consortia of *Rhizopus oryzae*, *A. flavus*, and *Spirulina* (Wang et al., 2025) have shown remarkable delignification abilities with enhanced enzyme synthesis, sugar liberation, and biogas slurry degradation, respectively.

2.3.3.2. Enzyme: Enzymatic pretreatment utilizes lignin-degrading enzymes, such as laccases and manganese peroxidase from white-rot fungi, in conjunction with cellulases and hemicellulases that hydrolyze cellulose and hemicellulose into fermentable sugars. This strategy offers high substrate specificity, operates under mild conditions with reduced energy demand, and minimizes equipment corrosion. By enhancing the release of fermentable sugars, enzymatic methods improve biofuel yields and overall bioconversion efficiency (Atitallah et al., 2019). However, the high cost of commercial enzymes remains a major limitation, constraining economic feasibility. Current research aims to lower these costs through on-site enzyme production by microorganisms (e.g., *A. niger*) and by improving enzyme stability and recyclability via immobilization techniques.

2.3.4. Combined pretreatment method

Combined pretreatment strategies integrate two or more methods, often from different categories (e.g., thermochemical, physicochemical), to achieve a more comprehensive and efficient disintegration of lignocellulosic biomass. By exploiting synergistic effects, this approach enhances sugar release while reducing the limitations associated with individual methods (Carvalheiro et al., 2024). Examples of such combined pretreatment strategies include stream explosion, Liquid hot water, ammonia-based [Fibre Expansion (FEX)], CO_2 explosion, Oxidative pretreatment, and Wet oxidation (Gao et al., 2024; Carvalheiro et al., 2024). Each pretreatment technique disrupts lignocellulosic biomass (LB) structures differently, with the selection depending on the type and composition of the biomass, which includes cellulose, hemicellulose, lignin, and sometimes starch. Consequently, yields and products vary across methods (Galbe and Wallberg, 2019). Overall, the combined pretreatment approaches offer several advantages over single pretreatment methods, particularly in biorefineries, including

enhanced efficiency under optimized conditions, cost reduction, better enzyme accessibility, higher conversion rates, reduced toxic by-products, and improved sustainability, thereby supporting both environmental and economic viability (Konan et al., 2024). Despite their effectiveness in disrupting lignocellulosic structures, combined approaches face industrial challenges, including high costs, energy demands, inhibitor generation, and complex downstream processing (Moodley et al., 2020). Developing post-pretreatment strategies that address these constraints, particularly the removal of inhibitors, remains critical to improving industrial feasibility.

2.4. Formation and impact of inhibitory compounds in pretreated lignocellulosic hydrolysate

Pretreatment of lignocellulosic biomass (LB) through physical, chemical, or biological routes enables the release of fermentable sugars from structural polysaccharides but simultaneously generates inhibitory by-products that impair hydrolysis and fermentation efficiency. These inhibitors originate from biomass components (cellulose, hemicellulose, lignin, extractives) or leached metals (such as copper, nickel, chromium, and iron) from pretreatment equipment (Bishop et al., 2024). The formation, nature, and concentration of these fermentation inhibitors depend largely on biomass compositional heterogeneity and pretreatment conditions such as temperature, pH, pressure, and chemical inputs (Soares et al., 2023). Early classifications of inhibitory compounds focused on short-chain organic acids, furans, and phenols. However, the discovery of new inhibitory compounds and a better understanding of their mode of action have birthed a new categorisation including sugar-derived aldehydes, aromatic compounds, short-chain organic acids, and aldehydes, and other inhibitors (Sjulander and Kikas, 2020) (Table 2.3).

2.4.1. Sugar-derived aldehyde inhibitors

Sugar-derived aldehydes, primarily furan derivatives and glycolaldehydes, arise from the degradation of cellulose and hemicellulose during pretreatment. Hemicellulose contains pentoses (D-xylose, L-arabinose) and hexoses (D-mannose, D-glucose, D-galactose), while cellulose is composed mainly of D-glucose (Rodrigues et al., 2024). Furan derivatives such as furfural and hydroxymethylfurfural (HMF) are particularly significant in fermentation due to their inhibitory and economic relevance (Ornaghi et al., 2020).

Table 2.3. Category and structural description of inhibitory compounds derivable from lignocellulosic biomass.

Category	Sub-category	Inhibitory compounds	Description	References
Sugar-derived Aldehydes (SDA)	Furans	Furfural ($C_5H_4O_2$)	An aromatic aldehyde with a furan ring and a formyl group (-CHO).	Esteban et al., 2018
		Hydroxymethylfurfural ($C_6H_6O_3$)	A furan ring substituted with a hydroxymethyl group (-CH_2OH) and a formyl group (-CHO).	Ornaghi et al., 2020
	Glycolaldehyde	Glycolaldehyde ($C_2H_4O_2$)	a hydroxy group (-OH) and an aldehyde group (-CHO) on a two-carbon chain.	Weng et al., 2024
Aromatic compounds	Phenolic compounds	Syringaldehyde ($C_9H_{10}O_4$)	A benzaldehyde derivative with two methoxy groups and one hydroxyl group.	
		Syringic acid ($C_9H_{10}O_5$)	A benzoic acid derivative with two methoxy groups and one hydroxyl group.	
		4-hydroxybenzaldehyde ($C_7H_6O_2$)	Benzaldehyde with a hydroxyl group at the para position.	
		4-hydroxy-coumaric acid (p-Coumaric Acid) ($C_9H_8O_3$)	Cinnamic acid derivative with a hydroxyl group at the para position.	de Andrade Bianchini et al., 2024
		Vanillin ($C_8H_8O_3$)	A benzaldehyde derivative with a methoxy group (-OCH_3) and a hydroxyl group (-OH).	Korányi et al., 2020
		Vanillic acid ($C_8H_8O_4$)	A benzoic acid derivative with one methoxy group and one hydroxyl group.	Al Mamari, 2021
		Salicylic acid ($C_7H_6O_3$)	A benzoic acid derivative with a hydroxyl group ortho to the carboxyl group.	Thirunavukkaras et al., 2024
		Ferulic acid ($C_{10}H_{10}O_4$)	A hydroxycinnamic acid derivative with a methoxy group and a hydroxyl group.	
		Coniferyl aldehyde ($C_{10}H_{10}O_3$)	phenylpropanoid aldehyde with a methoxy (-OCH_3) and an alkenyl group.	
		4-hydroxy-benzoic acid ($C_7H_6O_3$)	A benzoic acid derivative with a hydroxyl group at the para position.	
		Catechol ($C_6H_6O_2$)	A benzene ring with two hydroxyl groups in ortho positions.	
		Guaiacol ($C_7H_8O_2$)	A benzene ring with one hydroxyl group and one methoxy group.	
	Non-phenolic compounds	Benzyl alcohol (C_7H_8O)	A benzene ring attached to a methanol group (-CH_2OH).	
		Cinnamaldehyde (C_9H_8O)	A phenylpropanoid with an aldehyde group (-CHO) on a propenyl side chain.	
		Benzoic acid ($C_7H_6O_2$)	A benzene ring with a carboxyl group	Verma et al., 2024
		Cinnamic acid ($C_9H_8O_2$)	A phenylpropanoid with a carboxyl group (-COOH) on a propenyl side chain.	Sjulander and Kikas, 2020
		Para- and ortho-toluic acid ($C_8H_8O_2$)	Benzoic acids with a methyl group at the para (4th) or ortho (2nd) position relative to the carboxyl group.	de Andrade Bianchini et al., 2024
		3,4-dimethoxycinnamic acid ($C_{11}H_{12}O_4$)	Cinnamic acid with two methoxy groups (-OCH_3) at the 3rd and 4th positions.	
		Coumaroyl amide ($C_9H_9NO_2$)	The carboxylic group (-COOH) in p-Coumaric acid is replaced with an amide (-$CONH_2$)	
		Feruloyl amide ($C_{10}H_{11}NO_3$)	The carboxylic group (-COOH) in ferulic acid is replaced with an amide (-$CONH_2$)	
	Benzoquinones	p-Benzoquinone ($C_6H_4O_2$)	A cyclic compound with two ketone groups on opposite sides of a benzene ring.	Kimani et al., 2021
		2,6-Dimethoxybenzoquinone ($C_8H_8O_4$)	A benzoquinone with two methoxy groups (-OCH_3) at the 2nd and 6th positions.	
Short chain Organic compounds	Short-chain organic acids	Formic acid (CH_2O_2)	The simplest carboxylic acid with one carbon atom.	Mazzoli, 2021
		Acetic acid ($C_2H_4O_2$)	A two-carbon carboxylic acid with one carbonyl group.	Johannes and Xuan, 2024
		Lactic acid ($C_3H_6O_3$)	A hydroxycarboxylic acid with a hydroxyl group (-OH) and a carboxyl group (-COOH).	Duan et al., 2023
		Levulinic acid ($C_5H_8O_3$)	A ketocarboxylic acid with a ketone group and a carboxyl group.	Sjulander and Kikas, 2020;
	Short-chain organic Aldehydes	Formaldehyde (CH_2O)	Aldehyde, with a single carbon atom bonded to a hydrogen and an oxygen double bond.	Bayu et al., 2019
		Acetaldehyde (C_2H_4O)	A two-carbon aldehyde with one carbonyl group (-CHO).	Andérez-Fernández et al., 2022
Other inhibitors compounds	Sugars	Monomeric and oligomeric pentoses (e.g., xylose, $C_5H_{10}O_5$)	A 5-carbon sugar with an aldehyde group (aldopentose).	Rodrigues et al., 2024
		Glucose ($C_6H_{12}O_6$)	A 6-carbon aldose sugar with an aldehyde group.	
		Cellobiose ($C_{12}H_{22}O_{11}$)	A disaccharide made of two glucose molecules linked by a β (1→4) bond.	
	Metals	Metals	Ions of metals, such as copper, nickel, chromium and iron,	Bishop et al, 2024

Furfural is produced from pentose degradation under acidic, high-temperature conditions, where sugars like xylose undergo dehydration, releasing three water molecules to yield furfural (Esteban et al., 2018) (Eq. 2.1).

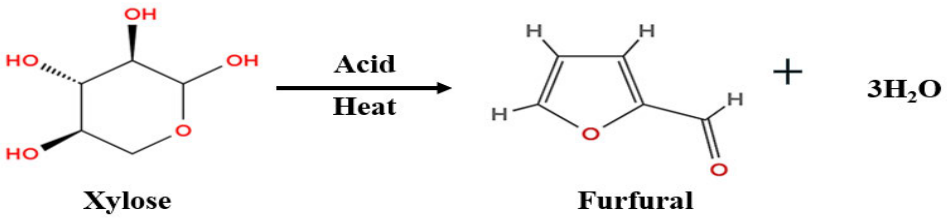

Xylose Furfural

Eq. 2.1

Furfural is a critical inhibitor in acid-pretreated lignocellulosic hydrolysates, with concentrations above 1.0 g/L impairing microbial vitality, growth rate, ethanol yield, and productivity (Jilani and Olson, 2023). In *S. cerevisiae*, furfural induces reactive oxygen species (ROS) accumulation, oxidative stress, and genomic instability, particularly when acting synergistically with other inhibitors (Ren et al., 2024). Its toxicity is further linked to the inhibition of intracellular enzymes, notably hexokinase, glyceraldehyde-3-phosphate dehydrogenase (GPD), alcohol dehydrogenase (ADH), and pyruvate dehydrogenase (PDH), thereby disrupting glycolysis and the TCA cycle (Lei et al., 2024).

Besides enzyme inhibition, furfural has been implicated in the disruption of vital cellular components of fermenting organisms, including vacuole and mitochondrial membranes, chromatin, and actin, while depleting ATP and NAD(P)H levels through enzymatic inhibition, cofactor depletion, and damage to membranes, genetic materials, and proteins (Saucedo-Gutierrez et al., 2024). Microbial cell can only modulate furfural toxicity at lower concentrations, transforming it into less harmful compounds such as furfuryl alcohol and furoic acid (Guarnieri et al., 2017). Hence, reducing the furfural concentration in preheated hydrolysate is critical for bioprocessing.

Hydroxymethylfurfural (HMF), formed by hexose dehydration during heat or acid pretreatment (Eq. 2.2), is abundant in hexose-rich substrates (e.g., molasses, fruit juices, starch, cellulosic) due to sugar caramelisation and Maillard reactions. HMF exhibits strong microbial toxicity, with concentrations above 1.0 g/L prolonging the lag phase and impairing growth and fermentation in *S. cerevisiae*. At high concentrations, HMF inhibits several enzymes, including alcohol dehydrogenase (ADH), pyruvate dehydrogenase (PDH), and aldehyde dehydrogenase

(ALDH) (Lei et al., 2024). However, under respirative and fermentative conditions, HMF can be converted to less toxic compounds such as 5-hydroxymethylfurfuryl alcohol (by reduction) and 5-hydroxymethylfuroic acid (by oxidation) (Eq. 2.2) (Messori et al., 2022).

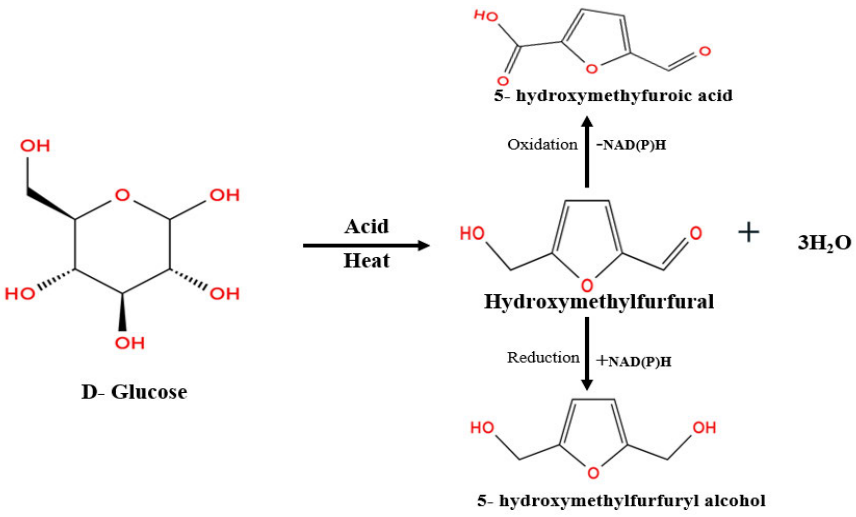

Eq. 2.2

Glycolaldehyde, a simple sugar-derived aldehyde containing both –CHO and –OH groups, is generated from hexose and pentose degradation during pretreatment under low water conditions that favour fragmentation reactions (Weng et al., 2024). During thermal or acid-catalyzed pretreatment, glucose ($C_6H_{12}O_6$) can be degraded to glycolaldehyde ($C_2H_4O_2$) and formaldehyde (C_2H_4O) through retro-aldol cleavage reactions involving splitting between C_2-C_3 and C_4-C_5 bonds of the glucose molecule. Xylose ($C_5H_{10}O_5$), on the other hand, disintegrates to glyceraldehyde ($C_3H_6O_2$) and glycolaldehyde ($C_2H_4O_2$), as shown in the reaction (Eq. 2.3) below. Glycolaldehyde is beneficial as a lone compound, playing significant roles in various biochemical processes. Nevertheless, it has been identified as a major inhibitor in the LB hydrolysates fermentation by *S. cerevisiae* (Jayakody et al., 2017). Glycolaldehyde covalently binds to macromolecules, including DNA, proteins, and cell membrane amino residues, disrupting essential cellular functions (Jayakody et al., 2017). Moreso, its inhibitory action extends to key glycolytic and metabolic enzymes, reducing growth rate, viability, and fermentation performance. Concentrations as low as 1–10 mM markedly hinder bioethanol production, underscoring the need for engineered yeast strains with improved tolerance (Jayakody et al., 2017).

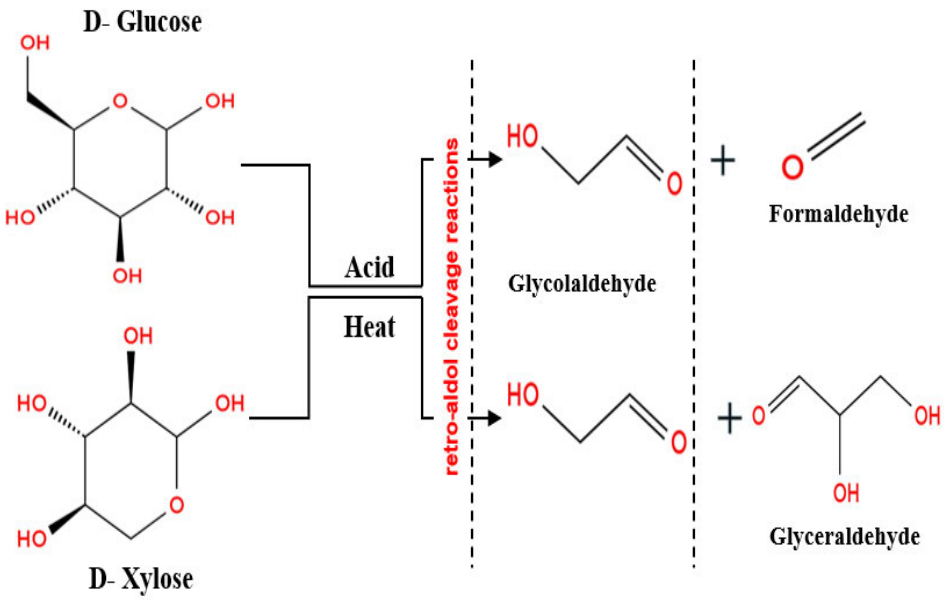

(Eq. 2.3)

2.4.2. Aromatic inhibitory compounds

Aromatic compounds, primarily derived from lignin and carbohydrate degradation during acid pretreatment, constitute a major class of fermentation inhibitors. Lignin, a heterogeneous aromatic polymer composed of coniferyl, coumaryl, and sinapyl alcohol monomers linked by strong C–C and ether bonds, releases aromatic derivatives upon disintegration (Korányi et al., 2020). The composition of these inhibitors depends on both the pretreatment method and the intrinsic lignin structure of the biomass (Sjulander and Kikas, 2020). The aromatic inhibitory compounds can be phenolic compounds, non-phenolic compounds or benzoquinones. Phenolic compounds are primarily identified by the presence of at least one hydroxyl group attached to an aromatic benzene ring (Al Mamari, 2021). Common examples, as shown in Fig. 2 .4, include syringaldehyde, coniferyl aldehyde, vanillin, vanillic acid, syringic acid, salicylic acid, 4-hydroxybenzaldehyde, 4-hydroxycoumaric acid, ferulic acid, feruloyl amide, 4-hydroxybenzoic acid, coumaroyl amide, catechol, and guaiacol (Thirunavukkaras et al., 2024). The formation of vanillin and vanillic acid is linked to the guaiacyl monomers of lignin, while syringic acid and syringaldehyde are generated from its syringyl monomers. The production of 4-hydroxybenzaldehyde is attributed to the p-hydroxyphenyl unit.

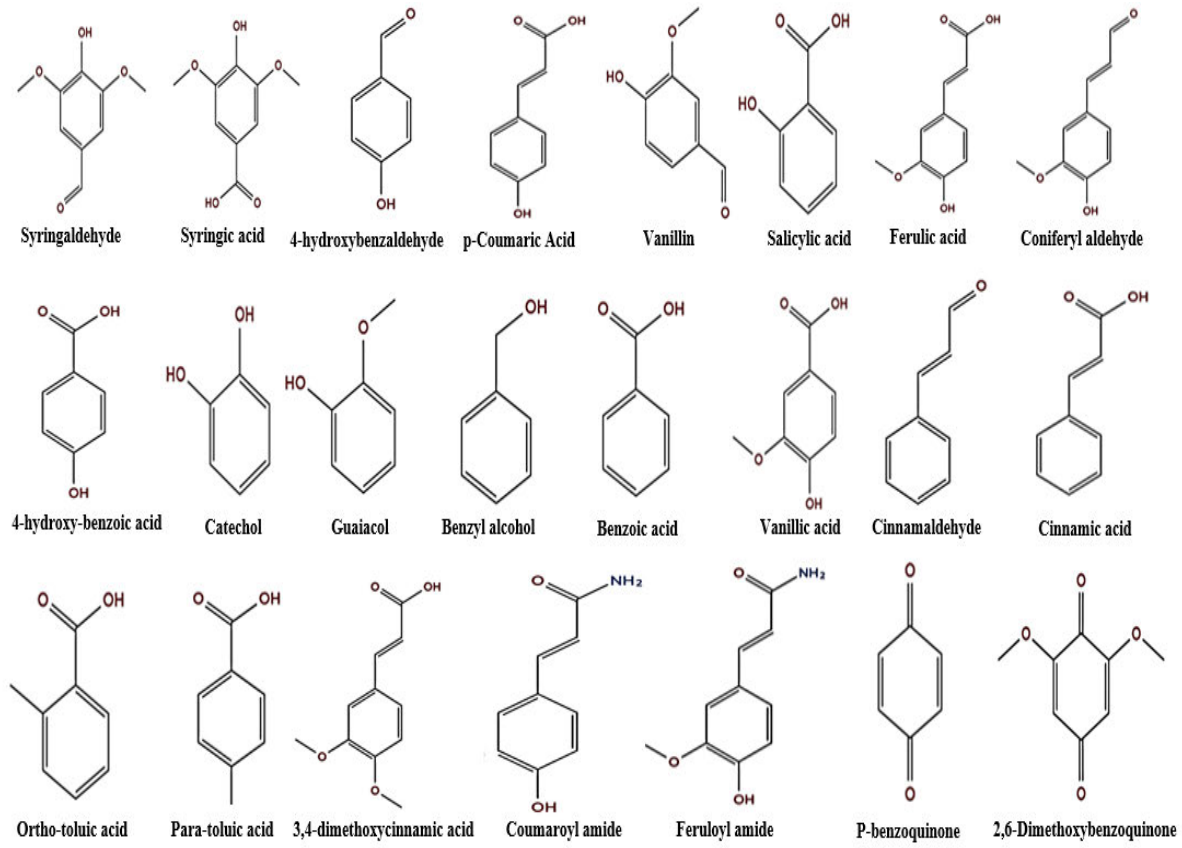

Figure 2.4. Aromatic inhibitory compounds.

Similarly, ferulic acid and 4-hydroxycinnamic acid are associated with the monolignol components coniferyl alcohol and coumarin alcohol, respectively (de Andrade Bianchini et al., 2024). Non-phenolic aromatic inhibitors, though lignin-derived, differ structurally from phenolics by the absence or position of hydroxyl groups. Examples include benzyl alcohol, cinnamaldehyde, and benzoic acid. Other classes include phenolic amides such as feruloyl and coumaroyl amides, and benzoquinones like 2,6-dimethoxybenzoquinone and p-benzoquinone (Verma et al., 2024). The inhibitory effects of phenolics vary depending on the pretreatment method. For instance, according to Chen et al. (2020), alkaline-derived phenolics exhibit high inhibition on *Zymomonas mobilis* fermentation, whereas those originating from ammonia fibre expansion (AFEX) exhibited comparatively milder effects (Chen et al., 2020). Vanillin and syringaldehyde inhibit glucose metabolism, with vanillin reducing hydrogen yield by 17% (Iglesias-Carres et al., 2022).

Phenolic amides inhibit nucleotide biosynthesis in *E. coli*, thereby impairing the purine and pyrimidine pathways (Kimani et al., 2021). Microbial resistance to these phenolic inhibitors is

strongly influenced by membrane composition (lipids, phospholipids, proteins), but inhibition mechanisms remain poorly understood. Their typically low concentrations in hydrolysates further complicate analysis, though their cumulative impact on fermentation efficiency is significant.

2.4.3. Short-chain organic inhibitory compounds

Short-chain organic inhibitors, formed during cellulose and hemicellulose hydrolysis, impede fermentation by impairing microbial activity (Mazzoli, 2021). Examples of this category of inhibitor include carboxylic acids [such as formic acid (CH_2O_2), acetic acid ($C_2H_4O_2$), lactic acid ($C_3H_6O_3$), levulinic acid ($C_5H_8O_3$)], and aldehydes such as formaldehyde (CH_2O) and acetaldehyde (C_2H_4O) (Sjulander and Kikas, 2020). Formic acid, the simplest carboxylic acid, is commonly formed during lignocellulose degradation at high temperature and acidity, mainly via catalytic hydrodeoxygenation of furfural and HMF (Andérez-Fernández et al., 2022). The formation of formic acid increases with pretreatment severity over time. Formic acid lowers fermentation pH, disrupts microbial metabolism, and inhibits enzymatic function, ultimately reducing ethanol productivity (Basera et al., 2024).

Acetic acid, mainly released during hemicellulose and lignin deacetylation, is the most prevalent acetyl-group inhibitor in bioethanol fermentation (Johannes and Xuan, 2024). Moreover, the presence of acetic acid in LB hydrolysate is observed across diverse pretreatment processes, with chemical pretreatment resulting in higher acetic acid formation. Notably, acetic acid lowers the pH of the fermentation medium, thereby acidifying the intracellular matrix, which is detrimental to microbial growth and activity (Johannes and Xuan, 2024). Acetic acid is particularly detrimental as it diffuses into cells, disrupts pH homeostasis, and impairs nutrient uptake, ultimately reducing microbial fermentation efficiency (Johannes and Xuan, 2024). Levulinic acid is formed during cellulose degradation under acidic, high-temperature conditions, which similarly compromises microbial membranes and enzyme activity, thereby reducing growth and fermentation efficiency (van der Maas et al., 2021).

Formaldehyde is a highly reactive compound biologically formed alongside glycolaldehyde ($C_2H_4O_2$) during the degradation of hexose sugar (glucose; $C_6H_{12}O_6$) through retro-aldol cleavage reactions (Bayu et al., 2019). At high concentrations, formaldehyde forms cross-links with proteins and nucleic acids, disrupting cellular functions and inhibiting microbial growth. Furthermore, formaldehyde effectively inhibits dihydrogen (H_2) production by [FeFe]-

hydrogenases by forming Fe-bound formaldehyde adduct. This adducts mimics a metal-hydrido species, effectively blocking the active site and halting hydrogen production (Duan et al., 2023). Acetaldehyde, on the other hand, is a byproduct of oxidative decarboxylation of pyruvate obtained during sugar dehydration to furfural and HMF. Acetaldehyde at high concentrations can disrupt cellular metabolism by interfering with enzyme activity and the glycolytic pathway, inducing oxidative stress, and impairing fermentation efficiency (Jayakody and Jin, 2021).

2.5. Strategies for mitigating the impact of inhibitory compounds in lignocellulosic hydrolysate

Inhibitory compounds from LB hydrolysate have proven detrimental to the overall efficiency of fermentation processes. Therefore, it is essential to minimize their presence and, consequently, their impact. Strategies to mitigate the impact of inhibitory compounds are crucial for improving the efficiency of biofuel production. Various approaches have been developed to mitigate the effect of inhibitory compounds. These include biological methods to enhance microbial tolerance and remove inhibitors prior to fermentation, as well as detoxifying hydrolysates using various physical, chemical, and combined approaches (Fig. 2.5), each offering distinct advantages and limitations.

2.5.1. Biological methods for microbial adaptation

Several biological adaptation strategies are adopted by microorganisms to withstand lignocellulose-derived inhibitors. These include in-situ detoxification via enzymes such as oxidoreductases and dehydrogenases, whose expression is upregulated in response to inhibitor exposure (Brandt et al., 2019). Regulatory genes also enhance resistance by modulating stress responses. Additionally, microbes can adjust metabolic pathways to mitigate inhibitory effects or utilize inhibitors as substrates. Another strategy involves membrane modifications to alter fluidity and permeability, thereby controlling inhibitor influx, while stress protectants (e.g., trehalose, spermidine, glutathione, and thioredoxin) stabilize cellular functions. Furthermore, cellular efflux mechanisms, facilitated by membrane transporters and pumps, collectively enhance microbial tolerance by removing intracellular inhibitors.

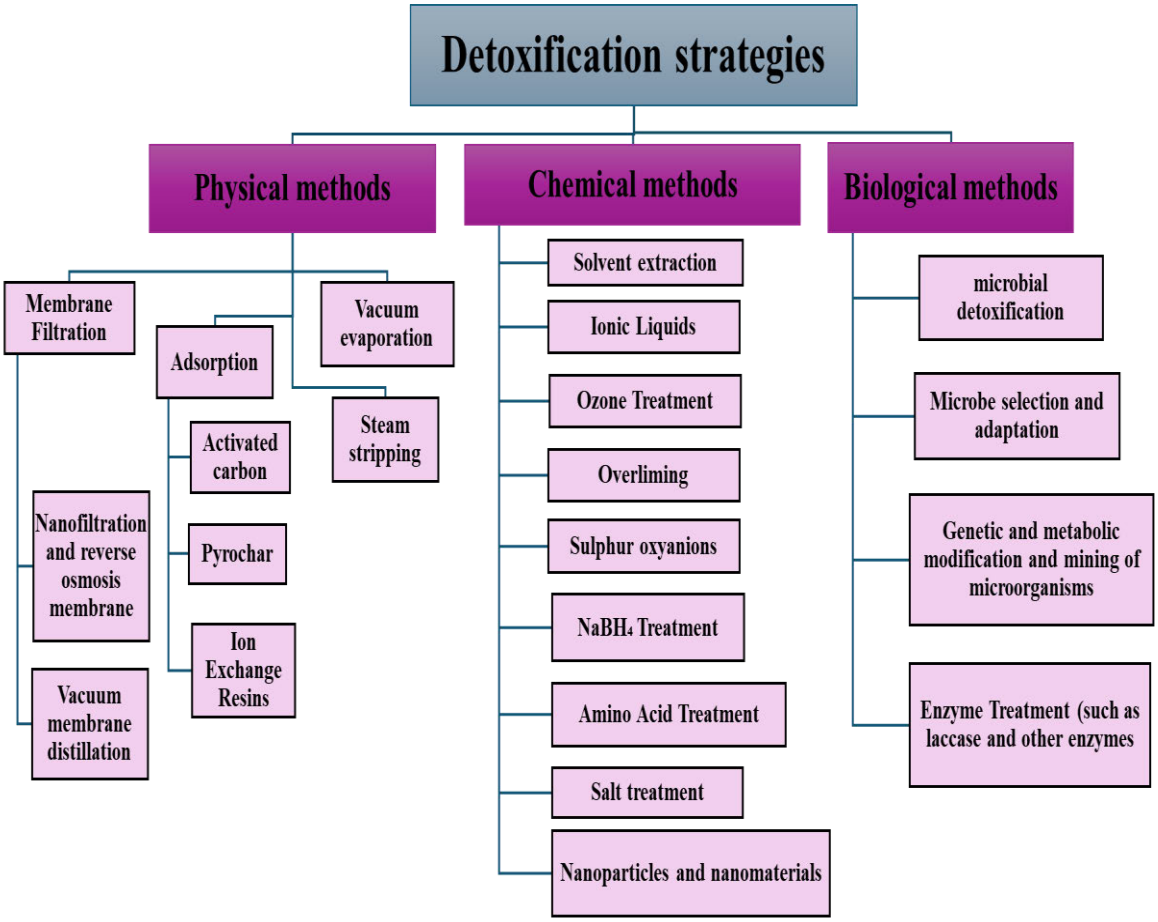

Figure 2.5. Strategies for removing inhibitory compounds from lignocellulosic biomass.

2.5.1.1. Direct microbial detoxification of lignocellulosic hydrolysates

Several microbial strains exhibit selective detoxification of lignocellulose-derived inhibitors. For instance, *Bordetella* sp. BTIITR efficiently removes furfural and HMF, achieving complete furfural and 80% HMF degradation from simulated hydrolysates within 16 hours, and 100% furfural, 94% HMF, and 82% acetic acid removal from sugarcane bagasse hydrolysate without sugar loss (Singh et al., 2017). Similarly, a modified *Acinetobacter baylyi* ADP1 strain degrades aromatic inhibitors such as benzoate and 4-hydroxybenzoate while sparing sugars (Singh et al., 2019). Among sixty-four yeast strains screened, *Pichia occidentalis* Y1′a and M1 reduced furfural, HMF, and acetic acid by 42.89% and 46.04%, respectively, after 96 hours (Soares et al., 2016). *Trichoderma reesei* has also been used to simultaneously detoxify hydrolysates and enhance carboxymethyl cellulase production via a feeding strategy with rice straw hydrolysate (Panda and Maiti, 2019). Optimization of process conditions further improves detoxification efficiency. For instance, *Amorphotheca resinae* ZN1, under optimized aeration and mixing, halved the detoxification time of dilute acid-treated corn stover hydrolysate from 96 to 36 hours

without reducing ethanol yield (He et al., 2016). Combining detoxifying and fermenting organisms presents additional advantages. Co-culturing ferulic acid-degrading *E. coli* with *T. reesei* increased ethanol production by 7.8% from rice straw hydrolysate (Zhang et al., 2017). Likewise, engineering a consortium of *Acinetobacter baylyi* ADP1 strains enhanced ethanol fermentation by *Kluyveromyces marxianus* through concurrent degradation of benzoate and 4-hydroxybenzoate (Singh et al., 2019).

2.5.1.2. Genetic and metabolic modification of microorganisms

Employing evolutionary engineering to develop microbial strains with enhanced tolerance to the toxicity of inhibitory compounds is a promising strategy for improving biofuel production. These adaptive techniques, including the development of multi-inhibitor resistance and adaptive laboratory evolution (ALE), have been shown to significantly enhance strain resilience and productivity. For example, ALE applied to *B. subtilis* produced strains capable of growth in 100% hydrolysate, with mutations in genes such as codY, katA, and perR conferring enhanced tolerance (Driessen et al., 2023). In *S. cerevisiae*, overexpression of CAR1 improved acetic acid tolerance by modulating nitrogen metabolism and stress response pathways (Xiong et al., 2024). Similarly, ALE of *Corynebacterium glutamicum* S9114, performed through serial transfers in corn stover hydrolysate over 128 days, yielded a strain with enhanced conversion of furfural, HMF, vanillin, syringaldehyde, 4-hydroxybenzaldehyde, and acetic acid (Wang et al., 2018).

In another study by Ren et al. (2024), X-ray was used in multiple rounds to induce mutations in *S. cerevisiae*, and the modified SCF-R4 mutant strain of *S. cerevisiae* enhanced furfural tolerance and reduced reactive oxygen species production. Similarly, heavy ion irradiation (HIR) combined with ALE generated vanillin-tolerant yeast mutants (H6, H7, X3, X8) with 3.4-fold higher resistance compared to wild type, linked to differentially expressed genes (FLO9, GRC3, PSP2, SWF1) involved in flocculation, rDNA transcription, mutation repair, and protein palmitoylation (Jia et al., 2024). Genes encoding aldo-keto reductases (GCY1, YPR1) with vanillin reductase activity also improved vanillin tolerance when overexpressed. Likewise, overexpression of ADH6, ALD6, ZWF1, YNL134C, and YJR096W in *S. cerevisiae* significantly increased μ_{max} under vanillin stress (Wang et al., 2016). Despite these advances, evolutionary adaptations often remain strain- or condition-specific and may be sensitive to environmental fluctuations.

2.5.1.3. Enzyme treatment

Common examples of enzymes employed are the laccases and peroxidases. Laccases are lignolytic oxidative enzymes (EC 1.10.3.2, AA1 family of multi-copper oxidases) widely used for detoxifying phenolic inhibitors in lignocellulosic hydrolysates (Tramontina et al., 2020). Laccases ensure the degradation and polymerization of aromatic compounds such as syringaldehyde, thereby reducing their toxicity. Both free and immobilized laccases, with or without mediators, have been employed for inhibitor detoxification. For example, 0.1 U/mL extracellular *Trametes maxima* IIPLC-32 laccase reduced phenolic inhibitors in sugarcane bagasse hydrolysate by 66% within 30 min (Suman et al., 2018), while *Myceliophthora thermophila* laccase removed 87% of phenolics from steam-pretreated olive tree pruning (Ibarra et al., 2023). Laccases' efficiency depends on redox potential. This is evident in lower detoxifying capability displayed by laccase with lower redox potential from *S. ipomoeae* in the oxidation of syringaldehyde and ferulic acid, while high-redox fungal laccases effectively oxidize ferulic acid, syringaldehyde, vanillin, p-coumaric acid, and other phenolics in preheated hydrolysate (De La Torre et al. 2017). Laccase activity can also be expanded with redox mediators, enabling detoxification of additional phenolic and ketone derivatives, as demonstrated by *T. versicolor* laccase by Saravanakumar et al. (2016). Laccase offers a green and sustainable approach to inhibitors' detoxification and minimizing environmental impact compared to chemical methods (Tramontina et al., 2020). Despite these potentials, laccase application faces limitations, including reduced sugar recovery due to β-glucosidase inhibition, poor stability under alkaline conditions, and product inhibition. To address these challenges, alkaline-tolerant laccases have been explored to improve stability under such conditions (Arefmanesh et al., 2022).

Peroxidases, on the other hand, are enzymes derived from plants and microorganisms, capable of degrading phenolic compounds and mitigating their inhibitory effects on fermentation. An example is the manganese peroxidases (MnP), a class of heme-containing glycoproteins produced by a wide range of wood-colonizing basidiomycetes, which oxidize Mn^{2+} to Mn^{3+}, and subsequently degrade phenols and dyes (Yee et al. 2018). Horseradish peroxidase from *Coprinus cinereus* has been used to remove 50 to 90% of total phenolics from LB hydrolysates (Tramontina et al., 2020). Likewise, Li et al. (2019) reported the enhancement of peroxidase activity as a lytic polysaccharide monooxygenase with improved detoxification via a reactive oxygen species (ROS) generation mechanism. Many other related biological enzymes have demonstrated ligninolytic properties directly or indirectly. For instance, aryl-alcohol oxidases

(AAOs), methanol oxidases (MOXs), and glyoxal oxidases (GLOXs) are capable of acting on alcohol-inhibitory molecules derived from lignin oxidation. The application of AAOs from *P. ostreatus* reportedly oxidized HMF, suggesting their potential broader application for detoxifying LB pretreatments (Serrano et al., 2019). Moreover, vanillyl-alcohol oxidases (VAOs) convert diverse para-substituted phenols into aromatic compounds such as vanillin and coniferyl alcohol. NADPH-dependent 1,4-benzoquinone reductases in yeast contribute to aromatic detoxification and oxidative stress mitigation, while overexpression of benzoquinone reductase in *Phanerochaete sordida* YK-624 enhanced metabolism of low-molecular-weight lignin fragments through quinone redox cycling and hydroxyl radical generation (Mori et al., 2016).

2.5.2. Physical detoxification approach

Physical detoxification methods remove inhibitors from lignocellulosic hydrolysates without introducing chemicals, enzymes, or microorganisms and their modifications. Physical detoxification can be achieved through membrane filtration, adsorption, evaporation, or steam stripping.

2.5.2.1. Membrane filtration: This is a size-exclusion separation process that effectively removes high-molecular-weight compounds and phenolic inhibitors from fermentable sugars. The technique operates by allowing smaller molecules to permeate a membrane while retaining larger ones. For instance, Pham et al. (2024) achieved lignin purification from mildly alkaline sugarcane extract using membrane filtration, with polysulfone membranes outperformed polyethersulfone membranes at a molecular weight of 10 kDa and 40 °C, while evaluating the effects of transmembrane pressure (bar), shear rate (s^{-1}), temperature (°C), and membrane molecular weight cut-off (kDa). Several modifications to membrane filtration, such as vacuum membrane distillation (VMD), layer-by-layer membranes, nanofiltration (NF), and reverse osmosis (RO), have been developed to enhance detoxification efficiency. Gupta et al. (2022) reported a hybrid NF-RO system in a comparative study that effectively removed inhibitors, including acetic acid, HMF, furfural, and vanillin, from hydrolysates while retaining fermentable sugars such as glucose, xylose, and arabinose. Similarly, Pan et al. (2019) demonstrated the high suitability of hybrid NF-RO systems (NF270, NF245, NF-Dow FilmTec, DK-GE Osmonics), achieving sugar retention rates above 94%. which translated to an increase in sugar titer from 38.4 g/L to 145.6 g/L, alongside inhibitor detoxification efficiencies of up to 80%. Moreover, Rathnayake et al. (2022) showed that the Alfa Laval NF99HF

nanomembrane purifies monosaccharides, retaining xylose (85%) and glucose (95%). Membrane performance depends on feed temperature, flux, pH, and solute concentration; however, fouling and high costs limit the large-scale feasibility.

2.5.2.2. Adsorption: Adsorption techniques utilize specialized porous solid-phase materials (adsorbents) to achieve selective physicochemical binding and subsequent removal of inhibitory species from fermentation hydrolysates. Examples of absorbents include activated carbon (AC) and pyrochar. Their adsorption efficacy is contingent upon a combination of adsorbent characteristics, such as surface area, pore size, and chemical properties, as well as prevailing environmental conditions, including temperature, pH, and contact time (Deng et al., 2018). This method offers an advantage over other physical methods by removing inhibitory compounds without modification, thereby allowing for the recovery of value-added inhibitors that can be further utilised industrially as valuable chemicals.

Activated carbon (AC) is produced from agricultural waste via thermochemical processes and effectively removes inhibitors, such as furfural, HMF, aromatic compounds, and short-chain organic acids, from hydrolysates (Sarawan et al., 2017). Preechakun et al. (2024) reported a 47.1–63.9% reduction of byproducts, including HMF and furfural, from hemicellulose-enriched sugarcane bagasse hydrolysate using AC with macroporous resin under 5-10% (w/v) loading, 4-70 °C, and 4 h treatment. Arminda et al. (2021) also achieved optimal removal (55% phenolics, 64% HMF, and 41% furfural) at 799.18 °C, a 4.88 impregnation ratio, and 101.38 min activation. However, sugar loss is a common occurrence. For example, AC from gasified açaí endocarp residues applied to sisal bagasse acid hydrolysate removed 52% of furfural, 100% of HMF, and 40.4% of acetic acid, but caused 17% sugar loss (do Nascimento et al., 2021).

Pyrochar, on the other hand, is produced via biomass pyrolysis (e.g., agricultural residues, wood chips, anaerobic digester sludge) and is a stable adsorbent with high surface area and porosity, applied in soil amendment, carbon sequestration, and lignocellulosic hydrolysate detoxification. Pyrochar from solid anaerobic digestates effectively removed >94% of HMF and 99% of furfural at 40 g/L within 24 h, while preserving sugars (Monlau et al., 2015). Pyrochar-based catalysts synthesized at 400 °C enhanced cellulose conversion by 16.00- 0.50%, outperforming hydrochar-based catalysts, which yielded 11.14% glucose and 29.54% HMF removal (Liu et al., 2020).

2.5.2.3. Ion exchange resins: Ion exchange resins detoxify lignocellulosic hydrolysates by selectively adsorbing inhibitors such as phenolics, furfural, and HMF, typically after pH adjustment to optimize adsorption. A typical example is the ion exchange resin-335, enabling 58.9 % removal of acetic acid, 61.3 % removal of formic acid, 63.4 % removal of levulinic acid, and 43.0 % reduction in furan derivatives from acidic corncob hydrolysate (ACH) after 30 min of treatment with 1 M NaOH (Han et al., 2025). Using hydrophobic resin XAD-4, sequentially pretreated Pine Forest litter hydrolysate showed substantial inhibitor removal, increasing ethanol yield from 22.51 to 27.38 g/L (Pandey and Negi, 2024). Similarly, anion-exchange resin 335 achieved 90.13% acetic acid, 92.58% furfural, and 94.85% lignin removal from acidic corncob hydrolysate (Han et al., 2022). Advances in resin technology aim to improve selectivity and adsorption capacity while reducing sugar loss.

2.5.2.4. Steam stripping and vacuum evaporation: Steam stripping involves injecting steam into hydrolysates to volatilize and remove volatile organic compounds (VOCs) and other inhibitors (Zimbardi et al., 2022). While effective for volatile inhibitors, the process requires high energy input for steam generation and can catalyze the degradation of long-chain compounds into short-chain inhibitors; non-volatile inhibitors remain largely unaffected. Meanwhile, vacuum evaporation reduces volatile inhibitors while concentrating reducing sugars in hydrolysates (Jin et al., 2023). However, both steam stripping and vacuum evaporation cause fermentable sugar losses and require significant energy input

2.5.3. Chemical detoxification

The chemical detoxification approach involves employing chemicals to remove or reduce the concentration of inhibitory compounds through precipitation, ionisation, and chemical reactions, thereby improving the fermentability of lignocellulosic hydrolysates. Various chemical strategies have been explored and developed to detoxify inhibitory compounds, each with unique mechanisms and effectiveness (Sjulander and Kikas, 2020). These methods include solvent extraction, ionic liquids, ozonolysis, overliming, and the addition of specific chemical agents, such as sodium borohydride, sulfur oxyanions, salts, and amino acids.

2.5.3.1. Solvent extraction: This is an extractive detoxification technique that can be achieved using solvent systems that simultaneously reduce inhibitor toxicity and generate solvents suitable for reuse. One promising approach is the deep eutectic solvents (DESs), which enhance bioprocess efficiency by selectively removing inhibitors from lignocellulosic hydrolysates. The extraction efficiency depends on the physicochemical properties of DESs, particularly their

ability to form hydrogen bonds and van der Waals interactions with inhibitor molecules (Makoś et al., 2020). Moreover, DESs are characterised by their low toxicity, biodegradability, and ease of synthesis, as well as their potential for regeneration, making them environmentally sustainable compared to conventional solvents (Cronin et al., 2020; Socas-Rodríguez et al., 2020). Beyond detoxification, DES-based extraction enables the recovery of high-purity lignin, improving the economic viability of lignocellulosic biorefineries. Despite these advantages, several challenges persist, including the need to optimize DES formulations to enhance inhibitor removal without significant sugar loss, ensuring the process is scalable for industrial applications, and evaluating the long-term environmental impacts of DES components.

2.5.3.2. Ionic liquids (ILs): Ionic liquids represent a promising approach for detoxifying fermentation inhibitors from lignocellulosic hydrolysates. This process involves the use of hydrophobic phosphonium ILs, such as phosphinate and neodecanoate, which selectively extract inhibitors while preserving fermentable sugars (Tonova et al., 2024). This selective extraction depends on process parameters, including temperature, pH, and the IL-to-hydrolysate ratio, which must be optimized to maximize inhibitor removal while minimizing sugar loss (Bhat et al., 2024). Additionally, IL regeneration and recycling improve process sustainability. Compared to ion-exchange resins, ILs achieve higher sugar retention, although resins may be more efficient for phenolic and furfural removal (Makoś-Chełstowska et al., 2023). Despite their effectiveness, the potential toxicity and cost of ILs remain limiting factors. Integrating ILs with complementary detoxification methods, such as membrane extraction or deep eutectic solvents (DESs), can enhance economic feasibility, reduce costs, and improve overall inhibitor removal efficiency (Makoś et al., 2020).

2.5.3.3. Ozone treatment: Ozone treatment, through ozonolysis, selectively oxidizes inhibitors without significant cellulose or sugar degradation, offering advantages over other oxidative treatment methods. At low dosages, it effectively reduces aromatic compounds, furfural, and HMF by approximately 50%, enhancing hydrolysate fermentability. However, due to the reactive nature of ozone, higher ozone dosages increase total acid content, particularly formic acid, leading to poor fermentability and rendering the hydrolysate less suitable for fermentation.

2.5.3.4. Overliming: Overliming is an LB detoxification mechanism that involves the introduction of alkaline agents like calcium hydroxide ($Ca(OH)_2$) to increase LB hydrolysate pH, facilitating the precipitation and removal of toxic compounds, furans, and phenolics, while

leaving some carboxylic acids, such as acetic acid, largely unaffected (Promta et al., 2024). For instance, in an optimized overliming detoxification study of sugarcane bagasse hydrolysate for bioethanol production, Promta et al. (2024) reported 38.37% removal of total furans and 50.02% removal of total phenolics at pH 9.5, 40°C, and a 60-minute reaction time, while poplar hydrolysates achieved 75.6% furan and 68.1% aromatic removal (Zhang et al., 2018). The effectiveness of overliming is dependent on parameters such as pH, temperature, and treatment duration. The pH level is critical, with a high pH (e.g., 12) improving inhibitor removal, but it can also cause up to 70% sugar loss (Zhang et al., 2018). To mitigate this drawback, optimizing detoxification processes and combining overliming with complementary methods can enhance overall effectiveness. For example, the sequential treatment of LB hydrolysate with overliming and activated carbon (AC) has proven to be more effective than either method alone, as AC can remove more phenolic acids, complementing the removal of dialdehydes and diketones (Zhang et al., 2018).

2.5.3.5. Sodium borohydride ($NaBH_4$) treatment: $NaBH_4$ acts as a reducing agent, reducing ketone and aldehyde groups to hydroxyls, neutralizing furans and phenolics, and preserving fermentable sugars (Cavka and Jönsson, 2013; Wang et al., 2020). Peinado et al. (2019) reported that treating olive-tree pruning hydrolysate with 0.03 mol/L $NaBH_4$ at pH 6.0 for 30 min detoxified ~100% of furans and 40% of phenolics, enabling previously unfermentable liquors to yield a 27% increase in bioethanol under optimal conditions. Cavka and Jönsson (2013) similarly reported that mild $NaBH_4$ treatment (20°C, pH 6.0) reduced inhibitors (aldehyde, p-benzoquinone, 2,6-dimethoxybenzoquinone, furfural) in Norway spruce and sugarcane bagasse hydrolysates, improving glucose consumption and raising bioethanol yield from 0.09 to 0.31 g/g and productivity from 0.05 to 0.57 g/L/h. Although $NaBH_4$ is a cost-effective detoxification method, its efficiency in removing inhibitors is generally lower than that of other techniques.

2.5.3.6. Sulfur oxyanions: Sulfur oxyanions, such as dithionite and sulfite reagents, act as reducing agents that neutralize toxic compounds in lignocellulosic hydrolysates via catalytic oxidation, targeting aldehydes and ketones and enhancing enzymatic hydrolysis and fermentation (Ilanidis et al., 2021). Sulfur oxyanions treatment of softwood hydrolysate at pH 5.5 or 8.5, 75 °C, by 5.0–12.5 mM intermediate dithionite concentration resulted in high bioethanol productivity and yield (Ilanidis et al., 2021).

2.5.3.7. Amino acid treatment: Amino acids with reactive side-chain functional groups, such as cysteine, histidine, and lysine, can react with carbonyl compounds in LB hydrolysates, forming less toxic products. Cysteine, for instance, utilises its thiol group to form thiazolidine carboxylic acids through Schiff base reactions with aldehydes, thereby mitigating inhibitory effects on yeast fermentation (Aboshi et al., 2022). Among various amino acids (including histidine, arginine, aspartic acid, and glutamic acid) evaluated by Liu et al. (2025), histidine demonstrated the highest inhibitor removal efficiency, of 91.2 %, a significant reduction in lignin content (from 35.7 % to 21.5 %), and an improvement in enzymatic hydrolysis efficiency, with glucose yields exceeding 60 % compared to 46.7 % in the control. In another report, detoxification of organosolv-pretreated pine hydrolysate with cysteine resulted in efficient removal of inhibitory compounds and enhanced butanol fermentation (Li et al., 2018). However, excessive cysteine can be toxic, limiting its application. Overall, physical, biological, and chemical detoxification methods face several constraints, including high costs, complex processes, long processing times, incomplete removal, toxicity, and potential loss of sugars. These limitations underscore the need for greener, sustainable, and selective strategies that maximize inhibitor removal while preserving fermentable sugars.

2.6. Nanoparticle-assisted detoxification: mechanisms and advances

Nanotechnology is a novel approach for detoxifying inhibitory compounds in pretreated LB hydrolysate, leveraging the unique physicochemical properties of nanoparticles (NPs), such as size, surface charge, and high surface area-to-volume ratio (Sanusi et al., 2021). The adsorption and degradative capacity of NPs is further influenced by reaction conditions such as temperature, pH, reaction time, pressure, stabilizing agents, mixing intensity, and redox potential (Sanusi et al., 2019). Together, these intrinsic properties and operational factors govern the effectiveness of NPs in inhibitor removal, ultimately enhancing the efficiency of biofuel production. The interaction between inhibitors and NPs may occur via selective or non-selective mechanisms, depending on the chemical nature of the inhibitors and the functionalization of the NPs' surface, which can be identified by characterization techniques and analytical tools. These include X-ray Diffraction (XRD) used to determine crystal structure, phase composition, and crystallite size; Transmission Electron Microscopy (TEM) which provide high-resolution images to determine morphology, particle size, and distribution; Scanning Electron Microscopy (SEM) which analyzes surface morphology and particle shape; Energy-Dispersive X-ray Spectroscopy (EDS/EDX) which determines elemental composition in conjunction with SEM or TEM, and Fourier Transform Infrared Spectroscopy (FTIR) which

identifies surface functional groups and chemical bonds on Fe_3O_4 NPs (Ayub et al., 2020). UV-Vis Spectroscopy analyzes optical properties and Photoluminescence (PL), which measures optical emission properties (Oluwalana and Ajibade, 2021). Other tools include Thermogravimetric Analysis (TGA) and Dynamic Light Scattering (DLS) (Ahmed et al., 2024). Overall, nano-adsorbents exhibit significant potential for targeted removal of process inhibitors through different chemical and physical interactions. Consequent to the unique properties of nanoparticles (NPs), their application as adsorbents in the detoxification of various inhibitory compounds from LB hydrolysate remains promising for downstream fermentation processes. The adsorption performance of NPs depends on their type, surface area, chemical properties, and affinity for target inhibitors. Nanoadsorbents can be broadly categorized as carbon-based nanomaterials (CBNs) (which generally include carbon nanotubes (CNTs), graphene, fullerenes, carbon nanowires, carbon nanofibers, and graphene); metal-based nanomaterials; nanocomposites; and functionalized nanoparticles. Metallic and metal oxide NPs, such as Fe_3O_4 and other metallic nanoparticles (Fe, Al, Ni, Co, Au), have been widely investigated due to their magnetic properties, which enable facile separation, recovery, and reusability (Sanusi et al., 2021).

High porosity, strong magnetism, and adaptability to surface functionalization further enhance their suitability for biofuel applications. Fe_3O_4 NPs surface can be functionalised using different materials to confer extra characteristics, enhancing their efficacy and specificity. An example is seen in a study by Bishop et al. (2024) on the surface modification of Fe_3O_4 nanoparticles using poly (ethylene glycol) (PEG), tri-sodium citrate (TSC), chitosan-coated, and k-carrageenan (k-C), which enhanced the removal of metal ion contents up to 42.74-fold from waste sugarcane molasses. Xiang et al. (2023) investigated the detoxification of acidic LB hydrolysates by two adsorbents, M-0 and M-1, synthesized with magnetic nanoparticles and lignin. M-1 demonstrated a high removal efficiency of 93.41% for ferulic acid and 53.12% for furfural, with minimal loss of sugar (Xiang et al., 2023). Moreover, metal-organic nanoframework (MOF-MIL-140C) tested by Li et al. (2021) demonstrated maximum adsorption capacities of 222.72, 240.38, 231.48, 207.04, and 60.79 mg/g for vanillin, syringaldehyde, ferulic acid, p-coumaric acid, and furfural, respectively.

The following section explores the application of nanoparticles in bioprocessing, with a focus on their mechanism of inhibitor removal and their application in bioethanol production.

2.6.1. Mechanisms of inhibitory compound removal from LB hydrolysates

The removal of inhibitory compounds from pretreated LB hydrolysate and other biochemical functions by NPs involve various interactions and adsorption mechanisms. Metallic nanomaterials (including Fe_3O_4) utilise various mechanisms (Fig. 2.6) such as adsorption by π-π interactions, hydrogen bonding and hydrophobic interactions, catalytic oxidation and degradation, complexation, surface functionalization, electrostatic interactions, and oxidation-reduction reactions (Table 2.4). Nanoparticle-inhibitor complexation occurs through chemical and physical interactions such as van der Waals forces, hydrogen bonding, π–π stacking, electrostatic interactions, and ionization of inhibitors (Dowlatabadi et al., 2019). The electrostatic interaction between nanoparticles and inhibitory compounds is critical, as the surface charges or functional groups of nanoparticles interact with charged inhibitory compounds in pretreated hydrolysates. For example, negatively charged Fe_3O_4-silica dioxide NPs interact with positively charged amino groups. The strength of NP-inhibitor adsorption can be assessed by measuring the zeta potential, which reveals the surface charge (Oluwalana et al., 2021). Additionally, electrostatic interactions can initiate NP surface functionalisation, enabling selective binding of target inhibitors to specific chemical groups (such as amines, thiols, and carboxyl groups), thereby facilitating their removal.

Fe_3O_4 nanoparticles can facilitate oxidation-reduction (redox) reactions that modify or neutralize inhibitory compounds in LB hydrolysates. In the oxidative state, Fe_3O_4 generates reactive oxygen species (ROS) via Fenton and Haber–Weiss reactions, degrading inhibitors into less harmful compounds (Mai and Hilt, 2017) while in the reductive state, zero-valent iron nanoparticles (nZVI) donate electrons to reduce furfural and HMF due to their high reactivity and ability to participate in redox reactions (Sulaiman et al., 2024). The adsorption of inhibitors such as phenolic compounds and furans is influenced by the nature of the adsorbent, the chemical properties of the inhibitors, and the conditions of the adsorption process. According to Li et al. (2021), phenolic adsorption involves π–π interactions, hydrophobic forces, and pH-dependent hydrogen bonding/metal coordination, whereas furfural adsorption is primarily driven by π-π and hydrophobic interactions. Xiang et al. (2023) also reported that magnetic lignin-based adsorbents (M-0 and M-1) removed ferulic acid (93.41%) and furfural (53.12%) with minimal sugar loss, primarily through π–π interactions and hydrogen bonding. Catalytic degradation is another mechanism by which nanoparticles (NPs) convert inhibitors into less toxic compounds.

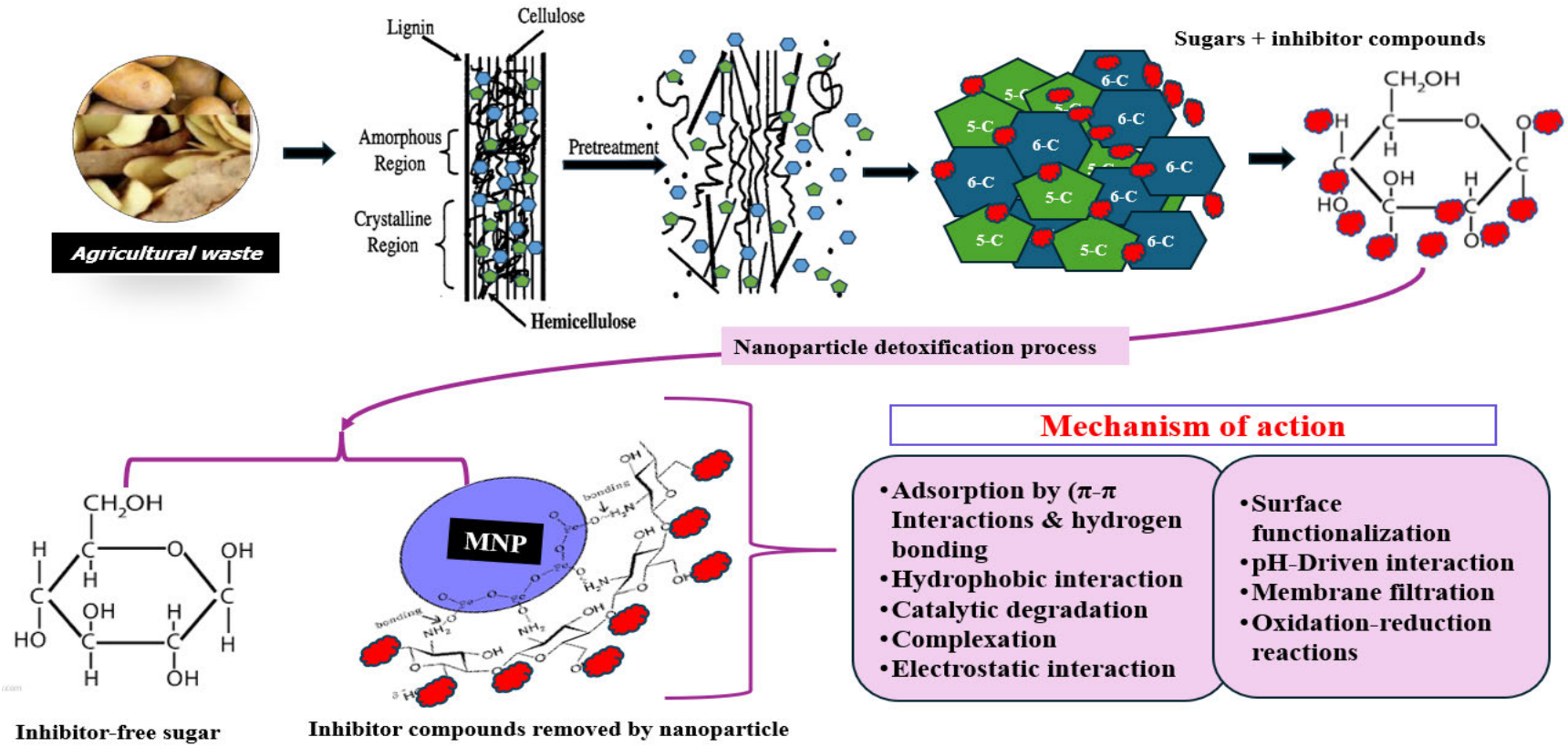

Figure 2.6. Detoxification mechanism of inhibitory compounds from LB.

Table 2.4. Mechanisms through which nanoparticles NPs remove inhibitory compounds from the hydrolysate of lignocellulosic biomass.

Mechanism	Description	Inhibitors Removable	Factors Influencing Efficiency	References
Adsorption by π-π Interactions and Hydrogen bonding	High surface area of nanoparticles provides numerous binding sites for inhibitor molecules.	Furfural, HMF, phenolics, organic acids	Nanoparticle surface area, porosity, functional groups, pH, temperature	Li et al., 2021
Hydrophobic Interaction	Nanoparticles with hydrophobic surfaces or coatings attract hydrophobic molecules, enhancing their removal.	Phenolics, lignin-derived compounds	Hydrophobicity of coating, solvent polarity	Xiang et al., 2023
Catalytic Degradation	Metal nanoparticles or metal oxide nanoparticles catalyze the conversion of inhibitors into less harmful compounds, reducing their toxicity.	Furfural, HMF	Catalyst type, particle size, reaction conditions (temperature, pressure, solvent)	Weerathunga et al., 2021 ; Pourali et al., 2022
Complexation	Metal ions in certain nanoparticles form complexes with inhibitors, removing them from the solution.	Organic acids, aromatic compounds	Metal ion type, solution pH, inhibitor structure	Khan et al., 2024
Surface Functionalization	Nanoparticles functionalized with specific chemical groups (e.g., amines, thiols, carboxyl) bind selectively to target inhibitors.	Aldehydes (HMF, furfural), organic acids	Type of functionalization, inhibitor concentration	Xiang et al., 2023
Membrane Filtration	Nanoporous materials enhanced with magnetic properties create membranes that selectively filter out inhibitors while allowing sugar passage.	Furfural, HMF, phenolic compounds	Pore size distribution, membrane material, operating conditions (pressure, flow rate)	Ma et al., 2024
Electrostatic Interaction	Surface-charged nanoparticles (such as Fe^{2+} and Fe^{3+} in Fe_3O_4-NP) interact with oppositely charged inhibitory compounds, facilitating binding and removal.	Organic acids, phenolic acids	Surface charge of nanoparticles, ionic strength	Sanusi et al., 2021
pH-Driven Interaction	Changes in pH influence the ionization of inhibitors and the surface charge of nanoparticles, affecting their removal efficiency.	Weak acids, phenolic compounds	Hydrolysate pH, isoelectric point of nanoparticles	Chen et al., 2017
Oxidation-Reduction Reactions	Nanoparticles facilitate redox reactions that modify or neutralize inhibitory compounds.	Phenolics, organic acids	Redox potential, nanoparticle composition	Oluwalana et al., 2021

The adsorption of inhibitors such as phenolic compounds and furans is influenced by the nature of the adsorbent, the chemical properties of the inhibitors, and the conditions of the adsorption process. According to Li et al. (2021), phenolic adsorption involves π–π interactions, hydrophobic forces, and pH-dependent hydrogen bonding/metal coordination, whereas furfural adsorption is primarily driven by π-π and hydrophobic interactions. Xiang et al. (2023) also reported that magnetic lignin-based adsorbents (M-0 and M-1) removed ferulic acid (93.41%) and furfural (53.12%) with minimal sugar loss, primarily through π–π interactions and hydrogen bonding. Catalytic degradation is another mechanism by which nanoparticles (NPs) convert inhibitors into less toxic compounds. For example, Fe_3O_4@GAC was shown to achieve a furfural degradation efficiency of 98.2% (Pourali et al., 2022), while Fe $(NiFe)O_4$-SiO_2 achieved 92.5% furfuryl alcohol yield via catalytic hydrogenation of furfural (Halilu et al., 2019). Moreover, NPs can enable photocatalytic and electrochemical degradation of furfural. For example, Au/γ-Al_2O_3 catalyzed oxidative esterification of HMF, reaching 99% conversion and 90% selectivity for dimethyl 2,5-furandicarboxylate (FDMC) at 45 °C (Weerathunga et al., 2021).

2.6.2. Impact of nanoparticle (Fe_3O_4 NPs) implementation on bioethanol production

Generally, LB valorisation for bioethanol production is achieved through multi-step processes, including pretreatment, hydrolysis, and fermentation, illustrated in Fig. 2.7. Magnetic nanoparticles (e.g., Fe_3O_4) have shown significant potential in enhancing these stages by acting as catalyst and electron transfer agents, detoxifiers of inhibitory compounds, or in improving microbial activity, some examples of which are summarized in Table 2.5. The inclusion of the nanoparticles in pretreatment has been reported to improve biomass degradation, ensure high sugar yield, and eliminate inhibitory by-products. Fe_3O_4 nanoparticles enhanced acid-pretreated corn stover hydrolysis, increasing xylose and glucose yields by 13-19% compared to the control. In addition, immobilized laccases on Cu^{2+}-modified magnetic nanoparticles achieved 40.76% degradation, improving cellulose-to-bioethanol conversion by 23.98%compared to non-treated biomass (Martinez et al., 2022). Similarly, nanobiocatalyst-assisted pretreatment of waste potato peels yielded higher bioethanol concentrations (0.93 g/g), 2.2-fold greater than previously reported (Sanusi et al., 2021).

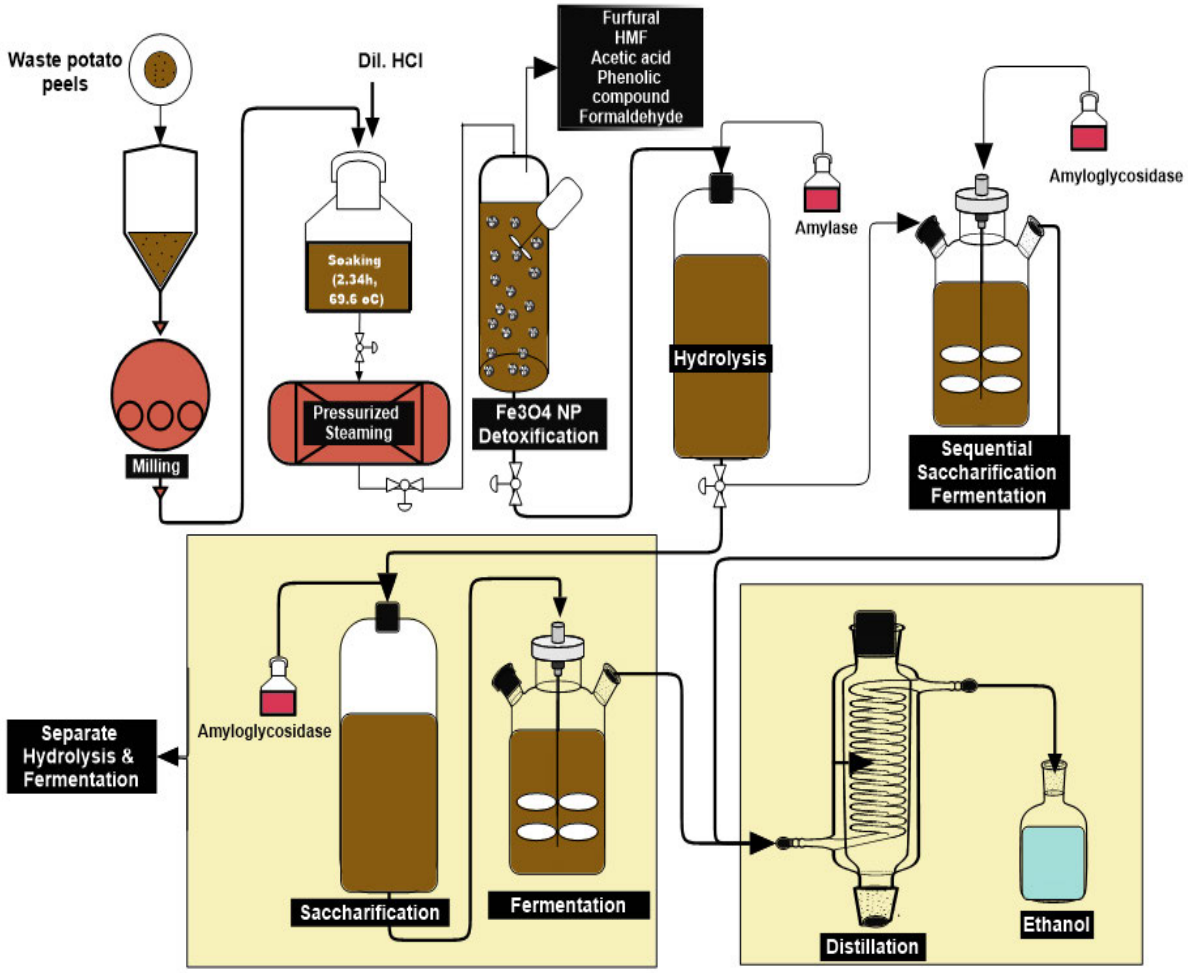

Figure 2.7. Typical implementation of Fe_3O_4 NP detoxification for bioethanol production.

Table 2.5. Nanoparticles in Bioethanol Production: Feedstock, Reaction Conditions, and Yield Improvements.

Feedstock	**Nanomaterial**	**Reaction Conditions**	**Microorganism**	**Nanoparticle Concentration**	**Yield / % Yield Increase**	**Remarks**	**Reference**
Golden trumpet flower (*Allamanda schotti*i L)	Cellulase-immobilised Fe_3O_4	Temp = 35°C, pH = 5.5, Time = 72 h	S. *cerevisiae* immobilised on Jute fibre, Sugarcane bagasse, Coconut coir, Sodium alginate, Free cells	-	235 g/L, 228 g/L, 218 g/L, 196 g/L, 182 g/L	Metallic nanoparticles enhance bioethanol production from various feedstocks	Vijayalakshmi et al., 2021
Sugarcane leaves	MnO_2	Temp = 70°C, pH = 4.8, Time = 2 h	-	-	21.96 g/L	Improved bioethanol yield	Cherian et al., 2015
Syngas	SiO_2–CH_3	Catalyst size = 76 nm, Temp = 37°C, Time = 60 h	*Clostridium ljungdahlii*	0.3 wt%	166.1%	Enhanced bioethanol yield	Kim et al., 2014
Syngas	$CoFe_2O_4$@SiO_2–CH_3	Catalyst size = 300 nm, Temp = 37°C, Time = 60 h	*Clostridium ljungdahlii*	0.3 wt%	213.5%	Superior bioethanol yield	Kim and Lee, 2016
Potato peel waste	NiO	Temp = 32.25°C, pH = 4.86, Time = 30 h	*Saccharomyces cerevisiae BY4743*	0.05 wt%	31.58 g/L, 59.96%	Improved product yield	Sanusi et al., 2020
Potato peel waste	ZnO	Temp = 38°C, pH = 4.86, Time = 5 days	*Saccharomyces cerevisiae*	150 mg/L	33.16%	Bioethanol yield increased	Attia et al., 2022
Rice straw	ZnO	Catalyst dosage = 0.05 wt%, Temp = 20–25°C, pH = 6–8, Time = 72 h	*Fusarium oxysporum*	200 mg/L	125.7%	ZnO nanoscale enhances bioethanol production	Gupta and Chundawat, 2020
Dairy yeast	Silicon dioxide	Temp = 37°C, pH = 7, Time = 36 h	Kluyveromyces *lactis*	-	150 g/L	Improved bioethanol production	Beniwal et al., 2018
Banana peel waste	NiO	-	*Pichia kudriavzevii* IFM 53048	0.01 wt%	190%	Enhanced bioethanol yield	Nduka et al., 2024

Various enzymes, such as β-glucosidase, β-Galactosidase, amylase, amyloglucosidase, cellulase, laccase, cellobiose, and xylanase, have been immobilized on nanomaterials to enhance catalytic potential and stability. Kaur et al. (2021) immobilised cellulase produced from *Aspergillus fumigatus* onto magnetic nanoparticles using glutaraldehyde as a cross-linking agent, achieving a binding efficiency of 65.55%. The immobilised enzyme attained a saccharification efficiency of 52.67% on pretreated rice straw hydrolysate and could be reused for up to four consecutive saccharification cycles, retaining 50.34% of its initial activity. Moreover, John et al. (2023) reported the immobilization of the hydrolytic enzyme cellulase on Fe_3O_4/GO/CS nanocomposites, achieving 99% activity retention after four reuse cycles. The process yielded 7.32 g/L ethanol from pretreated wheat bran and 7.05 g/L ethanol from pretreated rice bran following fermentation with *S. cerevisiae*.

Ingle et al. (2017) compared free and immobilized cellulase on iron oxide nanoparticles from *Alternaria alternata* for sugarcane bagasse hydrolysis at varying temperatures. During the first hydrolysis cycle, the free enzyme transforms 78% of cellulose into glucose and immobilizes only 72% after 24 h at 40 ^{o}C. Moreover, the immobilised cellulase was reused in two subsequent process cycles, with conversions of 68% and 52% cellulose into glucose, respectively. The reduction in enzymatic hydrolysis observed after the first cycle is consistent with the loss of enzyme (such as cellulase) activity reported earlier by Singhvi and Kim (2020). For β-galactosidase, Beniwal et al. (2018) demonstrated covalent immobilization of β-galactosidase from *Kluyveromyces lactis* enzyme on SiO_2 nanoparticles, conferring thermal/pH stability and effectiveness after 15 reuses for cheese whey hydrolysis.

Similarly, Park et al. (2018) observed enhanced thermal stability and catalytic activity for β-galactosidase immobilized on magnetic nanoparticles using p-nitrophenyl β-D-glucoside for bioethanol synthesis. Magnetite NPs (Fe_3O_4-NH_2) have been used to enhance bioethanol production via laccase immobilization for corn stover delignification. Cellulase-immobilized magnetic NPs improved the hydrolysis of golden trumpet flower (*Allamanda schottii* L.), followed by fermentation with *S. cerevisiae* immobilized on jute fibre, sugarcane bagasse, coconut coir, sodium alginate, and free cells, yielding 235, 228, 218, 196, and 182 g/L of bioethanol, respectively (Vijayalakshmi et al., 2021) (Table 2.5).

Cherian et al. (2015) examined *Aspergillus fumigatus* JCF-derived cellulase immobilized on MnO_2 nanoparticles retained 60% catalytic activity after five cycles and produced 21.96 g/L of

bioethanol using SSF. Immobilized nanobiocatalysts generally improve saccharification and thermostability compared to free enzymes. For example, glutaraldehyde-crosslinked *T. reesei* cellulase immobilized on MNPs hydrolyzed hemp hurd (Devi et al, 2021). Similarly, thermostable β-glucosidase from *A. niger* immobilized on MNPs achieved 93% immobilization efficiency and 50% activity retention after several cycles. Immobilized cellulases reused for five cycles exhibited stability across a wide pH and temperature range. In another case, cellulase immobilized for sugarcane leaf hydrolysis produced 22 g/L bioethanol, outperforming free enzyme systems (Singhvi and Kim, 2020).

Beyond acting as carriers for immobilised enzymes, Fe_3O_4 NP may be directly employed for inhibitor degradation or removal, independent of enzymatic activity, as shown by Bishop et al. (2024), who reported 29.05% and 53.53% reductions in 5-HMF and furfural, respectively. Sanusi et al. (2019) also suggested direct removal of inhibitory compounds after implementing Fe_3O_4 NP inclusion in the production of ethanol from PPW. However, the mechanisms underlying nanoparticle–inhibitor interactions remain poorly understood, highlighting the need for comprehensive studies. Such investigations are critical for optimizing detoxification strategies, improving microbial performance, and ultimately enhancing the efficiency and economic viability of bioprocesses.

2.7. Microbial fermentation of lignocellulosic hydrolysates

2.7.1. Bioethanol process development

Bioethanol production is achieved through multi-step processes, including pretreatment, hydrolysis, fermentation, and their modifications. Pretreatment disrupts the recalcitrant LB structure, releasing cellulose and hemicellulose, which are then hydrolysed into fermentable sugars (glucose, xylose, etc.), usually via enzymatic hydrolysis (Chohan et al., 2020). Meanwhile, these sugars are subsequently fermented into ethanol, with yield and productivity largely dependent on microorganism selection and process optimisation due to inhibitory compounds in hydrolysates. Bioethanol-producing microbes include *S. cerevisiae*, non-*Saccharomyces* yeasts (such as *Candida*, *Kloeckera*, *Hanseniaspora*, *Brettanomyces*, *Pichia*, *Lanchacea* and *Kluyveromyces* spp.), thermophilic microorganisms (such as *Geobacillus thermoglucosidasius* and *Thermoanerobacterium saccharolyticum*), and bacteria (such as *Zymomonas mobilis* and other microorganisms, including *Clostridium* species, which metabolise fermentable sugars under microaerophilic or anaerobic conditions to produce bioethanol (González-Gloria et al., 2024).

S. cerevisiae produces ethanol through the Embden-Meyerhof-Parnas (EMP) pathway, where intracellular glucose is converted to pyruvate coupled with the oxidation of NAD+ to NADH through glycolysis. Pyruvate is decarboxylated to acetaldehyde by pyruvate decarboxylase and subsequently reduced to ethanol by alcohol dehydrogenase, regenerating NAD^+ from NADH (Fig. 2.8). *S. cerevisiae* strains lack the ability to ferment pentose sugars (e.g., xylose and L-arabinose) due to the absence of key pentose-metabolising enzymes, limiting their efficiency on LB hydrolysate. In contrast, *Zymomonas mobilis* employs the Entner–Doudoroff pathway to generate pyruvate and, like *S. cerevisiae*, yields ~2 moles of ethanol per mole of hexose (Xia et al., 2019).

Moreso, acetogenic bacteria can produce ethanol via the Wood–Ljungdahl pathway using syngas as a substrate, which represents an alternative bioethanol production strategy (Jang et al., 2023). *P. stipitis* (also known as *Scheffersomyces stipitis*) is a non-conventional yeast capable of cellulosic ethanol production due to its natural ability to metabolise a broad spectrum of sugars (glucose, xylose, mannose, galactose, and cellobiose) present in saccharified lignocellulose. Unlike *S. cerevisiae*, *P. stipitis* metabolizes xylose, a five-carbon sugar (pentose), through a slightly different pathway called the pentose phosphate pathway (PPP). In this route, xylose is reduced to xylitol by xylose reductase (XR) using NADH/NADPH as a cofactor, oxidised to xylulose by xylitol dehydrogenase (XDH) using NAD^+, and phosphorylated by xylulokinase (XK) to xylulose-5-phosphate, which enters the PPP and links to glycolysis through pyruvate formation (Bertels et al., 2021). The ability of *P. stipitis* to naturally ferment xylose and, complementarily, glucose, makes it suitable for co-culture with *S. cerevisiae*, enabling efficient utilisation of both hexose and pentose sugars present in LB hydrolysates.

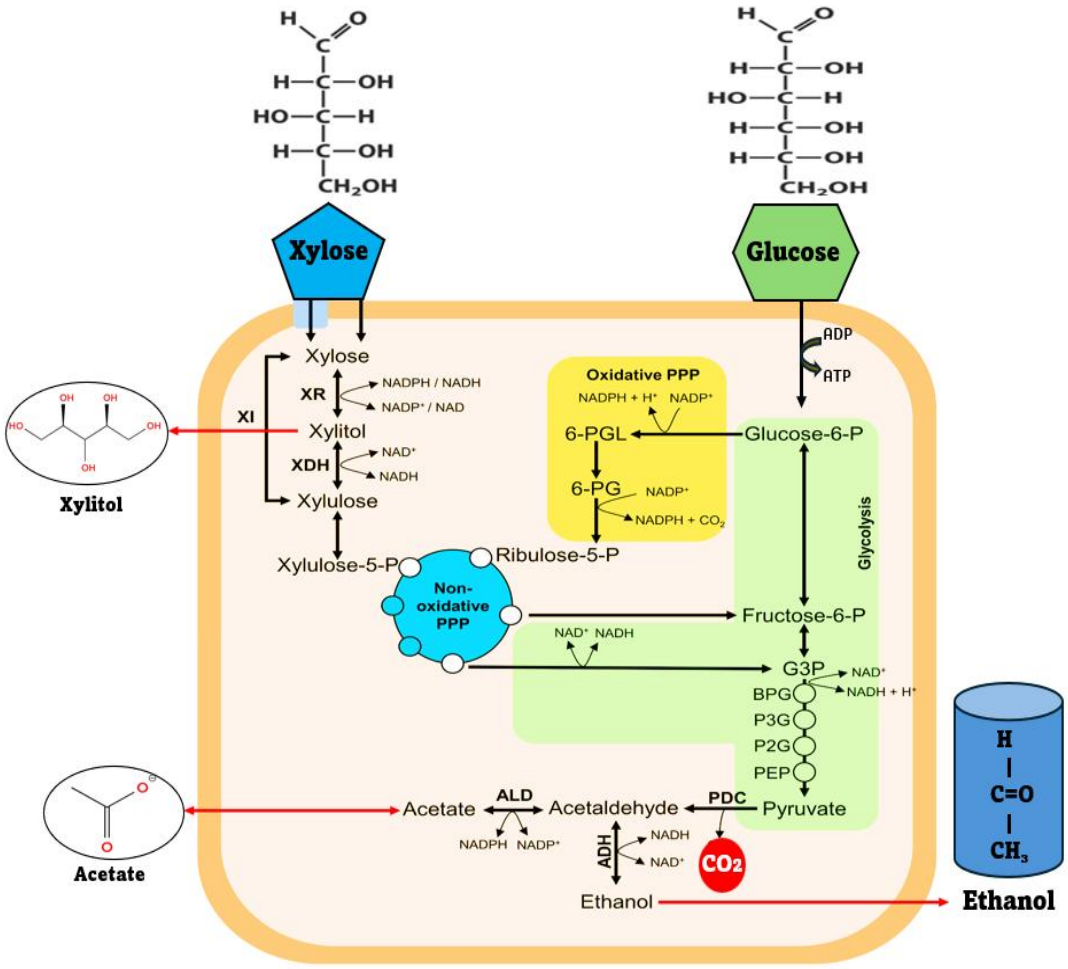

Figure 2.8. Glucose and xylose metabolism in yeasts (Adapted from Ochoa-Chacón et al., 2022)

XI, xylose isomerase; XR, xylose reductase; XDH, xylitol dehydrogenase; XK, xylulose kinase; PPP, pentose phosphate pathway; G3P, glyceraldehyde-3-phosphate; PDC, pyruvate decarboxylase; ADH, alcohol dehydrogenase; ALD, aldehyde dehydrogenase

2.7.2. Microbial fermentation mode

Beyond conventional batch, fed-batch, and continuous fermentation, several advanced strategies have been developed, including separate hydrolysis and fermentation (SHF), simultaneous saccharification and fermentation (SSF), pre-saccharification and SSF (PSSF), consolidated bioprocessing (CBP), and consolidated bio-saccharification (CBS), with more still under exploration. These approaches, which either separate or integrate key bioprocessing steps, significantly influence ethanol yield, downstream fermentation performance, and overall cost-effectiveness (Wang et al., 2024). SHF is a bioethanol production strategy in which

processing steps (i.e., pretreatment, enzyme production, saccharification, and fermentation) are conducted independently. This allows for optimization of each stage, leading to sugar-rich hydrolysates with minimal fermentation inhibitors, thereby enhancing ethanol yields (Lu et al., 2021). Notably, the inhibitors arising from each bioprocess step can be effectively managed in the controlled SHF environment. However, the independent nature of SHF increases operational costs due to the cumulative expenses incurred at each process step.

In the case of SSF, saccharification and fermentation occur concurrently in a single bioreactor, reducing operational costs and preventing sugar accumulation and its associated inhibition (Wang et al., 2024). However, SSF efficiency is often limited by differing optimal conditions for saccharification and fermentation, particularly high saccharification temperatures that can inhibit microbial activity, except in the case of thermophilic strains (Chavan et al., 2023). The pre-hydrolysis SSF is an upgrade of the SSF developed to avoid early carbon deficiency in SSF and to enhance the hydrolysis rate of cellulose or starch into glucose (Afedzi and Parakulsuksatid, 2023). PSSF (also known as fed-batch delayed SSF) is performed by exposing the pretreated hydrolysate to enzymatic degradation prior to the commencement of the SSF process. Consolidated Bioprocessing (CBP) integrates enzyme production, saccharification, and fermentation into a single system, utilizing engineered microorganisms that can simultaneously degrade lignocellulose and ferment sugars (Devi et al., 2021). CBP faces challenges such as inhibitor interference and inefficient utilization of sugar mixtures, as pretreatment-derived inhibitors can disrupt microbial cell membranes, protein synthesis, growth, and product formation (Lynd et al., 2022).

On a general note, the various fermentation strategies for bioethanol production offer both advantages and disadvantages in terms of nutrient retention and inhibitor control, and overall process cost. While simultaneous SSF offers low overall process costs, its practical application is often limited by challenges in process integration, such as enzyme adaptability and synchronizing saccharification with fermentation. To mitigate this drawback, enzyme optimization and microbial strain selection are employed to enhance synergistic efficiency (Zhang et al., 2024). Even with optimized SSF, co-utilization of pentose and hexose sugars may be inefficient, causing carbon catabolite repression where preferred sugars (e.g., glucose) inhibit metabolism of less preferred ones (e.g., xylose), leading to sugar accumulation, which results in catabolic or sugar inhibition and reduced ethanol yield (Policastro et al., 2021). This

limitation can be mitigated through microbial co-fermentation or co-culture to improve pentose utilization.

2.8. Co-fermentation strategies for enhanced ethanol yield

2.8.1. Co-fermentation strategies

The microbial co-fermentation (or co-culture) strategy in bioprocessing is a promising approach for enhancing product formation by cultivating multiple microbial strains with complementary metabolic pathways, enabling more efficient biomass conversion into value-added products (Miah et al., 2022). Co-culture systems can involve yeast–yeast, yeast–bacteria, or bacteria–bacteria interactions. Yeast-yeast co-cultures, such as *S. cerevisiae* with *Scheffersomyces stipitis* or *Torulaspora delbrueckii*, have been widely applied in ethanol and beer fermentations, respectively (Clausen and Junne, 2025). A typical yeast-bacteria system involves the co-inoculation of *Bacillus coagulans* and *Kluyveromyces marxianus* in synthetic media, enabling the simultaneous production of lactic acid (LA) from C_5 sugars (i.e., xylose) and bioethanol from C_6 (i.e., glucose/fructose), yielding 0.98 g/g LA and 0.51 g/g ethanol. In the same study, the valorisation of pomegranate peels achieved LA and bioethanol yields exceeding 90 % in comparison to the synthetic media (Demiray et al., 2024). Meanwhile, the starter cultures comprising *Lactobacillus delbrueckii* subs. *bulgaricus* ATCC BAA-365 and *Streptococcus thermophilus* LMG, routinely employed in the production of yogurt, are examples of bacteria co-cultures (Ulmer et al., 2023).

The choice of co-culture strategies adopted per time is dependent on the target product to be generated. In ethanol production, *S. cerevisiae* is commonly co-cultivated with yeasts such as *Scheffersomyces stipitis* (*P. stipitis*), *S. diastaticus*, *Kluyveromyces marxianus*, *Zymomonas mobilis*, and fungi like *Trichoderma reesei*. For instance, the co-culture of *S. cerevisiae* and *P. fermentans* in a single-vessel electrochemical bioreactor using wheat straw hydrolysate achieved a power density of 77.5 mW m^{-2} and an ethanol concentration of 8.7% (w/v) (Shrivastava and Sharma, 2024). Since the goal of downstream fermentation is the improvement or complete conversion of LB sugars (both pentoses and hexoses) into value-added products at minimal process cost, the simultaneous saccharification and co-fermentation (SSCF) involving *S. cerevisiae* and *P. stipitis* has emerged as a promising approach to ensure the complete sugar assimilation, thereby improving the overall process efficiency (Naseeruddin et al., 2021). The co-fermentation of *S. cerevisiae* and *P. stipitis* enables efficient utilization of both hexoses (by *S. cerevisiae*) and pentoses, particularly xylose (by *P. stipitis*), maximizing

sugar conversion from LB for higher ethanol yields (Miah et al., 2022). Different feedstocks have been explored using a co-culture of *S. cerevisiae* and *P. stipitis* to enhance ethanol production. For example, sweet sorghum juice fermented by the co-cultures of *P. stipitis–S. cerevisiae* and *P. stipitis–K. marxianus* yielded 29.45g/L and 31.87 g/L of ethanol, respectively (Phukoetphim et al., 2017). Immobilized co-cultures of *S. cerevisiae* PE-2 and *P. stipitis* achieved a 4-fold and 3-fold increase in ethanol productivity compared to monocultures of axenic *S. cerevisiae* and *P. stipitis,* respectively (Rodrigues et al., 2024). For instance, the co-fermentation of *S. cerevisiae* TA2 and *W. anomalus* HCJ2F significantly improved ethanol yield compared to the monocultures of *S. cerevisiae* TA2 and *W. anomalus* HCJ2F under laboratory conditions (Hawaz et al., 2024). Collectively, these findings highlight the promise of SSCF-based co-cultures in overcoming single-strain limitations, with further potential from introducing additional strains to metabolize residual sugars and enhance overall efficiency.

However, limited nutrient availability can trigger competition among microbial species, leading to the accumulation of metabolic by-products that inhibit cellular processes. For instance, co-cultivation of *Lactobacillus fermentum* with a wild *S. cerevisiae* strain during fuel ethanol fermentation of sugarcane juice and molasses resulted in reduced ethanol yields and higher residual sugar levels. The wild yeast exhibited slower sugar consumption rates and a strong preference for glucose over fructose, causing incomplete fermentation. Meanwhile, the presence of *L. fermentum* promoted the growth of contaminants such as *D. bruxellensis*, further aggravating fermentation inefficiencies (Reis et al., 2018). Such antagonistic microbial interactions, combined with the accumulation of inhibitors during LB hydrolysis and fermentation, can be effectively mitigated by applying nanoparticles either post-pretreatment or during hydrolysis (Mohapatra et al., 2020).

Furthermore, the simultaneous saccharification and co-fermentation (SSCF) strategy may face several limitations, necessitating precise control of environmental parameters, including pH, temperature, and oxygen levels, to maintain enzymatic efficiency and microbial activity. These limitations, however, can be mitigated through advanced process optimization strategies (Aruwajoye et al., 2017).

2.8.2. Role of oxygen, pH, and cofactor balance in mixed-sugar fermentation

The efficiency of mixed-sugar fermentation in LB hydrolysates, particularly by yeasts such as *S. cerevisiae* and *P. stipitis*, is strongly influenced by environmental factors, including oxygen availability, pH, and intracellular redox balance.

2.8.2.1. Oxygen: Oxygen functions as a critical metabolic modulator in yeast fermentation, exhibiting distinct roles across different species (Duncan et al., 2024). For yeasts like *S. cerevisiae*, a fermentative metabolism is sustained even in the presence of oxygen under high-sugar conditions. Nevertheless, oxygen is indispensable for cellular anabolism, specifically for the synthesis of crucial cellular components such as sterols and unsaturated fatty acids, which are vital for maintaining membrane integrity and stress tolerance during subsequent anaerobic fermentation. Consequently, providing a limited amount of oxygen (microaerobic conditions) is often beneficial for robust biomass growth and higher ethanol yields. *P. stipitis*, a facultative anaerobe, fundamentally requires oxygen for the efficient fermentation of xylose; however, the specific oxygen uptake rate is a critical parameter for maximizing ethanol production. *P.* (*Scheffersomyces*) *stipitis* requires a low and well-controlled level of oxygenation with an optimal K_La range between 12–18 h^{-1} (0.36 g dm^{-3} h^{-1} approximately) for yeast metabolism and efficient ethanol production from xylose (Fonseca et al., 2018). This is due to the redox imbalance that occurs under anaerobic conditions, which can lead to xylitol formation instead of ethanol. Aerobic conditions can alter the NAD+/NADH and NADP+/NADPH ratios, which are pivotal for maintaining redox balance (Tyibilika et al., 2024). This modulation of the cellular redox state directly impacts metabolic pathways and can influence the production of various fermentation by-products.

2.8.2.2. pH: The pH of the fermentation medium is a critical parameter that affects microbial growth, sugar uptake, enzyme activity, and process performance. Most fermenting yeasts, including *S. cerevisiae* and *P. stipitis*, exhibit optimal growth and ethanol production within a slightly acidic range, typically between pH 4.5 and 5.5 (Song et al., 2019). The toxigenic impact of weak acid (like acetic acid), which is commonly associated with fermentation processes, is highly dependent on the extracellular pH (Antunes and Sá-Correia, 2024). At a low extracellular pH (below its pKa of 4.76), acetic acid exists primarily in its protonated, undissociated form, which can passively diffuse across the cell membrane and dissociates within the cell with the higher intracellular pH, releasing a proton and causing intracellular acidification that disrupts pH homeostasis (Antunes and Sá-Correia, 2024). This metabolic stress forces the cell to expend significant energy to actively pump out protons, leading to ATP depletion and the inhibition of metabolic enzymes, which ultimately reduces fermentation efficiency (Garrigós et al, 2025). Therefore, maintaining an optimal pH is crucial for mitigating inhibitor toxicity and ensuring efficient fermentation.

2.8.2.3. Cofactor balance: The intracellular balance of redox cofactors, specifically the NAD+/NADH and NADP+/NADPH ratios, is a critical determinant of efficiency in mixed-sugar fermentation (Han et al., 2021). This is particularly evident in the native xylose metabolic pathway of *S. cerevisiae*, which utilizes xylose reductase (XR) and xylitol dehydrogenase (XDH). This pathway creates a redox imbalance because XR preferentially consumes NADPH, whereas XDH uses NAD+, leading to a cofactor mismatch that often results in xylitol accumulation and reduced ethanol yield. To circumvent this, metabolic engineering strategies often involve introducing NADH-preferring XR or a xylose isomerase (XI) pathway, which bypasses the cofactor-dependent initial step entirely (Zhu et al., 2021). In the case of *P. stipitis* (the native xylose metaboliser), which is more redox-balanced, the presence of fermentation inhibitors like furan aldehydes (e.g., furfural and HMF) further complicates cofactor balance. In this regard, the enzymatic detoxification of these compounds consumes NAD(P)H, resulting in a significant redox drain that depletes the cell's reducing power (Jilani and Olson, 2023). This redirection of metabolic flux has a negative impact on overall cell viability and productivity. Therefore, developing an integrated detoxification and co-fermentation system offers a promising solution that mitigates inhibitor toxicity and enhances the utilization of mixed sugars under optimized process conditions.

2.9. Bioprocess optimisation and kinetics modelling

2.9.1. Fermentation process optimisation

The optimization and scaling of bioprocesses are central to advancing industrial biotechnology (Moodley and Kana, 2017). Fermentation bioprocess performance and product formation are inherently complex and are influenced by numerous biochemical and engineering parameters, including fermentation conditions, the strain of fermenting microbe, substrate type, and bioreactor configuration (Rorke *et al*., 2017). In bioprocess optimization, the traditional one-variable-at-a-time (OVAT) approach, where a single factor is varied while all others are held constant, offers limited applicability in complex biological systems. This method overlooks potential interactions between variables, which are often crucial to the performance of fermentation processes (Ibrahim and Abdul Wahab, 2024). Additionally, OVAT is time-consuming, resource-intensive, and constrained in its ability to explore multi-dimensional design spaces, making it unsuitable for systems governed by nonlinear dynamics and synergistic effects. Modern optimization strategies address these shortcomings by employing statistically robust and computationally efficient tools that can model variable interactions and

predict optimal process conditions. The fundamental objective is to define a multi-dimensional response surface that accurately identifies the conditions yielding maximal product formation (Ibrahim and Abdul Wahab, 2024).

To this end, techniques such as Response Surface Methodology (RSM) and Artificial Neural Networks (ANN) have become essential tools in fermentation bioprocess optimization, enabling simultaneous evaluation of multiple parameters, improved precision, and facilitate the translation of lab-scale findings to scalable, industrial applications. RSM is an effective method for modelling and optimising, which employs statistical and mathematical techniques to design experiments, model responses, and determine optimal conditions by capturing both linear and nonlinear effects of process variables (Gaitonde et al., 2017). RSM employs designed experiments such as Central Composite (CCD) and Box–Behnken to fit a second-order polynomial model that describes the relationships between process variables (e.g., pH, temperature, agitation speed) and responses (e.g., biomass, product concentration). This approach reduces experimental runs without compromising statistical validity and has been widely applied in ethanol production, enzyme synthesis, and microbial biomass optimization (Rorke et al., 2017; Bishop et al., 2024). For instance, optimization of pH, temperature, and inoculum size in a co-culture of *B. licheniformis* and *S. cerevisiae* on wheat straw increased bioethanol yields from 4.11 g/L to 14.70 g/L upon scale-up (Sharma et al., 2021).

Beyond conventional statistical methods, Artificial Intelligence (AI)-based tools have emerged as powerful assets in modelling and optimization of bioenergy, biofuel, and bioproduct processes. AI enables real-time process monitoring, adaptive control, and dynamic optimization, allowing for the efficient exploration of complex process interactions. This reduces experimental demands from large variable spaces that are often impractical to assess experimentally and accelerates scale-up.

Key AI-driven tools include Evolutionary Algorithms, Genetic Algorithms (GA) (Izquierdo et al., 2024), and Artificial Neural Networks (ANN) (Mansour et al., 2024). These methods are increasingly applied for parameter optimization, process prediction, and performance enhancement. Among them, ANNs have proven particularly effective for modelling nonlinear, multivariate systems in bioprocessing. Structured as layered networks of interconnected neurons, ANNs learn from data by adjusting connection weights through training, enabling them to capture complex relationships between input variables and process responses. Their

applications extend to process monitoring, optimization, hybrid modeling, and data-driven forecasting in both upstream and downstream operations (Taiwo and Musonge, 2023).

In addition to technical process improvements, AI models also offer support for economic analysis and commercialization planning. Hybrid AI approaches such as ANN-GA systems for multi-objective optimization, convolutional neural networks (CNNs), and retrieval-augmented generation (RAG) embedded in large language models (LLMs) are being increasingly explored for smart decision-making in bioprocess design. These tools enable virtual experimentation, reduce time-to-scale, and support the development of robust, cost-effective, and scalable biorefinery systems.

2.9.2. Kinetic modelling

Bioprocess modelling encompasses the mathematical representation and simulation of biological, physical, and chemical phenomena underlying substrate conversion into valuable products (Fedailaine et al., 2015). In microbial systems, kinetic models such as the logistic, modified Gompertz, Luedeking-Piret, and modified Luedeking-Piret models are widely used to describe cell growth, product formation, and substrate utilization, offering insights into microbial metabolic regulation and process dynamics (Germec et al., 2019). These models, developed from experimental data, enable predictive analysis that supports process optimization and scale-up by improving design, enhancing yields, minimizing by-products, and ensuring efficient resource utilization for industrial applications (Kucharska et al., 2018).

Additionally, adsorption kinetics modelling and thermodynamic models have been adapted and implemented to provide further mechanistic understanding of processes involving adsorbents, particularly nanoparticles. include pseudo-first-order, pseudo-second-order, Elovich, and intraparticle (Weber–Morris) diffusion models (Ayub et al., 2020), while adsorption isotherms such as Langmuir, Freundlich, and Temkin are employed to characterize mechanisms and interactions between adsorbent (such as NPs) and adsorbate (inhibitory compounds), determining maximum adsorption process efficiency.

2.10. Scale-up in lignocellulosic bioethanol production

Process scale-up studies are essential for translating optimised laboratory-scale bioprocesses into commercially viable industrial operations (de Mello et al., 2024). The scale-up of a fermentation process requires several important engineering considerations, which ultimately

dictate process performance. Key scale-up variables for an industrial-scale ethanol fermentation process include bioreactor geometry, mass and heat transfer, mixing efficiency, power consumption, bulk rheology, cell viability, microenvironmental conditions, nutrient availability, bioreactor configuration, and overall product yield (Nzimande et al., 2025). Among these factors, efficient mixing is particularly critical for achieving homogeneous nutrient and gas distribution, uniform microorganism suspension, and optimal mass transfer, heat removal, and reaction kinetics (Bisgaard et al., 2021). The importance of mixing becomes even more evident in high-solids fermentations (>15–20% dry matter), where viscous slurries restrict both mixing and aeration. Under such conditions, oxygen transfer emerges as a key limitation, particularly for microorganisms like *P. stipitis*, where high cell densities in large-scale reactors exacerbate the challenge. Consequently, enhanced agitation is necessary to maintain solids in suspension and facilitate effective enzyme–microbe interactions. Optimized mixing regime parameters like constant power input per unit volume (P/V), constant impeller tip speed, Reynolds' number, impeller pumping capacity (V_P), fluid circulation time (t_c), scale of turbulence determination (λ) and shear stress (τ) have been used to determine the operational efficiency of semi-pilot scale process to determine scalability potential and enhance productivity, yield, and product quality (Nzimande et al,, 2025). Constant P/V refers to the amount of power required to operate the bioreactor relative to the volume of the input liquid media. Meanwhile, constant impeller tip speed refers to a fixed linear velocity at the outermost edge of an impeller (blade tip) during mixing or agitation processes, even when scaling up or changing equipment. V_{tip} is directly proportional to the product of impeller speed and the impeller diameter. The P/V measures energy efficiency and the bioreactors' energy requirements, while impeller tip speed reveals the relationship between mixing efficiency, mass and heat transfer, substrate utilization, shear stress, and microbial cells (Lemire et al., 2022). The impeller pumping capacity (V_P) represents the volume of liquid discharged by the stirrer per unit time (m^3/ s), while the fluid circulation time (t_c) is a function of the volume of the liquid phase (V_L) and pumping capacity (V_P). The degree of turbulence within the bioreactor directly affects broth homogeneity and fluid-phase mass transfer efficiency, which is governed by the energy dissipation caused by eddy formation and breakup. The scale of turbulence, which reflects the smallest eddies that contribute to effective mixing and mass transfer, is estimated using the Kolmogorov microscale (λ). This parameter is a function of the energy dissipation rate per unit mass (ε), which in turn is related to the specific power input (P/V_L). Shear stress (τ) in a bioreactor is the force per unit area exerted on fluid elements, arising from the friction of adjacent fluid layers moving at different velocities (Nzimande et al., 2025). The

Froude [Fr], volume [N_v], and geometry [N_g] numbers (non-dimensional bioreactor parameters) express the ratio of centrifugal to gravitational forces, the ratio of impeller diameter (agitation diameter) to bioreactor diameter in relation to the filling volume, and the ratio of impeller diameter to bioreactor diameter, respectively. Industrial-scale bioreactor design for bioethanol fermentation depends on the comprehensive understanding and precise application of these scale-up criteria. Several reports involving batch SSF systems and their modified configurations, when coupled with Rushton impeller-equipped bioreactors, have demonstrated considerable promise in scaling lignocellulosic ethanol production. Ethanol concentrations exceeding 40 g/L have been consistently reported across diverse substrates. For instance, pulp and paper sludge at 22% (w/v) in a 3 L bioreactor yielded 42.34 g/L of ethanol (Dey et al., 2022). Even higher titers were achieved with sugarcane bagasse at 20% (w/v), yielding 57.2 g/L (Raj and Krishnan, 2020), and with *Prosopis juliflora* at 20% (w/v) in a 5 L bioreactor, yielding 52.83 g/L (Gupta et al., 2016). Collectively, these findings demonstrate the feasibility of attaining industry-relevant ethanol concentrations under optimized mixing and agitation conditions.

The ethanol yields reported further underscore the efficiency of SSF conversion strategies in a scale-up scenario. For instance, oil palm trunk fibre yielded 0.72 g/g (Tareen et al., 2021), while sugarcane bagasse demonstrated conversion efficiencies of 94.65% (Raj and Krishnan, 2020). Such variation reflects the influence of feedstock composition and recalcitrance, as well as the interplay between solids loading, enzymatic accessibility, and microbial performance. Importantly, high-solid loading up to 30% (w/v) poses associated challenges, including viscosity and mass transfer limitations, necessitating higher mixing efficiency for the industrial viability of these processes. Therefore, maintaining suitable and optimal operational process parameters is vital to sustain the homogeneity of substrate–nutrient concentrations and temperature gradients, preserve microbial integrity, and maximize productivity and product quality at an industrial scale.

2.11. Research gaps and future perspectives

Despite significant advancements in LB bioethanol production, particularly with the valorization of potato peel waste (PPW), key research gaps persist. Addressing these gaps is essential to overcoming existing challenges and accelerating the transition to a commercially viable, truly sustainable bioethanol industry. While the modes of microbial inhibition by inhibitors such as furfural, HMF, acetic acid, phenolics, and their derivatives are well-

understood, detailed studies specifically quantifying and characterizing the precise concentrations and synergistic effects of these inhibitors within PPW hydrolysates remain scarce. Most studies emphasize ethanol yield without establishing a specific inhibitory profile, limiting the design of targeted detoxification strategies. Comprehensive profiling of PPW hydrolysates under varied pretreatment conditions is therefore essential. Furthermore, optimizing or developing novel detoxification methods specifically tailored for PPW hydrolysates, such as exploring the efficacy of advanced adsorption materials and selective alternatives that minimize sugar loss and reduce operational costs. Developing a fermentation strategy (such as synergistic combinations of *S. cerevisiae* and *P. stipitis*) that possesses enhanced tolerance to PPW-specific inhibitors or can metabolize these inhibitors in situ during fermentation is crucial. This approach facilitates a more consolidated and economically viable bioprocess.

Nanoparticle-assisted detoxification offers a promising avenue for efficient inhibitor removal due to their high surface area and catalytic properties, typical of Fe_3O_4 nanoparticles. However, a significant research gap exists regarding the scalable, cost-effective recovery and recycling of these nanoparticles after treatment. The long-term stability and reusability of nanoparticles in complex hydrolysate matrices also need further investigation. Further research should focus on developing advanced separation technologies for nanoparticle recovery (e.g., magnetic separation for iron oxide nanoparticles) that are both energy-efficient and economically viable at a large scale. Emphasis should be placed on designing nanoparticles with inherent properties that facilitate easy, complete recovery without compromising detoxification efficiency or structural integrity across multiple cycles.

To this end, bioprocess optimization is critical, as it provides a comprehensive understanding of process efficiency, productivity, and yield comparison, as well as process economics, and potential scale-up considerations that are vital for tailoring strategies to meet specific production goals. However, there is a paucity of studies on the optimization of key input parameters that form part of the feasible process conditions for synergistic nanoparticle detoxification, inoculum development, and SSCF strategy. Integrating Generative AI tools, such as Artificial Neural Networks (ANN), could advance optimization and sensitivity testing by combining numerical and qualitative insights while enabling dynamic adjustments for scale-up performance.

Furthermore, there is a dearth of knowledge on the kinetic modelling of *S. cerevisiae–P. stipitis* co-cultures, including growth dynamics, ethanol production, and sugar utilization from the detoxified hydrolysate, particularly, PPW. Such models are crucial for the industrial-scale-up of biofuels, such as ethanol, centred on waste utilisation and valorisation. Therefore, an in-depth understanding of these bioprocess kinetics is essential to enhance process feasibility, productivity, and design, thereby improving bioethanol yields and economic viability on a commercial scale.

Following process optimization and kinetic studies, transitioning laboratory-scale processes to industrial-sized production units remains challenging due to the need to ensure seamless integration of process operations such as pretreatment, enzymatic hydrolysis, and fermentation, while maintaining efficiency, increasing productivity, and minimizing energy consumption. Therefore, to achieve comparable conditions while maintaining product quality at larger scales, careful consideration of bioreactor geometry, hydrodynamic complexity, shear sensitivity, mass and heat transfer efficiency is required. Maintaining a uniform reactor environment and constant scale-up criteria such as constant V_{tip}, constant P/V, and revolution-per-second (rps) across scales is imperative for preserving biological activity and scale-up reproducibility. These considerations are essential for achieving economically viable bio-based production processes. Advancements in these approaches offer the potential to improve process efficiency, lower costs, and maximize resource utilization, thereby advancing the realization of sustainable and commercially viable LB biorefineries.

2.12. Conclusions

Lignocellulosic biomass bioethanol offers a renewable alternative to fossil fuels while promoting waste valorization within a circular bioeconomy. Potato peel waste, rich in fermentable carbohydrates (starch, cellulose, hemicellulose), represents a promising feedstock; however, pretreatment generates inhibitors (furfural, HMF, acetic acid, phenolics, formaldehyde) that interfere with microbial metabolism, reduce enzymatic activity, and severely limit fermentation efficiency. The detrimental impact of the inhibitory compounds is particularly pronounced in co-fermentation systems, where mixed cultures of hexose- and pentose-utilizing microorganisms, such as *Saccharomyces cerevisiae* and *Pichia stipitis*, synergistically metabolize mixed sugars in an inhibitor-laden environment. Nanoparticle-assisted detoxification (e.g., Fe_3O_4) emerged as a promising strategy, enabling effective removal of inhibitors while supporting co-fermentation for improved ethanol yields and

process stability. Integration with advanced process optimization and kinetic modelling further enhances predictive control and scalability.

Despite recent progress, critical gaps remain, including: (i) systematic optimization of nanoparticle detoxification parameters (dosage, pH, contact time, temperature); (ii) mechanistic elucidation of inhibitor–nanoparticle interactions; (iii) assessment of nano-detoxification impacts on microbial performance in co-culture systems; (iv) kinetic modelling of co-fermentation using detoxified hydrolysates; and (v) scale-up feasibility, particularly nanoparticle recovery, reusability, and energy efficiency. Addressing these gaps is essential for advancing nanoparticle-enabled PPW valorization toward economically viable, industrially scalable and environmentally sustainable bioethanol production technologies from agro-industrial residues.

References

Aboshi, T., Narita, K., Katsumi, N., Ohta, T. and Murayama, T., 2022. Removal of C9-aldehydes and-alcohols from melon juice via cysteine addition. Journal of the Science of Food and Agriculture, 102(13), 6131-6137. https://doi.org/10.1002/jsfa.11965.

Achinas, S., Li, Y., Achinas, V., Euverink, G. J. W., 2019. Biogas potential from the anaerobic digestion of potato peels: Process performance and kinetics evaluation. Energies, 12(12), 2311. https://doi.org/10.3390/en12122311.

Afedzi, A. E. K. and Parakulsuksatid, P., 2023. Recent advances in process modifications of simultaneous saccharification and fermentation (SSF) of lignocellulosic biomass for bioethanol production. Biocatalysis and Agricultural Biotechnology, 102961. https://doi.org/10.1016/j.bcab.2023.102961.

Aguilar-Reynosa, A., Romaní, A., Ma. Rodríguez-Jasso, R., Aguilar, C. N., Garrote, G., Ruiz, H.A. 2017. Microwave heating processing as alternative of pretreatment in second-generation biorefinery: An overview. Energy Conversion and Management, 136, 50-65. https://doi.org/10.1016/j.enconman.2017.01.004.

Ahmed, J., Sajjad, M., Shakir, H.A., Khan, M., Franco, M. and Irfan, M., 2024. Magnetic Nanocatalysts for Biofuel Production. In Agricultural Biomass Nanocatalysts for Green Energy Applications, 145-172. Singapore: Springer Nature Singapore. https://doi.org/10.1007/978-981-97-1623-4_7.

Al Mamari, H.H., 2021. Phenolic compounds: Classification, chemistry, and updated techniques of analysis and synthesis. Phenolic compounds-chemistry, synthesis, diversity, non-conventional industrial, pharmaceutical and therapeutic applications, 10. https://doi.org/10.5772/intechopen.98958.

Alio, M.A., Tugui, O.C., Rusu, L., Pons, A., Vial, C., 2020. Hydrolysis and fermentation steps of a pretreated sawmill mixed feedstock for bioethanol production in a wood biorefinery. Bioresour. Technol., 310, 123412. https://doi.org/10.1016/j.biortech.2020.123412.

Andérez-Fernández, M., Ferrero, S., Queiroz, J.P., Pérez, E., Álvarez, C.M., Martín, Á. and Bermejo, M.D., 2022. Formic acid production by simultaneous hydrothermal CO_2 reduction

and conversion of glucose and its derivatives. Journal of the Taiwan Institute of Chemical Engineers, 139, 104504. https://doi.org/10.1016/j.jtice.2022.104504.

Antunes, M. and Sá-Correia, I., 2024. The role of ion homeostasis in adaptation and tolerance to acetic acid stress in yeasts. FEMS Yeast Research, 24, p.foae016. https://doi.org/10.1093/femsyr/foae016.

Anu, A., Kuhad, R.C., Rapoport, A., Kumar, V., Singh, D., Kumar, V., Tiwari, S.K., Ahlawat, S. and Singh, B., 2024. Biological pretreatment of lignocellulosic biomass: An environment-benign and sustainable approach for conversion of solid waste into value-added products. Critical Reviews in Environmental Science and Technology, 54(10), 771-796. https://doi.org/10.1080/10643389.2023.2277670.

Anu, A., Kumar, V., Singh, D., 2021. A greener, mild, and efficient bioprocess for the pretreatment and saccharification of rice straw. Biomass Conversion and Biorefinery, 13, 4121-4133. https://doi.org/10.1007/s13399-021-01450-9.

Arapoglou, D., Varzakas, T., Vlyssides, A., Israilides, C., 2010. Ethanol production from potato peel waste (PPW). Waste Manag., 30, 1898-1902. https://doi.org/10.1016/j.wasman.2010.04.017.

Arefmanesh, M., Vuong, T.V., Nikafshar, S., Wallmo, H., Nejad, M. and Master, E.R., 2022. Enzymatic synthesis of kraft lignin-acrylate copolymers using an alkaline tolerant laccase. Applied microbiology and biotechnology, 106(8), 2969-2979. https://doi.org/10.1007/s00253-022-11916-z.

Arminda, M., Josúe, C., Cristina, D., Fabiana, S. and Yolanda, M., 2021. Use of activated carbons for detoxification of a lignocellulosic hydrolysate: Statistical optimisation. Journal of Environmental Management, 296, 113320. https://doi.org/10.1016/j.jenvman.2021.113320.

Aruwajoye, G. S., Faloye, F. D., Gueguim Kana, E. B., 2017. Soaking assisted thermal pre-treatment of cassava peels wastes for fermentable sugar production: process modelling and optimization, Energy Convers. Manage. 2017; 150: 558-556. http://dx.doi.org/10.1016/j.ijhydene.2014.01.163.

Ashokkumar, V., Venkatkarthick, R., Jayashree, S., Chuetor, S., Dharmaraj, S., Kumar, G., Chen, W.H. and Ngamcharussrivichai, C., 2022. Recent advances in lignocellulosic biomass

for biofuels and value-added bioproducts: A critical review. Bioresource technology, 344, 126195. https://doi.org/10.1016/j.biortech.2021.126195.

Atitallah, I. B., Antonopoulou, G., Ntaikou, I., Alexandropoulou, M., Nasri, M., Mechichi, T., Lyberatos, G., 2019. On the evaluation of different saccharification schemes for enhanced bioethanol production from potato peels waste via a newly isolated yeast strain of *Wickerhamomyces anomalus*. Bioresource Technology, 289, 121614. https://doi.org/10.1016/j.biortech.2019.121614.

Attia, Y. A., Abdelsalam, E. M., Saeed, S., Saleh, M. M., Samer, M., 2022. Bioethanol production from potato peels using *Saccharomyces cerevisiae* treated with ZnO and ZnO/g-C3N4 nanomaterials. Egypt J Chem., 65(13), 309-15. https://doi.org/10.21608/ejchem.2022.118978.5351.

Awogbemi, O.; Kallon, D.V.V.; Owoputi, A.O., 2022. Biofuel Generation from Potato PeelWaste: Current State and Prospects. Recycling, 7, 23. https:// doi.org/10.3390/recycling7020023.

Ayub, A., Raza, Z.A., Majeed, M.I., Tariq, M.R. and Irfan, A., 2020. Development of sustainable magnetic chitosan biosorbent beads for kinetic remediation of arsenic contaminated water. International journal of biological macromolecules, 163, 603-617. https://doi.org/10.1016/j.ijbiomac.2020.06.287.

Baral, N.R., Davis, R. and Bradley, T.H., 2019. Supply and value chain analysis of mixed biomass feedstock supply system for lignocellulosic sugar production. Biofuels, Bioproducts and Biorefining, 13(3), 635-659. https://doi.org/10.1002/bbb.1975.

Baramee, S., Siriatcharanon, A-k., Ketbot, P., Teeravivattanakit, T., Waeonukul, R., Pason, P., Tachaapaikoon, C., Ratanakhanokchai, K., Phitsuwan, P., 2020. Biological pretreatment of rice straw with cellulase-free xylanolytic enzyme-producing *Bacillus firmus* K-1: Structural modification and biomass digestibility. Renewable Energy, 160, 555-563. https://doi.org/10.1016/j.renene.2020.06.061.

Barampouti, E. M., Christofi, A., Malamis, D., Mai, S., 2023. A sustainable approach to valorize potato peel waste towards biofuel production. Biomass Conversion and Biorefinery, 13(9), 8197-8208. https://doi.org/10.1007/s13399-021-01811-4.

Basera, P., Chakraborty, S. and Sharma, N., 2024. Lignocellulosic biomass: insights into enzymatic hydrolysis, influential factors, and economic viability. Discover Sustainability, 5(1), 311. https://doi.org/10.1007/s43621-024-00543-5.

Bayu, A., Karnjanakom, S., Yoshida, A., Kusakabe, K., Abudula, A. and Guan, G., 2019. Polyoxomolybdates catalysed cascade conversions of cellulose to glycolic acid with molecular oxygen via selective aldohexoses pathways (an epimerization and a [2+4] Retro-aldol reaction). Catalysis Today, 332, 28-34. https://doi.org/10.1016/j.cattod.2018.05.034.

Beniwal, A., Saini, P., Kokkiligadda, A., Vij, S., 2018. Use of silicon dioxide nanoparticles for β-galactosidase immobilization and modulated ethanol production by co-immobilized K. marxianus and *S. cerevisiae* in deproteinized cheese whey. Food Sci Technol., 87, 553-61. https://doi.org/10.1016/j.lwt.2017.09.028.

Bertels, L.K., Fernández Murillo, L., Heinisch, J.J., 2021. The pentose phosphate pathway in yeasts-more than a poor cousin of glycolysis. Biomolecules, 11(5), 725. https://doi.org/10.3390/biom11050725.

Bhat, M.A., Bhat, M.A., Jan, S., Shah, A.A. and Jan, A.T., 2024. Lignocellulosic biomass in circular economy: A techno-transition in carbon neutrality towards sustainable energy production. Biomass and Bioenergy, 189, 107349. https://doi.org/10.1016/j.biombioe.2024.107349.

Bisgaard, J., Muldbak, M., Tajsoleiman, T., Rydal, T., Rasmussen, T., Huusom, J.K., Gernaey, K.V., 2021. Characterization of mixing performance in bioreactors using flow-following sensor devices. Chem. Eng. Res. Des. 174, 471-485. https://doi.org/10.1016/j.cherd.2021.08.008.

Bishop, B.D., Sanusi, I.A. and Kana, G.E., 2024. Enhanced substrate suitability of autoclave-assisted acid pre-treated waste sugarcane molasses: Pre-treatment optimization, sequential nano-based detoxification strategies, and bioproduct production. Biomass Conversion and Biorefinery, 1-14. https://doi.org/10.1007/s13399-024-06127-7.

Brandt, B.A., Jansen, T., Görgens, J.F., van Zyl, W.H., 2019. Overcoming lignocellulose-derived microbial inhibitors: advancing the *Saccharomyces cerevisiae* resistance toolbox. Biofuels, Bioproducts and Biorefining, 13(6), 1520-1536. https://doi.org/10.1002/bbb.2042.

Carvalheiro, F., Alves-Ferreira, J., Fernandes, M.C., Duarte, L.C., 2024. Integrated Processes of Pretreatment and Enzymatic Hydrolysis of Cellulosic Biomass. In: Bisaria, V. (eds) Handbook of Biorefinery Research and Technology: Biomass Logistics to Saccharification. Springer, Dordrecht. https://doi.org/10.1007/978-94-007-6308-1_74.

Cavka, A. and Jönsson, L.J., 2013. Detoxification of lignocellulosic hydrolysates using sodium borohydride. Bioresource Technology, 136, 368-376. https://doi.org/10.1016/j.biortech.2013.03.014.

Chen, K., Hao, S., Lyu, H., Luo, G., Zhang, S. and Chen, J., 2017. Ion exchange separation for recovery of monosaccharides, organic acids and phenolic compounds from hydrolysates of lignocellulosic biomass. Separation and Purification Technology, 172, 100-106. https://doi.org/10.1016/j.seppur.2016.08.004.

Chen, X., Zhai, R., Li, Y., Yuan, X., Liu, Z.H., Jin, M., 2020. Understanding the structural characteristics of water-soluble phenolic compounds from four pretreatments of corn stover and their inhibitory effects on enzymatic hydrolysis and fermentation. Biotechnology for biofuels, 13, 1-13. https://doi.org/10.1186/s13068-020-01686-z.

Cherian E, Dharmendirakumar M, Baskar G., 2015. Immobilization of cellulase onto MnO_2 nanoparticles for bioethanol production by enhanced hydrolysis of agricultural waste. Chinese J Catal. 36(8), 1223–1229. https://doi.org/10.1016/S1872-2067(15)60906-8.

Chohan, N. A., Aruwajoye, G. S., Sewsynker-Sukai, Y., Kana, E. G., 2020. Valorisation of potato peel wastes for bioethanol production using simultaneous saccharification and fermentation: Process optimization and kinetic assessment. Renewable Energy, 146, 1031-1040. https://doi.org/10.1016/j.renene.2019.07.042.

Clausen, A.K. and Junne, S., 2025. Recent advances in yeast and bacteria co-cultivation for bioprocess applications. World Journal of Microbiology and Biotechnology, 41(5), 170. https://doi.org/10.1007/s11274-025-04385-9.

Cronin, D.J., Chen, X., Moghaddam, L., Zhang, X., 2020. Deep eutectic solvent extraction of high‐purity lignin from a corn stover hydrolysate. ChemSusChem, 13(17), 4678-4690. https://doi.org/10.1002/cssc.202001243.

da Silva Machado, A., Ferraz, A., 2017. Biological pretreatment of sugarcane bagasse with basidiomycetes producing varied patterns of biodegradation. Bioresource Technology, 225, 17-22. https://doi.org/10.1016/j.biortech.2016.11.053.

Dahunsi, S.O., 2019. Mechanical pretreatment of lignocelluloses for enhanced biogas production: Methane yield prediction from biomass structural components. Bioresource technology, 280, 18-26. https://doi.org/10.1016/j.biortech.2019.02.006.

de Andrade Bianchini, I., Jofre, F.M., Lacerda, T.M., de Almeida Felipe, M.D.G., 2024. Xylitol Production by Candida tropicalis from Sugarcane Bagasse and Straw: an Adaptive Approach to Improve Fermentative Performance. BioEnergy Research, 17(2), 1041-1054. https://doi.org/10.1007/s12155-023-10709-0.

De La Torre, M., Martín-Sampedro, R., Fillat, Ú., Eugenio, M.E., Blánquez, A., Hernández, M., Arias, M.E., Ibarra, D., 2017. Comparison of the efficiency of bacterial and fungal laccases in delignification and detoxification of steam-pretreated lignocellulosic biomass for bioethanol production. Journal of Industrial Microbiology and Biotechnology, 44(11), 1561-1573. https://doi.org/10.1007/s10295-017-1977-1.

de Mello, A.F.M., de Souza Vandenberghe, L.P., Herrmann, L.W., Letti, L.A.J., Burgos, W.J.M., Scapini, T., Manzoki, M.C., de Oliveira, P.Z., Soccol, C.R., 2024. Strategies and engineering aspects on the scale-up of bioreactors for different bioprocesses. Systems Microbiology and Biomanufacturing, 4(2), 365-385. https://doi.org/10.1007/s43393-023-00205-z.

Demiray, E., González-Fernández, C. and Tomás-Pejó, E., 2024. *Kluyveromyces marxianus* and *Bacillus coagulans* co-cultivation: efficient co-production of bioethanol and lactic acid from pomegranate peels. Bioresource Technology Reports, 25, 101808. https://doi.org/10.1016/j.biteb.2024.101808.

Deng, F., Cheong, D.-Y. Aita, G.M. 2018. Optimization of activated carbon detoxification of dilute ammonia pretreated energy cane bagasse enzymatic hydrolysate by response surface methodology. Ind. Crops Prod., 115, 166-173. https://doi.org/10.1016/j.indcrop.2018.02.030.

Devi, A., Singh, A., Bajar, S. and Owamah, H.I., 2021. Nanomaterial in liquid biofuel production: applications and current status. Environmental Sustainability, 4(2), 343-353. https://doi.org/10.1007/s42398-021-00193-7.

Dey, P., Chakrabortty, S., Haldar, D., Sowmya, A., Rangarajan, V. and Ruiz, H.A., 2022. Kinetic model supported improved and optimized submerged production strategy of cellulase enzyme from newspaper waste biomass. Bioprocess and Biosystems Engineering, 45(8), 1281-1295. https://doi.org/10.1007/s00449-022-02741-9.

do Nascimento, B.F., de Araujo, C.M.B., do Nascimento, A.C., da Silva, F.L.H., de Melo, D.J.N., Jaguaribe, E.F., Cavalcanti, J.V.F.L., da Motta Sobrinho, M.A., 2021. Detoxification of sisal bagasse hydrolysate using activated carbon produced from the gasification of açaí waste. Journal of Hazardous Materials, 409, 124494. https://doi.org/10.1016/j.jhazmat.2020.124494.

Dowlatabadi, M., Jahangiri, M. and Farhadian, N. (2019) 'Prediction of chlortetracycline adsorption on the Fe3O4 nanoparticle using molecular dynamics simulation', Journal of Biomolecular Structure and Dynamics, 37(14), 3616-3626. https://doi.org/10.1080/07391102.2018.1521746.

Driessen, J.L., Johnsen, J., Pogrebnyakov, I., Mohamed, E.T., Mussatto, S.I., Feist, A.M., Jensen, S.I., Nielsen, A.T., 2023. Adaptive laboratory evolution of Bacillus subtilis to overcome toxicity of lignocellulosic hydrolysate derived from Distiller's dried grains with solubles (DDGS). Metabolic Engineering Communications, 16, e00223. https://doi.org/10.1016/j.mec.2023.e00223.

Duan, J., Veliju, A., Lampret, O., Liu, L., Yadav, S., Apfel, U.P., Armstrong, F.A., Hemschemeier, A., Hofmann, E., 2023. Insights into the Molecular Mechanism of Formaldehyde Inhibition of [FeFe]-Hydrogenases. Journal of the American Chemical Society, 145(48), 26068-26074. https://doi.org/10.1021/jacs.3c07800.

Duncan, J.D., Devillers, H., Camarasa, C., Setati, M.E. and Divol, B., 2024. Oxygen alters redox cofactor dynamics and induces metabolic shifts in *Saccharomyces cerevisiae* during alcoholic fermentation. Food Microbiology, 124, 104624. https://doi.org/10.1016/j.fm.2024.104624.

Esteban, J., Yustos, P., Ladero, M., 2018. Catalytic processes from biomass-derived hexoses and pentoses: A recent literature overview. Catalysts, 8(12), 637. https://doi.org/10.3390/catal8120637.

FAO. 2024. Agricultural production statistics 2010–2023. FAOSTAT Analytical Briefs, 96. Rome. https://openknowledge.fao.org/handle/20.500.14283/cd3755en.

Fatma, S., Hameed, A., Noman, M., Ahmed, T., Shahid, M., Tariq, M., Sohail, I. and Tabassum, R., 2018. Lignocellulosic biomass: a sustainable bioenergy source for the future. Protein and peptide letters, 25(2), 148-163. https://doi.org/10.2174/0929866525666180122144504.

Fedailaine, M., Moussi, K., Khitous, M., Abada, S., Saber, M., Tirichine, N., 2015. Modeling of the anaerobic digestion of organic waste for biogas production. Procedia Comput. Sci. 52, 730-737. https://doi.org/10.1016/j.procs.2015.05.086.

Felekis, V., Stavraki, C., Malamis, D., Mai, S., Barampouti, E. M., 2023. Optimisation of bioethanol production in a potato processing industry. Fermentation, 9(2), 103. https://doi.org/10.3390/fermentation9020103.

Fonseca, B.G., Mateo, S., Moya, A.J., Roberto, I.C., 2018. Biotreatment optimization of rice straw hydrolyzates for ethanolic fermentation with *Scheffersomyces stipitis*. Biomass and Bioenergy, 112, 19-28. https://doi.org/10.1016/j.biombioe.2018.02.003.

Gabhane, J., William, S.P., Gadhe, A., Rath, R., Vaidya, A.N. and Wate, S., 2014. Pretreatment of banana agricultural waste for bio-ethanol production: Individual and interactive effects of acid and alkali pretreatments with autoclaving, microwave heating and ultrasonication. Waste management, 34(2), 498-503. https://doi.org/10.1016/j.wasman.2013.10.013.

Gaitonde, V.N., Manjaiah, M., Maradi, S., Karnik, S.R., Petkar, P.M., Paulo Davim, J., 2017. In: Multiresponse Optimization in Wire Electric Discharge Machining (WEDM) of HCHCr Steel by Integrating Response Surface Methodology (RSM). Woodhead Publishing, 199-221. https://doi.org/10.1016/B978-0-85709-481-0.00007-0.

Galbe, M., Wallberg, O. 2019. Pretreatment for biorefineries: a review of common methods for efficient utilisation of lignocellulosic materials. Biotechnol Biofuels 12, 294. https://doi.org/10.1186/s13068-019-1634-1.

Gao, Y., Song, C., Usman, M., Zheng, Z., Meng, X., Shen, X., Cai, Y. and Wang, X., 2024. Pretreatment of wheat straw using ammonia-rich liquid fraction of digestate: Contribution of biological and non-biological components in methane yield. Industrial Crops and Products, 220, 119262. https://doi.org/10.1016/j.indcrop.2024.119262.

Garrigós, V., Picazo, C., Dengler, L., Ewald, J.C., Matallana, E. and Aranda, A., 2025. Cytosolic peroxiredoxin Tsa1 influences acetic acid metabolism and pH homeostasis in wine yeasts. Journal of Agricultural and Food Chemistry, 73(13), 8015-8025. https://doi.org/10.1021/acs.jafc.4c13199.

Germec, M., Demirel, F., Tas, N., Ozcan, A., Yilmazer, C., Onuk, Z., Turhan, I., 2017. Microwave-assisted dilute acid pretreatment of different agricultural bioresources for fermentable sugar production. Cellulose, 24(10), 4337-4353. https://doi.org/10.1007/s10570-017-1408-5.

Germec, M., Turhan, I., Karhan, M., Demirci, A. (2019). Kinetic modelling and techno-economic feasibility of ethanol production from carob extract-based medium in biofilm reactor. Applied Sciences 9(10), 2121. https://doi.org/10.3390/app9102121.

Ghodke, P.K., Anthony, C., Sharma, A.K., 2024. Bioprocessing of Agricultural and Forest Waste. Sustainable Production Innovations: Bioremediation and Other Biotechnologies, 367-393. https://doi.org/10.1002/9781119792888.ch13.

Ghoreishi, S., Løhre, C., Hermundsgård, D.H., Molnes, J.L., Tanase-Opedal, M., Brusletto, R., Barth, T., 2024. Identification and quantification of valuable platform chemicals in aqueous product streams from a preliminary study of a large pilot-scale steam explosion of woody biomass using quantitative nuclear magnetic resonance spectroscopy. Biomass Conversion and Biorefinery, 14(3), 3331-3349. https://doi.org/10.1007/s13399-022-02712-w.

González-Gloria, K.D., Tomás-Pejó, E., Amaya-Delgado, L., Rodríguez-Jasso, R.M., Loredo-Treviño, A., Singh, A., Hans, M., Martín, C., Kumar, S. and Ruiz, H.A., 2024. Biochemical and biorefinery platform for second-generation bioethanol: fermentative strategies and microorganisms. Fermentation, 10(7), 361. https://doi.org/10.3390/fermentation10070361.

Guarnieri, M.T., Franden, M.A., Johnson, C.W., Beckham, G.T., 2017. Conversion and assimilation of furfural and 5-(hydroxymethyl) furfural by *Pseudomonas putida* KT2440. Metabolic Engineering Communications, 4, 22-28. https://doi.org/10.1016/j.meteno.2017.02.001.

Gupta, R., Mehta, G. and Kuhad, R.C., 2016. Scale-up of abatement of fermentation inhibitors from acid hydrolysates for efficient conversion to ethanol as biofuel. Journal of Chemical Technology and Biotechnology, 91(6), 1826-1834. https://doi.org/10.1002/jctb.4775.

Gupta, K., Chundawat, T.S., 2020. Zinc oxide nanoparticles synthesized using *Fusarium oxysporum* to enhance bioethanol production from rice-straw. Biomass and Bioenergy, 143, 105840. https://doi.org/10.1016/j.biombioe.2020.105840.

Gupta, V.C., Singh, M., Prasad, S., Mishra, B.N. (2022). Sustainable and Economical Approaches in Utilizing Agricultural Solid Waste for Bioethanol Production. In: Baskar, C., Ramakrishna, S., Baskar, S., Sharma, R., Chinnappan, A., Sehrawat, R. (eds) Handbook of Solid Waste Management. Springer, Singapore. https://doi.org/10.1007/978-981-16-4230-2_40.

Halilu, A., Hussein Ali, T., Sudarsanam, P., Bhargava, S.K., 2019. Synthesis of fuel grade molecules from hydroprocessing of biomass-derived compounds catalyzed by magnetic Fe (NiFe)O_4SiO_2 nanoparticles. Symmetry, 11(4), 524. https://doi.org/10.3390/sym11040524.

Han, J., Gong, G., Wu, X. and Zha, J., 2021. Systematic Metabolic Engineering of *Saccharomyces cerevisiae* for Efficient Utilization of Xylose. In Emerging Technologies for Biorefineries, Biofuels, and Value-Added Commodities, 157-173. Cham: Springer International Publishing. https://doi.org/10.1007/978-3-030-65584-6_7.

Han, J., Xu, B., Wang, H., Huang, G., Zhang, X., Xu, Y., 2022. Purification of acidic lignocellulose hydrolysate using anion-exchange resin: Multicomponent adsorption, kinetic and thermodynamic study. Bioresource Technology, 351, 126979. https://doi.org/10.1016/j.biortech.2022.126979.

He, Y., Zhang, J., Bao, J., 2016. Acceleration of biodetoxification on dilute acid pretreated lignocellulose feedstock by aeration and the consequent ethanol fermentation evaluation. Biotechnology for biofuels, 9, 1-13. https://doi.org/10.1186/s13068-016-0438-9.

He, Z., Zhang, F., Tu, R., Jia, Z., Cheng, S., Sun, Y., Wu, Y., Shen, X., Jiang, E. and Xu, X., 2020. The influence of torrefaction on pyrolysed biomass: The relationship of bio-oil composition with the torrefaction severity. Bioresource Technology, 314, 123780. https://doi.org/10.1016/j.biortech.2020.123780.

Hernández-Beltrán, J.U., Hernández-De Lira, I.O., Cruz-Santos, M.M., Saucedo-Luevanos, A., Hernández-Terán, F. and Balagurusamy, N., 2019. Insight into pretreatment methods of lignocellulosic biomass to increase biogas yield: current state, challenges, and opportunities. Applied sciences, 9(18), 3721. https://doi.org/10.3390/app9183721.

Huang, W., Wachemo, A. C., Yuan, H., Li, X. (2019). Modification of corn stover for improving biodegradability and anaerobic digestion performance by *Ceriporiopsis subvermispora*. Bioresource Technology, 283, 76-85. https://doi.org/10.1016/j.biortech.2019.02.035.

Ibarra, D., Eugenio, M.E., Alvira, P., Ballesteros, I., Ballesteros, M., Negro, M.J., 2023. Effect of laccase detoxification on bioethanol production from liquid fraction of steam-pretreated olive tree pruning. Fermentation, 9(3), 214. https://doi.org/10.3390/fermentation9030214.

Ibrahim, S., Abdul Wahab, N., 2024. Optimizing neural network algorithms for submerged membrane bioreactor: A comparative study of OVAT and RSM hyperparameter optimization techniques. Water Science and Technology, 89 (7), 1701-1724. https://doi.org/10.2166/wst.2024.099.

Iglesias-Carres, L., Krueger, E.S., Herring, J.A., Tessem, J.S., Neilson, A.P., 2022. Potential of phenolic compounds and their gut microbiota-derived metabolites to reduce TMA formation: application of an in vitro fermentation high-throughput screening model. Journal of Agricultural and Food Chemistry, 70 (10), 3207-3218. https://doi.org/10.1021/acs.jafc.2c00247.

Ilanidis, D., Stagge, S., Alriksson, B. and Jönsson, L.J., 2021. Factors affecting detoxification of softwood enzymatic hydrolysates using sodium dithionite. Processes, 9(5), 887. https://doi.org/10.3390/pr9050887.

Ingle, A.P., Rathod, J., Pandit, R., da Silva, S.S. and Rai, M., 2017. Comparative evaluation of free and immobilized cellulase for enzymatic hydrolysis of lignocellulosic biomass for sustainable bioethanol production. Cellulose, 24(12), 5529-5540. https://doi.org/10.1007/s10570-017-1517-1.

Izquierdo, P.F., Coral, M.P., Benavides, F.O., 2024. Application of an artificial neural network coupled to a genetic algorithm for the production of polyphenols in *Parachlorella kessleri*

grown under mixotrophic conditions. Algal Res. 77, 103331. https://doi.org/10.1016/j.algal.2023.103331.

Jang, Y.S., Kim, W.J., Im, J.A., Palaniswamy, S., Yao, Z., Lee, H.L., Yoon, Y.R., Seong, H.J., Papoutsakis, E.T. and Lee, S.Y., 2023. Efforts to install a heterologous Wood-Ljungdahl pathway in *Clostridium acetobutylicum* enable the identification of the native tetrahydrofolate (THF) cycle and result in early induction of solvents. Metabolic Engineering, 77, 188-198. https://doi.org/10.1016/j.ymben.2023.04.005.

Javed, A., Ahmad, A., Tahir, A., Shabbir, U., Nouman, M. and Hameed, A., 2019. Potato peel waste-its nutraceutical, industrial and biotechnological applications. AIMS Agriculture and Food, 4(3), 807-823. https://doi.org/10.3934/agrfood.2019.3.807.

Jayakody, L.N., Ferdouse, J., Hayashi, N., Kitagaki, H., 2017. Identification and detoxification of glycolaldehyde, an unattended bioethanol fermentation inhibitor. Critical reviews in biotechnology, 37(2), 177-189. https://doi.org/10.3109/07388551.2015.1128877.

Jayakody, L.N. and Jin, Y.S., 2021. In-depth understanding of molecular mechanisms of aldehyde toxicity to engineer robust Saccharomyces cerevisiae. Applied Microbiology and Biotechnology, 105(7), pp.2675-2692. https://doi.org/10.1007/s00253-021-11213-1.

Jia, C., Chai, R., Zhang, M., Guo, X., Zhou, X., Ding, N., Lei, C., Dong, Z., Zhao, J., Ren, H., Lu, D., 2024. Improvement of *Saccharomyces cerevisiae* strain tolerance to vanillin through heavy ion radiation combined with adaptive laboratory evolution. Journal of Biotechnology, 394, 112-124. https://doi.org/10.1016/j.jbiotec.2024.08.014.

Jilani, S.B., Olson, D.G. 2023. Mechanism of furfural toxicity and metabolic strategies to engineer tolerance in microbial strains. Microb Cell Fact, 22, 221. https://doi.org/10.1186/s12934-023-02223-x.

Jin, T., Xing, X., Xie, Y., Sun, Y., Bian, S., Liu, L., Chen, G., Wang, X., Yu, X., Su, Y., 2023. Evaluation of preparation and detoxification of hemicellulose hydrolysate for improved xylitol production from quinoa straw. International journal of molecular sciences, 24(1), 516. https://doi.org/10.3390/ijms24010516.

Johannes, L.P., Xuan, T.D., 2024. Comparative Analysis of Acidic and Alkaline Pretreatment Techniques for Bioethanol Production from Perennial Grasses. Energies, 17(5), 1048. https://doi.org/10.3390/en17051048.

John, J.A., Samuel, M.S. and Selvarajan, E., 2023. Immobilized cellulase on Fe3O4/GO/CS nanocomposite as a magnetically recyclable catalyst for biofuel application. Fuel, 333, 126364. https://doi.org/10.1016/j.fuel.2022.126364.

Karimipour-Fard, P., Chio, C., Brunone, A., Marway, H., Thompson, M., Abdehagh, N., Qin, W. and Yang, T.C., 2024. Lignocellulosic biomass pretreatment: Industrial oriented high-solid twin-screw extrusion method to improve biogas production from forestry biomass resources. Bioresource Technology, 393, 130000. https://doi.org/10.1016/j.biortech.2023.130000.

Kaur, P., Taggar, M.S., Kalia, A., 2021. Characterization of magnetic nanoparticle–immobilized cellulases for enzymatic saccharification of rice straw. Biomass Conv. Bioref. 11, 955–969. https://doi.org/10.1007/s13399-020-00628-x.

Khan, P., Ali, S., Jan, R. and Kim, K.M., 2024. Lignin Nanoparticles: Transforming Environmental Remediation. Nanomaterials, 14(18), 1541. https://doi.org/10.3390/nano14181541.

Kim, Y.K., Lee, H., 2016. Use of magnetic nanoparticles to enhance bioethanol production in syngas fermentation. Bioresour. Technol., 204, 139-144. https://doi.org/10.1016/j.biortech.2016.01.001.

Kim, Y.K., Park, S.E., Lee, H., Yun, J.Y., 2014. Enhancement of bioethanol production in syngas fermentation with *Clostridium ljungdahlii* using nanoparticles. Bioresour Technol, 159, 446-50. https://doi.org/10.1016/j.biortech.2014.03.046.

Kimani, B.G., Kerekes, E.B., Szebenyi, C., Krisch, J., Vágvölgyi, C., Papp, T. and Takó, M., 2021. In vitro activity of selected phenolic compounds against planktonic and biofilm cells of food-contaminating yeasts. Foods, 10(7), 1652. https://doi.org/10.3390/foods10071652.

Knežević, A., Đokić, I., Tosti, T., Popović, S., Vukojević, J., 2021. Biological Pretreatment of Wheat Straw: Effect of Fungal Culturing on Enzymatic Hydrolysis of Carbohydrate. Polymers. https://doi.org/10.21203/rs.3.rs-227697/v1.

Kommoji, S., Gopinath, M., Sagar, P.S., Yuvaraj, D., Iyyappan, J., Varsha, A.J., Sunil, V. (2021). Lipid bioproduction from delignified native grass (*Cyperus distans*) hydrolysate by *Yarrowia lipolytica*. Bioresour. Technol., 324, 124659. https://doi.org/10.1016/j.biortech.2020.124659.

Konan, D., Rodrigue, D., Koffi, E. 2024. Combination of Technologies for Biomass Pretreatment: A Focus on Extrusion. Waste Biomass Valor 15, 4519-4540. https://doi.org/10.1007/s12649-024-02472-w.

Korányi, T.I., Fridrich, B., Pineda, A. and Barta, K., 2020. Development of 'lignin-first' approaches for the valorization of lignocellulosic biomass. Molecules, 25(12), 2815. https://doi.org/10.3390/molecules25122815.

Kostyniuk, A. and Likozar, B., 2024. Wet torrefaction of biomass waste into value-added liquid product (5-HMF) and high-quality solid fuel (hydrochar) in a nitrogen atmosphere. Renewable energy, 226, 120450. https://doi.org/10.1016/j.renene.2024.120450.

Kucharska, K., Hołowacz, I., Konopacka-Łyskawa, D., Rybarczyk, P., Kamiński, M., 2018. Key issues in modelling and optimization of lignocellulosic biomass fermentative conversion to gaseous biofuels. Renew. Energy. 129, 384-408. https://doi.org/10.1016/j.renene.2018.06.018.

Kumar, V., Yadav, S.K., Kumar, J., Ahluwalia, V., 2020. A critical review on current strategies and trends employed for removal of inhibitors and toxic materials generated during biomass pretreatment. Bioresource Technology, 299, 122633. https://doi.org/10.1016/j.biortech.2019.122633.

Lei, C., Guo, X., Zhang, M., Zhou, X., Ding, N., Ren, J., Liu, M., Jia, C., Wang, Y., Zhao, J., Dong, Z., 2024. Regulating the metabolic flux of pyruvate dehydrogenase bypass to enhance lipid production in *Saccharomyces cerevisiae*. Communications Biology, 7(1), 1399. https://doi.org/10.1038/s42003-024-07103-7.

Lemire, L., Pham, P.L., Durocher, Y., Henry, O., 2022. Practical considerations for the scale-up of Chinese hamster ovary (CHO) cell cultures. In *Cell Culture Engineering and Technology: In appreciation to Professor Mohamed Al-Rubeai*, 367–400. Cham: Springer International Publishing. https://doi.org/10.1007/978-3-030-79871-0_12.

Li, S., Qi, B., Luo, J., Zhuang, Y. and Wan, Y., 2021. Ultrafast selective adsorption of pretreatment inhibitors from lignocellulosic hydrolysate with metal-organic frameworks: Performance and adsorption mechanisms. Separation and Purification Technology, 275, 119183. https://doi.org/10.1016/j.seppur.2021.119183.

Li, F., Ma, F., Zhao, H., Zhang, S., Wang, L., Zhang, X., Yu, H., 2019. A lytic polysaccharide monooxygenase from a white-rot fungus drives the degradation of lignin by a versatile peroxidase. Applied and Environmental Microbiology, 85(9), 02803-18. https://doi.org/10.1128/AEM.02803-18.

Li, J., Shi, S., Tu, M., Via, B., Sun, F.F., Adhikari, S., 2018. Detoxification of organosolv-pretreated pine prehydrolysates with anion resin and cysteine for butanol fermentation. Applied biochemistry and biotechnology, 186, 662-680. https://doi.org/10.1007/s12010-018-2769-4.

Li, S., Qi, B., Luo, J., Zhuang, Y., Wan, Y., 2021. Ultrafast selective adsorption of pretreatment inhibitors from lignocellulosic hydrolysate with metal-organic frameworks: Performance and adsorption mechanisms. Separation and Purification Technology, 275, 119183. https://doi.org/10.1016/j.seppur.2021.119183.

Liang, S., McDonald, A.G. 2014. Chemical and thermal characterization of potato peel waste and its fermentation residue as potential resources for biofuel and bioproducts production. J Agric Food Chem. 62: 8421-8429. https://doi.org/10.1021/jf5019406.

Liu, Y.J., Li, B., Feng, Y., Cui, Q., 2020. Consolidated Bio-Saccharification: Leading Lignocellulose Bioconversion into the Real World. Biotechnol. Adv. 40, 107535. https://doi.org/10.1016/j.biotechadv.2020.107535.

Liu, Z., Madadi, M., Song, G., Sun, C., Yan, H., Lu, X., El-Gendy, N.S., Zhou, Q. and Sun, F., 2025. Insights into Histidine-Assisted Mitigation of Pretreatment-Derived Inhibitors for Sustainable Sugar Platform Biorefinery. Journal of Environmental Chemical Engineering, 13(6), 119821. https://doi.org/10.1016/j.jece.2025.119821.

Lu, J., Li, J., Gao, H., Zhou, D., Xu, H., Cong, Y., Zhang,W., Xin, F., Jiang, M., 2021. Recent Progress on Bio-Succinic Acid Production from Lignocellulosic Biomass. World J. Microbiol. Biotechnol., 37, 16. https://doi.org/10.1007/s11274-020-02979-z.

Lynd, L.R., Beckham, G.T., Guss, A.M., Jayakody, L.N., Karp, E.M., Maranas, C., McCormick, R.L., Amador-Noguez, D., Bomble, Y.J., Davison, B.H., Foster, C., 2022. Toward low-cost biological and hybrid biological/catalytic conversion of cellulosic biomass to fuels. Energy and Environmental Science, 15(3), 938-990. https://doi.org/10.1039/D1EE02540F.

Ma, Q., Lei, Q., Liu, F., Song, Z., Khusid, B., Zhang, W., 2024. Evaluation of commercial nanofiltration and reverse osmosis membrane filtration to remove per‐and polyfluoroalkyl substances (PFAS): Effects of transmembrane pressures and water matrices. Water Environment Research, 96(2), e10983. https://doi.org/10.1002/wer.10983.

Mai, T., Hilt, J.Z., 2017. Magnetic nanoparticles: Reactive oxygen species generation and potential therapeutic applications. Journal of Nanoparticle Research, 19, 1-10. https://doi.org/10.1007/s11051-017-3943-2.

Makoś, P., Słupek, E., Gębicki, J., 2020. Extractive detoxification of feedstocks for the production of biofuels using new hydrophobic deep eutectic solvents-Experimental and theoretical studies. Journal of Molecular Liquids, 308, 113101. https://doi.org/10.1016/j.molliq.2020.113101.

Makoś-Chełstowska, P., Słupek, E., Kucharska, K., Gębicki, J., 2023. Extractive detoxification of hydrolysates with simultaneous formation of deep eutectic solvents. Chemical and Process Engineering: New Frontiers. https://doi.org/10.24425/cpe.2023.146720.

Mansour, M., Ali, M. K., Berkani, M., Flahaut, S., Chaoua, S., Kamyab, H., Vasseghian, Y., Chaouche, N.K., 2024. Optimization of physicochemical parameters for lipopeptides surfactin production by *Bacillus halotolerans* under oat straw medium using Box-Behnken design and artificial neural networks. Sustain. Chem. Pharm. 37, 101419. https://doi.org/10.1016/j.scp.2023.101419.

Martínez, S.A.H., Melchor-Martínez, E.M., Hernández, J.A.R., Parra-Saldívar, R. and Iqbal, H.M., 2022. Magnetic nanomaterials assisted nanobiocatalysis systems and their applications in biofuels production. Fuel, 312, 122927. https://doi.org/10.1016/j.fuel.2021.122927.

Mazzoli, R., 2021. Current progress in production of building-block organic acids by consolidated bioprocessing of lignocellulose. Fermentation, 7(4), 248. https://doi.org/10.3390/fermentation7040248.

Messori, A., Fasolini, A., Mazzoni, R., 2022. Advances in Catalytic Routes for the Homogeneous Green Conversion of the Bio-Based Platform 5-Hydroxymethylfurfural. ChemSusChem, 15(13), e202200228. https://doi.org/10.1002/cssc.202200228.

Miah, R., Siddiqa, A., Chakraborty, U., Tuli, J.F., Barman, N.K., Uddin, A., Aziz, T., Sharif, N., Dey, S.K., Yamada, M. and Talukder, A.A., 2022. Development of high temperature simultaneous saccharification and fermentation by thermosensitive *Saccharomyces cerevisiae* and *Bacillus amyloliquefaciens*. Scientific Reports, 12(1), 3630. https://doi.org/10.1038/s41598-022-07589-3.

Ming, C., Dilokpimol, A., Zou, C., Liao, W., Zhao, L., Wang, M., De Vries, R.P., Kang, Y., 2019. The quest for fungal strains and their co-culture potential to improve the enzymatic degradation of Chinese distillers' grain and other agricultural wastes. International Biodeterioration and Biodegradation, 144, 104765. https://doi.org/10.1016/j.ibiod.2019.104765.

Mohapatra, S., Ranjan Mishra, R., Nayak, B., Chandra Behera, B., Das Mohapatra, P.K. 2020. Development of Co-Culture Yeast Fermentation for Efficient Production of Biobutanol from Rice Straw: A Useful Insight in Valorization of Agro Industrial Residues. Bioresour. Technol., 318, 124070. https://doi.org/10.1016/j.biortech.2020.124070.

Monlau, F., Sambusiti, C., Antoniou, N., Zabaniotou, A., Solhy, A., Barakat, A., 2015. Pyrochars from bioenergy residue as novel bio-adsorbents for lignocellulosic hydrolysate detoxification. Bioresource technology, 187, 379-386. https://doi.org/10.1016/j.biortech.2015.03.137.

Moodley, P. and Kana, E.G., 2017. Comparison of a two-stage and a combined single-stage salt-acid based lignocellulosic pretreatment for enhancing enzymatic saccharification. Industrial Crops and Products, 108, 219-224. https://doi.org/10.1016/j.indcrop.2017.06.048.

Moodley, P., Sewsynker-Sukai, Y. and Kana, E.G., 2020. Progress in the development of alkali and metal salt catalysed lignocellulosic pretreatment regimes: Potential for bioethanol production. Bioresource Technology, 310, p.123372. https://doi.org/10.1016/j.biortech.2020.123372.

Mori, T., Koyama, G., Kawagishi, H., Hirai, H., 2016. Effects of homologous expression of 1, 4-benzoquinone reductase and homogentisate 1, 2-dioxygenase genes on wood decay in hyper-lignin-degrading fungus *Phanerochaete sordida* YK-624. Current Microbiology, 73, 512-518. https://doi.org/10.1007/s00284-016-1089-6.

Mulat, D. G., Huerta, S. G., Kalyani, D., Horn, S. J., 2018. Enhancing methane production from lignocellulosic biomass by combined steam explosion pretreatment and bioaugmentation with cellulytic bacterium *Caldicellulosiruptor bescii*. Biotechnology for Biofuels, 11(1), 19. https://doi.org/10.1186/s13068-018-1025-z.

Mushtaq, Q., Ishtiaq, U., Joly, N., Qazi, J. I., Martin, P., 2024. Amylase and cellulase production from newly isolated Bacillus subtilis using acid treated potato peel waste. Microorganisms, 12(6), 1106. https://doi.org/10.3390/microorganisms12061106.

Naseeruddin, S., Desai, S., Venkateswar Rao, L., 2021. Co-culture of *Saccharomyces cerevisiae* (VS3) and *Pichia stipitis* (NCIM 3498) enhances bioethanol yield from concentrated *Prosopis juliflora* hydrolysate. 3 Biotech 11, 21. https://doi.org/10.1007/s13205-020-02595-6.

Nduka, F.O., Onwurah, I.N.E., Obeta, C.J., Nweze, E.J., Nkwocha, C.C., Ujowundu, F.N., Eje, O.E. and Nwigwe, J.O., 2024. Effect of nickel oxide nanoparticles on bioethanol production by *Pichia kudriavzveii* IFM 53048 using banana peel waste substrate. Environmental Technology, 45(16), 3283-3302. https://doi.org/10.1080/09593330.2023.2215450.

Han, J., Pyo, S.H. and Xu, Y., 2025. Ultrasound-assisted regeneration of ion exchange resins for efficient detoxification of lignocellulosic hydrolysate in biorefinery. Renewable Energy, 252, 123568. https://doi.org/10.1016/j.renene.2025.123568.

Nzimande, S.N., Sanusi, I.A., Yobo, K., Ramchuran, S.O. and Kana, G.E., 2025. Process development for antifungal production by *Bacillus subtilis* BS20: nanoparticle supplementation, process optimization and preliminary scale-up studies. Bioprocess and Biosystems Engineering, 1-12. https://doi.org/10.1007/s00449-025-03205-6.

Ochoa-Chacon, A., Martinez, A., Poggi-Varaldo, H.M., Villa-Tanaca, L., Ramos-Valdivia, A.C. and Ponce-Noyola, T., 2022. Xylose metabolism in bioethanol production: *Saccharomyces cerevisiae* vs non-*Saccharomyces* yeasts. BioEnergy Research, 15(2), 905-923. https://doi.org/10.1007/s12155-021-10340-x.

Olatunji, K.O., Ahmed, N.A., Ogunkunle, O., 2021. Optimization of biogas yield from lignocellulosic materials with different pretreatment methods: a review. Biotechnol. Biofuels 14, 159. https://doi.org/10.1186/s13068-021-02012-x.

Oluwalana, A.E., Ajibade, P.A., 2021. Structural, optical and photocatalytic studies of oleylamine capped PbS nanoparticles. Opt Quant Electron 53(2), 1-13. https://doi.org/10.1007/s11082-020-02636-7.

Onyeaka, H., Hart, A., Obileke, K., 2025. Enhancing carbon neutrality: the role of biomass in CO2 uptake. In Advances in Sustainable Applications of Microalgae (pp. 73-93). Elsevier Science Ltd. https://doi.org/10.1016/B978-0-443-22127-9.00003-2.

Ornaghi, H.L., Ornaghi, F.G., Neves, R.M., Monticeli, F., Bianchi, O., 2020. Mechanisms involved in thermal degradation of lignocellulosic fibers: a survey based on chemical composition. Cellulose, 27, 4949-4961. https://doi.org/10.1007/s10570-020-03132-7.

Osman, A.I., Mehta, N., Elgarahy, A.M., Al-Hinai, A., Al-Muhtaseb, A.a.H., Rooney, D.W., 2021. Conversion of biomass to biofuels and life cycle assessment: a review. Environmental Chemistry Letters 19, 4075-4118. https://doi.org/10.1007/s10311-021-01273-0.

Ovejero-Pérez, A., Nakasu, P.Y., Hopson, C., Costa, J.M. and Hallett, J.P., 2024. Challenges and opportunities on the utilisation of ionic liquid for biomass pretreatment and valorisation. npj Materials Sustainability, 2(1), 7. https://doi.org/10.1038/s44296-024-00015-x.

Ozer Uyar, G. E., Uyar, B., 2023. Potato peel waste fermentation by Rhizopus oryzae to produce lactic acid and ethanol. Food Science and Nutrition, 11(10), 5908-5917. https://doi.org/10.1002/fsn3.3670.

Pan, L., He, M., Wu, B., Wang, Y., Hu, G., Ma, K., 2019. Simultaneous concentration and detoxification of lignocellulosic hydrolysates by novel membrane filtration system for bioethanol production. Journal of Cleaner Production, 227, 1185-1194. https://doi.org/10.1016/j.jclepro.2019.04.239.

Panda, S.K., Maiti, S.K., 2019. An approach for simultaneous detoxification and increment of cellulase enzyme production by *Trichoderma reesei* using rice straw. Energy Sources, Part A: Recovery, Utilization, and Environmental Effects, 41(22), 2691-2703. https://doi.org/10.1080/15567036.2019.1568641.

Pandey, A.K., Negi, S., 2024. Enhanced ethanol production using hydrophobic resin detoxified Pine forest litter hydrolysate and integrated fermentation process development supplementing molasses. Environmental Science and Pollution Research, 31(46), 57386-57396. https://doi.org/10.1007/s11356-023-30185-5.

Park, H.J., Driscoll, A.J., Johnson, P.A., 2018. The development and evaluation of B-glucosidase immobilized magnetic nanoparticles as recoverable biocatalysts. Biochem. Eng. J. 133, 66-73. https://doi.org/10.1016/j.bej.2018.01.017.

Pathak, P. D., Mandavgane, S. A., Puranik, N. M., Jambhulkar, S. J., Kulkarni, B. D. (2017). Valorization of potato peel: a biorefinery approach. Critical Reviews in Biotechnology, 38(2), 218-230. https://doi.org/10.1080/07388551.2017.1331337.

Peinado, S., Mateo, S., Sánchez, S., Moya, A.J., 2019. Effectiveness of sodium borohydride treatment on acid hydrolyzates from olive-tree pruning biomass for bioethanol production. BioEnergy Research, 12, 302-311. https://doi.org/10.1007/s12155-019-09979-4.

Pham, N.T.T., Beaufils, N., Peydecastaing, J., Behra, P., Pontalier, P.Y., 2024. Lignin Purification from Mild Alkaline Sugarcane Extract via Membrane Filtration. Clean Technologies, 6(2), 750-766. https://doi.org/10.3390/cleantechnol6020038.

Phukoetphim N, Salakkam A, Laopaiboon P, Laopaiboon L. 2017. Kinetic models for batch ethanol production from sweet sorghum juice under normal and high gravity fermentations: Logistic and modified Gompertz models. Journal of biotechnology; 243: 69-75. https://doi.org/10.1016/j.jbiotec.2016.12.012.

Policastro, G., Giugliano, M., Luongo, V., Napolitano, R., Fabbricino, M., 2021. Carbon catabolite repression occurrence in photo fermentation of ethanol-rich substrates. Journal of Environmental Management, 297, 113371. https://doi.org/10.1016/j.jenvman.2021.113371.

Pourali, P., Fazlzadeh, M., Aaligadri, M., Dargahi, A., Poureshgh, Y., Kakavandi, B., 2022. Enhanced three-dimensional electrochemical process using magnetic recoverable of Fe_3O_4@ GAC towards furfural degradation and mineralization. Arabian Journal of Chemistry, 15(8), p.103980. https://doi.org/10.1016/j.arabjc.2022.103980.

Preechakun, T., Pongchaiphol, S., Raita, M., Champreda, V., Laosiripojana, N., 2024. Detoxification of hemicellulose-enriched hydrolysate from sugarcane bagasse by activated

carbon and macroporous adsorption resin. Biomass Conversion and Biorefinery, 14(13), 14559-14574. https://doi.org/10.1007/s13399-022-03596-6.

Promta, T., Thonkamdee, P., Sasujit, K., 2024. Optimization of overliming detoxification of sugarcane bagasse hydrolysate by using response surface methodology for bio-ethanol production. Maejo International Journal of Energy and Environmental Communication, 6(1), 1–10. https://doi.org/10.54279/mijeec.v6i1.253749.

Rai, A. K., Al Makishah, N. H., Wen, Z., Gupta, G., Pandit, S., Prasad, R., 2022. Recent developments in lignocellulosic biofuels, a renewable source of bioenergy. Fermentation, 8(4), 161. https://doi.org/10.3390/fermentation8040161.

Raj, K. and Krishnan, C., 2020. Improved co-production of ethanol and xylitol from low-temperature aqueous ammonia pretreated sugarcane bagasse using two-stage high solids enzymatic hydrolysis and *Candida tropicalis*. Renewable Energy, 153, 392-403. https://doi.org/10.1016/j.renene.2020.02.042.

Rajak, R.C., Saha, P., Singhvi, M.S., Kwak, D., Kim, D., Lee, H., Deshmukh, A.R., Bu, Y., Kim, B.S., 2021. An eco-friendly biomass pretreatment strategy utilizing reusable enzyme-mimicking nanoparticles for lignin depolymerization and biofuel production. Green Chem. https://doi.org/10.1039/D1GC01456K.

Rao, J., Lv, Z., Chen, G., Peng, F., 2023. Hemicellulose: Structure, chemical modification, and application. Progress in Polymer Science, 140, 101675. https://doi.org/10.1016/j.progpolymsci.2023.101675.

Rathnayake, B., Valkama, H., Ohenoja, M., Haverinen, J. and Keiski, R.L., 2022. Evaluation of nanofiltration membranes for the purification of monosaccharides: influence of pH, temperature, and sulfates on the solute retention and fouling. Membranes, 12(12), 1210. https://doi.org/10.3390/membranes12121210.

Reis, V.R., Bassi, A.P.G., Cerri, B.C., Almeida, A.R., Carvalho, I.G., Bastos, R.G., Ceccato-Antonini, S.R., 2018. Effects of feedstock and co-culture of *Lactobacillus fermentum* and wild *Saccharomyces cerevisiae* strain during fuel ethanol fermentation by the industrial yeast strain PE-2. AMB Express, 8(1), 23. https://doi.org/10.1186/s13568-018-0556-9.

Ren, J., Zhang, M., Guo, X., Zhou, X., Ding, N., Lei, C., Jia, C., Wang, Y., Zhao, J., Dong, Z., Lu, D., 2024. Furfural tolerance of mutant *Saccharomyces cerevisiae* selected via ionizing radiation combined with adaptive laboratory evolution. Biotechnology for Biofuels and Bioproducts, 17(1), 117. https://doi.org/10.1186/s13068-024-02562-w.

Reza, M., Bertinetto, C., Kesari, K.K., Engelhardt, P., Ruokolainen, J., Vuorinen, T., 2019. Cellulose elementary fibril orientation in the spruce S 1-2 transition layer. Sci. Rep. 9 (1), 1-7. https://doi.org/10.1038/s41598-019-40303-4.

Ribeiro, G. F., Junior, A. B., 2023. The global energy matrix and use of agricultural residues for bioenergy production: A review with inspiring insights that aim to contribute to deliver solutions for society and industrial sectors through suggestions for future research. Waste Management and Research, 41(8), 1283-1304. https://doi.org/10.1177/0734242X231154149.

Rodrigues, P.D.O., Corrêa, A.G., Baffi, M.A., Pasquini, D., 2024. Potential applications of hemicellulose. In Handbook of Biomass (697-727). Singapore: Springer Nature Singapore. https://doi.org/10.1007/978-981-99-6727-8_27.

Rorke, D.C.S., Suinyuy, T.N., Kana, E.B.G., 2017. Microwave-assisted chemical pre-treatment of waste sorghum leaves: Process optimization and development of an intelligent model for determination of volatile compound fractions. Bioresource Technology, 224, 590–600. http://dx.doi.org/10.1016/j.biortech.2016.10.048.

Roy, S., Dikshit, P.K., Sherpa, K.C., Singh, A., Jacob, S., Rajak, R.C., 2021. Recent nanobiotechnological advancements in lignocellulosic biomass valorization: A review. Journal of Environmental Management, 297, 113422. https://doi.org/10.1016/j.jenvman.2021.113422.

Ruguo, H.U., 1999. A Computer-Aided Statistical Approach. In: Boca Raton. (eds) Food Product Design. CRC Press. 125-176.

Sanusi, A.I., Suinyuy, T. N., Kana, G.E.B., 2021. Impact of nanoparticle inclusion on bioethanol production process kinetics and inhibitor profile. Biotechnology Reports,29, 1-12. https://doi.org/10.1016/j.btre.2021.e00585.

Sanusi, I.A., Suinyuy, T.N., Lateef, A., Kana, G.E.B., 2020. Effect of nickel oxide nanoparticles on bioethanol production: Process optimization, kinetic and metabolic studies. Process Biochem, 92, 386-400. https://doi.org/10.1016/j. procbio.2020.01.029.

Sanusi, I. A., Faloye, F.D., Gueguim Kana, E. B. 2019. Impact of various metallic oxide nanoparticles on ethanol production by *Saccharomyces cerevisiae* BY4743: screening, kinetic study and validation on potato waste." Catalysis Letters 149(7), 2015-2031. https://doi.org/10.1007/s10562-019-02796-6.

Saravanakumar, T., Park, H.S., Mo, A.Y., Choi, M.S., Kim, D.H., Park, S.M., 2016. Detoxification of furanic and phenolic lignocellulose derived inhibitors of yeast using laccase immobilized on bacterial cellulosic nanofibers. Journal of Molecular Catalysis B: Enzymatic, 134, 196-205. https://doi.org/10.1016/j.molcatb.2016.11.006.

Sarawan, C., Suinyuy, T. N., Sewsynker-Sukai, Y., Gueguim Kana, E.B., 2019. Optimized activated charcoal detoxification of acid-pretreated lignocellulosic substrate and assessment for bioethanol production, Bioresource Technology, 286, 1-10. https://doi.org/10.1016/j.biortech.2019.121403.

Saucedo-Gutierrez, J.J., Escamilla-García, M., Amaro-Reyes, A., Carrillo-Garmendia, A., Madrigal-Pérez, L.A., Regalado-González, C., Granados-Arvizu, J.Á., 2024. Differential impacts of furfural and acetic acid on the bioenergetics and fermentation performance of *Scheffersomyces stipitis*. Fungal Genetics and Biology, 174, p.103914. https://doi.org/10.1016/j.fgb.2024.103914.

Serrano, A., Calviño, E., Carro, J., Sánchez-Ruiz, M.I., Cañada, F.J., Martínez, A.T., 2019. Complete oxidation of hydroxymethylfurfural to furandicarboxylic acid by aryl-alcohol oxidase. Biotechnology for biofuels, 12(1), 217. https://doi.org/10.1186/s13068-019-1555-z.

Sharma, S., Jha, P.K., Panwar, A., 2021. Production of bioethanol from wheat straw via optimization of co-culture conditions of *Bacillus licheniformis* and *Saccharomyces cerevisiae*. Discover Energy, 1(1), 5. https://doi.org/10.1007/s43937-021-00004-4.

Shrivastava, A., Sharma, R.K., 2024. Evaluation of co-culture system to produce ethanol and electricity from wheat straw hydrolysate using *Saccharomyces cerevisiae* and *Pichia fermentans*. Biomass Conv. Bioref. 14, 9407-9416. https://doi.org/10.1007/s13399-022-02914-2.

Singh, A., Bedore, S.R., Sharma, N.K., Lee, S.A., Eiteman, M.A., Neidle, E.L., 2019. Removal of aromatic inhibitors produced from lignocellulosic hydrolysates by *Acinetobacter baylyi*

ADP1 with formation of ethanol by *Kluyveromyces marxianus*. Biotechnology for biofuels, 12, pp.1-11. https://doi.org/10.1186/s13068-019-1434-7.

Singh, B., Verma, A., Mandal, P.K. and Datta, S., 2017. A biotechnological approach for degradation of inhibitory compounds present in lignocellulosic biomass hydrolysate liquor using *Bordetella* sp. BTIITR. Chemical engineering journal, 328, 519-526. https://doi.org/10.1016/j.cej.2017.07.059.

Singhvi, M.S., Gokhale, D.V., 2019. Lignocellulosic biomass: hurdles and challenges in its valorization. Appl. Microbiol. Biotechnol. 103, 9305-9320. https://doi.org/10.1007/s00253-019-10212-7.

Singhvi, M., Kim, B.S., 2020. Current developments in lignocellulosic biomass conversion into biofuels using nanobiotechology approach. Energies, 13(20), 5300. https://doi.org/10.3390/en13205300.

Sjulander, N., Kikas, T., 2020. Origin, impact and control of lignocellulosic inhibitors in bioethanol production: A review. Energies, 13(18), 4751. https://doi.org/10.3390/en13184751.

Soares, L.B., da Silveira, J.M., Biazi, L.E., Longo, L., de Oliveira, D., Furigo Junior, A., Ienczak, J.L., 2023. An overview on fermentation strategies to overcome lignocellulosic inhibitors in second-generation ethanol production using cell immobilization. Critical Reviews in Biotechnology, 43(8), 1150-1171. https://doi.org/10.1080/07388551.2022.2109452.

Soares, L.C., Chandel, A.K., Pagnocca, F.C., Gaikwad, S.C., Rai, M., da Silva, S.S., 2016. Screening of yeasts for selection of potential strains and their utilization for in situ microbial detoxification (ISMD) of sugarcane bagasse hemicellulosic hydrolysate. Indian Journal of Microbiology, 56, 172-181. https://doi.org/10.1007/s12088-016-0573-9.

Socas-Rodríguez, B., Santana-Mayor, A., Herrera-Herrera, A.V., Rodríguez- Delgado, M. A., 2020. Deep eutectic solvents, in: Green Sustainable Process for Chemical and Environmental Engineering and Science, 123–177, https://doi.org/ 10.1016/B978-0-12-817386-2.00005-6.

Soltaninejad, A., Jazini, M., Karimi, K., 2022. Sustainable bioconversion of potato peel wastes into ethanol and biogas using organosolv pretreatment. Chemosphere, 291, 133003. https://doi.org/10.1016/j.chemosphere.2021.133003.

Song, G., Madadi, M., Meng, X., Sun, C., Aghbashlo, M., Sun, F., Ragauskas, A.J., Tabatabaei, M., Ashori, A., 2024. Double in-situ lignin modification in surfactant-assisted glycerol organosolv pretreatment of sugarcane bagasse towards efficient enzymatic hydrolysis. Chemical Engineering Journal, 481, 148713. https://doi.org/10.1016/j.cej.2024.148713.

Song, Y., Cho, E.J., Park, C.S., Oh, C.H., Park, B.J. and Bae, H.J., 2019. A strategy for sequential fermentation by *Saccharomyces cerevisiae* and *Pichia stipitis* in bioethanol production from hardwoods. Renewable Energy, 139, 1281-1289. https://doi.org/10.1016/j.renene.2019.03.032.

Soni, S.K., Sharma, B. Sharma, A., Thakur, B., Soni, R., 2023. Exploring the potential of potato peels for bioethanol production through various pretreatment strategies and an in-house-produced multi-enzyme system. Sustainability, 15, 9137. https://doi.org/10.3390/su15119137.

Subedi, S., Ghimire, Y.N., Gautam, S., Poudel, H.K. and Shrestha, J., 2019. Economics of potato (Solanum tuberosum L.) production in terai region of Nepal. Archives of Agriculture and Environmental Science, 4(1), 57-62. https://doi.org/10.26832/24566632.2019.040109.

Sulaiman, W.K., Azeez, L., Adebisi, S.A., Wahab, O.O., Agbaogun, B.K., 2024. Exploring zero-valent iron nanoparticles (nZVI) for Bisphenol A removal: Experimental investigations and Monte-Carlo simulation insights. Water Practice and Technology, 19(8), 3416-3438. https://doi.org/10.2166/wpt.2024.209.

Suman, S.K., Khatri, M., Dhawaria, M., Kurmi, A., Pandey, D., Ghosh, S., Lata Jain, S., 2018. Potential of *Trametes maxima* IIPLC-32 derived laccase for the detoxification of phenolic inhibitors in lignocellulosic biomass prehydrolysate. International Biodeterioration and Biodegradation, 133, 1-8. https://doi.org/10.1016/j.ibiod.2018.05.009.

Taiwo, A.E., Musonge, P., 2023. Comparative evaluation of bioethanol fermentation process parameters using RSM, ANN and ANFIS. Biofuels, Bioproducts and Biorefining, 17(4), 961-975. https://doi.org/10.1002/bbb.2490.

Tareen, A.K., Sultan, I.N., Songprom, K., Laemsak, N., Sirisansaneeyakul, S., Vanichsriratana, W. and Parakulsuksatid, P., 2021. Two-step pretreatment of oil palm trunk for ethanol production by thermotolerent *Saccharomyces cerevisiae* SC90. Bioresource Technology, 320, 124298. https://doi.org/10.1016/j.biortech.2020.124298.

Thirunavukkarasu, A., Hedenström, M., Sparrman, T., Nilsson, M.B., Schleucher, J. and Öquist, M., 2024. Unraveling the dynamics of lignin chemistry on decomposition to understand its contribution to soil organic matter accumulation. Plant and Soil, 1-18. https://doi.org/10.1007/s11104-024-07066-y.

Tonova, K., Zhivkova, S., Lazarova, M. and Mustafa, A., 2024. Extraction by ionic liquids for the case of detoxification of lignocellulosic hydrolysates. Reaction Chemistry and Engineering, 9(10), 2610-2622. https://doi.org/10.1039/D4RE00154K.

Tramontina, R., Brenelli, L.B., Sodré, V., Franco Cairo, J.P., Travália, B.M., Egawa, V.Y., Goldbeck, R., Squina, F.M., 2020. Enzymatic removal of inhibitory compounds from lignocellulosic hydrolysates for biomass to bioproducts applications. World Journal of Microbiology and Biotechnology, 36, 1-11. https://doi.org/10.1007/s11274-020-02942-y.

Tsegaye, B., Balomajumder, C., Roy, P., 2018. Biodegradation of wheat straw by *Ochrobactrum oryzae* BMP03 and *Bacillus* sp. BMP01 bacteria to enhance biofuel production by increasing total reducing sugars yield. Environmental Science and Pollution Research International, 25(30), 30585-30596. https://doi.org/10.1007/s11356-018-3056-1.

Tyibilika, V., Setati, M.E., Bloem, A., Divol, B., Camarasa, C., 2024. Exploring fermentative metabolic response to varying exogenous supplies of redox cofactor precursors in selected wine yeast species. FEMS Yeast Research, 24, p.foae029. https://doi.org/10.1093/femsyr/foae029.

Ulmer, A., Veit, S., Erdemann, F., Freund, A., Loesch, M., Teleki, A., Zeidan, A.A., Takors, R., 2023. A two-compartment fermentation system to quantify strain-specific interactions in microbial co-cultures. Bioengineering, 10(1), 103. https://doi.org/10.3390/bioengineering10010103.

van der Maas, L., Driessen, J.L., Mussatto, S.I., 2021. Effects of inhibitory compounds present in lignocellulosic biomass hydrolysates on the growth of *Bacillus subtilis*. Energies, 14(24), 8419. https://doi.org/10.3390/en14248419.

Varella, L.Y., Mesquita, A.Z., de Rezende, D.B., Mourão, I.G., Cren, É.C., Lopes, N.P., Silva, W.G., Alonso, T.C., 2024. Experimental evaluation of the use of gamma radiation in sugarcane bagasse (*Saccharum* spp.) as a pretreatment for bioethanol production. Radiation Physics and Chemistry, 218, 111611. https://doi.org/10.1016/j.radphyschem.2024.111611.

Verma, S., Hariwal, M., Patel, P., Shah, P., Kumar, S., 2024. Plants Retaliating Defense Strategies against Herbivores. In Plant Elicitor Peptides: New Tool for Sustainable Agriculture, 149-170. Singapore: Springer Nature Singapore. https://doi.org/10.1007/978-981-97-6374-0_7.

Vijayalakshmi, S., Govindarajan, M., Al-Mulahim, N., Ahmed, Z., Mahboob, S., 2021. Cellulase immobilized magnetic nanoparticles for green energy production from *Allamanda schottii* L: Sustainability research in waste recycling. Saudi journal of biological sciences, 28(1), 901-910. https://doi.org/10.1016/j.sjbs.2020.11.034.

Wang, X., Liang, Z., Hou, J., Bao, X., Shen, Y., 2016. Identification and functional evaluation of the reductases and dehydrogenases from *Saccharomyces cerevisiae* involved in vanillin resistance. BMC biotechnology, 16, 1-9. https://doi.org/10.1186/s12896-016-0264-y.

Wang, X., Khushk, I., Xiao, Y., Gao, Q., Bao, J., 2018. Tolerance improvement of Corynebacterium glutamicum on lignocellulose derived inhibitors by adaptive evolution. Applied Microbiology and Biotechnology, 102, 377-388. https://doi.org/10.1007/s00253-017-8627-4.

Wang, W., Wang, X., Zhang, Y., Yu, Q., Tan, X., Zhuang, X. and Yuan, Z., 2020. Effect of sodium hydroxide pretreatment on physicochemical changes and enzymatic hydrolysis of herbaceous and woody lignocelluloses. Industrial Crops and Products, 145, 112145.

Wang, Y., Zhang, Y., Cui, Q., Feng, Y., Xuan, J., 2024. Composition of Lignocellulose Hydrolysate in Different Biorefinery Strategies: Nutrients and Inhibitors. Molecules, 29(10), 2275. https://doi.org/10.3390/molecules29102275.

Wang, R., Xu, Y., Wang, D., 2025. Differences in brewing characteristics between saccharifying microorganisms, Rhizopus and Aspergillus, for the fermentation of rice wine. Food Bioscience, 106328. https://doi.org/10.1016/j.fbio.2025.106328.

Weerathunga, H., Sarina, S., Zhu, H.Y., Waclawik, E.R., 2021. Oxidative esterification of 5-hydroxymethylfurfural into dimethyl 2, 5-furandicarboxylate using gamma alumina-supported gold nanoparticles. ACS omega, 6(7), 4740-4748. https://doi.org/10.1021/acsomega.0c05541.

Weng, C., Peng, X., Han, Y., 2021. Depolymerization and conversion of lignin to value-added bioproducts by microbial and enzymatic catalysis. Biotechnol. Biofuels 14, 84. https://doi.org/10.1186/s13068-021-01934-w.

Weng, Y.J., Ding, Z.Y., Li, Y.C., Wu, Y.F., Xu, Y.Y., Chen, R., Zhao, X.L., Wang, H.Y., Zhang, D.L., Zhang, Y.L., 2024. Oxygen vacancies enriched Ir/WO x catalysts for the directly chem-catalytic conversion of cellulose to ethanol. Tungsten, 1-12. https://doi.org/10.1007/s42864-024-00293-x.

Xia, J., Yang, Y., Liu, C.G., Yang, S. and Bai, F.W., 2019. Engineering *Zymomonas mobilis* for robust cellulosic ethanol production. Trends in biotechnology, 37(9), 960-972. https://doi.org/10.1016/j.tibtech.2019.02.002.

Xiang, H., Dai, K., Kou, J., Wang, G., Zhang, Z., Li, D., Chen, C., Wu, J., 2023. Selective adsorption of ferulic acid and furfural from acid lignocellulosic hydrolysate by novel magnetic lignin-based adsorbent. Separation and Purification Technology, 307, 122840. https://doi.org/10.1016/j.seppur.2022.122840.

Xiong, L., Wang, Y.T., Zhou, M.H., Takagi, H., Qin, J., Zhao, X.Q., 2024. Overexpression of arginase gene CAR1 renders yeast *Saccharomyces cerevisiae* acetic acid tolerance. Synthetic and Systems Biotechnology, 9(4), 723-732. https://doi.org/10.1016/j.synbio.2024.05.013.

Yadav, K.S., Naseeruddin, S., Prashanthi, G.S., Sateesh, L. and Rao, L.V., 2011. Bioethanol fermentation of concentrated rice straw hydrolysate using co-culture of *Saccharomyces cerevisiae* and *Pichia stipitis*. Bioresource technology, 102(11), 6473-6478. https://doi.org/10.1016/j.biortech.2011.03.019.

Yee, K.L., Jansen, L.E., Lajoie, C.A., Penner, M.H., Morse, L., Kelly, C.J., 2018. Furfural and 5-hydroxymethyl-furfural degradation using recombinant manganese peroxidase. Enzyme and Microbial Technology, 108, 59-65. https://doi.org/10.1016/j.enzmictec.2017.08.009.

Zahoor, Wang, W., Tan, X., Imtiaz, M., Wang, Q., Miao, C., Yuan, Z., Zhuang, X., 2021. Rice straw pretreatment with KOH/urea for enhancing sugar yield and ethanol production at low temperature. Industrial Crops and Products 170, 113776. https://doi.org/10.1016/j.indcrop.2021.113776.

Zhang, Q., Huang, H., Han, H., Qiu, Z., Achal, V., 2017. Stimulatory effect of in-situ detoxification on bioethanol production by rice straw. Energy, 135, 32-39. https://doi.org/10.1016/j.energy.2017.06.099.

Zhang, Y., Xia, C., Lu, M., Tu, M., 2018. Effect of overliming and activated carbon detoxification on inhibitors removal and butanol fermentation of poplar prehydrolysates. Biotechnology for biofuels, 11, 1-14. https://doi.org/10.1186/s13068-018-1182-0.

Zhang, Z., Zhang, X., Qi, S., Na, Q., Zhao, K., Yu, Z., Tan, Z., Ying, H. and Zhu, C., 2024. Constructing a chemoenzymatic strategy for enhancing the efficiency of selectively transforming 5-hydroxymethylfurfural to furan carboxylic acid. Green Chemistry, 27(3), pp.642-649. https://doi.org/10.1039/D4GC04735D.

Zhu, Y., Zhang, J., Zhu, L., Jia, Z., Li, Q., Xiao, W. and Cao, L., 2021. Minimize the xylitol production in *Saccharomyces cerevisiae* by balancing the xylose redox metabolic pathway. Frontiers in Bioengineering and Biotechnology, 9, 639595. https://doi.org/10.3389/fbioe.2021.639595.

Zimbardi, F., Viola, E., Arcieri, G., Valerio, V. and Carnevale, M., 2022. A novel method to detoxify steam-exploded biomass and produce a substrate for biorefinery. Processes, 10(12), 2611. https://doi.org/10.3390/pr10122611.

Zondi, A. S., Sanusi, I. A., Sewsynker-Sukai, Y., Beukes, L. S., Kana, G. E. (2025). Nano-based co-valorization, detoxification, and fermentation of potato waste and black liquor for bioethanol production. Biomass Conversion and Biorefinery, 1-13. https://doi.org/10.1007/s13399-025-06515-7.

Zytner, P., Kumar, D., Elsayed, A., Mohanty, A., Ramarao, B.V., Misra, M., 2023. A review on polyhydroxyalkanoate (PHA) production through the use of lignocellulosic biomass. RSC sustainability, 1(9), 2120-2134. https://doi.org/10.1039/D3SU00126A.

CHAPTER 3

Nano-based surface adsorption detoxification of process inhibitors for improved bioethanol productivity

This chapter has been published in *Bioresource Technology Reports* (25, 101783) with the title: Nano-based surface adsorption detoxification of process inhibitors for improved bioethanol productivity, https://doi.org/10.1016/j.biteb.2024.101783. The published paper is presented in the following pages.

The supplementary material can be accessed from https://ars.els-cdn.com/content/image/1-s2.0-S2589014X24000240-mmc1.docx.

Bioresource Technology Reports 25 (2024) 101783

Contents lists available at ScienceDirect

Bioresource Technology Reports

journal homepage: www.sciencedirect.com/journal/bioresource-technology-reports

Nano-based surface adsorption detoxification of process inhibitors for improved bioethanol productivity

Adeniyi P. Adebule [a], Isaac A. Sanusi [a,b], E.B. Gueguim Kana [a,*]

[a] University of KwaZulu-Natal, School of Life Sciences, Private Bag X01, Scottsville 3209, South Africa
[b] University of Fort Hare, Fort Hare Institute of Technology, Private Bag X1314, Alice 5700, South Africa

ARTICLE INFO

Keywords:
Nanoparticles
Detoxification
Inhibitors
Saccharification
Adsorption

ABSTRACT

The presence of inhibitory compounds in pretreated hydrolysates has limited the productivity of lignocellulosic based (LCB) bioethanol production. Tackling this limitation through nano-based hydrolysate detoxification remain understudied. Therefore, this study modelled and optimized a Fe_3O_4 nanoparticle-based detoxification of five (5) process inhibitors to improve bioethanol productivity. The detoxification mechanism was assessed by analysing recovered Fe_3O_4 nanoparticle (NP) using Fourier infrared spectroscopy (FTIR), transmission electron microscopy (TEM), photocatalysis, and UV-spectrophotometry. Under optimized conditions Fe_3O_4 NP adsorbent achieved high removal efficiencies for furfural (1.65-fold), 5-hydromethylfurfural (1.21-fold), phenol (1.95-fold), acetic acid (3.25-fold), and formaldehyde (1.55-fold), without sugar loss. Surface adsorption and complexation were identified mechanisms in the inhibitor removal with pH and initial inhibitor concentration as the principal influencing factors. The optimized detoxified hydrolysate (ODH) achieved a high saccharification efficiency of 88.95 % and substantial bioethanol yield of 0.504 g/g. These results highlight the efficiency, mechanisms, and desirability of using nano-size adsorbent in the detoxification of pretreated hydrolysate.

1. Introduction

Non-renewable fossil fuels have been the main source of global energy for many years and have failed to fulfil today's most significant requirements for a healthy environment. This has resulted in global quest for alternative, renewable, and environmentally friendly energy sources such as lignocellulosic-based energy sources (Tian et al., 2018). Lignocellulosic biomass, specifically agro-industrial starch-based wastes, has enormous potential as a feedstock for biofuel production (Tian et al., 2018). In a typical biofuel production involving lignocellulosic feedstock valorization, substrate pretreatment is essential to facilitate the disintegration of their complex structural components towards maximum fermentable sugar recovery. Several conventional pretreatment techniques (including biological, physical, chemical, and physicochemical methods) have been applied to enhance biofuel production from lignocellulosic feedstocks (Rorke et al., 2017). Chemical pretreatments such as acid pretreatment, when employed under severe process conditions, release useful carbohydrates such as starch, cellulose, and hemicellulose, as well as inhibitory compounds (Rorke et al., 2017). These inhibitors result from the non-selective conversion of hexose and pentose carbohydrates to different forms. Also, the concentration and chemical composition of these inhibitors in pretreated hydrolysate are based on the severity of the pretreatment conditions implemented (Rorke et al., 2017). Moreover, the toxicity of these inhibitory compounds on bioprocesses differs in terms of their mode of action and intensity. Key inhibitory compounds associated with lignocellulosic biomass pretreatment include acetic acid, phenolics, furan derivatives (furfural, 5-hydroxymethyl furfural), and formaldehydes. These inhibitory compounds induce prolonged lag phases, diminish cell growth rates, impede cell biomass formation, and disrupt metabolic activities, thereby undermining the overall quality and productivity of the desired product. Furthermore, they are known to obstruct enzyme activities, resulting in diminished enzymatic and cellular functions. This poses a major bottleneck to the commercialization of lignocellulosic-based biofuels. For these reasons, it is imperative to eliminate or lower the concentration of process inhibitors in pretreated hydrolysates, as this is crucial in mitigating their adverse effects on saccharifying enzymes, and enhancing sugar fermentability (Gupta et al., 2017). Hence, there has been greatly growing interest in developing effective techniques for pretreated hydrolysate detoxifocation and among these techniques, adsorption has shown great efficacy (Al-Hetlani et al., 2022).

* Corresponding author.
E-mail address: kanag@ukzn.ac.za (E.B.G. Kana).

https://doi.org/10.1016/j.biteb.2024.101783
Received 2 November 2023; Received in revised form 5 February 2024; Accepted 9 February 2024
Available online 11 February 2024

Various detoxification strategies have been explored to mitigate the impact of inhibitory substances in lignocellulosic fermentation processes (Rorke et al., 2017). Different adsorbents including activated charcoal have been used in the detoxification of pretreated hydrolysates (Sajab et al., 2019; Zhu et al., 2022), but with many limitations such as low adsorption capacity, lower surface area as well as the challenge of isolation and regeneration of activated charcoal after the adsorption process is completed (Gupta et al., 2017; Sarawan et al., 2019; Al-Hetlani et al., 2022). New detoxification adsorbents such as nanoparticles (NPs) or nano-based adsorbents are desired for the removal of inhibitory compounds. Nanomaterials, such as Fe_3O_4 NPs possess a high adsorption capacity, a large surface area to volume ratio, multi-surface functional potential, and specificity that could enhance the elimination of inhibitory compounds in pretreated hydrolysates. The incorporation of NPs for inhibitory compound detoxification could improve the kinetics and productivity of bioprocessing due to the aforementioned functionalities (Sanusi et al., 2021). Despite the merits of incorporating nanoparticles (NPs) in bioprocesses, there is a need for an efficient detoxification strategy capable of removing inhibitors from pretreated lignocellulosic hydrolysate as well as simultaneously improving microbial fermentation. Understanding nanoparticle-based detoxification dynamics on fermentation inhibitors will provide additional insights into lignocellulosic bioprocessing design towards improving product yields (Akalın et al., 2013). Hence, this study aimed to enhance the detoxification process of pretreated waste potato peel hydrolysate using nanoparticles as well as elucidate the mechanisms of process inhibitor removal (using a combination of techniques, including Fourier transform infrared spectroscopy (FTIR), scanning electron microscopy with energy dispersive X-ray spectroscopy (SEM-EDS), and transmission electron microscopy (TEM), photoluminescence, and UV-spectroscopy). Moreover, most of the previous work employing nanoadsorbents focuses on removal of pollutants from wastewater (Al-Hetlani et al., 2022) or the removal of fewer inhibitors at higher adsorbents concentration (100 g/L) (Zhu et al., 2022). This study extends the potential of magnetic nanomaterials particularly Fe_3O_4 nanoadsorbent for the removal of multiple process inhibitory compounds, namely furfural, 5-hydromethylfurfural, phenol, acetic acid, and formaldehyde from pretreated lignocellulosic hydrolysate in singular detoxification process while sugar loss was simultaneously prevented.

2. Materials and methods

2.1. Substrate preparation

Waste potato peel (WPP) used in this study was obtained from Pietermaritzburg metropolis, KwaZulu-Natal province, South Africa. Oven-dried (at ≤55 °C) waste potato peel (WPP) was pulverised to particle size ≤2 mm and kept moisture-free at ambient temperature until further use. The compositional analysis of WPP was analysed using National Renewable Energy Laboratory (NREL) standard protocols and the Megazyme starch kit (Megazyme, Ireland) (Sluiter et al., 2008). The native PPW contained 52.14 % starch, 10 % hemicellulose, 4.03 % cellulose, and 6.07 % lignin.

2.2. Pretreatment of WPP

The WPP was pretreated using soaking-assisted thermal pretreatment (SATP), as detailed by Sanusi et al. (2019). In summary, 0.92 % (*v*/*v*) HCl solution was added to an Erlenmeyer flask containing WPP (5 %) with a working volume of 100 mL. Subsequently, the mixture was immersed in a water bath without agitation for 2.34 h at 69.6 °C and then autoclaving for 5 min at 121 °C. The obtained pretreated hydrolysate was used for initiating the detoxification.

2.3. Nanoparticle synthesis and screening for inhibitors detoxification

Iron (III) oxide nanoparticles (Fe_3O_4 NP), iron (II) oxide nanoparticle (Fe_2O_3 NP), and zerovalent iron nanoparticles (Fe [0] NP) were prepared by co-precipitation using previously outlined protocols (Sanusi et al., 2019; Khaghani and Ghanbari, 2016). A preliminary detoxification study with nanoparticles was conducted using the pretreated WPP hydrolysate (Section 2.2). Varied concentrations of each of the NPs (0.01 and 0.1 g/L) were evaluated at low (3.0) and high (8.0) pH for a 240 min at 30 °C (Fig. 1A and B). The most efficient detoxification process (the Fe_3O_4 NP-incorporated process) was thereafter modelled, optimized, and validated. The reusability of Fe_3O_4 NP was also assessed (Fig. 1C and D).

2.4. Model development for inhibitory compound detoxification

The response surface methodology (RSM) Box-Behnken design is an ideal modelling and optimisation technique that can be used to elucidate the linear and non-linear interactions of process factors to determine the best process conditions (Abuhena et al., 2022a; Abuhena et al., 2022b). The RSM was used to generate 29 independent experimental runs (Table 1). The model input parameter ranges consisted of nanoparticle concentration (0–0.5 % *w*/*v*), pH (2.0–8.0), temperature (25–60 °C), and contact time (10–300 min), respectively (Sanusi et al., 2019; Hong et al., 2021). The resultant responses were furfural (g/L), 5-hydroxymethylfurfural (HMF) (g/L), phenol (g/g), acetic acid (g/L), formaldehyde (g/L), reducing sugar (g/L), and sugar loss (%). The data obtained were fitted to a polynomial model equation (Eq. (1)) to assess the interactive effects of input parameters for the process inhibitor removal.

$$Y = \alpha_0 + \alpha_1 x_1 + \alpha_2 x_2 + \alpha_3 x_3 + \alpha_{11} x_1 2 + \alpha_{22} x_2 2 + \alpha_{33} x_3 2 + \alpha_{12} x_1 x_2 + \alpha_{13} x_1 x_3 + \alpha_{23} x_2 x_3 \quad (1)$$

Y represents the response output, α_0 is the intercept, $\alpha_1 x_1$ to $\alpha_3 x_3$ are the linear coefficients, $\alpha_{11} x_1^2$ to $\alpha_{33} x_3^2$ are the quadratic coefficients, and $\alpha_{12} x_1 x_2$ to $\alpha_{23} x_2 x_3$ represent the interaction of coefficients. This model was evaluated for fitness using the analysis of variance (ANOVA) (using Design Expert version 12). The optimum detoxification set points for the responses (furfural, HMF, acetic acid, phenol, reducing sugar, and sugar loss) were obtained by solving the polynomial equations, and these set points were hence validated experimentally.

2.5. Hydrolysate detoxification and nanoparticle recyclability

A 100 mL working volume of the pretreated WPP hydrolysates was placed in 250 mL Erlenmeyer flasks. Subsequently, the detoxification, as illustrated in Fig. 2 for the entire detoxification scheme, was carried out by adding Fe_3O_4 NP appropriately. The pH, process temperature, and contact time were adjusted according to the specifications in Table 1, with a consistent 120 rpm maintained for all runs. A sample was taken from each detoxification flask to determine the percentage detoxification efficiency (DE) using Eq. (2).

$$\%DE = \frac{C_o - C_t}{C_o} \times 100 \quad (2)$$

where C_o and C_t are the inhibitor concentrations (g/L) at the initial time and at time (t), respectively.

To understand the mechanism of the inhibitor removal, additional investigations on the adsorption process and surface interactions between the Fe_3O_4-NP adsorbent and inhibitors were carried out using FTIR, TEM, photoluminescence emission, and optical absorption.

Also, the recyclability of Fe_3O_4 nanoparticle was conducted following the methodology outlined by Al-Hetlani et al. (2022), and the degradation efficiency (DE) (Fig. 1B) was evaluated under the same detoxification conditions utilised in the validation experiment.

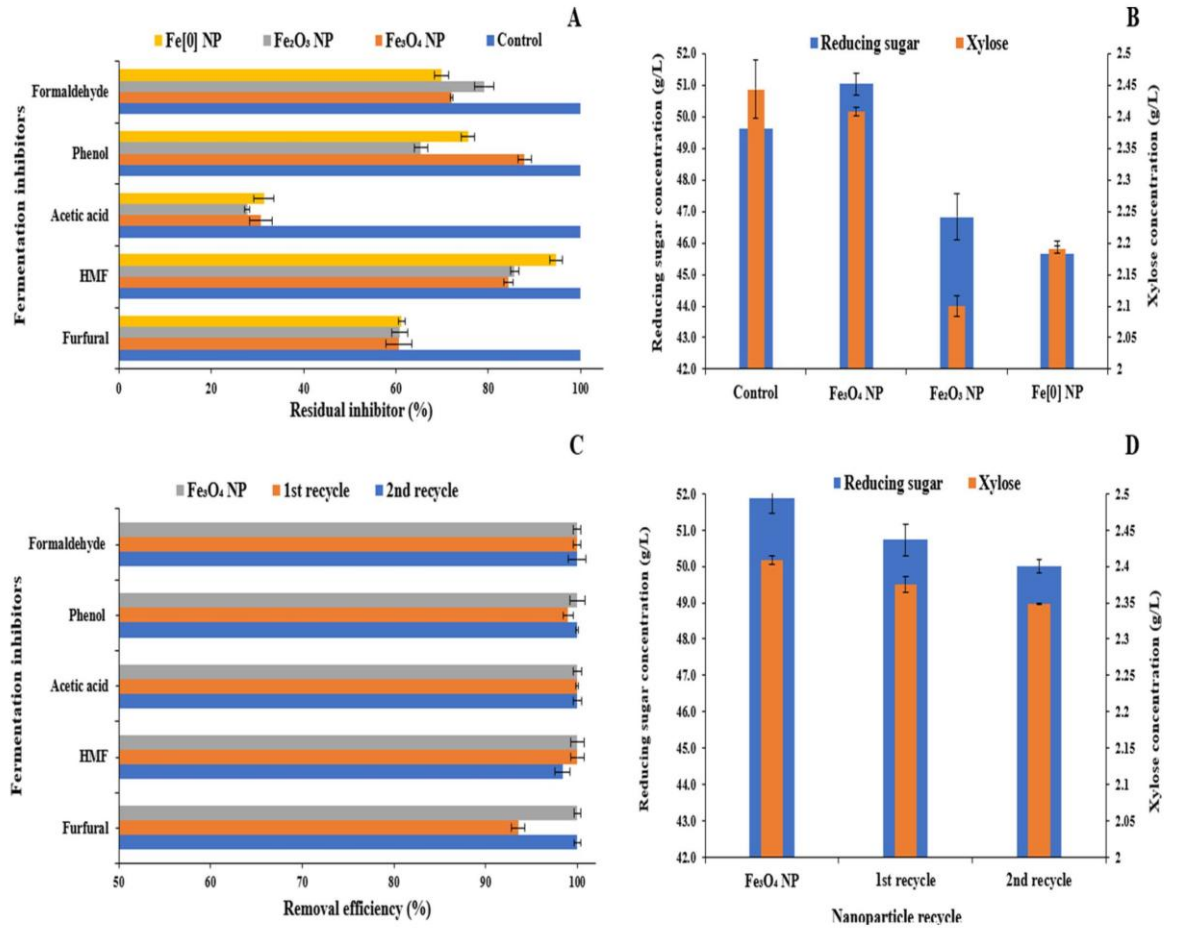

Fig. 1. Effect of iron oxide nanoparticle valency (Fe_3O_4, Fe_2O_3 and Fe [0) on detoxification efficiency (A), Adsorption–desorption study for the reusability of the Fe_3O_4 nanoparticles (B).

2.6. Artificial neural network model for predictive inhibitor removal

Artificial neural network (ANN) was used to develop an intelligent model to predict the removal of process inhibitor under Fe_3O_4 NP detoxification conditions. The inputs included contact time, heating temperature, nanoparticle concentration, and pH while the outputs were furfural (g/L), HMF (g/L), phenol (g/g), acetic acid (g/L), formaldehyde (g/L), reducing sugar (g/L) and sugar loss (%).

Following Rorke et al. (2017) guidelines regarding ANN, the experimental data set was divided into 75 % for training and 25 % for validation of the study. The network was trained using a back propagation algorithm with the goal of achieving a minimum net error on the validation data set while preventing overtraining or memorization. The accuracy of the intelligent model was assessed using regression analysis and coefficient of determination (R^2). This illustrates the model's ability to accurately predict the fermentation inhibitor removal efficiency. The experimental data were normalized according to the equation (Eq. (3)) below:

$$e_i = \frac{e_i - E_{min}}{E_{max} - E_{min}} \tag{3}$$

where e_i is the normalized data and E_{min} and E_{max} denote the minimum and maximum values.

Furthermore, sensitivity test and knowledge discovery study was carried out to determine the rate and direction of output change when each input was varied from its minimum to maximum values, while remaining inputs were kept at their median value (Rorke et al., 2017). Subsequently, the mathematical function relating the inputs and inhibitory compounds removal was derived from the developed model.

2.7. Bioethanol production

Prior to fermentation, the stored yeast (*Saccharomyces cerevisiae* BY4743) was revived and cultivated using previously developed seed-culture method (Sanusi et al., 2019). Subsequently, this seed-culture was used as inoculum in sterilized broth fermentation medium (composition previously specified in Sarawan et al. (2019)) containing the non-detoxified hydrolysate and the optimized detoxified pretreatment hydrolysate subjected to the simultaneous saccharification and fermentation (SSF) processes. The SSF processes (detailed protocol in Sanusi et al. (2019)), were conducted using a 100 mL working volume in a sterilized 250 mL flask. Under aseptic conditions, aliquots (2 mL) were collected from the flask at intervals of 3 h until 24 h and stored at −20 °C for the determination of ethanol concentration (EC), xylose, and reducing sugars (RSs).

2.8. Analytical procedures

The synthesised NPs and the recovered NP after the hydrolysate detoxification were characterized by FTIR, SEM-EDX and TEM. Additionally, the Perkin Elmer LS 45 fluorescence and the Perkin Elmer Lambda 25 UV–Vis spectrometers were utilised to assess the photo-

Table 1
RSM Box-Behnken experimental design of the nano-based inhibitor detoxification.

Run	Nanoparticle Conc. (w/v %)	Temperature (°C)	Contact Time (min)	pH	Reducing sugar (g/L)	Sugar Loss (%)	Furfural (g/L)	HMF (g/L)	Acetic Acid (g/L)	Phenol (g/g)	Formaldehyde (g/L)
1	0.25	25	155	8	48.000	3.28	0.742	0.129	2.042	0.426	1.250
2	0.25	25	10	5	48.414	2.45	0.857	0.231	3.783	0.068	1.200
3	0.5	42.5	155	8	44.900	9.53	1.035	0.147	4.864	0.557	1.436
4	0	42.5	155	2	50.048	0.00	1.200	0.145	10.629	0.098	1.150
5	0.5	42.5	155	2	47.807	3.67	1.002	0.000	8.227	0.041	1.243
6	0.25	42.5	300	8	46.920	5.46	1.271	0.054	5.225	0.521	1.205
7	0.25	60	155	2	51.000	0.00	0.924	0.000	8.227	0.047	1.200
8	0.25	42.5	10	2	53.129	0.00	0.951	0.000	7.987	0.074	1.419
9	0.5	25	155	5	46.546	6.21	0.500	0.112	4.023	0.044	1.280
10	0.25	42.5	155	5	52.803	0.00	0.732	0.165	3.243	0.092	1.030
11	0.25	42.5	155	5	52.760	0.00	0.731	0.165	3.423	0.053	1.030
12	0.25	25	300	5	49.091	1.08	0.939	0.203	3.843	0.050	1.151
13	0.25	60	10	5	50.000	0.00	0.970	0.188	3.003	0.086	1.145
14	0.25	42.5	300	2	48.554	2.16	0.961	0.000	7.747	0.026	1.226
15	0	60	155	5	49.254	0.75	1.268	0.237	2.402	0.160	1.200
16	0	42.5	155	8	46.266	6.77	1.148	0.276	1.261	0.333	1.200
17	0.5	42.5	10	5	47.760	3.76	0.600	0.166	3.543	0.101	1.200
18	0.25	42.5	155	5	52.196	0.00	0.750	0.165	2.222	0.098	1.030
19	0.25	60	155	8	45.800	7.71	0.900	0.117	2.162	0.638	1.292
20	0	42.5	300	5	48.647	1.98	1.200	0.328	2.642	0.154	1.208
21	0	25	155	5	48.000	3.28	1.100	0.282	2.042	0.077	1.202
22	0.5	42.5	300	5	43.204	12.94	0.624	0.377	2.582	0.008	1.100
23	0.25	42.5	10	8	46.966	5.36	1.000	0.126	1.201	0.351	1.223
24	0.25	42.5	155	5	52.850	0.00	0.731	0.218	3.003	0.059	1.030
25	0.25	42.5	155	5	52.700	0.00	0.700	0.218	2.762	0.020	1.030
26	0	42.5	10	5	46.219	6.87	1.021	0.258	1.982	0.068	1.139
27	0.25	60	300	5	47.480	4.33	1.150	0.275	2.762	0.071	1.053
28	0.25	25	155	2	48.741	1.79	0.982	0.000	6.906	0.077	1.214
29	0.5	60	155	5	45.145	9.03	0.766	0.212	3.003	0.077	1.119

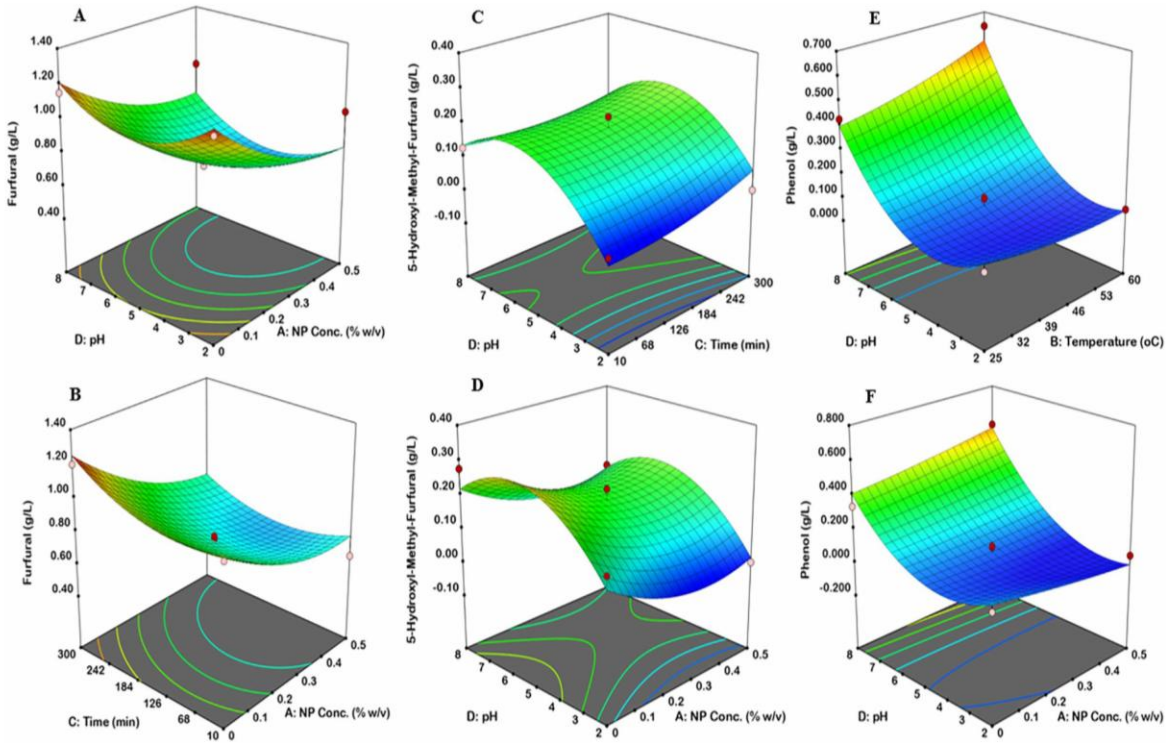

Fig. 2. Three-dimensional response surface graphs representing the interactive effects of: furfural [(A) pH and Fe_3O_4 NP concentration (% *w/v*), (B) time (min) and Fe_3O_4 NP concentration (% w/v)]; HMF [(C) pH and time (min), (D) pH and Fe_3O_4 NP concentration (% w/v)]; phenol [(E) pH and temperature (°C) and (F) pH and Fe_3O_4 NP concentration (% w/v)].

luminescence emission and optical absorption respectively of both the synthesised NPs and the recovered NP after the detoxification process. The hydrolysate RSs were quantified using the Miller assay, while the glucose and xylose concentrations in g/L were analysed using the Megazyme kits (Megazyme, Wicklow, Ireland). The ethanol concentration was measured with a Vernier ethanol vapour sensor (LABQUEST12

sensor, USA). Furfural, HMF, phenol, formaldehyde, and acetic acid in g/L were determined following standard conventional protocols as described in previous studies (Omran and Coughlin, 2020). And the bioethanol yield, productivity, saccharification efficiency and sugar utilization were determined using Eqs. (4)–(7), respectively.

$$Bioethanol\ yield\ (g/g) = \frac{Maximum\ ethanol\ concentration\ (g/L)}{Utilized\ glucose\ (g/L)} \quad (4)$$

$$Bioethanol\ productivity\ (g/l/h) = \frac{Maximum\ ethanol\ concentration\ (g/l)}{Fermentation\ period\ (h)} \quad (5)$$

$$Saccharification\ efficiency\ (\%) = \frac{Reducing\ sugar\ release\ (g/L)\ x\ 0.9}{\text{Initial starch concentration (g/L)}} \times 100 \quad (6)$$

$$Sugar\ utilisation\ (\%) = \frac{Initial\ sugar\ content - final\ sugar\ content}{Initial\ sugar\ content} \times 100 \quad (7)$$

3. Results

3.1. Nanoparticle characterization

The SEM-EDX elemental composition of the prepared NPs (see supplementary document) reveals prominent metallic and oxygen units. Additionally, trace amounts of carbon, sulphur, chlorine, silicon, and aluminium were detected. The transmission electron microscopy (TEM) micrograph illustrates that Fe_3O_4, Fe_2O_3, and Fe [0] particles are approximately spherical, with average sizes of 39, 47, and 55 nm, respectively. The nanoparticles' shape, size, and surface charge contribute to their exceptional properties, including catalytic properties and surface-to-volume ratio. The absorption bands for Fe_3O_4, Fe_2O_3, and Fe [0] at 800, 1000, and 1110 nm, respectively, are indicative of their peaks. Metal oxide nanoparticles and hydroxides typically display peak absorption in the fingerprint region below the 1000 nm wavelength due to interatomic vibrations. Additional peaks within the absorption range from 3800 to 800 cm^{-1} can be attributed to the presence of various functional groups (–CH_3, –CH_2, =C–H, –C–H, C=O, –OH, and NH groups) with distinct stretching vibrations.

3.2. Preliminary nanoparticle's screening for detoxification of inhibitors

A preliminary assessment of the effectiveness of Fe_3O_4, Fe_2O_3, and Fe [0] nanoparticles (NPs) in removing the inhibitors and recovering sugar in pretreated hydrolysate under various detoxification conditions. Fig. 1A illustrates the detoxification potential of these NPs at NPs concentration (0.01 or 0.1 g/L), pH (3.0 or 8.0) temperature of 30 °C, and 240 min exposure period. Fe_3O_4 NPs (at 0.01 g/L, pH 3) exhibited the highest inhibitor removal efficiency for furfural (39.4 %), HMF (17.44 %), formaldehyde (28.0 %), acetic acid (69.2 %), and phenol (12.2 %), with improved reducing sugar recovery (51.03 g/L) and no sugar loss. In contrast, Fe_2O_3 and Fe [0] nanoparticles showed lower inhibitor removal efficiencies and sugar losses of 5.65 % and 7.99 %, respectively. Moreover, the xylose content after the detoxification process using Fe_3O_4 was 2.8 g/L with 0 % xylose loss, while with Fe_2O_3 and Fe [0] NPs, xylose concentrations of 2.47 g/L and 2.57 g/L were obtained, respectively. Overall, Fe_3O_4 nanoparticles demonstrated the highest detoxification potential, leading to their selection for further studies.

3.3. Development of the RSM models

The experimental data from the designed model are presented in Table 1. The ANOVA data were used to assess the statistical significance of the models for the detoxification process, while minimizing sugar loss (Table 2). The *p*-values, ranging from 0.0001 to 0.0132, were deemed significant (values <0.05) (Nwabueze, 2010). The low p-values (<0.0001–0.0132) and F values (3.47–43.97) underscore the model's significance. The R^2 value >0.776 indicates that the models could account for over 77 % of the variations in the observed data. These observations suggest the model's suitability to illustrate the correlation among selected factors. Thus, the quadratic model obtained in this study could predict inhibitor removal under a nano-based detoxification regime. The final polynomial Eqs. (8)–(14), relating inhibitor concentrations, reducing sugar, and sugar loss to the coded factors A, B, C, and D (nanoparticle concentration, process temperature, process time, and pH), are presented below.

The dual interactions of pH and nanoparticle concentration were the most significant parameters in the detoxification model for HMF, acetic acid, reducing sugar, and sugar loss. Temperature and pH were significant for phenol removal. Also, the perturbation curve of detoxification of furfural, HMF, phenol, acetic acid, and formaldehyde plots (see supplementary document) revealed varying levels of detoxification effects on the inhibitor removal. The steepness of the perturbation curvature highlighted the importance of each variable, with pH and NP concentration having the predominant influence on the detoxification rate in this order: pH > NP concentration > time > temperature. During the detoxification process, increases in variables (especially NP concentration and pH) led to increased sugar losses (up to 6.1 %). However, this was lower compared to the inhibitor removal rate, confirming that sugar and inhibitors were not selectively adsorbed by the nanoparticles. Similar observation has been reported by Hong et al. (2021) for the removal of process inhibitors using activated carbon.

$$\begin{aligned} Furfural =& 7.288 - 2.009A + 0.716B + 0.622C + 0.0634D \\ &+ 0.245AB - 0.388AC + 0.212AD + 0.244BC + 0.539BD \\ &+ 0.654CD + 1.056A^2 + 0.599B^2 + 1.156C^2 + 1.872D^2 \end{aligned} \quad (8)$$

$$\begin{aligned} HMF =& 0.186 - 0.043A + 0.006B + 0.022C + 0.059D \\ &+ 0.036AB + 0.035AC + 0.004AD + 0.029BC \\ &- 0.003BD - 0.018CD + 0.064A^2 - 0.006B^2 \\ &+ 0.0218C^2 - 0.130D^2 \end{aligned} \quad (9)$$

Table 2
Analysis of Variance (ANOVA) for the developed inhibitor detoxification model.

Model Output	Sum of Squares	DF	Mean Square	F-value	p-value	R^2	
Reducing sugar	195.98	14	14.00	43.97	<0.0001	0.9778	Significant
Sugar loss	329.35	14	23.53	24.24	<0.0001	0.9778	Significant
Furfural	0.9269	14	0.0662	3.47	0.0132	0.7762	Significant
HMF	0.2532	14	0.0181	6.11	0.0009	0.8594	Significant
Acetic acid	156.52	14	11.18	14.20	<0.0001	0.9342	Significant
Phenol	0.8296	14	0.0593	25.89	<0.0001	0.9626	Significant
Formaldehyde	0.2401	14	0.0171	3.61	0.0109	0.7840	Significant

DF = degree of freedom.

$$\text{Acetic acid} = 2.931 + 0.441A - 0.09B + 0.275C - 2.747D - 0.345AB - 0.405AC + 1.501AD - 0.0751BC - 0.300BD + 1.066CD + 0.181A^2 - 0.194B^2 + 0.069C^2 + 2.591D^2 \quad (10)$$

$$\text{Phenol} = 0.064 - 0.005A + 0.028B + 0.007C + 0.205D - 0.013AB - 0.045AC + 0.07AD + 0.001BC + 0.06BD + 0.054CD + 0.010A^2 + 0.022B^2 - 0.008C^2 + 0.194D^2 \quad (11)$$

$$\text{Formaldehyde} = 10.30 + 0.232A - 0.2417B - 0.319C + 0.129D - 0.397AB - 0.423AC + 0.358AD - 0.106BC + 0.140BD + 0.440CD + 0.843A^2 + 0.628B^2 + 0.581C^2 + 1.567D^2 \quad (12)$$

$$\text{Total Reducing sugar} = 52.662 - 1.089A - 0.0091B - 0.716C - 1.702D - 0.664AB - 1.746AC + 0.219AD - 0.799BC - 1.115BD + 1.132CD - 3.685A^2 - 1.976B^2 - 2.112C^2 - 1.893D^2 \quad (13)$$

$$\text{Sugar loss} = -6.113 + 2.195A + 0.0189B + 1.443C + 3.430D + 1.337AB + 3.518AC - 0.441AD + 1.611BC + 2.246BD - 2.282CD + 7.426A^2 + 3.981B^2 + 4.255C^2 + 3.815D^2 \quad (14)$$

where the linear coefficients (A: nanoparticle concentration, B: process temperature, C: process time, D: pH), interaction coefficient (AB, AC, AD, BC, BD, and CD), quadratic coefficients (A^2, B^2, C^2 and D^2), manifest both antagonistic (indicated by negative [−] signs) and synergistic (indicated by positive [+] signs) effects on the output variables.

3.4. Interactive effect of detoxification input variables on the response outputs

Figs. 2 and 3 depict the interactive effects of the input parameters on the inhibitor removal, reducing sugar concentrations, and sugar loss. A simultaneous increase in pH and nanoparticles concentration from 2 to 8 and 0 to 0.5 % (*w/v*), respectively, resulted in a decrease in furfural concentration from 1.2 to 0.7 g/L (Fig. 2A). Similarly, maintaining the pH at the minimum value while increasing Fe_3O_4 NP concentration from 0 to 0.5 % (w/v) resulted in a decrease in furfural concentration from 1.20 to 0.76 g/L. The pairwise increase in Fe_3O_4 NP concentration and contact time (10–300 min) led to a reduction in furfural concentration from 1.1 g/L to 0.70 g/L (Fig. 2B).

In addition, the simultaneous increase in pH and Fe_3O_4 NP concentration from 2 to 8 and 0 to 0.5 % (*w/v*), respectively, resulted in an increase in HMF concentration from 0.11 to 0.19 g/L, followed by a subsequent decline to 0.14 g/L (Fig. 2C and D). Interestingly, an increase in the Fe_3O_4 NP concentration at the minimum pH value (2) demonstrated a sharp decrease in HMF content from 0.11 to 0 g/L.

Moreover, an increase in temperature (25–60 °C), while maintaining a constant minimum pH, led to a reduction in phenol concentration from 0.1 to 0.03 g/g (Fig. 2E). Similarly, an increment in Fe_3O_4 NP concentration while keeping the pH at the minimum value of 2.0 resulted in a decrease in phenol concentration from 0.12 to 0 g/g (Fig. 2F).

Furthermore, the acetic acid concentration decreased from 8.9 to 2.5 g/L when both the pH and exposure time increased simultaneously (Fig. 3A). Remarkably, with the pairwise increase in pH and concentration from 2 to 8 and 0 to 0.5 % (*w/v*) respectively, there was a reduction in acetic acid content from 8.9 to 1.07 g/L (Fig. 3B).

Additionally, the formaldehyde concentration was reduced from 1.28 g/L to 1.03 g/L with the pairwise increase in contact time and pH (Fig. 3C). The combination of a rise in pH and an increase in the concentration of Fe_3O_4 NP from 2 to 8 and 0 to 0.5 % (*w/v*), respectively, was effective in reducing formaldehyde concentration from 1.26 g/L to 1.03 g/L (Fig. 3D).

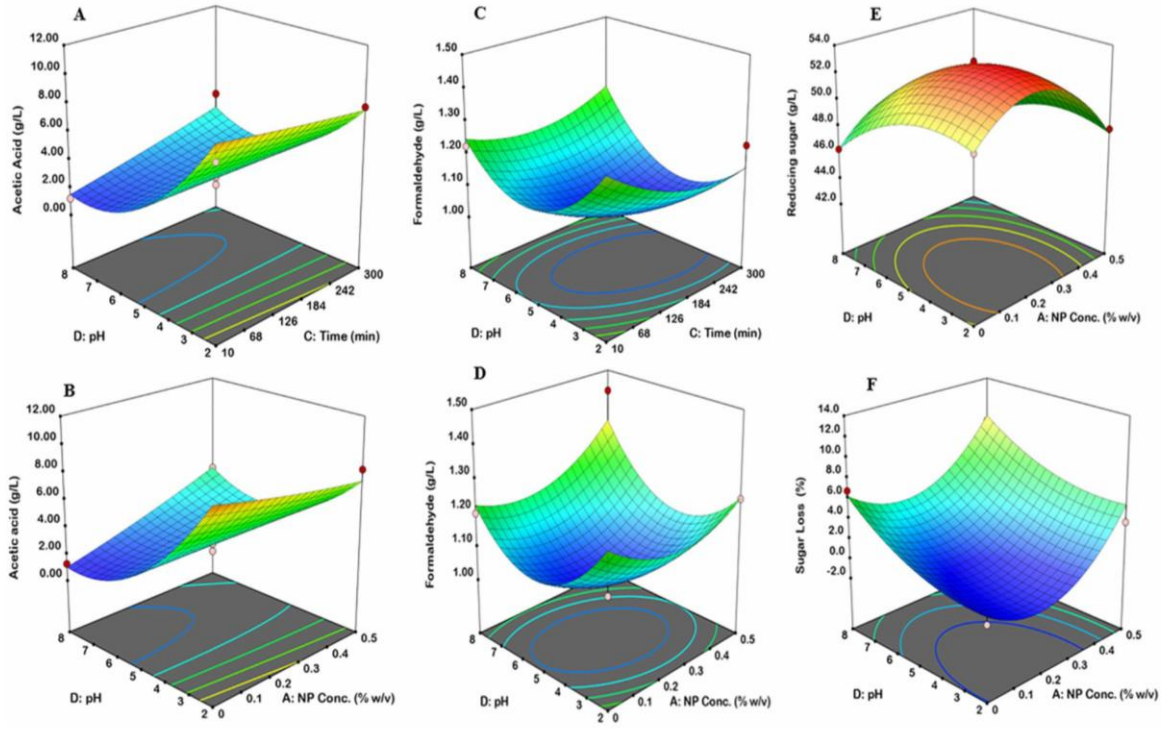

Fig. 3. Three-dimensional response surface graphs representing the interactive effects of: acetic acid [(A) pH and time (min), (B) pH and Fe_3O_4 NP concentration (% w/v)]; formaldehyde [(C) pH and time (min), (D) pH and Fe_3O_4 NP concentration (% w/v)]; reducing sugar [(E) pH and Fe_3O_4 NP concentration (% w/v)], sugar loss [(F) pH and Fe_3O_4 NP concentration (% w/v)].

The impact of detoxification on sugar loss, a concurrent increase in pH () and Fe_3O_4 NP concentration (0 to 0.5 % w/v) resulted in an initial increase in reducing sugar concentration (50.4–52.8 g/L), followed by a sharp decline from 52.8 g/L to 45.4 g/L (Fig. 3E). Likewise, increasing NP concentration (0 to 0.5 % w/v) and maintaining pH at 2.0, reduced sugar concentration from 52.8 to 48.69 g/L with 5.3 % sugar loss. Similarly, the simultaneous increase in pH and Fe_3O_4 NP concentration resulted in an increasing sugar loss from 0.0 to 9.8 % (Fig. 3F). Also, when the Fe_3O_4 NP concentration is maintained at the minimum value and the pH is increased from 2 to 8, a reduction in reducing sugar from 50.4 to 46.4 g/L and a corresponding increase in sugar loss from 0.0 to 5.9 % were observed.

3.5. Experimental validation of the optimized model

The model predicted optimized conditions for Fe_3O_4 NP concentration, temperature, contact time, and pH as 0.021 % (w/v), 35.37 °C, 12.74 min, and 4.14, respectively. The validated values for furfural, HMF, phenol, acetic acid, formaldehyde, reducing sugar, and sugar loss were 0.6652 g/L, 0.1487 g/L, 0.008 g/g, 4.324 g/L, 0.9667 g/L, 51.028 g/L, and 0 %, respectively. These values were in agreement with the predicted values for furfural (0.711 g/L), HMF (0.1831 g/L), phenol (0.010 g/g), acetic acid (3.903 g/L), formaldehyde (0.963 g/L), reducing sugar (49.949 g/L), and sugar loss (1.618 %) (supplementary material). The results demonstrate a 40 % reduction in furfural, 24 % in HMF, 69 % in acetic acid, 49 % in phenol, and 35 % in formaldehyde, coupled with a 3 % increase in reducing sugar, achieved in this present study. This is comparable to previous reports (Table 3).

3.6. Detoxification mechanisms

The FTIR spectra of Fe_3O_4 NP and detox-Fe_3O_4-NP (Fe_3O_4 NP recovered after detoxification) are depicted in Fig. 4A. The peak at 555 cm^{-1}, observed for both the Fe_3O_4-NP and detox-Fe_3O_4-NP, corresponds to the vibration of the Fe—O bond. The IR spectra peak at 2943 cm^{-1} found in detox-Fe_3O_4-NP correspond to the asymmetric and symmetric C—H stretching vibrations. The strong band at 1643 cm^{-1} represents a mono-substituted C=C stretching of alkene. Meanwhile, the peaks at 1535 and 1404 cm^{-1} are related to the C=O stretching vibrations of amide and the bending vibrations of -NH_2 groups, respectively. Furthermore, the peak around 1380 cm^{-1} is assigned to the phenol hydroxyl (O—H) bending vibrations.

Comparing the obtained spectrum for the Fe_3O_4 NP with detox-Fe_3O_4-NP, the peaks at 3843, 1632, 1160, 880, and 555 cm^{-1} become less steep in the detox-Fe_3O_4-NP and acquire broader spectra at 1160 and 880 cm^{-1}, respectively. This strongly indicates the presence of amino, phenolic, aldehyde, amine, and hydroxyl groups of various inhibitors in complexation with Fe (III) of the Fe_3O_4 NP adsorbent (Cao et al., 2014). Moreover, the sharp characteristic adsorption peak at 580 cm^{-1} related to the Fe—O bond vibration of Fe_3O_4 appearing in the detox-Fe_3O_4-NP spectrum further shows the retention of the magnetic Fe_3O_4 NP property after detoxification (Fan et al., 2017).

Similarly, Fig. 4B presents the photoluminescence spectra of the Fe_3O_4 NP and detox-Fe_3O_4-NP at varying dilutions (A1 - A3 and B1 - B3), respectively, with an excitation wavelength of 350 nm. The Fe_3O_4-NP (A1- A3) exhibited sharp emission bands at 380 nm and broad emission bands at 446 nm. In contrast, detox-Fe_3O_4-NP showed sharp emission bands at 410 nm and broad emission bands at 465 nm. Also, the emission maxima observed at 380 and 410 nm wavelengths were assigned to the transition of trapped electrons from donor levels to the valence band (Tohidi and Jamshidi-Ghaleh, 2015). A change in the wavelength could have resulted in lower energy excitation observed in the detox-Fe_3O_4-NP compared to that of the Fe_3O_4 NP. This difference could be attributed to the change in the particle size of the detox-Fe_3O_4-NP (increased after the detoxification process) compared to that of the Fe_3O_4 NP particle size (see supplementary document).

Additionally, the optical absorption spectra of Fe_3O_4 NPs and detox-Fe_3O_4-NPs were assessed using UV spectroscopy in the range of 200–700 nm (Fig. 5A and B, respectively). Detox-Fe_3O_4-NP spectra notably differed from that of Fe_3O_4 NP, particularly between 200 and 240 nm and 320–380 nm, underscoring the differences in particle size. This aligns with literature that particle size influences optical properties (Wang et al., 2019).

Furthermore, TEM micrograph of the nanoparticles exhibited variations for both Fe_3O_4 NP and detox-Fe_3O_4-NP (see supplementary document). Particle sizes ranged from 11.66 to 29.64 nm (average size = 20.08 nm) for Fe_3O_4 NP and 29.34 to 56.18 nm (average size = 44.84 nm) for detox-Fe_3O_4-NP. Remarkably, Fe_3O_4 NP size increased by over 2-fold post-detoxification, most probably due to inhibitor adsorption onto the nanoparticle's surface or ligand complexation with inhibitors.

Table 3
Comparison of inhibitor detoxification processes and effect on sugar recovery.

Substrate	Detoxification conditions	Removal efficiency and sugar loss	Reference
Waste potato peels hydrolysate	Fe_3O_4 NP, 0.021%w/v, pH 4.14, 12.74 min, 35.4 °C	Furfural-40 %, Phenol-24 %, Acetic acid-69 %, HMF-17 %, Sugar recovery-51.02 g/L, Sugar loss-0 %	This study
Spruce hydrolysate	NaOH, pH, 10, 1 h	Furan aldehydes-18 %, Phenols-8 %, Sugar loss-4 %	Larsson et al., 1999
Bagasse hydrolysate	Ca $(OH)_2$, pH 9, 60 °C, 30 min	Furan aldehydes-69 %, Phenols-35 %, Sugar loss-15 %	Martinez et al., 2001
Spruce hydrolysate	Ca $(OH)_2$, pH 12, 60 °C, 170 h	Furan aldehydes-100 %, Phenols-150 %, Sugar loss-68 %	Millati et al., 2002
Corn stover hydrolysate	Ca $(OH)_2$, pH 10, 50 °C, 0.5 h	Sugar loss-13 %	Mohagheghi et al., 2006
Oil palm empty fruit bunch fibre	AC-Fe (III)/Fox	Furfural- 0.2 %	Sajab et al., 2019
Sorghum leaf waste	Activated charcoal (AC) (5%w/v), pH 3.76, 134.73 min, 25 °C	Furfural-98 %, Acetic acid-37 %, HMF-88 %, Sugar loss-7 %	Sarawan et al., 2019
Corn stover	Lignin NP	Furfural-98.7 %, Acetic acid-47.8 %, Formic acid-28.1 %, Levulinic acid- 0 %, HMF- 0 %	Zhu et al., 2022

3.7. Recyclability of Fe_3O_4 nanoparticle for detoxification

The regenerated Fe_3O_4 NP was reused in the detoxification process, with the adsorbent (Fe_3O_4 NP) demonstrating high detoxification efficiency in two (2) cycles for all the inhibitors evaluated (Fig. 1C and D). Interestingly, detoxification was maintained at 100 % after the second cycle. Similar observations were presented in Sun et al. (2021) and Al-Hetlani et al. (2022), who reported recycling of chitosan-modified Fe_3O_4-ATP (3 times) and AC-$COFe_2O_4$ (5 times) respectively.

3.8. Input parameter sensitivity test

The sensitivity of the dependent response variable (see supplementary document) is reflected by a steep slope or curvature in the plot (Oh et al., 1995). Table 4 depicts the sensitivity testing outcome elucidated with different model equations. The concentrations of the inhibitors were not significantly impacted until the process temperature was >35 °C (see supplementary document). The relationship exhibited by both temperatures and the various inhibitors fitted both sigmoid and polynomial regression equations (Table 4). In the same vein, exposure time showed varying impacts on the removal of inhibitory compounds

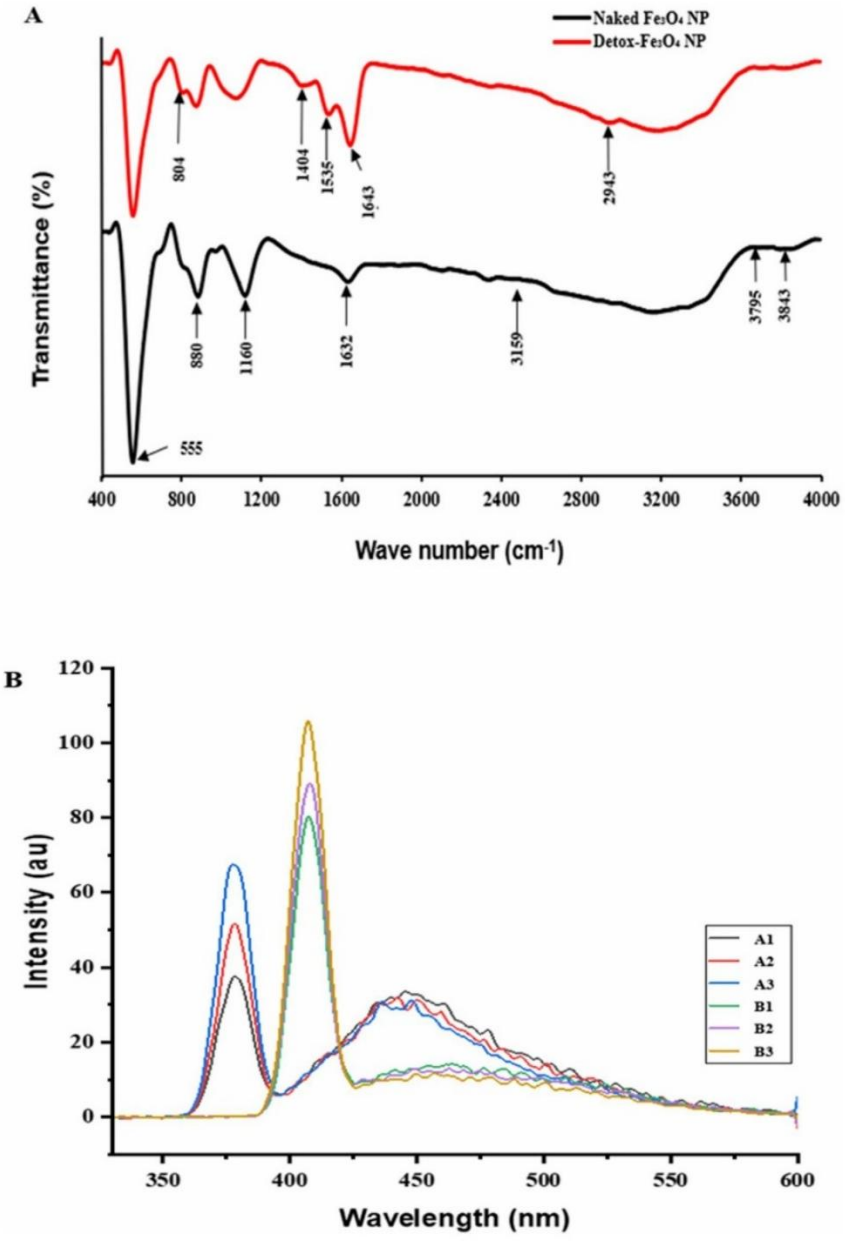

Fig. 4. **(A)** FTIR spectra of Naked and Detox-Fe_3O_4 NPs, **(B)** Photoluminescence emission spectra [A1-A3: dilutions of Naked Fe_3O_4-NP, B1-B3: dilution of Detox-Fe_3O_4-NP].

(see supplementary document). Specifically, furfural, HMF, and phenol were best adsorbed between 10 and 60 min. Further exposure per time led to a sharp decrease in their adsorption on the nano adsorbent. Conversely, acetic acid and formaldehyde adsorbed consistently until 120 min before slowly increasing for the rest of the process. These relationships between inhibitors, adsorbent, and time fitted various non-linear model types ranging from rational Weibull, DR-Hill, reciprocal quadratic to polynomial regression for furfural, HMF, acetic acid, phenol, and formaldehyde, respectively. The highest furfural removal efficiency (30 %) was achieved at pH 5, while HMF was better adsorbed at pH 3. The influence of pH on furfural and HMF was best illustrated by sinusoidal and rational models, respectively. Continuous adsorption for acetic acid and formaldehyde was observed at pH <6. On the contrary, phenol concentration remained constant from pH 2 to 5 before observing a sharp increment up to pH 9, which was better illustrated by the DR-Hill model.

3.9. Bioethanol production using optimal detoxified hydrolysate

Bioethanol production, *S. cerevisiae* growth, and sugar utilization for both non-detoxified hydrolysate (NDSSF) and optimally detoxified hydrolysate (ODSSF) are presented in Fig. 6, respectively. Both the NDSSF and ODSSF processes displayed a brief lag phase of 3 h. A noteworthy escalation in bioethanol concentration was observed from 4.74 to 23.20 g/L (NDSSF) and 5.09 to 25.96 g/L (ODSSF) between the 3rd and 9th hours (Fig. 6A). This corresponded with an increase in yeast growth (Fig. 6B) and sugar utilization (Fig. 6C). It was evident that ethanol production was notably higher using the optimally detoxified hydrolysate. In Table 5, the ODSSF (2.885 g/L/h) showed higher ethanol productivity (ethanol yields = 0.504 g/g). In contrast, the NDSSF exhibited an ethanol productivity of 2.578 g/L/h (ethanol yields = 0.494 g/g). Moreover, the higher productivity and yield achieved in ODSSF align consistently with higher saccharification efficiency (88.95 %) compared

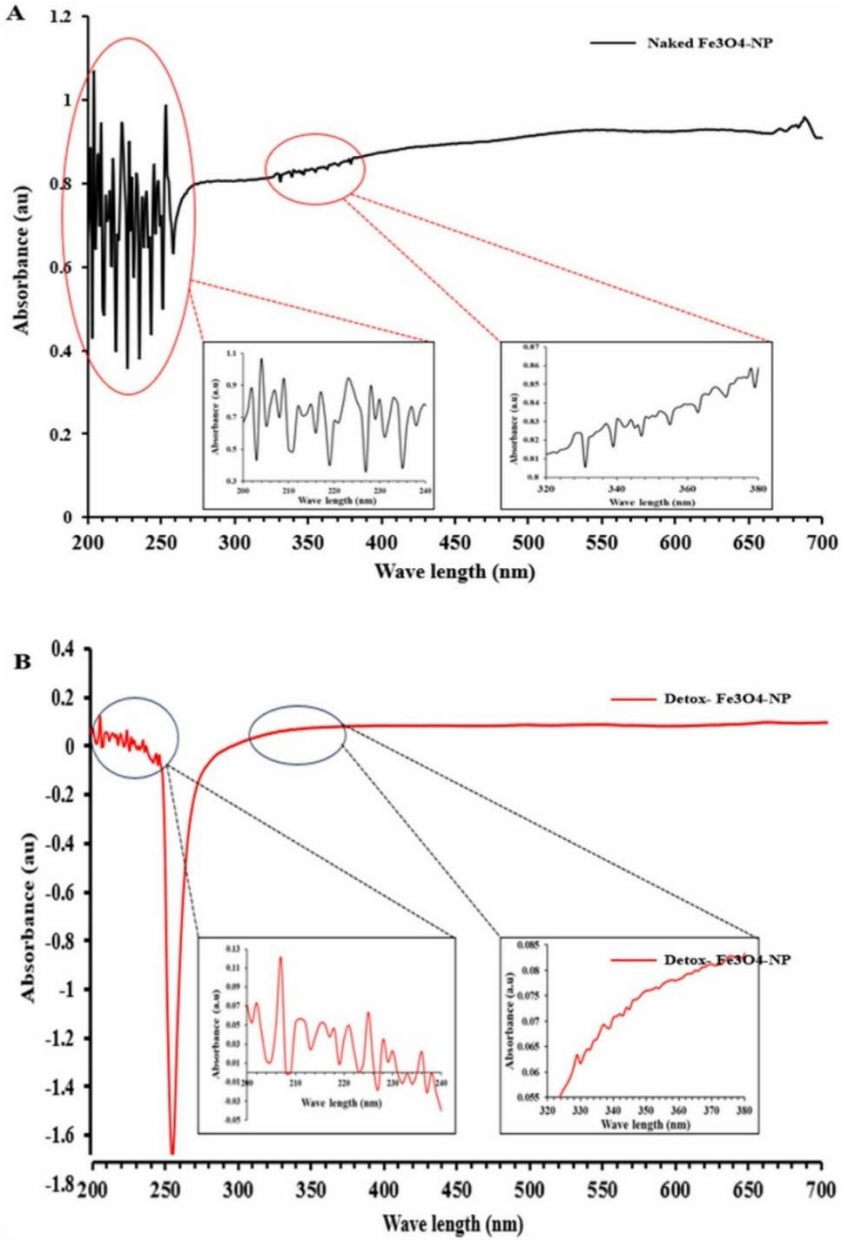

Fig. 5. **(A)** UV–vis absorption spectra of Naked-Fe_3O_4 NP, **(B)** UV–vis absorption spectra of Detox-Fe_3O_4 NP.

to that obtained in the NDSSF (85.15 %) (Table 5).

4. Discussion

4.1. Fe_3O_4 NP as an adsorbent

In the present study, the detoxification potential of the NPs strongly depends on their exceptional properties such as size, surface charge, and surface area to volume ratio (Sanusi et al., 2021). The inhibitors could bind to the active sites of the NPs, selectively and non-selectively, depending on the NP's surface and functional properties of the inhibitors, which influence their removal rate. For instance, the large specific surface area of Fe_3O_4 NPs provided more adsorption sites, consequently resulting in higher detoxification efficiency (Zhang et al., 2023). Hence, nano-adsorbents have the desirable abilities to interact with and adsorb process inhibitors through their chemical and physical properties. The regenerated Fe_3O_4 NP was reused in the detoxification process with the adsorbent (Fe_3O_4 NP) demonstrating high detoxification efficiency (~100 %) in two (2) cycles for all the inhibitors evaluated. This could be attributed to the large surface area of the nanoparticle providing sufficient adsorbent or attachment points (which have not been overloaded) for the inhibitors (Al-Hetlani et al., 2022). The sharp characteristic adsorption peak related to the Fe—O bond vibration of Fe_3O_4 appearing in the detox-Fe_3O_4-NP spectrum further showed the retention of inherent Fe_3O_4 NP property as well as the presence of vacant sites on Fe_3O_4 NP after detoxification (Fan et al., 2017). This further confirms the potential reuseability of the Fe_3O_4 NP recovered after detoxification. The use of magnetic Fe_3O_4 NP, with its added benefits such as reusability, could reduce detoxification costs, consequently reducing the overall capital investment in lignocellulosic bioethanol production.

Table 4
Model equations illustrating the inhibitors removal pattarn with input parameters varied within their boundaries.

Eq.	Detoxification process input: output	Equation type	Model equation form	Fitted model	R^2 value
(i)	Fe_3O_4NP conc: Furfural	DR-Hill	$y = \alpha + \frac{\theta x^{\eta}}{k^{\eta} + x^{\eta}}$	$y = 1.13 + \frac{-0.69x^{1.27}}{0.23^{1.27} + x^{1.27}}$	0.99
(ii)	Fe_3O_4NP conc: HMF	Polynomial regression (degree = 4)	$y = a + bx + cx^2 + dx^3 + ex^4$	$y = 0.279 – 0.187x - 2.97x^2 + 12x^3 – 12.5x^4$	0.99
(iii)	Fe_3O_4NP conc: Acetic acid	DR- Weibull	$y = \gamma + (1-\gamma)(1 - e^{-\beta x^{\alpha}})$	$y = 2.71 + (1 - 2.71)\left(1 - e^{0.48x^{1.12}}\right)$	0.99
(iv)	Fe_3O_4NP conc: Phenol	DR-Hill	$y = \alpha + \frac{\theta x^{\eta}}{k^{\eta} + x^{\eta}}$	$y = 0.098 + \frac{-0.045x^{2.56}}{0.088^{2.56} + x^{2.56}}$	0.99
(v)	Fe_3O_4NP conc: Formaldehyde	DR- Multistage 4	$y = \gamma + (1-\gamma)\left(1 - e^{-\beta_1 x - \beta_2 x^2 - \beta_3 x^3 - \beta_4 x^4}\right)$	$y = 1.16 + (1 - 1.16)\left(1 - e^{5.69x - 0.012x^2 + 0.045x^3 - 0.046x^4}\right)$	0.98
(vi)	Temp: Furfural	Polynomial regression (degree = 5)	$y = a + bx + cx^2 + dx^3 + ex^4 + fx^5$	$y = 3.04 – 0.31x + 0.017x^2 – 0.0005x^3 + (6.3 \times 10^{-6} x^4) – (3.26 \times 10^{-8} x^5)$	0.99
(vii)	Temp: HMF	DR-Hill	$y = \alpha + \frac{\theta x^{\eta}}{k^{\eta} + x^{\eta}}$	$y = 0.25 + \frac{-0.079x^{-9.72}}{47.5^{-9.72} + x^{-9.72}}$	0.99
(viii)	Temp: Acetic acid	Sinusoidal	$y = a + b\ cos\ (cx + d)$	$y = 2.96 + 0.135\ cos\ (0.102x - 0.16)$	0.99
(ix)	Temp: Phenol	Reciprocal quadratic	$y = \frac{1}{a + bx + cx^2}$	$y = \frac{1}{20 + 0.08x - 0.003x^2}$	
(x)	Exp. Time: Furfural	Rational model	$y = \frac{a + bx}{1 + cx + dx^2}$	$y = \frac{0.69 + 0.02x}{1 + 0.029x - 0.000019x^2}$	0.99
(xi)	Exp. Time: HMF	Weibull model (sigmoidal)	$y = \left(a - be^{-cx^d}\right)$	$y = \left(0.30 - 0.14e^{-(2.7\times10^{-5})x^{2.70}}\right)$	0.99
(xii)	Exp. Time: Acetic acid	DR-Hill	$y = \alpha + \frac{\theta x^{\eta}}{k^{\eta} + x^{\eta}}$	$y = 3.20 + \frac{-0.29x^{3.46}}{47.5^{3.46} + x^{3.46}}$	0.96
(xiii)	Exp. Time: Phenol	Reciprocal quadratic	$y = \frac{1}{a + bx + cx^2}$	$y = \frac{1}{18.9 + 0.0005x - 0.00005x^2}$	0.99
(xiv)	Exp. Time: Formaldehyde	Polynomial regression (degree = 5)	$y = a + bx + cx^2 + dx^3 + ex^4 + fx^5$	$y = 1.21 + 0.0012x - 0.00006x^2 + 4.77 \times 10^{-7} x^3$	0.99
(xv)	pH: Furfural	Sinusoidal	$y = a + b\ cos\ (cx + d)$	$y = 0.89 + 0.137\ cos\ (1.02x - 1.76)$	0.99
(xvi)	pH: HMF	Rational model	$y = \frac{a + bx}{1 + cx + dx^2}$	$y = \frac{0.013x - 0.032}{1 - 0.39x + 0.046x^2}$	0.92
(xvii)	pH: Acetic acid	MMF	$y = \frac{ab + cx^d}{b + x^d}$	$y = \frac{2.26(0.0004) + 8.39x^{-6.05}}{0.0004 + x^{-6.05}}$	0.99
(xviii)	pH: Phenol	DR-Hill	$y = \alpha + \frac{\theta x^{\eta}}{k^{\eta} + x^{\eta}}$	$y = 0.046 + \frac{0.46x^{14.25}}{6.53^{14.25} + x^{14.25}}$	0.99
(xix)	pH: Formaldehyde	Polynomial regression (degree = 5)	$y = a + bx + cx^2 + dx^3 + ex^4 + fx^5$	$y = 2.17 – 1.28x - 0.64x^2 – 0.15x^3 + 0.017x^4 – 0.0007x^5$	0.99

4.2. *Effect of model development on inhibitor removal*

The optimized nano detoxification process from this research could be utilised to theoretically predict the inhibitor removal. The sensitivity of the responses to the input parameters is demonstrated by the significant impact of these factors on all the responses. This is corroborated by the perturbation curve of the detoxification plots, which reveals the response of the functional dependent variable as the level of the independent variable changes when other independent variables are fixed at their centre point (Oh et al., 1995). As observed, the importance of each variable shows significant and differing levels of detoxification parameter effects on the removal of process inhibitors. This observed pattern indicates that the nano-adsorbent did not exhibit selective adsorption of sugar and inhibitors (Hong et al., 2021).

Looking at the interactive effects of the input parameters on inhibitor detoxification, reducing sugar concentrations, and sugar loss, summarily, the presence of Fe_3O_4 NP in the solution in synergy with other input parameters is likely to have catalysed the oxidative process by increasing the production of hydroxyl radicals, facilitating the degradation of furfural. This aligns with the findings of Román-Leshkov et al. (2006), confirming that a further increase in catalyst concentration resulted in a significant (60.9 %) reduction in HMF. This reduction was attributed to the decomposition of HMF into levulinic and formic acids by the acidic active sites on the catalyst surface. Also, the effects of these input parameters on the rate of inhibitor attachment to the Fe_3O_4 NP surface could be attributed to the mechanisms of each inhibitor removal. These mechanisms are closely linked to the chemical structures and functional groups possessed by the inhibitors and the nano-sized adsorbent (Sarawan et al., 2019).

After the process optimization and validation, the results demonstrate a 40 % reduction in furfural, 24 % in HMF, 69 % in acetic acid, 49 % in phenol, and 35 % in formaldehyde, coupled with a 3 % increase in reducing sugar was achieved in this present study. The results of the present study were compared with previous reports (Table 3). Zhu et al. (2022) documented the removal efficiency of acetic acid, HMF, and furfural as 47.8 %, >5 %, and 98.7 %, respectively, using lignin nanoparticles. Likewise, using activated charcoal, observed higher inhibitor removal efficiency for furfural (93 %), acetic acid (14 %) and HMF (96 %), but a total sugar loss of 9 %. Also, Sarawan et al. (2019) using activated charcoal, reporting removal efficiency of 98 %, 88 %, and 37 % for furfural, HMF, and acetic acid, respectively, with a 7 % sugar loss. The higher removal efficiency of inhibitors with no sugar loss and the high recyclability of the nano-sized adsorbent suggest that Fe_3O_4 nanoparticle-based hydrolysate detoxification is desirable for the economic viability of lignocellulosic-based ethanol production. The varying impacts exhibited by Fe_3O_4 NPs on each inhibitor are largely attributed to the different chemical structures and functional groups possessed by the inhibitors and the nano-sized adsorbent.

4.3. *Fe_3O_4 NP detoxification mechanisms*

Comparing the spectrum of Fe_3O_4 NP with detox-Fe_3O_4-NP (Fig. 3A), a strong indication of the amino, phenolic, aldehyde, amine, and hydroxyl groups on the various inhibitors in complexation with Fe (III) of the Fe_3O_4 NP adsorbent was observed (Cao et al., 2014). Similarly, the photoluminescence spectra (Fig. 3A) showed high transition levels due to the recombination of excitons (inhibitors) on the nano surface (Wang et al., 2019; Ajibade et al., 2020), further confirming the inhibitor

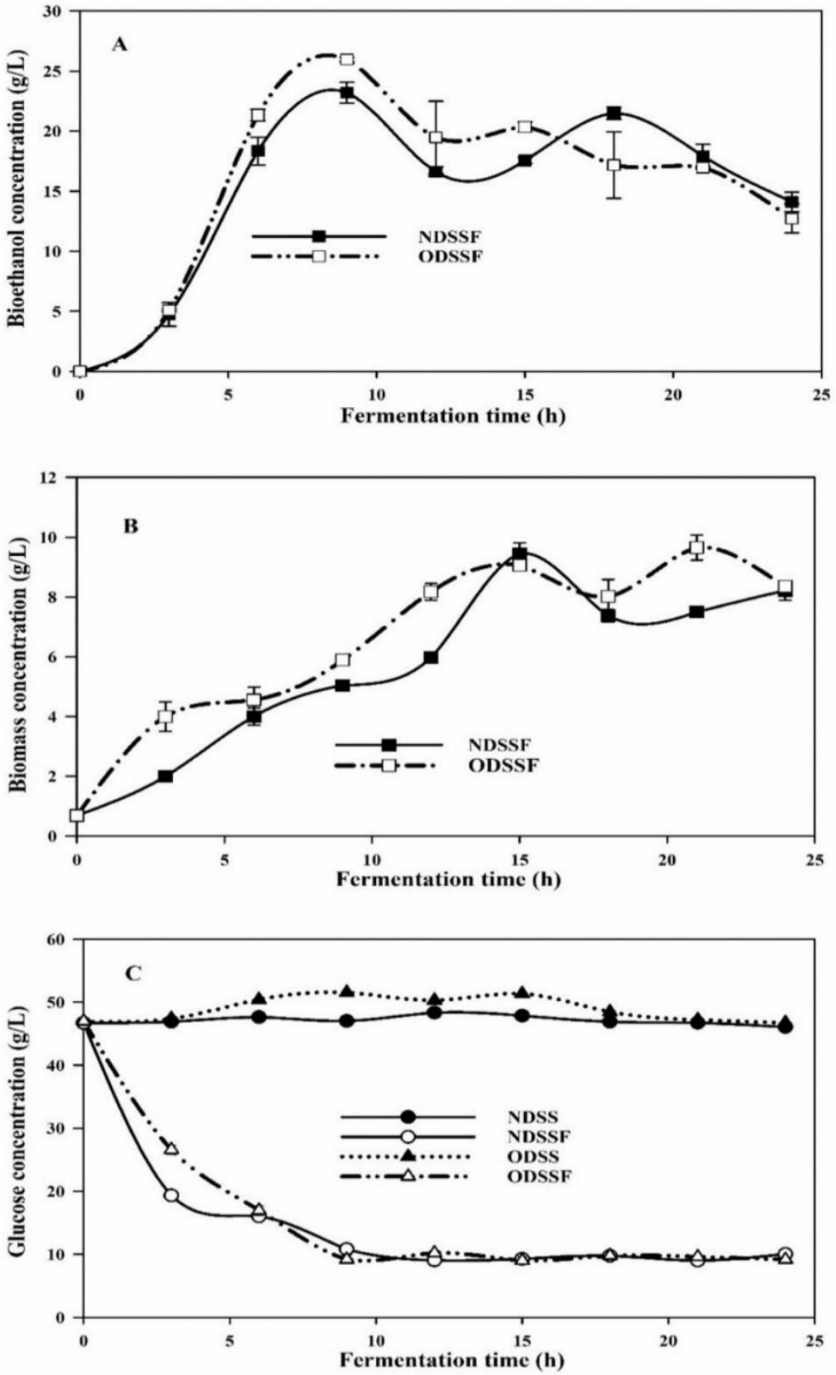

Fig. 6. Production of bioethanol under NDSSF and ODSSF (**A**) conditions; *S. cerevisiae* growth during bioethanol production using NDSSF and ODSSF (**B**): Sugar utilization under NDSS, NDSSF, ODSS, ODSSF (**C**).

Table 5
Performance of SSF with detoxified and non-detoxified hydrolysates.

Fermentation modes	NDSSF	ODSSF
Sugar utilization (%)	80.71 ± 0.034^a	80.47 ± 0.120^a
Saccharification efficiency (%)	83.41 ± 0.976^a	88.95 ± 0.757^b
Bioethanol yield (g/g)	0.494 ± 0.018^a	0.504 ± 0.004^b
Bioethanol concentration (g/L)	23.204 ± 0.420^a	25.964 ± 0.092^b
Bioethanol productivity (g/L/h)	2.578 ± 0.048^a	2.885 ± 0.010^b

The superscripts "a" and "b" indicate pairwise similarity or statistical difference in the output between the fermentation modes (NDSSF and ODSSF).

removal. Also, the observable broader spectrum was due to the effective passivation of the trapped luminescence caused by the inhibitors' compound during detoxification. This further elucidates the influence of adsorbed inhibitors on the luminescent properties of Fe_3O_4 nanoparticles. These observations can further be attributed to the differences in wavelength of the samples. The higher the wavelength, the lower the energy excitation of the sample. A change in the wavelength could have resulted in lower energy excitation observed in detox-Fe_3O_4-NP compared to that of the Fe_3O_4 NP. This difference could be due to the change in particle size; the detox-Fe_3O_4-NP particle size has increased after the detoxification process (see supplementary document).

Additionally, the optical absorption spectra of Fe_3O_4 NP and the detox-Fe_3O_4-NP were evaluated using UV spectroscopy (Fig. 4). The spectra showed that both Fe_3O_4 NP and the detox-Fe_3O_4-NP displayed distinct variations in absorption wavelengths, further affirming the differences in the particle properties due to the absence or presence of attached inhibitors.

In addition, the particle size of the nanoparticles obtained from the TEM micrograph displayed variations in both the Fe_3O_4 NP and the detox-Fe_3O_4-NP (see supplementary document). Moreover, the increase in the detox-Fe_3O_4-NP particle size was due to the adsorbed inhibitors on the surface of the Fe_3O_4 NP. The average size of 20.08 nm was observed for the Fe_3O_4 NP and 44.84 nm for the detox-Fe_3O_4-NP. Notably, the particle size of the Fe_3O_4 NP increased by >2-fold after the detoxification process and attributed to the adsorption of the inhibitors to the nanoparticle's surface or the ligand complexation of the nanoparticle with the inhibitors.

Furthermore, the inhibitor speciation and surface charge of the Fe_3O_4 NP were likely influenced by the pH of the system (Sanusi et al., 2019). The oxidation rate and immobilization rate on iron oxide are strongly pH-dependent (Lu et al., 2008). Similarly, pH plays a crucial role in influencing the adsorption mechanism of detoxifiers, such as Fe_3O_4 NP in this case (Mussatto and Roberto, 2004). Under specific pH conditions, especially pH <5 (as observed in the optimal pH of 4.14 in this study), there is likely a higher migration of inhibitors to the surface of Fe_3O_4 NP (Zhang et al., 2023). Additionally, a change in the pH of the system could have caused the precipitation and/or volatility of inhibitors. Reports have demonstrated that the inclusion of nanoparticles in bioprocessing can modulate the system pH as well as buffering the system to a significant extent (Sanusi et al., 2019). Under non-optimal pH conditions, there could be a higher competition among the different available inhibitory ions, hindering the migration of individual inhibitors to the target site on the Fe_3O_4 NP surface.

Additionally, the electrostatic attraction due to the difference in charge of the inhibitor and the surface charge of Fe_3O_4 NP resulted in the promotion of inhibitor removal. Moreover, the removal capacity of Fe_3O_4 NP is higher at high inhibitor concentrations, which could be explained simply by the fact that at higher inhibitor concentrations, the driving force for the migration of inhibitors to Fe_3O_4 NP is higher resulting surface binding (Cheng et al., 2022). For instance, in this study, acetic acid, furfural, and formaldehyde, which had higher initial concentrations of 14.052 g/L, 1.098 g/L, and 1.341 g/L (final concentration: 4.324 g/L, 0.663 g/L, and 0.966 g/L), respectively, were the most detoxified from the pretreated hydrolysate. Compared to inhibitors (HMF, phenol) with lower initial concentrations (0.195 g/L, 0.0156 g/g), the removal rate was lower (final concentration: 0.161 g/L, 0.0137 g/g), respectively. Also, adsorption is an electrochemical process that requires a driving force that could be influenced by the initial inhibitor concentration. Moreover, the physiochemical properties of these inhibitors such as the chemical structure and the functional group could influence their adsorption. Hence, high inhibitory compound concentration, chemical structure and the functional group of the inhibitors resulted in higher inhibitor adsorption rate in the pretreated hydrolysate, leading to a lowering of the ion constituent of the medium and, consequently, the overall charge potential of the system.

Moreover, the higher specific surface area has been proven to provide more adsorption sites, thus yielding higher inhibitor removal efficiency (Zhang et al., 2023). On the other hand, the high adsorption capacity of Fe_3O_4 NP on the inhibitory compound due to the presence of numerous vacant sites and subsequent increase in Fe_3O_4 NP concentration must have led to repulsive forces between the dominating ions, hindering their accessibility (Jin et al., 2023). On the other hand, the Fe_3O_4 NP adsorbent has the potential to interact with inhibitory compounds to form ligands as well as complexes (complexation) due to their chelating capacities with the available functional groups of these inhibitors. Additionally, Fe_3O_4 nanoparticles probably achieved inhibitory compound removal through a radical degradation mechanism (Mani et al., 2018; Zeng et al., 2014).

Likewise, the sensitivity testing revealed that the NP concentration had differing impacts on each inhibitor, exhibiting different model equations, mostly a dose-response (DR) relationship (Table 4) with a threshold concentration at 0.2 % *w/v*. Moreover, the concentrations of the inhibitors were not significantly impacted until the process temperature was >35 °C (see supplementary document). It is noteworthy that pH influenced the inhibitor removal process remarkably, such that as pH increased above 5, the detoxification process was negatively impacted, thereby indicating higher sensitivity.

4.4. Effect of detoxified hydrolysate on bioethanol production

The bioethanol productions under NDSHF, ODSHF, NDSSF, and ODSSF processes are illustrated in Fig. 5A and B, respectively. NDSHF and ODSHF exhibited a shorter lag phase (2 h) compared to the 3 h lag time observed in the NDSSF and ODSSF processes. A significant increase in bioethanol concentration was noted from 5.82 to 19.57 g/L (NDSHF), 6.09 to 20.85 g/L (ODSHF), 4.74 to 23.20 g/L (NDSSF), and 5.09 to 25.96 g/L (ODSSF) between 3 and 9 h (Fig. 5A and B). This coincided with an increase in yeast growth (Fig. 4C–D) and sugar utilization (Fig. 5E–F). Further increases in ethanol concentration were observed for NDSHF (19.77 g/L) at 18 h and ODSHF (21.44 g/L) at 15 h. In both ODSHF and ODSSF processes, higher ethanol amounts of 21.443 g/L and 25.964 g/L were recorded. The nano-based detoxification approach diminishes the negative effects of inhibitors in the hydrolysates through probable inhibitory compound adsorption, chelation, and neutralization chemistry principles. Aside from acting as a detoxifier, Fe_3O_4 NP increases the hydrolytic rate due to its large surface area to volume ratio, enabling *S. cerevisiae* to bind onto the active sites of the molecule. This subsequently stimulates biochemical processes for enhanced enzymatic activities. Additionally, the NP aids mass transfer, *S. cerevisiae* growth, and the metabolic pathway for high ethanol production.

The ODSHF (2.317 g/L/h) and NDSHF (2.17 g/L/h) exhibited lower ethanol productivity, with corresponding ethanol yields of 0.44 g/g and 0.431 g/g, respectively. In ODSSF and NDSSF, ethanol productivity was 2.885 and 2.578 g/L/h, translating to yields of 0.504 and 0.494 g/g, respectively. Ethanol yield and productivity were higher in both detoxified processes (ODSHF and ODSSF) compared to NDSHF and NDSSF. Furthermore, the high productivity and yield achieved in ODSSF and ODSHF are consistent with saccharification efficiencies of 88.95 % and 85.15 %, respectively (Table 5). The positive outcomes observed in ODSSF and ODSHF can also be attributed, in part, to the reduction of inhibitory compounds in the pretreated hydrolysate. This reduction promotes the metabolic and growth kinetics of *S. cerevisiae*. This is supported by the enhanced specific growth rate observed with *S. cerevisiae* under the conditions of ODSSF and ODSHF. Fermentation inhibitors, such as acetic acid and furfural, are known to impede bioethanol formation by negatively affecting cell growth due to the accumulation of anions from acid dissociation, resulting in detrimental intracellular conditions (Gupta et al., 2017; Faramarzi et al., 2019). Additionally, furfural causes the build-up of reactive oxygen species (ROS) within the cell, leading to impairment of cellular organelles such as the vacuole, mitochondrial membranes, chromatin, and actin (Qiu and Jiang, 2017; Sanusi et al., 2021). Furthermore, a previous study has shown that Fe_3O_4 NP exhibits an electropositive affinity and interaction with glucose, enhancing substrate-cell contact for high ethanol productivity (Sanusi et al., 2021). Therefore, the presence of Fe_3O_4 NP could have impacted the processes not only as a detoxifying agent but also as a biocatalyst, enhancing *S. cerevisiae* metabolic activities and growth, ultimately improving overall process performance (Sanusi et al., 2021). Notably, after the exponential phase (>9 h), ethanol concentration decreased, corresponding with a gradual deceleration in yeast growth and the onset of the stationary phase (Fig. 5C and D). Decrease in ethanol concentration can be attributed to glucose depletion, ethanol oxidation, and the build-up of organic acids (Shafaghat et al., 2010). Additionally, the reversible conversion of ethanol to aldehydes by

alcohol dehydrogenases (ADHs), in combination with a reduction in NAD+ or NADP+, could result in a decrease in ethanol concentration during fermentation (De Smidt et al., 2008). Another reason could be the accumulation of excess ethanol in the fermentation broth, leading to the deactivation of essential ethanol-producing enzymes such as pyruvate decarboxylase and alcohol dehydrogenase (Raj et al., 2014).

5. Conclusion

The study successfully demonstrated the efficacy of nanoparticle-based detoxification of pretreated WPP hydrolysate without sugar loss. Fe_3O_4 nanoparticles efficiently removed these inhibitors through surface adsorption and complexation of inhibitory compounds. Interestingly, the detoxification process also enhanced saccharification efficiency and *S. cerevisiae* growth kinetics, achieving high specific growth rate (1.18-fold increment). This translated to significant bioethanol productivity (2.885 g/L/h) and yield (0.504 g/g). These findings underscore a need for an efficient detoxification strategy towards improved and a cost effective lignocellulosic-based bioethanol production.

Funding

Not applicable.

CRediT authorship contribution statement

Adeniyi P. Adebule: Writing – review & editing, Writing – original draft, Visualization, Validation, Software, Methodology, Investigation, Formal analysis, Data curation, Conceptualization. **Isaac A. Sanusi:** Writing – review & editing, Visualization, Validation, Supervision, Project administration, Methodology, Formal analysis, Data curation, Conceptualization. **E.B. Gueguim Kana:** Conceptualization, Writing – review & editing, Resources, Supervision.

Declaration of competing interest

The authors: Adebule P. Adeniyi, Isaac A. Sanusi, Gueguim E.B. Kana declare there are no conflict of interest in this work.

Data availability

Data will be made available on request.

Acknowledgments

The authors thankfully acknowledge Cynthia Matyumza from the Microscopy and Microanalysis Unit, University of KwaZulu-Natal, Pietermaritzburg campus for providing all the necessary help in carrying out the SEM and TEM analyses.

Appendix A. Supplementary data

Supplementary data to this article can be found online at https://doi.org/10.1016/j.biteb.2024.101783.

References

Abuhena, M., Al-Rashid, J., Azim, M.F., Barman, N.C., Khan, M.N., Kabir, M.G., Rasul, N. M., Huang, Z., Akter, S., Huq, M.A., 2022a. Optimization of *Bacillus subtilis*-based fermentation of anaerobic digestate and biohazard-free application in endophyte-assisted hardening of micropropagated plantlets for increasing survivability. Biocatal. Agric. Biotechnol. 45, 102512 https://doi.org/10.1016/j.bcab.2022.102512.

Abuhena, M., Al-Rashid, J., Azim, M.F., Khan, M.N., Kabir, M.G., Barman, N.C., Rasul, N. M., Akter, S., Huq, M.A., 2022b. Optimization of industrial (3000*L*) production of *Bacillus subtilis* CW-S and its novel application for minituber and industrial-grade potato cultivation. Sci. Rep. 12, 11153. https://doi.org/10.1038/s41598-022-15366-5.

Ajibade, P.A., Sikakane, B.M., Botha, N.L., Oluwalana, A.E., Omondi, B., 2020. Synthesis and crystal structures of bis (dibenzyl dithiocarbamato) Cu (II) and Ag (I) complexes: Precursors for $Cu_{1.8}S$ and Ag_2S nano-photocatalysts. J. Mol. Struct. 1221, 1–9. https://doi.org/10.1016/j.molstruc.2020.128791.

Akalın, M.K., Karagöz, S., Akyüz, M., 2013. Application of response surface methodology to extract yields from stinging nettle under supercritical ethanol conditions. J. Supercrit. Fluids 84, 164–172. https://doi.org/10.1016/j.supflu.2013.10.004.

Al-Hetlani, E., D'Cruz, B., Amin, M.O., Madkour, M., 2022. Effective magnetic nanoadsorbent based on a carbonaceous/spinel ferrite nanocomposite for the removal of pharmaceutical pollutants from wastewater. Environ. Sci. Water Res. Technol. 8, 998–1010. https://doi.org/10.1039/d1ew00495f.

Cao, C., Xiao, L., Chen, C., Shi, X., Cao, Q., Gao, L., 2014. In situ preparation of magnetic Fe_3O_4/chitosan nanoparticles via a novel reduction precipitation method and their application in adsorption of reactive azo dye. Powder Technol. 260 (7), 90–97. https://doi.org/10.1016/j.powtec.2014.03.025.

Cheng, H., Zhang, J., Chen, Y., Zhang, W., Ji, R., Song, Y., Li, W., Bian, Y., Jiang, X., Xue, J., Han, J., 2022. Hierarchical porous biochars with controlled pore structures derived from co-pyrolysis of potassium/calcium carbonate with cotton straw for efficient sorption of diethyl phthalate from aqueous solution. Bioresour. Technol. 346 (126604), 1–9. https://doi.org/10.1016/j.biortech.2021.126604.

De Smidt, O., Du Preez, J.C., Albertyn, J., 2008. The alcohol dehydrogenases of Saccharomyces cerevisiae: a comprehensive review. FEMS Yeast Res. 8, 967–978. https://doi.org/10.1111/j.1567-1364.2008.00387.x.

Fan, H.-L., Zhou, S.-F., Jiao, W.-Z., Qi, G.-S., Liu, Y.-Z., 2017. Removal of heavy metal ions by magnetic chitosan nanoparticles prepared continuously via high-gravity reactive precipitation method. Carbohydr. Polym. 174, 1192–1200. https://doi.org/10.1016/j.carbpol.2017.07.050.

Faramarzi, S., Anzabi, Y., Fararizadeh-Malmiri, H., 2019. Selenium supplementation during fermentation with sugar beet molasses and saccharomyces cerevisiae to increase bioethanol production. Green Process. Synth. 8 (1), 622–628. https://doi.org/10.1515/gps-2019-0032.

Gupta, R., Gautam, S., Shukla, R., Kuhad, R.C., 2017. Study of charcoal detoxification of acid hydrolysate from corncob and its fermentation to xylitol. J. Environ. Chem. Eng. 5, 4573–4582. https://doi.org/10.1016/j.jece.2017.07.073.

Hong, J.W., Gam, D.H., Kim, J.H., Jeon, S.J., Kim, H.S., Kim, J.W., 2021. Process development for the detoxification of fermentation inhibitors from acid pretreated microalgae hydrolysate. Molecules 26 (2435), 1–14. https://doi.org/10.3390/molecules26092435.

Jin, X., Lu, Y., Zhang, H., Ju, Y., Zeng, X., Li, X., Chen, J., Liu, Z., Yu, S., Wang, S., 2023. Synthesis and application of ion-exchange magnetic microspheres for deep removal of trace acetic acid from DMAC waste liquid. Nanomaterials 13, 509. https://doi.org/10.3390/nano13030509.

Khaghani, S., Ghanbari, B., 2016. Microwave synthesis of Fe_2O_3 and ZnO nanoparticles and evaluation its application on grain iron and zinc concentrations of wheat (*Triticum aestivum* L.) and their relationships to grain yield. J. Nanostruct. 6 (2), 149–155. https://doi.org/10.7508/JNS.2016.02.007.

Larsson, S., Palmqvist, E., Hahn-Hägerdal, B., Tengborg, C., Stenberg, K., Zacchi, G., Nilvebrant, N., 1999. The generation of fermentation inhibitors during dilute acid hydrolysis of softwood. Enzyme Microb. Technol. 24 (3–4), 151–159.

Lu, Y.W., Huang, C.P., Huang, Y.H., Lin, C.P., Chen, H.T., 2008. Effect of pH on the oxidation of ferrous ion and immobilization technology of iron hydro(oxide) in fluidized bed reactor. Sep. Sci. Technol. 43 (7), 1632–1641. https://doi.org/10.1080/01496390801973656.

Mani, A., Kulandaivellu, T., Govindaswamy, S., Mohan, A.M., 2018. Fe_3O_4 nanoparticle-encapsulated mesoporous carbon composite: an efficient heterogeneous Fenton catalyst for phenol degradation. Environ. Sci. Pollut. Res. Int. 25 (21), 20419–20429. https://doi.org/10.1007/s11356-017-9663-4.

Martinez, A., Rodriguez, M.E., Wells, M.L., York, S.W., Preston, J.F., Ingram, L.O., 2001. Detoxification of dilute acid hydrolysates of lignocellulose with lime. Biotechnol. Prog. 17, 287–293. https://doi.org/10.1021/bp0001720.

Millati, R., Niklasson, C., Taherzadeh, M.J., 2002. Effect of pH, time, and temperature of overliming on detoxification of dilute acid hydrolyzates for fermentation by *Saccharomyces cerevisiae*. Process Biochem. 38, 515–522. https://doi.org/10.1016/S0032-9592%2802%2900176-0.

Mohagheghi, A., Ruth, M., Schnell, D.J., 2006. Conditioning hemicellulose hydrolysates for fermentation: effects of overliming pH on sugar and ethanol yields. Process Biochem. 41, 1806–1811. https://doi.org/10.1016/J.PROCBIO.2006.03.028.

Mussatto, S.I., Roberto, I.C., 2004. Alternatives for detoxification of diluted-acid lignocellulosic hydrolyzates for use in fermentative processes: a review. Bioresour. Technol. 93 (1), 1–10. https://www.ncbi.nlm.nih.gov/pubmed/14987714.

Oh, S.J., Rheem, S.S., Sim, J.H., Kim, S.K., Baek, Y.G., 1995. Optimizing conditions for the growth of Lactobacillus casei YIT 9018 in tryptone-yeast extract-glucose medium by using response surface methodology. Appl. Environ. Microbiol. 61, 3809–3814. https://doi.org/10.1128/aem.61.11.3809-3814.1995.

Omran, A.P., Coughlin, C.B., 2020. Bial's test, a simple method for formaldehyde detection. Bial's test, a simple method for formaldehyde detection. Biomed. J Sci. Tech. Res. 27 (3), 20860–20863. https://doi.org/10.26717/bjstr.2020.27.004515.

Qiu, Z., Jiang, R., 2017. Improving *Saccharomyces cerevisiae* ethanol production and tolerance via RNA polymerase II subunit Rpb7. Biotechnol. Biofuels 10, 125. https://doi.org/10.1186/s13068-017-0806-0.

Raj, S.B., Ramaswamy, S., Plapp, B.V., 2014. Yeast alcohol dehydrogenase structure and catalysis. Biochemistry 53, 5791–5803. https://doi.org/10.1021/bi5006442.

Román-Leshkov, Y., Chheda, J.N., Dumesic, J.A., 2006. Phase modifiers promote efficient production of hydroxymethylfurfural from fructose. Science 312 (5782), 1933–1937. https://doi.org/10.1126/science.1126337.

Rorke, D.C.S., Suinyuy, T.N., Gueguim Kana, E.B., 2017. Microwave-assisted chemical pretreatment of waste sorghum leaves: Process optimization and development of an intelligent model for determination of volatile compound fractions. Bioresour. Technol. 224, 590–600. https://doi.org/10.1016/j.biortech.2016.10.048.

Sajab, M.S., Santanaraj, J., Mohammad, A.W., Kaco, H., Harum, S., 2019. Detoxification of lignocellulosic hydrolysates by in situ formation of Fe [0] nanoparticles on activated carbon. Bioresources 14 (4), 8614–8626. https://doi.org/10.15376/biores.14.4.8614-8626.

Sanusi, A.I., Faloye, F.D., Kana, E.G.B., 2019. Impact of various metallic oxide nanoparticles on ethanol production by *Saccharomyces cerevisiae* BY4743: Screening, kinetic study and validation on Potato waste. Catal. Lett. 149 (7), 2015–2031. https://doi.org/10.1007/s10562-019-02796-6.

Sanusi, A.I., Suinyuy, T.N., Kana, G.E.B., 2021. Impact of nanoparticle inclusion on bioethanol production process kinetic and inhibitor profile. Biotechnol. Rep. 29 (1–12), e00585 https://doi.org/10.1016/j.btre.2021.e00585.

Sarawan, C., Suinyuy, T.N., Sewsynker-Sukai, Y., Gueguim Kana, E.B., 2019. Optimized activated charcoal detoxification of acid-pretreated lignocellulosic substrate and assessment for bioethanol production. Bioresour. Technol. 286, 1–10. https://doi.org/10.1016/j.biortech.2019.121403.

Shafaghat, H., Najafpour, G.D., Rezaei, S.P., Sharifzadeh, M., 2010. Optimal growth of Saccharomyces cerevisiae (PTCC 24860) on pretreated molasses for ethanol production: application of response surface methodology. Chem. Ind. Chem. Eng. Q. 16 (2), 199–206. https://doi.org/10.2298/CICEQ100201029S.

Sluiter, A., Hames, B., Ruiz, R., Scarlata, C., Sluiter, J., Templeton, D., Crocker, D., 2008. NREL Technical Report, NREL/TP-510-42618. In: http://www.nrel.gov/biomass/analytical_procedures.html.

Sun, P., Zhang, W., Zou, B., Zhou, L., Ye, Z., Zhao, Q., 2021. Preparation of EDTA-modified magnetic attapulgite chitosan gel bead adsorbent for the removal of Cu (II), Pb (II), and Ni (II). Int. J. Biol. Macromol. 182, 1138–1149. https://doi.org/10.1016/j.ijbiomac.2021.04.132.

Tian, S.-Q., Zhao, R.-Y., Chen, Z.-C., 2018. Review of the pretreatment and bioconversion of lignocellulosic biomass from wheat straw materials. Renew. Sust. Energ. Rev. 91, 483–489. https://doi.org/10.1016/j.rser.2018.03.113.

Tohidi, T., Jamshidi-Ghaleh, K., 2015. Effect of TEA on photoluminescence properties of PbS nanocrystalline thin films. Appl. Phys. A Mater. Sci. Process. 118, 1247–1258. https://doi.org/10.1007/s00339-014-8823-3.

Wang, Y., Szokolova, K., Nasir, M., Sofer, Z., Pumera, M., 2019. Layered crystalline and amorphous platinum disulfide (PtS2): contrasting electrochemistry. Chem. Eur. J. 25, 7330–7338. https://doi.org/10.1002/chem.201900331.

Zeng, T., Zhang, X., Wang, S., Ma, Y., Niu, H., Cai, Y., 2014. Assembly of a nanoreactor system with confined magnetite core and shell for enhanced Fenton-like catalysis. Chem. Eur. J. 20, 6474–6481. https://doi.org/10.1002/chem.201304221.

Zhang, Y., Tang, Y., Yan, R., Li, J., Li, C., Liang, S., 2023. Removal performance and mechanisms of aqueous Cr (VI) by biochar derived from waste hazelnut shell. Environ. Sci. Pollut. Res. 30, 97310–97318. https://doi.org/10.1007/s11356-023-28603-9.

Zhu, J., Jiao, N., Zhang, H., Xu, G., Xu, Y., 2022. Detoxification of lignocellulosic pre-hydrolysate by lignin nanoparticles, prepared from biorefinery biowaste, to enhance ethanol production. Bioprocess Biosyst. Eng. 45, 1011–1018. https://doi.org/10.1007/s00449-022-02720-0.

CHAPTER 4

Adsorption kinetics and thermodynamics of Fe_3O_4-nanoparticle-based detoxification of process inhibitors in pretreated waste potato peel hydrolysate

This chapter has been published in *Bioresource Technology Reports* (102185) with the title: Adsorption kinetics and thermodynamics of Fe_3O_4-nanoparticle-based detoxification of process inhibitors in pretreated waste potato peel hydrolysate, https://doi.org/10.1016/j.biteb.2025.102185. The published paper is presented in the following pages.

Bioresource Technology Reports 31 (2025) 102185

Contents lists available at ScienceDirect

Bioresource Technology Reports

journal homepage: www.sciencedirect.com/journal/bioresource-technology-reports

Adsorption kinetics and thermodynamics of Fe_3O_4-nanoparticle-based detoxification of process inhibitors in pretreated waste potato peel hydrolysate

Adeniyi P. Adebule, Isaac A. Sanusi *, Gueguim E.B. Kana

University of KwaZulu-Natal, School of Life Sciences, Pietermaritzburg campus, South Africa

ARTICLE INFO

Keywords:
Adsorption kinetics
Fe_3O_4 nanoadsorbent
Inhibitors
Hydrolysate
Detoxification

ABSTRACT

This study evaluates the efficiency of Fe_3O_4 nanoparticle adsorbent based on contact time, pH, temperature, inhibitors' initial concentration and nanoadsorbent dosage in the removal of inhibitory compounds (ICs) in pretreated waste potato peel hydrolysate using batch adsorption studies. The results revealed chemisorptive interaction between the nanoadsorbent and the ICs. The adsorption of phenol and HMF closely followed the Langmuir model (R^2 = 0.997 and 0.966, respectively). Meanwhile, acetic acid and formaldehyde adsorption followed the Freundlich model (R^2 = 0.985 and 0.980, respectively), whereas furfural followed the Temkin model (R^2 = 0.970). Moreover, the ΔG^0 (the thermodynamics) decreased with increasing temperature, implying that the nature of the adsorption process is spontaneous (shown by ΔS^0) and endothermic (indicated by ΔH^0), except for furfural inhibitor. Fe_3O_4-nano-based adsorbent demonstrates a multi-adsorption mechanism capable of both uniform and variable binding, primarily relying on strong interactions with adsorbate molecules, which is consistent with chemisorptive mechanisms.

1. Introduction

Lignocellulosic biomasses (LB) are abundant, renewable and widely available resource that can be used for sustainable energy production (Adebule et al., 2024). Lignocellulosic-based bioprocess energy production involves a pretreatment process that releases not only cellulose, hemicellulose, and starch components but also inhibitory byproducts such as phenol, furfural, acetic acid and 5-hydroxymethylfurfural (HMF) (Kag et al., 2022; Adebule et al., 2024). These inhibitory compounds have been implicated in prolonging the lag phase of growth of fermentation microbes and causing metabolic process interference (Bishop et al., 2024). This ultimately reduces the efficiency and the productivity of the process. Additionally, they have been shown to suppress and inhibit enzymatic activities, resulting in impaired overall enzymatic and cellular functions (Becerra et al., 2022). The presence of these fermentation inhibitors and their interference in lignocellulosic-based bioprocessing highlighting the critical significance of their removal in pretreated hydrolysate (Sanusi et al., 2020). Many removal attempts have been investigated using different adsorbents such as nanoparticles (NPs), until now there is a dearth of studies on the adsorption kinetics and the thermodynamics of inhibitory compound removal in pretreated hydrolysate. Understanding the adsorption kinetics and the effect of temperature on the inhibitory compound removal process will provide valuable insights in the detoxification of pretreated lignocellulosic hydrolysate design towards improving yields (Adebule et al., 2024). Additionally, this will offer clarity on the dynamics of the adsorption mechanisms of nanoadsorbent in inhibitory compound removal.

Nanotechnology has been used for the removal of inhibitory compounds (Bishop et al., 2024). Nanotechnology application with its desirable advantages is one of the newest modalities adopted to mitigate the impact of inhibitory compounds in bioprocessing. Different nanoadsorbents and nanoparticles (NPs) types, both inorganic and organic, have displayed varying adsorption capacities when implemented to detoxify pretreated hydrolysates (Fan et al., 2017; Sanusi et al., 2021; Rezaei et al., 2023; Adebule et al., 2024; Zondi et al., 2025). On the other hand, detoxification adsorbents such as activated charcoal and activated clay have been used in the detoxification of pretreated hydrolysate, but these adsorbents have low adsorption efficiency and cannot be easily reused (Adebule et al., 2024). Novel absorbents like Fe_3O_4 nanoparticle with higher efficiency and recyclable in the detoxification of pretreated hydrolysates is desirable. Moreover, nanoparticles such as Fe_3O_4 nanoparticle has high adsorption capacity, low toxicity, multi-surface

* Corresponding author.
E-mail address: Sanusia@ukzn.ac.za (I.A. Sanusi).

https://doi.org/10.1016/j.biteb.2025.102185
Received 19 February 2025; Received in revised form 1 May 2025; Accepted 15 June 2025
Available online 19 June 2025

functional potential, and magnetic properties (Igwegbe et al., 2020; Rezaei et al., 2023; Qais et al., 2023; Alshandoudi et al., 2024). Other desirable aspect in the use of Fe_3O_4 NPs adsorbent is its easy reusability due to its magnetic property, low cost and scalability due to its recyclability potential (Adebule et al., 2024).

Although the proposed mechanisms for IC removal involve surface adsorption, chelation, and complexation, with pH, initial inhibitor concentration, and nanoparticle functionality being key influencing factors, further investigation is needed to fully understand the adsorption mechanism (Oluwalana and Ajibade, 2021; Ajibade et al., 2021; Meena et al., 2023; Adebule et al., 2024). Presently, there is a dearth of literature on the adsorption kinetic, isotherm and the thermodynamics of bioprocess inhibitory compound removal, especially, the adsorption kinetics and the thermodynamics of Fe_3O_4-NP adsorbent during IC removal in pretreated waste potato peels (WPP) hydrolysate has not been reported. Given the abovementioned research gap this work aims to conduct a comprehensive adsorption study of Fe_3O_4-NP adsorbent for the removal of phenol, furfural, acetic acid, formaldehyde and 5-hydroxymethylfurfural inhibitory compounds in pretreated WPP hydrolysate. The main objectives of this work was to: (1) elucidate the adsorption kinetics and mechanisms of Fe_3O_4-NP for the detoxification of these inhibitory compounds from pretreated WPP hydrolysate using Pseudo-first order (PFO), Pseudo-second-order (PSO), Elovich and intra-particle diffusion models, and (2) study the adsorption isotherm and thermodynamics of IC removal processes via Langmuir, Freundlich and Temkin's isotherms to further elucidate the adsorptive modality of Fe_3O_4-NP adsorbent in removing phenol, furfural, acetic acid, formaldehyde and 5-hydroxymethylfurfural in the pretreated hydrolysate.

2. Materials and methods

2.1. Chemicals used

The various chemicals utilised in this study were of reagent grade and applied without prior modification or purification. Iron (II) sulfate heptahydrate ($FeSO_4.7H_2O$, 97 %), sodium hydroxide (NaOH), GR-grade furfural, 5-hydroxymethylfurfural (HMF), phenol, formaldehyde, and acetic acid (CH_3COOH, 99 %). Deionised water obtained from an Elix Milli Q water deioniser was employed throughout the experiments.

2.2. Preparation and characterisation of Fe_3O_4 NP

Iron (III) oxide nanoparticles (Fe_3O_4 NP) were synthesised using the co-precipitation protocol described by Sanusi et al. (2019). A 0.1 M of $FeSO_4{\cdot}7H_2O$ was prepared, and the pH of this solution was adjusted to 12 by the dropwise addition of 1 M sodium hydroxide (NaOH), and the final volume was brought to 200 mL. Fe_3O_4 NP was precipitated from the solution by subjecting the solution to microwave radiation (700 W) for 10 min. The resulting Fe_3O_4 NP were dried in an oven at 70 °C, and the dried Fe_3O_4 NP was thereafter characterised.

The elemental unit of Fe_3O_4 NP was examined with scanning electron microscopy (SEM, ZEISS EVO/LS15, United Kingdom). Transmission electron microscopy (TEM, JEM-1400, JEOL, USA) was employed to determine the particle size and shape of the NPs. Moreover, the synthesised Fe_3O_4 NPs functional group was examined by Fourier Transform Infrared (FTIR) spectroscopy (Spectrum 100, PerkinElmer, USA) across the FTIR spectra range of 500 and 4000 cm^{-1}. Subsequently, the ultra-violet visible (UV–vis) absorption spectral properties of the Fe_3O_4 NPs were obtained with ultra-violet visible spectrophotometry (200–700 nm). Furthermore, Fe_3O_4 NP was characterised using X-ray diffraction. X-ray diffraction patterns were collected using a Malvern Panalytical Aeris diffractometer. This system employed Fe-filtered Co-Kα radiation, a PIXcel detector, and automatic slits. Phase identification was performed with X'Pert Highscore Plus software (Oluwalana and Ajibade, 2021). The average crystallite sizes were determined by solving the Debye–Scherrer's equation: $\left(D = \frac{k\lambda}{\beta\cos\theta}\right)$. In the equation, "D" represents the average crystallite size, k is the shape factor (0.94), λ is the X-ray wavelength (1.5406 Å), "β" the full width at half-maximum (FWHM), and "θ" is Bragg's angle of the diffraction peak. Moreover, the Brunauer-Emmett- Teller (BET) method was used to determine the surface area of Fe_3O_4 NP by nitrogen adsorption-desorption isotherms using Anton Paar's Nova 800 analyzer (USA). Furthermore, Barrett–Joyner–Halenda (BJH) method was used to determine the pore volume and size distribution of Fe_3O_4 NP.

2.3. Point of zero charge of Fe_3O_4 NPs adsorbent

The point of zero charge (PZC) of the Fe_3O_4 NP was determined by implementing the modified salt addition method outlined by Ayub et al. (2020). Twenty-seven (9 triplicates) Erlenmeyer flasks were each filled with a 40 mL aliquot of 0.1 M $NaNO_3$ solution. The $NaNO_3$ solution was adjusted to a range of pH values from 3.0 to 11.0. Afterwards, the Fe_3O_4 NP (0.021 g) was added into each flask and stirred at 150 rpm in an orbital shaker at 30 °C for 48 h. Subsequently, the solutions were filtered, and the final pH values of the filtrates were recorded accordingly. The changes in pH (ΔpH) values were thereafter estimated by finding the difference between initial pH (pH_i) and final pH (pH_f) values ($\Delta pH = pH_f - pH_i$) of the solutions. The point of zero charge (PZC) is the pH value at which the change in pH (ΔpH) is zero, indicating a neutral surface charge on the Fe_3O_4 nanoparticles. This value was determined graphically by plotting the initial pH against ΔpH (Altun and Ecevit, 2024).

2.4. Inhibitory compound derivation and detoxification

2.4.1. Inhibitory compound derivation

Acid pretreatment such as the present study releases useful carbohydrates from pretreated waste potato peel (WPP) as well as inhibitory compounds. The observed inhibitors in the pretreated WPP are obtained from the non-selective conversion of hexose and pentose carbohydrates (Adebule et al., 2024). Some inhibitory compounds associated with pretreated WPP that were analyzed in this study were acetic acid, phenol, furfural, 5-Hydroxymethyl furfural, and formaldehydes.

2.4.2. Detoxification of inhibitory compound by Fe_3O_4 NP adsorbent

The detoxification potential of Fe_3O_4 NP for the removal of furfural, HMF, acetic acid, phenol, and formaldehyde inhibitors derived from the pretreated WPP hydrolysate was investigated under optimal detoxification conditions of Fe_3O_4 NP adsorbent concentration of 0.021 % *w/v*, pH of 4.14, temperature of 35.37 °C and 12.74 min contact time. The solution mixture was continuously stirred at 120 rpm, after which the magnetic nanoadsorbent was separated and recovered by exposing it to a stronger magnetic field using an external magnet. The concentrations of inhibitory compounds (furfural, HMF, acetic acid, phenol and formaldehyde) in the experimental samples were determined using standard protocol. Furfural was quantified using the UV–Vis spectrophotometric method for quantitative determination at 280 nm (A280) (Adebule et al., 2024). 5-Hydroxymethylfufural (HMF) was also determined spectrophotometrically as descrbed by de Andrade et al. (2017). Quantification of phenol was achieved spectrophotometrically (at 540 nm) using ferric chloride as a colour indicator reagent (Apostică et al., 2018). Bial's test (orcinol-HCl method) was employed to determine the concentration of formaldehyde (Omran and Coughlin, 2020). While the acid-base titration method was employed to determine the concentration of acetic acid (Adebule et al., 2024).

2.5. Batch adsorption study

The batch adsorption study was conducted for phenol, furfural, acetic acid, formaldehyde and 5-hydroxymethylfurfural inhibitory

compounds. The initial pH's effect on the adsorption of ICs was determined under various pH conditions (1.0, 2.0, 3.0, 4.0, 5.0, 6.0, 7.0, and 8.0). The effect of Fe_3O_4 NP adsorbent concentration, was obtained with 0.005, 0.010, 0.02, 0.03, 0.04, 0.05, 0.075, and 0.1 g in 100 mL of pretreated WPP hydrolysate. Furthermore, the impact of temperature on inhibitor adsorption was investigated at different temperatures (20 °C, 25 °C, 30 °C, 35 °C, 40 °C, 45 °C, 50 °C, 55 °C, and 60 °C) under optimum setpoints (including Fe_3O_4-NPs =0.021 g; t = 12.74 min, and pH = 4.14 (Adebule et al., 2024)). For each batch study, an appropriate concentration of Fe_3O_4-NP was added to 100 mL pretreated WPP hydrolysate; the pH of the solution was similarly adjusted using 1 M HCl/ NaOH solution, and the adsorption temperature was fixed accordingly. Thereafter, the mixture was shaken (120 rpm) for 12.74 min at 35.37 °C. The reduction in the inhibitory compounds' concentrations was determined, as stated in section 2.4.

2.5.1. Adsorption efficiency

The adsorption efficiency (% AE) of the adsorbent and the adsorption capacity (q_t) over time (t) were evaluated (using Eq. 1 and 2) by estimating the difference between the initial and the final inhibitory compound (furfural, HMF, phenol, acetic acid, and formaldehyde) concentration (Al-Hetlani et al., 2022).

$$\%AE = \frac{(C_0 - C_t)}{C_0} \times 100 \tag{1}$$

$$q_t = \frac{(C_0 - C_t)\,V}{m} \tag{2}$$

Eq. (3) was solved to determine the equilibrium adsorption capacity (q_e [g/g]) (Al-Hetlani et al., 2022),

$$q_e = \frac{(C_0 - C_e)\,V}{m} \tag{3}$$

where C_0 represents the initial inhibitor concentration (g/L), C_t is the concentration at time t (g/L), C_e is the equilibrium concentration (g/L). V denotes the volume (L) of the hydrolysate used, while m refers to the mass (g) of Fe_3O_4 NP (g).

2.5.2. Adsorption Kinetics

The adsorption kinetic study investigated the reaction time required to achieve equilibrium under optimum conditions. Briefly, Fe_3O_4 NP (0.021 g) was added to 100 mL pretreated WPP hydrolysate with an initial pH value adjusted to 4.14 (with 1 M HCl and NaOH solutions) and agitated (120 rpm.) at predefined time intervals of 4, 5, 6, 8, 10, 12, 14, 16, 20, 30, and 60, min using 35.37 °C as the process temperature. The change in concentration of furfural, HMF, acetic acid, phenol, and formaldehyde were thereafter determined as stated in section 2.4.

The pseudo-first and pseudo-second-order kinetic models were used to evaluate the adsorption rates of the inhibitors. These kinetic models are presented by eqs. (4) and (5), respectively:

$$\mathrm{In}(q_e - q_t) = \mathrm{In}\, q_e - k_1 t \tag{4}$$

$$\frac{t}{q_t} = \frac{1}{q_e} t + \frac{1}{k_2 (q_e^2)} \tag{5}$$

In this context, q_e denotes the equilibrium adsorptions of inhibitors, while q_t represents the adsorption capacity at a given time 't' (min). The pseudo-first-order and the pseudo-second-order models' rate constant are represented by k_1 (min $^{-1}$) and k_2 (g\g. min), respectively. For the pseudo-first-order kinetics, plotting ln (q_e - q_t) against time yielded q_e (from the intercept) and k_1 (from the slope). In the case of the second-order kinetics, the equilibrium adsorption capacity (q_e) and the rate constant (k_2) were determined from the intercept and slope, respectively, of plots of t/q_t versus time. To further elucidate the mechanism through which inhibitors bind to the active sites on the nanoadsorbent (Fe_3O_4-NP) surface and gain deeper insight into the adsorption behaviour of this highly homogeneous adsorbent, the intraparticle diffusion and Elovich, models were employed as expressed in eqs. 6 and 7, respectively.

$$q_t = k_p t^{1/2} \tag{6}$$

$$q_t = \left(\frac{1}{\beta}\right)\mathrm{In}(\alpha\beta) + \left(\frac{1}{\beta}\right)\mathrm{In} \tag{7}$$

where α, the initial adsorption rate (mg g^{-1} h^{-1}) and β, the desorption constant (g mg^{-1}), represent the Elovich constants; meanwhile, the intraparticle diffusion model's rate constant is denoted as k_p (mg g^{-1} $h^{-1/2}$).

2.5.3. Adsorption isotherms and thermodynamics studies

Hundred millilitres of the pretreated WPP hydrolysate containing initial concentrations (C_0) of 0.026, 0.94, 0.828, 1.643, 9.488 g/L of phenol, furfural, HMF, formaldehyde and acetic acid, respectively. Fe_3O_4-NP (0.021 g) were added to 100 mL pretreated WPP hydrolysate with a pH of 4.14 and were utilised to examine the effect of the initial concentrations of inhibitor at 35.37 °C for 12.74 min with a shaking frequency of 120 rpm. The difference in the concentrations of furfural, 5-HMF, phenol, acetic acid, and formaldehyde were afterwards determined. The adsorption isotherm models (including Langmuir, Freundlich, and Temkin) were critical in evaluating the adsorption capacity of adsorbent at equilibrium and its interaction with the adsorbate (inhibitory compounds). The Adsorption isotherm models (Langmuir, Freundlich, and Temkin) were calculated using eqs. 8, 9 and 10, respectively.

$$\frac{C_e}{q_e} = \frac{1}{q_{m(K_L)}} + \frac{C_e}{q_m} \tag{8}$$

$$In\, q_e = In\, K_f + \left(\frac{1}{n}\right) In C_e \tag{9}$$

$$q_e = \mathrm{B_t} In\, K_t + B_t In C_e \tag{10}$$

The Langmuir adsorption constant K_L (L/g) reflects the affinity of the adsorption sites, while C_e (g/L) denotes the inhibitor's equilibrium concentration. q_e is the amount of inhibitor adsorbed at equilibrium, and q_m represents the maximum adsorption capacity. Meanwhile, K_F ((g/g) $(L/g)^{1/n}$) and n are the Freundlich isotherm constants that indicate the adsorption capacity and adsorption intensity, respectively. K_t (Lmg^{-1}) represents the equilibrium binding (Temkin isotherm) constant, which corresponds to the maximum binding energy. The separation factor (R_L), expressed by eq. (4), characterises the isotherm shape: favourable ($0 < R_L < 1$), unfavourable ($R_L > 1$), irreversible ($R_L = 0$), or linear ($R_L = 0$) (Juang et al., 1997).

$$R_L = \frac{1}{1 + K_L C_e} \tag{11}$$

The thermodynamic characteristics of the reaction process were elucidated by estimating the thermodynamic constants for the adsorption process based on the following equations:

$$\Delta G = -RT lnK \tag{12}$$

$$\Delta G = \Delta H - T\Delta S \tag{13}$$

$$InK = \frac{\Delta S}{R} - \frac{\Delta H}{R} \times \frac{1}{T} \tag{14}$$

ΔG (Gibbs free energy) is expressed in kJ/mol, while temperature (T) is in Kelvin. R, the gas constant, is 8.314×10^{-3} kJ/K·mol. K is derived from the adsorption capacity (qe, in g/g) divided by the inhibitor's equilibrium concentration (Ce, in g/L).

Table 1
Key FTIR shifts on Detox- Fe_3O_4 NP and accompanying inhibitors-functional groups.

FTIR shift wavenumber (cm^{-1})	Assigned functional group	Likely inhibitor source	Interpretation
554	Fe–O stretching vibration	–	Reduction in the Fe—O peak (Reduced magnetite)
880	O–H bending / C—H deformation	Possibly phenol, HMF	Indicates aromatic or alcohol-related C–H/ O–H deformation
1100	S=O or C—O stretching	HMF, acetic acid	Interaction with oxygenated species (e.g., alcohol, acid groups)
1240–1404	C–O / C—H bending (aryl/ alkyl)	Phenol, furfural	Binding of aromatic rings or alkyl substitutions
1535–1645	C=O and C=C stretching (aromatic/ aliphatic)	Furfural, HMF, formaldehyde	Strong carbonyl or aromatic group interaction with Fe_3O_4
1632	H–O–H bending / C=O stretching	Formaldehyde, HMF	Interaction of aldehyde or water molecules
2940	C–H stretching (alkyl)	Acetic acid, HMF, phenol	Surface adsorption of alkyl-containing inhibitors
3159–3758	O–H stretching (hydroxyl groups)	Phenol, alcohols	Broadband indicates hydroxyl surface groups that reduce after detox interaction
3865	Free O—H (non-bonded)	–	Possibly O—H acquire from synthesis

3. Results and discussion

3.1. Profile of Fe_3O_4 NP adsorbent

The morphology of the Fe_3O_4 NP and the detox-Fe_3O_4-NP, their elemental compositions as well as the elemental mapping were revealed using SEM (See supplementary document). The presence of the metal and the oxygen units in the metallic oxide NP was confirmed by their strong signals. Trace quantity of precursor utilised in the NP's synthesis and the grid coated with carbon employed in the SEM examination, including carbon, sulphur, copper, and silicon, were discovered in the NP. While the inhibitors conferred the presence of additional elements on the detox-Fe_3O_4-NP. The reduction in iron (Fe) and increase in C and O elemental weight of detox-Fe_3O_4-NP (the elemental weight at this point differs remarkably) must have resulted from the Fe-binding and surface adsorption of the inhibitory compounds. Elemental mapping (See supplementary document) revealed a uniform distribution of iron and oxygen across the surface of the NP (Ecer et al., 2022).

Likewise, the TEM micrographs for Fe_3O_4 NP and detox-Fe_3O_4-NP exhibited closely packed, roughly circular-shaped nanoparticle with varied nanoparticle sizes. It was found that Fe_3O_4 NP had an initial size range of 11.66 to 29.64 nm, with an average size of 20.08 ± 3.08 nm. Following detoxification, the NPs increased in size, ranging from 29.34 to 56.18 nm and averaging 44.84 nm as revealed by the particle size distribution histogram (See supplementary document). This doubling in Fe_3O_4 NP size post-detoxification suggests likely adsorption of inhibitory compounds onto the nanoparticle surface or ligand complexation with the inhibitors or both (Sanusi et al., 2020; Adebule et al., 2024; Bishop et al., 2024; Zondi et al., 2025).

Table 2
BET surface area analysis of Fe_3O_4 and Detox- Fe_3O_4 NP.

Samples	Surface area (m^2/ g)	Pore diameter (nm)	Pore volume (cm^3/ g)
Fe_3O_4	59.650	3.39186	0.152908
Detox- Fe_3O_4 NP	58.834	3.41471	0.088764

The FTIR spectra for both Fe_3O_4 NP and the detoxified Fe_3O_4 NP (Fe_3O_4 NP recovered after detoxification) showed the chemical composition and molecular interactions of the ICs and the adsorbent (See supplementary document). Both samples show a peak at 555 cm^{-1}, indicative of Fe—O bond vibration (Liu et al., 2021). In the detox-Fe_3O_4-NP spectrum, a peak at 2943 cm^{-1} correspond to C—H stretching vibrations (both asymmetric and symmetric) (Meena et al., 2025a; Meena et al., 2025b). Notably, the band at 1643 cm^{-1} was prominent and corresponds to the C=C stretching of a monosubstituted alkene and H-O-H bending. Furthermore, the peaks at 1535 cm^{-1} are associated with C=O stretching in amides and 1404 cm^{-1} indicated NH_2 bending vibrations. A characteristic broad OH band around 880 cm^{-1} is indicative of the presence of FeOOH (Granath et al., 2021), while the band at 1120 cm^{-1} may correspond to SO_4^{2-} (Lavrynenko and Bolbukh, 2014) likely introduced during the synthesis process. Additionally, the peak around 1380 cm^{-1} corresponds to the bending vibrations of the phenol hydroxyl (O—H) group, while the broad stretching vibrations between 3028 cm^{-1} and 3400 cm^{-1} indicate the presence of O—H groups in both samples (Cao et al., 2024). Compared to Fe_3O_4 NP, the spectrum of detox- Fe_3O_4-NP shows a reduction in peak intensity at 3843, 1632, 1160, 880, and 555 cm^{-1}, while the peaks at 1160 and 880 cm^{-1} appear broader (Table 1). This suggests a strong interaction between Fe (III) in Fe_3O_4 NP and functional groups such as phenolic, amine, amino, aldehyde, and hydroxyl from various inhibitors (Cao et al., 2014). Moreover, the detox-Fe_3O_4-NP spectrum displays a distinct peak at 580 cm^{-1}, which is characteristic of Fe—O bond vibration in Fe_3O_4. This observation further supports the conclusion that the detoxification process does not compromise the inherent properties of Fe_3O_4 NP (Fan et al., 2017).

Furthermore, the sharp and well-defined XRD peaks confirm the high crystallinity and uniformity of both the naked Fe_3O_4 NP and the detox-Fe_3O_4-NP recovered post-detoxification process (See supplementary document). The distinct diffraction pattern and narrow peaks further confirm their crystalline nature. The seven peaks at 21.29°, 35.17°, 41.51°, 50.59°,61.88°, 65.95° and 75.40° correspond to the electron diffraction process occurring in the crystal planes (220), (311), (400), (422), (440), (546), and (533). These diffraction patterns are characteristic of Fe_3O_4 nanoparticles. The diffraction pattern of detox-Fe_3O_4-NP showed additional diffraction peaks [such as Fe_2O_3 (Hematite) and $HFeO_2$ (goethite)] were found in phases other than Fe_3O_4, indicating its difference from the pure synthesised Fe_3O_4 NP, probably caused by Fe_3O_4 oxidation or reduction by the adsorbed inhibitors (Fan et al., 2017). Moreover, aside from a prominent peak at $2\theta = 41.51°$, all other peaks remained unchanged from their original positions before and after the inhibitory compound adsorption. This observation confirms that the inhibitors adhere to the Fe_3O_4 NP through a surface adsorption process involving physicochemical interactions between the nanoadsorbent's surface and the inhibitors via surface complexation. By comparison, the percentage occurrence of magnetite was estimated to be 87.7 % for the Fe_3O_4 NP, and 70.1 % for the detox-Fe_3O_4-NP. The retention of the high percentage of magnetite in the detox-Fe_3O_4-NP allows for efficient separation from aqueous solutions when an external magnetic field was applied (Adebule et al., 2024). These findings demonstrate that both the detox-Fe_3O_4-NP and naked Fe_3O_4 NP are relatively rich in iron oxide. However, the width of Fe_3O_4 NPs was higher than detox-Fe_3O_4-NP, indicating a reduction in the crystallite sizes of the detox-Fe_3O_4-NP (Meena and Surela, 2024). The average crystalline sizes of Fe_3O_4 NP and detox-Fe_3O_4 -NP calculated using Debye-Scherrer's equation are 13.37 ± 1.526 nm and 18.33 ± 1.475 nm.

The optical properties of the absorption spectra of naked Fe_3O_4 and detox-Fe_3O_4 NPs were examined using UV spectroscopy, covering between 200 and 400 nm wavelength (See Supplementary Document). The spectra revealed significant variations in absorption wavelengths for both Fe_3O_4 NP and detox-Fe_3O_4-NP. Significant differences were

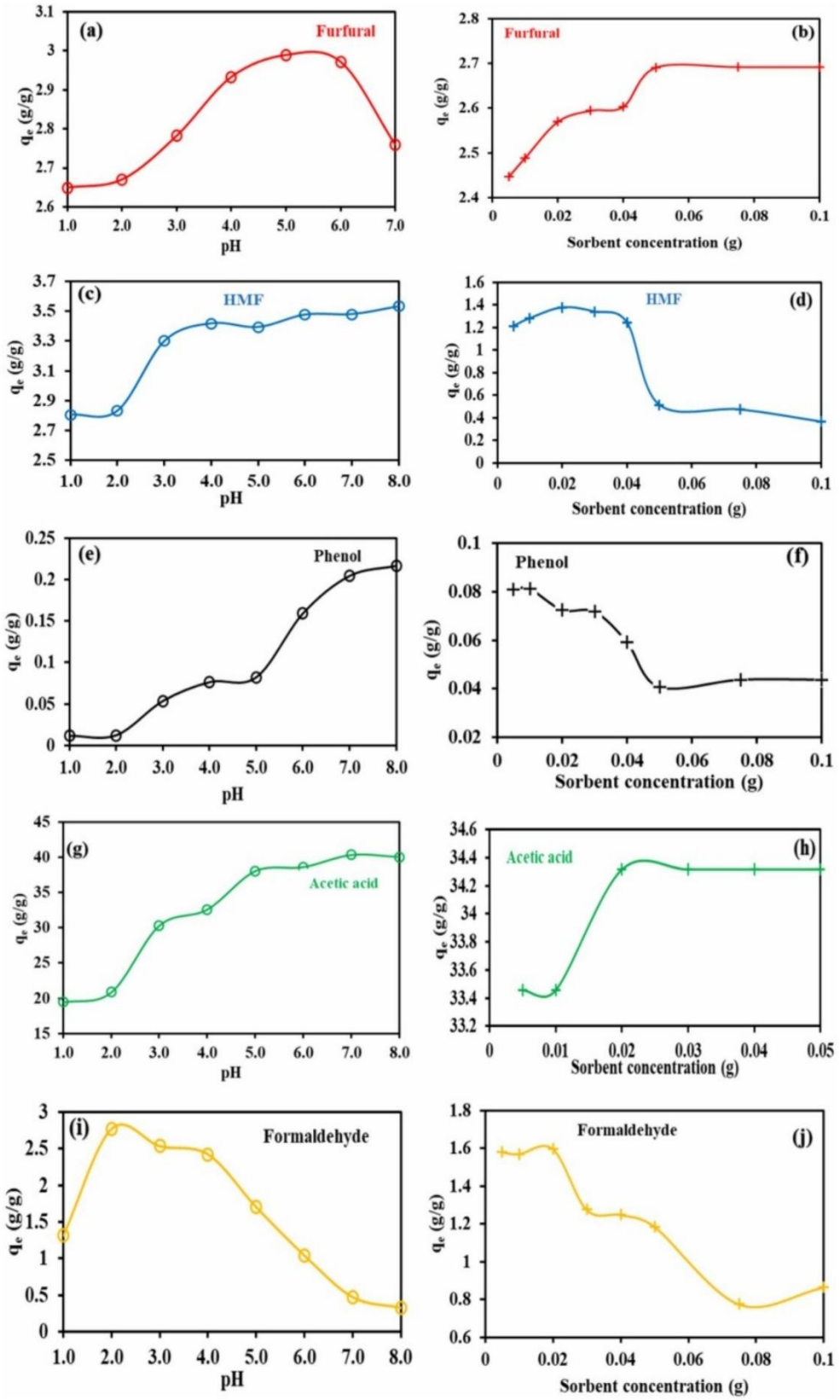

Fig. 1. The effect of pH and sorbent concentration on the adsorption of inhibitors.

observed in the detox-Fe_3O_4-NP spectra compared to Fe_3O_4 NP, particularly in the 200–240 nm ranges, similarly within 320–380 nm ranges, indicating alterations in particle size. The variation in the particle size can be ascribed to the presence or absence of inhibitors on the Fe_3O_4 NP absorbent surfaces. These further substantiate the results obtained for the TEM and FTIR analyses and are consistent with Wang et al. (2019), who reported that nanoparticle size influences optical properties.

The results (Table 2) of the Brunauer-Emmett-Teller (BET) include the surface area, pore volume, and diameter of Fe_3O_4 NP and the detox-Fe_3O_4-NP. An adsorbent's surface area and porosity are key determinants of its properties. A larger surface area provides more adsorption sites, consequently enhancing the adsorption of these inhibitors (Xiang et al., 2023). The naked Fe_3O_4-NP exhibited a relatively large surface area (59.650 m^2/g) and pore volume (0.1529 cm^3/g) (Table 2). After the adsorption of the inhibitors on the detox-Fe_3O_4-NP, the surface area and pore size diminished to 58.834 m^2/g and 0.0888 cm^3/g, respectively. The reduction in the surface area and pore size could be ascribed to the adherence of adsorbates (inhibitory compounds) to the surface of Fe_3O_4 NP, subsequently reducing available active sites. Moreover, the pore diameter of Fe_3O_4 NP and the detox-Fe_3O_4-NP was 3.39 nm and 3.41 nm, respectively (Table 2). The pore is responsible for efficient molecular diffusion and interaction, thereby ensuring the enhancement of the nanomaterial's catalytic and adsorption efficiency (Khojasteh et al., 2024). The minimal reduction in surface area (~2.35 %) and slight pore diameter suggest that the Fe_3O_4 NP maintained their structural integrity but experienced slight modifications and structural alterations due to the interaction of the inhibitor and the nanoparticles.

To further understand the adsorption process of the inhibitory compounds, the PZC isoelectric point of Fe_3O_4 NP was obtained by the plot of pH_i versus ΔpH to obtain the pH_{pzc} values for Fe_3O_4 NP (See supplementary document). The pH_{pzc} value of 5.0 obtained indicates the pH at which the net electrical charge of the nanomaterial is neutral (Altun and Ecevit, 2024). The low point of zero charges exhibited by Fe_3O_4 NP indicates a persistent negative surface charge across a wide pH range, facilitating the adsorption of positively charged ions from the pretreated hydrolysate. This justified the remarkable performance of the Fe_3O_4 NP absorbent in this study. The pH_{pzc} ranges earlier reported by Zhao et al. (2016) and Ayub et al. (2020), from 2.0 to 9.05, agree with the findings in this study. For instance, the pH_{pzc} value of 5.9 was recorded for the effective decontamination of water containing bivalent heavy metals using amorphous MnO_4 (Zhao et al., 2016). This indicates MnO_2 was less negatively charged compared to that of Fe_3O_4 NPs in the current study. In another study, the magnetic chitosan composite exhibited a higher PZC value (7.7), indicating positive charges (Ayub et al., 2020). The combination of this magnetic chitosan composite and Fe_3O_4 NP absorbent in this study could be an excellent absorbent for the removal of the different inhibitory compounds present in the pretreated hydrolysate.

The photoluminescence spectra (excitation wavelength of 350 nm) were recorded for both Fe_3O_4 NP adsorbent and detox-Fe_3O_4-NP at different dilutions (See Supplementary Document). The Fe_3O_4 NP adsorbent displayed distinct emission peaks at 380 nm, along with broader bands at 446 nm. Meanwhile, after detoxification, these peaks shifted to 410 nm and 465 nm, respectively, in the detox-Fe_3O_4-NP. The peak for Fe_3O_4 NP adsorbent at 446 nm may be attributed to a high transition level caused by the surface state excitons recombination (Hone and Dejene, 2018). Broad emission exhibited by the Fe_3O_4 NP adsorbent at 380 and 410 nm wavelengths is indicative of Stokes' shift and trapped luminescence. This emission presented peaks at 380 and 410 nm, corresponding to electron transitions from donor levels to the valence band. (Oluwalana and Ajibade, 2021). The shift in wavelength observed in detox-Fe_3O_4-NP, compared to the Fe_3O_4 NP adsorbent, may be attributed to lower energy excitation. As highlighted earlier, this change in wavelength could stem from the post-adsorption of inhibitory compounds by the detox-Fe_3O_4-NP, which increases its particle size.

3.2. Inhibitory compound adsorption study

3.2.1. Effect of pH on inhibitory compound adsorption

The impact of varying pH on the simultaneous removal of furfural, HMF, phenol, acetic acid, and formaldehyde while maintaining constant temperature (35.37 °C), Fe_3O_4 NP adsorbent concentration (0.021 g), contact time (12.74 min), is illustrated in Fig. 1. At an initial concentration of 0.940 g/L, furfural was gradually removed from pH 1.0–5.0. The removal efficiency diminished from 66.77 % to 61.64 % over this range, suggesting higher migration of inhibitors to the surface of Fe_3O_4 NP at lower pH conditions, especially pH <5 (Adebule et al., 2024). Conversely, HMF (at an initial concentration of 0.8272 g/L) showed no noticeable removal effect at pH 1.0 and 2.0. However, a further increase in pH beyond 2.0 improved adsorption capacity up to 3.42 g/g at pH of 4.0 but reduced to 3.39 g/g at pH 5.0. The adsorption capacity (3.53 g/g) increased slightly when the pH was increased to pH 8.0. Meanwhile, for the phenol and acetic acid, an increase in pH value from 1.0 to 8.0 enhanced phenol and acetic acid removal remarkably, resulting in high adsorption capacities of 0.125 g/g and 40.32 g/g, corresponding to 100 % and 89.24 % removal efficiency, respectively. Moreover, formaldehyde exhibited a contrasting trend, with its adsorption capacity significantly reduced from 2.78 g/g at the acidic pH of 2.0 to 0.33 g/g at the alkaline pH of 8.0. The adsorption capacity of Fe_3O_4 NP for formaldehyde was maximised at pH 2.0. Subsequent increases in pH led to a continuous decrease in the adsorbent's performance. pH plays a critical role in determining the adsorption mechanism of adsorbents such as Fe_3O_4 NP (Adebule et al., 2024). For instance, pH could influence an adsorption process by affecting the electrostatic properties of the adsorbent surface and the equilibrium of adsorbate-adsorbent interactions, thereby determining the overall adsorption capacity. At low pH (acidic conditions), positively charged inhibitor compounds and H^+ ions compete for adsorption sites on the adsorbent surface. Conversely, at higher pH (basic conditions), the electrostatic attraction between the cationic inhibitor and the negatively charged surface strengthens adsorption, leading to deprotonation of surface groups. Furthermore, non-optimal pH can hinder inhibitor migration to target sites on the Fe_3O_4 NP surface due to increased competition among inhibitory ions (Adebule et al., 2024). These suboptimal pH levels can also significantly affect system modulation and buffering, thereby influencing the adsorption process (Sanusi et al., 2019).

3.2.2. Effect of nano-adsorbent concentration on the adsorption inhibitory compounds

The impact of adsorbent (Fe_3O_4 NP) concentration variation on the removal of furfural, HMF, acetic acid, phenol, and formaldehyde under optimal conditions is illustrated in Fig. 1. At a 0.940 g/L initial furfural concentration, increasing the concentration of Fe_3O_4 NP from 0.005 g to 0.02 g resulted in slight increase in the adsorption capacity (q_e) from 2.55 g/g to 2.82 g/g. However, a further increase in the nanoadsorbent concentration to 0.05 g led to a decrease in adsorption capacity to 2.45 g/g. Moreover, the furfural removal percentage was lowest for Fe_3O_4 NP concentration at 0.05 g (54.67 %) and highest at 0.02 g (62.97 %) Fe_3O_4 NP concentration. Further increase in the adsorbent concentration beyond 0.05 g up to 0.10 g, the adsorption capacity improved, reaching approximately 2.6 g/g. The observed increase in adsorption with higher Fe_3O_4 NP concentrations suggests that more available adsorption sites facilitate furfural uptake.

Fig. 1 shows the effect of Fe_3O_4 NP dosage on HMF removal. Raising the concentration of Fe_3O_4 NP from 0.01 g to 0.05 g yielded an adsorption capacity of 1.37 g/g and a 35 % HMF removal efficiency. This improvement likely results from the increased availability of adsorption sites for HMF molecules at higher adsorbent doses. With further increase in the adsorbent concentration beyond 0.05 g up to 0.10 g, the adsorption capacity retarded to 0.368 g/g. This decrease in HMF adsorption capacity at high adsorbent concentration might be attributed to the low availability of HMF molecules per unit mass of the

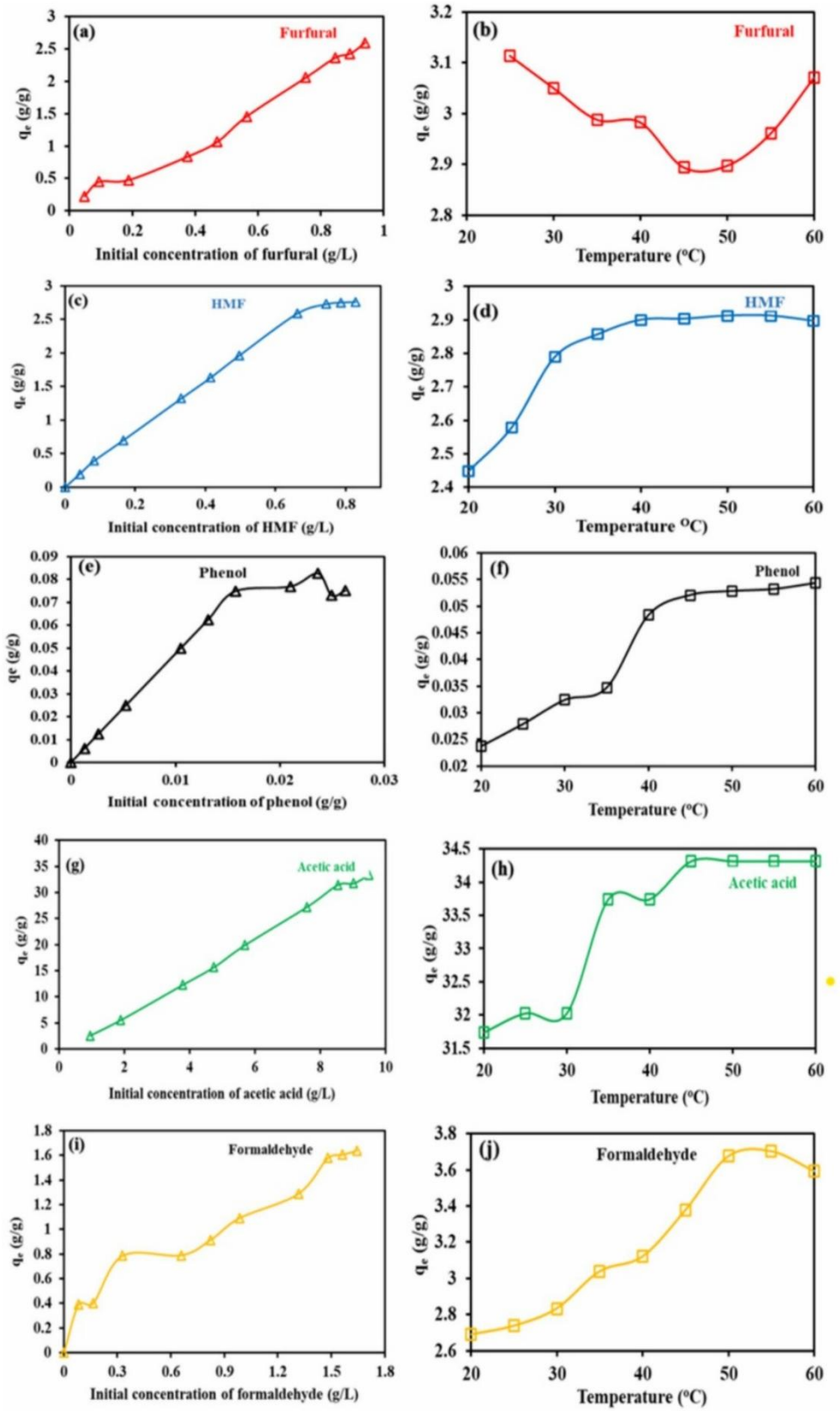

Fig. 2. The effect of inhibitors' initial concentration (a, c, e, g, and i) and temperature (b, d, f, h, and j) on the adsorption by Fe_3O_4-nanoparticle.

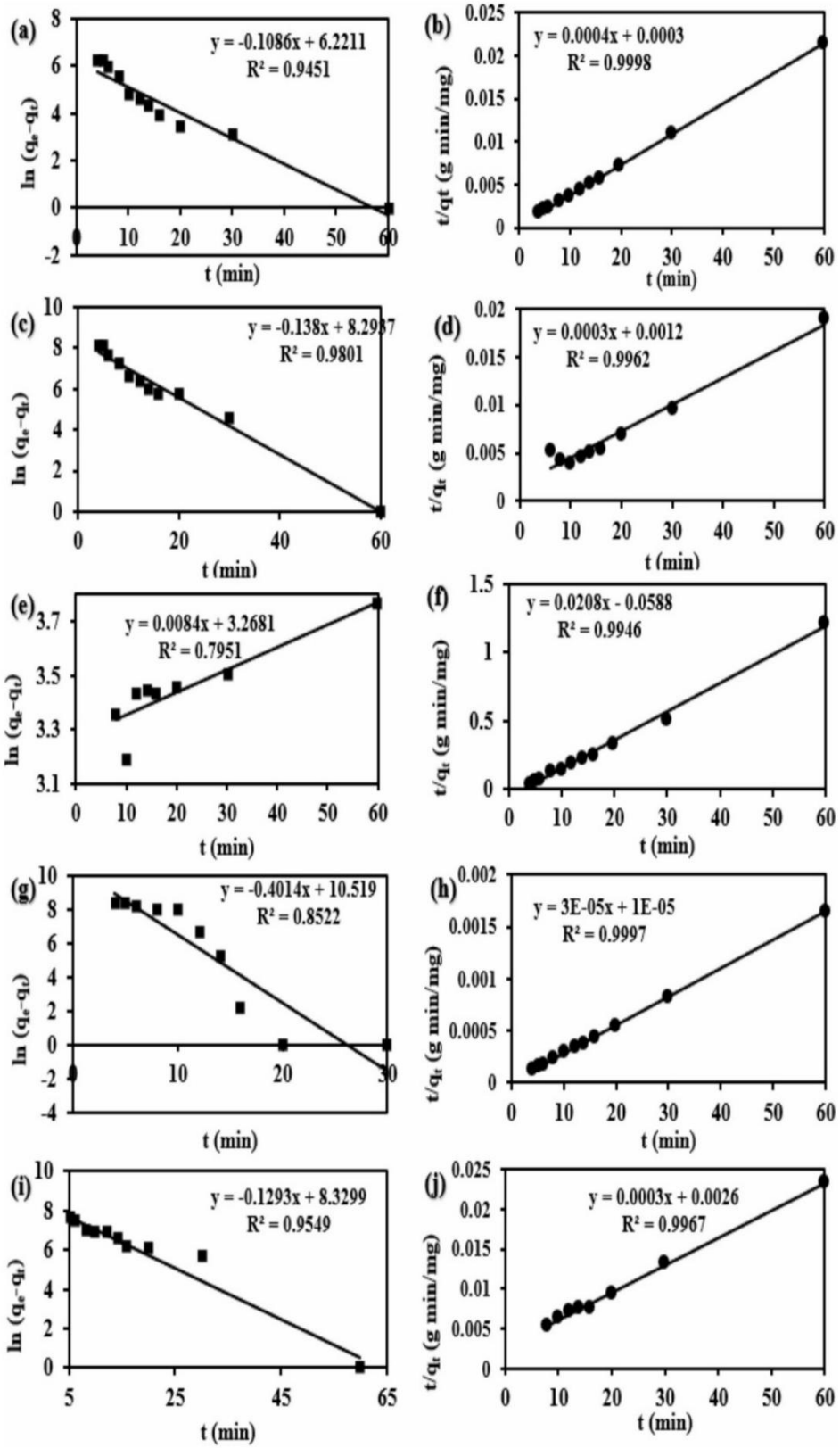

Fig. 3. Pseudo-first order (a, c, e, g, and i) and Pseudo-second order (b, d, f, h, and j) kinetic model for the adsorption of fermentation inhibitors by Fe_3O_4-NP. Note: furfural (a and b); HMF (c & d); phenol (e and f); acetic acid (g and h); formaldehyde (i and j).

Table 3
Kinetics parameters of the adsorption of fermentation inhibitors by Fe_3O_4 nanoadsorbent.

Models	Parameters	Furfural	HMF	Phenol	Acetic acid	Formaldehyde
Pseudo-first order	K_1 (min^{-1})	−0.0018	−0.0023	0.00014	−0.0067	−0.0022
	q_e ($mg\ g^{-1}$)	503.26	3998.6	26.26	37,012.1	4146.0
	R^2	0.9451	0.9801	0.7951	0.8522	0.9549
Pseudo-second order	K_2 ($g\ mg^{-1}\ min^{-1}$)	4.8×10^{-4}	7.5×10^{-5}	-7.36×10^{-3}	9.0×10^{-5}	3.5×10^{-5}
	q_e ($mg\ g^{-1}$)	2631.58	3333.3	48.08	33,333.33	3333.33
	R^2	0.9998	0.9962	0.995	0.9997	0.9967
Elovich	α ($g/g\ min^{-1}$)	68.79	0.6019	-9.320×10^{-6}	7.1×10^{6}	0.4624
	β (g/g)	2.938	0.4114	−71.429	0.4273	1.1795
	R^2	0.9511	0.929	0.7684	0.7244	0.8868
Intra-particle diffusion model	K_{diff}	0.1953	1.715	−6.1825	1.6334	0.3702
	C_i	1.945	−3.3003	90.625	29.654	0.2111
	R^2	0.9007	0.8987	0.6465	0.7396	0.7304

adsorbent. Likewise, phenol removal by Fe_3O_4 NP at varying concentrations is represented in Fig. 1. An improved adsorption capacity from 0.06 to 0.081 g/g was obtained by increasing adsorbent concentration from 0.01 to 0.05 g. Given the limited adsorption capacity of Fe_3O_4 NP for phenol removal, Fe_3O_4 NP as an adsorbent might not be sufficiently effective for phenol removal in the pretreated hydrolysate. Furthermore, acetic acid removal capacity was lower as the nanoadsorbent concentration increased from 0.005 and 0.01 g (Fig. 1). However, accelerated acetic acid removal was observed for nanoadsorbent concentrations from 0.02 to 0.05 g, exhibiting higher adsorption capacity (34.42 g/g) and removal efficiency (75.95 %). Beyond this nanoadsorbent concentration range, a reduction in the adsorption capacity (33.17 g/g) of acetic acid was observed. Thus, Fe_3O_4 NP concentration between 0.02 and 0.05 g can serve as an effective range dose for acetic acid removal. Meanwhile, the variation in Fe_3O_4 NP concentration from 0.005 and 0.01 g was effective in formaldehyde removal with adsorption capacity >1.57 g/g. Conversely, as the Fe_3O_4 NP concentration increased from 0.02 g to 0.075 g, its adsorption capacity for formaldehyde decreased from 1.60 g/g to 0.77 g/g.

3.2.3. *Effect of inhibitors' initial concentration on the adsorption process*

The effects of the initial concentration of fermentation inhibitors (furfural, HMF, acetic acid, phenol, and formaldehyde) on the adsorption performance of the adsorbent (Fe_3O_4 NP) were investigated, and these are shown in Fig. 2. A series of experiments using initial concentrations of 0.940 g/L for furfural, 0.8272 g/L for HMF, 0.026 g/g for phenol, 9.488 g/L for acetic acid, and 1.643 g/L for formaldehyde was understudied while maintaining optimal condition for temperature (35.37 °C), pH (4.14), contact time (12.74 min) and Fe_3O_4 NP concentration (0.021 g). Increasing the concentration of inhibitors from 5 % to 100 % yielded a corresponding increase in adsorption capacity. Specifically, adsorption capacities increased from 0.224 g/g to 2.593 g/g for furfural, 0.197 g/g to 2.761 g/g for HMF, 0.006 g/g to 0.075 g/g for phenol, 2.26 g/g to 33.458 g/g for acetic acid, and 0 g/g to 1.64 g/g for formaldehyde. This indicates direct proportionality such that as the rate of adsorption site saturation increases, initial inhibitor concentration increases. However, 100 % adsorption efficiency was attained when the inhibitors' concentrations were below 10 %. This observation can be attributed to the strong interaction between the inhibitor and the nanoadsorbent's surface active sites, coupled with the inhibitor's mass transfer limitations within the hydrolysate. However, once the nanoadsorbent active sites reaches saturation, adsorption efficiency declines at higher inhibitor concentrations. This implied that the Fe_3O_4 NP nanoadsorbent was responsive and actively removing inhibitors until the active site deposition was optimum (Abdel-Hady et al., 2023).

3.2.4. *Effect of temperature on inhibitory compound adsorption*

Fig. 2 also shows the effect of temperature on the simultaneous adsorption of furfural, HMF, phenol, acetic acid, and formaldehyde while maintaining a constant Fe_3O_4 NP concentration (0.021 g), contact time (12.74 min) and pH (4.14). The adsorption capacity of HMF and phenol showed a steep increment from 20 °C to 45 °C before their adsorption capacities slightly plateaued with further increase in temperature up to 60 °C. While acetic acid exhibited q_e increment between 30 °C and 45 °C but showed no further improvement beyond this temperature. The effect of temperature increment on formaldehyde was remarkably low, with q_e increasing from 2.69 g/g (at 20 °C) to 3.71 g/g (at 60 °C). The observed increase in adsorption capacity at temperatures up to 45 °C likely results from two temperature-driven effects: increased surface excitation on the nanoadsorbent, creating additional adsorption sites, and enhanced diffusion of the inhibitor's volatile components within the Fe_3O_4 NP's large surface area (Altun and Ecevit, 2024). The adsorption rate and catalytic degradation process of substances have been identified to be significantly influenced by the operating temperature (Valizadeh et al., 2022). However, the negative effect of temperature on adsorption in other instances may be due to the increased Brownian motion of molecules within the solution and the weakening of adsorbate-adsorbent interactions initiated at higher temperatures (Li et al., 2021). A comparable temperature-dependent adsorption trend in the adsorption of furfural and phenolic acids using the multi-organic framework material MIL-140C under varying temperature conditions was reported by Li et al. (2021).

3.3. *Adsorption removal efficiency and kinetic modelling*

The adsorption rate and efficiency of the nanoadsorbent (Fe_3O_4 NP) in the ICs removal were evaluated (See Supplementary Document). Furfural, HMF, acetic acid, and formaldehyde were rapidly adsorbed within the first 10 min. The nanoadsorbent exhibited increasing adsorption efficiency over time, reaching equilibrium within 20 min. The final adsorption efficiencies were 62 % for furfural, 73 % for HMF, 81 % for acetic acid, and 28 % for formaldehyde. Phenol differs remarkably, exhibiting its highest adsorption efficiency (73.8 %) after 6 min, followed by sharp retardation in the adsorption efficiency (40 %).

Furthermore, kinetic modelling, using pseudo-first-order (PFO), pseudo-second-order (PSO) (Fig. 3), intra-particle diffusion and Elovich models, was performed to elucidate further the mechanism of interactions between ICs and the Fe_3O_4 nanoadsorbent's active sites.

Adsorption kinetics for ICs depend upon the availability of active sites on the Fe_3O_4 NP surface. As shown in Table 3, the PSO model best describes the adsorption process, exhibiting good linearity and a high correlation coefficient ($R^2 > 0.901$ for all the inhibitory compounds analyzed) compared to the other three models. Moreover, the experimental adsorption capacity (q_e) fitted well with the PSO model. This fit indicates that the adsorption of all five inhibitor compounds followed a chemisorption mechanism. This aligns with previous findings by Xiang et al. (2023) using a novel magnetic lignin-based adsorbent for selective ferulic acid and furfural adsorption from acidic lignocellulosic hydrolysate, as well as Ilahi et al. (2020) on the use of starch-maghemite composite for the removal of arsenic pollutant from water. The results show an inverse proportionality between adsorption efficiency and the rate of adsorption, with both the adsorption rate and efficiency being

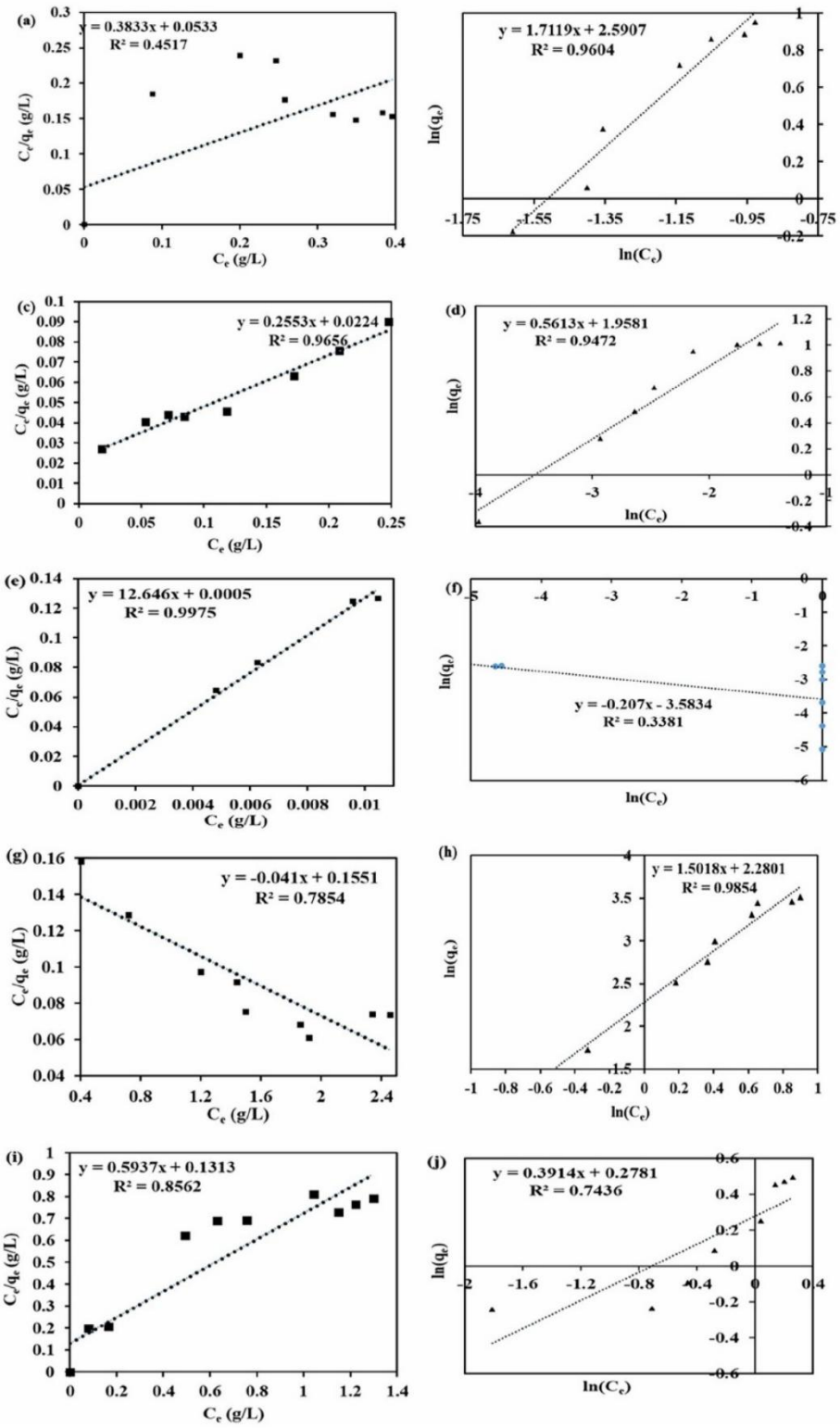

Fig. 4. Langmuir (a, c, e, g, and i) and Freundlich (b, d, f, h, and j) kinetic model for the adsorption of fermentation inhibitors by Fe_3O_4-NP. Note: furfural (a and b); HMF (c & d); phenol (e and f); acetic acid (g and h); formaldehyde (i and j).

Table 4
Isotherm parameters of the adsorption of the inhibitors by Fe_3O_4 nanoadsorbent.

Models	Parameters	Furfural	HMF	Phenol	Acetic acid	Formaldehyde
Langmuir isotherm	Q_{max} (g/g)	2.609	3.917	0.079	24.390	1.684
	K_L (L mg^{-1})	0.0072	0.011	25.29	0.264	0.0045
	R^2	0.452	0.966	0.997	0.785	0.856
	R_L	0.99	0.99	0.601–0.968	0.285–0.889	0.99
Freundlich isotherm	N	0.584	1.782	−4.831	0.666	1.284
	K_F ((mg g^{-1}) (L $mg^{-1})^{1/n}$)	13.339	7.086	0.028	9.778	1.344
	R^2	0.960	0.947	0.338	0.985	0.980
Temkin Isotherm	B_T (J mol^{-1})	2.720	0.901	−0.007	24.881	0.918
	K_t (L mg^{-1})	6.542	103.8	0.001	1.546	4.489
	R^2	0.970	0.944	0.337	0.924	0.958

influenced by the duration of exposure of the nanoadsorbent to the pretreated hydrolysate. Similarly, adsorption efficiency declines as active sites become saturated over time (Al-Hetlani et al., 2022). This reduction is primarily attributed to repulsive forces between inhibitor molecules already adsorbed on the nanoadsorbent and those remaining in the pretreated hydrolysate. Further increase in adsorption efficiency observed after equilibrium time for furfural and formaldehyde is probably due to adsorbate-to-adsorbate interaction once the nanoadsorbent's active sites are saturated. The outcome of the present study reveals the dual influence of both the nanoadsorbent concentration and inhibitor concentration during the adsorption process (Ayub et al., 2020).

3.4. Adsorption isotherms of the inhibitor removal

Fig. 4 shows the adsorption data fitting for furfural, HMF, acetic acid, phenol, and formaldehyde using Langmuir and Freundlich isotherm models. Table 4 presents the fitted variables and their corresponding correlation coefficients. Comparing the models, the best fit (R^2 of 0.997 and 0.966) was recorded for phenol and HMF, respectively, with the Langmuir model. This implies a predominantly monolayer adsorption process (El Bakri et al., 2024). Langmuir model has been known to describe a system where monolayer adsorption of inhibitor compounds occurs on the surface of the Fe_3O_4 NPs with a specific number of adsorption sites (Sierra et al., 2020). However, multilayer adsorption was observed for the acetic acid and formaldehyde, having recorded better empirical data fitting to the Freundlich model with R^2 values of 0.985 and 0.980, respectively. This further shows that there are unequal available heterogeneous sites at these active sites, each with varied adsorption energy and interacting molecules (Kakavandi et al., 2013). This attribute might be conferred by the simultaneous adsorption of varying adsorbates on the surface of the Fe_3O_4 NPs. This agrees with previous reports that the Freundlich isotherm model is suitable for describing the adsorption of molecules that are either monolayer or multilayer on the heterogeneous surface of the adsorbent. While both the Freundlich (R^2 = 0.960) and Temkin (R^2 = 0.970) models fit the furfural adsorption data, the slightly higher R^2 value for the Temkin model suggests it provides a better description of the adsorption process by the Fe_3O_4 NPs adsorbent (Fig. 5). This suggests that the adsorption process using Fe_3O_4 NPs involves chemisorption, where adsorption energy is influenced by the adsorbent-adsorbate interactions (Maryanti et al., 2020; Valizadeh et al., 2022). This highlights the complexity of chemical interactions between absorbed molecules owing to the heterogeneous distribution of binding energies at the active sites on Fe_3O_4 NPs. This observation agrees with Temkin's assumption of uniformly distributed binding energy across the surface of the adsorbent. Moreover, the analysis of adsorption isotherm data resulted in the maximum adsorption capacities of 2.609 g/g for furfural, 3.917 g/g for HMF, 0.079 g/g for phenol, 24.39 g/g for acetic acid, and 1.684 g/g for formaldehyde. This adsorption capacity reveals the efficiency of the adsorption process and indicates the removal capability of Fe_3O_4 NPs for acetic acid (the most adsorbed), while formaldehyde is the least adsorbed.

In addition, the separation factor (R_L) values between 0 and 1 for all the inhibitors investigated in this study indicated the favourability of the inhibitor's adsorption to the surface of Fe_3O_4 NP. Furthermore, the values obtained for formaldehyde adsorption indicated that adsorption was favourable and heterogenic at the surface of Fe_3O_4 NP with fewer interactions between adsorbed ions. This differs for acetic acid with a higher 1/n value of 1.5, indicating less favourable adsorption where adsorption is not proportionate to the concentration of absorbate. However, a cooperative adsorption mechanism might be promoted, with more interactions between adsorbed ions. In summary, Fe_3O_4 NP adsorption mechanisms occur through multi-molecular, monolayer, and multilayer adsorption with varying interaction energies, indicating its versatility in detoxifying inhibitors. Also, the models suitably evaluate the data and give insight into the surface properties of the adsorbent (Fe_3O_4 NP), providing important information on adsorption capacity, binding affinity, and the mechanism of inhibitor removal by the adsorbent.

3.5. Thermodynamics of the inhibitory compound removal

Thermodynamic properties (Gibbs free energy change (ΔG°), entropy (ΔS°) and enthalpy (ΔH°) of ICs adsorption onto the Fe_3O_4 NP adsorbent were determined by estimating the adsorption isotherms across a temperature range of 293 K to 333 K (293 K, 298 K, 303 K, 308 K, 313 K, 318 K, 323 K, 328 K, and 333 K). Fig. 5 illustrates the effects of temperature on adsorption capacity. Adsorption increased with temperature for most compounds, except for furfural. The slopes and the intercept of the ln *Kd* versus 1/*T* plots were used to estimate the values of ΔH^o and ΔS^o. Table 5 shows the thermodynamic parameters with negative ΔG^o values across all temperatures, indicating that the adsorption process is spontaneous and feasible in nature (Sun et al., 2021). The negative ΔG^o values increase with increasing temperatures (298 to 333 K) from −5.005 to −7.144 kJ/mol (HMF), −0.277 to −3.60 kJ/mol (phenol), −5.895 to −6.916 kJ/mol (acetic acid), and − 2.226 to −3.87 kJ/mol (formaldehyde), showing that high temperature influences the adsorption process, due to increased process spontaneity. More so, the positive values of both ΔH° and ΔS° suggest that the adsorption process is endothermic and accompanied by increased randomness at the adsorbent-adsorbate interface (Meena et al., 2024). An exception was observed in the case of furfural adsorption, which is exothermic in nature with negative ΔH° value (−7.193 kJ/mol.K) and ΔS° (−4.406 J/mol K), which is consistent with negative enthalpy and entropy thermodynamic report on furfural removal from liquid effluents by commercial activated carbon (Cuevas et al., 2014). This could be due to the formation of strong intermolecular or chemical bonds, such as hydrogen bonding or π-π interactions, during the reaction involving furfural, which typically aligns with the observation in the hydrogenation of furfural to form furfuryl alcohol (Pino et al., 2019). Additionally, the negative ΔS° value shows that the furfural molecules were adsorbed systematically at the solid-liquid interface due to reduced randomness in the adsorption process (Abdel-Hady et al., 2023). However, the negative ΔG confirmed the spontaneity and feasibility of the adsorption process.

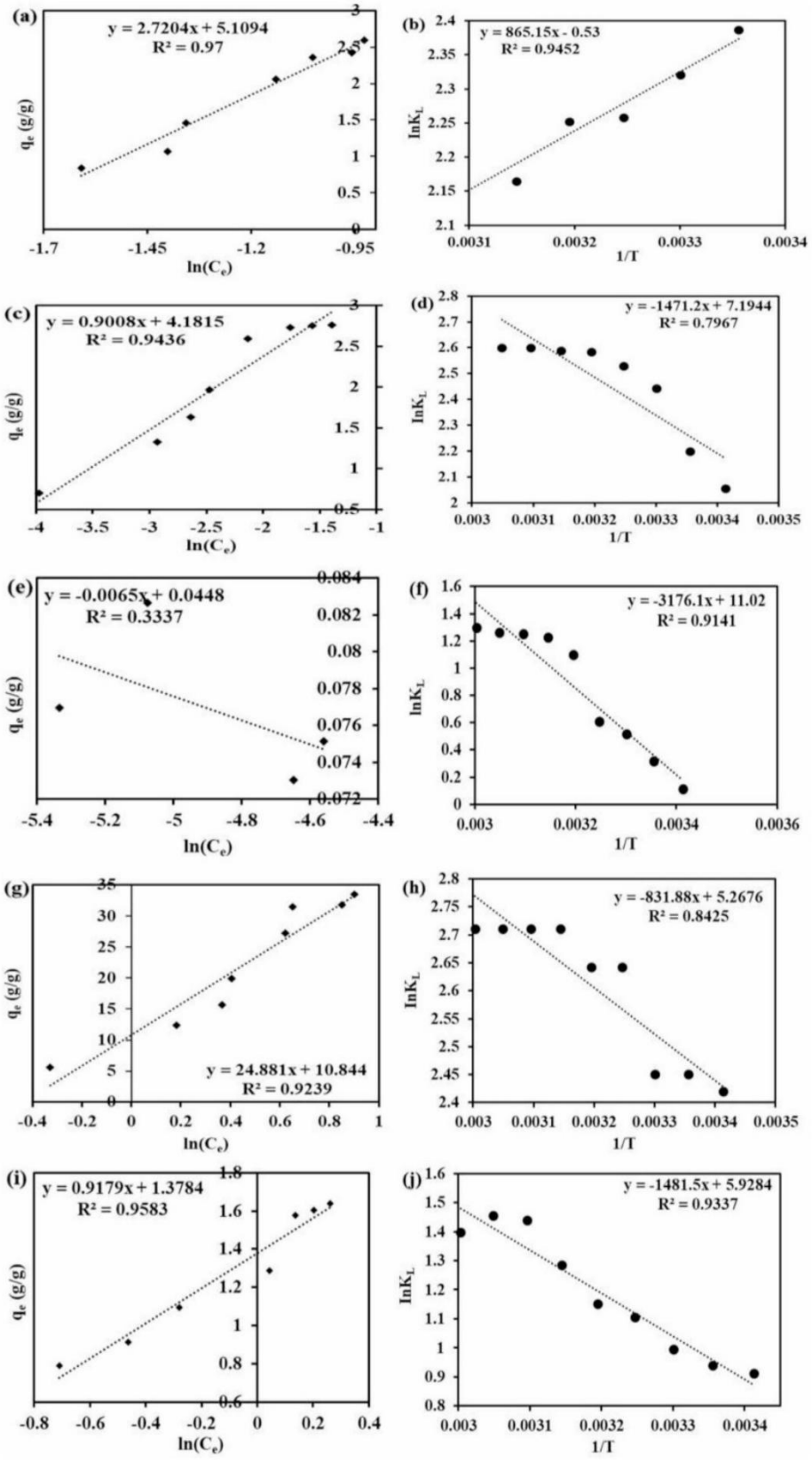

Fig. 5. Temkin isotherm (a, c, e, g, and i) and thermodynamics study (b, d, f, h, and j) kinetic model for the adsorption of fermentation inhibitors by Fe_3O_4-NP. Note: furfural (a and b); HMF (c and d); phenol (e and f); acetic acid (g and h); formaldehyde (i and j).

Table 5
Fe_3O_4 nanoadsorbent adsorption thermodynamic of the inhibitor removal.

Absorbate		Temperature (Kelvin)									ΔH^0 (kJ/mol.k)	ΔS^0 (J/mol.K)
		293	298	303	308	313	318	323	328	333		
Furfural	ΔG^0 (kJ/mol)	−5.132	−5.913	−5.847	−5.781	−5.861	−5.723	−5.822	−6.082	−6.484	−7.193	−4.406
HMF	ΔG^0 (kJ/mol)	−5.005	−5.445	−6.156	−6.475	−6.725	−6.843	−6.983	−7.092	−7.144	12.232	59.814
Phenol	ΔG^0 (kJ/mol)	−0.277	−0.784	−1.296	−1.554	−2.864	−3.242	−3.360	−3.445	−3.600	26.406	91.620
Acetic acid	ΔG^0 (kJ/mol)	−5.895	−6.071	−6.173	−6.767	−6.876	−7.166	−7.279	−7.392	−7.504	6.916	43.793
Formaldehyde	ΔG^0 (kJ/mol)	−2.226	−2.331	−2.505	−2.834	−2.994	−3.400	−3.868	−3.966	−3.870	12.317	49.289

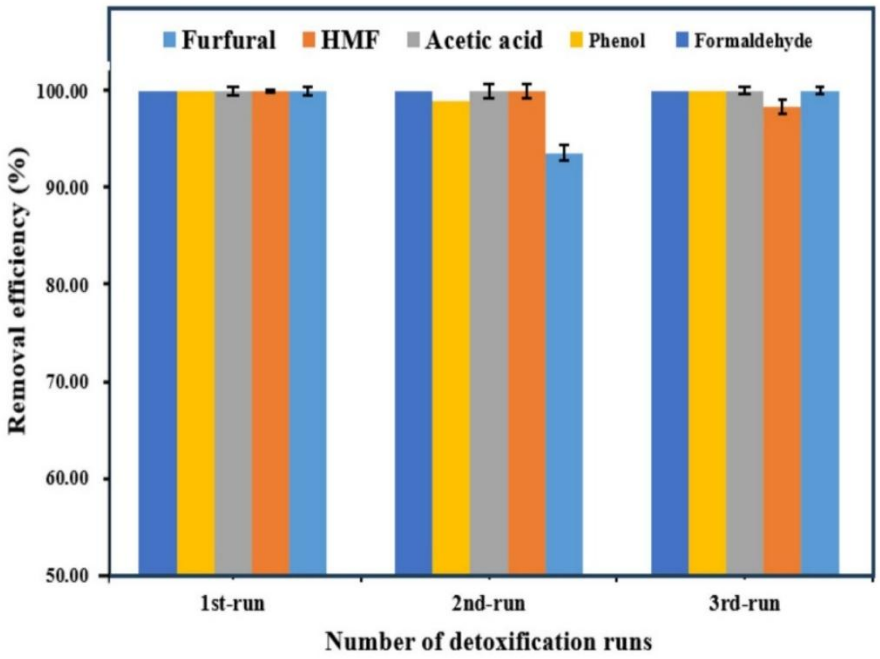

Fig. 6. Reusability of Fe_3O_4 NP after three detoxification runs.

3.6. *Reusability potential of Fe_3O_4 nanoparticle for IC detoxification*

The stability and reusability of the Fe_3O_4 NP nano-adsorbent for potential industrial detoxification were tested by performing three detoxification cycles (Rezaei et al., 2023). The fresh and regenerated Fe_3O_4 NPs were reused in the detoxification process and demonstrated high efficiency across all three runs for all evaluated inhibitors (Fig. 6). Interestingly, the Fe_3O_4 NP maintained approximately 100 % stability for detoxification even after the third run (Fig. 6). This observation aligns with findings by Qais et al. (2023), where Nano-ZnO achieved three runs of ionic dye acid blue 92 (AB 92) removal from aqueous solutions. In contrast, Meena et al. (2024) reported a higher reusability of five recycling runs for the removal of rhodamine B (RhB) dye from aqueous samples using a fabricated polyaniline-coated porous and fibrous nanocomposite (PCTWC), which exhibited at least 80.18 % removal effeciency. Thus, this study has demonstrated the reusability of the magnetic Fe_3O_4 NP with potential to reduce detoxification cost and facilitates its industrial application.

3.7. *Inhibitory compound adsorption mechanism*

The potential mechanism relating to the adsorption of furfural, HMF, acetic acid, phenol, and formaldehyde is presented in Fig. 7. Specifically, Fe_3O_4 NP exhibits hydrophilic characteristics due to the surface hydroxyl (-OH) groups promoting the adsorption of hydrophilic compounds such as HMF, acetic acid, and formaldehyde. The polar hydroxyl (-OH) and aldehyde (-CHO) groups exhibited by HMF, the carboxyl (-COOH) end of acetic acid, the polar carbonyl (-CHO) group of formaldehyde, the hydroxyl (-OH) group in phenol structure, and the aldehyde (-CHO) present in furfural molecule can easily form hydrogen bonds with water, making them relatively hydrophilic. Consequently, their easy attachment to the surface of Fe_3O_4 NP adsorbent and removal from the pretreated hydrolysate. Hence, the interactions between the Fe_3O_4 NP, the inhibitor molecules, as well as the nanoadsorbent removal mechanism, were strongly influenced by hydrogen bonds, π–π interactions, π-hydrogen bonding and electrostatic interactions. Additionally, the attachment and removal of these inhibitors were substantiated by the results from the TEM, XRD, FTIR and UV spectroscopy (See supplementary document). Additionally, the surface functionalisation of Fe_3O_4 NP initiated by the adsorption of the inhibitors, enables adsorbate-absorbate molecules binding. The pH_{pzc} of the nanoadsorbent is 5.0, signifying that the nanoadsorbent surface is negatively charged. A pH higher than this value (5.0) will stimulate electrostatic interaction between the Fe_3O_4 NP and the inhibitor molecules. Also, a positively charged surface (pH_{pzc}>5.0) will enhance the attraction of negatively charged components of the inhibitor, thereby improving the adsorption process.

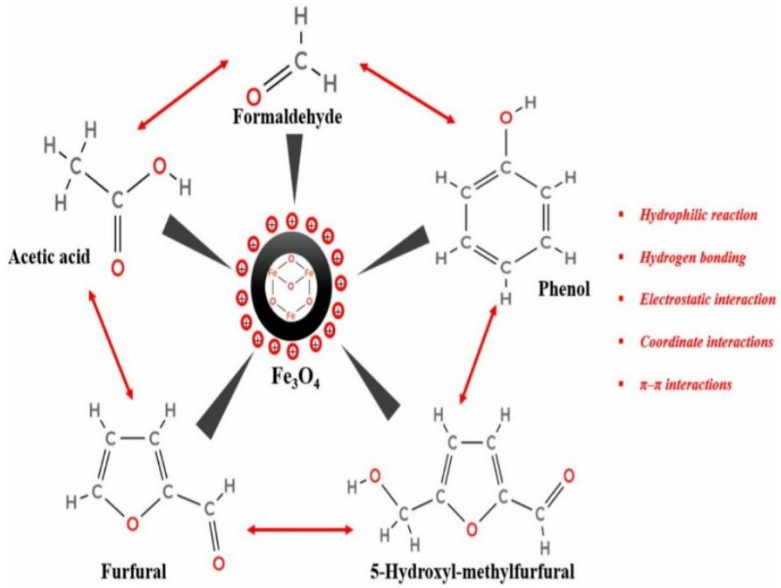

Fig. 7. Schematic illustration of the adsorption mechanism of Fe_3O_4 -NP for inhibitors.

4. Conclusion

The removal of the ICs (furfural, HMF, acetic acid, phenol, and formaldehyde) from pretreated hydrolysate using Fe_3O_4 nanoadsorbent were successfully studied. The structural and chemical nature of the Fe_3O_4 nanoadsorbent pre- and post-adsorption were revealed by SEM-EDS, TEM, FTIR, XRD, BET, PZC and UV spectrophotometry confirming the formation of inhibitor-nanoadsorbent interactions. Adsorbent dosage, initial inhibitor concentration, temperature, pH, and exposure time have a strong influence on the adsorption capacity and adsorption efficiency. In addition, the removal processes of ICs by Fe_3O_4 NP adsorbent involve diffusion within the particles, binding to active sites, adsorbate-absorbate interaction and the chemisorption process. The potential bond forces involved in the adsorption include hydrogen bonds, π–π interactions, π-hydrogen bonding and electrostatic interactions. The adsorption isotherm data fitted the Freundlich, Langmuir and Temkin models. These models revealed the homogenous monolayer (phenol and HMF) and heterogeneous multilayer (acetic acid and formaldehyde) of the adsorption processes. Generally, Fe_3O_4 NP adsorbent exhibited multi-molecular layer adsorption of the inhibitors. The thermodynamics coefficients (ΔG^0, ΔS^0 and ΔH^0) indicated that the ICs adsorption onto Fe_3O_4 NP adsorbent was predominantly spontaneous and endothermic. The study provides significant insights into the potential of Fe_3O_4 nanoadsorbent in the removal of the inhibitory compounds (ICs) from pretreated hydrolysate towards improving productivity and yield in lignocellulosic-based bioprocessing.

CRediT authorship contribution statement

Adeniyi P. Adebule: Writing – review & editing, Writing – original draft, Visualization, Validation, Software, Methodology, Investigation, Formal analysis, Data curation, Conceptualization. **Isaac A. Sanusi:** Writing – review & editing, Writing – original draft, Visualization, Validation, Supervision, Resources, Methodology, Data curation, Conceptualization. **Gueguim E.B. Kana:** Writing – review & editing, Supervision, Resources, Conceptualization.

Declaration of competing interest

The authors: Adeniyi P. Adebule, Isaac A. Sanusi and E.B. Gueguim Kana declare there are no conflict of interest in this work.

Appendix A. Supplementary data

Supplementary data to this article can be found online at https://doi.org/10.1016/j.biteb.2025.102185.

Data availability

Data will be made available on request.

References

Abdel-Hady, E.E., Mohamed, H.F., Hafez, S.H., Fahmy, A.M., Magdy, A., Mohamed, A.S., Ali, E.O., Abdelhamed, H.R., Mahmoud, O.M., 2023. Textural properties and adsorption behavior of Zn–Mg–Al layered double hydroxide upon crystal violet dye removal as a low cost, effective, and recyclable adsorbent. Sci. Rep. 13 (1), 6435. https://doi.org/10.1038/s41598-023-33142-x.

Adebule, A.P., Sanusi, I.A., Kana, G.E.B., 2024. Nano-based surface adsorption detoxification of process inhibitors for improved bioethanol productivity. Bioresource Technology Reports 25, 101783. https://doi.org/10.1016/j.biteb.2024.101783.

Ajibade, P.A., Oluwalana, A.E., Mphahlele, L.L.R., 2021. Effect of temperature on the morphological, optical, and photocatalytic properties of CdS quantum dots. Opt. Quant. Electron. 53, 342. https://doi.org/10.1007/s11082-021-02978-w.

Al-Hetlani, E., D'Cruz, B., Amin, M.O., Madkour, M., 2022. Effective magnetic nanoadsorbent based on a carbonaceous/spinel ferrite nanocomposite for the removal of pharmaceutical pollutants from wastewater. Environ. Sci.: Water Res. Technol. 8, 998–1010. https://doi.org/10.1039/d1ew00495f.

Alshandoudi, L.M., Alkindi, S.R., Alhatmi, T.Y., Hassan, A.F., 2024. Synthesis and characterization of nano zinc oxide/zinc chloride–activated carbon composite based on date palm fronds: adsorption of methylene blue. Biomass Convers. Biorefinery 14 (15), 17219–17233. https://doi.org/10.1007/s13399-023-03815-8.

Altun, T., Ecevit, H., 2024. Fabrication and characterization of Halloysite–Fe_3O_4–Ag nanocomposite as efficient catalyst for metronidazole degradation by using sodium borohydride: artificial neural network modeling. Mater. Chem. Phys. 317, 129145. https://doi.org/10.1016/j.matchemphys.2024.129145.

Apostică, A.G., Ichim, T.A.T.I.A.N.A., Radu, V.M., Bulgariu, L.A.U.R.A., 2018. Simple and rapid spectrophotometric method for phenol determination in aqueous media. Bul. Inst. Polit. Iaşi 64 (3), 9–18.

Ayub, A., Raza, Z.A., Majeed, M.I., Tariq, M.R., Irfan, A., 2020. Development of sustainable magnetic chitosan biosorbent beads for kinetic remediation of arsenic contaminated water. Int. J. Biol. Macromol. 163, 603–617. https://doi.org/10.1016/j.ijbiomac.2020.06.287.

Becerra, M.L., Prieto, G.A., Rendueles, M., Diaz, M., 2022. Biological transformations of furanic platform molecules to obtain biomass-derived furans: a review. Biomass Convers. Biorefinery 1-19. https://doi.org/10.1007/s13399-022-03535-5.

Bishop, D.C.B., Sanusi, A.I., Kana, G.E.B., 2024. Enhanced substrate suitability of autoclave-assisted acid pre-treated waste sugarcane molasses: Pre-treatment

optimization, sequential nano-based detoxifcation strategies, and bioproduct production. Biomass Convers. Biorefinery. https://doi.org/10.1007/s13399-024-06127-7.

Cao, C., Xiao, L., Chen, C., Shi, X., Cao, Q., Gao, L., 2014. In situ preparation of magnetic Fe3O4/chitosan nanoparticles via a novel reduction precipitation method and their application in adsorption of reactive azo dye. Powder Technol. 260 (7), 90–97. https://doi.org/10.1016/j.powtec.2014.03.025.

Cao, S., Zhu, R., Wu, D., Su, H., Liu, Z., Chen, Z., 2024. How hydrogen bonding and π–π interactions synergistically facilitate mephedrone adsorption by bio-sorbent: an in-depth microscopic scale interpretation. Environ. Pollut. 342, 123044. https://doi.org/10.1016/j.envpol.2023.123044.

Cuevas, M., Quero, S.M., Hodaifa, G., López, A.J.M., Sánchez, S., 2014. Furfural removal from liquid effluents by adsorption onto commercial activated carbon in a batch heterogeneous reactor. Ecol. Eng. 68, 241–250.

de Andrade, J.K., de Andrade, C.K., Komatsu, E., Perreault, H., Torres, Y.R., da Rosa, M. R., Felsner, M.L., 2017. A validated fast difference spectrophotometric method for 5-hydroxymethyl-2-furfural (HMF) determination in corn syrups. Food Chem. 228, 197–203. https://doi.org/10.1016/j.foodchem.2017.01.158.

Ecer, Ü., Sahan, T., Zengin, A., Gubbuk, I.H., 2022. Decolorization of Rhodamine B by silver nanoparticle–loaded magnetic sporopollenin: characterization and process optimization. Environ. Sci. Pollut. Res. 29, 79375–79387. https://doi.org/10.1007/s11356-022-21416-2.

El Bakri, A., El Boujaady, H., Ferraa, N., Bennani-Ziatni, M., 2024. The removal of phenol through adsorption onto synthetic calcium phosphates–a study encompassing analyses of kinetics and thermodynamics. Ecological Engineering & Environmental Technology (EEET) 25 (4), 301–315. https://doi.org/10.12912/27197050/184155.

Fan, H.L., Zhou, S.F., Jiao, W.Z., Qi, G.S., Liu, Y.Z., 2017. Removal of heavy metal ions by magnetic chitosan nanoparticles prepared continuously via high-gravity reactive precipitation method. Carbohydr. Polym. 174, 1192–1200. https://doi.org/10.1016/j.carbpol.2017.07.050.

Granath, T., Löbmann, P., Mandel, K., 2021. Oxidative precipitation as a versatile method to obtain ferromagnetic Fe_3O_4 nano-and mesocrystals adjustable in morphology and magnetic properties. Part. Part. Syst. Charact. 38 (3), 2000307. https://doi.org/10.1002/ppsc.202000307.

Hone, F.G., Dejene, F.B., 2018. Studies the effects of bath pH and lead molar concentrations on the structural, optical and electrical properties of lead sulphide thin films prepared by chemical route. J. Mater. Sci. Mater. Electron. 29, 13188–13199. https://doi.org/10.1007/s10854-018-9443-z.

Igwegbe, C.A., Onukwuli, O.D., Ighalo, J.O., Okoye, P.U., 2020. Adsorption of cationic dyes on Dacryodes edulis seeds activated carbon modified using phosphoric acid and sodium chloride. Environ. Process. 1151-71. https://doi.org/10.1007/s40710-020-00467-y.

Ilahi, S., Narayan, P., Tara, N., Pal, S., Ali, S., 2020. Arsenic removal from water by starch functionalized maghemite nano-adsorbents: thermodynamics and kinetics investigations. Colloid and Interface Science Communications 36, 100263. https://doi.org/10.1016/j.colcom.2020.100263.

Juang, R.S., Wu, F.C., Tseng, R.L., 1997. The ability of activated clay for the adsorption of dyes from aqueous solutions. Environ. Technol. 18 (5), 525–531. https://doi.org/10.1080/09593331808616568.

Kag, S., Kukreti, N., Ruhal, R., Mann, S., Sharma, J., Kataria, R., 2022. Recent technologies for lignocellulose biomass conversion to bioenergy and biochemicals. In: Nandabalan, Y.K., Garg, V.K., Labhsetwar, N.K., Singh, A. (Eds.), Zero Waste Biorefinery. Energy, Environment, and Sustainability. Springer. https://doi.org/10.1007/978-981-16-8682-5_2.

Kakavandi, B., Jonidi, A., Rezaei, R., Nasseri, S., Ameri, A., Esrafily, A., 2013. Synthesis and properties of Fe_3O_4-activated carbon magnetic nanoparticles for removal of aniline from aqueous solution: equilibrium, kinetic and thermodynamic studies. Iranian Journal of Environmental Health Science & Engineering 10, 1–9. https://doi.org/10.1186/1735-2746-10-19.

Khojasteh, H., Mohammadi-Aghdam, S., Heydaryan, K., Sharifi, N., Aspoukeh, P., Khanahmadzadeh, S., Khezri, B., 2024. Optimization of Fe_3O_4@ SiO_2/Ag/AgCl/CdS nanocomposite via response surface methodology: an efficient visible-light photocatalyst for methyl orange degradation. J. Sol-Gel Sci. Technol. 111 (2), 362–380. https://doi.org/10.1007/s10971-024-06458-x.

Lavrynenko, O.M., Bolbukh, Y.M., 2014. Structural features of the iron-oxygen nanoparticles formed when the rotation-corrosion dispersion method is applied. Nano Studies 9, 127–148. https://inis.iaea.org/records/nesad-pet38.

Li, S., Qi, B., Luo, J., Zhuang, Y., Wan, Y., 2021. Ultrafast selective adsorption of pretreatment inhibitors from lignocellulosic hydrolysate with metal-organic frameworks: performance and adsorption mechanisms. Sep. Purif. Technol. 275, 119183. https://doi.org/10.1016/j.seppur.2021.119183.

Liu, Y., Cao, S., Xi, C., Su, H., Chen, Z., 2021. A new nanocomposite assembled with metal organic framework and magnetic biochar derived from pomelo peels: a highly efficient adsorbent for ketamine in wastewater. J. Environ. Chem. Eng. 9, 106207. https://doi.org/10.1016/j.jece.2021.106207.

Maryanti, R., Nandiyanto, A.B.D., Manullang, T.I.B., Hufad, A., Sunardi, S., 2020. Adsorption of dye on carbon microparticles: Physicochemical properties during adsorption, adsorption isotherm and education for students with special needs. Sains Malays 49, 2949–2960. https://doi.org/10.17576/jsm-2020-4912-09.

Meena, P.L., Surela, A.K., 2024. Review on polyaniline-based nanocomposite heterogeneous catalysts for catalytic reduction of hazardous water pollutants. RSC Adv. 14 (37), 26801–26819. https://doi.org/10.1039/D4RA02550D.

Meena, P.L., Saini, J.K., Surela, A.K., Mordhiya, B., Chhachhia, L.K., Meena, K.S., 2023. Fabrication of polyaniline-supported MnO_2 nanocomposite for removal of water pollutant: kinetic and isotherm studies. ChemistrySelect 8 (25). https://doi.org/10.1002/slct.202300724.

Meena, P.L., Saini, J.K., Surela, A.K., Poswal, K., Chhachhia, L.K., 2024. Fabrication of polyaniline-coated porous and fibrous nanocomposite with granular morphology using tea waste carbon for effective removal of rhodamine B dye from water samples. Biomass Convers. Biorefinery 14, 1711–1730. https://doi.org/10.1007/s13399-021-02267-2.

Meena, P.L., Surela, A.K., Chhachhia, L.K., Meena, J., Meena, R., 2025a. Investigation of the photocatalytic potential of C/N-co-doped ZnO nanorods produced via a mechano-thermal process. Nanoscale Advances 7, 1335–1352. https://doi.org/10.1039/D4NA00890A.

Meena, P.L., Surela, A.K., Chhachhia, L.K., Kumar, N., 2025b. Dye sensitized photoactivation of ZnO/Zn (NCN) nanocomposites obtained via solvent free mechanothermal process and their photocatalytic application. Ceram. Int. 51 (4), 4891–4903. https://doi.org/10.1016/j.ceramint.2024.11.462.

Oluwalana, A.E., Ajibade, P.A., 2021. Structural, optical and photocatalytic studies of oleylamine capped PbS nanoparticles. Opt. Quant. Electron. 53 (2), 1–13. https://doi.org/10.1007/s11082-020-02636-7.

Omran, A.P., Coughlin, C.B., 2020. Bial's test, a simple method for formaldehyde detection. Bial's test, a simple method for formaldehyde detection. Biomedical Journal of Scientific & Technical Research 27 (3), 20860–20863. https://doi.org/10.26717/bjstr.2020.27.004515.

Pino, N., López, D., Espinal, J.F., 2019. Thermochemistry and kinetic analysis for the conversion of furfural to valuable added products. J. Mol. Model. 25, 26. https://doi.org/10.1007/s00894-018-3908-0.

Qais, D.S., Islam, M.N., Othman, M.H.D., Mahmud, H.E., Quayum, M.E., Islam, M.A., Ismail, I.M.I., Habib, A., 2023. Nano-zinc oxide fibers: synthesis, characterization, adsorption of acid blue 92 dye, isotherms, thermodynamics and kinetics. Emerging Contaminants 9 (2), 100224. https://doi.org/10.1016/j.emcon.2023.100224.

Rezaei, B., Yari, P., Sanders, S.M., Wang, H., Chugh, V.K., Liang, S., Mostufa, S., Xu, K., Wang, J.P., Gómez-Pastora, J., Wu, K., 2023. Magnetic nanoparticles: a review on synthesis, characterization, functionalization, and biomedical applications. Small 20 (5), 2304848. https://doi.org/10.1002/smll.202304848.

Sanusi, A.I., Faloye, F.D., Kana, E.B.G., 2019. Impact of various metallic oxide nanoparticles on ethanol production by *Saccharomyces cerevisiae* BY4743: screening, kinetic study and validation on potato waste. Catal. Lett. 149 (7), 2015–2031. https://doi.org/10.1007/s10562-019-02796-6.

Sanusi, A.I., Sewsynker-Sukai, Y., Kana, E.B.G., 2021. Nanotechnology in bioprocess development: applications of nanoparticles in the generation of biofuels. In: Microbial Nanobiotechnology. Springer. https://doi.org/10.1007/978-981-33-4777-9_6.

Sanusi, A.I., Suinyuy, T.N., Lateef, A., Gueguim Kana, E.B., 2020. Effect of nickel oxide nanoparticles on bioethanol production: Process optimization, kinetic and metabolic studies. Process Biochem. 92, 386–400. https://doi.org/10.1016/j.procbio.2020.01.029.

Sierra, P.V., Eric, T., José, G., Hernández, F.L., 2020. Arsenic sorption on chitosan-based sorbents: comparison of the effect of molybdate and tungstate loading on As (V) sorption properties. J. Polym. Environ. 28, 934–947. https://doi.org/10.1007/s10924-020-01654-6.

Sun, P., Zhang, W., Zou, B., Zhou, L., Ye, Z., Zhao, Q., 2021. Preparation of EDTA-modified magnetic attapulgite chitosan gel bead adsorbent for the removal of Cu (II), Pb (II), and Ni (II). Int. J. Biol. Macromol. 182, 1138–1149. https://doi.org/10.1016/j.ijbiomac.2021.04.132.

Valizadeh, K., Bateni, A., Sojoodi, N., Ataabadi, M.R., Behroozi, A.H., Maleki, A., You, Z., 2022. Magnetized inulin by Fe_3O_4 as a bio-nano adsorbent for treating water contaminated with methyl orange and crystal violet dyes. Sci. Rep. 12 (1), 22034. https://doi.org/10.1038/s41598-022-26652-7.

Wang, Y., Szokolova, K., Nasir, M., Sofer, Z., Pumera, M., 2019. Layered crystalline and amorphous platinum disulfide (PtS2): contrasting electrochemistry. Chemistry A European Journal 25, 7330–7338. https://doi.org/10.1002/chem.201900331.

Xiang, H., Dai, K., Kou, J., Wang, G., Zhang, Z., Li, D., Chen, C., 2023. Selective adsorption of ferulic acid and furfural from acid lignocellulosic hydrolysate by novel magnetic lignin-based adsorbent. Sep. Purif. Technol. 307, 122840. https://doi.org/10.1016/j.seppur.2022.122840.

Zhao, J., Liu, J., Ning, L., Wang, W., Nan, J., Zhao, Z., Cui, F., 2016. Highly efficient removal of bivalent heavy metals from aqueous systems by magnetic porous Fe3O4-MnO2: adsorption behavior and process study. Chem. Eng. J. 304, 737–746. https://doi.org/10.1016/j.cej.2016.07.003.

Zondi, A.S., Sanusi, I.A., Sewsynker-Sukai, Y., Beukes, L.S., Kana, E.B.G., 2025. Nano-based co-valorization, detoxification, and fermentation of potato waste and black liquor for bioethanol production. Biomass Conv. Bioref. https://doi.org/10.1007/s13399-025-06515-7.

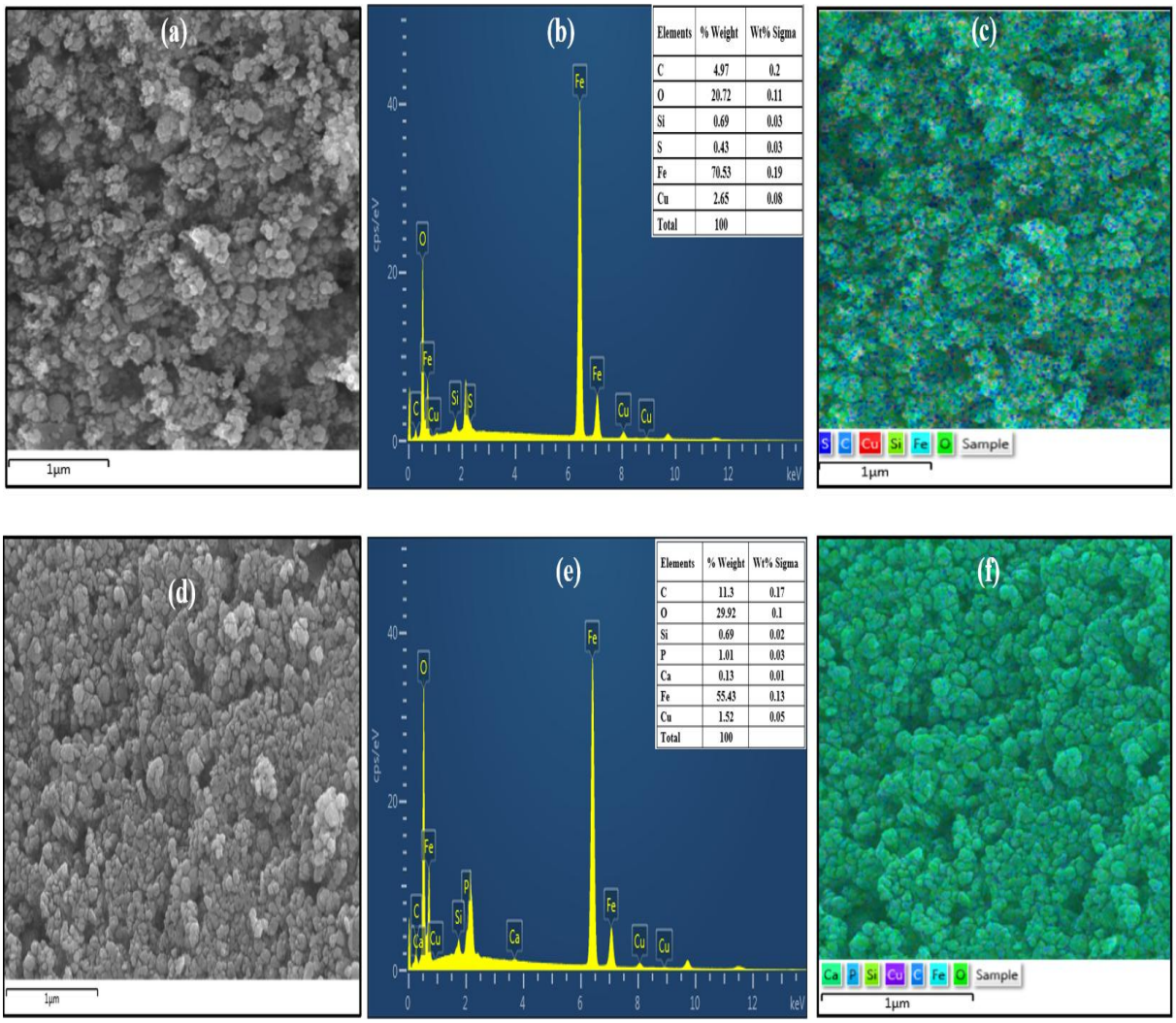

Figure S4. 1. SEM image [(a) and (d)], EDX spectra [(b) and (e)], Elemental maps [(c) and (f)] of Fe_3O_4-NP and detox-Fe3O4-NP

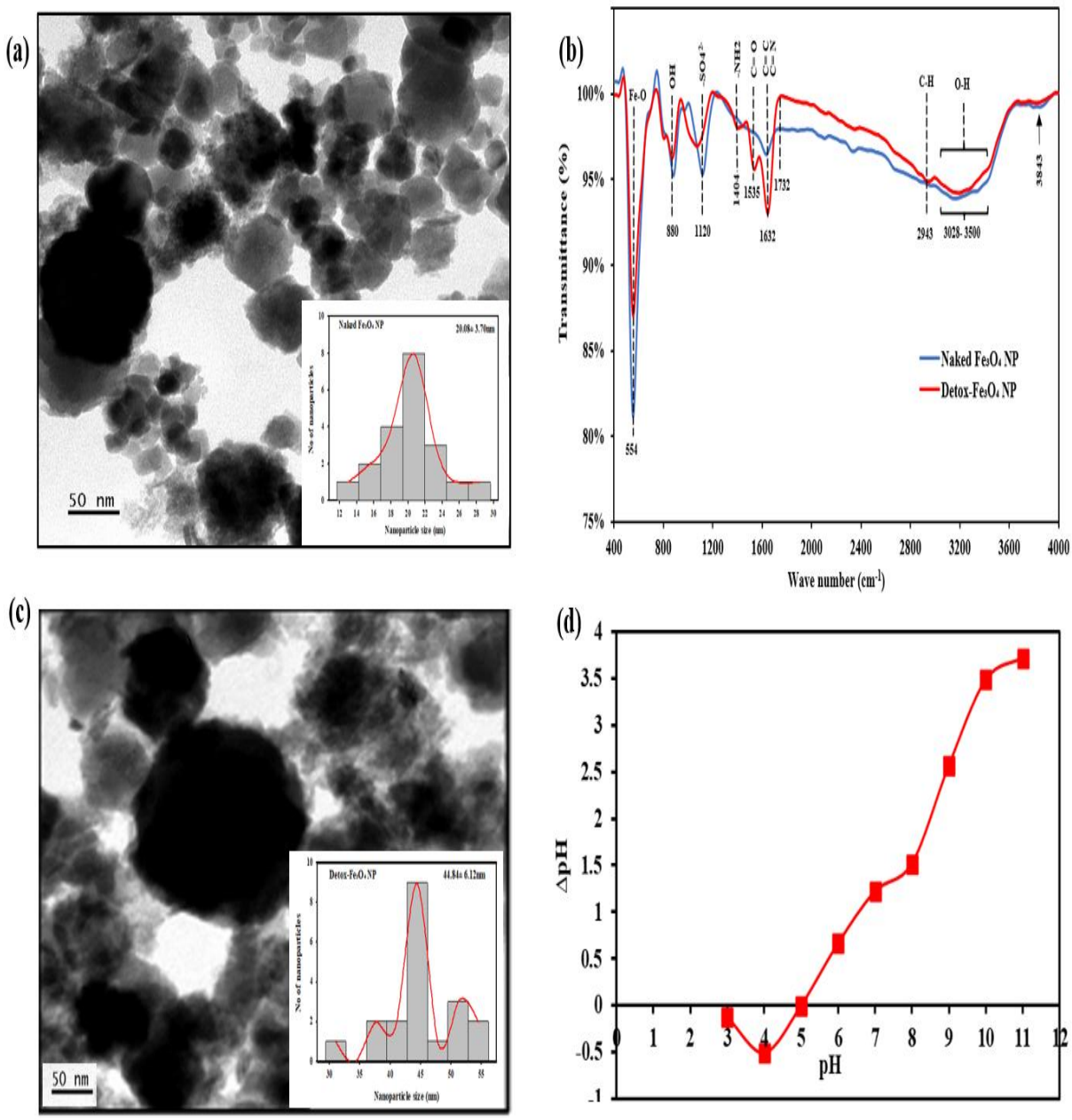

Figure S4. 2. TEM image with distribution histogram [(a) and (c)], FTIR spectra (b) of Fe_3O_4-NP and detox-Fe_3O_4-NP and pHpzc graph of Fe_3O_4-NP (d)

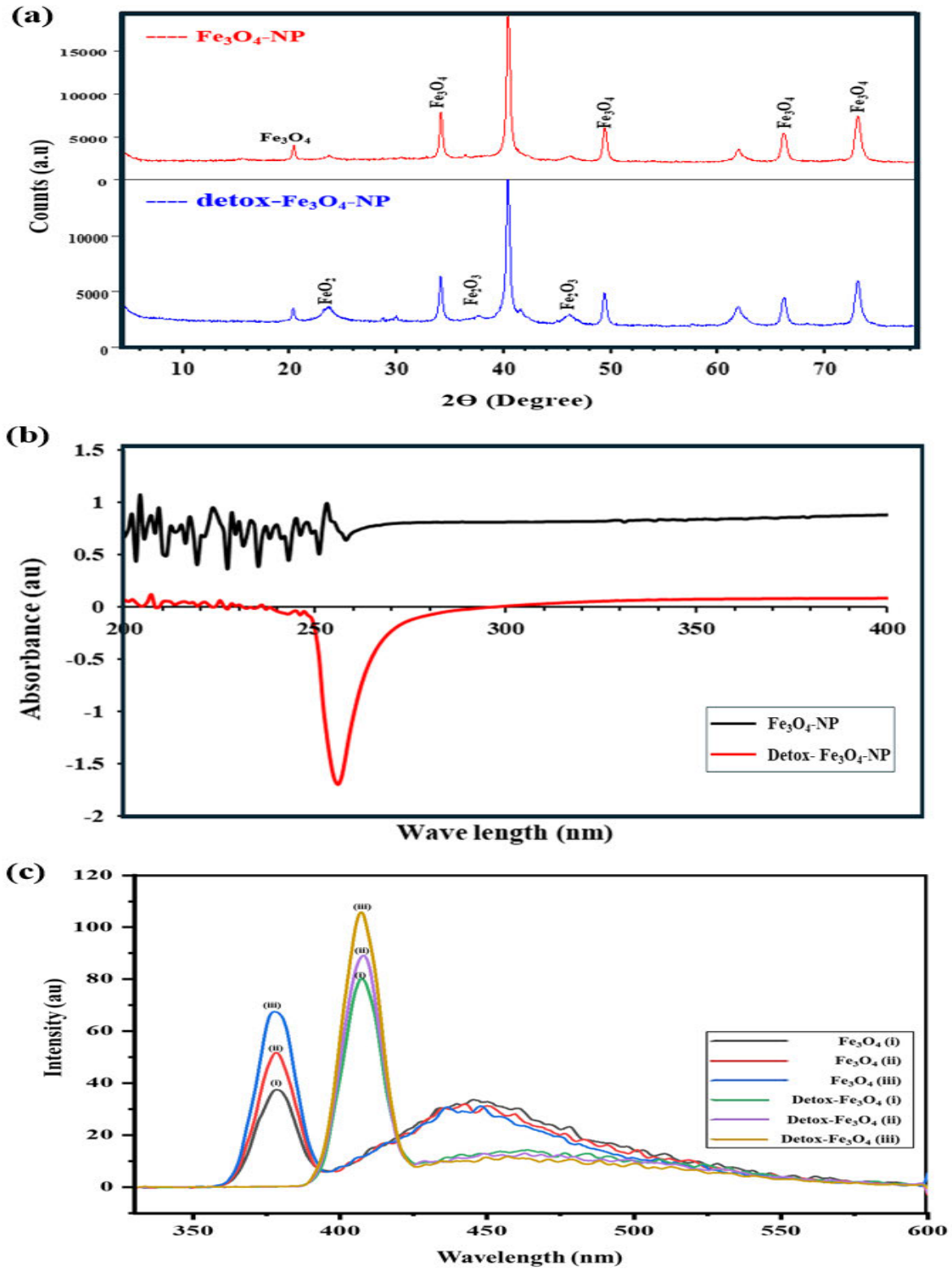

Figure S4. 3. (a) XRD patterns, (b) UV-Vis absorption, and (c) Photoluminescence emission spectra of Fe_3O_4-NP and detox-Fe_3O_4-NP

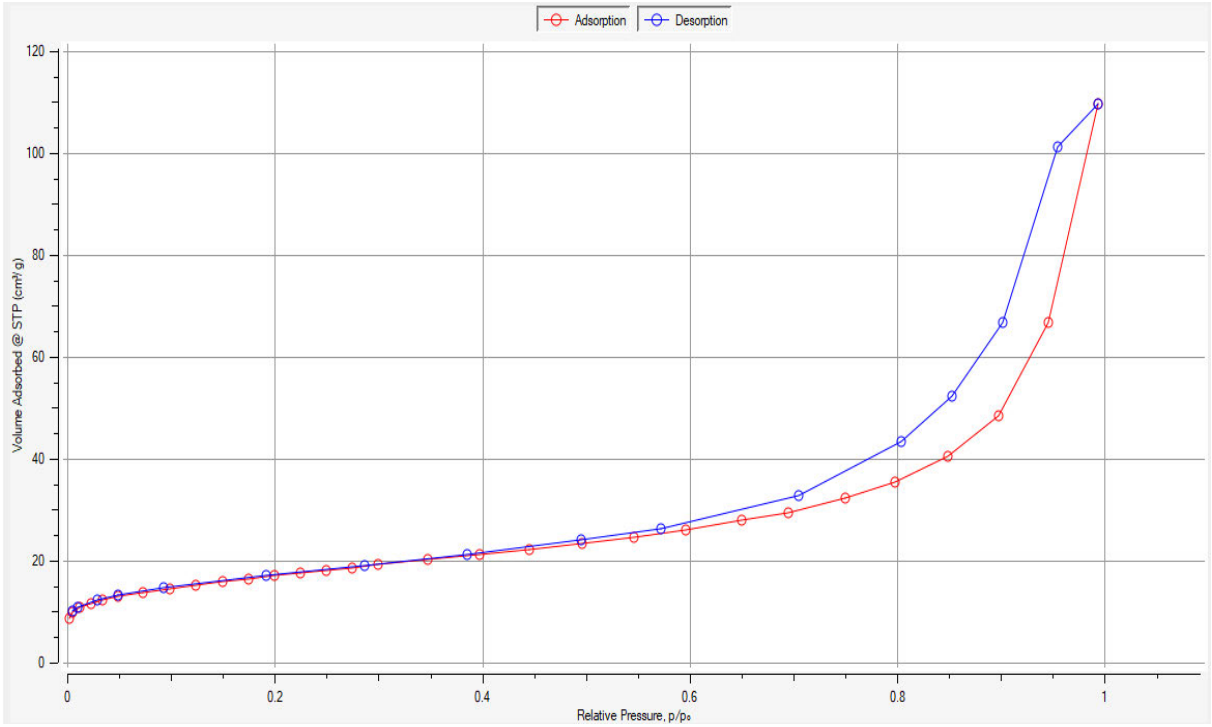

Figure S4. 4. BET Isotherm of Fe_3O_4 NP

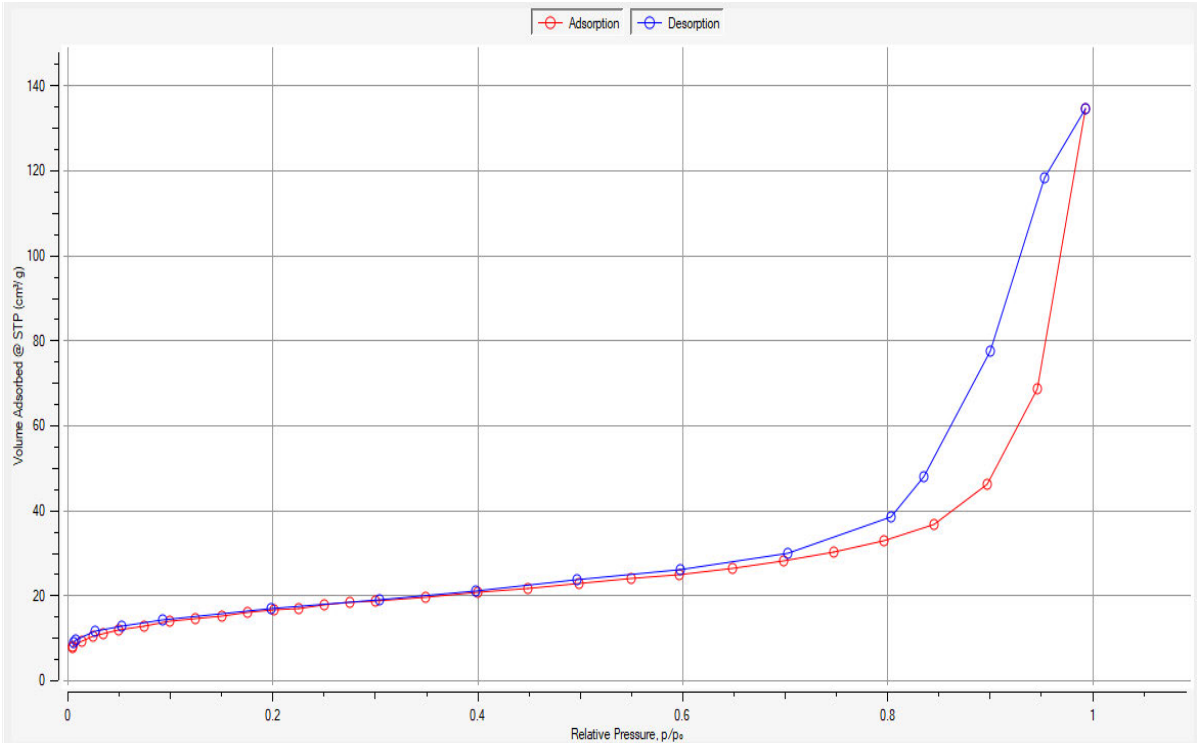

Figure S4. 5. BET Isotherm of Detox- Fe_3O_4 NP

CHAPTER 5

Growth-associated and non-growth-associated bioethanol production kinetics from nanoadsorbent-detoxified pretreated hydrolysate

This chapter has been published with the title: Growth-associated and non-growth-associated bioethanol production kinetics from nano-adsorbent-detoxified pretreated hydrolysate. *Catalysis Letters*, *155*(3): 96. https://doi.org/10.1007/s10562-024-04868-8. The published paper is presented in the following pages.

Catalysis Letters (2025) 155:96
https://doi.org/10.1007/s10562-024-04868-8

Growth-associated and Non-growth-associated Bioethanol Production Kinetics from Nanoadsorbent-Detoxified Pretreated Hydrolysate

Adeniyi P. Adebule[1] · Isaac A. Sanusi[1] · Gueguim E. B. Kana[1]

Received: 18 August 2024 / Accepted: 29 September 2024

Abstract

Lignocellulosic-based (LCB) bioethanol production is challenged by the presence of inhibitory compounds in pretreated LCB hydrolysates limiting productivity. The negative impact of these inhibitory compounds on LCB bioethanol production kinetics remain understudied. Hence, this study modelled the kinetics of bioethanol fermentation using nanoadsorbent-detoxified potato peel waste (PPW) hydrolysate. Four different fermentation processes under both separate hydrolysis and fermentation (SHF) and simultaneous saccharification and fermentation (SSF) conditions, including A (SHF with non-detoxified hydrolysate), B (SSF with non-detoxified hydrolysate), C (SHF with detoxified hydrolysate), and D (SSF with detoxified hydrolysate) were evaluated for bioethanol productivity. Higher productivity of 1.23 and 1.16-fold increments were recorded for fermentation processes C and D. Thereafter, the experimental data for cell growth, bioethanol production and substrate utilisation were well-fitted by the logistic function, modified Gompertz, and Luedeking-Piret models respectively. Moreover, the obtained root-mean-square error (RMSE) and mean square error (MSE) were low, while the accuracy factor (AF), bias factor (BF), slope and regression coefficient (R^2) were close to 1. The bioethanol production processes were largely growth-associated (α) as α values (g ethanol/g substrate) were higher than β values (g ethanol/g substrate/h). The models were effectively implemented, demonstrating their usefulness to elucidate bioethanol productivity kinetics for improved process design and the development of large-scale bioethanol production.

Graphical Abstract

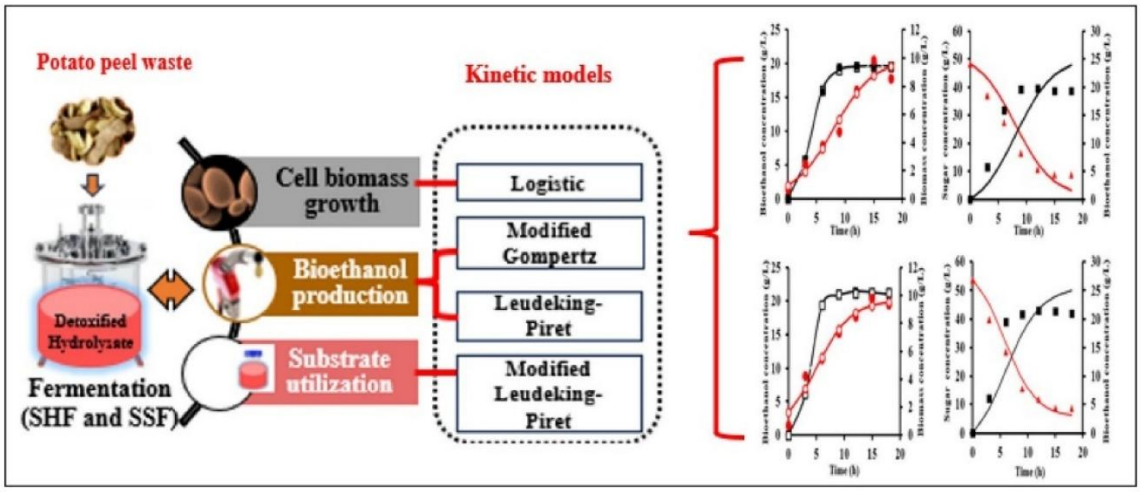

Keywords Bioethanol · Detoxified hydrolysate · Growth-associated · Kinetics · Substrate utilisation

Extended author information available on the last page of the article

Published online: 21 January 2025

Abbreviations

μ_{max}	Maximum specific growth rate (h^{-1})
X_o	Initial cell concentration (g/L)
X_{max}	Maximum cell concentration (g/L)
P_m	Maximum potential bioethanol concentration
$r_{p,m}$	Maximum bioethanol production rate (g/L/h),
t_L	Lag time (h)
A	Growth associate constant (g P/g X)
β	Non-growth associate constants (g P/g X. h)
Γ	Substrate utilisation coefficient (g S/g X)
Δ	Maintenance coefficient (g S/g X. h)
MGM	Modified Gompertz model
LP	Leudeking-Piret model
MLP	Modified Leudeking-Piret model
PPW	Potato peel waste
SSF	Simultaneous Saccharification and fermentation
SHF	Separate Hydrolysis and Fermentation
Process A	Non-detoxified separate hydrolysis and fermentation
Process C	Optimised detoxified separate hydrolysis and fermentation
Process B	Non-detoxified simultaneous saccharification and fermentation
Process D	Optimised detoxified simultaneous saccharification and fermentation
RMSE	Root-mean-square-error
MSE	Mean-square-error
AF	Accuracy factor
BF	Bias factor
R^2	Regression coefficient
Q_X	Maximum specific growth rate
Q_P	Maximum production rate
Q_S	Maximum substrate utilisation rate
SU	Sugar utilisation
TY	Theoretical ethanol yield

1 Introduction

The rapid depletion of fossil fuel reserves and the escalating associated environmental issues such as pollution, global warming, and the greenhouse effect resulting from the widespread use of petroleum fuels have underscored the urgent need for renewable and sustainable energy sources [1]. This transition is crucial not only for the generation of biofuels but to mitigate the negative environmental impact of using petroleum fuels [1]. Alternatively, this renewable energy can be sourced biologically using agro-industrial waste such as potato peel [2, 3]. One of the environmental significances of potato production on a global scale is the huge generation of potato peel waste (PPW) (which is approximately 15–40% of the whole crop) [4]. Consequently, employing a biorefinery approach to enhance PPW utilisation offers significant advantages in managing PPW towards value-added products production. The PPW is rich in starch, an ideal substrate that can be hydrolysed to release high fermentable carbohydrates such as glucose and xylose. This strategy seamlessly harmonises with the broader goal of fostering a circular economy and promoting sustainable development [5].

One of such valuable biofuels derived from the beneficiation of PPW is bioethanol. Bioethanol from waste such as PPW is a biodegradable biofuel with high octane, and it generates reduced CO_2 emissions during combustion, which is associated with a lower risk of ozone formation than fossil fuels [6, 7]. Although large-scale bioethanol production from waste materials has been explored, several bottlenecks still exist, including the release of fermentation inhibitors (such acetic acid, furfural, 5-hydromethylfurfural and phenol) during feedstock pretreatment [1]. These inhibitors negatively impact fermentation productivity by obstructing enzyme activities through imbalances in cellular electrochemical gradients, elongated lag phase, and the inhibition of product formation. Hence, detoxification of these inhibitory compounds in pretreated hydrolysate is imperative to limit their negative effects on bioprocessing [2, 8–10]. The efficacy of this detoxification process has prompted the investigation into the utilisation of the detoxified hydrolysate for bioethanol production [2]. However, the kinetics of microbial cell growth, product formation, and substrate consumption using the detoxified hydrolysate have not been well studied. Interestingly, kinetic models such as logistic, modified Gompertz, Luedeking-Piret, and modified Luedeking-Piret models could provide insight as well as capture information about the metabolic activity and dynamics of a fermentation process, which is desirable for bioprocess design, implementation, and scaling up [11, 12]. Moreover, elucidating the relationship of product formation to growth-associated, non-growth-associated and mixed-growth-associated is imperative to process development and scale up.

The logistic model describes the change in cell content as a function of the cell growth rate, initial cell concentration, and highest cell concentration under sufficient substrate availability. In contrast, the modified Gompertz model describes cell growth-related product formation based on the lag time of bioethanol formation, the highest production rate, and the highest bioethanol concentration obtained [13]. Additionally, the Luedeking-Piret (LP) model and its modified form (modified Luedeking-Piret) give additional insight into product formation by correlating biomass growth and substrate consumption rate [14]. Even though there are many studies with kinetic models on bioethanol production, to the best of our knowledge, there are scarcity of study on kinetic model of bioethanol fermentation using optimised detoxified pretreated potato peel waste under the separate hydrolysis

and fermentation (SHF) and simultaneous saccharification and fermentation (SSF) processes.

Therefore, in this study, comparative bioethanol fermentation using SHF and SSF fermentation modes was implemented using optimised detoxified and non-detoxified pretreated PPW hydrolysate. In addition, the logistic function, the modified Gompertz model, the Luedeking-Piret, and the modified Luedeking-Piret kinetic models were employed to further elucidate the cell growth metabolism and bioethanol formation dynamics through nonlinear regression analyses.

2 Materials and Methods

2.1 Sample Preparation

The experimental study's feedstock (potato peel waste) was collected from food vendors in the Pietermaritzburg metropolis, KwaZulu-Natal province, South Africa (29.5418◦ S, 30.4077◦ E). The substrate was immediately dried at 50–55 °C for 48 h in a laboratory oven (Scientific series 2000, South Africa) to reduce the moisture content and then milled to a particle size of 1–2 mm using a laboratory miller. The composition analysis of milled waste potato peels shows 52% starch, 14% structural carbohydrate, 4% cellulose, 10% hemicellulose, 6% lignin, 13.21% crude protein, 10.76% ash, and 0.43% fat.

2.2 Hydrolysate Preparation and Detoxification

The milled PPW was pretreated using optimised process parameters previously reported by Aruwajoye et al. [15], and the detoxification of inhibitors (such as furfural, 5-hydromethyl furfural, phenolic compound, formaldehyde, and acetic acid) from the pretreated hydrolysate was carried out using the optimised protocol detailed in Adebule et al. [2]. Briefly, the substrate pretreatment was carried out in 250 mL Schott bottles with a working volume of 100 mL. In the pretreatment reactor, 0.92 (% v/v) HCl solution was added to the milled PPW (5%w/v) soaked at 69.62 °C for 2.34 h in a water bath. Following the above process, the bottles were autoclaved at 121 °C for 5 min [15]. For the hydrolysate detoxification, Fe_3O_4 NP (0.021 w/v%) was added to 100 mL of pretreated hydrolysate of PPW maintained at pH 4.14 and 35.37 °C for 12.74 min [2]. The detoxified hydrolysate was thereafter used for the SHF and SSF bioethanol production.

2.3 Fermentation Processes

2.3.1 Inoculum Cultivation and Fermentation Media

The viability of *Saccharomyces cerevisiae* was maintained aseptically on a double-strength yeast peptone dextrose (YPD) slant (20 g/L yeast extract, 40 g/L peptone, 40 g/L dextrose, and 20 g/L agar). Before fermentation, a 250 mL Erlenmeyer conical flask containing 100 mL of YPD broth medium was inoculated with *S. cerevisiae* and grown at 30 °C, 120 rpm, to attain an exponential growth as the fermentation seed culture. The broth fermentation medium contained separately the non-detoxified (ND) PPW hydrolysate [Process A and B] and the optimised detoxified (OD) PPW hydrolysate [Process C and D] as the sole carbon source, yeast extract (5 g), $(NH_4)_2SO_4$ (1 g), KH_2PO_4 (2 g) and $MgSO_4$ (1 g) per litre autoclaved at 121 °C for 15 min to obtain a sterile medium.

2.3.2 Fermentation Modes

The bioethanol fermentation modes implemented were the separate hydrolysis and fermentation (SHF) and the simultaneous saccharification and fermentation (SSF). The fermentation designs at various stages of the processes are shown in Fig. 1. The SHF and SSF modes were obtained with enzymatic liquefaction, saccharification, and fermentation performed separately and sequentially. Both fermentation processes were carried out in 250 ml Erlenmeyer flasks with a working volume of 100 ml. A 10% v/v inoculation of the starter culture (*S. cerevisiae*) with an initial cell count estimate of 10^7 cells/mL was aseptically transferred to the fermentation flasks. The SSF processes (B and D) with a solid loading of 5%, and an amylase loading of 0.212 mL for the liquefaction stage at 90 °C, pH 7, for 60 min. Subsequently, for the saccharification process, 0.295 mL of amyloglucosidase, fermentation broth, and 10% v/v *S. cerevisiae* inoculum broth were added. Afterwards, SSF experiment was incubated at 35 °C and 120 rpm for 24 h until sugar concentration was depleted.

On the other hand, for the SHF experiment, the liquefaction, the saccharification, and the fermentation stages as indicated above were carried out separately. The SHF experiment was also incubated at 35 °C and 120 rpm over 24 h until sugar concentration was depleted. Sample aliquots (1 mL) were extracted from the processes (A, B, C and D) every three (3) hours intervals and stored at 4 °C for further analyses (residual sugar, bioethanol, and biomass concentrations). The data obtained were subsequently used for the kinetic estimation and modelling.

2.4 Analytical Methods

Biomass concentration (g/L) was determined by correlating the cell count of *S. cerevisiae* with its dry cell weight using a predetermined standard calibration curve.

The ethanol concentration (g/L) in the gas phase of the fermentation process was estimated using an ethanol

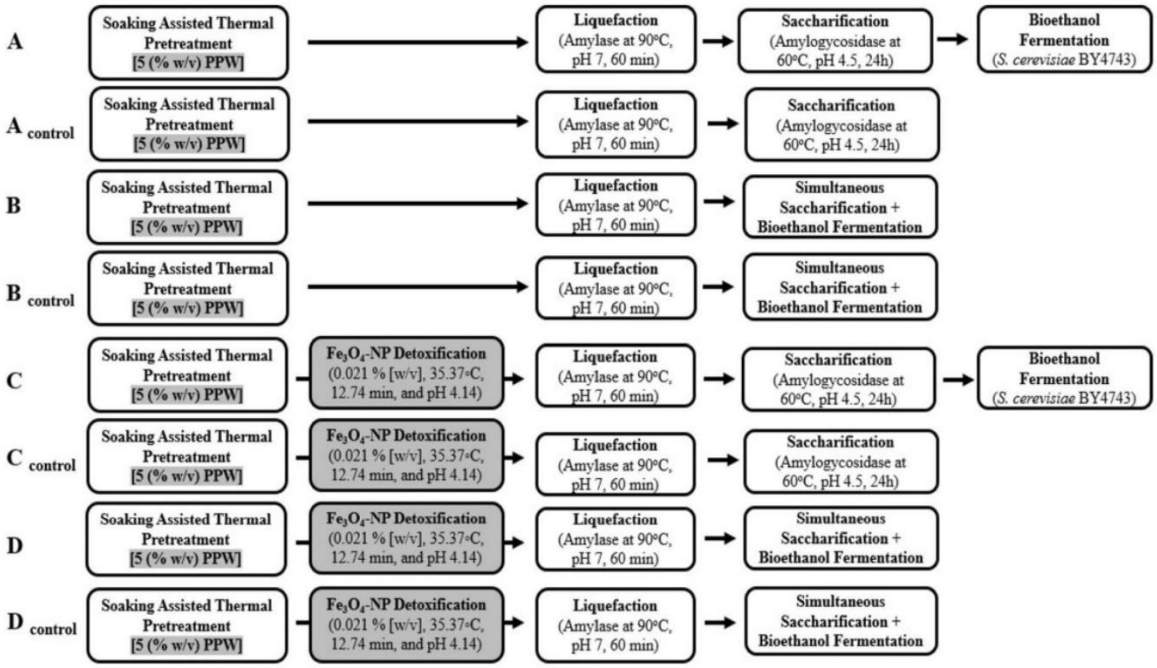

Fig. 1 Flow diagram showing stages of SHF and SSF for media A, B, C, and D. The controls were not exposed to fermentation. A: Non-detoxified separate hydrolysis and fermentation. A $_{control}$: Non-detoxified separate hydrolysis (without fermentation). B: Non-detoxified simultaneous saccharification and fermentation. B $_{control}$: Non-detoxified simultaneous saccharification (without fermentation). C: Optimised detoxified separate hydrolysis and fermentation. C $_{control}$: Optimised detoxified separate hydrolysis (without fermentation). D: Optimised detoxified simultaneous saccharification and fermentation. D $_{control}$: Optimised detoxified simultaneous saccharification (without fermentation)

vapour sensor (ETH-BTA LABQUEST12, Vernier Software and Technology, USA).

Reducing sugar content per litre was determined using the 3,5–dinitro salicylic acid method [16], while the glucose content (g/L) was quantified using the Megazyme glucose assay kit (Megazyme, Ireland).

2.5 Kinetic Parameters and Model Development

Fermentation kinetics parameters were estimated according to the equations presented in Table 1, and Fig. S1 (supplementary document). Linear and non-linear regression forms of logistic function, modified Gompertz, Luedeking-Piret, and modified Luedeking-Piret models were implemented for cell growth, product formation, and sugar consumption to predict the kinetic dynamic of bioethanol fermentation of the processes (A, B, C and D) under either SSF or SHF. The non-linear regression estimations were carried out using the Microsoft Excel Solver (Ms. Solver™) spreadsheet-based program and compared with the model parameters obtained by linear fitting to ascertain improved model accuracy.

2.5.1 Cell Growth Kinetics Using Logistic Function Model

The logistic function model represents the cell growth dynamics from the initiation of the log phase to the stationary phase. Equation (1) represents the exponential and stationary phases of cell growth.

$$X = \frac{X_0 \cdot \exp\left(\mu_{max} \cdot t\right)}{1 - \left(\frac{X_0}{X_{\max}}\right) \cdot \left(1 - \exp\left(\mu_{max} \cdot t\right)\right)} \quad (1)$$

Here, X denoted the biomass concentration (g/L), X_0 is the initial cell concentration, X_{max} is the maximum cell concentration, and μ_{max} is the maximum specific growth rate at specific times (t) during the cells' exponential and stationary growth phases.

Also, μ_{max} and X_0 of the cell growth were graphically evaluated using the slope and the y-shift of the plot of $\ln\left(\frac{X}{X_{max}-X}\right)$ and time (t) was derived from Eq. (2). Equation (2) arises from the rearrangement of Eq. (1)

Table 1 Kinetic parameters of PPW fermentation

	Parameter	Symbol	Unit	Equation
1	Biomass growth	ΔX	g/L	X_{max}—X_{min}
2	Ethanol production	ΔP	g/L	P_{max}—P_{min}
3	Sugar utilisation	ΔS	g/L	S_{max}—S_{min}
4	Biomass yield	$Y_{X/S}$	g/g	ΔX/ΔS
5	Ethanol yield	$Y_{P/S}$	g/g	ΔP/ΔS
6	Ethanol production per biomass	$Y_{P/X}$	g, ethanol/g, biomass	ΔP/ΔX
7	Sugar consumption per biomass	$Y_{S/X}$	g, sugar/g, biomass	ΔS/ΔX
8	Maximum specific growth rate	Q_X	g/L/h	$(dX/dt)_{max}$
9	Maximum production rate	Q_P	g/L/h	$(dP/dt)_{max}$
10	Maximum substrate utilisation rate	Q_S	g/L/h	$-(dS/dt)_{max}$
11	Glucose utilisation yield	SUY	%	$(\Delta S/S_{max})\times 100$
12	Theoretical ethanol yield	TY	G	$Y_{P/S}$ / 0.511

X_{min}, P_{min}, and S_{min} represent the minimum cell biomass, ethanol, and sugar concentrations (g/L), respectively, while X_{max}, P_{max}, and S_{max} are the maximum biomass, ethanol, and sugar concentrations (g/L). The linear equation of the steepest part of the biomass, ethanol, and sugar concentrations against time was obtained using $y = ax + b$, where Q_X, Q_P, and Q_S are the slopes, respectively (See supplementary document)

$$\ln\left(\frac{X}{X_{max}-X}\right) = \mu_{max}.t - \ln\left(\frac{X_{max}-X_0}{X_0}\right) \quad (2)$$

2.5.2 Product Formation Kinetics

Empirical bioethanol data from fermentation processes (A, B, C and D) were fitted to the modified Gompertz and Luedeking-Piret models [17, 18]. The modified Gompertz model (Eq. 3) depicts the relationship between the bioethanol concentration (P), the potential maximum bioethanol concentration (P_m), the maximum bioethanol production rate ($r_{p,m}$) and the lag time (t_L) from the inception of the fermentation to the exponential productivity.

$$P = P_m.\exp\left\{-\exp\frac{r_{p,m}.\exp(1)}{P_m}.(t_L - t) + 1\right\} \quad (3)$$

The Luedeking-Piret model (Eq. 4) was also implemented to fit the experimental bioethanol production data. Product formation kinetics using the Luedeking-Piret model mainly consist of growth and non-growth-associated factors. The rate of product formation depends on the total biomass concentration (x) and the growth rate (dx/dt) in linear form, as shown below.

$$\frac{dP}{dt} = \alpha\frac{dx}{dt} + \beta X \quad (4)$$

The non-growth dependent constant (β) value was estimated using $\frac{\left(\frac{dP}{dt}\right)_{stationaryPhase}}{X_m}$ since (dx/dt) = 0 and X = X_{max} in the stationary growth phase.

On the other hand, to determine the value of the growth-dependent constant (α), the P is obtained from Eq. 5 derived from Eq. 4.

$$dP = \alpha dX + \beta\int X(t)d(t) \quad (5)$$

Moreover, using Eq. (1) for X_t when Eq. (5) is integrated by the initial condition P = P_0 at t = 0, the change in product concentration with time was determined following Eq. 6.

$$P = P_0 + aX_0\left(\frac{\exp(\mu_{max}\cdot t)}{1-\left(\frac{X_0}{X_{max}}\right)\cdot(1-\exp(\mu_{max}\cdot t))} - 1\right) + \beta\frac{x_{max}}{\mu_{max}\ln\left(1-\frac{X_0}{x_{max}(1-e^{\mu max t})}\right)} \quad (6)$$

Thereafter, Eq. (6) was used for the derivation of Eq. (7).

$$P = P_0 + \alpha A(t) + \beta B(t) \quad (7)$$

$$\text{where } A(t) = X_0\left(\frac{\exp(\mu_{max}\cdot t)}{1-\left(\frac{X_0}{X_{max}}\right)\cdot(1-\exp(\mu_{max}\cdot t))} - 1\right) = \frac{x_{max}}{\mu_{max}\ln\left(1-\frac{X_0}{x_{max}(1-e^{\mu max t})}\right)}$$

The growth-dependent product formation constant (α) was therefore obtained as the slope of the plot of [P-P_0—$\beta B(t)$] against $A(t)$, as derived from Eq. (7).

2.5.3 Substrate Utilisation Kinetics

The modified Luedeking-Piret (MLP) model (Eq. 8) accounts for substrate (S) conversion to cell mass (X) and product (P) formation, as well as substrate consumption for maintenance [18]. The experimental data under non-detoxified and detoxified substrate utilisation were used to fit the model.

$$-\frac{dS}{dt} = \gamma\frac{dX}{dt} + \delta X \tag{8}$$

The maintenance coefficient (δ) was obtained in the stationary phase (where $X = X_{max}$) by plotting the biomass concentration as a function of time, assuming that dP/dt = 0 in the stationary phase, according to $\delta = \frac{\beta}{Y_{\frac{p}{s}}} + Ke = \frac{-\frac{dS}{dt}stationary}{X_m}$

To determine the values of γ, Eq. (8) is firstly solved with the initial condition S = So; t = 0, which was thereafter rearranged to derive Eq. (9). The γ values were obtained as the slopes of the plots of [S_0—S—δB(t)] versus A(t) following Eq. (9).

$$S = S_0 - \gamma X_0\left(\frac{\exp\left(\mu_{\max}\cdot t\right)}{1-\left(\frac{X_0}{X_{\max}}\right)\cdot\left(1-\exp\left(\mu_{\max}\cdot t\right)\right)} - 1\right) + \delta\frac{X_{\max}}{\mu_{\max}\ln\left(1-\frac{X_0}{X_{\max}\left(1-e^{\mu_{\max}t}\right)}\right)}S_0 - \gamma A(t) - \delta B(t) \tag{9}$$

2.6 Validation of Models

Notably, the root-mean-square-error (RMSE), mean-square-error (MSE), accuracy factor (AF), bias factor (BF), and regression coefficient (R^2) are standard statistical metrics for the evaluation of model performance and fitness. Therefore, the RMSE (Eq. 10) and MAE (Eq. 11) were used to validate models.

$$RMSE = \sqrt{\frac{1}{n}\sum_{t=1}^{n}\left(x_t - y_t\right)^2},\ t = 1,2,3,\ \ldots,\ n \tag{10}$$

$$MAE = \left(\frac{1}{n}\sum_{t=1}^{n}\left|x_t - y_t\right|\right),\ t = 1,2,3,\ \ldots,\ n \tag{11}$$

Additionally, the slope of each model was evaluated by plotting predicted versus experimental data to determine the R^2 values. Meanwhile, BF and AF, which further validate the kinetic models, were determined using Eqs. 12 and 13, respectively. Also, an idea kinetic model would have AF = BF = 1 in the case of no structural deviation, illustrating the exact match between actual observation and model predictions. If 1 ≤ AF < 1.20, the model is "good," if 1.20 ≤ AF ≤ 1.30, the model is "acceptable," and if AF > 1.30, the model is "unacceptable." If 0.95 ≤ BF ≤ 1.11, the model is "good," if 0.87 ≤ BF < 0.95 or 1.11 < BF ≤ 1.43, the model is "acceptable," and if BF < 0.87 or BF > 1.43, the model is "unacceptable" [19, 20].

$$BF = 10^{\sum_{t=1}^{n}\frac{\log\left(x_t/y_t\right)}{n}},\ t = 1,2,3,\ \ldots,\ n \tag{12}$$

$$AF = 10^{\sum_{t=1}^{n}\frac{\log\left(y_t/x_t\right)}{n}},\ t = 1,2,3,\ \ldots,\ n \tag{13}$$

where n is the number of observations (n = 7), and xt and yt represent the experimental and predicted data at a time 't' (g/L), respectively. A mathematical model should preferably have low RMSE and MAE; however, AF, BF, R^2, and slope values should be close to 1 [14, 21].

2.7 Statistical Analysis

The experimental data obtained from the study was analyzed with Statistical Software Package for the Social Sciences (IBM SPSS) version 24.0. While the Duncan's multiple comparison test was performed at a 5% level of significance (p = 0.05).

3 Results and Discussion

3.1 Bioethanol Fermentation Performance

Fig. 2A represents the bioethanol production for the fermentation processes (A, B, C, and D). A rapid increase in bioethanol concentration from 5.82 to 19.57 g/L (A), 6.09 to 20.85 g/L (C), 4.74 to 23.20 g/L (B), and 5.09 to 25.96 g/L (D) was observed from 3 to 9 h (Fig. 2A). An additional increase in ethanol concentrations was observed from 9 to 12 h for fermentation process A (19.77 g/L) and fermentation process C (21.44 g/L). Meanwhile, fermentation processes B and D already demonstrated peak bioethanol production of 23.20 g/L and 25.96 g/L, respectively. Upon comparing the fermentation performance of the detoxified processes (Processes C and D) with the non-detoxified control experiments (Processes A and B), higher bioethanol concentrations were observed for the detoxified processes [22, 23]. The reduction in ethanol concentration in all the fermentation processes as shown in Fig. 2A, and this can be attributed to glucose depletion, ethanol oxidation, and the accumulation of organic acids [24–28]. Furthermore, the reversible conversion of ethanol to aldehydes by alcohol dehydrogenases (ADHs), coupled with a reduction in NAD + or NADP +, could lead to a decline in ethanol

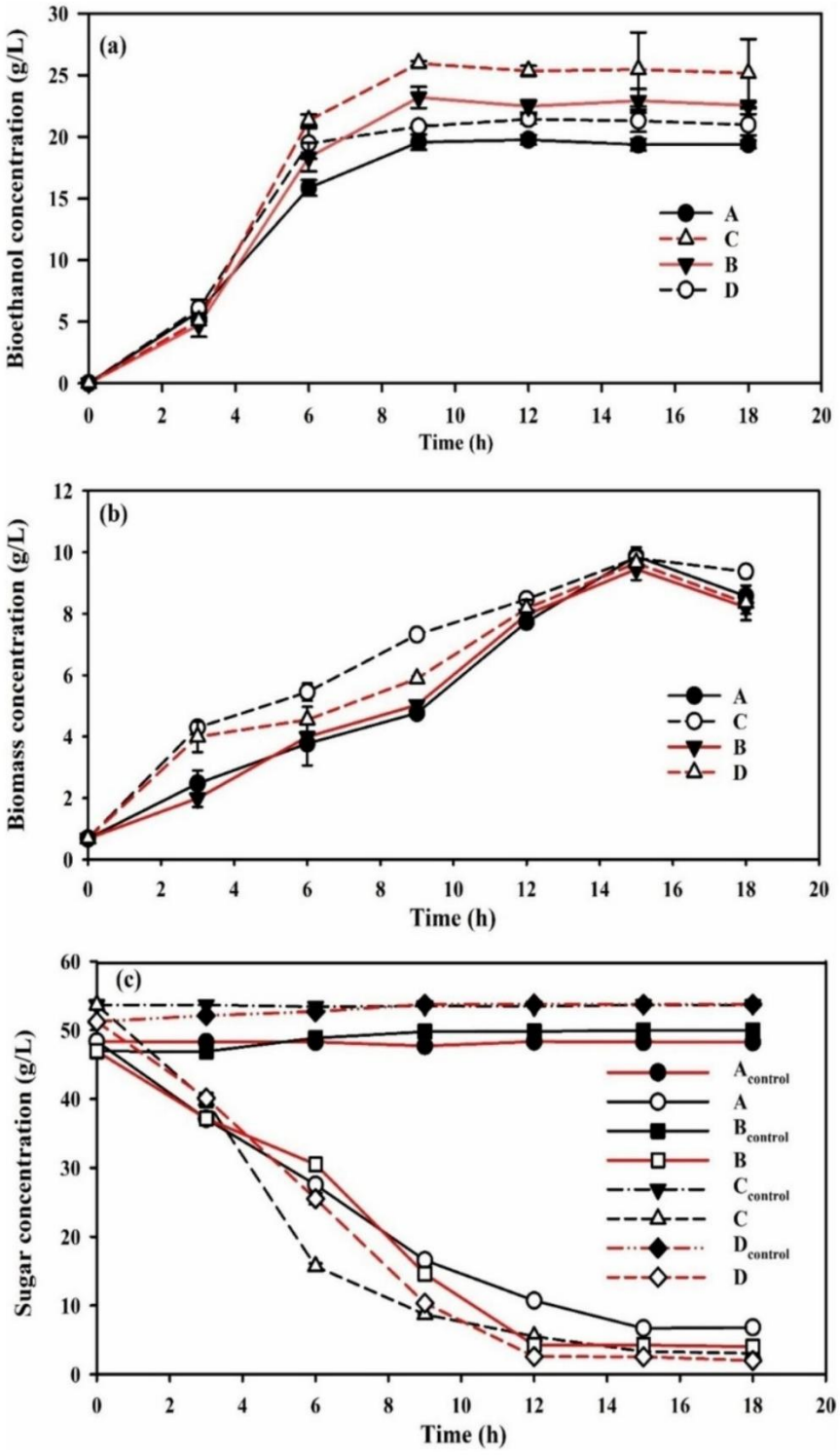

Fig. 2 Fermentation profile Media A, B, C and D conditions: Bioethanol production (**a**), Cell biomass concentration (**b**) and Sugar utilisation (**c**)

concentration during fermentation. Excessive ethanol accumulation in the fermentation broth might also deactivate crucial ethanol-producing enzymes, such as pyruvate decarboxylase and alcohol dehydrogenase [29].

Moreover, the bioethanol maximum production rates (Q_P) of 2.644 and 3.243 g/L/h (Table 2), corresponding to bioethanol yields ($Y_{P/S}$) of 0.498 and 0.424 g/g, and product yield per biomass ($Y_{P/X}$) of 2.151 and 2.349 g/g, were

Table 2 Fermentation kinetic parameters of experimental and predicted data of cell biomass, bioethanol production and substrate utilisation

Parameters	Medium							
	A	B	C	D	A	B	C	D
Cell growth kinetics (X)	Experimental				Logistic model			
ΔX (g/L)	9.190	8.770	9.130	8.970	8.472	8.205	7.903	7.928
$Y_{X/S}$ (g/g)	0.221	0.192	0.180	0.173	0.203	0.179	0.156	0.153
Q_X (g/L/h)	0.547	0.587	0.620	0.563	0.564	0.590	0.617	0.554
μ_{max} (h^{-1})	0.293	0.331	0.340	0.312	0.284	0.325	0.323	0.258
Bioethanol kinetics (P)	Experimental							
ΔP (g/L)	19.768	23.204	21.443	25.964	19.660	23.051	21.186	25.925
$Y_{P/X}$ (g/g)	2.151	2.626	2.349	2.895	2.139	2.628	2.320	2.890
$Y_{P/S}$ (g/g)	0.498	0.507	0.424	0.501	0.472	0.503	0.419	0.501
Q_P (g/L/h)	2.643	3.056	3.243	3.556	2.679	3.100	3.239	3.581
TY (g/g)	0.975	0.992	0.830	0.980	0.924	0.984	0.820	0.980
	Experimental							
ΔP (g/L)	19.768	23.204	21.443	25.964	18.765	22.347	21.697	25.375
$Y_{P/X}$ (g/g)	2.151	2.626	2.349	2.895	2.042	2.548	2.376	2.829
$Y_{P/S}$ (g/g)	0.498	0.507	0.424	0.501	0.450	0.488	0.429	0.490
Q_P (g/L/h)	2.643	3.056	3.243	3.556	1.883	2.209	2.193	2.502
TY (g/g)	0.975	0.992	0.830	0.980	0.888	0.955	0.840	0.959
Substrate utilisation kinetics (S)	Experimental							
ΔS (g/L)	41.673	45.761	50.603	51.775	46.574	46.943	53.663	51.216
$Y_{S/X}$ (g/g)	4.535	5.218	4.947	5.772	5.068	5.335	5.877	5.710
Q_S (g/L/h)	3.423	3.457	5.177	4.574	3.481	3.247	5.069	4.017
SU (%)	86.17	91.93	94.29	96.27	96.31	100	100	100.0

achieved for fermentation processes A and C, respectively. Moreover, 3.056 and 3.556 g/L/h Q_P values were obtained for Media B and D, corresponding to $Y_{P/S}$ (0.507 and 0.501 g/g) and $Y_{P/X}$ (2.626 and 2.895 g/g), respectively. The bioethanol maximum production rate was slightly lower in both detoxified processes compared to the non-detoxified processes. On the other hand, the Q_P obtained in processes C and D was consistent with the higher $Y_{P/X}$ (2.349 g/g and 2.895 g/g), respectively [22, 23]. It also aligned with maximum substrate utilisation rate (Q_S) and sugar utilisation (SU) for both processes C (5.177 g/L/h, 94.29%) and D (4.574 g/L/h, 96.27%). This surpassed the values of 3.423 g/L/h and 86.17% for processes A, and 3.457 g/L/h and 91.9% for processes B.

The growth patterns of *S. cerevisiae* over time in fermentation processes A—D are illustrated in Fig. 2B. Lag phases were short for the detoxified processes, followed by exponential growth from 2 to 15 h. This growth pattern correlated with significant glucose consumption (> 86%) (Fig. 2B). Moreover, the maximum specific growth rates (μ_{max}) in Fig. 3a, d, g, j, showed fermentation process C had higher μ_{max} of 0.340 h^{-1} compared to A (0.298 h^{-1}) (Table 2). Conversely, the fermentation process B demonstrated a slightly higher μ_{max} of 0.331 h^{-1} compared to 0.312 h^{-1} obtained from the D. The elevated μ_{max} values (> 0.31) observed for fermentation processes C and D provide additional evidence for the robustness of *S. cerevisiae* growth and metabolic activities under the detoxified fermentation conditions. Furthermore, the maximum growth rate (Q_X) of 0.620 g/g for fermentation process C was higher than the 0.547 g/g obtained from A, underscoring the importance of inhibitor removal on the processes. The positive impact of the detoxified hydrolysate on the fermentation processes can be attributed to the reduction in inhibitory compounds concentration and the improved sugar utilization associated with the detoxified hydrolysate. Additionally, the improved performance was due to the enhanced enzymatic hydrolysis, which typically increases the overall efficiency of fermentative processes. [23, 24, 30]. Moreso, reducing process inhibitor concentrations that inhibit bioethanol formation efficiency by adversely impacting cell growth through detrimental intracellular conditions supports the high productivity obtained in both fermentation processes C and D [24, 25]. These adverse effects on cellular activities stem from (1) the accumulation of anions resulting from acid dissociation, (2) the impediment of ethanol production by obstructing the anaerobic growth of *S. cerevisiae*, (3) the accumulation of reactive oxygen species (ROS) within the cell, and (4) interference with glycolytic pathways through enzyme inactivation (Glyceraldehyde-3-phosphate dehydrogenase, alcohol dehydrogenase (ADH), and hexokinase are a few glycolytic enzymes that are typically adversely impacted) [26, 27, 29].

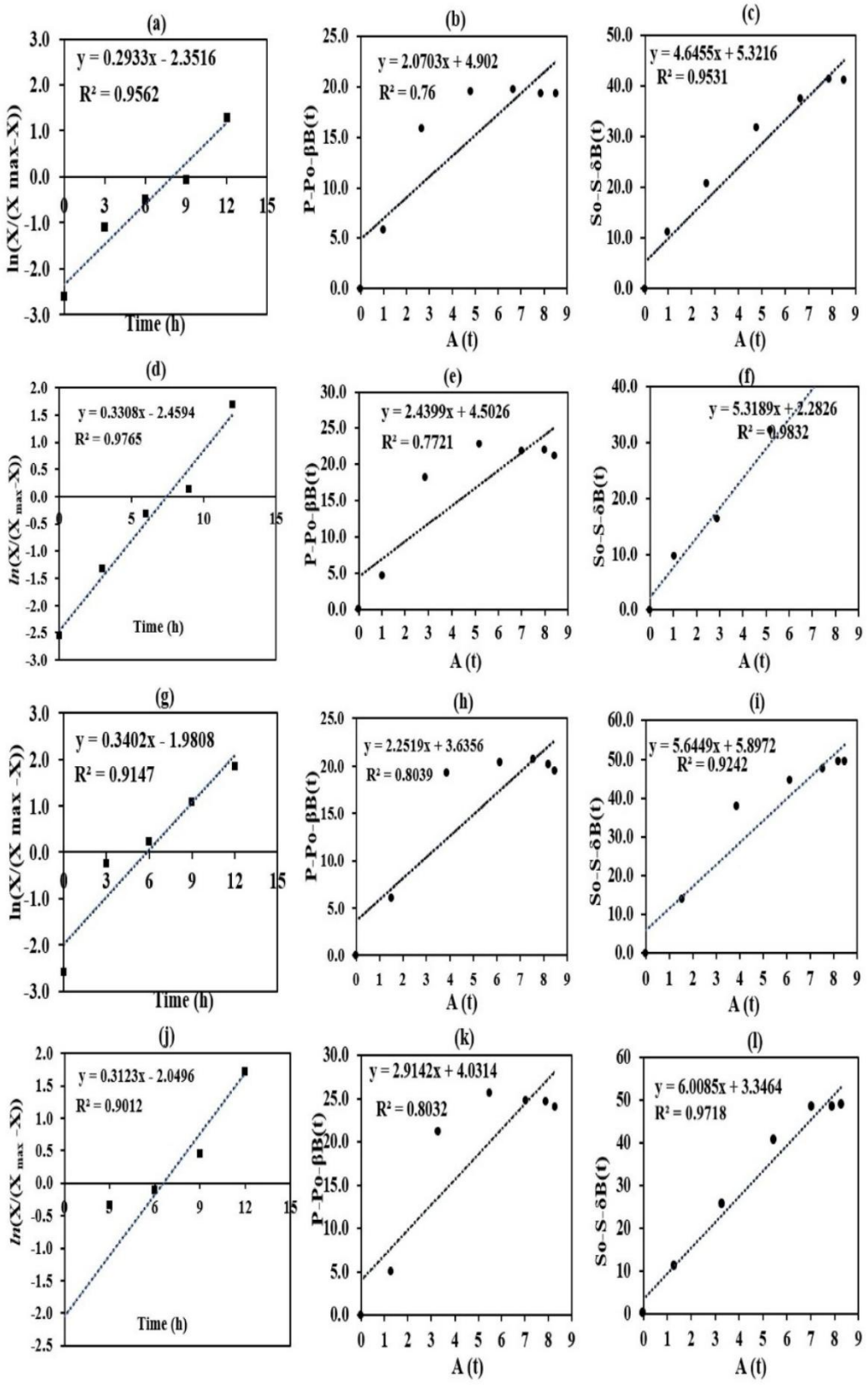

Fig. 3 Determination of μ_{max} α, γ under Process A [(**a**), (**b**), (**c**)]; B [(**d**), (**e**), (**f**)]; C [(**g**), (**h**), (**i**)] and D [(**j**), (**k**), (**l**)], respectively

The μ_{max} obtained in this study was higher compared to previous reports using undetoxified hydrolysate of sugar beet juice (0.169 h^{-1}) [31], sweet sorghum juice (0.154 h^{-1}) [32], food waste (0.135 h^{-1}) [33], and corn cobs (0.216 h^{-1}) using different strains of *S. cerevisiae*. In this study, the μ_{max} values obtained with fermentation processes C and D are highly favourable for industrial process upscaling. Elevated growth rates stimulate respiro-fermentative cellular activities, enhancing fermentative capacity for increased productivity.

3.2 Cell growth kinetics

In this study, the logistic model was applied and assessed for its potential to accurately predict biomass production dynamics from experimental data. The logistic model predicted the maximum specific growth rate (μ_{max}), biomass yield ($Y_{X/S}$), and the maximum growth rate (Q_X) that aligned with the experimentally derived values (Table 2). Table 3 shows that X_0 varied between 0.784 g/L and 1.611 g/L for all the fermentation processes. Remarkably, process D exhibited the highest maximum cell concentration (X_{max}) of 9.983 g/L compared to 9.955 g/L (A), 9.268 g/L (B), and 9.657 g/L (C). Also, the maximum specific growth rates (μ_{max}) obtained for the logistic model were above 0.025 h^{-1}; this is highly desirable for industrial process scale-up [24].

Moreover, high coefficients of determination (R^2) (0.954, 0.960, 0.966 and 0.937) and slopes (0.965, 0.969, 0.950 and 0.934) were observed for fermentation processes A, B, C and D, respectively (Table 2). Signifying the model's capability in elucidating the growth of *S. cerevisiae* under the fermentation processes [14]. The model was further validated with RMSE and MEA; the obtained RMSE and MEA values ranged from 0.515 to 0.594 g/L and 0.463 to 0.575 g/L, respectively. These also demonstrated a solid agreement between experimental and predicted biomass concentration data. Additionally, the effectiveness of the logistic model in predicting cell biomass concentrations was validated by the obtained BF values ($1.011 \leq BF \leq 1.035$) and AF values ($1.062 \leq AF \leq 1.106$), further underscoring the logistic model as a helpful tool that can be employed to improve the growth kinetics of fermenting microbes.

3.3 Bioethanol Production Kinetics

3.3.1 Kinetics of Bioethanol Production Using the Modified Gompertz Model

The modified Gompertz model (MGM) exhibited high and satisfactory R^2 values for the fermentation processes (A = 0.999, C = 0.999, B = 0.998, and D = 0.999) (Table 3), showing the model could explain significant fractions of the total variation in the observed data. Fermentation process C showed higher maximum potential bioethanol concentration (P_m) and maximum bioethanol production rate ($r_{p,m}$) of 21.18 g/L and 6.93 g/L/h, respectively, compared to 19.67 g/L (P_m) and 4.358 g/L/h ($r_{p.m}$) for process A. Similarly, fermentation process D exhibited higher P_m (25.93 g/L) and $r_{p.m}$ (6.88 g/L/h) compared to process B (23.05 g/L,

Table 3 Validation of model parameters for logistic and modified Gompertz (MG) models

		Process A	Process B	Process C	Process D
	Parameters	Cell growth			
Logistic model	X_0 (g/L)	0.929	0.784	1.611	1.566
	X_{max} (g/L)	9.955	9.268	9.657	9.983
	μ_{max} (h^{-1})	0.284	0.325	0.323	0.258
	R^2	0.954	0.965	0.966	0.950
	RMSE (g/L)	0.594	0.514	0.530	0.591
	MEA (g/L)	0.575	0.497	0.463	0.574
	Slope	0.960	0.969	0.937	0.934
	BF	1.025	1.011	1.029	1.035
	AF	1.106	1.084	1.062	1.089
		Bioethanol production			
MGM	P_m (g/L)	19.674	23.053	21.187	25.925
	$r_{p.m}$ (g/L/h)	4.358	5.671	6.931	6.883
	t_L (h)	1.679	2.204	2.123	2.297
	R^2	0.999	0.998	0.999	0.999
	RMSE (g/L)	0.245	0.331	0.137	0.222
	MEA (g/L)	0.226	0.251	0.118	0.177
	Slope	0.999	0.999	1.000	1.000
	BF	1.001	1.001	1.000	1.001
	AF	1.013	1.013	1.006	1.007

P_m, and 5.67 g/L/h, $r_{p,m}$). The enhanced bioethanol productivity observed in fermentation processes C and D can be attributed to the detoxified hydrolysate employed [2]. The significance of using detoxified hydrolysate in bioethanol fermentation has been highlighted above. Also, the presence of Fe_3O_4 nanoparticles might have stimulated and enhanced enzymatic and metabolic activities towards improving process performance [9, 23, 24]. Nanoparticles' significant roles in synthesising cytochromes and ferroxins (Fd) biomolecules have been reported [24]. These biomolecules are crucial for cellular energy metabolism and significantly influence cellular activity and overall productivity [24]. Given that higher production rates are preferred at large scales, the high $r_{p,m}$ attained in the current work using detoxified hydrolysate is desirable. However, marginally prolonged lag times of 2.12 and 2.30 h were observed in the fermentation processes C and D, respectively, in contrast to the control experiment 1.68 h. An indication of an extended adaptation period for the yeast under C and D process conditions is required for a shortened lag phase. The MGM predictions (19.67 g/L, 23.05 g/L, 21.19 g/L, and 25.93 g/L) align closely with the experimental bioethanol concentrations (19.79 g/L, 21.44 g/L, 23.20 g/L and 25.96 g/L), for fermentation processes A, B, C, and D, respectively, confirming the reliability of the findings in the present study. Similarly, the bioethanol production per biomass ($Y_{P/X}$), bioethanol yield ($Y_{P/S}$), and maximum production rate (Q_P) predicted by the MGM ranged from 2.139 g/g to 2.890 g/g, 0.419 g/g to 0.501 g/g and 2.68 g/L/h to 3.58 g/L/h, respectively. This is closely aligned with the obtained experimental results (2.151- 2.895 g/g, 0.424- 0.507 g/g, and 2.664- 3.556 g/L/h respectively). Likewise, in Table 3, the RMSE and MAE values ranged between 0.137 g/L and 0.331 g/L and 0.118 g/L and 0.251 g/L, respectively, strongly supporting the obtained results as well as indicating a low computation error. Notably, fermentation processes C and D had the least AF values of 1.006 and 1.007, confirming the accuracy of the MGM predictions. The proximity of BF and AF to 1 underscores the model's reliability in predicting bioethanol production [14]. Overall, the MGM accurately predicted the kinetic parameters, aligning closely with the observed results in this study.

3.3.2 Kinetics of Bioethanol Production Using the Luedeking-Piret Model

The growth associate constant (α) and non-growth associate constants (β) estimates for all the fermentation processes are summarised in Table 4. The estimated constants were derived using linear regression (graphical) and non-linear regression approaches (Ms Excel Solver) to compare model prediction accuracy. The non-growth associate constants (β) for bioethanol production was close to zero, ranging from 0.0011 to 0.0133 (g P/g X. h). While, the growth-associated constants (α) of 2.070 g P/g X, 2.252 g P/g X, 2.440 g P/g X and 2.914 g P/g X obtained by linear regression were lower compared to 2.805 g P/g X, 2.770 g P/g X, 3.105 g P/g X, and 3.515 g P/g X estimated by Excel Solver™ tool for

Table 4 Comparative prediction and validation of model parameters for Luedeking-Piret, and Modified Luedeking-Piret models

		Linear regression estimation				Non-linear regression estimation			
	Parameters	Process A	Process B	Process C	Process D	Process A	Process B	Process C	Process D
LP	Bioethanol production								
	α (g *P*/g *X*)	2.0703	2.4399	2.2519	2.9142	2.8051	3.1049	2.7696	3.5150
	β (g *P*/g *X*. h)	0.0011	0.0133	0.0129	0.0105	0.0011	0.0133	0.0129	0.0105
	R^2	0.762	0.788	0.821	0.814	0.762	0.791	0.824	0.815
	RMSE (g/L)	6.104	6.135	5.031	5.964	4.587	4.871	3.962	4.904
	MEA (g/L)	4.902	5.894	4.921	4.062	3.713	3.633	2.927	3.531
	Slope	0.762	0.795	0.829	0.819	1.032	1.001	1.010	0.982
	BF	1.624	1.433	1.33	1.289	1.253	1.174	1.122	1.102
	AF	1.624	1.433	1.33	1.291	1.384	1.284	1.222	1.201
MLP	Substrate utilisation								
	γ (g S/g *X*)	4.646	5.319	5.645	6.0085	5.5223	5.790	6.6527	6.543
	δ (g *S*/g *X*. h)	0.0045	0.0078	0.0086	0.0019	0.0045	0.0078	0.0086	0.0019
	R^2	0.953	0.983	0.924	0.973	0.956	0.986	0.932	0.973
	RMSE (g/L)	6.467	3.540	8.283	4.659	4.331	2.354	5.672	2.533
	MEA (g/L)	5.649	2.641	6.690	4.318	3.588	1.896	4.351	2.058
	Slope	0.937	0.956	0.898	0.966	1.116	1.042	1.061	1.075
	BF	0.722	0.704	0.559	0.720	1.134	0.984	0.899	1.022
	AF	1.386	1.421	1.789	1.476	1.395	1.211	1.225	1.125

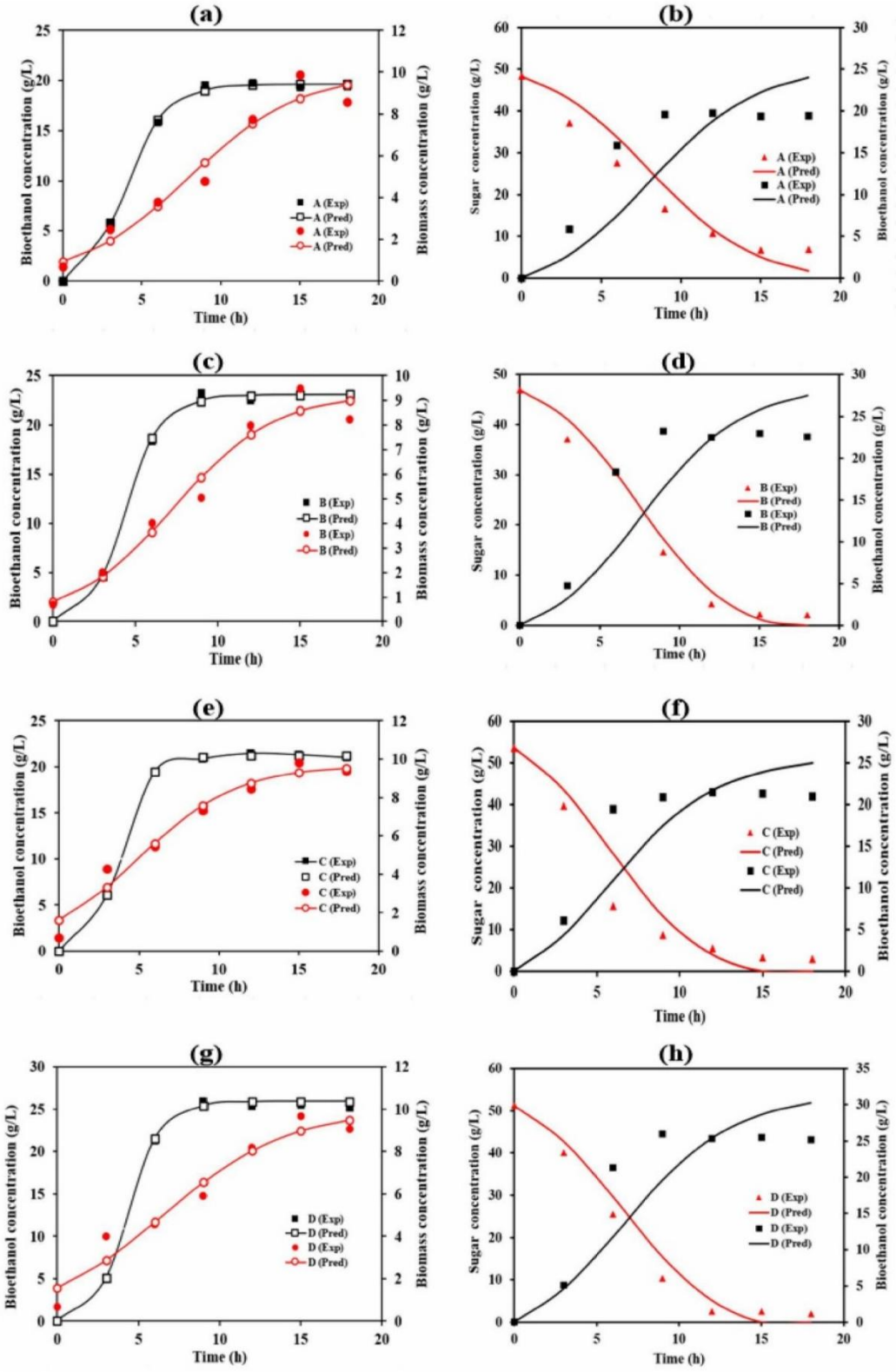

Fig. 4 Cell biomass concentration, ethanol production and substrate consumption curves of Processes A, B, C, and D fitted by the logistic model and MG model [(**a**), (**c**), (**e**), and (**g**)], LP model and MLP model [(**b**), (**d**), (**f**), and (**h**)], respectively

fermentation processes A, B, C, and D, respectively. Moreover, the regression coefficient (R^2) observed for both estimations was relatively close, ranging from 0.762 to 0.824. However, the slope, which is a derivative of experimental versus predicted data, varied significantly in both estimations, with the nonlinear fitting giving a slope value closer to 1, within the range of 0.982—1.032, while the range of 0.762—0.829 was obtained graphically (Fig. 3 and Fig. 4). On the other hand, the RMSE and MAE were much lower using the Excel Solver™ tool (Table 4) with values all below 4.904 g/L and 3.713 g/L, respectively. Meanwhile, the RMSE and MAE from the graphical estimation were as high as 6.135 g/L and 5.894 g/L, respectively, indicating a higher model error. The results obtained from the non-linear fitting by Excel Solver™ indicated that the LP model was desirable in predicting the bioethanol concentrations due to the BF values ($1.102 \leq BF \leq 1.289$) and AF values between the range of 1.201 to 1.284, except for 1.384 obtained for fermentation process A prediction. However, the BF and AF values derived from graphically predicted data were $1.289 \leq BF \leq 1.624$ and $1.291 \leq AF \leq 1.624$ (Table 4). Since the BF and AF of the graphical model are above the acceptable range of 0.87 to 1.43 and 1.0 to 1.30, respectively (except in process D), the model can be declared unacceptable [34]. Hence, the Ms Solver™ (non-linear fitting) Leudeking-Piret-derived parameters are preferable and acceptable for bioethanol production kinetics modelling.

Furthermore, Fig. 5 shows the comparative plot of the observed (experimental) and predicted bioethanol production data from the LP model. The result obtained for $\alpha \neq 0$ and $\beta \neq 0$ confirmed that fermentation processes are mainly growth-related (If $\alpha \neq 0$ and $\beta = 0$, product formation is growth associated but If $\alpha = 0$ and $\beta \neq 0$, product formation is non-growth associated) [14]. However, other influences could have contributed to higher β obtained, particularly in detoxified processes (C and D), include the presence of nanoparticles and the detoxified hydrolysate used for the fermentation process. The experimental kinetic parameters related to bioethanol production were also estimated using data from the LP model (Table 2). The results indicated that the values of ΔP, $Y_{P/X}$, $Y_{P/S}$, and TY obtained by the LP model were close but slightly lower than the experimental results, except in the values of $Y_{P/X}$ (2.376 g/g), $Y_{P/S}$ (0.429 g/g), and TY (0.840 g/g) for process C (Table 2). In the case of the maximum volumetric productivities the highest Qp of 2.502 g/L/h was obtained for fermentation process D (A = 1.883, B = 2.209 and C = 2.193). This further corroborated the desirability of hydrolysate detoxification and the SSF process employed compared to the other processes. Evidently, LP model acceptably represented all experimental data and gave a better understanding of the bioethanol formation kinetics, with high corroboration with results in existing literature.

3.4 Substrate Consumption Kinetics

The substrate utilisation rate is a function of cell growth rate, product formation, and rate of substrate uptake rate for δ obtained using the modified Luedeking-Piret model. Table 4 summarises the substrate utilisation (γ) (g S/g X) and maintenance coefficient (δ) (g S/g X.h) estimates for all the fermentation processes (A, B, C and D). The values of δ were low and ranged from 0.0019 to 0.0086 g S/g X.h. The δ is intricately related to specific growth and substrate uptake rates for cellular maintenance [14]. The values of δ derived from the current study were similar to previous reports by Jiménez-Islas et al. [35] and Suresh et al. [36], with values of δ close to zero, except Chang et al. [37] (Table 5). The higher δ-values reported by Chang et al. [37] indicate that an important part of the carbon source used was employed to maintain the fermenting organism during growth. Similar to Sect. 3.4, the estimated constants derived using a non-linear regression approach (Ms Excel Solver) gave better model prediction than linear regression obtained graphically. The substrate utilisation coefficient (γ) was highest for fermentation processes C (6.653 g S/g X) and D (6.543 g S/g X) (Table 4).

Moreover, cellular maintenance during fermentation involves energy expenditure to repair damaged components and ensure cellular equilibrium. While the rate of sugar utilisation is mainly a function of the substrate uptake rate, cell growth rate, cellular maintenance, and product formation [38, 39]. The low δ obtained in this study can be attributed to the conditions of the fermentation medium, specifically the detoxified substrate hydrolysate to which the fermenting organisms are exposed. [39]. The observation in this study aligns with the findings of Germec et al. [14], Liu et al. [38] and Teo and Ooi [40], who similarly reported low δ values ranging from 0.0012 to 0.0284 g S/gX.h. The low δ values signify that the yeasts utilise sugars in the detoxified hydrolysate towards high bioethanol and biomass production.

Furthermore, the substrate utilisation coefficients (γ) were validated by fitting the data obtained through non-linear and linear regression analysis. Table 4 shows the non-linear fitting derivatives (5.522, 5.790, 6.653 and 6.543 g S/gX) and linear fitting estimation (4.646, 5.319, 5.645 and 6.009 gS/gX) for fermentation processes A, B, C and D, respectively. The RMSE, MAE, AF, BF and R^2 obtained in this study were within acceptable levels. Desirably, the high regression coefficient (R^2) observed for both estimates ranged from 0.924 to 0.986 (Fig. 5). This further affirms the suitability of modified Leudeking-Piret for estimating substrate utilisation. Additionally, the kinetic parameters related to sugar utilisation were predicted using the data obtained from the MLP model. The results are represented in Table 2 compared to the parameters obtained experimentally. The results indicated that the predicted values of ΔS and SUY with the

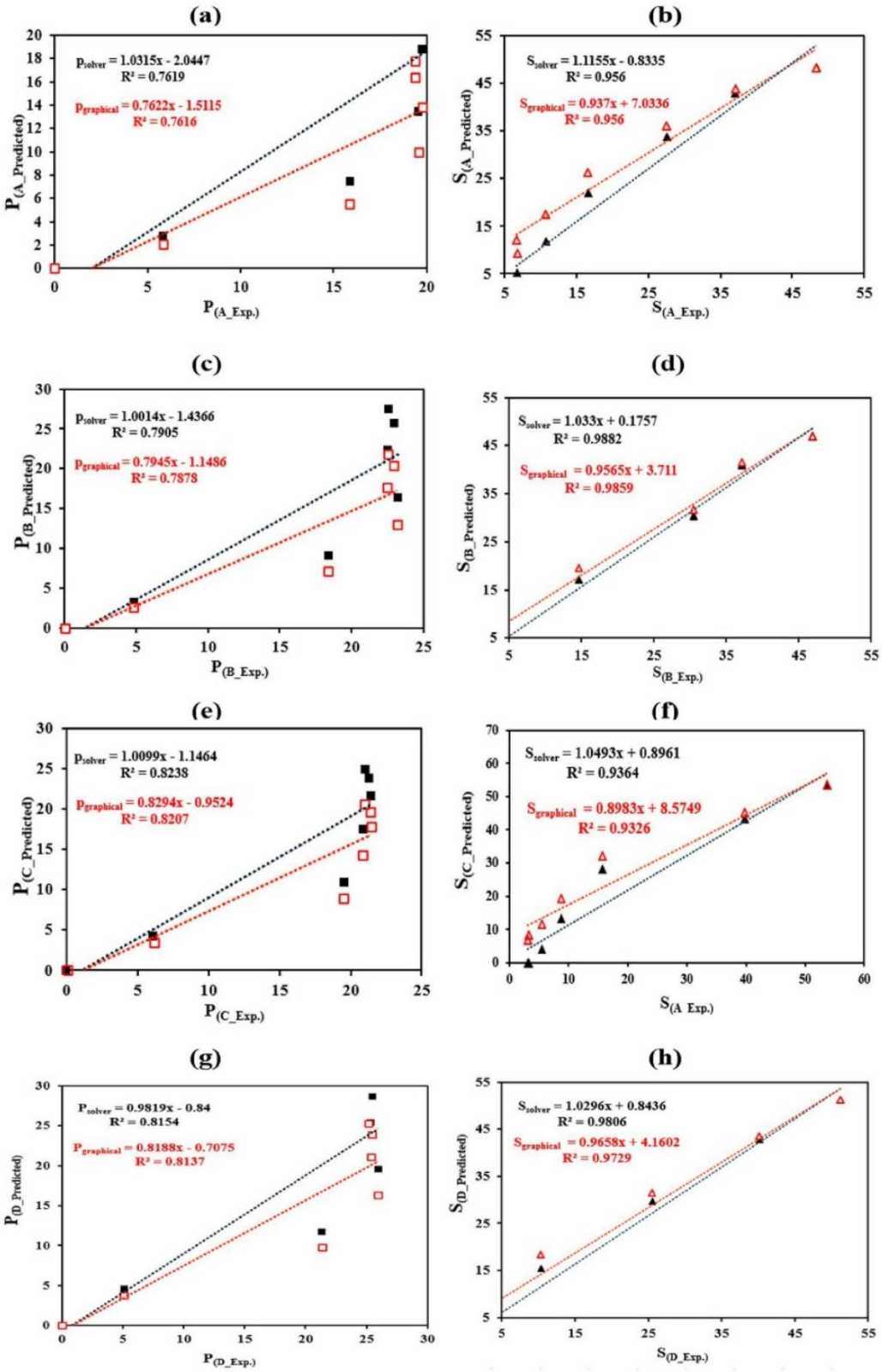

Fig. 5 LP and MLP models prediction comparison using Ms Excel model solver tool and graphical method in relation to R^2 and slope for Process A [(**a**) & (**b**)]; B [(**c**) & (**d**)]; C [(**e**, **f**)] and D [(**g**) & (**h**)], respectively

Table 5 Kinetic model coefficients obtained with the logistic, MG, LP and MLP model compared to previous studies

Substrate	Microorganism	X_0	X_{max}	μ_{max}	P_m	$r_{p,m}$	t_L	α	β	γ	δ	Ref
Process A	*S. cerevisiae* BY4743	0.929	9.955	0.284	19.67	4.358	1.679	2.8051	0.0011	5.5223	0.0045	This study
Process B	*S. cerevisiae* BY4743	0.784	9.268	0.325	23.05	5.671	2.204	3.1049	0.0133	5.790	0.0078	This study
Process C	*S. cerevisiae* BY4743	1.611	9.657	0.323	21.19	6.931	2.123	2.7696	0.0129	6.6527	0.0086	This study
Process D	*S. cerevisiae* BY4743	1.566	9.983	0.258	25.93	6.883	2.297	3.5150	0.0105	6.543	0.0019	This study
Red Beet Juice	*S. cerevisiae* ATCC 9763	-	5.31	0.379	-	-	-	4.5326	0.1047	0.074	0.095	Jiménez-Islas et al. [35]
Crude whey	*Kluveromyces marxianus*	-	12.80	0.095	-	-	-	0.733	0	3.3846	0.135	Suresh et al. [36]
Waste cotton hydrolysate	*Escherichia coli*	-	3.75	0.21	-	-	-	0.05	0.29	0.25	0.47	Chang et al. [37]
Red Beet Juice	*S. cerevisiae ITD00196*	-	6.35	0.467	-	-	-	5.3184	-0.044	0.0732	-0.0848	Jiménez-Islas et al. [35]
Glucose	*S. cerevisiae* BY4743	0.24	1.80	0.54	2.56	0.31	1.58	-	-	-	-	Sanusi et al. [24]
Sugar beet	*S. cerevisiae*	2.602	9.473	0.213	69.85	4.54	2.21	-	-	-	-	Dodić et al. [31]

MLP model were slightly higher than their experimental values. Besides, the MLP model estimated somewhat higher values of $Y_{S/X}$ than the experimental values. Expectedly, the ΔS and $Y_{S/X}$ were highest for Process D (51.216 g/L; 5.71 g/g). Moreover, the maximum volumetric sugar utilisation rates (Qs) in fermentation process A, B, C, and D, predicted to be 3.481, 3.247, 5.069, and 4.017 g/L/h, were in good agreement with the experimental results of 3.423, 3.457, 5.177, and 4.574 g/L/h, respectively (Table 2). Overall, the predicted results were highly compatible with the experimental sugar utilisation kinetics, further highlighting the suitability of the implemented model.

3.5 Comparison of the Kinetics of the Bioethanol Fermentation Process

The results obtained in the current study were comparable to findings from prior research. In this study, fermentation process D yielded a maximum bioethanol production of 25.96 g/L, this showed a 2.77-fold and 1.50-fold improvement over the yield obtained by Srimachai et al. [41] and Ariyajaroenwong et al. [42], respectively. Additionally, the maximum bioethanol production rate of 6.88 g/L/h exceeded the rates reported by Rorke and Gueguim Kana [43] and Dodić et al. [31] by 13.23-fold and 1.51-fold, respectively (Table 5).

Similarly, as shown in Table 5, the growth and non-growth associate constants were compared to previous studies. The α (4.533 gP/gX) and β (0.1047 gP/gX.h) values were obtained for the production of bioethanol from pretreated corn stover using *S. cerevisiae* ATCC 9763 [35]. Also, Chang et al. [37] reported bioethanol formation kinetics using *E. coli* to ferment waste cotton hydrolysate, yielding high β values of 0.29 gP/gX.h with corresponding α values of 0.05 gP/gX, which is a non-growth-related process. The growth associate constant and non-growth associate constant obtained in the present study were higher than those observed by Jiménez-Islas et al. [35] and Chang et al. [37] above.

Moreover, γ value of 5.723 g S/g X was earlier reported by Germec et al. [14], whereas lower γ value of 0.074 g S/g X and 3.3846 g S/g X were reported by Suresh et al. [36] and Jiménez-Islas et al. [35] respectively compared to the present study. However, a higher γ value (8.2 g S/g X) was reported using *Kluyveromyces fragilis*-NCIM 0557 for the bioethanol fermentation from sugarcane bagasse [44].

Notably, the α, β, γ and δ values obtained in this study were comparable with previous reports and desirable for high-performing bioprocessing. Specifically, significantly lower values of β and δ were observed in this study, strong evidence of growth-associated processes, enhanced metabolic activities and lower cell maintenance requirement due to the process conditions implemented [14]. Lower δ

indicates less energy required to repair damaged cellular components and ensure cellular equilibrium towards high metabolic activities and product formation. This also indicates that *S. cerevisiae* dependence on the substrate was mainly for biomass and bioethanol production [14].

4 Conclusion

This study reports on the kinetics of bioethanol production by *S. cerevisiae* using detoxified PPW hydrolysate. The kinetic models implemented include logistic function, modified Gompertz, Luedeking-Piret, and modified Luedeking-Pire models through linear and non-linear regression. Predicted results closely matched experimental data, especially using nonlinear regression fitting, highlighting the efficacy of the models in predicting the dynamics of the fermentation processes. Interestingly, inhibitory compound detoxification significantly improved fermentation performance in fermentation process D, which resulted in the highest P_m (25.925 g/L) and X_{max} (9.983 g/L). The improved metabolic performance in process D was predominantly growth-associated ($\alpha = 3.515$ g P/g X and $\gamma = 6.543$ g S/g X), with a low cell maintenance coefficient (δ) value (0.0019 g S/g X. h). The generated kinetic knowledge in this study provides additional insight on bioethanol formation towards improved process performance, optimisation and commercial upscaling.

Supplementary Information The online version contains supplementary material available at https://doi.org/10.1007/s10562-024-04868-8.

Author contributions Adebule P. Adeniyi, Sanusi A. Isaac, and Gueguim EB. Kana conceived the experiments; Adebule P. Adeniyi performed the experiments, analysed the data, and wrote the manuscript for publication with the help and guidance of Sanusi A. Isaac and Gueguim EB. Kana.

Funding Open access funding provided by University of KwaZulu-Natal.

Data availability Data from the study will be made available on request.

Declarations

Conflict of interest The authors declare there are no conflicts of interest in this work.

References

1. Rorke DCS, Suinyuy TN, Kana EBG (2017) Microwave-assisted chemical pretreatment of waste sorghum leaves: process optimization and development of an intelligent model for determination of volatile compound fractions. Bioresour Technol 224:590–600. https://doi.org/10.1016/j.biortech.2016.10.048
2. Adebule AP, Sanusi AI, Kana EBG (2024) Nano-based surface adsorption detoxification of process inhibitors for improved bioethanol productivity. Bioresour Technol Rep 25:101783. https://doi.org/10.1016/j.biteb.2024.101783
3. Sanusi AI, Faloye FD, Kana EBG (2019) Impact of various metallic oxide nanoparticles on ethanol production by *Saccharomyces cerevisiae* BY4743: screening, kinetic study and validation on potato waste. Catal Lett 149:2015–2031. https://doi.org/10.1007/s10562-019-02796-6
4. Barampouti EM, Christofi A, Malamis D, Mai S (2023) A sustainable approach to valorize potato peel waste towards biofuel production. Biomass Conv Biorefinery 13:8197–8208. https://doi.org/10.1007/s13399-021-01811-4
5. Cristóbal J, Caldeira C, Corrado S, Sala S (2018) Techno-economic and profitability analysis of food waste biorefineries at European level. Bioresour technol 259:244–252. https://doi.org/10.1016/j.biortech.2018.03.016
6. Aruwajoye GS, Kassim A, Saha AK, Kana EBG (2020) Prospects for the improvement of bioethanol and biohydrogen production from mixed starch-based agricultural wastes. Energies 13:6609. https://doi.org/10.3390/en13246609
7. Thangavelu SK, Ahmed AS, Ani FN (2016) Review on bioethanol as alternative fuel for spark ignition engines. Energy Rev 56:820–835. https://doi.org/10.1016/j.rser.2015.11.089
8. Sankaran R, Parra-Cruz RA, Pakalapati H, Show PL, Ling TC, Chen W, Tao Y (2019) Recent advances in the pretreatment of microalgal and lignocellulosic biomass: a comprehensive review. Bioresour Technol 298:122476. https://doi.org/10.1016/j.biortech.2019.122476
9. Sanusi AI, Suinyuy TN, Kana EGB (2021) Impact of nanoparticle inclusion on bioethanol production process kinetic and inhibitor profile. Biotechnol Rep 29:1–12. https://doi.org/10.1016/j.btre.2021.e00585
10. Banerjee S, Rout S, Banerjee S, Atta A, Das D (2019) Fe_2O_3 nanocatalyst aided transesterification for biodiesel production from lipid-intact wet microalgal biomass: a biorefinery approach. Energ Convers Manage 195:844–853. https://doi.org/10.1016/j.enconman.2019.05.060
11. Di Fraia S, Sharmila VG, Banu JR, Massarotti N (2023) A comprehensive review on upscaling of food waste into value-added products towards a circular economy: holistic approaches and life cycle assessments. Trends Food Sci & Technol. https://doi.org/10.1016/j.tifs.2023.104288
12. Almquist J, Cvijovic M, Hatzimanikatis V, Nielsen J, Jirstrand M (2014) Kinetic models in industrial biotechnology improving cell factory performance. Metab Eng 24:38–60. https://doi.org/10.1016/j.ymben.2014.03.007
13. Moodley P, Kana EBG (2019) Bioethanol production from sugarcane leaf waste: effect of various optimized pre-treatments and fermentation conditions on process kinetics. Biotechnol Rep 24:1–8. https://doi.org/10.1016/j.btre.2019.e00329

14. Germec M, Turhan I, Karhan M, Dermirci A (2019) Kinetic modeling and techno-economic feasibility of ethanol production from carob extract based medium in biofilm reactor. Appl Sci 9(2121):1–19. https://doi.org/10.3390/app9102121
15. Aruwajoye GS, Faloye FD, Kana EBG (2017) Soaking assisted thermal pretreatment of cassava peels wastes for fermentable sugar production: process modelling and optimization. Energy Convers Manag 150:558–566. https://doi.org/10.1016/j.enconman.2017.08.046
16. Bishop BDC, Sanusi AI, Kana EBG (2024) Enhanced substrate suitability of autoclave-assisted acid pre-treated waste sugarcane molasses: pre-treatment optimization, sequential nano-based detoxification strategies, and bioproduct production. Biomass Convers and Biorefinery. https://doi.org/10.1007/s13399-024-06127-7
17. Yatmaz E, Germec M, Erkan SB, Turhan I (2022) Modeling of ethanol fermentation from carob extract–based medium by using *Saccharomyces cerevisiae* in the immobilized-cell stirred tank bioreactor. Biomass Convers Biorefinery 12:5241–5255. https://doi.org/10.1007/s13399-020-01154-6
18. Zheng Y, Zhao C, Li X, Xia M, Wang X, Zhang Q, Yan Y, Lang F, Song J, Wang M (2022) Kinetics of predominant microorganisms in the multi-microorganism solid-state fermentation of cereal vinegar. LWT 159:113209. https://doi.org/10.1016/j.lwt.2022.113209
19. Ross T (1996) Indices for performance evaluation of predictive models in food microbiology. J Appl Microbiol 81:501–508. https://doi.org/10.1111/J.1365-2672.1996.TB03539.X
20. Germec M, Karhan M, Dermirci A, Turhan I (2022) Kinetic modeling, sensitivity analysis, and techno-economic feasibility of ethanol fermentation from non-sterile carob extract-based media in *Saccharomyces cerevisiae* biofilm reactor under a repeated-batch fermentation process. Fuel 324:124729. https://doi.org/10.1016/j.fuel.2022.124729
21. Germec M, Turhan I (2021) Predicting the experimental data of the substrate specificity of *Aspergillus niger* inulinase using mathematical models, estimating kinetic constants in the Michaelis-Menten equation, and sensitivity analysis. Biomass Convers and Biorefinery 2021:1–12. https://doi.org/10.1007/s13399-021-01830-1
22. Bansal R, Katyal P, Jain D (2021) Enzymatic and acidic hydrolysis of cull potatoes for production of fermentable sugars. Starch-Stärke 74:210202. https://doi.org/10.1002/star.202100202
23. Sanusi I, Aruwajoye G, Revaprasadu N, Sewsynker-Sukai Y, Meyer LE, Kana EBG (2022) A novel autoclave-assisted nanoparticle pre-treatment for improved sugar recovery from potato peel waste: process optimisation, nanoparticle recyclability and bioethanol production. Biomass Convers and Biorefinery. https://doi.org/10.1007/s13399-022-03574-y
24. Sanusi AI, Suinyuy TN, Lateef A, Kana EBG (2020) Effect of nickel oxide nanoparticles on bioethanol production: process optimization, kinetic and metabolic studies. Process Biochem 92:386–400. https://doi.org/10.1016/j.procbio.2020.01.029
25. Faramarzi S, Anzabi Y, Fararizadeh-Malmiri H (2019) Selenium supplementation during fermentation with sugar beet molasses and *Saccharomyces cerevisiae* to increase bioethanol production. Green Process Synth 8(1):622–628. https://doi.org/10.1515/gps-2019-0032
26. Gupta R, Gautam S, Shukla R, Kuhad RC (2017) Study of charcoal detoxification of acid hydrolysate from corncob and its fermentation to xylitol. J Environ Chem Eng 5:4573–4582. https://doi.org/10.1016/j.jece.2017.07.073
27. Richardson TL, Harner NK, Bajwa PK, Trevors JT, Lee H (2011) Approaches to deal with toxic inhibitors during fermentation of lignocellulosic substrates. In: Zhu J, Zhang X, Pan XJ (eds) Sustainable production of fuels, chemicals, and fibers from forest biomass. ACS Symposium Series; American Chemical Society, Washington
28. Naghshbandi MP, Tabatabaei M, Aghbashlo M, Gupta VK, Sulaiman A, Karimi K, Moghimi H, Maleki M (2019) Progress toward improving ethanol production through decreased glycerol generation in *Saccharomyces cerevisiae* by metabolic and genetic engineering approaches. Renew Sustain Energy Rev 1(115):109353. https://doi.org/10.1016/j.rser.2019.109353
29. Raj SB, Ramaswamy S, Plapp BV (2014) Yeast alcohol dehydrogenase structure and catalysis. Biochem 53:5791–5803. https://doi.org/10.1021/bi5006442
30. Choong YY, Norli I, Abdullah AZ, Yhaya MF (2016) Impacts of trace element supplementation on the performance of anaerobic digestion process: a critical review. Bioresour Technol 209:369–379. https://doi.org/10.1016/j.biortech.2016.03.028
31. Dodic JM, Vucurovic DG, Dodic SN, Grahovac JA, Popov SD, Nedeljkovic NM (2012) Kinetic modelling of batch ethanol production from sugar beet raw juice. Appl Energy 99:192–197. https://doi.org/10.1016/j.apenergy.2012.05.016
32. Phukoetphim N, Salakkam A, Laopaiboon P, Laopaiboon L (2017) Kinetic models for batch ethanol production from sweet sorghum juice under normal and high gravity fermentations: logistic and modified Gompertz models. J Biotech 243:69–75. https://doi.org/10.1016/j.jbiotec.2016.12.012
33. Yan S, Chen X, Wu J, Wang P (2013) Pilot-scale production of fuel ethanol from concentrated food waste hydrolysates using *Saccharomyces cerevisiae* H058. Bioprocess Biosyst Eng 36(7):937–946. https://doi.org/10.1007/s00449-012-0827-9
34. Sumner J, Jenson I, Ross T (2012) Using predictive microbiology to benefit the Australian meat industry. Woodhead Publishing Series in Food Sci, Technol and Nutr. https://doi.org/10.1533/9780857096937.5.276
35. Jiménez-Islas D, Páez-Lerma J, Soto-Cruz NO, Gracida J (2014) Modelling of ethanol production from red beet juice by *Saccharomyces cerevisiae* under thermal and acid stress conditions. Food Technol Biotechnol. 52: 93–100. http://hrcak.srce.hr/file/175265.
36. Suresh S, Srivastava V, Sakthivel S, Arisutha S (2018) Kinetic modeling of ethanol production for substrate–microbe system. In Biorefining of Biomass to Biofuels; Springer: Heidelberg. https://doi.org/10.1007/978-3-319-67678-4_16.
37. Chang D, Yu Z, Islam Z, Zhang H (2015) Mathematical modeling of the fermentation of acid-hydrolyzed pyrolytic sugars to ethanol by the engineered strain *Escherichia coli* ACCC 11177. Appl Microbiol Biotechnol 99:4093–4105. https://doi.org/10.1007/s00253-015-6475-7
38. Liu L, Zhang Z, Wang J, Fan Y, Shi W, Liu X, Shun Q (2019) Simultaneous saccharification and co-fermentation of corn stover pretreated by H_2O_2 oxidative degradation for ethanol production. Energy 168:946–952. https://doi.org/10.1016/J.ENERGY.2018.11.132
39. Sathendra-Elumalai R, Ramanujam P, Tawfik MA, Ravichandran P, Gurunathan B (2023) Optimization and kinetics modelling for enhancing the bioethanol production from banana peduncle using *Trichoderma reesei* and *Kluveromyces marxianus* by co-pretreatment methods. Sustain Energy Technol Assess 56:103129. https://doi.org/10.1016/j.seta.2023.103129
40. Teoh Y, Ooi Z (2016) Evaluation of unstructured kinetic models for the production of bioethanol from banana and pineapple wastes. Bioresources 11:4295–4305. https://doi.org/10.15376/BIORES.11.2.4295-4305
41. Srimachai T, Nuithitikul K, O-thong S, Kongjan P, Panpong K (2015) Optimization and kinetic modeling of ethanol production from oil palm frond juice in batch fermentation. Energy Procedia 79:111–118. https://doi.org/10.1016/j.egypro.2015.11.490

42. Ariyajaroenwong P, Laopaiboon P, Salakkam A, Srinophakun P, Laopaiboon L (2016) Kinetic models for batch and continuous ethanol fermentation from sweet sorghum juice by yeast immobilized on sweet sorghum stalks. J Taiwan Inst Chem Eng 66:210–216. https://doi.org/10.1016/j.jtice.2016.06.023
43. Rorke DCS, Kana EBG (2017) Kinetics of bioethanol production from waste sorghum leaves using *Saccharomyces cerevisiae* BY4743. Fermentation 3:19. https://doi.org/10.3390/fermentation3020019
44. Sasikumar E, Viruthagiri T (2008) Optimization of process conditions using response surface methodology (RSM) for ethanol production from pretreated sugarcane bagasse: kinetics and modeling. Bioenergy Res 1:239–247. https://doi.org/10.1007/s12155-008-9018-6

Authors and Affiliations

Adeniyi P. Adebule[1] · Isaac A. Sanusi[1] · Gueguim E. B. Kana[1]

✉ Gueguim E. B. Kana
kanag@ukzn.ac.za

[1] School of Life Sciences, University of KwaZulu-Natal, Private Bag X01, Scottsville 3209, South Africa

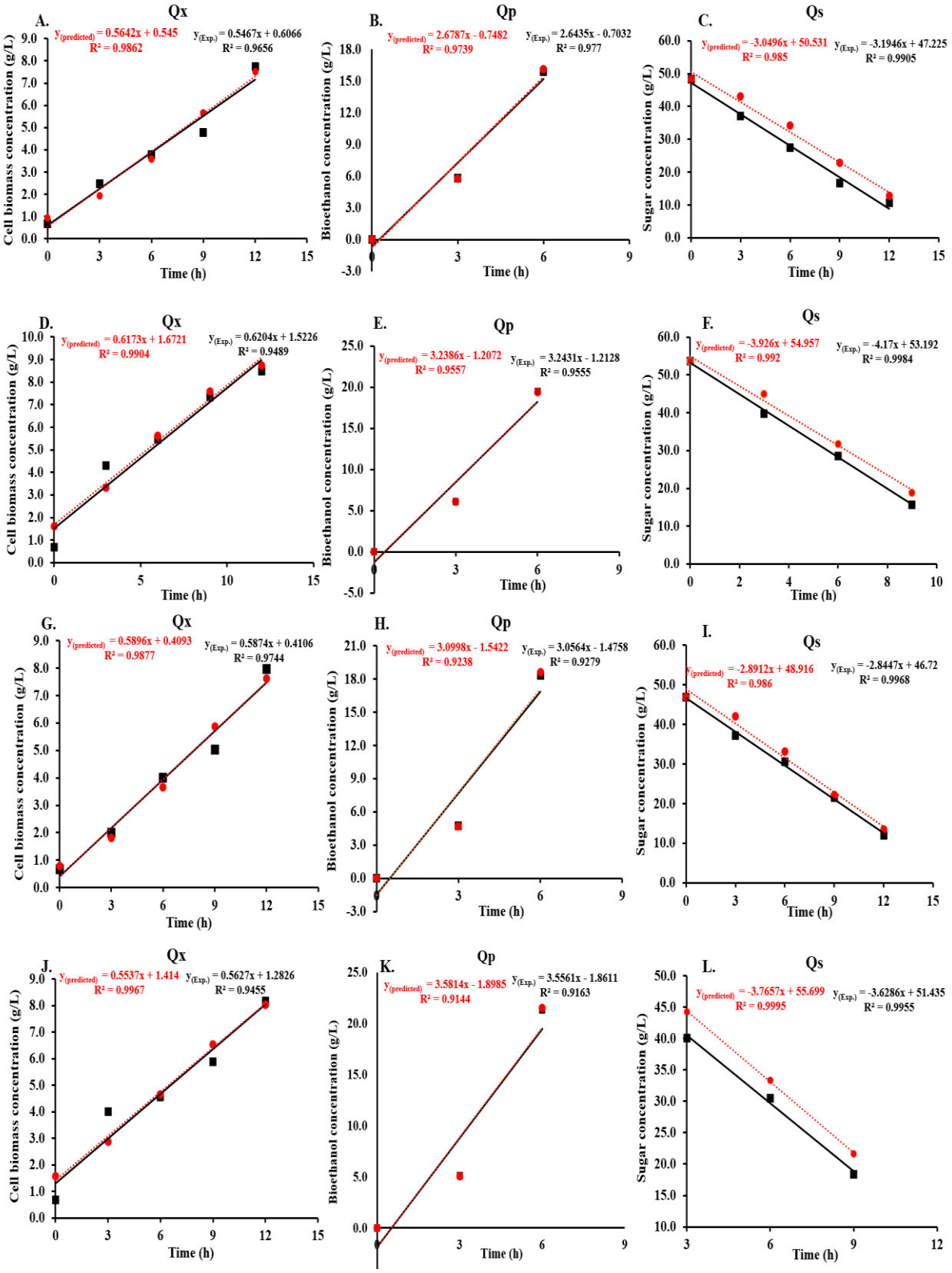

Figure S5. 1. Fermentation kinetic parameters (Qx, Qp, and Qs) of experimental and predicted data related to cell biomass, bioethanol production and substrate utilization. NDSHF (A, B, C); ODSHF (D, E, F); NDSSF (G, H, I); and ODSSF (J, K, L).

CHAPTER 6

Improved ethanol production via optimised co-fermentation of *Saccharomyces cerevisiae* and *Pichia stipitis* post-nanoparticle-detoxification of pretreated waste potato peel

This chapter has been accepted in the journal *Biomass Conversion and Biorefinery* with the title: Waste-based *Pichia stipitis* inoculum development for co-fermentation of nanoparticle-detoxified pretreated potato peel hydrolysate. The manuscript is presented in the following pages.

Improved bioethanol production via optimised co-fermentation of *Saccharomyces cerevisiae* and *Pichia stipitis* post-nanoparticle-detoxification of pretreated waste potato peel hydrolysate

Adeniyi P. Adebule, Isaac A. Sanusi*, E.B. Gueguim Kana

University of KwaZulu-Natal, School of Biological Sciences (Microbiology), Private Bag X01, Scottsville 3209, South Africa

Abstract

This study explores bioethanol fermentation from detoxified hydrolysate using *S. cerevisiae*, *P. stipitis*, and their co-culture. Model-based optimisation of *Pichia stipitis* inoculum development (PSID) was performed by evaluating the effects of waste lubricant oil (WLO) concentration (%), temperature (°C), and incubation time (h) on fermentation efficiency. Similarly, simultaneous saccharification and co-fermentation (SSCF) processes were modelled and optimised to establish the impact of solid loading, co-inoculation time and inoculation ratio. Upon validation of the PSID model, the addition of waste lubricant oil as a carbon source enhanced *P. stipitis* growth and reduced cultivation time by fivefold. Biomass concentrations of 9.62 g/L for *S. cerevisiae*, 7.97 g/L for *P. stipitis*, and 14.17 g/L for the co-culture (1:4) were achieved. The most desirable optimised co-fermentation conditions were achieved at a zero-hour co-inoculation time, an inoculation ratio of 1:4 (*S. cerevisiae* to *P. stipitis*), and a 10% solid loading. The validation predicted co-fermentation condition yielded 48.7 g/L and 0.505 g/g bioethanol concentration and yield, thereby achieving a fermentation efficiency of 99%. The reliability of the process outcome was established by the consistency of the kinetic models' predictions with the experimental data. Optimisation and kinetic findings obtained from this study provided significant knowledge for the development of simultaneous saccharification co-fermentation and the synergistic interaction of co-culture with inoculum development, size proportion, and time of inoculation for bioethanol production processes using detoxified hydrolysate of PPW.

Keywords: ***Pichia stipitis*, detoxified hydrolysate, co-fermentation, kinetics, inoculum ratio**.

Correspondence: Sanusia@ukzn.ac.za/Isaacsanusi7@gmail.com; Tel.: +27616181662

Abbreviations

μ_{max}	Maximum specific growth rate (h^{-1})
X_o	Initial cell concentration (g/L)
X_{max}	Maximum cell concentration (g/L)
P_m	Maximum potential bioethanol concentration
$r_{p,m}$	Maximum bioethanol production rate (g/L/h),
t_L	Lag time (h)
A	Growth associate constant (g P/g X)
β	Non-growth associate constants (g P/g X. h)
Γ	Substrate utilisation coefficient (g S/g X)
Δ	Maintenance coefficient (g S/g X. h)
MGM	Modified Gompertz model
MLP	Modified Leudeking-Piret model
PSID	*Pichia stipitis* inoculum development
PPW	Potato Peel Waste
WLO	Waste lubricant oil
Sc	*Saccharomyces cerevisiae*
Ps	*Pichia stipites*
SSF	Simultaneous saccharification and fermentation
SSCF	Simultaneous saccharification and co-fermentation
Sc-SSF $_{mono}$	Monoculture of *Saccharomyces cerevisiae*
Ps-SSF $_{mono}$	Monoculture of *Pichia stipites*
ScPs-SSF $_{co\text{-}culture}$	Co-culture of *Saccharomyces cerevisiae* + *Pichia stipitis*
TSU	Total sugar utilisation (%)
GU	Glucose utilisation (%)
XU	Xylose utilisation (%)
BY	Bioethanol yield (g/g)
BC	Bioethanol concentration (g/L)
BP	Bioethanol productivity (g/L/h)
FPE	Fermentation process efficiency (%)

6.1. Introduction

The impact of fossil fuel consumption on the environment and climate change has led to a growing interest in producing biofuels such as bioethanol (Lainez at al., 2019). Bioethanol as fuel has a clean-burning, high-octane rating and can be produced from various lignocellulosic feedstocks, including agricultural waste, forestry residues, and municipal waste (Lainez at al., 2019; Tian et al., 2018; Mankar et al., 2021). Although lignocellulosic biomass wastes, such as potato peel, are inexpensive, renewable, and sustainable, with the potential for cost-effective bioethanol production, their efficient conversion remains limited by several challenges. Some of these bottlenecks include low fermentable sugar yield, high pretreatment costs, and the presence of process inhibitors in the pretreated hydrolysate (Vanmarcke et al., 2021). Moreover, a single microbial strain used for fermentation can often not ferment the multiple sugars present simultaneously and efficiently in pretreated lignocellulosic hydrolysate, leading to low ethanol yields (Magocha et al., 2018). Another drawback is enzyme inhibition caused by the accumulation of glucose during the saccharification process (Diaz et al., 2014). Therefore, simultaneous saccharification and fermentation (SSF) can be an alternative to prevent enzyme inhibition, provide shorter processing times, decrease energy demand, and eventually reduce production costs (Sanusi et al., 2020). Simultaneous saccharification and fermentation (SSF) is a one-step process that combines the enzymatic hydrolysis of lignocellulosic biomass and fermentation into a single process. The SSF process has several advantages over separate hydrolysis and fermentation processes, including reduced process time, increased ethanol yield, and reduced enzyme cost (Behera et al., 2022). The SSF process has been successfully implemented for bioethanol production from various lignocellulosic feedstocks, including corn stover, switchgrass, sugarcane bagasse, potato peel, and residue (Jiang et al., 2019; Li et al., 2021).

Furthermore, the choice of microbial strain and the inoculum development have been reported to play a significant role in the efficiency and yield of bioethanol production (Adegoye et al., 2021). Although *S. cerevisiae* has been extensively used in ethanol production, its potential is hindered by the inability to effectively utilise the xylose component of sugar released during the pretreatment and hydrolysis of lignocellulosic biomasses. Therefore, a system capable of utilising xylose alongside *S. cerevisiae* will enhance ethanol yield and productivity. *Scheffersomyces* (*Pichia) stipitis* has been reported as one of the most promising yeasts for xylose utilisation in ethanol conversion and can be employed alongside other yeasts to improve ethanol productivity through co-fermentation (Raina et al., 2020; Yadav et al., 2011). For

instance, the co-culture of conventional yeast (such as *S. cerevisiae*) and non-conventional yeast (such as *Zymomonas sp*., *Aspergillus niger,* and *P. stipitis*) has been reported to improve the efficiency of bioproduct formation from lignocellulosic biomass (Singh et al., 2014; Goncalves et al., 2016; Izmirlioglu and Demirci, 2017; Raina et al., 2020).

In the case of *S. cerevisiae* and *P. stipitis*, their co-fermentation has the potential to completely metabolise glucose and xylose in pretreated hydrolysate, leading to an enhanced bioethanol yield and productivity (Wu et al., 2023; Naseeruddin et al., 2021). Co-culturing these strains could enhance the economics of ethanol production from pretreated waste lignocellulosic biomass hydrolysate. Factors such as solid loading, co-inoculation time, and inoculum ratio are important in determining the efficiency of any co-fermentation process (Călugăr et al., 2024). Moreover, the typical cultivation period for *P. stipitis* during inoculum development exceeds 18 hours, potentially lengthening the overall process time (Yadav et al., 2011; Santosh et al., 2017). Although *P. stipitis* is favourable for co-fermentation due to its ability to ferment xylose, its prolonged lag phase during inoculum development before fermentation can be a limitation. Shortening this phase will be beneficial to the overall process. Therefore, optimising inoculum development to reduce this extended lag phase is necessary (Galbraith et al., 2018).

In cultivating *P. stipitis* as a seed culture, several carbon sources can be included in its growth medium. *P. stipitis* has been reported to utilise glucose, mannose, and galactose but best utilises pentose sugar (e.g. xylose) (Rouhollah et al., 2007). To enhance the growth of *P. stipitis,* supplementation with alternative carbon sources could be important. Glycerol and methanol were reported by Liu et al. (2019) and Caspeta et al. (2012) for the cultivation of *Aspergillus oryzae* and *Pichia pastori*, respectively. While xylose is available from pretreated lignocellulosic biomass hydrolysate, methanol and glycerol are costly, priced at approximately USD 1 and USD 10 per kg, respectively, and contribute significantly to overall bioprocess costs. Therefore, investigating cost-effective alternative carbon sources, which are often considered “waste” (such as waste lubricant oil and spent oil), is imperative. The untreated hydrocarbon waste footprint on the environment has caused significant pollution and constraints on sustainability. The industrial discharge of waste lubricant oil and its constituents have been documented (Eregie and Jamal-Ally, 2019). This waste requires extensive treatment to reduce contaminants before discharging into water bodies, often involving significant capital investment, energy consumption, and greenhouse gas emissions. Interestingly, spent coolant lubricant oil, also known as waste lubricant oil (WLO), is mainly composed of hydrocarbons, including aliphatic compounds with alkyl groups and carbon chain lengths ranging from C_7 to C_9, as well as aromatic compounds with a carbon chain length of C_8 (Eregie and Jamal-Ally,

2019). Moreover, residual nutritional components (like soluble organic compounds, nitrogen, and protein) arising from the isomerisation of the WLO could further stimulate *P. stipitis* growth, as seen with *Scenedesmus vacuolatus*. Given these considerations, the use of untreated industrial lubricant oil as a substitute for either methanol or glycerol in the inoculum development process for *P. stipitis* could be a more practical and cost-effective approach, reducing inoculum development costs and contributing to a cleaner environment.

To the best of our knowledge, there are no reports on the development of *P. stipitis* inoculum using a waste-based formulation. Furthermore, research on the potential of *P. stipitis* inoculum development using waste carbon sources, such as waste lubricant oil, as a carbon source in media formulation to shorten the cultivation period is scarce. Therefore, the study aims to assess the co-fermentation of *S. cerevisiae* and *P. stipitis* in simultaneous saccharification and bioethanol production using nano-detoxified pretreated hydrolysate. To achieve this, the following specific objectives were carried out: (1) improvement of *P. stipitis* inoculum using waste oil-based media, (2) determination of the optimal inoculum ratio and sequential inoculation timing for maximum ethanol production, (3) assessment of the impact of monoculture and co-culture on ethanol production, (4) evaluation of the co-culturing of *S. cerevisiae* and *P. stipitis* for simultaneous saccharification and fermentation (SSF) and simultaneous saccharification and co-fermentation (SSCF) using nano-detoxified waste potato peel hydrolysate, followed by an analysis of the process kinetics.

6.2. Materials and methods

6.2.1. Sample preparation

Potato peel waste, used as the feedstock for the experimental study, was collected from food vendors in the Pietermaritzburg metropolitan area, KwaZulu-Natal province, South Africa (29.5418 ° S, 30.4077 ° E). The peels were immediately dried at 50-55 °C for 48 h in a laboratory oven (Scientific series 2000, South Africa) to reduce the remaining moisture content and were subsequently milled to a particle size of 1-2 mm using a centrifugal miller (Retsch ZM-1, South Africa). The composition analysis of milled potato peel waste (52 % starch, 14 % structural carbohydrate, 4 % cellulose, 10 % hemicellulose, 6 % lignin, 13.21% crude protein, 10.76 % ash, and 0.43 % fat) was determined using the National Renewable Energy Laboratory method (Sluiter et al., 2008), and the total starch content was measured using the Megazyme starch kit (Megazyme, Ireland). However, the waste lubricant oil used was obtained from a local aluminium recycling company in Pietermaritzburg, South Africa. Its composition, as

reported by Eregie and Jamal-Ally (2019), includes hydrocarbons containing aliphatic compounds with alkyl groups and carbon chain lengths ranging from C7 to C9, as well as aromatic compounds with carbon chain lengths of C8.

6.2.2. Pretreatment of potato peel waste (PPW) and hydrolysate detoxification

The milled PPW were pretreated using optimised process parameters previously reported by Aruwajoye et al. (2017), and the detoxification of inhibitors (such as furfural, 5-hydro-methyl furfural, phenolic compound, formaldehyde, and acetic acid) from the pretreated hydrolysate was carried out using the protocol detailed in Adebule et al. (2024). For the pretreatment, 0.92% (v/v) HCl solution with 10% PPW solid loading was soaked in a water bath without shaking at 69.6°C for 2.34 h, then autoclaved for 5 minutes at 121°C. The optimised detoxification conditions implemented were Fe_3O_4 NP concentration (0.021 w/v%), temperature (35.37 °C), contact time (12.74 min), and pH (4.14) to simultaneously remove inhibitor compounds such as furfural, 5-hydroxymethylfurfural, phenol, acetic acid, and formaldehyde, without sugar loss (Adebule et al., 2024). The detoxified hydrolysate was thereafter employed for ethanol production.

6.2.3. Yeast activation and inoculum development

The yeasts employed in this study were *S. cerevisiae* BY4743 and *P. stipitis*. Resuscitations of *S. cerevisiae* and *P. stipitis* were separately maintained using standard media and conditions (Santosh et al., 2017; Sanusi et al., 2019). The fermenting yeasts were sub-cultured on respective media every two weeks. Moreover, using different carbon sources based on a previous study by Caspeta et al. (2012) enhanced the inoculum development of *P. pastoris*, which is similar to *P. stipitis*. Hence, a preliminary screening involving six (6) carbon sources (glucose, xylose, methanol, glycerol, waste lubricant oil, and spent vegetable cooking oil) was first conducted to determine the most suitable for *P. stipitis* inoculum development. A colony of *P. stipitis* grown for 24-48 hrs at 35 °C was transferred separately into a 250 mL Erlenmeyer flask containing 100 mL of sterilised broth with and without (1 % v/v) glucose, xylose, methanol, glycerol, waste lubricant oil, or spent vegetable cooking oil. All cultures underwent incubation at 35 °C in an orbital shaker (120 rpm) for 48 hours, with biomass concentration as the growth efficiency index. Consequently, the carbon source for *P. stipitis* inoculum development was modelled and optimised to investigate the possibility of shortening incubation time and inoculation temperature.

6.2.4. Modelling and optimisation of the *Pichia stipitis* inoculum development (PSID)

The response surface methodology (RSM) was employed for the modelling and optimisation of key growth input parameters, including incubation temperature, time, and inclusion of waste lubricant for *P. stipitis* inoculum development (Yang and Zhang, 2018). The experimental design consisted of seventeen (17) runs (See supplementary document). The input parameters were incubation time (6- 48 h), temperature (25- 45 ºC), and lubricant oil inclusion (0- 2 %v/v), while the output was *P. stipitis* biomass concentration (spores/mL). The experimental biomass data were fitted to the quadratic polynomial equation (Eq. 6.1), relating the input parameters to the response (*P. stipitis* biomass concentration).

$$Y = \alpha_0 + \alpha_1 x_1 + \alpha_2 x_2 + \alpha_3 x_3 + \alpha_{11} x_1^2 + \alpha_{22} x_2^2 + \alpha_{33} x_3^2 + \alpha_{12} x_1 x_2 + \alpha_{13} x_1 x_3 + \alpha_{23} x_2 x_3 \quad \text{Eq. (6.1)}$$

Where: Y = *P. stipitis* biomass concentration, coefficient relating the interception of the plane with the axis of response, $\alpha_1 x_1$ to $\alpha_3 x_3$ are the linear coefficients, $\alpha_{11} x_{21}$ to $\alpha_{33} x_{23}$ are the quadratic coefficients, and $\alpha_{12} x_1 x_2$ to $\alpha_{23} x_2 x_3$ represent the interaction of coefficients. The model was further evaluated using the analysis of variance (ANOVA). The optimal inoculum setpoints for the response were obtained by resolving the polynomial equation, and these setpoints were subsequently validated experimentally.

The validation experiment was performed using the predicted optimised input conditions as specified by the developed model. In addition, for the control experiments, waste lubricant oil (YPX) was replaced with glycerol (YPXgly), Methanol (YPXmeth) (Jia et al., 2022), and waste vegetable oil (YPXveg) separately, and the experiments were carried out under the same parameters used for the validation experiment.

6.2.5. Simultaneous saccharification and co-fermentation (SSCF) process condition

The pre-treated and detoxified PPW hydrolysate was liquefied (Sanusi et al., 2020) to obtain a fermentation slurry. The SSF processes were then carried out with a 100 mL working volume in a 250 mL Erlenmeyer flask. Flasks containing liquefied detoxified PPW slurry (50 mL), fermentation media (40 mL), 15 Units/g of glucoamylase (Amyloglucosidase), and 10% (v/v) inoculum were incubated at the required temperatures for 24 h at 120 rpm. The preliminary SSCF experiments, one variable at a time, were set up in phases to achieve the following: (i) co-inoculation ratio, (ii) time-course for co-inoculation, and (iii) sugar prioritisation. Afterwards, a co-fermentation model was developed for bioethanol production.

To obtain the best inoculum ratio for the co-fermentation, the *S. cerevisiae* (Sc) (primary metaboliser) and *P. stipitis* (Ps) (secondary metaboliser) at varying ratios (1:4, 2:3, 1:1, 3:2, 4:1) were inoculated respectively with the total inoculum size of 10%. Thereafter, to achieve the most suitable time for the introduction of these inocula, the best seed inoculum ratio (1:4 of Sc to Ps) was introduced with 2% (v/v) *S. cerevisiae* and 8% (v/v) *P. stipitis* at an interval of 0 h, 3 h, 6 h, up to 24 h.

6.2.6. RSM experimental design and optimisation of the SSCF process

The RSM (Box-Behnken design) was used to model and optimise bioethanol production. The three independent co-fermentation parameters, solid loading (A), co-inoculation time (B), and inoculation ratio (C), were the input parameters, with the bioethanol concentration and bioethanol yield as the response outputs. The input parameters were varied in the range of 5 to 15 g, 0 to 24 h and 1 to 5, respectively (Table 6.1). The inoculation ratio *S. cerevisiae* (Sc) to *P. stipitis* (Ps) at varying proportions of 4:1, 3:2, 2.5:2.5, 2:3 and 1:4 was represented by 1, 2, 3, 4, and 5, respectively. The choice of model process parameters and their ranges were chosen from literature and previous studies by Liu et al. (2019); Mohapatra et al. (2020); and Gao et al. (2021). A total of seventeen (17) independent experimental runs were generated and carried out. The experimental data were fitted to a quadratic polynomial model relating the input variables to the output parameters (Y), the bioethanol concentration and bioethanol yield, according to Equation (6.1), using Design-Expert software (Stat-Ease Inc., USA). Validation experiments were conducted under optimised conditions. Sample analysis was conducted every 3 h. The validation experiments with their corresponding control experiments (not inoculated) were performed in replicates. The optimised co-fermentation experiments were conducted to further understand the sugar utilisation mechanism and prioritisation. Each seed cultures were used to inoculate the fermenting media singly, serving as the positive control. Meanwhile, the fermenting media uninoculated with either of the organisms served as the negative control. All experiments were incubated at 35 °C and 120 rpm for 24 hrs. The control experiments (uninoculated) were subjected to the same conditions as the corresponding experiments. A sample of 1 mL was aseptically removed from each experimental setup at regular intervals (3 h). The extracted sample was thereafter used for biomass, glucose, and xylose concentrations.

Table 6.1. Box-Behnken design of different process input parameters for bioethanol concentration and bioethanol yield by co-fermentation.

Run	Input parameters			Output			
	A: Solid loading (g)	B: Co-inoculation time (hr)	C: Inoculation ratio	Ethanol concentration (g/L)	Predicted Ethanol concentration (g/L)	Ethanol yield (g/g)	Predicted Ethanol yield (g/g)
1	10	12	3	34.2787	34.24	0.362888	0.3625
2	5	12	1	23.0647	22.56	0.448233	0.4451
3	10	12	3	34.2294	34.24	0.362366	0.3625
4	10	12	3	34.2134	34.24	0.362197	0.3625
5	15	12	5	37.504	38.01	0.322801	0.3259
6	10	12	3	34.2166	34.24	0.362231	0.3625
7	10	0	5	48.475	47.49	0.513176	0.5004
8	10	12	3	34.2635	34.24	0.362727	0.3625
9	15	24	3	31.0219	29.84	0.267009	0.2565
10	10	24	1	34.77	35.76	0.368089	0.3809
11	5	0	3	24.94	26.12	0.484677	0.4952
12	5	24	3	24.1789	23.70	0.469886	0.4602
13	15	0	3	39.6346	40.12	0.341139	0.3508
14	15	12	1	28.5	28.69	0.245303	0.2431
15	5	12	5	24.179	23.99	0.469887	0.4721
16	10	24	5	34.073	34.75	0.36071	0.3681
17	10	0	1	36.39	35.72	0.385239	0.3778

6.2.7. Analytical methods

The pretreated PPW samples (non-detoxified and optimally detoxified) were examined using a Scanning Electron Microscope (SEM) (Model ZEISS-EVO/LS15, United Kingdom) to ascertain the impact of detoxification on the morphological features. The samples were mounted onto aluminum grid coated and gold sputter coated before viewing to obtain suitable photomicrographs. Similarly, Fourier Transform Infrared (FTIR) spectroscopy was used to examine functional group changes on a Spectrum 100 (PerkinElmer, USA). The FTIR spectra were recorded between 500 and 4000 cm−1. Optical absorption measurements were done on Perkin Elmer Lambda 25 UV-Vis Spectrometer.

Biomass concentration (g/L) was determined for both *S. cerevisiae* and *P. stipitis* by relating their spore counts to the dry cells' weight using a pre-determined standard curve (Sanusi et al., 2019). Reducing sugar content per litre was determined using the 3,5–dinitro salicylic acid method, while glucose and xylose concentrations were analysed using the Megazyme glucose kit (K-GLUC) and Megazyme xylose kit (©Megazyme, Wicklow, Ireland) respectively.

The carbon dioxide (CO_2) and nitrogen (N_2) gas were analysed using a portable multi-gas analyser (SKZ industrial. Shandong, China) for potential fermentative pathways determination (Abdel-Rahman et al., 2011). Ethanol concentration was measured in the gaseous phase using an ethanol vapour sensor (ETH-BTA, Vernier Software, and Technology, Beaverton, USA) (Adebule et al., 2025). Moreover, the bioethanol yield, productivity, sugar utilisation, and saccharification efficiency were determined using Eq. 6.2 – 6.6.

$$Bioethanol\ \ yield\ (\mathrm{BY})(g/g) = \frac{Maximum\ ethanol\ \ concentration\ (g/L)}{Utilized\ sugar\ (g/L)} \quad \text{(Eq. 6.2)}$$

$$Bioethanol\ productivity\ (\mathrm{BP})\ (g/L/h) = \frac{Maximum\ ethanol\ concentration\ (g/L)}{Fermentation\ period\ (h)} \quad \text{(Eq. 6.3)}$$

$$Fermentation\ process\ efficiency\ (FPE)\ (\%) = \frac{Maximum\ ethanol\ concentration\ (g/L)}{\text{Theoretical yield (g/L)}} \times 100 \quad \text{(Eq. 6.4)}$$

$$Glucose\ utilisation\ (\mathrm{GU})\ (\%) = \frac{Initial\ glucose\ content - final\ glucose\ content}{Initial\ glucose\ content} \times 100 \quad \text{(Eq. 6.5)}$$

$$Xylose\ utilisation\ (\mathrm{XU})\ (\%) = \frac{Initial\ xylose\ content - final\ xylose\ content}{Initial\ xylose\ content} \times 100 \quad \text{(Eq. 6.6)}$$

6.2.8. Kinetic modeling

6.2.8.1. Cell growth kinetics

The logistic growth model in its integrated form (Eq. 6.7) was used to estimate *S. cerevisiae* and *P. stipitis* under simultaneous saccharification and co-fermentation. The equation relates biomass (X) to the initial cell concentration (X_0), maximum cell concentration (X_{max}), and maximum specific growth rate (μ_{max}) at specific times (t) during the exponential and stationary growth phases of the yeast cells.

$$X = \frac{X_0 \cdot \exp(\mu_{max} \cdot t)}{1 - \left(\frac{X_0}{X_{\max}}\right) \cdot (1 - \exp(\mu_{max} \cdot t))} \quad \text{(Eq. 6.7)}$$

6.2.8.2. Product formation kinetics

To estimate the kinetics of product formation, the combination of growth and non-growth-associated production factors were considered. The bioethanol data obtained from the SSCF processes were fitted into the modified Gompertz and the Luedeking–Piret models. As indicated in Eq. (6.8), the modified Gompertz model depicts the relationship between the bioethanol concentration (P) to the potential maximum bioethanol concentration (Pm), maximum bioethanol production rate ($r_{p,m}$), and the lag time (t_L) from the inception of the fermentation to the exponential phase.

$$P = P_m \cdot \exp\left\{-\exp\frac{r_{p.m} \cdot \exp(1)}{P_m} \cdot (t_L - t) + 1\right\} \quad \text{(Eq. 6.8)}$$

where P is the bioethanol concentration (g/L), Pm is the potential maximum bioethanol concentration (g/L), $r_{p,m}$ is the maximum bioethanol production rate (g/L/h), and t_L is the lag time (h) for bioethanol production.

Following the Luedeking–Piret model, the rate of product formation depends on the total biomass concentration (X) and the growth rate dX/dt in linear, differential, and integrated forms, as shown in Eqs. (6.9), (6.10) and (6.11), respectively.

$$\frac{dP}{dt} = \alpha \frac{dx}{dt} + \beta X \quad \text{(Eq. 6.9)}$$

$$dP = \alpha \, dX + \beta \int X(t) \, d(t) \quad \text{(Eq. 6.10)}$$

$$P = P_0 + aX_0\left(\frac{\exp(\mu_{max}\cdot t)}{1-\left(\frac{X_0}{X_{max}}\right)\cdot(1-\exp(\mu_{max}\cdot t))} - 1\right) + \beta\frac{x_{max}}{\mu_{max}} ln\left(1 - \frac{X_0}{x_{max}}(1 - e^{u_{max}t})\right) \quad \text{(Eq. 6.11)}$$

where α and β are the product formation constants of the fermentation conditions. If α = 0 and β ≠ 0, product formation is non-growth associated and if α ≠ 0 and β = 0, product formation is growth-associated (Germic et al., 2019). β can be estimated using $\frac{\left(\frac{dP}{dt}\right)_{stationary\ Phase}}{X_{max}}$ since at the stationary phase of growth dX/dt = 0 and X= X_{max}.

P is the bioethanol concentration (g/L), while X, X_0, X_{max}, and μ_{max} represent the cell biomass concentration, initial cell biomass concentration, maximum cell biomass concentration, and maximum specific growth rate at specific times (t) during the exponential and stationary growth phases of the yeast cells, respectively.

6.2.8.2. Substrate utilisation kinetics

The substrate utilisation kinetic was estimated using the modified Luedeking-Piret (MLP) model (Eq. 6.12), which accounts for substrate conversion to the cell mass and product and substrate consumption for maintenance. The integrated form of Eq. (6.12) with initial conditions S= S0, t= 0 is depicted by Eq. (6.13).

$$-\frac{dS}{dt} = \gamma\frac{dx}{dt} + \delta X \quad \text{(Eq. 6.12)}$$

$$S = S_0 - \gamma X_0\left(\frac{\exp(\mu_{max}\cdot t)}{1-\left(\frac{X_0}{X_{max}}\right)\cdot(1-\exp(\mu_{max}\cdot t))} - 1\right) + \delta\frac{X_{max}}{\mu_{max}} ln\left(1 - \frac{X_0}{X_{max}}(1 - e^{u_{max}t})\right) \quad \text{(Eq. 6.13)}$$

Equation 6.13 can be alternatively written as follows (Eq. 6.14)

$$S = S_0 - \gamma A(t) + \delta B(t) \quad \text{(Eq. 6.14)}$$

where γ and δ are the substrate utilisation constants of the fermentation condition. When [S_0-S- δ B(t)] is plotted versus A(t), γ is found from the slope of the plot. At the stationary phase where X= Xmax, δ can be determined by plotting the biomass concentration as a function of time, assuming that dP/dt = 0, using $\frac{\beta}{Y_{\frac{p}{s}}} + Ke = \delta = \frac{-\frac{dS}{dt}stationary}{X_{max}}$

All estimations were performed using Microsoft® Excel solver ® (Germec et al., 2019; Adebule et al., 2025). The presented data represent the means of replicate values (n = 2). All outcomes were expressed as mean ± standard deviation for each fermentation output.

6.3. Results and discussion

6.3.1. *Pichia stipitis* inoculum development (PSID) model development

The preliminary screening, using xylose (YPX) as the sole carbon source, resulted in a higher yeast (*P. stipitis*) load of 2.04×10^6 CFU/mL compared to 1.00×10^5 CFU/mL observed for glucose (YPG) after cultivation at 30°C and 120 rpm for 24 h. Then, xylose was combined with different secondary carbon sources (waste lubricant oil, methanol, glycerol, and waste vegetable oil). The $YPX_{Lub.\ oil}$ produced the highest load of 4.16×10^6 CFU/mL, followed by the $YPXv_{eg}$ (2.97×10^6 CFU/mL), YPX_{meth} (2.79×10^6 CFU/mL), and YPX_{gly} (2.20×10^6 CFU/mL) and was therefore considered for inoculum development model design. The yeast load with corresponding input parameters obtained from the experimental runs is shown in the supplementary document. The fitness of the PSID model was evaluated using the Analysis of Variance (ANOVA) (See supplementary materials). The model F-value of 12.46 indicates that the regression equations can interpret the response trends, while the lack of significant fit implies good model fitness. The P-value of the model was determined as 0.0016, which is less than 0.05, indicating model and parameter significance (Bishop et al., 2024). The incubation time was the most significant of the three PSID model input parameters ($p = 0.0007$), followed by temperature ($p = 0.0049$) and waste oil inclusion ($p = 0.0113$). However, the combined effect of waste oil inclusion and temperature significantly affected model development ($p = 0.0158$). Notably, waste lubricant oil contains residual nutritional components, including soluble organic compounds, nitrogen, protein, fatty acids, and carboxylic acids (Eregie and Jamal-Ally, 2019). These components likely played a crucial role in stimulating the growth and development of *P. stipitis* (Bhattacharya et al., 2015). Also, temperature plays a key role in enzymes' optimal functioning and ensuring efficient glucose uptake during fermentation. In addition, the coefficient of determination (R^2) value is a statistic that measures the proportion of variation in the output values that can be attributed to the input variables. The developed PSID model yielded an R^2 of 0.9412, indicating that the model can account for 94% of the variation in the response. These statistical indices suggest that the developed models positively correlated the input parameters and the response (yeast load). The model polynomial Eq. (6.15) was generated

for yeast load (CFU/mL), representing the input parameters for the response variable. Thus, the quadratic model obtained could predict *P. stipitis* inoculum development.

Yeast load (CFU/mL) = 4. 46 x 10^6 + 780000 A -550125 B + 464375 C -179000 AB + 393000 AC -762750 BC -413525 A^2 -404275 B^2 -802275 C^2 (Eq. 6.15).

Where A, B, and C represent the incubation time, temperature, and waste lubricant oil, respectively.

6.3.2. Interactive effects of process input variables on the yeast load

The PSID model observed a maximum yeast load of 5.27×10^6 CFU/mL for run 17 under inoculum development conditions of 1% v/v, 25ºC, and 48h for waste lubricant oil inclusion (WLO), temperature, and incubation time, respectively. On the other hand, a minimum yeast load of 2.21×10^6 CFU/mL was obtained for run 5 (2% v/v WLO, 45ºC temperature, and 27h incubation time). The 3D-RSM plots and contour (Fig. 6.1) show the interactive effects of the different input variables on the output (yeast load). The combined interaction between temperature and incubation time and their impact on yeast load (CFU/mL) (Fig. 6.1a) showed an increase in incubation time from 6h to 48h, resulting in a sharp increase in the yeast load from 2.74×10^6 CFU/mL to 5.27×10^6 CFU/mL. On the other hand, by increasing both the temperature and incubation time concurrently, an improved yeast cell growth was observed until the midpoint (4.47 × 10^6 CFU/mL), after which a steady decline set in. Lower yeast load (< 2.40 ×10^6 CFU/mL) was obtained at minimum incubation time (6h) when the temperature was increased from 25 - 45ºC.

The negative influence of temperature on the yeast load can be attributed to its effects on yeast bioactivities and metabolism. High temperatures will halt bioactivities such as heat-sensitive enzymatic activities of the cell, and in extreme situations, complete inhibition of microbial growth could be observed. Moreover, at elevated temperatures (>42 ºC), the cellular transportation of materials across the cellular membrane is altered, leading to the accumulation of toxic inhibitory compounds within the cell (Rorke and Gueguim Kana, 2017). The impact of the interaction of waste lubricant oil inclusion and incubation time on the yeast load (Fig. 6.1b) showed the concurrent increase in the WLO concentration (0 - 1 %v/v) and incubation time (6 - 35h) resulted in an increased yeast load from 2.70×10^6 CFU/mL to 4.48×10^6 CFU/mL. Further, an increase in WLO concentration from 1% v/v to 2%v/v caused a slight decline in yeast load (4.58×10^6 CFU/mL).

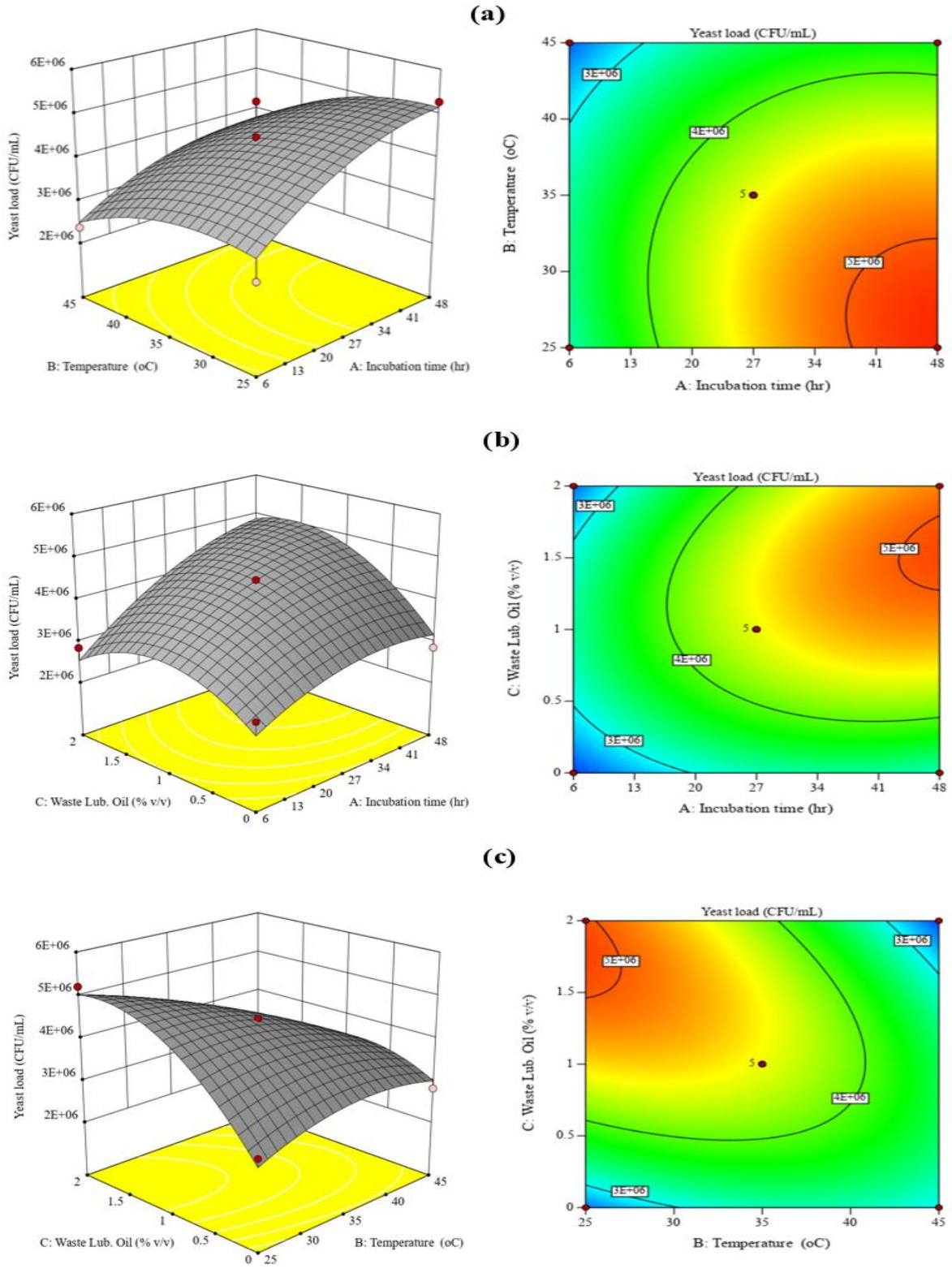

Figure 6.1. The RSM 3D and contour plots showing the interactive effects of the different input variables (a) temperature (°C) and incubation time (h), (b) incubation time (h) and WLO (% v/v), and (c) temperature (°C) and WLO (% v/v) on yeast load (CFU/mL).

The highest yeast load (5.04×10^6 CFU/mL) was recorded when WLO was maintained at slightly above 1% v/v and incubation time increased from 6 - 48h. The results reveal a strong relationship between WLO and incubation time in influencing the growth of *P. stipitis*. Typically, *Pichia sp.* cultivation requires >24h to achieve exponential growth or obtain a desirable concentration inoculum size. For instance, according to Li et al. (2021), *P. kluyveri* achieved exponential growth after 48 h at 32 ºC incubation. The results in the present study are remarkable as the inoculum size of desirable concentration was obtained at a shorter time <24h. Moreover, this study showed the efficacy of utilising WLO as a carbon source for *P. stipitis* inoculum development, substantially reducing the incubation period. This can be attributed partly to the efficient utilisation of WLO by *P. stipitis* as a carbon source, promoting the release of growth factors and consequently shortening the lag phase.

The pairwise interaction of temperature and WLO concentration on the yeast load revealed that concurrent increase in temperature (25 to 45 ºC) and WLO concentration (0 to 2 %v/v), occasioning an initial increase in yeast load from 2.77×10^6 CFU/mL to 4.47×10^6 CFU/mL at mid-point. Further increase in the temperature parameter above 35 ºC led to a substantial decline in yeast load from 4.47×106 CFU/mL to approximately 2.21×10^6 CFU/mL. However, by continuously increasing WLO concentration from 0 to 2 %v/v at 25 ºC, yeast load appreciated from 2.77×10^6 CFU/mL to 5.21×10^6 CFU/mL. Usually, several factors influence yeast growth; however, temperature (as mentioned above) has been shown to have the most drastic effect that could potentially influence the growth pattern of microorganisms.

6.3.3. PSID Model validation and comparison with previous studies

The experimental validation of the PSID model was conducted at the predicted set points of 1.52% WLO, 25 ºC, and 6h incubation time. The model predicted a yeast load of 3.32×10^6 CFU/mL; meanwhile, 3.55×10^6 CFU/mL was obtained from the experimental validation. This translates to a difference of 6.62 % compared to the model's prediction, which is considered negligible. It also indicates the high accuracy and precision of the developed RSM model, which is highly reliable for prediction. The 1.52% WLO validated in this study is lower in concentration compared to the optimal methanol concentration of 5–10 g/L employed, enhancing monellin production in *P. pastoris* fed-batch fermentation through an efficient online methanol/sorbitol co-feeding strategy (Abdel-Rahman et al., 2011). Moreover, the six (6) hour incubation time recorded is 4-fold lower than the 22–24 h incubation time reported by Mohapatra et al. (2020). Apart from the >4- to 5-fold reduction in incubation time derived from

adopting WLO, it effectively replaces glycerol and methanol for cell growth and protein expression (Abdel-Rahman et al., 2011) in *Pichia* sp. cultivation. Achieving exponential growth for *P. stipitis* at 25 °C, which is lower than the 30 °C temperature reported by Mohapatra et al. (2020), offers a cost-effective approach to inoculum development and fermentation process. The desirability of the optimal process conditions lies in the aim to minimise incubation time while guaranteeing the utilisation of WLO within an optimal range. This is particularly critical, as the cultivation of *P. stipitis* requires more than 24 hours to achieve exponential growth during the development of the inoculum.

6.3.4. Characterisation of substrates

Morphological changes and distortions characterising the native, pretreated, and detoxified potato peel waste were analysed with scanning electron microscopy (Fig. 6. 2a, b, and c). The native PPW sample (Fig. 6. 2a) exhibited a smooth, intact structure compared to the pre-treated and detoxified biomass. The outer layer of the biomass was mainly composed of structural polysaccharides enclosed within the intact cell walls. However, the pre-treated and detoxified samples exhibited distinct structural changes, including fragmentation, extreme cavitation, and disintegration of cellular integrity compared to the native sample. Similar observations on different biomasses have been reported in the literature when using other pre-treatment techniques such as acid, alkaline, and salt (Guo et al., 2016; Aruwajoye et al., 2017; Thakur et al., 2021).

The structural changes of the pre-treated biomass might be attributed to the destabilisation and alteration of the rigid lignocellulosic cell wall structure during delignification (Moodley and Kana, 2019). Fig. 6.2c, which represents detoxified PPW, differs slightly morphologically from Fig. 6.2b (pretreated but non-detoxified) regarding reduced structural porosity. This must have been caused by the influence of the Fe_3O_4 nanoparticle filling some pores (Sanusi et al., 2020).

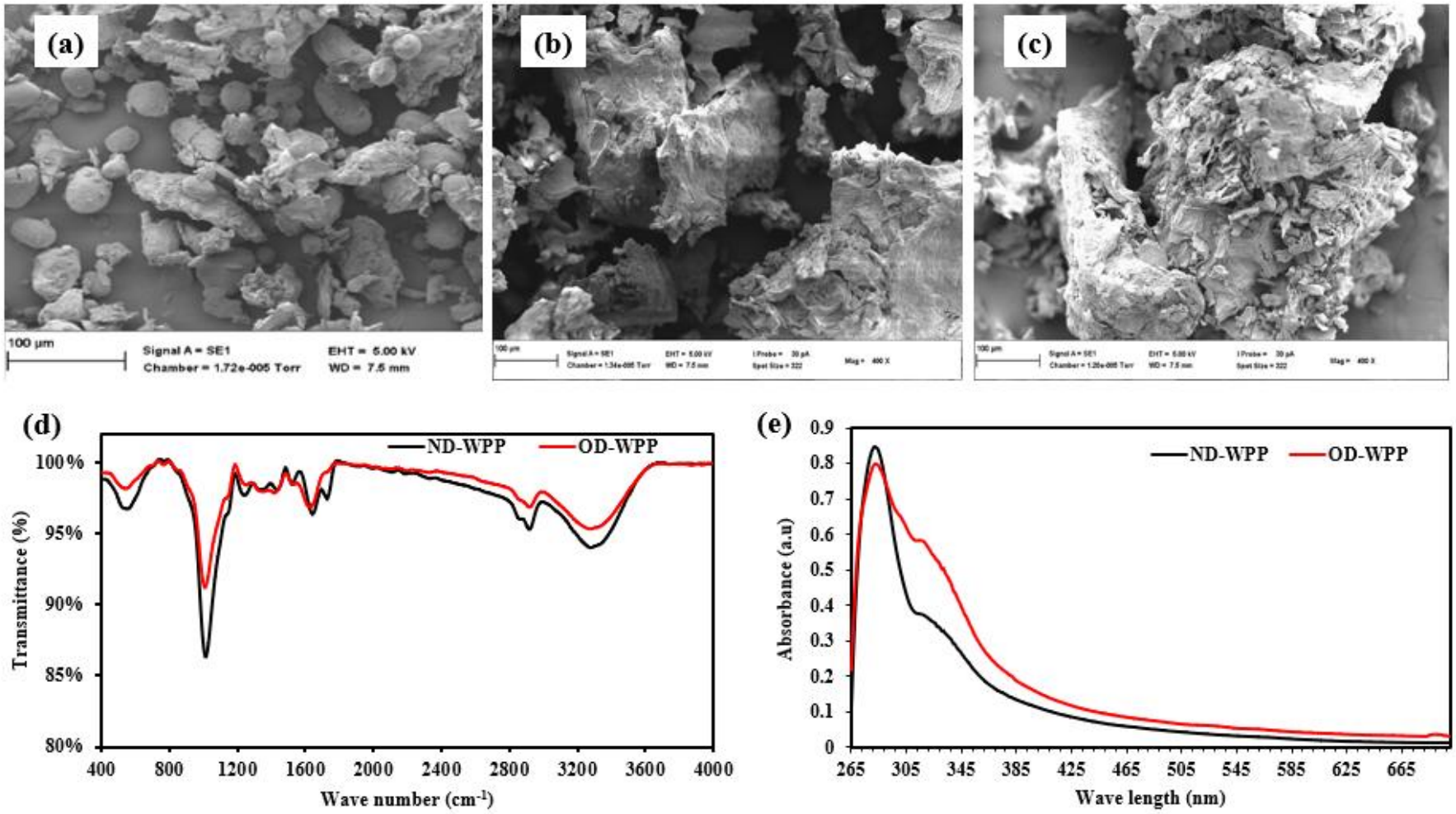

Figure 6.2. Scanning Electron Micrographs of native potato peel waste (a), pretreated potato peel waste (b), nano-adsorbent detoxified potato peel waste (c), FTIR spectra of non-detoxified and detoxified potato peel waste (d), UV–vis absorption spectra of non-detoxified and detoxified potato peel waste.

The structural disruptions observed in the non-detoxified (Fig. 6.2b) and detoxified (Fig. 6.2c) pre-treated PPW are substantiated by the modifications revealed by the FTIR analysis. Structural changes observed before and after detoxification were indicated by variations in the banding patterns of the non-detoxified and detoxified pre-treated PPW FTIR spectra (Fig. 6.2d). The characteristic broad band of 3290 cm^{-1} is assigned to the asymmetric stretching vibration of the hydroxyl (O-H) group, which represents alcohols and phenols. The broadening of the bands in 1760 to 2800 cm^{-1} associated with the O-H stretching of the hydrogen bonds of amylose and amylopectin (from starch granules) was equally distributed in the non-detoxified and detoxified PPW samples. Both spectra exhibited sharp peaks at 2920 cm^{-1}, corresponding to the asymmetric and symmetric C-H stretching vibrations showing the distinguishing feature of cellulose (Zhang et al., 2020).

The OD-PPW showed a higher transmittance (lower absorption) than the ND-PPW, suggesting a reduction in aliphatic content after detoxification. Another prominent band at 1011 cm^{-1} was assigned to C-H bending and C-O stretching vibrations associated with crystalline and amorphous attributes of starch (Aruwajoye et al., 2017; Govindaraju et al., 2021). The low-intensity peak at 1220 cm^{-1} and 1616 cm^{-1} belongs to the aromatic ring vibration and C=O stretching characteristic of carbonyl groups (e.g., aldehydes, ketones), which were slightly more intense in the non-detoxified PPW than in the detoxified PPW, indicating a reduction in carbonyl-containing compounds post-detoxification (Zhang et al., 2020). The strong band at 1643 cm^{-1} represents a mono-substituted C=C stretching of an alkene. Similarly, absorption peak stretching from 1600–1800 cm^{-1} can be attributed to C=O stretching vibrations of acetyl and ester groups in hemicellulose and lignin. However, eradicating the absorption peak in 1730 cm^{-1} reflects the potential impact of nano-detoxification in removing lignin. Previous reports on biomass pre-treatment have recorded similar banding patterns (Aruwajoye et al., 2017). By comparing the obtained spectra for the non-detoxified and detoxified PPW, the peaks at 3290, 2920, 1640, 1011, 880, and 550 cm^{-1} became less steep in the detoxified PPW. This indicated a reduction in the sample's functional groups of amino, phenolic, aldehyde, amine, and hydroxyl group components, integral to various fermentation inhibitors. The FTIR analysis of the non-detoxified and optimised detoxified waste potato peel samples substantiated the occurrence of structural alterations during the nanoparticle detoxification process, leading to the disentangling and removal of inhibitor compounds.

Additionally, the optical absorption spectra of the non-detoxified (NDH) and optimised detoxified (ODH) waste potato peel samples were analysed using UV spectroscopy in the range of 260–700 nm (Fig. 6. 2e). The NDH sample shows a higher overall absorbance compared to the ODH sample in the UV region, indicating a higher concentration of UV-absorbing compounds in the non-detoxified sample. Both samples exhibited prominent peaks around 270–280 nm. However, the NDH sample differs significantly from the ODH sample, with a higher peak absorbance (Thakur et al., 2021). After the peak, the absorbances for both samples decline. The NDH sample shows a steeper decline, indicating the presence of multiple absorbing species. Meanwhile, the ODH sample shows a more gradual decline, indicating a more homogeneous and reduced concentration of absorbing compounds. However, in the visible region (above 400 nm), the absorbance for both samples is low, but the NDH sample still showed slightly higher absorbance than the ODH sample. This slight difference further confirmed the presence of additional compounds in the non-detoxified sample. The reduction in absorbance at these wavelengths suggests effective detoxification.

6.3.5. Co-inoculation and co-fermentation study

6.3.5.1. Preliminary screening on the effect of seed culture ratio variation and time of inoculation on bioethanol production

Fig. 6.3 showed the SSCF seed inoculum comprising both *S. cerevisiae* (Sc) and *P. stipitis* (Ps) at varying proportions (1:4, 2:3, 2.5:2.5, 3:2, 4:1). The corresponding ethanol production for the different inoculation ratios is shown in Fig. 6.3a. All fermentation ratios exhibited short lag times ranging from 0 to 5 h, except for ScPs (1:4) (8 h). The variation in lag time is probably due to differences in the dynamism of interactions between the two species. The quality of seed cultures is pivotal in determining the overall performance of the process, especially in a co-culture scenario. To establish a co-culture system effectively, selecting suitable organisms and culture conditions is crucial (Gao et al., 2021). Given the optimal co-inoculation ratio of 1:4 (*S. cerevisiae* to *P. stipitis*), glucose accumulation is anticipated due to the low starting volume of *S. cerevisiae*, which may potentially impede ethanol production (Liu et al., 2019).

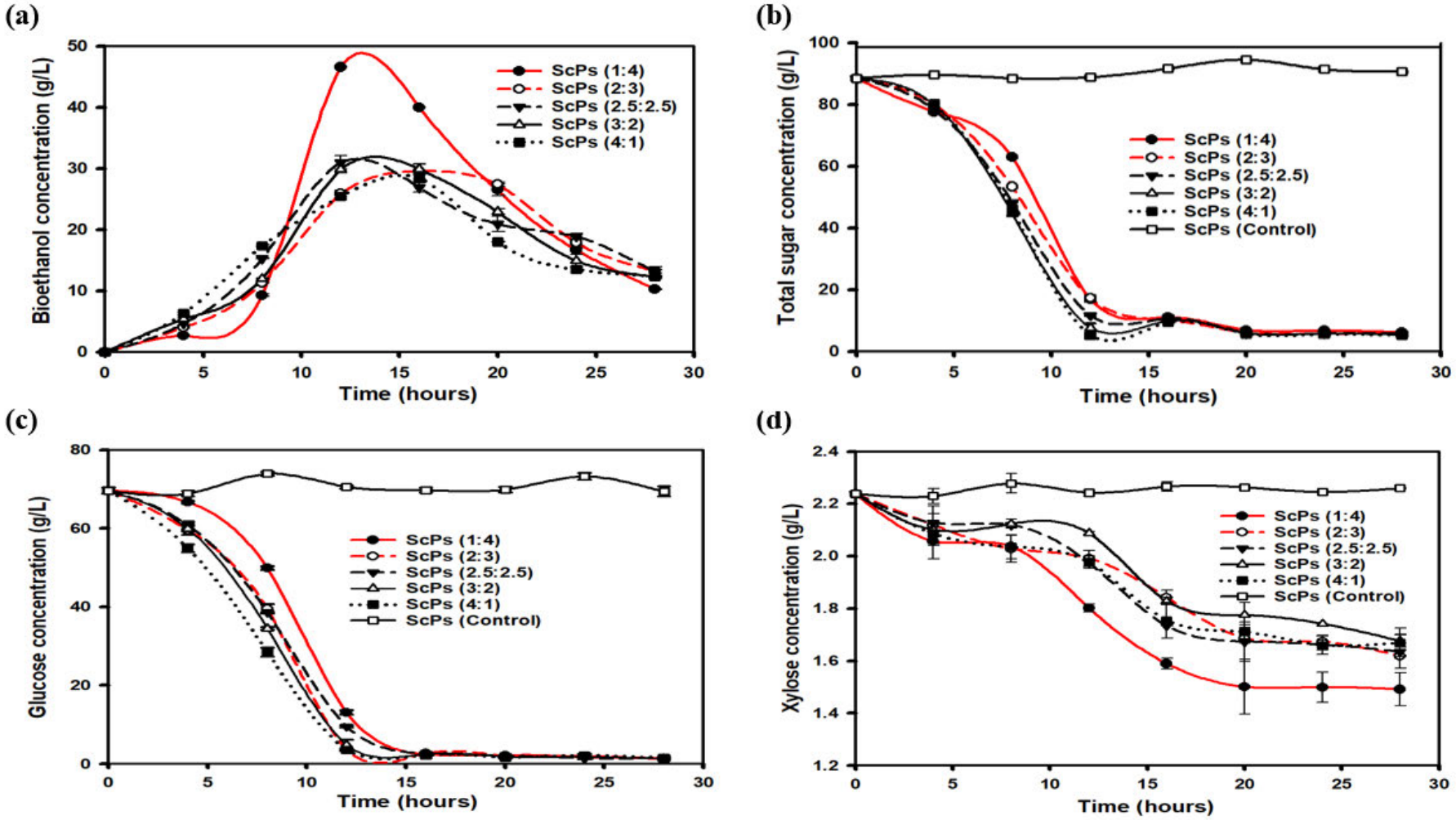

Figure 6.3. Influence of seed cultures ratio variation on ethanol production through co-fermentation. ScPs (represents the ratio of *S. cerevisiae* to *P. stipitis*).

However, the synchronous utilisation of the fermentable sugars (glucose and xylose) prevented sugar accumulation to inhibit bioethanol production in the ScPs-SSF process. Moreover, the dual ability of *P. stipitis* to utilise glucose and xylose simultaneously must have mitigated glucose accumulation (Okonkwo et al., 2016), thereby preventing process inhibition (Miah et al., 2022).

The highest maximum bioethanol concentration (46.61 g/L) recorded for the co-fermentation under varying ratios was obtained from ScPs (1:4) after 12h of fermentation. While the ScPs (2:3) showed a maximum bioethanol concentration of 29.58 g/L after 16h, ScPs (1:1), 31.02 g/L after 12h, ScPs (3:2), 29.94 g/L also after 16h, and ScPs (4:1), 28.50 g/L after 16h. Once peak bioethanol production was attained across all five processes, a subsequent decrease in bioethanol production occurred throughout the remaining fermentation period, primarily attributable to nutrient exhaustion and depletion of fermentable sugars. The total sugar, glucose, and xylose consumption observed during the corresponding bioethanol productions at all ratios is shown in Fig. 6.3b, 6.3c, and 6.3d. Notably, a consistent degradation of xylose was observed across all ratios, with the most substantial degradation observed with ScPs (1:4). The variation in substrate consumption is due to dynamic interactions among fermenting species, influenced by carbon sources and substrate bioavailability (Nielsen et al., 2000). In an earlier study conducted by Liu et al. (2019), *S. cerevisiae* and *Candida tropicalis* (3:1 ratio) yielded the highest bioethanol concentration (10.92 g/100mL) in comparison with various *S. cerevisiae* and *C. tropicalis* ratios (4:1, 3:1, 2:1, 1:1, 1:2, 1:3, and 1:4). In another study, *S. cerevisiae* and *P. stipitis* inoculum ratios of 2:2% (v/v) favoured the highest butanol concentration of 3.1 g/L using rice straw substrate (Mohapatra et a., 2020).

To further optimise interactions between the two species for improved productivity, the most appropriate timing for introducing each species at 4-hour intervals was determined using the most productive inoculation ratio [(ScPs (1:4)] (Section 3.4.1). As shown in Fig. 6 .4, the introduction of *P. stipitis* at a complementary ratio (4) to *S. cerevisiae* (1) at zero (0) hours yielded the maximum bioethanol production of 43.11 g/L. This was also achieved in the shortest fermentation period (12h). Inoculation times of 4 h, 8 h, 12 h, 16 h, 20 h, 24 h, and 28 h yielded bioethanol concentrations of 33.43 g/L, 34.35 g/L, 37.0 g/L, 38.14 g/L, 37.71 g/L, 36.07 g/L, and 34.84 g/L, respectively.

6.3.5.2. Bioethanol production by monoculture of *S. cerevisiae* and *P. stipitis*

The detoxified hydrolysate, containing total reducing sugar, glucose, and xylose concentrations of 98.11 g/L, 72.71 g/L, and 2.33 g/L, respectively, was fermented separately by *S. cerevisiae* and *P. stipitis* for bioethanol production, serving as a positive control. The bioethanol obtained under SSF conditions with *S. cerevisiae* (Sc-SSF_{mono}) and *P. stipitis* (Ps-SSF_{mono}) was depicted in Fig. 6 .4, with the Ps-SSF showing no lag phase, but a short lag phase (<5h) was observed in Sc-SSF_{mono}. The Sc-SSF_{mono} produced a bioethanol concentration of 36.40 g/L, with a glucose utilisation of 94.3% and a fermentation efficiency of 73.3%, resulting in bioethanol yield of 0.377 g/g and productivity of 3.03 g/L/h after 12 hours (Table 6.2). Then, a gradual decrease in bioethanol production was observed afterwards until the 24^{th} hour.

On the other hand, *P. stipitis* (Ps-SSF_{mono}) produced bioethanol concentration of 0.894 g/L after 9h followed by a steady decline. The resulting bioethanol yield and productivity were 0.01 g/L and 0.10 g/L/h, respectively (Table 6.2). Although *P. stipitis* primarily utilises xylose and can metabolise glucose synergistically with xylose, its performance in glucose metabolism was found inefficient in this study (Song et al., 2019). Although both xylose and glucose were fermented, xylose was preferentially utilised for bioethanol production from the detoxified hydrolysate. The high bioethanol concentration achieved in the Sc-SSF_{mono} process in this study is similar to the 36.04 g/L reported in the SSF process by Sanusi et al. (2021). Also, comparing previous studies on bioethanol production, the ethanol concentration in the Sc-SSF_{mono} process was 4.8 times and 6.6 times higher than those reported by Arapoglou et al. (2010) and Hashem and Darwish (2010), which were 7.67 g/L and 5.52 g/L, respectively.

The bioethanol productivities of 3.03 g/L/h (Sc-SSF_{mono}) and 0.10 g/349 L/h (Ps-SSF_{mono}) achieved in this study can be favourably compared with findings from previous research. For instance, Arapoglou et al. (2010) and Khawla et al. (2012) reported lower bioethanol productivities of 0.15 g/L/h and 0.25 g/L/h, respectively, when compared to the 3.03 g/L/h obtained in Sc-SSF_{mono}. Likewise, the 3.03 g/L/h productivity from Sc-SSF_{mono} was higher than the results reported by Sanusi et al. (2021) and Izmirlioglu and Demirci (2016). The variations in bioethanol productivity can be primarily attributed to the pre-detoxification of the hydrolysate in the present study, the differences in yeast strains and the specific fermentation conditions employed.

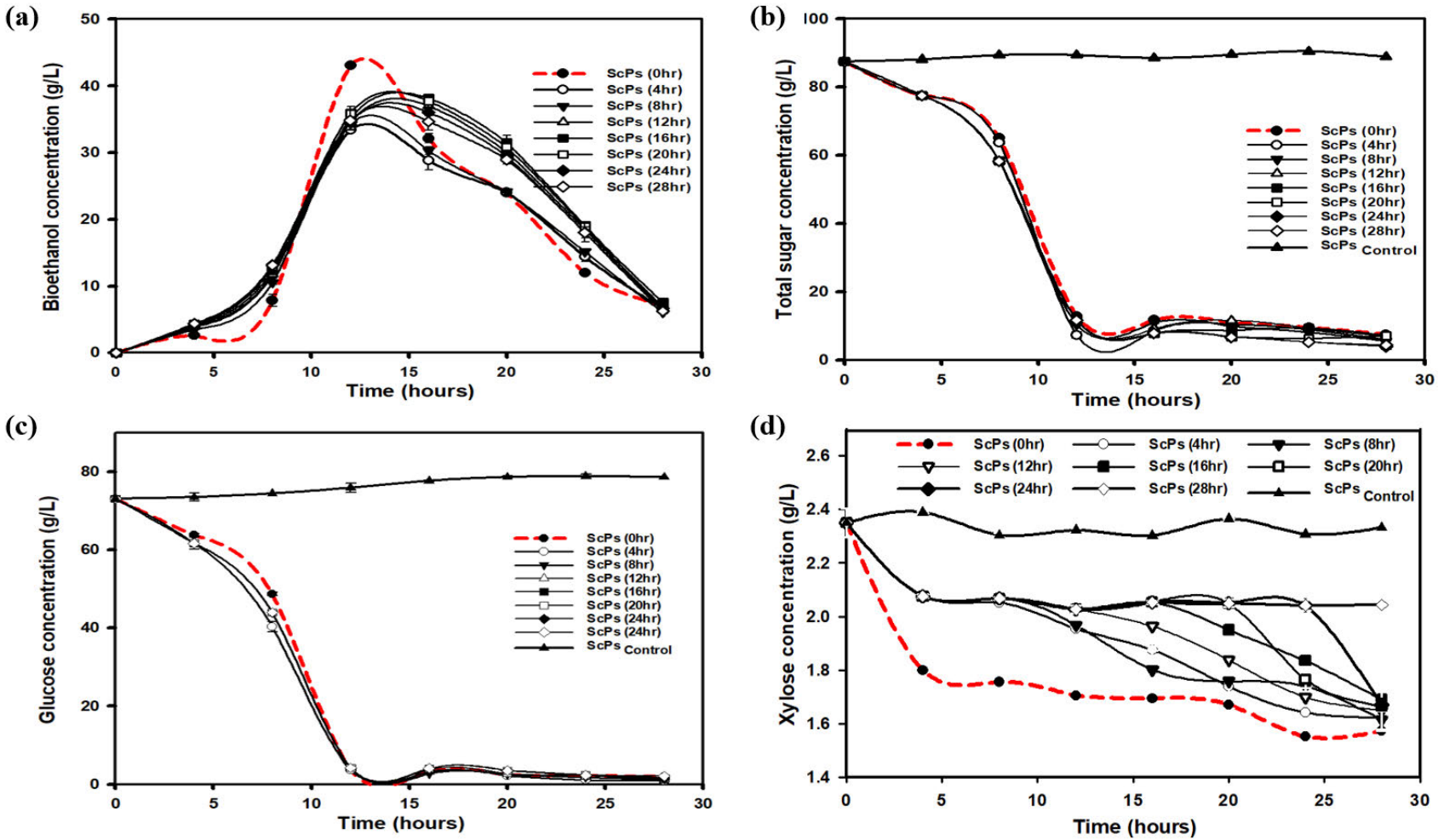

Figure 6.4. Production of bioethanol and sugar utilisation from different inoculation timing by co-fermentation.

6.3.5.3. Co-fermentation model development and optimisation

The experimental conditions, along with the corresponding bioethanol concentration and yields, are presented in Table 6.1. Experimental data were used to develop two polynomial equations relating the ethanol concentration and yield to the input variables as shown in Equations (6.16) and (6.17) below:

$$\text{Bioethanol concentration} = 34.24 + 5.04\,A - 3.17\,B + 2.69C - 1.96\,AB + 1.97\,AC - 3.20\,BC - 7.21\,A^2 + 2.91\,B^2 + 1.28\,C^2 \quad \text{(Eq. 6.16)}$$

$$\text{Bioethanol yield} = 0.362 - 0.087\,A - 0.032\,B + 0.027\,C - 0.015\,AB + 0.014\,AC - 0.034\,BC - 0.004\,A^2 - 0.032\,B^2 + 0.013\,C^2 \quad \text{(Eq. 6.17)}$$

Where A, B and C represent the solid loading (g), co-inoculation time (h) and inoculation ratio, respectively. The validity of the fitted models was evaluated using analysis of variance (ANOVA) (see Supplementary Tables S3). P-values < 0.05 indicated the model and parameter significance, while high F-values indicate that response trends can be interpreted by the regression equations (Chaganti et al., 2012). The bioethanol concentration and yield models displayed high F-values of 77.09 and 76.90 with low p-values, both < 0.0001, respectively. The coefficient of determination (R^2) values of the models was 0.99 for bioethanol concentration and yield, thus indicating that both models can explain 99.0% of the variability in the observed experimental data. High model fitness is reflected in the coefficient of determination (R^2) value, which ranges between 0.80 and 1.00 (Eregie et al., 2023). The significance of the individual input parameters was determined based on their p-values (see Supplementary Tables S3), with solid loading ($p < 0.0001$), co-inoculation time ($p < 0.0001$), and inoculation ratio ($p = 0.0001$) indicating significant effects on the bioethanol concentration. Similar p-values were obtained for bioethanol yield, except for the inoculation ratio, with a p-value of 0.0002. Remarkably, the interactive effect of all variables had a significant impact on the bioethanol concentration and yield. The p-values of the pairwise interactions of solid loading and co-inoculation time (0.0051 and 0.0326); solid loading and inoculation ratio (0.005 and 0.041); co-inoculation time and inoculation ratio (0.0003 and 0.0005) were obtained for bioethanol concentration and yield, respectively. The solid loading affects the efficiency of mass and heat transfer in the SSF process. A high solid loading results in higher viscosity, which can reduce enzyme diffusion, thereby negatively affecting sugar release for yeast cell growth and bioethanol production (Aguilar-Reynosa et al., 2017). Meanwhile, a low solid loading will result in a shortage of sugar

for product formation. The timing of co-inoculation can influence the metabolic interactions between different microbial species (Bingol et al., 2024). In the production of bioethanol, the co-culture of different yeast strains was optimised by adjusting the inoculation sequence to enhance sugar fermentation efficiency (Sharma et al., 2021). However, the ratio of different microbial inoculums is critical for balancing growth and product formation (Sanchez-Cuasapud et al., 2024).

6.3.5.4. Interactive effects of process parameters on bioethanol concentration and yield

The co-fermentation input parameters, along with their corresponding bioethanol concentrations and yields, are shown in Table 1. Bioethanol concentration ranged from 23.06 to 48.48 g/L, whilst the yields ranged from 0.26 to 0.51 g/g. For runs 1, 3, 4, 6 and 8, where all the process inputs were at their median values, the SSCF process resulted in bioethanol concentrations ranging from 34.22 to 34.28 g/L and yields (0.362 to 0.363 g/g). The lowest bioethanol concentration (23.06 g/L) was obtained at 5 g solid loading, with a complementary higher yield of 0.44 g/g (run 2). This is because bioethanol production depended mainly on the concentration of sugars. With 10 g solid loading, an incubation ratio 1 of 4 of S. cerevisiae to *P. stipitis* (represented as 5), and a zero-hour co-inoculation time (run 7), the highest bioethanol concentration (48.48 g/L) and yield (0.51 g/g) were produced. The three-dimensional (3D) response surface graphs (Fig. 6.5a to f) illustrate the interactive effects of the process parameters on bioethanol concentration and yield. Figures 6.5a and 5b show the pairwise interaction between solid loading and co-inoculation time, while maintaining the inoculation ratio at its median value (3). A simultaneous increase in solid loading from 5.0 to 15.0 g and co-inoculation time from 0 to 24 h led to an initial increment in the bioethanol concentration from 24.94 to 34.28 g/L (at mid-point) and reduced to 31.02 g/L after further simultaneous increment of the solid loading and co-inoculation time (Fig. 6. 5a). However, bioethanol yield reduced significantly from 0.485 to 0.267 g/g under the same condition (Fig. 6. 5b). Maintaining the co-inoculation time at a minimum (0 h) and increasing the solid loading from 5 to 13g increased the bioethanol concentration to 41.8 g/L. Contrastingly, the yield reduced from 0.485 to 0.341 g/g. A slight reduction in bioethanol concentration, from 24.94 to 24.18 g/L, was observed when the solid loading was at a minimum and the co-inoculation time increased from 0 to 24 hours. Similarly, bioethanol yields are slightly reduced, from 0.485 to 0.470 g/g, by increasing the co-inoculation time from 0 to 24 h.

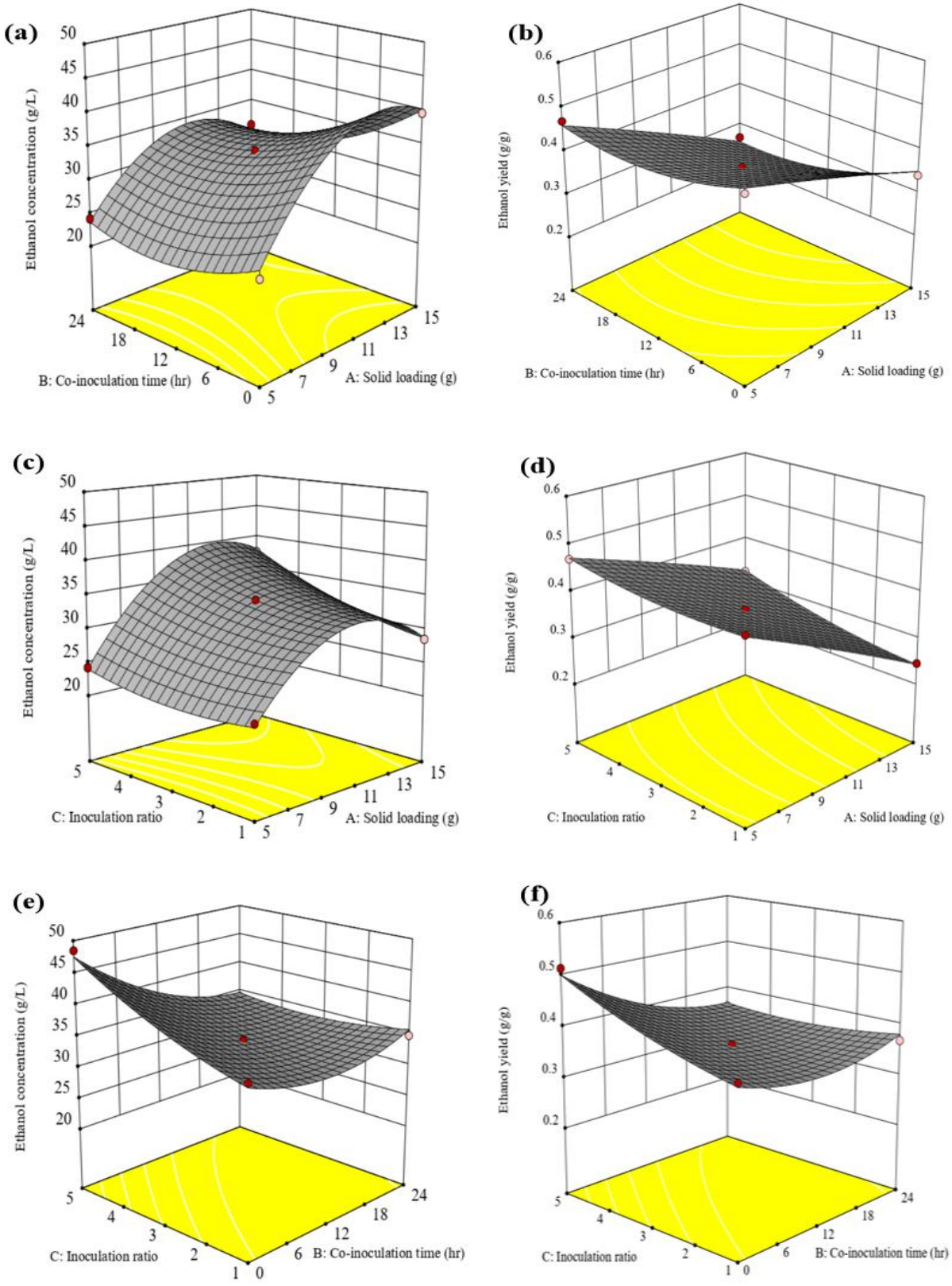

Figure 6.5. The 3D plot showing the interactive effect of the process parameters: solid loading and co-inoculation time (a and b), solid loading and inoculation ratio (c and d), co-inoculation time and inoculation ratio (f and g) on ethanol concentration and yield, respectively.

Generally, the low bioethanol yield obtained in this study can be attributed to poor mixing at high solid loadings. Poor mixing is known to negatively influence the viscosity of fermentation system, which causes ineffective mass and heat transfer as well as a reduction in the enzyme efficiency (Chohan et al., 2020). Additionally, poor mixing arising from high solid loading could lead to nutrient concentration gradients, which may result in sugar-osmotic pressure effects on the fermenting microorganisms, forcing the yeast cells to channel their metabolic processes towards cell maintenance and biomass growth (Sewsynker-Sukai and Kana, 2018). As solid loading increases, the conversion of sugars can decrease due to reduced saccharification efficiency. Moreover, Zhu et al. (2020) reported that, at high solid loading, the severity of low-temperature inhibition (LTI) in corn stover was accompanied by decreased sugar conversion and bioethanol yield. Chohan et al. (2020) previously investigated the optimisation of bioethanol production from potato peel waste using simultaneous saccharification and fermentation, with inputs of temperature, pH, and solid loading (5 to 20 g). The optimised solid loading (12.70 % w/v) obtained was slightly higher than 10 g recorded in this study. Generally, pretreated potato peel waste exhibits higher viscosity at higher solid loadings.

The interactive effect of solid loading and inoculation ratio on bioethanol concentration and yield, while maintaining the co-inoculation time at its centre point is shown in Fig. 6c and d, respectively. For the inoculation ratios, 1, 2, 3, 4, and 5 represent 4:1, 3:2, 1:1, 2:3, and 1:4 ratios of *S. cerevisiae* to *P. stipitis*, respectively. The bioethanol concentration increased from 23.06 to 34.28 g/L (at the midpoint) and further to 37.50 g/L with a pairwise increment in the solid loading and inoculation ratio from 5.0 to 15 g and from 1 to 5, respectively. On the other hand, bioethanol yield decreased continuously from 0.448 to 0.323 g/g (Fig. 6 .5d). A slight increase in bioethanol concentration (23.06 to 24.18 g/L) was observed as the inoculation ratio increased continuously while the solid loading remained at a minimum (5 g). In contrast, the yield increased from 0.448 to 0.470 g/g under the same conditions. Moreover, bioethanol concentration increased from 23.06 to 33.1 g/L (with about 13 g solid loading) and reduced to 28.5 (at 15 g solid loading) when the inoculum ratio was kept at 1 (i.e. 4:1 of *S. cerevisiae* to *P. stipitis*). Meanwhile, under the same conditions, bioethanol yield decelerated from 0.448 to 0.245 g/g. However, the highest bioethanol concentration point (~ 40g) of the solid loading and inoculation ratio 3D-graph was observed at an inoculum ratio of 5 (i.e. 1:4 of *S. cerevisiae* to *P. stipitis*). As higher inoculum concentrations of specific yeast in a co-fermentation process can generally lead to increased fermentation efficiency and bioethanol yield, they can also

affect the dynamics of fermentation, substrate utilisation, and product formation (Zhu et al., 2021; Kaur et al., 2020). Therefore, achieving a balanced inoculum ratio and the inoculum-to-substrate ratio is essential for optimising fermentation conditions and achieving desired outcomes in bioethanol production.

The pairwise impact of co-inoculation time and inoculation ratio on bioethanol concentration and yield, while the solid loading is kept at its median value, is shown in Fig. 6e and f, respectively. The 3D graph (Fig. 6 .5e) revealed that simultaneous increases in co-inoculation time and inoculation ratio, from 0 to 24 h and 1 to 5, resulted in a continuous reduction in bioethanol concentration from 36.39 to 34.07 g/L. Meanwhile, bioethanol yield reduced from 0.385 to 0.361 g/g (Fig. 6. 5f). Similarly, bioethanol concentration and yield reduced from 36.39 to 34.77 g/L and 0.385 to 0.368 g/g, respectively, with an inoculation ratio of 1 and the co-inoculation time being increased from up to 24 h. Conversely, adopting a zero-hour co-inoculation time and increasing the inoculation ratio from 1 to 5 resulted in an increment in bioethanol concentration and yield from 36.39 to 48.48 g/L and from 0.385 to 0.51 g/g, respectively. This indicated that a 1:4 ratio of *S. cerevisiae* to *P. stipitis* enhanced bioethanol production throughout the process.

The presence of non-*Saccharomyces* yeasts (*P. stipitis*) likely reduced the maximum population of *S. cerevisiae*, thereby affecting the overall fermentation kinetics. Typically, 1:4 of *S. cerevisiae* to *P. stipitis* means that *P. stipitis* amounted to 80% of the entire inoculum size. In multi-starter fermentations, non-*Saccharomyces* yeasts often become dominant, while *S. cerevisiae* eventually dominates by the end of fermentation (Zhu et al., 2021). Moreover, the results from this study indicated a general reduction in bioethanol concentration and yield when co-inoculation was implemented after zero hours. This corroborated the importance of co-inoculation time in bioethanol formation. The interaction between different microbial strains during co-inoculation can lead to either antagonistic or synergistic effects, depending on the timing of inoculation of the specific yeast. The timing of yeast introduction, whether simultaneous or sequential, affects the fermentation process. Sequential inoculation, where non-*Saccharomyces* yeasts are introduced first, followed by *S. cerevisiae*, can result in lower bioethanol production and distinct metabolite profiles (Devanthi et al., 2018; Diez-Ozaeta et al., 2022). However, in the case of this study, the co-inoculation of both *S. cerevisiae* and *P. stipitis* at a 1:4 ratio at the beginning of the process facilitated rapid adaptation and synergy between the two microbes. Additionally, since *P. stipitis* possesses the ability to utilise both

hexose and pentose sugars, the availability of both sugars in the system gives room for less competition between the microbes.

6.3.5.5. Experimental validation of the developed co-fermentation RSM models

The experimental validation under the optimal conditions was conducted in duplicates to maximise the bioethanol concentration and yield. The predicted optimum conditions for maximum bioethanol concentration (47.49 g/L) and yield (0.50 g/g) were 10% solid loading, zero-hour co-inoculation time, and a 1:4 inoculation ratio of *S. cerevisiae* to *P. stipitis*. The optimised conditions produced a slightly higher bioethanol concentration of 48.73 g/L and a yield of 0.505 g/g, both of which were higher than the model prediction. Figure 6.6 illustrates the ethanol concentration achieved by the co-culture of *S. cerevisiae* and *P. stipitis* (ScPs-$SSF_{co\text{-}culture}$) using detoxified potato peel hydrolysate. The ScPs-$SSF_{co\text{-}culture}$ process demonstrated a steady increase in bioethanol production, reaching 16 g/L at 9 hours, followed by an exponential surge at 12 hours, culminating in a peak bioethanol production of 48.73 g/L. Beyond this peak, a decrease in bioethanol concentration was observed for the remainder of the 24-hour fermentation period, likely due to nutrient depletion, sugar consumption, and the rising ethanol concentration.

This trend corresponds with the medium's sugar concentration reduction from 95.74 g/L to 0.99 g/L (accounting for approximately 99% of total sugar utilisation), as detailed in Table 6.2. Sugar consumption in the medium appeared to favour *S. cerevisiae* over *P. stipitis*, given the higher availability of glucose than xylose. *S. cerevisiae* showed a preferential metabolism of glucose over xylose. In addition, the higher fermentative efficiency (98.25%) observed in ScPs-SSF could be partly attributed to the use of detoxified hydrolysate and the synergistic effect of the co-fermenting microorganisms. The maximum bioethanol concentrations achieved by the ScPs-$SSF_{co\text{-}culture}$ were 1.34-fold and 54.5-fold higher than the Sc-SSF_{mono} (36.40 g/L) and Ps-SSF_{mono} (0.8935 g/L). Moreover, the bioethanol yield and maximum productivity obtained for ScPs-$SSF_{co\text{-}culture}$ in the present study were 0.505 g/g and 4.06 g/L/h, respectively, higher than bioethanol yield (0.39 g/g) and bioethanol productivity (0.39 g/L/h) obtained from the batch fermentation of glucose-xylose mixture by co-culture of *S. cerevisiae* V30 and *P. stipitis* CCY39502 (Kordowaska-Wiater et al., 2001).

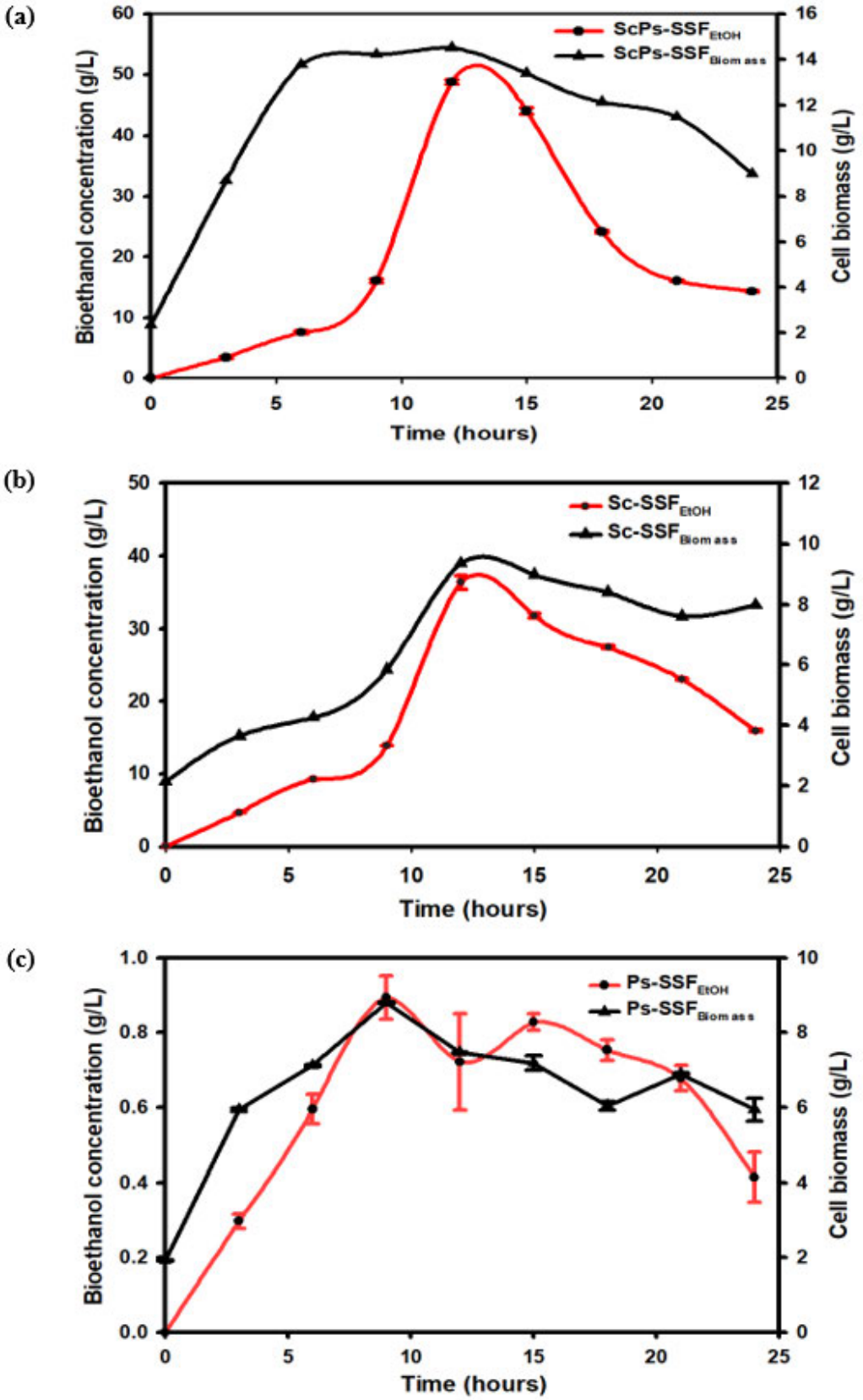

Figure 6.6. The profile of bioethanol production and cell biomass of the monoculture of (a) *S. cerevisiae* [Sc-SSF], (b) *P. stipitis* [Ps-SSF], and (c) their co-culture [ScPs-SSF].

Table 6.2. Fermentation parameters of single and co-culture of *S. cerevisiae* and *P. stipitis*

Fermentation mode	TSU (%)	GU (%)	XU (%)	BC (g/L)	BY (g/g)	BP (g/L/h)	FPE (%)
Sc-SSF	94.41	94.33	7.36	36.4	0.377	3.03	73.35
Ps-SSF	20.47	24.63	38.85	0.89	0.01	0.1	1.95
ScPs-SSF	98.96	99.67	63.27	48.71	0.505	4.06	98.25

TSU: Total sugar utilisation**, GU:** Glucose utilisation**, XU:** Xylose utilisation**, BY:** Bioethanol yield**, BC:** Bioethanol concentration**, BP:** Bioethanol productivity**, TY:** Theoretical yield**, FPE:** Fermentation process efficiency. [Note: TY (g/L) and FPE (%) were calculated in terms of total reducing sugar for Sc-SSF, Ps-SSF and ScPs-SSF, respectively].

In comparison with previous studies, the ethanol produced in this study was approximately 2.34 times higher than that reported by Singh et al. (2014), who obtained a bioethanol concentration of 20.8 g/L from the co-culture of *S. cerevisiae* and *P. stipitis* using rice husk substrate. Moreover, the ethanol production recorded in this study was 1.92-fold, 1.65-fold, and 1.53-fold higher than 25.39 g/L obtained in the co-culture of *Trichoderma reesei* and *Kluveromyces marxianus* using banana peduncle (Rouhollah et al., 2007), 29.45 g/L by *P. stipitis- S. cerevisiae* and 31.87 g/L by *P. stipitis- K. marxianus* (Phukoetphim et al., 2017), respectively. The SSF co-culture using lignocellulosic biomass offers a potential ethanol production process with high ethanol yield and shortened fermentation time, leading to reduced process costs.

6.3.6. Fermentation kinetics

6.3.6.1. Yeast growth kinetics using the logistic model

High kinetics coefficient of determination (R^2) of 0.918, 0.953, and 0.991 were obtained for Sc-SSF_{mono}, Ps-SSF_{mono}, ScPs-$SSF_{co\text{-}culture}$, respectively (Table 6.3), indicating the model sufficiently defines the growth of both fermenting organisms in both monoculture and co-culture systems. The notable short lag phase expedited the onset of the exponential growth phase in all the simultaneous saccharification and fermentation (SSF) systems. The increased yeast cell growth after the lag phase was associated with sugar utilisation of 94.33%, 24.63%, and 98.43% for the Sc-SSF_{mono}, Ps-$SSF_{mono,}$ and ScPs-$SSF_{co\text{-}culture}$ processes, respectively (Fig. 6. 6). High 0.247 h^{-1} maximum specific growth rate was recorded for Sc-SSF_{mono}, this value

represents a viable fermentation process which could enhance process economics and productivity at a large scale.

In both the Sc-SSF$_{mono}$ and Ps-SSF$_{mono}$ systems, the initial and maximum cell concentrations (X_0 and X_{max}) were recorded as 1.86 g/L and 9.62 g/L, and 1.97 g/L and 7.97 g/L, respectively. Meanwhile, the co-culture fermentation system (ScPs-SSF$_{co\text{-}culture}$) demonstrated higher values with X_0 and X_{max} reaching 2.13 g/L and 14.17 g/L. These results are consistent with the experimental observations for Sc-SSF$_{mono}$ (X_0: 2.14 g/L, X_{max}: 9.35 g/L) and Ps-SSF$_{mono}$ (X_0: 1.92 g/L, X_{max}: 8.80 g/L). The slightly lower maximum cell concentrations recorded for Ps-SSF$_{mono}$ compared to Sc-SSF$_{mono}$ can be attributed to the higher glucose concentration (72.71 g/L) in the medium compared to xylose concentration (2.33 g/L).

Table 6.3. Kinetics of cell growth and bioethanol production under monoculture and co-culture SSF

		Sc-SSF	Ps-SSF	ScPs-SSF
		Cell growth		
Logistic model	X_0 (g/L)	1.857	1.986	2.129
	X_o (g/L) [Exp]	2.135	1.922	2.331
	X_{max} (g/L)	9.620	7.967	14.169
	X_{max} (g/L) [Exp]	9.353	8.880	14.509
	U_{max} (h^{-1})	0.247	0.695	0.752
	R^2	0.918	0.953	0.991
		Bioethanol production		
MGM	P_m (g/L)	32.593	0.820	46.394
	$r_{p.m}$ (g/L/h)	4.438	0.149	97.938
	t_L (h)	4.304	1.087	8.836
	R^2	0.877	0.959	0.980
LP	α (g *P*/g *X*)	2.928	0.111	1.365
	β (g *P*/g *X*. h)	0.1646	0.0012	0.1075
	R^2	0.884	0.914	0.733
		Sugar utilisation		
MLP	γ (g S/g *X*)	11.426	2.896	7.5833
	δ (g *S*/g *X*. h)	0.0039	0.0047	0.0013
	R^2	0.951	0.940	0.80

μ_{max}=maximum specific growth rate, X_o=initial cell concentration, X_{max}=maximum cell concentration, P_m=maximum potential bioethanol concentration, $r_{p,m}$=maximum bioethanol production rate, t_L=lag time, PPW= Potato peel waste, MGM = Modified Gompertz Model, LP=Luedeking-Piret, MLP= Modified Luedeking-Piret.

This study recorded a higher maximum cell concentration in both monoculture and co-culture systems, comparably higher than the 5.145 g/L obtained for bioethanol production using sweet sorghum juice as substrate (Dodic et al., 2012) and 8.0 g/L recorded after sugar beet juice was metabolized for bioethanol production also using *S. cerevisiae* as the fermenting microbes (Richardson et al., 2011). Although the X_{max} of 14.17 g/L recorded in this study from the co-culture system was slightly lower than 15.0 g/L obtained from the co-culture of *Trichoderma reesei* and *Kluveromyces marxianus* using banana peduncle, a higher maximum specific growth rate (μ_{max}) of 0.752 h^{-1} was achieved in this study. This is 5.78-fold higher (0.13 h^{-1}) compared to that reported by Sathendra-Elumalai et al. (2023).

The results suggest that the co-culture system promoted rapid cell growth and cellular productivity more effectively. This can be attributed, in part, to the favourable process conditions and the use of detoxified hydrolysate (inhibitory compounds removed) (Adebule et al., 2024). Fermentation inhibitory compounds, such as furfural, 5-hydroxymethylfurfural, acetic acid, and phenolic compounds have been known to hinder cell growth, enzyme activation, and metabolic activities. These inhibitors can increase intracellular pH, impacting the specific growth rate and cell mass yield per ATP and interfering with the glycolytic process (Teoh and Ooi, 2016). This highlights the critical role of hydrolysate detoxification in bioprocessing efficiency.

6.3.6.2. Bioethanol production kinetics using modified Gompertz and Luedeking-Piret models

The modified Gompertz model exhibited high R^2 values of 0.877 (Sc-SSF_{mono}), 0.959 (Ps-SSF_{mono}), and 0.980 (ScPs-$SSF_{co\text{-}culture}$). The maximum potential bioethanol concentration (P_m) of 46.39 g/L with a lag time (t_L) of 8.84 h was obtained for ScPs-$SSF_{co\text{-}culture}$. Meanwhile, Sc-SSF_{mono} and Ps-SSF_{mono} had a P_m of 32.59 g/L and 0.82 g/L, respectively, with tL of 4.30 h and 1.09 h (Table 6.3). The model predictions were consistent with the experiment's maximum bioethanol concentration for Sc-SSF_{mono} (36.40 g/L), Ps- SSF_{mono} (0.89 g/L), and ScPs-$SSF_{co\text{-}culture}$ (48.73 g/L).

Also, with the Leudeking-Piret model, a good coefficient of determination (R^2) of 0.884 (Sc-SSF_{mono}), 0.914 (Ps-SSF_{mono}), and 0.733 (ScPs-$SSF_{co\text{-}culture}$) was achieved (See Supplementary Material). In the various fermentation protocols, the non-growth-associated constant for bioethanol formation (β) ranged from 0.0012 to 0.164 gP/gX.h (Table 6.3). On the other hand,

the growth-associated constants (α) for bioethanol were determined as 2.928, 0.111, and 1.365 gP/gX for Sc-SSF_{mono}, Ps- SSF_{mono}, and ScPs-$SSF_{co\text{-}culture}$, respectively. The results indicated that, with $\alpha \neq 0$ and β not close to zero except for Ps-SSF_{mono} (0.0012). The overall kinetic results of this model further underscore the influence of other process factors beyond cell growth, which could include the use of detoxified hydrolysate and the incorporation of nanoparticles. In an earlier report, Liu et al. (2019) modelled bioethanol production, obtaining α (2.392 gP/gX) and β (0.013 gP/gX.h) from pretreated corn stover through the co-culture of *S. cerevisiae* and *C. tropicalis* from which the bioethanol production was concluded to be influenced mainly by growth-associated factors due to the very small β value. In another study, Teoh and Ooi (2016) obtained lower values for α (0.3661 gP/gX) and β (-0.0036 gP/gX.h) in the growth-associated bioethanol formation from banana and pineapple wastes by the co-fermentation of *A. terrus* and *K. marxianus*. However, higher values of α (5.3143 gP/gX and 4.5326 gP/gX) alongside their corresponding β values (-0.044 gP/gX.h and 0.1047 gP/gX.h) were reported in the kinetic modelling of bioethanol production from red beet juice utilising two distinct *S. cerevisiae* strains (ITD00196 and ATCC 9763), respectively. These values were higher than those obtained in the present study. Notably, in both cases of product formation (ATCC 9763 and ITD00196), growth association was evident, as the β values were significantly smaller than the respective α values (Germec et al., 2019). This underscores the variability in the bioethanol formation kinetics. Summarily, the obtained parameters from these models, including the maximum potential bioethanol concentration (P_m), lag time (t_L), the maximum bioethanol production rate ($r_{p,m}$), growth and non-growth associate constants (α and β) presented in Table 6.3, gave a better understanding on the bioethanol formation kinetics in both monoculture and co-culture system.

6.3.6.3. Substrate utilisation kinetics

Substrate consumption typically conforms to the Modified Luedeking-Piret model (Germec et al., 2019; Liu et al., 2019; Sathendra-Elumalai et al., 2023). The experimental data on substrate utilisation over time for the SSF bioprocesses using Sc-SSF_{mono}, Ps-$SSF_{mono,}$ and their co-culture (ScPs-$SSF_{co\text{-}culture}$), were fitted to the Modified Luedeking-Piret model (Fig. 6. 7). The resultant values of γ and δ obtained for Sc-SSF_{mono}, Ps-$SSF_{mono,}$ and ScPs-$SSF_{co\text{-}culture}$ were 11.426, 2.896 and 6.892 (g S/g X) and 0.0039, 0.0047 and 0.0029 (g S/g X. h), respectively (Table 6.3). The maintenance coefficient (δ) is intricately linked to the specific growth rate and substrate uptake rate for cellular maintenance (Germec et al., 2019). Cellular maintenance

during fermentation entails energy expenditure for repairing damaged cellular components and ensuring cellular equilibrium. The variation in δ obtained in this study can be attributed to the variations in the substrate utilisation pathway by the monoculture or the co-culture of the fermenting organisms. As depicted in Table 6.3, the δ values for Sc-SSF_{mono}, Ps-SSF_{mono}, and ScPs-$SSF_{co\text{-}culture}$ were notably low, signifying that the yeasts predominantly utilise sugars in the detoxified hydrolysate for biomass and bioethanol production. Fig. 6.7 (b, d and f) illustrates the sugar utilisation profiles of Sc-SSF_{mono}, Ps-SSF_{mono}, and ScPs-$SSF_{co\text{-}culture}$. The total sugar, glucose concentration, and xylose concentrations rapidly decreased before 12 h, followed by a gradual decline in sugar utilisation and reduced bioethanol production from 12 h to 24 h. The simultaneous utilisation of glucose and xylose indicates that *S. cerevisiae* and *P. stipitis* used their respective substrates to produce bioethanol concurrently. Therefore, the relationship between substrate consumption and bioethanol synthesis, cell growth, and maintenance energy can be estimated from the residual total reducing sugar.

This observation in the current study, aligns with findings by Germec et al. (2019), Liu et al. (2019), and Teo and Ooi (2016), who similarly reported low δ values ranging from 0.0012 to 0.0284 g S/g X.h. The substrate utilisation coefficient (γ) was highest for Sc-SSF (11.426 g S/g X), underscoring the substantial presence of glucose (72.71 g/L) in the medium. In contrast, the ScPs-SSF displayed a lower γ value of 6.892 g S/g X due to the competition between *S. cerevisiae* and *P. stipitis* for available substrates. Notably, the Ps-SSF demonstrated the lowest γ of 2.896 g S/g X, a result intricately linked to the substrate's limited xylose content (2.33 g/L). Similarly, a high γ value (8.2 g S/g X) was reported using *Kluyveromyces. fragilis*-NCIM 0557 for bioethanol fermentation from sugarcane bagasse (Sasikumar and Viruthagiri, 2008).

6.3.7. Potential fermentation pathway

The monitoring of CO_2 production and N_2 gas was conducted to provide valuable insights into fermentation progress and the co-culture of *S. cerevisiae* and *P. stipitis* for bioethanol production. Fermentable sugars were metabolised by yeast via anaerobic respiration, producing ethanol and carbon dioxide. Similarly, the crude protein from the PPW, as well as peptone and yeast extract derived from the fermentation broth, serve as nitrogen sources for the growth and metabolic activities of the fermenting microorganisms (Nancib et al., 1991).

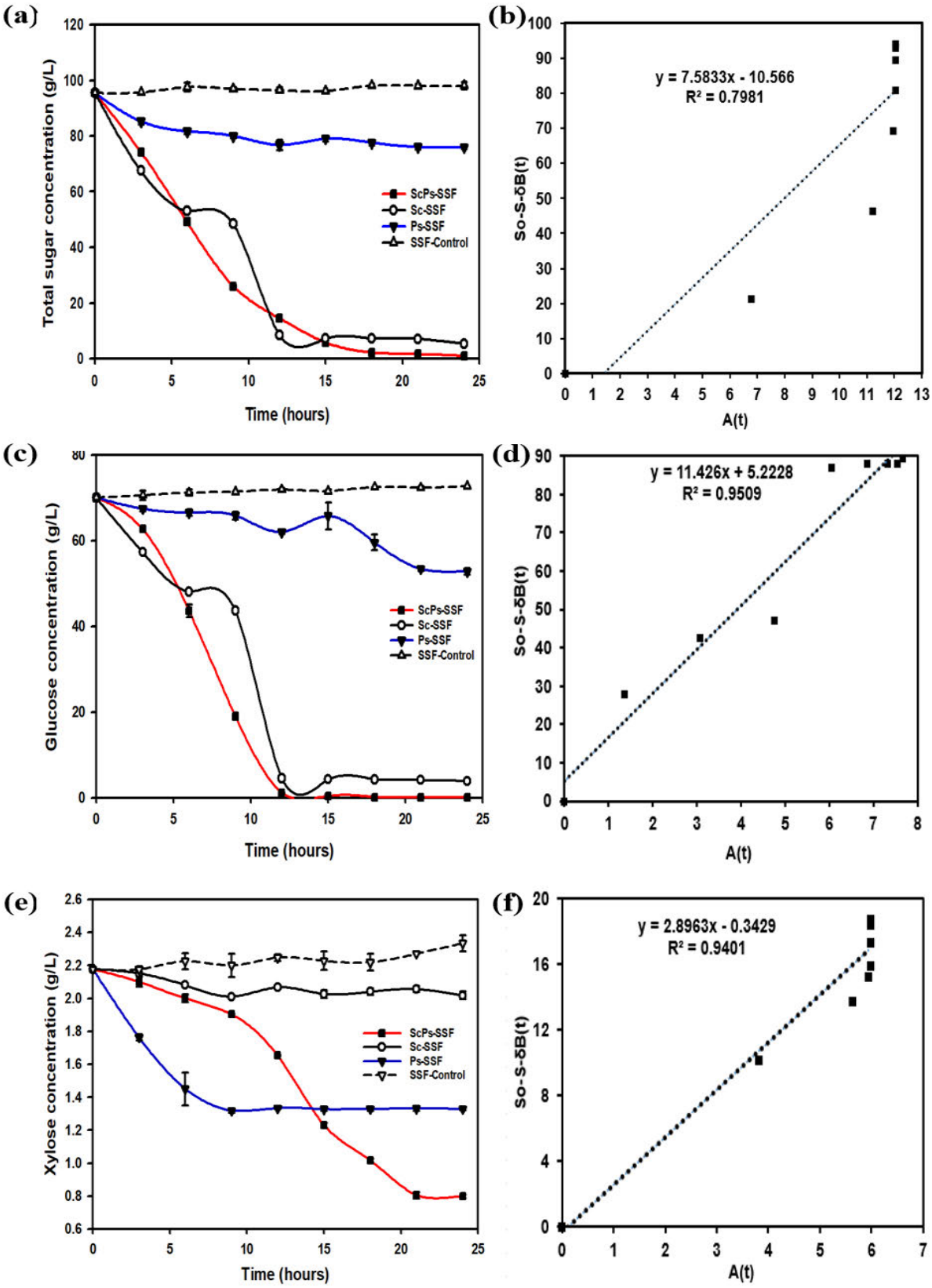

Figure 6.7. The profile of sugar utilisation (a, c and e), and MLP kinetics of Sc-SSF (b), Ps-SSF (d) and ScPs-SSF (f).

The CO_2 released commenced a short while after inoculation with corresponding depletion in N_2 concentration, presumably indicating the onset of ethanol fermentation (See Supplementary Material). The release of CO_2 during the fermentation process showed a steady increase, starting at 3 h, from 12.79% to a peak of 63.61% by 12 hours. This increase in CO_2 corresponded with a decrease in nitrogen (N_2) levels (which dropped from 87.20% to 36.08%) during the same period (See Supplementary Material). Following the peak in CO_2 release and a subsequent decline in carbon dioxide production, this pattern suggested an initial active phase of microbial metabolism (resulting in maximum CO_2 production) and the climax of metabolic activity. Notably, an increase in N_2 gas release was observed as CO_2 production declined after 24 hours of fermentation, suggesting a shift in microbial activity or dynamics. This rise in N_2 release could be associated with the role of peptone stabilising enzyme activity and yeast extract in growth and acetate assimilation after glucose depletion during fermentation (Nancib et al., 1991).

Concurrently with CO_2 generation, the bioethanol concentration increased from 0 to 48.73 g/L over the initial 12 h, subsequently decreasing to 14.33 g/L after 24 h. Evidently, within the ScPs-SSF, as sugars are metabolised (from 98.12 g/L to 13.47 g/L) to produce ethanol, CO_2 is released as a byproduct, playing a crucial role in regulating gas and pH levels in the system. Also, the presence of CO_2 gas could facilitate effective mixing and the exclusion of oxygen from the system. Additionally, it provides an adequate carbon source for yeast cells, allowing their growth and the continuation of the fermentation process (Guadalupe-Daqui et al., 2023). Consequently, more carbon is channelled towards bioethanol production than other cellular activities. Moreover, the diminished CO^2 production after the stationary phase of the fermentation process can be attributed to the preferential favouring of the acidic metabolic pathway (Wimonsong and Nitisoravut, 2015).

6.4. Conclusion

This study highlighted the beneficial synergistic impact of co-culturing *S. cerevisiae* and *P. stipitis* in fermenting detoxified pretreated potato peel waste hydrolysate under optimised conditions. It identified optimal conditions for bioethanol fermentation by co-fermentation of *S. cerevisiae* and *P. stipites*. Likewise, the study established that an inoculum ratio of 1:4 (*S. cerevisiae* to *P. stipitis*) and zero-hour inoculation time were the most effective strategies for maximising bioethanol production from detoxified pretreated potato peel waste hydrolysate. The optimised co-culture strategy yielded impressive results, including maximum specific

growth rate (μ_{max}) (ScPs-$SSF_{co\text{-}culture}$-0.752 h-1), glucose utilisation (99%), bioethanol productivity (4.06 g/L/h), yield (0.505 g/g), and higher bioethanol concentration (48.73 g/L). The kinetic models provided accurate predictions consistent with the experimental data, affirming their reliability. The concurrent utilisation of glucose by *S. cerevisiae* and xylose by *P. stipitis* in the co-culture system increased (>30%) bioethanol production compared to using only *S. cerevisiae* or *P. stipites*. This underscores the significance of the co-culture strategy in enhancing bioethanol production efficiency from pretreated potato peel waste hydrolysate.

References

Abdel-Rahman, M. A., Tashiro, Y., Sonomoto, K., 2011. Lactic acid production from lignocellulose-derived sugars using lactic acid bacteria: overview and limits. J. Biotechnol., 156(4), 286–301. https://doi.org/10.1016/j.jbiotec.2011.06.017.

Adebule, A. P., Sanusi, A. I., Gueguim Kana, E. B., 2024. Nano-based surface adsorption detoxification of process inhibitors for improved bioethanol productivity. Bioresour. Technol. Rep., 101783. https://doi.org/10.1016/j.biteb.2024.101783.

Adebule, A. P., Sanusi, I. A., Kana, G. E. B., 2025. Growth-associated and non-growth-associated bioethanol production kinetics from nanoadsorbent-detoxified pretreated hydrolysate. Catal. Lett., 155, 96. https://doi.org/10.1007/s10562-024-04868-8.

Adegboye, M. F., Ojuederie, O. B., Talia, P. M., Babalola, O. O., 2021. Bioprospecting of microbial strains for biofuel production: metabolic engineering, applications, and challenges. Biotechnol. Biofuels., 14, 5. https://doi.org/10.1186/s13068-020-01853-2.

Aguilar-Reynosa, A., Romaní, A., Rodríguez-Jasso, R. M., Aguilar, C. N., Garrote, G., Ruiz, H. A., 2017. Comparison of microwave and conduction-convection heating autohydrolysis pretreatment for bioethanol production. Bioresour. Technol., 243, 273–283. https://doi.org/10.1016/j.biortech.2017.06.103.

Arapoglou, D., Varzakas, T., Vlyssides, A., Israilides, C., 2010. Ethanol production from potato peel waste (PPW). Waste Manag., 30, 1898–1902. https://doi.org/10.1016/j.wasman.2010.04.017.

Aruwajoye, G. S., Faloye, F. D., Gueguim Kana, E. B., 2017. Soaking-assisted thermal pre-treatment of cassava peel wastes for fermentable sugar production: process modelling and optimisation. Energy Convers. Manage., 150, 558–567. https://doi.org/10.1016/j.ijhydene.2014.01.163.

Behera, S. S., Saranraj, P., Ray, R. C., 2022. Microbial bioethanol fermentation technologies—recent trends and future prospects. In Biofuels and Biorefining, Elsevier, 75–108. https://doi.org/10.1016/B978-0-12-824116-5.00011-8.

Bhattacharya, M., Guchhait, S., Biswas, D., Dattan, S., 2015. Waste lubricating oil removal in a batch reactor by mixed bacterial consortium: a kinetic study. Bioprocess Biosyst. Eng., 38, 2095–2106. https://doi.org/10.1007/s00449-015-1449-9.

Bingol, E., Qi, A., Karandeni-Dewage, C., Ritchie, F., Fitt, B. D., Huang, Y. J., 2024. Co-inoculation timing affects the interspecific interactions between phoma stem canker pathogens *Leptosphaeria maculans* and *Leptosphaeria biglobosa*. Pest Manag. Sci., 80(5), 2443–2452. https://doi.org/10.1002/ps.7799.

Bishop, B. D., Sanusi, I. A., Kana, G. E., 2024. Enhanced substrate suitability of autoclave-assisted acid pre-treated waste sugarcane molasses: pre-treatment optimization, sequential nano-based detoxification strategies, and bioproduct production. Biomass Convers. Biorefin., 27, 1–4. https://doi.org/10.1007/s13399-024-06127-7.

Călugăr, P. C., Coldea, T. E., Pop, C. R., Stan, L., Socaci, S. A., Ranga, F., Hegheș, S. C., Geană, E. I., Mudura, E., 2024. Effect of co-inoculation of *Saccharomyces* and non-*Saccharomyces* yeasts and nutrients addition during malolactic fermentation on apple cider composition. Food Biosci., 60, 104314. https://doi.org/10.1016/j.fbio.2024.104314.

Caspeta, L., Shoaie, S., Agren, R., Nookaew, I., Nielsen, J., 2012. Genome-scale metabolic reconstructions of *Pichia stipitis* and *Pichia pastoris* and in silico evaluation of their potentials. BMC Syst. Biol., 6, 24. https://doi.org/10.1186/1752-0509-6-24.

Chohan, N. A., Aruwajoye, G. S., Sewsynker-Sukai, Y., Kana, E. G., 2020. Valorisation of potato peel wastes for bioethanol production using simultaneous saccharification and fermentation: process optimization and kinetic assessment. Renew. Energy, 146, 1031–1040. https://doi.org/10.1016/j.renene.2019.07.042.

Devanthi, P. V. P., Linforth, R., Onyeaka, H., Gkatzionis, K., 2018. Effects of co-inoculation and sequential inoculation of *Tetragenococcus halophilus* and *Zygosaccharomyces rouxii* on soy sauce fermentation. Food Chem., 240, 1–8. https://doi.org/10.1016/j.foodchem.2017.07.094.

Diaz, J. T., Chinn, M., Truong, V. D., 2014. Simultaneous saccharification and fermentation of industrial sweet potatoes for ethanol production and anthocyanins extraction. Ind. Crops Prod., 62, 53–60. https://doi.org/10.1016/j.indcrop.2014.07.032.

Diez-Ozaeta, I., Lavilla, M., Amárita, F., 2022. Effect of inoculation strategy with autochthonous *Oenococcus oeni* strains on aroma development in Rioja Alavesa Tempranillo wines. LWT, 162, 113399. https://doi.org/10.1016/j.lwt.2022.113399.

Dodić, J. M., Vučurović, D. G., Dodić, S. N., Grahovac, J. A., Popov, S. D., Nedeljković, N. M., 2012. Kinetic modelling of batch ethanol production from sugar beet raw juice. Appl. Energy, 99, 192–197. https://doi.org/10.1016/j.apenergy.2012.05.016.

Eregie, S. B., Jamal-Ally, S. F., 2019. Comparison of biodegradation of lubricant wastes by *Scenedesmus vacuolatus* vs a microalgal consortium. Bioremediation J., 23, 277–301. https://doi.org/10.1080/10889868.2019.1671792.

Eregie, S. B., Sanusi, I. A., Kana, G. E., Ademola, O. O., 2023. Synergistic effect of process parameters and nanoparticles on spent lubricant oil waste biodegradation by UV-exposed *Scenedesmus vacuolatus*: process modelling, kinetics and degradation pathways. Bioresour. Technol. Rep., 24, 101627. https://doi.org/10.1016/j.biteb.2023.101627.

Galbraith, S. C., Bhatia, H., Liu, H., Yoon, S., 2018. Media formulation optimisation: current and future opportunities. Curr. Opin. Chem. Eng., 22, 42–47. https://doi.org/10.1016/j.coche.2018.08.004.

Gao, C. H., Cao, H., Cai, P., Sørensen, S. J., 2021. The initial inoculation ratio regulates bacterial coculture interactions and metabolic capacity. ISME J., 15, 29–40. https://doi.org/10.1038/s41396-020-00751-7.

Germec, M., Turhan, I., Karhan, M., Dermirci, A., 2019. Kinetic modeling and techno-economic feasibility of ethanol production from carob extract based medium in biofilm reactor. Appl. Sci., 9, 2121, 1–19. https://doi.org/10.3390/app9102121.

Gonçalves, F. A., Ruiz, H. A., dos Santos, E. S., Teixeira, J. A., de Macedo, G. R., 2016. Bioethanol production by *Saccharomyces cerevisiae*, *Pichia stipitis* and *Zymomonas mobilis* from delignified coconut fibre mature and lignin extraction according to biorefinery concept. Renew. Energy, 94, 353–365. https://doi.org/10.1016/j.renene.2016.03.045.

Govindaraju, I., Chakraborty, I., Baruah, V. J., Sarmah, B., Mahato, K. K., Mazumder, N., 2021. Structure and morphological properties of starch macromolecule using biophysical techniques. Starch-Stärke, 73(1–2), 2000030. https://doi.org/10.1002/star.202000030.

Guadalupe-Daqui, M. M., Goodrich-Schneider, R. M., Sarnoski, P. J., Carriglio, J. C., Sims, C. A., Pearson, B. J., MacIntosh, A. J., 2023. The effect of CO_2 concentration on yeast fermentation: rates, metabolic products, and yeast stress indicators. J. Ind. Microbiol. Biotechnol., 50(1), 1–9. https://doi.org/10.1093/jimb/kuad001.

Guo, X., Shu, S., Zhang, W., Hao, J., 2016. Synergetic degradation of corn cob with inorganic salt or hydrogen peroxide and electron beam irradiation. ACS Sustain. Chem. Eng., 4, 1099–1105. https://doi.org/10.1021/acssuschemeng.5b01168.

Hashem, M., Darwish, S. M. I., 2010. Production of bioethanol and associated by-products from potato starch residue stream by *Saccharomyces cerevisiae*. Biomass Bioenergy, 34, 953–959. https://doi.org/10.1016/j.biombioe.2010.02.003.

Izmirlioglu, G., Demirci, A., 2017. Simultaneous saccharification and fermentation of ethanol from potato waste by co-cultures of *Aspergillus niger* and *Saccharomyces cerevisiae* in biofilm reactors. Fuel, 202, 260–270. https://doi.org/10.1016/j.fuel.2017.04.047.

Izmirlioglu, G., Demirci, A., 2016. Improved simultaneous saccharification and fermentation of bioethanol from industrial potato waste with co-cultures of *Aspergillus niger* and *Saccharomyces cerevisiae* by medium optimisation. Fuel, 185, 684–691. https://doi.org/10.1016/j.fuel.2016.08.035.

Jia, L., Li, T., Yang, Z., Li, T., Ding, J., 2022. Enhancing monellin production in Pichia pastoris fed-batch fermentation through an efficient on-line methanol/sorbitol co-feeding strategy. J. Clean. Prod., 369, 133350. https://doi.org/10.1016/j.jclepro.2022.133350.

Jiang, S., Xu, P., Tao, F., 2019. L-Lactic acid production by *Bacillus coagulans* through simultaneous saccharification and fermentation of lignocellulosic corncob residue. Bioresour. Technol. Rep., 6, 131–137. https://doi.org/10.1016/j.biteb.2019.02.005.

Kaur, S., Kaur, K., Bhushan, B., Kaur, M., Hans, M., 2020. Inoculum size and age studies on single and mixed strain fermentation of grape juice. J. Pure Appl. Microbiol., 14(3), 2027–2036. https://doi.org/10.22207/JPAM.14.3.54.

Khawla, B. J., Sameh, M., Imen, G., Donyes, F., Dhouha, G., Raoudha, E. G., Oumèma, N. E., 2014. Potato peel as feedstock for bioethanol production: a comparison of acidic and enzymatic hydrolysis. Ind. Crops Prod., 52, 144–149. https://doi.org/10.1016/j.indcrop.2013.10.025.

Kordowska-Wiater, M., Targoński, Z., 2001. Ethanol production on the media containing glucose and xylose by coculture of *Pichia stipitis* CCY39501 and respiratory deficient mutant of *Saccharomyces cerevisiae* V30. Electron. J. Pol. Agric. Univ. Food Sci. Technol., 4(2), 15–28.

Lainez, M., Ruiz, H. A., Arellano-Plaza, M., Martínez-Hernandez, S., 2019. Bioethanol production from enzymatic hydrolysates of *Agave salmiana* leaves comparing *S. cerevisiae* and *K. marxianus*. Renew. Energy, 138, 1127–1133. https://doi.org/10.1016/j.renene.2019.02.058.

Li, X., Liu, S.-Q., 2021. Effect of co-inoculation and sequential inoculation of *Lactobacillus fermentum* and *Pichia kluyveri* on pork hydrolysates fermentation. Food Biosci., 44, 101400. https://doi.org/10.1016/j.fbio.2021.101400.

Liu, L., Zhang, Z., Wang, J., Fan, Y., Shi, W., Liu, X., Shun, Q., 2019. Simultaneous saccharification and co-fermentation of corn stover pretreated by H_2O_2 oxidative degradation for ethanol production. Energy, 168, 946–952. https://doi.org/10.1016/j.energy.2018.11.132.

Magocha, T. A., Zabed, H., Yang, M., Yun, J., Zhang, H., Qi, X., 2018. Improvement of industrially important microbial strains by genome shuffling: current status and future prospects. Bioresour. Technol., 257, 281–289. https://doi.org/10.1016/j.biortech.2018.02.118.

Mankar, A. R., Pandey, A., Modak, A., Pant, K. K., 2021. Pretreatment of lignocellulosic biomass: a review on recent advances. Bioresour. Technol., 334, 125235. https://doi.org/10.1016/j.biortech.2021.125235.

Miah, R., Siddiqa, A., Chakraborty, U., Tuli, J. F., Barman, N. K., Uddin, A., Aziz, T., Sharif, N., Dey, S. K., Yamada, M., Talukder, A. A., 2022. Development of high temperature simultaneous saccharification and fermentation by thermosensitive *Saccharomyces cerevisiae* and *Bacillus amyloliquefaciens*. Sci. Rep., 12(1), 3630. https://doi.org/10.1038/s41598-022-07589-3.

Mohapatra, S., Mishra, R. R., Nayak, B., Behera, B. C., Mohapatra, P. K. D., 2020. Development of co-culture yeast fermentation for efficient production of biobutanol from rice straw: a useful insight in valorization of agro-industrial residues. Bioresour. Technol., 318, 124070. https://doi.org/10.1016/j.biortech.2020.124070.

Moodley, P., Gueguim Kana, E. B., 2019. Bioethanol production from sugarcane leaf waste: effect of various optimised pre-treatments and fermentation conditions on process kinetics. Biotechnol. Rep., 24, e00329. https://doi.org/10.1016/j.btre.2019.e00329.

Nancib, N., Branlant, C., Boudrant, J., 1991. Metabolic roles of peptone and yeast extract for the culture of a recombinant strain of *Escherichia coli*. J. Ind. Microbiol., 8(3), 165–169. https://doi.org/10.1007/BF01575849.

Naseeruddin, S., Desai, S., Rao, V. L., 2021. Co-culture of *Saccharomyces cerevisiae* (VS3) and *Pichia stipitis* (NCIM 3498) enhances bioethanol yield from concentrated *Prosopis juliflora* hydrolysate. 3 Biotech., 11, 21. https://doi.org/10.1007/s13205-020-02595-6.

Nielsen, A. T., Tolker-Nielsen, T., Barken, K. B., Molin, S., 2000. Role of commensal relationships on the spatial structure of a surface-attached microbial consortium. Environ. Microbiol., 2, 59–68. https://doi.org/10.1046/j.1462-2920.2000.00084.x.

Okonkwo, C. C., Azam, M. M., Ezeji, T. C., Qureshi, N., 2016. Enhancing ethanol production from cellulosic sugars using *Scheffersomyces* (*Pichia*) *stipitis*. Bioprocess Biosyst. Eng., 39(7), 1023–1032. https://doi.org/10.1007/s00449-016-1580-2.

Phukoetphim, N., Salakkam, A., Laopaiboon, P., Laopaiboon, L., 2017. Kinetic models for batch ethanol production from sweet sorghum juice under normal and high gravity fermentations: logistic and modified Gompertz models. J. Biotechnol., 243, 69–75. https://doi.org/10.1016/j.jbiotec.2016.12.012.

Raina, N., Slathia, P. S., Sharma, P., 2020. Experimental optimisation of thermochemical pretreatment of sal (Shorea robusta) sawdust by Central Composite Design study for bioethanol production by co-fermentation using *Saccharomyces cerevisiae* (MTCC-36) and *Pichia stipitis* (NCIM-3498). Biomass Bioenergy, 143, 105819. https://doi.org/10.1016/j.biombioe.2020.105819.

Richardson, T. L., Harner, N. K., Bajwa, P. K., Trevors, J. T., Lee, H., 2011. Approaches to deal with toxic inhibitors during fermentation of lignocellulosic substrates. In: Zhu, J., Zhang, X., Pan, X. J. (Eds.), Sustainable Production of Fuels, Chemicals, and Fibers from Forest Biomass. ACS Symposium Series, American Chemical Society, Washington, DC, 1067, 171–202. https://doi.org/10.1021/bk-2011-1067.ch007.

Rorke, D. C. S., Gueguim Kana, E. B., 2017. Kinetics of bioethanol production from waste sorghum leaves using *Saccharomyces cerevisiae* BY4743. Fermentation, 3, 19. https://doi.org/10.3390/fermentation3020019.

Rouhollah, H., Iraj, N., Giti, E., Sorah, A., 2007. Mixed sugar fermentation by *Pichia stipitis*, *Saccharomyces cerevisiae*, and an isolated xylose fermenting *Kluyveromyces marxianus* and their cocultures. Afr. J. Biotechnol., 6, 1110–1114. https://doi.org/10.5897/AJB2007.000-2144.

Sanchez-Cuasapud, D. D. R., Botero-Botero, L. R., Hincapié-Pérez, M., 2024. Inoculation and microelements: two important factors for enhanced conidiogenesis of *Trichoderma asperellum* in solid and liquid fermentation. Rev. Fac. Nac. Agron. Medellín, 77(1), 10601–10609. https://doi.org/10.15446/rfnam.v77n1.108175.

Santosh, I., Ashtavinayak, P., Amol, D., Sanjay, P., 2017. Enhanced bioethanol production from different sugarcane bagasse cultivars using co-culture of *Saccharomyces cerevisiae* and *Scheffersomyces* (*Pichia*) *stipitis*. J. Environ. Chem. Eng., 5, 2861–2868. https://doi.org/10.1016/j.jece.2017.05.045.

Sanusi, A. I., Suinyuy, T. N., Kana, G. E. B., 2021. Impact of nanoparticle inclusion on bioethanol production process kinetic and inhibitor profile. Biotechnol. Rep., 29, e00585. https://doi.org/10.1016/j.btre.2021.e00585.

Sanusi, I., Suinyuy, T. N., Lateef, A., Gueguim Kana, E. B., 2020. Effect of nickel oxide nanoparticles on bioethanol production: process optimisation, kinetic and metabolic studies. Process Biochem., 92, 386–400. https://doi.org/10.1016/j.procbio.2020.01.029.

Sanusi, I. A., Faloye, F. D., Gueguim Kana, E. B., 2019. Impact of various metallic oxide nanoparticles on ethanol production by *Saccharomyces cerevisiae* BY4743: screening, kinetic study and validation on potato waste. Catal. Lett., 149, 2015–2031. https://doi.org/10.1007/s10562-019-02796-6.

Sasikumar, E., Viruthagiri, T., 2008. Optimisation of process conditions using response surface methodology (RSM) for ethanol production from pretreated sugarcane bagasse: kinetics and modeling. Bioenergy Res., 1, 239–247. https://doi.org/10.1007/s12155-008-9018-6.

Sathendra-Elumalai, R., Ramanujam, P., Tawfik, M. A., Ravichandran, P., Gurunathan, B., 2023. Optimisation and kinetics modelling for enhancing the bioethanol production from

banana peduncle using *Trichoderma reesei* and *Kluyveromyces marxianus* by co-pretreatment methods. Sustain. Energy Technol. Assess., 56, 103129. https://doi.org/10.1016/j.seta.2023.103129.

Sewsynker-Sukai, Y., Gueguim-Kana, E. B., 2018. Simultaneous saccharification and bioethanol production from corn cobs: process optimisation and kinetic studies. Bioresour. Technol., 262, 32–41. https://doi.org/10.1016/j.biortech.2018.04.056.

Sharma, S., Jha, P. K., Panwar, A., 2021. Production of bioethanol from wheat straw via optimisation of co-culture conditions of *Bacillus licheniformis* and *Saccharomyces cerevisiae*. Discov. Energy, 1, 1–8. https://doi.org/10.1007/s43937-021-00004-4.

Singh, A., Bajar, S., Bishnoi, N. R., 2014. Enzymatic hydrolysis of microwave alkali pretreated rice husk for ethanol production by *Saccharomyces cerevisiae*, *Scheffersomyces stipitis* and their co-culture. Fuel, 116, 699–702. https://doi.org/10.1016/j.fuel.2013.08.072.

Sluiter, A., Hames, B., Ruiz, R., Scarlata, C., Sluiter, J., Templeton, D., Crocker, D., 2008. Determination of structural carbohydrates and lignin in biomass. Technical Report NREL/TP-510-42618. National Renewable Energy Laboratory.

Song, Y., Cho, E. J., Park, C. S., Oh, C. H., Park, B. J., Bae, H. J., 2019. A strategy for sequential fermentation by *Saccharomyces cerevisiae* and *Pichia stipitis* in bioethanol production from hardwoods. Renew. Energy, 139, 1281–1289. https://doi.org/10.1016/j.renene.2019.03.032.

Teoh, Y., Ooi, Z., 2016. Evaluation of unstructured kinetic models for the production of bioethanol from banana and pineapple wastes. Bioresources, 11, 4295–4305. https://doi.org/10.15376/BIORES.11.2.4295-4305.

Thakur, M., Rai, A. K., Mishra, B. B., Singh, S. P., 2021. Novel insight into valorisation of potato peel biomass into type III resistant starch and maltooligosaccharide molecules. Environ. Technol. Innov., 24, 101827. https://doi.org/10.1016/j.eti.2021.101827.

Tian, S.-Q., Zhao, R.-Y., Chen, Z.-C., 2018. Review of the pretreatment and bioconversion of lignocellulosic biomass from wheat straw materials. Renew. Sustain. Energy Rev., 91, 483–489. https://doi.org/10.1016/j.rser.2018.03.113.

Vanmarcke, G., Demeke, M. M., Foulquié-Moreno, M. R., Thevelein, J. M., 2021. Identification of the major fermentation inhibitors of recombinant 2G yeasts in diverse lignocellulose hydrolysates. Biotechnol. Biofuels, 14, 92. https://doi.org/10.1186/s13068-021-01935-9.

Wimonsong, P., Nitisoravut, R., 2015. Comparison of different catalysts for fermentative hydrogen production. J. Clean Energy Technol., 3(2), 128–131. https://doi.org/10.7763/JOCET.2015.V3.181.

Wu, Y., Wen, J., Wang, K., Su, C., Chen, C., Cui, Z., Cai, D., Cheng, S., Cao, H., Qin, P., 2023. Understanding the dynamics of the *Saccharomyces cerevisiae* and *Scheffersomyces stipitis* abundance in co-culturing process for bioethanol production from corn stover. Waste Biomass Valor., 14, 43–55. https://doi.org/10.1007/s12649-022-01861-3.

Yadav, S. K., Naseeruddin, S., Prashanthi, G. S., Sateesh, L., Venkateswar-Rao, L., 2011. Bioethanol fermentation of concentrated rice straw hydrolysate using co-culture of *Saccharomyces cerevisiae* and *Pichia stipitis*. Bioresour. Technol., 102, 6473–6478. https://doi.org/10.1016/j.biortech.2011.03.019.

Yang, Z., Zhang, Z., 2018. Production of (2R,3R)-2,3-butanediol using engineered Pichia pastoris: strain construction, characterization and fermentation. Biotechnol. Biofuels, 11, 35. https://doi.org/10.1186/s13068-018-1031-1.

Zhang, C., Dong, L., Wu, J., Qiao, S., Xu, W., Ma, S., Zhao, B., Wang, X., 2020. Intervention of resistant starch 3 on type 2 diabetes mellitus and its mechanism based on urine metabonomics by liquid chromatography–tandem mass spectrometry. Biomed. Pharmacother., 128, 110350. https://doi.org/10.1016/j.biopha.2020.110350.

Zhu, J. Q., Zong, Q. J., Li, W. C., Chai, M. Z., Xu, T., Liu, H., Fan, H., Li, B. Z., Yuan, Y. J., 2020. Temperature profiled simultaneous saccharification and co-fermentation of corn stover increases ethanol production at high solid loading. Energy Convers. Manag., 205, 112344. https://doi.org/10.1016/j.enconman.2019.112344.

Zhu, X., Torija, M. J., Mas, A., Beltran, G., Navarro, Y., 2021. Effect of a multistarter yeast inoculum on ethanol reduction and population dynamics in wine fermentation. Foods, 10(3), 623. https://doi.org/10.3390/foods10030623.

CHAPTER 7

Process pilot scale-up and kinetic evaluation of co-fermentation of detoxified pretreated potato peel hydrolysate for sustainable bioethanol production

This chapter has been submitted to *Frontiers in Microbiology* journal with the title: Process scale-up and kinetic evaluation of co-fermentation of *Saccharomyces cerevisiae* and *Pichia stipitis* for sustainable bioethanol production from detoxified pretreated potato peel hydrolysate.

Process pilot scale-up and kinetic evaluation of co-fermentation of detoxified pretreated potato peel hydrolysate for sustainable bioethanol production

Adeniyi P. Adebule, Isaac A. Sanusi, E.B. Gueguim Kana*

[1]University of KwaZulu-Natal, School of Biological Sciences (Microbiology), Pietermaritzburg Campus, Private Bag X01, Scottsville 3209, South Africa

Abstract

This study explored the scale-up and kinetic dynamics of simultaneous saccharification and co-fermentation (SSCF) of bioethanol from detoxified PPW hydrolysate using the co-culture of *Saccharomyces cerevisiae* and *Pichia stipitis*. The 13L pilot-scale bioreactor was operated at a rotational speed of 1.58 rps, with an impeller tip speed (V_{tip}) of 0.35 m/s, and a power input of 0.012W, closely replicating the hydrodynamic conditions of the 2L laboratory-scale bioreactor operated at 2.0 rps, V_{tip} of 0.35 m/s, and 0.012W. This resulted in high bioethanol concentration (43.62 g/L), yield (0.472 g/g), and conversion efficiency (92.4%), which significantly reduced specific power consumption to 1.2 W/m³. The power consumption per unit volume (P/V_L) was 10-fold lower compared to the P/V_L obtained in the 2 L bioreactor. Meanwhile, a 0.79-fold decrease in shear stress was achieved in pilot pilot-scale bioreactor, resulting in low cell damage. The kinetic models implemented fitted the experimental data for the cell biomass production, bioethanol production, and substrate utilization, with coefficient of determination (R^2) close to 1. The bioethanol production was predominantly growth-associated, as indicated by higher α (g ethanol/g substrate) than β (g ethanol/g substrate/h) values. Furthermore, the derived nutrient-rich effluent, with a high total organic carbon (TOC) content (78% g/g), holds potential for cultivating microalgae. These findings provided valuable insights for industrial bioprocesses design and optimizing large-scale sustainable bioethanol production, and the downstream valorisation potentials of fermentation effluents.

Keywords: **Bioethanol, Co-fermentation, Detoxification, Kinetics, Process Scale-up.**

Abbreviations

μ_{max}	Maximum specific growth rate (h^{-1})
X_o	Initial cell concentration (g/L)
X_{max}	Maximum cell concentration (g/L)
P_m	Maximum potential bioethanol concentration
$r_{p,m}$	Maximum bioethanol production rate (g/L/h),
t_L	Lag time (h)
A	Growth associate constant (g P/g X)
β	Non-growth associate constants (g P/g X. h)
Γ	Substrate utilisation coefficient (g S/g X)
Δ	Maintenance coefficient (g S/g X. h)
BY	Bioethanol yield (g/g)
BC	Bioethanol concentration (g/L)
BP	Bioethanol productivity (g/L/h)
FPE	Fermentation process efficiency (%)
LM	Logistic model
LPM	Leudeking-Piret model
MGM	Modified Gompertz model
MLPM	Modified Leudeking-Piret model
MSE	Mean-square-error
PPW	Potato peel waste
RMSE	Root-mean-square-error
SSCF	Simultaneous saccharification and co-fermentation
TOC	Total organic carbon
TSU	Total sugar utilisation (%)

7.1. Introduction

Amidst the growing demand for decarbonization, the global shift toward renewable biofuels, and the pursuit of a sustainable bioeconomy, the production of low-carbon liquid biofuels, particularly bioethanol, has attracted substantial research and industrial interest (Olughu et al., 2023). Bioethanol, as a leading global biofuel, offers significant functional and environmental benefits, positioning it as a compelling alternative to fossil-derived gasoline due to its high combustion efficiency, high octane number, and reduced greenhouse gas emissions (Bello et al., 2020). Moreover, in economic terms, the global bioethanol market size is predicted to reach approximately USD 174.98 billion by 2034, expanding at a Compound Annual Growth Rate (CAGR) of 5.12% from 2024 to 2034 (Bidwai and Shivarkar, 2024). Highlighting the urgent need for large scale waste-based bioethanol production. These waste residues such as potato peel waste possess significant potential for large scale bioconversion of waste into bioethanol and other high-value bioproducts and have thus attracted growing global attention in recent decades (Chohan et al., 2020; Sanusi et al., 2021; FAO, 2024; Sanusi et al., 2024; Mushtaq et al., 2024; Adebule et al., 2024).

Despite significant progress in laboratory-scale bioethanol production, the economic feasibility and environmental sustainability of scaling up potato peel waste (PPW)-to-ethanol bioprocesses require thorough and systematic evaluation (Mohit et al., 2024). In principle, the design of industrial-scale microbial fermentation processes is fundamentally dependent on a complex interplay of factors, including growth conditions, nutrient formulation, target product, microbial strain's cellular machinery (gene functions, enzyme kinetics), bioreactor geometry, and fluid dynamics.

However, during process scale-up, microbial fermentation systems are often subjected to altered physical conditions, such as fluid dynamics, oxygen and heat transfer limitations, inhomogeneous nutrient distributions, and variations in shear stress, which negatively impact cell physiology and metabolic performance, hindering optimal process performance. For example, insufficient mixing in large-scale stirred tank reactors might cause localized zones of substrate depletion or accumulation of inhibitory metabolites, resulting in metabolic shifts that compromise bioethanol yield and productivity (Kumar et al., 2024). Addressing these scale-up challenges requires a deep understanding of both the microbial response to biophysical changes and the fluid dynamic behaviour of the bioreactor system for fast-tracking the transition from laboratory-scale to industrial scale (Torrelas et al., 2023).

Commonly employed scale-up criteria in fermentation processes include constant specific power input (P/V), constant volumetric mass transfer coefficient (kLa), constant impeller tip speed (shear), and constant mixing time. These factors are intricately related to mass transfer, mixing activity, power consumption, bulk rheology, cell viability, and nutrient availability within the bioreactor (de Mello et al., 2024). Also, scaling up a bioprocess can significantly impact process kinetics and, consequently, affect process productivity. Therefore, an in-depth understanding of the process kinetics (such as logistic kinetic, Modified Gompertz and Luedeking-Piret models) of cell growth, bioethanol formation, and substrate utilization is imperative for bioprocess design, optimization, and scaling up (Du et al., 2022; Germec et al., 2022; Adebule et al., 2025).

To the best of our knowledge, there is a dearth of comprehensive reports on the scaling up of bioethanol production by co-fermentation of *S. cerevisiae* and *P. stipitis* using Fe_3O_4 nanoparticle-detoxified, pretreated potato peel waste (PPW) hydrolysate, particularly coupled with an in-depth kinetic evaluation. This study, therefore, evaluate the potential transition from laboratory-scale to pilot scale in co-fermentation SSF-based bioethanol production using Fe_3O_4 nanoparticle-detoxified pretreated PPW hydrolysate. In addition, kinetic models (including the Logistic, Modified Gompertz, and Luedeking-Piret equations) were developed and validated to understand as well as predict metabolic activities of *S. cerevisiae* and *P. stipitis* co-cultures during the co-fermentation process. Finally, the potential for downstream beneficiation of the fermentation effluent was explored through compositional analysis.

7.2. Materials and methods

7.2.1. Sample preparation

The potato peel waste (PPW) used in the study was collected from food vendors in the Pietermaritzburg metropolitan area, KwaZulu-Natal province, South Africa. The peels were immediately dried at 50-55°C for 48 h in a laboratory oven (Scientific series 2000, South Africa) and thereafter milled to a particle size of 1-2 mm using a centrifugal miller (Retsch ZM-1, South Africa). The composition analysis of milled potato peel wastes reveals 52% starch, 14% structural carbohydrate, 4% cellulose, 10% hemicellulose, 6% lignin, 13.21% crude protein, 10.76% ash, and 0.43% fat. The Fe_3O_4 nanoparticle used for the study was prepared by co-precipitation using the method of Prochazkova et al. (2013) and characterized as outlined in Adelabu et al. (2024).

7.2.2. Pretreatment of potato peel waste and hydrolysate detoxification

The milled PPW were pretreated using optimised process parameters previously reported by Aruwajoye et al. (2017), and the detoxification of inhibitors (such as furfural, 5-hydroxymethyl furfural, phenolic compounds, formaldehyde, and acetic acid) from the pretreated hydrolysate was carried out using the protocol detailed in Adebule et al. (2024). For the pretreatment, 0.92% (v/v) HCl solution with 10% PPW solid loading was soaked in a water bath without shaking at 69.6°C for 2.34 h, then autoclaved for 5 minutes at 121°C. The detoxification conditions implemented were Fe_3O_4 NP concentration (0.021 w/v%), temperature (35.37 °C), contact time (12.74 min), and pH (4.14), resulting in 40% (furfural), 24% (HMF), 69% (acetic acid), 49% (phenol), and 35% (formaldehyde) simultaneous removal from pretreated PPW hydrolysate. The resultant detoxified hydrolysate was thereafter channelled for the present study.

7.2.3. Liquefaction process

The liquefaction process was performed in 250 mL Schott bottles (100 mL working volume). At the onset of the liquefaction process, the pH of the detoxified pretreated PPW hydrolysate was adjusted to neutral (pH 7), followed by the addition of 0.212 mL (125 Unit/g) amylase (Sigma-Aldrich, South Africa) loading, which was selected based on our previous optimisation studies (Sanusi et al., 2021). The slurry was later incubated at 90 °C and at 100 rpm for 60 min. This was followed by a denaturation step, during which the slurry mixture was heated to 96 °C for 10 min and subsequently cooled to room temperature.

7.2.4. Inoculum preparation

S. cerevisiae and the yeast *P. stipitis* were obtained from the Department of Microbiology, University of KwaZulu-Natal (Pietermaritzburg), South Africa. Activation of the *S. cerevisiae* and *P. stipitis* were conducted by incubating them separately in yeast peptone dextrose (YPD) (100 mL) media (containing (g/L); yeast extract,10; peptone, 20 and glucose, 20) and yeast peptone xylose plus (YPXmeth) (100 mL) media (containing (g/L); yeast extract, 20; peptone, 30; xylose, 20; dipotassium hydrogen phosphate (KH_2PO_4), 0.05 and methanol, 1 %v/v) were incubated at 30 ºC and 120 rpm for 24– 48 h of incubation time. The cultures were cultivated separately in 250 mL Erlenmeyer flasks containing 100 mL of YPD and YPXmeth medium (pH 5–6) until the OD values reached approximately 0.600 to 0.870 at OD600 and OD610 nm, corresponding to around 2.0×10^6 to 3.0×10^6 cells/mL respectively.

7.2.5. Simultaneous saccharification and co-fermentation (SSCF) for bioethanol production

The SSCF processes were carried out in 2 L (Bio/CelliGen 115, New Brunswick, USA) and 13 L (Labfors-INFORS HT, Switzerland) bioreactors under anaerobic environments with working volumes of 1 L and 10 L, respectively. The detoxified pretreated hydrolysate PPW and fermentation nutrient broth were fed to the sterilized bioreactors. Subsequently, 15 Unit/g of amyloglucosidase (Sigma-Aldrich, South Africa) and 10% v/v seed culture (containing a ratio of 1 to 4 of *S. cerevisiae* to *P. stipitis*) were added to the bioreactors containing the liquified detoxified pretreated hydrolysate PPW and fermentation nutrient broth, to initiate the simultaneous saccharification and fermentation. The nutrient broth contains yeast extract (5 g/L), KH_2PO_4 (2 g/L), $MgSO_4$ (1 g/L) and $(NH_4)_2SO_4$ (1 g/L) All the SSCF experiments were performed in replicate at 35 °C and 120 rpm for a 24 h incubation time for each batch culture as described below:

(i) 1 L batch system: Hydrolysate from the liquefied detoxified pretreated potato peels (500 mL containing 100 g of pretreated substrate) and nutrient broth (400 mL containing nutrients for a litre working volume) were fed to the sterilised bioreactor and then inoculated with 100 mL (i.e. 10% v/v) seed culture containing 20 mL of *S. cerevisiae* and 80 mL of *P. stipitis*, making up a 1:4 ratio. This was followed by fermentation at an optimal pH (5.8) and temperature (35 °C) for 24 h. Two (2) fixed Rushton turbine blade disk impellers provided agitation at 120 rpm (2 rps), circulation time (t_c) of 4.35 s, while utilising 0.012 W Power and 1.2 W/m^3 [Power to Volume ratio (P/V_L)].

ii) 10 L batch system: The fermentation broth comprised of the liquefied detoxified pretreated potato peels hydrolysate (5L containing 1kg of the pretreated substrate), and nutrient broth (4 L containing nutrients for a 10-litre working volume) was fed to the sterilised bioreactor and then inoculated with 1L (10% v/v) *S. cerevisiae* and *P. stipitis* seed culture at ratio 1:4. The fermentation was carried out at pH 5.8, temperature 35 ◦C and an agitation of 95 rpm (1.58 rps).

7.2.6. Scale-up parameters

7.2.6.1. Bioreactor geometric and mechanical specifications

The key structural and geometric characteristics of the two bioreactor systems used in this study are presented in Table 7.1. Both scales of the stirred-tank reactor were fitted with Rushton-type turbine impellers. The 2.0 L bioreactor vessel was operated at a working volume of 1.0 L, while

the pilot-scale unit has a working volume of 10 L (13 L total capacity), translating to 50–80% of the maximum volume to maintain similar liquid height-to-diameter ratios and mixing regimes across scales. Each reactor is a right circular cylinder of height h and internal diameter D. The 2L bioreactor measures a height (h) of 0.237 m and a diameter (D) of 0.125 m, yielding a height-to-diameter ratio (h/D) of 0.75:1, and static height (H) of the culture broth within this reactor was 0.09 m, whereas the pilot-scale bioreactor (13L) unit measures h = 0.427 m and D = 0.200 m (h/D = 1.63:1), and a static broth height of 0.326 m. The 2L-bioreactor impeller diameter is *di* = 0.054 m (t = 0.001 m), and the pilot-scale is *di* = 0.070 m (t = 0.002 m). The dimensionless impeller-to-vessel diameter ratio (*di/D*) is maintained at 0.43 (2L-bioreactor) and 0.35 (pilot-scale bioreactor).

Table 7.1. Bioreactor geometry employed in the co-fermentation processes.

Bioreactor configurations	**2 L bioreactor**	**13 L bioreactor**
Bioreactor capacity (m^3)	0.002	0.013
Working volume (m^3)	0.001	0.01
Bioreactor height [h] (m)	0.237	0.427
Bioreactor diameter [D] (m)	0.125	0.200
Static height of broth [H] (m)	0.09	0.326
Number of impellers (N)	2	2
Impeller diameter [di] (m)	0.054	0.070
Impeller thickness (m)	0.001	0.002
Geometric factor (fc)	0.633	0.857
Geometric number	0.432	0.350
Geometric ratio (h/D)	0.75:1	1.63:1
Power number (N_p)	5.20	10.40
Volume number (N_v)	0.512	1.25
Broth density [ρ] (kg/m^3)	1025	1025
Broth viscosity [η] (Pa s)	4.9×10^{-2}	4.9×10^{-2}
Kinematic viscosity [*v*] (m^2/s)	4.73×10^{-5}	4.73×10^{-5}
Impeller type	Rushton turbine	Rushton turbine

7.2.6.2. Bioreactor hydrodynamic and rheological properties

The fermentation broth was characterised by a density (ρ) of 1025 kg/m³ and a viscosity (η) of 4.9×10^{-2} Pa s, resulting in a kinematic viscosity (v) of $4.73\times10^{-5}m^2/s$ for both systems. Geometric factors (f_c) of 0.633 (2L bioreactor) and 0.857 (13L pilot-scale bioreactor) were calculated using standard mixing correlations. The power number (*NP*) of 5.20 (2 L bioreactor) and 10.40 (13 L bioreactor) inform the power requirement per unit volume (P/V_L) under turbulent conditions. Meanwhile, the fermenting media uninoculated with either of the organisms, subjected to the same conditions as per the corresponding test experiments, served as the control. The sample's aliquots were routinely withdrawn aseptically from each experimental setup at regular intervals (3 hours) for analytical purposes. The sample was centrifuged (10,000 rpm, 5 min, 4°C), and the supernatant was then used for determining bioethanol, biomass, and sugar concentrations.

7.2.6.3. Determination of scale-up parameters

The parameters (Table 7.2) used for the bioreactors at both scales were constant power consumption per unit volume (P/V_L), impeller tip speed (V_{tip}), Reynolds' number, impeller pumping capacity (V_P), fluid circulation time (t_c), scale of turbulence determination (λ) and shear stress (γ).

7.2.6.3.1. Constant impeller tip speed (V_{tip}) and constant power consumption

Constant impeller tip speed refers to maintaining a fixed linear velocity during mixing or agitation processes. It also elucidates the relationship between shear stress and microbial cells (Marques et al., 2010; Lemire et al., 2022). The V_{tip} (using Eq. 7.1) is directly proportional to the product of impeller speed and the impeller diameter (Pérez et al., 2018). Meanwhile, the power consumption per unit of volume was calculated according to Eq. 7.2,

$$v_{tip} = \pi din \quad \text{(Eq. 7.1)}$$

$$Power\ consumption = \frac{P}{V_L} \quad \text{(Eq. 7.2)}$$

Table 7.2. Rheology and hydrodynamic parameters of fermentation criteria.

Parameters	2 L bioreactor	13 L bioreactor
Rotational speed [n] (rpm/rps)	120/2	95/1.58
Impeller tip speed [V_{tip}] (m/s)	0.34	0.35
Power [P] (W)	0.012	0.012
Power consumption [P/V_L] (W/m^3)	12	1.2
Pumping capacity [V_P] (m^3/s)	2.3×10^{-4}	3.9×10^{-4}
Fluid circulation time [t_c] (s)	4.35	25.64
Energy dissipation rate [ε] (m^2/s^3)	1.17×10^{-2}	1.17×10^{-3}
Kolmogorov scale of turbulence [λ] (m)	1.73×10^{-3}	3.08×10^{-3}
Shear rate [γ] (s^{-1})	20	15.8
Shear stress [τ] (Pa)	0.98	0.7742
Froude number	0.022	0.018

7.2.6.3.2. Pumping capacity

The impeller pumping capacity (V_P) represents the volume of liquid discharged by the stirrer per unit time (m^3/ s). This was determined using Eq. 7.3 (Qazizada, 2016).

$$V_p = N_f n di^3 \quad \text{(Eq. 7.3)}$$

Where N_f is the flow number ($N_f = 0.72$ for Rushton turbine and low viscosity fluid), *di* is the impeller diameter, and *n* is the impeller speed.

7.2.6.3.3. Fluid circulation time

Fluid circulation time (t_c) is a function of the volume of the liquid phase (V_L) and pumping capacity (V_P). This was determined using Eq. 7. 4 below.

$$t_c = {}^{V_L}/_{V_P} \quad \text{(Eq. 7.4)}$$

7.2.6.3.4. Scale of turbulence determination

The degree of turbulence within the bioreactor directly affects broth homogeneity and fluid-phase mass transfer efficiency, which is governed by the energy dissipation caused by eddy formation and breakup. The scale of turbulence, reflecting the smallest eddies that contribute to effective mixing and mass transfer, was estimated using the Kolmogorov microscale (λ).

This parameter is a function of the energy dissipation rate per unit mass (ε), which in turn is related to the specific power input (P/V_L). The scale of turbulence Kolmogorov microscale (λ) was estimated using Eq. 7.5.

$$\lambda=\nu^{3}\varepsilon^{1/4} \quad \text{(Eq. 7.5)}$$

where λ = Kolmogorov microscale, ν = kinematic viscosity, ε= energy dissipation rate (ε) (i.e. turbulence energy per unit mass of liquid). Note that $\varepsilon=([N_p \rho n^3 di^5]/V)$, where N_p is the power number (dimensionless), 'n' impeller speed (rps), 'd_i' impeller diameter, and 'V' working volume of the liquid (m^3)

7.2.6.3.5. Shear rate (γ) and shear stress (τ)

The shear rate resulting from the mixing system was obtained by Eq. 7.6, where n is the mixing speed (rps) and k is the geometric constant for a standard Rushton impeller (k = 10 for Rushton turbine). Other the other hand, the shear stress (τ) in a bioreactor is the force per unit area exerted on fluid elements, arising from the friction of adjacent fluid layers moving at different velocities. For Newtonian fluids, shear stress can be estimated using Eq. 7.7.

$$\gamma=kn \quad \text{(Eq. 7.6)}$$

$$\tau=\mu\gamma \quad \text{(Eq. 7.7)}$$

Where τ is the shear stress (Pa), μ is the dynamic viscosity of the fluid (Pa·s), $\dot{\gamma}$ is the shear rate (s^{-1})

7.2.6.3.6. Non-dimensional bioreactor configuration

The dimensionless numbers were calculated using Eqs. 7.8 to 7.10. Froude number expresses the ratio of centrifugal to gravitational forces, while the volume number and the geometric number depict the ratio of impeller diameter to bioreactor diameter in relation to the filling volume.

$$Froude\ number\ (Fr) = \frac{n^2 \cdot d_o}{g} \quad \text{(Eq. 7.8)}$$

$$V\ olume\ number\ (N_v) = V_L/d^3 \quad \text{(Eq. 7.9)}$$

$$Geometric\ number\ (Ng) = d_o/d \quad \text{(Eq. 7.10)}$$

Where d (m) is the bioreactor diameter, d_o (m) the agitation diameter, n (s^{-1}) the shaking frequency, V_L (m^3) the liquid volume, and g (m/s^2) the gravitational acceleration.

7.2.7. Analytical methods

Biomass concentration (g/L) was determined for both *S. cerevisiae* and *P. stipitis* by relating their spore counts to the dry cells' weight using a pre-determined standard curve (Sanusi et al., 2019; Adebule et al., 2025). Reducing sugar content per litre was determined using the 3,5–dinitro salicylic acid method (Bishop et al., 2024), xylose concentrations (g/L) were determined using Megazyme xylose kit (©Megazyme, Wicklow, Ireland), while the glucose concentration was equal to the difference between the total sugar concentration and the xylose concentration (Liu et al., 2019). The viscosity and density of the broth were determined as described by Pérez et al. (2018) and Deniz et al. (2015), respectively. All determinations were carried out in replicate. Bioethanol concentration was measured in the gaseous phase using an ethanol vapour sensor (ETH-BTA, Vernier Software and Technology, Beaverton, USA). Moreover, bioethanol yield, productivity, sugar utilization, and fermentation efficiency were calculated using Equations 7.11–7.14 (Table 7.3).

7.2.8. Process kinetic modelling and validation

The process kinetic model was subsequently performed through non-linear regression analysis using Microsoft Excel Solver™ (Ms Solver™) (Adebule et al., 2025), based on Equations 7.15–7.19 (Table 7.3). The specific growth rates (μ) of the fermenting microbes were calculated using Equation 7.15, where X_2 and X_1 are biomass dry weights (g/L) at t_2 and t_1, respectively. The logistic model equation (Eq. 7.16) was used to define the correlation of cell dry weight (X) at a definite time (t) during active cell growth and static phases of cell growth to initial cell dry weight (X_0), maximum cell dry weight (X_{max}) and maximum specific growth rate (μ_{max}). The experimental data of the bioethanol production over time were fitted into the modified Gompertz model (MGM) and the Leudeking-piret model (LPM). The MGM relates the bioethanol concentration (P) to the production lag time (t_L), the maximum bioethanol production rate ($r_{p,m}$), and the potential maximum bioethanol concentration (P_m), in the period from the start of the fermentation process to the exponential phase of bioethanol production (h) as shown in Eq. 7.17. The LPM (Eq. 7.18) function by relating rate of product formation to the total biomass concentration (X) and the growth rate (μ). The substrate utilisation kinetics were estimated using the modified Luedeking-Piret (MLP) model (Eq. 7.19), which accounts for substrate conversion to the cell mass and product as well as the substrate consumption for cellular maintenance.

Table 7.3. Parameters for scaling up of bioethanol production from detoxified pretreated potato peel waste

Parameters	Formula	Equation
Bioethanol yield (BY) (g/g)	$\frac{Maximum\ ethanol\ \ concentration\ \left(\frac{g}{L}\right)}{Utilized\ sugar\ (g/L)}$	**7.11**
Bioethanol productivity (BP)((g/L)/h)	$\frac{Maximum\ ethanol\ concentration\ \left(\frac{g}{L}\right)}{Fermentation\ period\ (h)}$	**7.12**
Fermentation process efficiency (FPE) (%)	$\frac{Maximum\ ethanol\ concentration\ \left(\frac{g}{L}\right)}{\text{Theoretical yield}\ \left(\frac{g}{L}\right)} \times 100$	**7.13**
Sugar utilisation (GU) (%)	$\frac{Initial\ sugar\ content - final\ sugar\ content}{Initial\ sugar\ content} \times\ 100$	**7.14**
Specific growth rate (μ)	$(\mu) = \frac{\ln X_2 - \ln X_1}{t_2 - t_1}$	**7.15**
Logistic model	$X = \frac{X_0 . \exp(\mu_{max} . t)}{1 - \left(\frac{X_0}{X_{max}}\right) . (1 - exp(\mu_{max} . t))}$	**7.16**
Modified Gompertz model	$P = P_m \,.\exp\left\{-\exp\left[\frac{r_{p.m}\,.\exp(1)}{P_m}\right].(t_L - t) + 1\right\}$	**7.17**
Luedeking-Piret (MLP) model	$P = P_0 + aX_0\left(\frac{\exp(\mu_{max}\cdot t)}{1 - \left(\frac{X_0}{X_{max}}\right)\cdot(1 - \exp(\mu_{max}\cdot t))} - 1\right) + \beta\frac{x_{max}}{\mu_{max}} ln\left(1 - \frac{X_0}{x_{max}}(1 - e^{u_{max}t})\right)$	**7.18**
Modified Luedeking-Piret (MLP) model	$S = S_0 - \gamma X_0\left(\frac{\exp(\mu_{max}\cdot t)}{1 - \left(\frac{X_0}{X_{max}}\right)\cdot(1 - \exp(\mu_{max}\cdot t))} - 1\right) + \delta\frac{X_{max}}{\mu_{max}} ln\left(1 - \frac{X_0}{X_{max}}(1 - e^{u_{max}t})\right)$	**7.19**

Notably, the root-mean-square error (RMSE), mean-square error (MSE), and regression coefficient (R^2) are standard statistical metrics for evaluating model performance and fitness. Therefore, the RMSE (Equation 7.20) and MAE (Equation 7.21) were used to validate these models.

$$\text{RMSE} = \sqrt{\frac{1}{n}\sum_{t=1}^{n}(x_t - y_t)^2}, \qquad t = 1, 2, 3, \ldots\ldots\ldots\ldots\ldots\ldots.., n \qquad \text{(Eq. 7.20)}$$

$$\text{MAE} = \left(\frac{1}{n}\sum_{t=1}^{n}|x_t - y_t|\right), \qquad t = 1, 2, 3, \ldots\ldots\ldots\ldots\ldots\ldots.., n \qquad \text{(Eq. 7.21).}$$

7.2.9. Elemental analysis of SSCF process effluent

For the elemental analysis, the bioethanol fermentation effluent was prepared by filtering through a 0.45 µm nylon filter syringe prior to analysis. The concentrations of Ca, K, Na, Mg, and P were tested using Inductively Coupled Plasma Atomic Emission Spectroscopy (ICP-OES), following the standard methods for the examination of water and wastewater (APHA, 1998). The total organic carbon (TOC) was measured by oxidizing the wastewater samples using high-temperature oxidation with a platinum catalyst, generating carbon dioxide that was then detected by a Non-Dispersive Infrared (NDIR) detector. The total nitrogen was assessed using the Kjeldahl method, based on the accumulative concentration of Kjeldahl nitrogen, nitrates, and nitrites (Goyal et al., 2022).

7.3. Results and discussion

7.3.1. SSCF scale-up

7.3.1.1. Effects of constant scale-up criteria on process performance

The SSCF process was subjected to scale-up evaluation in 2 L and 13 L bioreactors under anaerobic conditions with working volumes of 1 L and 10 L, respectively, over a 24-hour period. The experimental profiles for bioethanol concentration, cell biomass accumulation, total reducing sugar, and glucose-xylose consumption associated with the 1 L and 10 L scale-up processes are illustrated in Figs. 7.1., 7.2., 7.3., and 7.4., respectively.

Figure 7.1. represents the bioethanol concentration obtained from the 1 L and 10 L scales using detoxified pretreated potato peel hydrolysate as the substrate. Both scales demonstrated a continuous exponential surge in bioethanol production after a short lag phase (>3 h) from 2.85

g/L to 43.84 g/L (1 L scale) and from 3.70 g/L to 43.62 g/L (10 L pilot scale) at the 12th hour of fermentation. The stationary fermentation stage occurred between 12h - 18h, before a general decline in bioethanol production was observed for the remainder of the 24-hour fermentation period, likely due to nutrient depletion, sugar consumption, ethanol oxidation, and organic acid (acetic acid) formation (Chohan et al., 2020). This trend was corroborated by the growth dynamics of the cell biomass, comprising the total cell estimation of both *S. cerevisiae* and *P. stipitis* involved in the co-fermentations, as shown in Fig. 7.2. Brief lag phases were observed, followed by exponential growth from 2 to 12 hours. This growth pattern correlated with significant sugar consumption (~95%), as shown in Fig. 7.3, and glucose-xylose consumption (Fig. 7.4) on both scales.

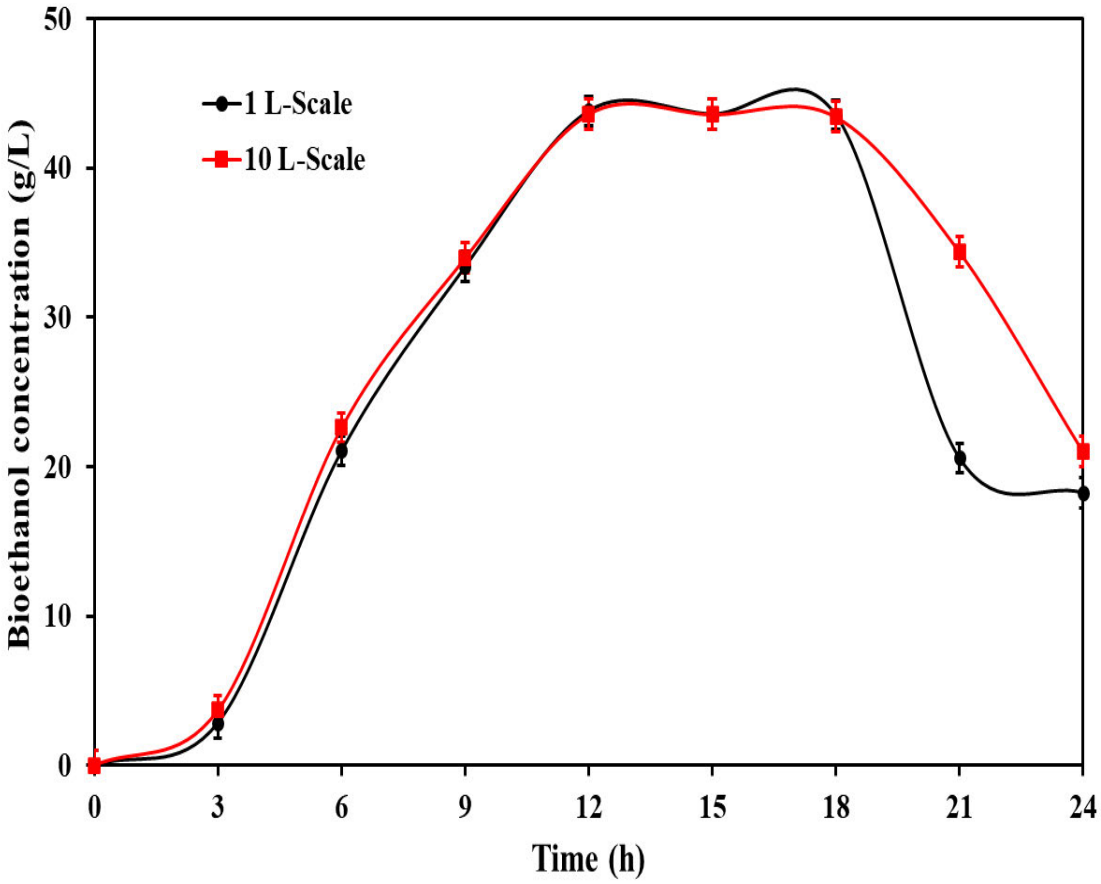

Figure 7.1. Bioethanol production profile for SSCF scale-up

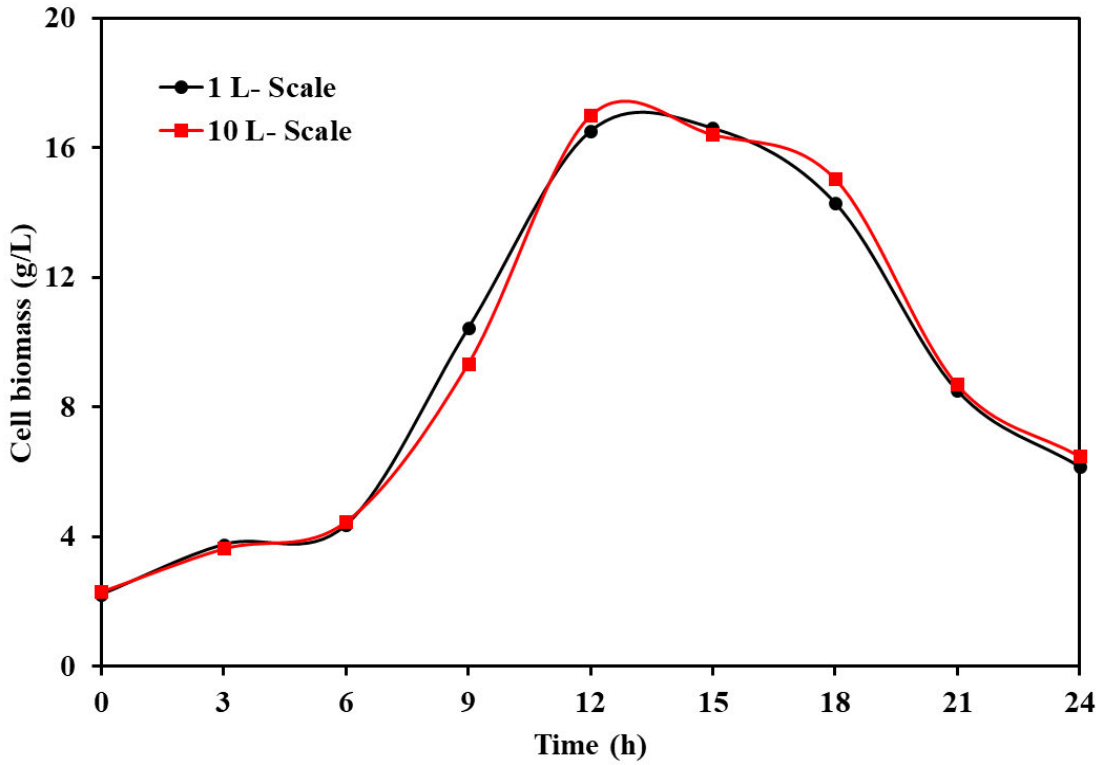

Figure 7.2. Cell biomass profile for SSCF scale-up

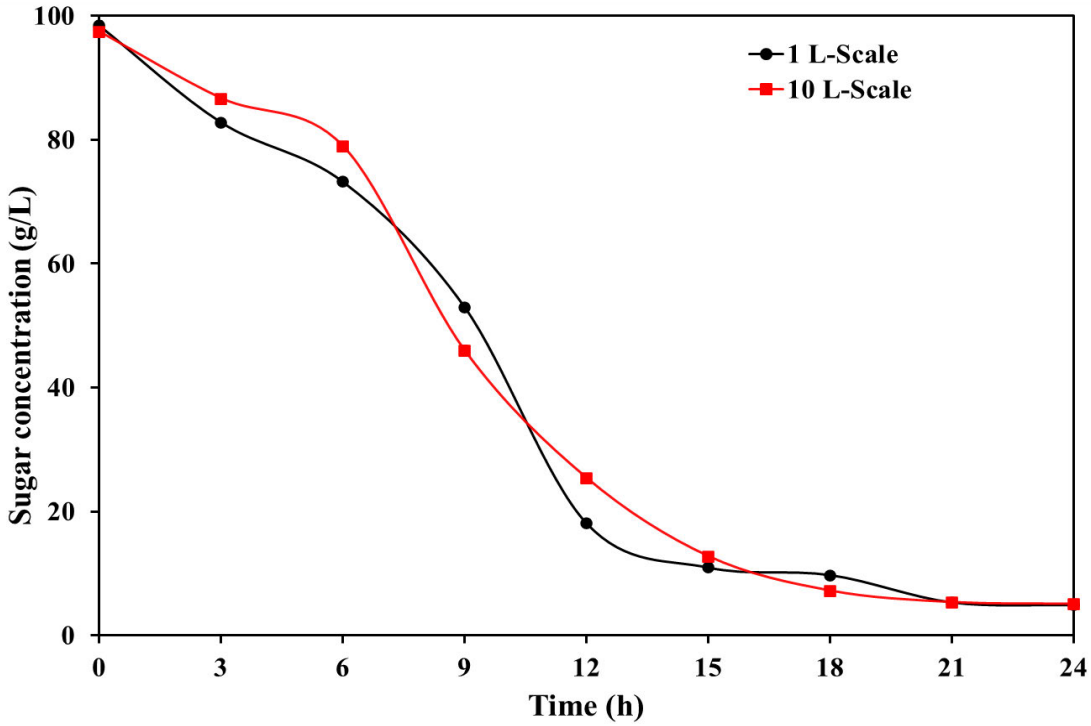

Figure 7.3. Total sugar concentration profile for SSCF scale-up

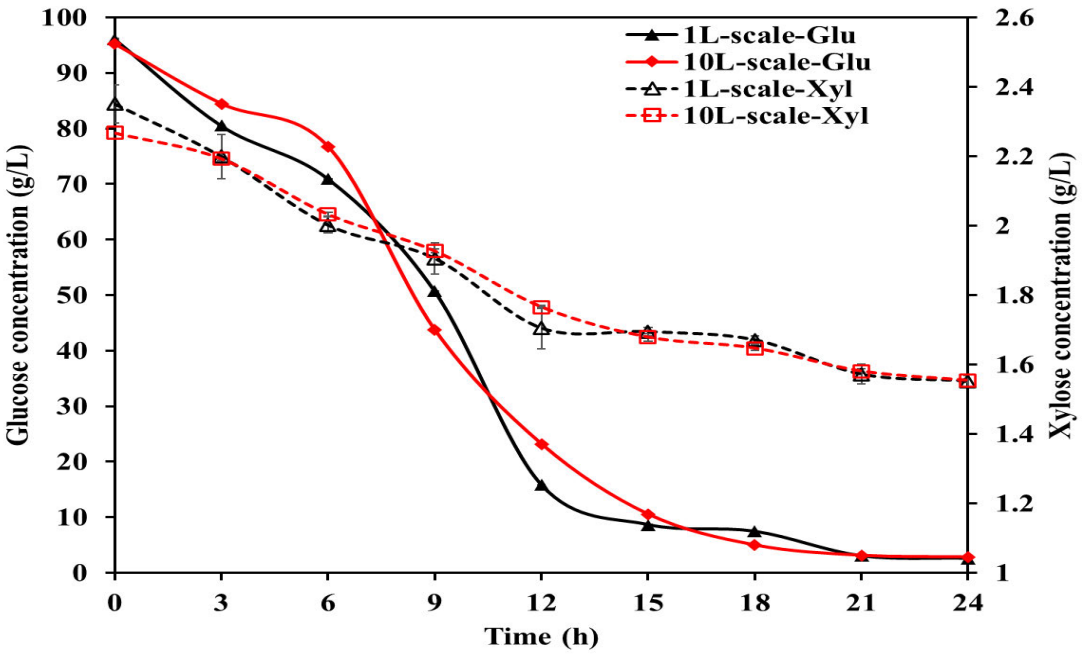

Figure 7.4. Glucose and xylose concentration profile for SSCF scale-up

The initial microbial concentration (X_0) was 2.216 g/L and 2.297 g/L for 1L and 10L scale, respectively, while the maximum microbial concentrations (X_{max}) were 16.60 g/L and 16.99 g/L. The 1L scale and 10L scale exhibited maximum specific growth rates (μ_{max}) of 0.292 and 0.250 h^{-1}, respectively. The higher μ_{max} from the 1L-scale-up does not translate to higher X_{max}; however, this resulted in higher bioethanol concentration (43.84 g/L). The μ_{max} obtained in both scale-up systems was higher comparable to previous reports using undetoxified hydrolysate of sugar beet juice (0.169 h^{-1}) (Dodić *et al*. 2012), sweet sorghum juice (0.154 h^{-1}) (Phukoetphim *et al*., 2017), food waste (0.135 h^{-1}), and corn cobs (0.216 h^{-1}) (Sewsynker-Sukai and Gueguim Kana, 2018) using different strains of *S. cerevisiae*, which further substantiates the favourability of the system in industrial process scale-up. Also, in the presence of sufficient substrate concentration and reduced inhibitory compound concentration, elevated growth rates stimulate respiro-fermentative cellular activities, enhancing fermentative capacity for increased productivity (Nduka et al., 2024).

The overall bioethanol fermentation performance in both scales is further revealed in Table 7.4. The bioethanol yield (g/g), which reflects the efficiency of substrate-to-ethanol conversion, remained consistently high across both scales. At the 1-litre scale, a yield of 0.469 g/g was recorded, while the 10-litre scale slightly outperformed it with a yield of 0.472 g/g.

Table 7.4. Bioethanol fermentation parameters for the SSCF process scale-up.

Parameters	1 Litre scale	10 Litres scale
Bioethanol concentration (g/L)	43.84	43.62
Bioethanol yield (g/g)	0.469	0.472
Bioethanol productivity (g/L/h)	3.653	3.635
Theoretical ethanol concentration (g/L)	47.81	47.21
Total sugar utilization (%)	95.0	94.8
Fermentation process efficiency (%)	91.7	92.4

This marginal increase at the larger scale was a positive indication of the scale-up success. Furthermore, achieving a maximum bioethanol yield within 12 hours of fermentation highlighted the efficiency of the SSCF process, enabling accelerated fermentation kinetics and a potential for high bioethanol productivity within a shortened fermentation period, thereby contributing to reduced overall process costs. Moreover, the 1-litre scale had a productivity of 3.653 g/L/h, and the 10-litre scale had a productivity of 3.635 g/L/h. The bioethanol yield and maximum productivity in both scales were higher than bioethanol yield (0.39 g/g) and bioethanol productivity (0.39 g/L/h) obtained by Kordowaska-Wiater et al. (2001) from the batch fermentation of glucose-xylose mixture by co-culture of *S. cerevisiae* V30 and *P. stipitis* CCY39502. Similarly, the outcomes of the present study were comparable to that of other studies in literatures (Rouhollah et al., 2007; Singh et al., 2014; Salakkam et al., 2023).

Further, the bioreactor operating parameters provide critical insights into the hydrodynamic conditions that underpin these consistent fermentation outcomes (Afedzi et al., 2022). The power consumption per unit volume (P/V_L) decreased dramatically from 12 W/m³ in the 2 L bioreactor to 1.2 W/m³ in the 13 L bioreactor, indicating a significant improvement in energy efficiency at the larger scale. This reduction in specific power input is often a desirable outcome in large-scale bioprocesses due to economic considerations.

Associated with the reduced specific power input (P) at the larger scale, parameters related to mixing intensity and micro-environment for cells also changed. The pumping capacity (V_P) increased, from 2.3×10^{-4} m^3/s to 3.9×10^{-4} m^3/s, which is expected with a larger impeller and working volume. The fluid circulation time (t_c) significantly increased from 4.35 s (2 L) to

25.64 s (13 L), implying longer periods for fluid elements to traverse the bioreactor, which is expected to impact cellular metabolism (Gao et al., 2022). However, the highly efficient sugar utilization (over 94%) and consistent bioethanol concentration suggest that the overall mixing provided by the optimised impeller tip speed was sufficient to mitigate any detrimental effects of longer circulation times in the 13L bioreactor system. Moreover, the rheological properties of the fermentation broth (e.g., low viscosity) may allow for faster diffusion and mixing, even with longer bulk circulation times (Gholamipour-Shirazi and Mossige, 2024; Estrada-García et al., 2024). Likewise, the Froude number, a dimensionless ratio indicating the balance of inertial forces to gravitational forces, also decreased slightly, suggesting relatively less surface turbulence at the larger scale (Mishra et al., 2023). The energy dissipation rate (ϵ) decreased by an order of magnitude (from 1.17×10^{-2} m^2/s^3 to 1.17×10^{-3} m^2/s^3), directly correlating with the lower power consumption per unit volume, translating to the Kolmogorov scale of turbulence (λ) increased from 1.73×10^{-3} m to 3.08×10^{-3} m, indicating larger eddy sizes at the 13 L scale (Petry and Salzig, 2021). Similarly, the shear rate (γ) and shear stress (τ) decreased at the larger scale (from 20 s^{-1} and 0.98 Pa to 15.8 s^{-1} and 0.7742 Pa, respectively). The observation reduction in shear stress and shear rate at the larger scale is beneficial for microbial fermentations, as high shear environments can be detrimental to cell viability and productivity, particularly for shear-sensitive microorganisms (Kheirkhah et al., 2022). The maintenance of high cell viability and metabolic activity, as evidenced by consistent bioethanol yield and sugar utilisation, suggests that the lower shear conditions in the 13 L bioreactor were favourable. The overall fermentation performance suggests that the 10-L pilot-scale design strategy provide a robust and scalable platform for industrial bioethanol production. This system achieves lower specific power consumption while preserving high metabolic efficiency in the *S. cerevisiae* and *P. stipitis* co-culture under varying hydrodynamic conditions. By prioritizing impeller tip speed over constant power input during scale-up, the approach offers an energy-efficient bioreactor design framework that facilitates faster process optimization for industrial applications.

7.3.1.2. Growth kinetics of the co-culture of *S. cerevisiae and P. stipitis* using logistic model

The experimental data for cell dry weight over time, for both scales, were fitted to the logistic function model (Figs. 7.5A and B), yielding a high coefficient of determination (R^2) > 0.90. This demonstrates the suitability of the logistic function in describing the growth dynamics of the coculture of *S. cerevisiae* and *P. stipitis*, as evaluated using these scale-up criteria. The logistic model-predicted maximum specific growth rate (μ_{max}) of 0.280 h^{-1} (1L-scale-up) and

0.266 h^{-1} (10L-scale-up) was consistently aligned with the experimentally derived μ_{max} value of 0.292 h^{-1} and 0.250 h^{-1}, respectively (Table 7.5). The maximum specific growth rates (μ_{max}) obtained from the logistic model were above 0.025 h^{-1} indicating highly desirability for industrial process scale-up (Sewsynker-Sukai and Gueguim Kana, 2018).

The root-mean-square error (RMSE) and mean-square error (MSE), which are standard statistical metrics for evaluating model performance and assessing its accuracy, were employed to validate the model. The RMSE values were 1.859 g/L and 1.938 g/L, while the MEA values were 1.473 g/L and 1.561 g/L for 1L-scale and 10L-scale, respectively, demonstrating a strong agreement between experimental and predicted cell biomass data (Adebule et al., 2025). However, the lower RMSE and MEA obtained for the 1L-scale corroborate the higher R^2 (0.9076), confirming a slightly better, but negligible, fitting compared to the 10L-scale.

7.3.1.3. Bioethanol production kinetics for 1L and 10L-scales using the modified Gompertz model and Luedeking-Piret model

Empirical data on bioethanol formation during fermentation were fitted to the modified Gompertz and Luedeking-Piret models to elucidate the kinetics of bioethanol production in both scale systems. The MGM exhibited satisfactory fit, with an R^2 of approximately 0.995, indicating that the model explained a significant fraction of the total variation in both scales (Figs. 7.5C and 7.5D). Both 1L and 10L-scales demonstrated similarly high maximum potential bioethanol concentration (P_m) (44.70 and 44.45 g/L) and maximum bioethanol production rate ($r_{p,m}$) of 6.58 and 6.54 g/L/h, respectively, as shown in Table 7.5. The observed similar P_m and $r_{p,m}$ values obtained from both scales might be attributed to similar rotational speed [n] and the impeller tip speed (V_{tip}). Given that higher production rates are preferred at large scales, the high $r_{p,m}$ (> 6.5 g/L/h) attained in the scale-up study substantiates the desirability of this strategy for industrial bioethanol production.

A marginally short lag time (t_L) of 2.91 and 2.66 hours observed indicated a short adaptation period for yeast cells under both scales' geometry, rheology, and hydrodynamics conditions. The close alignment between the MGM predictions and experimental bioethanol concentrations confirms the reliability of findings in the present study, as observed in the comparison between 43.84 g/L (experimental) and 44.70 g/L (predicted) for the 1L-scale, and 43.62 g/L (experimental) and 44.45 g/L (predicted) for the 10L-scale. However, the higher predicted values from the Modified Gompertz model serve as an indicator of potential

efficiency beneficiation, providing a benchmark for scale-up and further guiding optimisation trajectory.

The growth-associated product formation coefficient (α) and non-growth-associated product formation coefficient (β) estimated for both scale systems by the Leudeking-Piret model are summarised in Table 7.5. Both scales exhibited close to zero β-values of 0.0042 g P/g X. h (1L-scale) to 0.0004 g P/g X. h (10L-scale), while the α-values obtained were 3.373 g P/g X and 4.744 g P/g X. Figures 7.5E and 7.5F show the comparative plotting of both the observed (experimental) and predicted bioethanol production data from the LP model. The coefficients of determination (R^2) obtained were greater than 0.94 in both scales, indicating the model's significance and fitness. The results obtained for $\alpha \neq 0$ and $\beta \neq 0$ (but close to 0) confirmed that the bioethanol fermentation processes are mainly growth-associated, as $\alpha \neq 0$ and β are close to zero, opposing the non-growth-associated condition where $\alpha = 0$ and $\beta \neq 0$ (Germec et al., 2022).

On the other hand, the RMSE and MAE used to validate both production formation models, were lowest for the MGM (1.184 and 0.887 g/L [1L-scale]) and (1.124 and 0.847 g/L [10-L-scale]) compared to the LPM (3.353 and 2.461 g/L[1L-scale]) and (4.744 and 3.487 g/L [10-L-scale]), which further corroborated that MGM was a better fit model to explain the bioethanol production formation dynamics in relation to cell biomass accumulation. In comparison with previous studies, bioethanol production modelled from pretreated corn stover using a co-culture of *S. cerevisiae* and *C. tropicalis* was reported to have lower kinetic parameters: α = 2.392 gP/gX and β = 0.013 gP/gX·h (Liu et al., 2019). The bioethanol production was concluded to be influenced mainly by growth-associated factors, as indicated by the very small β value. In contrast, Jiménez-Islas et al. (2014) reported considerably higher α values (5.3143 and 4.5326 gP/gX) for bioethanol production from red beet juice using two *S. cerevisiae* strains (ITD00196 and ATCC 9763), with corresponding β values of -0.044 and 0.1047 gP/gX·h, respectively. Despite the differences, both cases exhibited growth-associated bioethanol production, as evidenced by the relatively small β values compared to α. The combined derivatives of the MGM and LPM offer valuable insights into the dynamics of bioethanol biosynthesis in both the 1L-scale and 10L-scale systems.

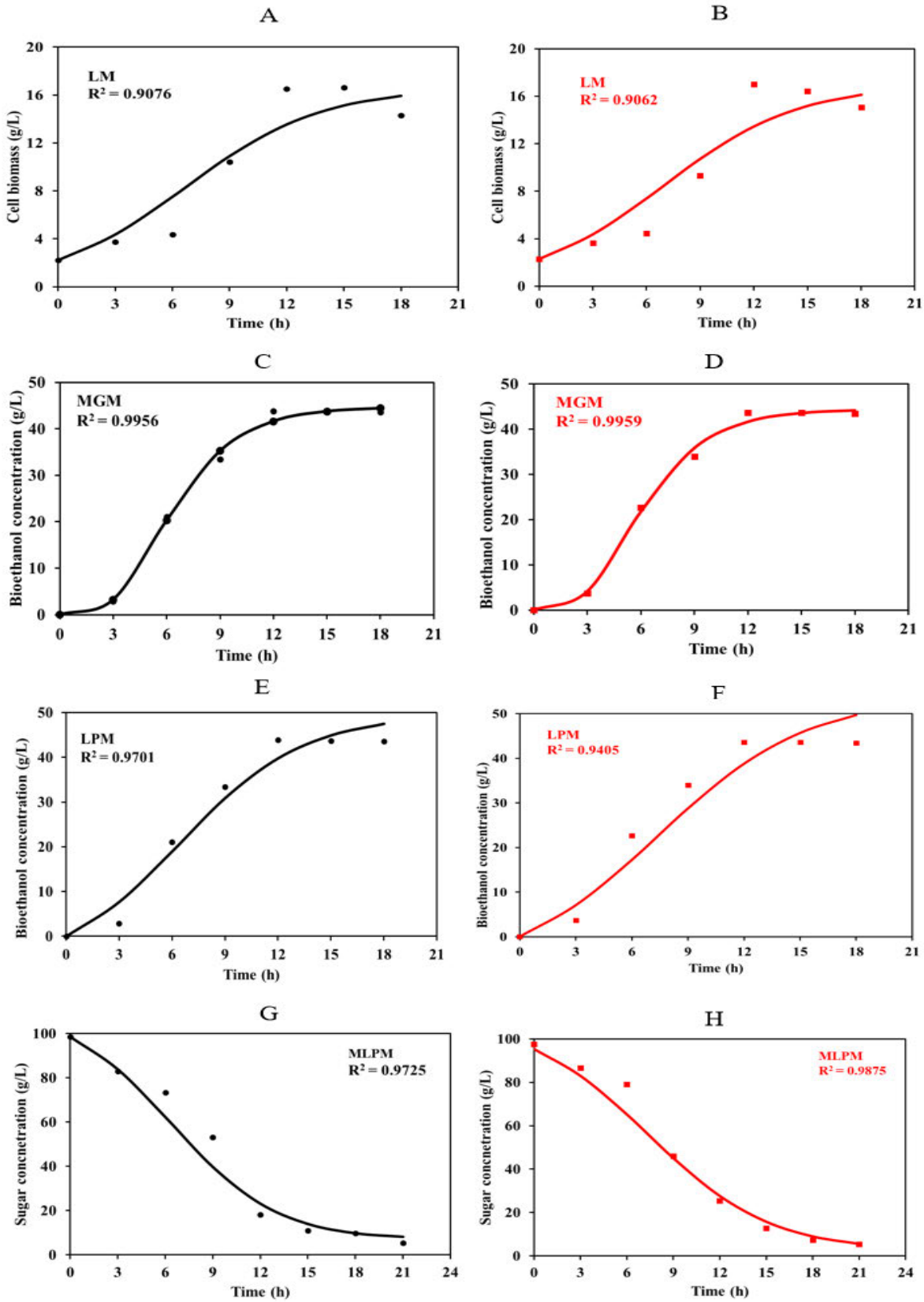

Figure 7.5. Cell biomass concentration, bioethanol production and substrate consumption curves of 1L and 10L-scale fitted by the logistic model (A and B); MG model (C and D); LP model (E and F) and MLP model (G and H), respectively.

Table 7.5. Kinetic model parameters for the SSCF process scale-up.

Models	Parameters	1 L scale-up	10 L scale-up
	Cell growth		
Exponential phase	μ_{max} (h^{-1})	0.292	0.250
	X_0 (g/L)	2.216	2.297
	X_{max} (g/L)	16.604	16.989
Logistic model	μ_{max} (h^{-1})	0.280	0.266
	R^2	0.9076	0.9062
	RMSE	1.859	1.938
	MEA	1.473	1.561
	Bioethanol production		
MGM	P_m (g/L)	44.703	44.451
	$r_{p.m}$ (g/L/h)	6.577	6.538
	t_L (h)	2.910	2.659
	R^2	0.9956	0.9959
	RMSE	1.184	1.124
	MEA	0.887	0.847
LP	α (g *P*/g *X*)	3.373	3.660
	β (g *P*/g *X*. h)	0.0042	0.0004
	R^2	0.9701	0.9405
	RMSE	3.353	4.744
	MEA	2.461	3.487
	Sugar utilisation		
MLP	γ (g S/g *X*)	6.524	6.611
	δ (g *S*/g *X*. h)	0.0090	0.0058
	R^2	0.9725	0.9875
	RMSE	6.245	4.458
	MEA	4.348	2.568

μ_{max}= maximum specific growth rate, X_0= initial cell concentration, X_{max}= maximum cell concentration, P_m= maximum potential bioethanol concentration, $r_{p,m}$= maximum bioethanol production rate, t_L=lag time

7.3.1.4. Substrate utilization kinetics in 1L and 10L-scales using the modified Luedeking Piret model.

Empirical data on substrate utilization over time for the scale-up systems were fitted to the Modified Luedeking-Piret model (Figs 7.5 G and H). This typically resulted in R^2 values >0.97, confirming the model's high significance in describing the substrate utilization kinetics (Germec et al., 2019; Adebule et al., 2025). The modified Luedeking-Piret model quantifies substrate consumption kinetics by elucidating substrate utilization based on growth-associated (γ, g S/g X) and maintenance-associated (δ) components to identifies whether substrate consumption shifts toward maintenance (higher δ) or growth (higher γ). This is important for enabling targeted process adjustments during scale-up. For instance, hydrodynamic heterogeneity such as gradients in nutrient distribution, dissolved oxygen, or shear stress can alter microbial metabolic behaviour. In the case of this scale-up study, the resultant values of γ and δ obtained for the 1 L-scale were 6.524 g S/g X, 0.009g S/g X·h, and for the 10 L-scale were 6.611 g S/g X, 0.0058g S/g X·h, respectively (Table 7.5). These indicate robust microbial growth or product synthesis efficiency and minimal energy expenditure on maintenance (Germec et al., 2022; Adebule et al., 2025), since the maintenance coefficient (δ) is intricately linked to the specific growth rate and substrate uptake rate for cellular maintenance (Germec et al., 2019).

Cellular maintenance during fermentation entails energy expenditure for repairing damaged cellular components and ensuring cellular equilibrium. As depicted in Table 7.5, the δ values for both scales were notably low, signifying that the yeasts minimise substrate "wastage" on non-productive maintenance processes and predominantly utilise sugars for biomass growth and bioethanol production during the scale up process. Interestingly, the values of δ derived from this study are similar to those reported earlier by Jiménez-Islas et al. (2014) and Suresh et al. (2018), with δ values close to zero. Moreover, γ values ranging from 5.3409 to 5.723 g S/g X were earlier reported by Germec et al. (2019), whereas lower γ values of 0.074 g S/g X and 3.3846 g S/g X were reported by Suresh et al. (2018) and Jiménez-Islas et al. (2014). However, a higher γ value (8.2 g S/g X) was reported by using *Kluyveromyces fragilis*-NCIM 0557 for bioethanol fermentation from sugarcane bagasse (Sasikumar and Viruthagiri, 2008). The high substrate utilization coefficient (γ) was substantiated by higher sugar concentrations (98.49 g/L and 97.43 g/L) in the fermentation medium. For the 1-litre-scale and 10L pilot-scale, high γ values exceeding 6.52 g S/g X and low δ values not above 0.0058 g S/g X/h under scaled

conditions confirm an efficient sugar-to-ethanol conversion with minimal metabolic overhead. This underscores the importance of bioreactor design choices (e.g., impeller tip speed and revolutions per second) for sustaining metabolic efficiency at larger scales.

The bioethanol production performance in this study compares favourably with previous large-scale reports (Table 7.6.) utilizing various lignocellulosic substrates and SSCF strategies in Rushton impeller-equipped bioreactors. For instance, the 10.0 L bioethanol concentration (43.62 g/L) was approximately 3.02% higher than the 42.34 g/L reported by Dey et al. (2021) using pulp and paper sludge at a 3.0 L scale with 22% (w/v) solids loading. Furthermore, it surpassed the 19.7 g/L reported by Um and Hanley (2008) using Solka Floc (purified cellulose) under fed-batch with 20% solids, by approximately 121.42%.

Moreover, Tareen et al. (2021) reported a significantly higher bioethanol concentration of 51.66 g/L and an impressive yield of 0.72 g/g using oil palm trunk fibre at a 1.0 L scale with a 20% (w/v) solid loading, employing an SSF strategy. The superior performance observed by Tareen et al. (2021) could be attributed to the substrate type (oil palm trunk fibre) and the higher solid loading of 20% contributing to the higher bioethanol produced. Zhang et al. (2010) achieved an ethanol concentration of 43.9 g/L, comparable to both scales in this study. However, this output was obtained from corn stover in a 5.0 L bioreactor with a high 30.0% (w/v) solids load, as against the 10% solid loading using detoxified PPW. This is a strong indicator of the efficiency of waste potato peel conversion. Suggesting the potential to maintain high performance during scale-up for the valorisation of waste potato peel into bioethanol.

7.3.2. Evaluation of fermentation effluent for potential valorisation

The effluent elemental components (Table 7.7) include dissolved Ca (< 1.25 mg/L), K (13.2 mg/L), Mg (2.06 mg/L), Na (241 mg/L), and P (3.98 mg/L). The electrical conductivity of the effluent (at 25°C) was 1760 mS/m, suspended solids (at 105 °C) was 12160 mg/L, total dissolved solids (at 180 °C) was 32020 mg/L, total solids (at 105 °C) was 5.5 %m/m, and TOC was 78 % g/g. Potassium and magnesium are vital cofactors that play key roles in photosynthesis, osmoregulation, and enzyme activation. Potassium and magnesium support both autotrophic growth in microalgae (Jiang et al., 2016; Castillo et al., 2021; Huai et al., 2022; Shan et al., 2023). For instance, increased magnesium concentrations significantly enhanced the biomass and lipid yield of *Chlorella vulgaris* and *Scenedesmus obliquus*, high lipid yield is beneficial for biodiesel production (Gorain et al., 2013).

Table 7.6. Bioethanol concentration and yield during the SSCF scale up in comparison to other studies.

Substrate	**Fermentation strategy**	**Impeller Type**	**Total Solids Load**	**Vessel Volume**	**Concentration (g/L), Yield (g/g)**	**Reference**
PPW (nano-detoxified hydrolysate)	Batch SSCF	Rushton	10% (w/v)	1.0 L	43.84 g/L, 0.469 g/g	This study
PPW (nano-detoxified hydrolysate)	Batch SSCF	Rushton	10% (w/v)	10.0 L	43.62 g/L, 0.472 g/g	This study
Pulp and paper sludge	Fed-batch SSF	Rushton	22% (w/v)	3.0 L	42.34 g/L, 0.53 (g/g)	(Dey et al., 2021)
Oil palm trunk fibre	S-SSF	Rushton	20% (w/v)	1.0 L	51.66%, 0.72 (g/g)	(Tareen et al., 2021a)
Sugarcane bagasse	Fed-batch PSSF	Rushton	20% (w/v)	1.0 L	57.2 g/L, 94.65%	(Raj and Krishnan, 2020)
Solka Floc	Fed-batch PSSF	Rushton	20%	3.0 L	19.7 g/L, 68.6%	(Um and Hanley, 2008b)
Corn stover	Fed-batch PSSF	Rushton	30.0% (w/v)	5.0 L	43.9 g/L, -	(Zhang et al., 2010)
Prosopis juliflora (Mesquite)	Fed-batch PSSF	Rushton	20.0% (w/v)	5.0 L	52.83 g/L, 0.45 (g/g)	(Gupta et al., 2012)

Table 7.7. Chemical composition of fermentation effluent.

Components (Elements)	Units	Value
pH	–	4.8
Density	kg/m³	1.1677
Dissolved Calcium	mg Ca/L	< 1.25
Potassium	mg K/L	13.2
Magnesium	mg Mg/L	2.06
Sodium	mg Na/L	241
Total Phosphorus	mg P/L	3.98
Electrical Conductivity at 25°C	mS/m	1760
Suspended solids at 105 °C	mg/L	12160
Total dissolved solids at 180 °C	mg/L	32020
Total solids at 105 °C	% m/m	5.5
Total organic carbon	% g/g	78

Similarly, *Chlorella vulgaris* exhibited a maximum growth rate of 0.482/day on the ninth day at a magnesium concentration of 5 mg/LMg^{2+}, as observed in a study investigating the effects of magnesium concentration (5, 10, and 15 mg/L) on freshwater green algae (Salman et al., 2023). Also, phosphorus, particularly at approximately 4 mg L^{-1}, is often a limiting nutrient crucial for nucleic acid and ATP biosynthesis. thereby reducing or eliminating the need for external phosphate additions. For example, phosphorus source and concentration significantly influenced the growth, chlorophyll a, total lipid, and fatty acid content of the diatom *Chaetoceros lorenzianus* (Zhang et al., 2025).

Moreover, the lignocellulosic fermentation waste effluent presents a significant organic load, evidenced by its remarkably high TOC of 78% (dry weight of solids), indicating a substantial organic load (Park et al., 2022). Organic carbon can serve as a carbon source for heterotrophic microorganisms, supporting their growth and the synthesis of valuable products (e.g., bioplastics, enzymes, organic acids, single-cell protein), making the effluent an excellent feedstock for such processes. Furthermore, channelling the fermentation effluent for anaerobic digestion (AD) could result in the microbial degradation of organic matter in the absence of oxygen, yielding biogas, a renewable energy. Besides, the AD process could effectively reduce the chemical oxygen demand (COD) and biochemical oxygen demand (BOD) of the effluent,

thereby mitigating downstream treatment costs and environmental impact towards sustainable approach to waste valorization.

Beyond bioenergy and biomass, fermentative acidogenic effluents could be an ideal medium suited for the synthesis of bioplastic precursors. Polyhydroxyalkanoate (PHA)-accumulating bacteria can channel organic acids and sugars into intracellular polyester granules. Studies have demonstrated robust PHA yields from fermentation residues under non-sterile conditions, underscoring the feasibility of this valorisation route (Fu et al., 2023). Integrating PHA production alongside algae cultivation, enzyme generation, and anaerobic digestion creates multiple revenue streams, significantly enhancing the circularity and economic resilience of biorefineries (Saratale et al., 2021). The acidic pH in these fermentation effluents indicates the presence of organic acids. While this pH might suit acidophilic microorganisms, pH adjustment is required for neutralophiles. Effective implementation would require process optimization and neutralization for many microbial applications, while high suspended solids call for centrifugation or microfiltration to prevent light-penetration losses in photobioreactors for microalgae growth (Salman et al., 2023). The residual solids comprising yeast biomass and unconverted lignocellulosic fragments can be valorized as biofertilizers (Chojnacka, 2023) or soil amendments, as demonstrated by increased crop yields when vinasse is applied to leafy vegetables compared to conventional NPK treatments (Clairmont et al., 2016).

Bioethanol fermentation acidogenic effluent, often considered a waste product, is a complex matrix rich in various organic and inorganic compounds. The effluent's potential as a nutrient source for generating other valuable products or supporting the growth of microalgae, offering a potential pathway for a circular biorefining system.

7.4. Conclusion

This study successfully demonstrated the scale-up of detoxified, pretreated waste potato peel (PPW) hydrolysate using the co-fermentation of *S. cerevisiae* and *P. stipitis* for sustainable bioethanol production. High fermentation performance was achieved, with an ethanol concentration of 43.62 g/L, a yield of 0.472 g/g, and 95% sugar utilization, as the process was scaled from laboratory (1 L) to pilot (10 L) scale. This success was attributed to the consistent geometric, rheological, and hydrodynamic characteristics maintained throughout the scale-up. Notably, a tenfold reduction in specific power consumption was achieved by maintaining a constant impeller tip speed (V_{tip}). Additionally, the fermentation effluent, rich in essential

elements, has potential for use in microalgae cultivation and biofertilizer. These findings underscored the technical feasibility and cost-effectiveness of using PPW as a substrate, highlighting its significant potential for waste valorization and sustainable large-scale bioethanol production in a circular bioeconomy scenario.

References

Adebule, A.P., Sanusi, I.A., Kana, E.G., 2024. Nano-based surface adsorption detoxification of process inhibitors for improved bioethanol productivity. Bioresource Technology Reports, 25: 101783. https://doi.org/10.1016/j.biteb.2024.101783.

Adebule, A.P., Sanusi, I.A., Kana, G.E.B., 2025. Growth-associated and Non-growth-associated Bioethanol Production Kinetics from Nanoadsorbent-Detoxified Pretreated Hydrolysate. Catalysis Letters, 155: 96. https://doi.org/10.1007/s10562-024-04868-8.

Afedzi, A.E.K., Rattanaporn, K., Parakulsuksatid, P., 2022. Impeller selection for mixing high-solids lignocellulosic biomass in stirred tank bioreactor for ethanol production. Bioresource Technology Reports, 17: 100935. https://doi.org/10.1016/j.biteb.2021.100935.

American Public Health Association (APHA), 1998. Standard methods for the examination of water and wastewater. Am. Public Heal. Assoc., Washington, DC. 20th ed. 3120, 3–37.

Aruwajoye, G.S., Faloye, F.D., Gueguim Kana, E., 2019. Process optimisation of enzymatic saccharification of soaking-assisted and thermal pretreated cassava peel waste for bioethanol production. Waste Biomass Valorization, 1–12. https://doi.org/10.1007/s12649-018-00562-0.

Aruwajoye, G.S., Faloye, F.D., Kana, E.G., 2017. Soaking-assisted thermal pretreatment of cassava peel waste for fermentable sugar production: process modelling and optimisation. Energy Conversion and Management, 150: 558–566. https://doi.org/10.1016/j.enconman.2017.08.046.

Aruwajoye, G.S., Sewsynker-Sukai, Y., Kana, E.G., 2020. Valorisation of cassava peels through simultaneous saccharification and ethanol production: Effect of prehydrolysis time, kinetic assessment and preliminary scale up. Fuel, 278: 118351. https://doi.org/10.1016/j.fuel.2020.118351.

Barampouti, E.M., Christofi, A., Malamis, D., et al., 2023. A sustainable approach to valorize potato peel waste towards biofuel production. Biomass Conv. Bioref., 13: 8197–8208. https://doi.org/10.1007/s13399-021-01811-4.

Bello, S., Galán-Martín, Á., Feijoo, G., Moreira, M.T., Guillén-Gosálbez, G., 2020. BECCS based on bioethanol from wood residues: Potential towards a carbon-negative transport and side-effects. Applied Energy, 279: 115884. https://doi.org/10.1016/j.apenergy.2020.115884.

Bidwai, S., Shivarkar, A., 2024. Fuel Ethanol Market Size, Share and Trends 2024 to 2034. Chemical and Material, Report code: 5239. https://www.precedenceresearch.com/fuel-ethanol-market.

Bishop, B.D.C., Sanusi, A.I., Kana, E.B.G., 2024. Enhanced substrate suitability of autoclave-assisted acid pre-treated waste sugarcane molasses: pre-treatment optimization, sequential nano-based detoxification strategies, and bioproduct production. Biomass Convers. Biorefin., 27: 1–4. https://doi.org/10.1007/s13399-024-06127-7.

Castillo, T., Ramos, D., García-Beltrán, T., Brito-Bazan, M., Galindo, E., 2021. Mixotrophic cultivation of microalgae: an alternative to produce high-value metabolites. Biochemical Engineering Journal, 176: 108183. https://doi.org/10.1016/j.bej.2021.108183.

Chohan, N.A., Aruwajoye, G.S., Sewsynker-Sukai, Y., Gueguim Kana, E.B., 2020. Valorisation of potato peel wastes for bioethanol production using simultaneous saccharification and fermentation: Process optimization and kinetic assessment. Renewable Energy, 146: 1031–1040. https://doi.org/10.1016/j.renene.2019.07.042.

Chojnacka, K., 2023. Valorization of biorefinery residues for sustainable fertilizer production: a comprehensive review. Biomass Conv. Bioref., 13: 14359–14388. https://doi.org/10.1007/s13399-023-04639-2.

Clairmont, C., Bibi, N.A., Oudho, H., Vickram, P., 2016. An Evaluation of ‘Vinasse’ (Bio-Ethanol Effluent) and Vermicompost as Soil Amendments for Cash Crop Production. Greener Journal of Agricultural Sciences, 6(9): 256–261. https://doi.org/10.15580/GJAS.2016.9.092816148.

de Mello, A.F.M., de Souza Vandenberghe, L.P., Herrmann, L.W., Letti, L.A.J., Burgos, W.J.M., Scapini, T., Manzoki, M.C., de Oliveira, P.Z., Soccol, C.R., 2024. Strategies and engineering aspects on the scale-up of bioreactors for different bioprocesses. Systems Microbiology and Biomanufacturing, 4(2): 365–385. https://doi.org/10.1007/s43393-023-00205-z.

Deniz, I., Imamoglu, E., Vardar Sukan, F., 2015. Evaluation of scale-up parameters of bioethanol production from Escherichia coli KO11. Turkish Journal of Biochemistry, 40(1). https://doi.org/10.5505/tjb.2015.33603.

Dey, P., Rangarajan, V., Nayak, J., Das, D.B., Wood, S.B., 2021. An improved enzymatic pre-hydrolysis strategy for efficient bioconversion of industrial pulp and paper sludge waste to bioethanol using a semi-simultaneous saccharification and fermentation process. Fuel, 294: 120581. https://doi.org/10.1016/j.fuel.2021.120581.

Dodić, J.M., Vučurović, D.G., Dodić, S.N., Grahovac, J.A., Popov, S.D., Nedeljković, N.M., 2012. Kinetic modelling of batch ethanol production from sugar beet raw juice. Applied Energy, 99: 192–197. https://doi.org/10.1016/j.apenergy.2012.05.016.

Du, Y.H., Wang, M.Y., Yang, L.H., Tong, L.L., Guo, D.S., Ji, X.J., 2022. Optimization and scale-up of fermentation processes driven by models. Bioengineering, 9(9): 473. https://doi.org/10.3390/bioengineering9090473.

Estrada-García, J., Hernández-Aguilar, E., Gutiérrez-Casiano, N., Méndez-Contreras, J.M., 2025. Monitoring of rheological parameters in the anaerobic fermentation process to obtain bioethanol from craft brewer's spent grain using brewer's spent yeast and *Saccharomyces cerevisiae* S-04. Biomass Conv. Bioref., 15: 15585–15602. https://doi.org/10.1007/s13399-024-06271-0.

FAO, 2024. FAO guide to new International Day of Potato sets scene for first-ever observance on May 30. www.fao.org/newsroom/detail/fao-guide-to-new-international-day-of-potato-sets-scene-for-first-ever-observance-on-may-30/en.

Fu, X., Xu, H., Zhang, Q., Xi, J., Zhang, H., Zheng, M., Xi, B., Hou, L.A., 2023. A review on polyhydroxyalkanoates production from various organic waste streams: feedstocks, strains, and production strategy. *Resources, Conservation and Recycling*, 198: 107166. https://doi.org/10.1016/j.resconrec.2023.107166.

Gao, H.L., Wen, Z.N., Sun, B.C., Zou, H.K., Chu, G.W., 2022. Intensification of ozone mass transfer for wastewater treatment using a rotating bar reactor. *Chemical Engineering and Processing – Process Intensification*, 176: 108946. https://doi.org/10.1016/j.cep.2022.108946.

Germec, M., Karhan, M., Dermirci, A., Turhan, I., 2022. Kinetic modeling, sensitivity analysis, and techno-economic feasibility of ethanol fermentation from non-sterile carob extract-based media in *Saccharomyces cerevisiae* biofilm reactor under a repeated-batch fermentation process. *Fuel*, 324: 124729. https://doi.org/10.1016/j.fuel.2022.124729.

Germec, M., Turhan, I., Karhan, M., Dermirci, A., 2019. Kinetic modeling and techno-economic feasibility of ethanol production from carob extract-based medium in biofilm reactor. *Appl. Sci.*, 9: 2121, 1–19. https://doi.org/10.3390/app9102121.

Gholamipour-Shirazi, A., Mossige, E.J.L., 2024. Impact of mixing on flavor and aroma development in fermented foods. *arXiv preprint arXiv:2412.10190.* https://doi.org/10.48550/arXiv.2412.10190.

Gonçalves, F.A., Ruiz, H.A., Silvino dos Santos, E., Teixeira, J.A., de Macedo, G.R., 2016. Bioethanol production by *Saccharomyces cerevisiae*, *Pichia stipitis* and *Zymomonas mobilis* from delignified coconut fibre mature and lignin extraction according to biorefinery concept. *Renew. Energy*, 94: 353–365. https://doi.org/10.1016/j.renene.2016.03.045.

Gorain, P.C., Bagchi, S.K., Mallick, N., 2013. Effects of calcium, magnesium and sodium chloride in enhancing lipid accumulation in two green microalgae. *Environmental Technology*, 34(13–14): 1887–1894. https://doi.org/10.1080/09593330.2013.812668.

Goyal, K., Singh, N., Jindal, S., Kaur, R., Goyal, A., Awasthi, R., 2022. Kjeldahl method. *Adv. Tech. Anal. Chem.*, 1(1): 105. https://doi.org/10.2174/9789815050233122010011.

Gupta, R., Kumar, S., Gomes, J., Kuhad, R.C., 2012. Kinetic study of batch and fed-batch enzymatic saccharification of pretreated substrate and subsequent fermentation to ethanol. *Biotechnol. Biofuels*, 5: 16. https://doi.org/10.1186/1754-6834-5-16.

Huai, B., Wu, Y., Liang, C., Tu, P., Mei, T., Guan, A., Yao, Q., Li, J., Chen, J., 2022. Effects of calcium on cell wall metabolism enzymes and expression of related genes associated with peel creasing in citrus fruits. *PeerJ*, 10: e14574. https://doi.org/10.7717/peerj.14574.

IEA Bioenergy, 2024. Country Report 2024: South Africa. Retrieved from https://www.ieabioenergy.com/wpcontent/uploads/2024/12/CountryReport2024_SouthAfrica_final.pdf.

Izmirlioglu, G., Demirci, A., 2017. Simultaneous saccharification and fermentation of ethanol from potato waste by co-cultures of *Aspergillus niger* and *Saccharomyces cerevisiae* in biofilm reactors. *Fuel*, 202: 260–270. https://doi.org/10.1016/j.fuel.2017.04.047.

Jiang, L., Pei, H., Hu, W., Hou, Q., Han, F., Nie, C., 2016. Biomass production and nutrient assimilation by a novel microalga, *Monoraphidium sp.* sDEC-17, cultivated in a high-ammonia wastewater. *Energy Conversion and Management*, 123: 423–430. https://doi.org/10.1016/j.enconman.2016.06.060.

Jiménez-Islas, D., Páez-Lerma, J., Soto-Cruz, N.O., Gracida, J., 2014. Modelling of ethanol production from red beet juice by *Saccharomyces cerevisiae* under thermal and acid stress conditions. *Food Technol. Biotechnol.*, 52: 93–100.https://hrcak.srce.hr/118561.

Kheirkhah, T., Neubauer, P., Junne, S., 2023. Controlling *Aspergillus niger* morphology in a low shear-force environment in a rocking-motion bioreactor. *Biochemical Engineering Journal*, 195: 108905. https://doi.org/10.1016/j.bej.2023.108905.

Kim, S.R., Ha, S.J., Wei, N., Oh, E.J., Jin, Y.S., 2012. Simultaneous co-fermentation of mixed sugars: a promising strategy for producing cellulosic ethanol. *Trends Biotechnol.*, 30(5): 274–282. https://doi.org/10.1016/j.tibtech.2012.01.005.

Kordowska-Wiater, M., Targoński, Z., 2001. Ethanol production on the media containing glucose and xylose by coculture of *Pichia stipitis* CCY39501 and respiratory deficient mutant of *Saccharomyces cerevisiae* V30. *Electron. J. Pol. Agric. Univ. Food Sci. Technol.*, 4(2): 15–28.

Kumar, M., Kumar, D., Singh, S., Chopra, S., Mahmood, S., Bhatia, A., 2024. Quality by design perspective for designing foam-based formulation: current state of art. *Curr. Pharm. Des.*, 30(6): 410–419. https://doi.org/10.2174/0113816128289965240123074111.

Lemire, L., Pham, P.L., Durocher, Y., Henry, O., 2022. Practical considerations for the scale-up of Chinese hamster ovary (CHO) cell cultures. In *Cell Culture Engineering and Technology: In appreciation to Professor Mohamed Al-Rubeai*, 367–400. Cham: Springer International Publishing. https://doi.org/10.1007/978-3-030-79871-0_12.

Liu, L., Zhang, Z., Wang, J., Fan, Y., Shi, W., Liu, X., Shun, Q., 2019. Simultaneous saccharification and co-fermentation of corn stover pretreated by H_2O_2 oxidative degradation for ethanol production. *Energy*, 168: 946–952. https://doi.org/10.1016/j.energy.2018.11.132.

Liu, T., Wang, Y., Li, J., Yu, Q., Wang, X., Gao, D., Wang, F., Cai, S., Zeng, Y., 2021.\ Effects from Fe, P, Ca, Mg, Zn and Cu in steel slag on growth and metabolite accumulation of microalgae: a review. *Appl. Sci.*, 11(14): 6589. https://doi.org/10.3390/app11146589.

Magocha, T.A., Zabed, H., Yang, M., Yun, J., Zhang, H., Qi, X., 2018. Improvement of industrially important microbial strains by genome shuffling: current status and future prospects. *Bioresour. Technol.*, 257: 281–289. https://doi.org/10.1016/j.biortech.2018.02.118.

Mantashe, S.G., 2021. Government gazette: Draft amendment regulations regarding the mandatory blending of biofuels with petrol and diesel. Department of Mineral Resources and Energy, *Staatskoerant*, 12 Maart 2021, No. 44265. www.gpwonline.co.za.

Marques, M.P., Cabral, J.M., Fernandes, P., 2010. Bioprocess scale-up: quest for the parameters to be used as criterion to move from microreactors to lab-scale. *J. Chem. Technol. Biotechnol.*, 85(9): 1184–1198. https://doi.org/10.1002/jctb.2387.

Mishra, S., Kumar, V., Sarkar, J., Rathore, A.S., 2023. Mixing and mass transfer in production-scale mammalian cell culture reactor using coupled CFD-species transport-PBM validation. *Chem. Eng. Sci.*, 267: 118323. https://doi.org/10.1016/j.ces.2022.118323.

Mohit, M., Xu, M., Kurnia, J.C., Mujumdar, A.S., Sasmito, A.P., 2025. A multi-scale multi-stage model for spray freezing of binary solutions. *Drying Technol.*, 43(1–2): 197–213. https://doi.org/10.1080/07373937.2024.2442490.

Mushtaq, Q., Ishtiaq, U., Joly, N., Spalletta, A., Martin, P., 2024. Harnessing *Bacillus subtilis* QY5 PP784163 for bioethanol production from potato peel waste and nutrient recovery for animal feed: maximizing resource efficiency. *Fermentation*, 10(10): 523. https://doi.org/10.3390/fermentation10100523.

Mvelase, L., Ferrer, S., 2024. The economywide impact of bioethanol production in South Africa. *Energy Conversion and Management: X*, 24: 100729. https://doi.org/10.1016/j.ecmx.2024.100729.

Nduka, F.O., Onwurah, I.N.E., Obeta, C.J., Nweze, E.J., Nkwocha, C.C., Ujowundu, F.N., Eje, O.E., Nwigwe, J.O., 2024. Effect of nickel oxide nanoparticles on bioethanol production by *Pichia kudriavzveii* IFM 53048 using banana peel waste substrate. *Environ. Technol.*, 45(16): 3283–3302. https://doi.org/10.1080/09593330.2023.2215450.

Olughu, O.O., Tabil, L.G., Dumonceaux, T., Mupondwa, E., Cree, D., Li, X., 2023. Technoeconomic analysis of a fungal pretreatment-based cellulosic ethanol production. *Results Eng.*, 19: 101259. https://doi.org/10.1016/j.rineng.2023.101259.

Park, J.W., Kim, S.Y., Noh, J.H., Bae, Y.H., Lee, J.W., Maeng, S.K., 2022. A shift from chemical oxygen demand to total organic carbon for stringent industrial wastewater regulations: utilization of organic matter characteristics. *J. Environ. Manag.*, 305: 114412. https://doi.org/10.1016/j.jenvman.2021.114412.

Pérez, R.P., Suárez, J.G., Diaz, E.N., Rodríguez, R.S., Menéndez, E.C., Balaguer, H.D., Lasa, A.M., 2018. Scaling-up fermentation of *Escherichia coli* for production of recombinant P64k protein from *Neisseria meningitidis*. *Electron. J. Biotechnol.*, 33: 29–35. https://doi.org/10.1002/cite.202100041.

Petry, F., Salzig, D., 2021. Impact of bioreactor geometry on mesenchymal stem cell production in stirred-tank bioreactors. *Chem. Ing. Tech.*, 93(10): 1537–1554. https://doi.org/10.1002/cite.202100041.

Pham, P.J., Hernandez, R., French, W.T., Estill, B.G., Mondala, A.H., 2011. A spectrophotometric method for quantitative determination of xylose in fermentation medium. *Biomass Bioenergy*, 35(7): 2814–2821. https://doi.org/10.1016/j.biombioe.2011.03.006.

Phukoetphim, N., Salakkam, A., Laopaiboon, P., Laopaiboon, L., 2017. Kinetic models for batch ethanol production from sweet sorghum juice under normal and high gravity fermentations: logistic and modified Gompertz models. *J. Biotechnol.*, 243: 69–75. https://doi.org/10.1016/j.jbiotec.2016.12.012.

Polat, E., Yüksel, E., Altınbaş, M., 2020. Mutual effect of sodium and magnesium on the cultivation of microalgae *Auxenochlorella protothecoides*. *Biomass Bioenergy*, 132: 105441. https://doi.org/10.1016/j.biombioe.2019.105441.

Qazizada, M.E., 2016. Design of a batch stirred fermenter for ethanol production. *Procedia Eng.*, 149: 389–403. https://doi.org/10.1016/j.proeng.2016.06.684.

Raina, N., Slathia, P.S., Sharma, P., 2020. Experimental optimisation of thermochemical pretreatment of sal (*Shorea robusta*) sawdust by Central Composite Design study for bioethanol production by co-fermentation using *Saccharomyces cerevisiae* (MTCC-36) and *Pichia stipitis* (NCIM-3498). *Biomass Bioenergy*, 143: 105819. https://doi.org/10.1016/j.biombioe.2020.105819.

Raj, K., Krishnan, C., 2020. Improved co-production of ethanol and xylitol from low-temperature aqueous ammonia pretreated sugarcane bagasse using two-stage high solids enzymatic hydrolysis and *Candida tropicalis*. *Renew. Energy*, 153: 392–403. https://doi.org/10.1016/j.renene.2020.02.042.

Rodríguez-Martínez, B., Coelho, E., Gullón, B., Yáñez, R., Domingues, L., 2023. Potato peels waste as a sustainable source for biotechnological production of biofuels: process optimization. *Waste Manag.*, 155: 320–328. https://doi.org/10.1016/j.wasman.2022.11.007.

Rouhollah, H., Iraj, N., Giti, E., Sorah, A., 2007. Mixed sugar fermentation by *Pichia stipitis*, *Saccharomyces cerevisiae*, and an isolated xylose-fermenting *Kluyveromyces marxianus* and their cocultures. *Afr. J. Biotechnol.*, 6: 1110–1114. http://dx.doi.org/10.5897/AJB2007.000-2144.

Salakkam, A., Phukoetphim, N., Laopaiboon, P., Laopaiboon, L., 2023. Mathematical modeling of bioethanol production from sweet sorghum juice under high gravity fermentation: applicability of Monod-based, logistic, modified Gompertz and Weibull models. *Electron. J. Biotechnol.*, 64: 18–26. https://doi.org/10.1016/j.ejbt.2023.03.004.

Salman, J.M., Grmasha, R.A., Stenger-Kovács, C., Lengyel, E., Al-Sareji, O.J., Al-Cheban, A.M.A., Meiczinger, M., 2023. Influence of magnesium concentrations on the biomass and biochemical variations in the freshwater algae *Chlorella vulgaris*. *Heliyon*, 9(1): e13072. https://doi.org/10.1016/j.heliyon.2023.e13072.

Sanusi, I., Suinyuy, T.N., Lateef, A., Gueguim Kana, E.B., 2020. Effect of nickel oxide nanoparticles on bioethanol production: process optimisation, kinetic and metabolic studies. *Process Biochem.*, 92: 386–400. https://doi.org/10.1016/j.procbio.2020.01.029.

Sanusi, A.I., Faloye, F.D., Kana, E.G.B., 2019. Impact of various metallic oxide nanoparticles on ethanol production by *Saccharomyces cerevisiae* BY4743: screening, kinetic study and validation on potato waste. *Catal. Lett.*, 149(7): 2015–2031. https://doi.org/10.1007/s10562-019-02796-6.

Sanusi, A.I., Suinyuy, T.N., Kana, G.E.B., 2021. Impact of nanoparticle inclusion on bioethanol production process kinetic and inhibitor profile. *Biotechnol. Rep.*, 29: e00585. https://doi.org/10.1016/j.btre.2021.e00585.

Sanusi, I., Aruwajoye, G., Revaprasadu, N., Sewsynker-Sukai, Y., Meyer, E.L., Kana, E.B.G., 2024. A novel autoclave-assisted nanoparticle pre-treatment for improved sugar recovery from potato peel waste: process optimisation, nanoparticle recyclability and bioethanol production. *Biomass Convers. Biorefin.*, 14(13): 13941–13953. https://doi.org/10.1007/s13399-022-03574-y.

Saratale, R.G., Cho, S.-K., Saratale, G.D., Kumar, M., Bharagava, R.N., Varjani, S., Kadam, A.A., Ghodake, G.S., Palem, R.R., Mulla, S.I., Kim, D.S., Shin, H.S., 2021. An overview of recent advancements in microbial polyhydroxyalkanoates (PHA) production from dark fermentation acidogenic effluents: a path to an integrated bio-refinery. *Polymers*, 13(24): 4297. https://doi.org/10.3390/polym13244297.

Sasikumar, E., Viruthagiri, T., 2008. Optimisation of process conditions using response surface methodology (RSM) for ethanol production from pretreated sugarcane bagasse: kinetics and modeling. *Bioenergy Res.*, 1: 239–247. https://doi.org/10.1007/s12155-008-9018-6.

Sewsynker-Sukai, Y., Gueguim-Kana, E.B., 2018. Simultaneous saccharification and bioethanol production from corn cobs: process optimisation and kinetic studies. *Bioresour. Technol.*, 262: 32–41. https://doi.org/10.1016/j.biortech.2018.04.056.

Shan, S., Manyakhin, A.Y., Wang, C., Ge, B., Han, J., Zhang, X., Zhou, C., Yan, X., Ruan, R., Cheng, P., 2023. Mixotrophy, a more promising culture mode: multi-faceted elaboration of carbon and energy metabolism mechanisms to optimize microalgae culture. *Bioresour. Technol.*, 386: 129512. https://doi.org/10.1016/j.biortech.2023.129512.

Singh, A., Bajar, S., Bishnoi, N.R., 2014. Enzymatic hydrolysis of microwave alkali pretreated rice husk for ethanol production by *Saccharomyces cerevisiae*, *Scheffersomyces stipitis* and their co-culture. *Fuel*, 116: 699–702. https://doi.org/10.1016/j.fuel.2013.08.072.

Suresh, S., Srivastava, V., Sakthivel, S., Arisutha, S., 2018. Kinetic modeling of ethanol production for substrate–microbe system. In *Biorefining of Biomass to Biofuels*. Springer, Berlin/Heidelberg, Germany, 361–372. https://doi.org/10.1007/978-3-319-67678-4_16.

Tareen, A.K., Punsuvon, V., Sultan, I.N., Khan, M.W., Parakulsuksatid, P., 2021a. Cellulase addition and pre-hydrolysis effect of high solid fed-batch simultaneous saccharification and ethanol fermentation from a combined pretreated oil palm trunk. *ACS Omega*. https://doi.org/10.1021/acsomega.1c03111.

Torrellas, M., Pietrafesa, R., Ferrer-Pinós, A., Capece, A., Matallana, E., Aranda, A., 2023. Optimizing growth and biomass production of non-*Saccharomyces* wine yeast starters by overcoming sucrose consumption deficiency. *Front. Microbiol.*, 14: 1209940. https://doi.org/10.3389/fmicb.2023.1209940.

Um, B.H., Hanley, T.R., 2008. High-solid enzymatic hydrolysis and fermentation of solka floc into ethanol. *J. Microbiol. Biotechnol.*, 18: 1257–1265. PMID: 18667854.

Wu, Y., Wen, J., Wang, K., Su, C., Chen, C., Cui, Z., Cai, D., Cheng, S., Cao, H., Qin, P., 2023. Understanding the dynamics of the *Saccharomyces cerevisiae* and *Scheffersomyces stipitis* abundance in co-culturing process for bioethanol production from corn stover. *Waste Biomass Valorization*, 14(1): 43–55. https://doi.org/10.1007/s12649-022-01861-3.

Yadav, S.K., Naseeruddin, S., Prashanthi, G.S., Sateesh, L., Venkateswar-Rao, L., 2011. Bioethanol fermentation of concentrated rice straw hydrolysate using co-culture of *Saccharomyces cerevisiae* and *Pichia stipitis*. *Bioresour. Technol.*, 102: 6473–6478. https://doi.org/10.1016/j.biortech.2011.03.019.

Zhang, J., Chu, D., Huang, J., Yu, Z., Dai, G., Bao, J., 2010. Simultaneous saccharification and ethanol fermentation at high corn stover solids loading in a helical stirring bioreactor. *Biotechnol. Bioeng.*, 105: 718–728. https://doi.org/10.1002/bit.22593.

Zhang, J., Xia, X., Wang, J., Chen, X., Li, J., Zeng, G., Duan, X., Han, Q., Peng, R., 2025. Effects of phosphorus sources on the growth, chlorophyll a and total lipids production, and

fatty acids composition in *Chaetoceros lorenzianus*. *J. Appl. Phycol.*, 1–8. https://doi.org/10.1007/s10811-025-03493-1.

Zondi, A.S., Sanusi, I.A., Sewsynker-Sukai, Y., Beukes, L.S., Kana, G.E., 2025. Nano-based co-valorization, detoxification, and fermentation of potato waste and black liquor for bioethanol production. *Biomass Convers. Biorefin.*, 1–13. https://doi.org/10.1007/s13399-025-06515-7.

CHAPTER 8

General discussion

8.1. Introduction

The study focused on the enhancement of bioethanol production through an optimized simultaneous saccharification and co-fermentation (SSCF) process, utilizing optimally detoxified pretreated potato peel waste (PPW) hydrolysate as substrate. This approach addresses a major bottleneck in lignocellulosic bioconversion, which is the inhibitory effects of fermentation-inhibiting compounds generated during biomass pretreatment. This chapter provides a thematic synthesis and critical discussion of the experimental findings presented throughout this study.

8.2. Fe_3O_4 nanoparticle-based detoxification

Magnetic Fe_3O_4 nanoparticles (NPs) demonstrated high efficacy as adsorbents for removing key inhibitors from pretreated PPW hydrolysate. Under optimized conditions (≈0.021% w/v NPs, 35°C, 12.7 min, pH 4.14) established via Response Surface Methodology (RSM), high removal efficiencies were achieved with no sugar loss. Specifically, Fe_3O_4 NPs adsorbent achieved removal efficiencies for furfural (1.65-fold), 5-hydroxymethylfurfural (1.21-fold), phenol (1.95-fold), acetic acid (3.25-fold), and formaldehyde (1.55-fold). These findings compare favourably with previous studies. Zhu et al. (2022) achieved removal efficiencies of 47.8% for acetic acid, >5% for HMF, and 98.7% for furfural using lignin nanoparticles. Similarly, Sarawan et al. (2019) reported removal efficiencies of 98%, 88%, and 37% for furfural, HMF, and acetic acid, respectively, using activated charcoal, albeit with a 7% sugar loss.

The characteristic profile and adsorption mechanism of Fe_3O_4 nanoparticles (NPs), pre and post-detoxification, were elucidated to reveal chemisorption, hydrogen bonding, π–π stacking, and electrostatic interactions adsorption mechanisms between inhibitor molecules and NPs surface sites as the primary detoxification mechanisms (Meena et al., 2025). Specifically, the particle size of Fe_3O_4 NPs increased from 20.08 nm to 44.84 nm (>2-fold) post-detoxification, due to surface adsorption of inhibitors and possible ligand complexation between the nano-adsorbent and the inhibitory compounds. Moreover, the hydroxylated Fe_3O_4 NPs surface, bearing hydroxyl groups and Fe (III) sites, facilitated these interactions through hydrogen

bonding, coordination with functional groups, and π–π interactions with aromatic inhibitors. FTIR analysis confirmed binding functional groups of phenolic-OH (phenol), and aldehyde-CHO (furfural, 5-hydroxymethylfurfural, and formaldehyde) to the surface of Fe_3O_4-NPs (Cao et al., 2014). The multi-modal adsorption, combining strong chemisorption (ligand binding to Fe (III)) with weaker interactions (van der Waals, π–π), underpins the high removal efficiencies.

Moreover, adsorption kinetics modelling provided further insight into the adsorption capacity, binding affinity, and underlying mechanisms. The adsorption kinetics followed a pseudo-second-order model, indicating that chemisorption is a rate-limiting step. The Langmuir model best fits phenol and HMF, indicating monolayer adsorption on homogeneous surface sites (El Bakri et al., 2024), while acetic acid and formaldehyde adsorption followed the Freundlich model, suggesting heterogeneous multilayer adsorption (Yang et al., 2024). The Temkin isotherm describes interactions where adsorption energy decreased with surface coverage, indicating chemisorption influenced by adsorbent–adsorbate interactions (Maryanti et al., 2020). The thermodynamics of the detoxification process indicated that the removal of the inhibitory compound was generally endothermic, except in the case of furfural. Additionally, the employed sensitivity analysis identified pH and Fe_3O_4 NPs adsorbent dosage as the two vital factors influencing the detoxification process, while temperature and contact time had lesser impacts within the tested range (Rorke et al., 2017).

Furthermore, the adsorption capacity increased with NPs concentration until site saturation occurred. pH exhibited a non-linear influence on the detoxification process, consistent with the known point of zero charge (PZC) behaviour of the adsorbent and inhibitor speciation (Ayub et al., 2020). The PZC of Fe_3O_4 NPs (~5.0) resulted in a positively charged surface under acidic conditions, enhancing the adsorption of weakly acidic inhibitors such as acetic acid. Furfural removal was most effective near pH 5, where the nanoparticle surface remained slightly positive, while HMF adsorption peaked at pH ~3. Formaldehyde exhibited consistent adsorption across the acidic pH range. In contrast, phenol adsorption increased significantly at higher pH values due to the formation of phenolate ions. These trends highlight the critical role of surface charge and inhibitor speciation, both of which are pH-dependent in the adsorption mechanism (Yang et al., 2025).

Further insight into the adsorption process performance was revealed by the shifts in –OH and Fe–O stretching vibrations observed post-adsorption, confirming the retention of Fe_3O_4 NPs' structural integrity and the presence of available adsorption sites post-detoxification (Fan et al.,

2017). Additionally, the regenerated Fe_3O_4 NPs maintained a high detoxification efficiency (~100%) over two detoxification cycles, likely due to their large surface area providing sufficient active sites for adsorption without saturation (Al-Hetlani et al., 2022). The higher detoxification efficiency with no sugar loss, coupled with the high recyclability of the nano-adsorbent, suggests that Fe_3O_4 nanoparticle-based hydrolysate detoxification could be a sustainable approach to obtain highly processable and fermentable hydrolysate.

8.3. Fermentation strategy: SHF vs. SSF

The nanoparticle-assisted detoxification process yielded a highly processable hydrolysate rich in fermentable sugars and low in inhibitory compounds. The detoxified hydrolysate was employed in simultaneous saccharification and fermentation (SSF) as well as separate hydrolysis and fermentation (SHF), to establish the most favourable fermentation strategy for the detoxified pretreated PPW. The SSF process demonstrated enhanced overall bioethanol yield and productivity relative to the SHF process. Specifically, SSF achieved a sugar utilization rate exceeding 94%, notably higher than the 91.9% recorded for SHF. Consequently, SSF generated approximately 25.96 g/L bioethanol concentration, compared to 23.20 g/L bioethanol produced under the SHF process. Moreover, the experimental data from bioethanol production over time fitted the modified Gompertz model with a high correlation coefficient (R^2) > 0.99, revealing a short lag phase (< 2.3 h) and high maximum production rates ($r_{p,m}$: 6.88 g/L·h). Furthermore, the Luedeking-Piret modelling demonstrated a predominantly growth-associated bioethanol production, characterized by a high growth-associated product formation coefficient (α = 3.515 g P/g X) and near-zero non-growth-associated product formation coefficient (β). This finding was further corroborated by substrate utilization kinetics, which yielded low maintenance coefficients ($\delta \approx 0.0019$ g S/g X·h). This value closely aligns with those reported by Germec et al. (2019), who observed similar δ values (0.0013–0.0016 g S/g X·h) using *S. cerevisiae* in a carob extract-based medium. Such low maintenance coefficients indicate minimal sugar consumption for non-productive cellular processes, such as repair and maintenance, thereby suggesting that a substantial proportion of the available carbon was efficiently directed toward bioethanol synthesis (Germec et al., 2019). In addition, the effective removal of inhibitory compounds translated to enhanced *S. cerevisiae* growth, evidenced by a maximum specific growth rate (μ_{max}) of 0.31 h^{-1}. This rate surpasses those reported for undetoxified hydrolysates, such as sugar beet juice (0.169 h^{-1}) (Dodic et al., 2012), sweet sorghum juice (0.154 h^{-1}) (Phukoetphim et al., 2017), and food waste (0.135 h^{-1}) (Yan

et al., 2013). The interplay between substrate utilization and biomass growth for improved bioethanol production in the SSF process further substantiated the critical role of inhibitor detoxification in hydrolysate processability, as well as its role in suppressing non-growth-associated maintenance metabolism and redirecting microbial metabolic activity towards growth-associated bioethanol production. In addition to the direct detoxification effect, the presence of Fe_3O_4 nanoparticles may have contributed to enhanced glycolytic flux and bioethanol yield, potentially aligning with the nanomaterial-mediated enhancements reported by Sanusi et al. (2021). Notably, the α, β, γ, and δ values obtained were comparable to those in previous reports and desirable for high-performance bioprocessing. Specifically, significantly lower values of the non-growth-associated and maintenance constants, β and δ, indicated less energy requirement for cellular repair and maintenance. This enables more energy to be directed toward metabolic activities and product formation, presenting a significant economic advantage for industrial applications by reducing energy consumption in large-scale operations (Germec et al., 2019).

However, despite the enhanced fermentability observed in SSF processes, the inefficient bioconversion of xylose released during biomass pretreatment remained a critical concern, limiting overall bioethanol yield. This limitation underscores the necessity for co-fermentation strategies involving xylose-fermenting yeasts. The co-fermentation strategy has been identified as a viable solution to this challenge by enabling the simultaneous and efficient utilisation of both glucose and xylose, thereby improving overall sugar conversion and bioethanol productivity, as observed in the present study.

8.4. SSCF optimization

In order to maximise utilisation of PPW-derived hexose and pentose sugars, an optimised simultaneous saccharification and co-fermentation (SSCF) process was developed using a co-culture of *Saccharomyces cerevisiae* (a hexose fermenter) and *P. stipitis* (a pentose fermenter). High bioethanol production (48.7 g/L), with a fermentation efficiency of 99%, a productivity of 4.06 g/L·h, and a yield of 0.505 g ethanol/g total sugar was achieved through simultaneous inoculation at 0 h with a 1:4 inoculum ratio (*S. cerevisiae*: *P. stipitis*) using the optimally detoxified PPW hydrolysate. The coculture of *S. cerevisiae* and *P. stipitis* significantly outperformed the monoculture system, achieving a 34% increase in bioethanol concentration. The enhanced performance is attributed to the synergistic advantages of co-fermentation, which is attributed to complementary sugar utilization and enhanced substrate conversion

efficiency. These findings are consistent with previous reports, which demonstrate that co-cultivation enhances mixed-sugar fermentation, thereby increasing bioethanol yield, production rate, and reducing fermentation time (Miah et al., 2022; Sathendra-Elumalai et al., 2023). The SSCF process kinetics and modelling were analysed using the Logistic, Gompertz, and Luedeking–Piret models to describe biomass growth, substrate consumption, and bioethanol production dynamics. The results demonstrated that detoxification of the hydrolysate significantly enhanced metabolic performance, as reflected in improved cell growth (X_{max} = 14.17 g/L), maximum specific growth rate (μ_{max} = 0.752 h^{-1}), and sugar conversion efficiency (98.43%). The Luedeking–Piret model provided critical insights, revealing that bioethanol production was predominantly growth-associated, with a high growth-associated coefficient (α = 1.365 g/g) and a minimal non-growth-associated coefficient (β = 0.11 g/g·h). The substrate utilization kinetics also showed low maintenance coefficients (δ) of 0.0013 g/g·h which aligns with findings by Germec et al. (2019), Liu et al. (2019), and Teo and Ooi (2016), who similarly reported low δ values ranging from 0.0012 to 0.0284 g S/g X.h., indicating efficient metabolic flux toward bioethanol production rather than biomass maintenance. Model validation using experimental data demonstrated a strong correlation, with R^2 values approximately 0.99, confirming the reliability of the kinetic models under the optimised SSCF conditions. Moreover, real-time monitoring of CO_2 and N_2 emissions revealed distinct metabolic shifts during fermentation: early-stage CO_2 evolution coincided with bioethanol production peaks, while subsequent N_2 release could be associated with the role of peptone stabilising enzyme activity and yeast extract in growth and acetate assimilation after glucose depletion during fermentation (Nancib et al., 1991; Guadalupe-Daqui et al., 2023). These insights validate the industrial viability of co-culture systems, where optimized parameters collectively enhance productivity while reducing process time and cost. In view of the fermentation performance, the SSCF was further subjected to a preliminary scale-up and kinetic studies.

8.5. Process scale-up

For industrial relevance and sustainable bioethanol production, the preliminary scale-up (from 1 L to 10 L) of the optimized SSCF process was successfully carried out. The non-gassed power (P) was maintained at 0.012 W across the two scales. For the 1 L scale-up, the impeller agitation speed [n] operated at 2.0 revolutions per second (rps), corresponding to impeller tip speed [V_{tip}] (0.34 m/s). In the 10 L scale-up, the agitation speed was adjusted to 1.58 rps and

V_{tip} (0.35 m/s) to maintain similar conditions operated at 35 °C and pH 5.78. Maintaining tip speed during scale-up reduced the specific power input from 12 W/m^3 (1L) to 1.2 W/m^3, significantly improving energy efficiency. This reduction altered the bioreactor hydrodynamics, with circulation time increasing from 4.35 s to 25.64 s, while shear stress decreased from 0.98 Pa to 0.77 Pa, thereby mitigating cell damage risks (Kheirkhah et al., 2022). Despite extended mixing cycles in the pilot-scale, high sugar conversion (>94%) and bioethanol yields indicated that mass transfer was not a limiting factor. The efficient substrate-enzyme interaction and microbial uptake suggest that the mixing conditions were sufficient to ensure effective accessibility of fermentable sugars throughout the system. The stability and efficiency of the scaled-up system can be attributed to three interrelated factors: (i) the low viscosity of the fermentation broth, which facilitated efficient substrate diffusion even with prolonged circulation times (Gholamipour-Shirazi and Mossige, 2024); (ii) reduced shear rate (γ = 20 to 15.8 s^{-1}), which preserved cell viability and reduced mechanical stress (Petry and Salzig, 2021); and (iii) enhanced microbial activities conferred by nanoparticle-mediated detoxification, which enabled robust fermentation process (Nduka et al., 2024). Additionally, during the scale-up, reduced energy dissipation rates ($\varepsilon = 1.17 \times 10^{-2}$ to 1.17×10^{-3} m^2/s^3) and increased eddy sizes (λ = 1.73 to 3.08 mm) demonstrated hydrodynamic similarity, rather than volumetric power equivalence, which is critical for effective scaling process. These findings support the feasibility of energy-efficient, high-productivity SSCF at larger scales, particularly for shear-sensitive microbial consortia when employed in lignocellulosic bioethanol production (Afedzi et al., 2022; Gao et al., 2022).

Moreover, both 1L and 10L-scales demonstrated similarly high maximum potential bioethanol concentration (P_m) (44.70 and 44.45 g/L) and maximum bioethanol production rate ($r_{p,m}$) of 6.58 and 6.54 g/L/h, respectively. The observed similar P_m and $r_{p,m}$ values obtained from both scales may be attributed to similar rotational speed [n] of 2 revolutions per second [rps] (1 L bioreactor) to 1.58 rps (10 L bioreactor) and the impeller tip speed (V_{tip}) of 0.34 m/s and 0.35 m/s, respectively in addition to other reasons highlighted above. Given that higher production rates are preferred at large scales, the high $r_{p.m}$ (> 6.5 g/L/h) attained in the scale-up study substantiates the desirability of this strategy for industrial bioethanol production. The growth-associated product formation coefficient (α) and non-growth-associated product formation coefficient (β) were estimated for both scales using the Leudeking-Piret model. Both scales exhibited close to zero β-values of 0.0042 g P/g X. h (1L-scale) to 0.0004 g P/g X. h (10L-scale), while the α-values obtained were 3.373 g P/g X and 4.744 g P/g X, respectively. This

also indicated bioethanol production was primarily growth-associated, with minimal energy diverted to maintenance (Germec et al., 2019). The low maintenance coefficient (δ) for substrate utilization (0.0058–0.009 gS/gX·h) further underscored efficient carbon channelling toward biomass and bioethanol production.

8.6. Scientific contributions of the study

This work provided novel insights into the complex interactions between Fe_3O_4 nanoparticles and inhibitory compounds within a bioprocessing context. To our knowledge, this research represents the first demonstration of integrating magnetic Fe_3O_4 nanoparticles (NPs) for detoxification within a simultaneous saccharification and co-fermentation (SSCF) process for pretreated PPW. The detailed surface characterization and adsorption study of post-detoxification-harvested Fe_3O_4 nanoparticles elucidated the multimodal mechanisms (chemisorption, hydrogen bonding, π–π stacking, and electrostatic interactions) through which functional groups of various inhibitors interact with Fe_3O_4 nanoparticles. Furthermore, the optimized SSCF system achieved synergistic sugar utilization and maximized bioethanol yield, underscoring the benefits of integrating advanced detoxification with co-culture strategies. These insights deepen the fundamental understanding of nano-adsorbent behaviour in complex bioprocessing environments, both at laboratory scale and semi-pilot scale.

The application of response surface methodology (RSM) and artificial neural network (ANN) models for optimizing nanoparticle-assisted detoxification steps enabled the optimization of critical parameters, including nanoparticle (NP) dose, pH, and contact time, to achieve maximal inhibitor removal efficiency. Further to this, the adsorption isotherm modeling and thermodynamics study, in conjunction with nanoparticle characterization, confirmed the mechanism of inhibitor detoxification. The modelling and optimisation of the SSCF process provide a framework for co-culturing *S. cerevisiae* and *P. stipitis* to enhance the bioconversion of fermentable sugars, thereby improving bioethanol production. The process kinetic modelling framework, incorporating logistic, modified Gompertz, and Luedeking–Piret models, satisfactory described the fermentation process dynamics, establishing relationships between biomass growth, substrate conversion, and product formation. The study established a comprehensive and adaptable framework to guide future research.

8.7. Practical/Industrial relevance

The developed process achieves industrial scalability using the optimally detoxified PPW hydrolysate, underscoring its commercial potential. The applicability of this process, particularly in regions with abundant PPW, such as South Africa, China, India and the USA, is highly promising for biofuel production. Furthermore, the generation of a nutrient-rich fermentation effluent offers potential additional value, aligning with the circular economy concept. Additionally, PPW-derived bioethanol presents a significant potential reduction in carbon footprint, representing a sustainable and renewable alternative to fossil fuels.

8.8. Limitations and research frontiers

Key challenges should be resolved further to promote the industrial applicability of this study's findings:

i. *Process generalizability and substrate specificity:* The process developed in this study is most applicable to starch-rich residues such as potato peel waste (PPW). While the process is effective for the current feedstock, its applicability to other pretreated lignocellulosic biomasses needs to be evaluated. Feedstocks with different starch contents or inhibitor profiles might require re-optimization of the detoxification and fermentation protocols to achieve similar or satisfactory results.

ii. *Incomplete Detoxification:* Although the major inhibitory compounds were effectively removed, trace-level residues might persist post-detoxification and could exert inhibitory effects on sensitive microbial strains during extended or continuous fermentation processes. Furthermore, the interactive and potentially synergistic effects among residual inhibitors was not fully captured by the current developed models.

iii. *Economic considerations:* A comprehensive techno-economic and life-cycle assessment is essential to validate the commercial viability of this approach. Key factors requiring evaluation include the cost-effectiveness of nanoparticle regeneration, enzyme dosing strategies, and energy inputs associated with mixing and process operation.

8.9. Summary and outlook

This study advances the understanding of enhancing *S. cerevisiae* and *P. stipitis* co-culture dynamics, particularly in glucose-xylose co-metabolism, by coupling kinetic modelling of co-

culture metabolism with optimally detoxified hydrolysate. The findings provide a practicable framework for the effective valorization of other lignocellulosic biomasses. Moreover, addressing existing knowledge gaps in nanoparticle inhibitor interactions and their impact on fermentation dynamics offers additional mechanistic insight into how detoxification influences bioethanol production, thereby underpinning the practicability of a nano-enabled SSCF strategy for lignocellulosic bioethanol production. These findings demonstrate the feasibility of a novel nanoparticle-integrated SSCF strategy for lignocellulosic bioethanol bioprocessing. The key conclusions and actionable recommendations from this research are presented in the final chapter.

References

Afedzi, A.E.K., Rattanaporn, K., Parakulsuksatid, P., 2022. Impeller selection for mixing high-solids lignocellulosic biomass in stirred tank bioreactor for ethanol production. Bioresource Technology Reports, 17, p.100935. https://doi.org/10.1016/j.biteb.2021.100935.

Al-Hetlani, E., D'Cruz, B., Amin, M.O., Madkour, M., 2022. Effective magnetic nanoadsorbent based on a carbonaceous/spinel ferrite nanocomposite for the removal of pharmaceutical pollutants from wastewater. Environ. Sci.: Water Res. Technol. 8, 998–1010. https://doi.org/10.1039/d1ew00495f.

Ayub, A., Raza, Z.A., Majeed, M.I., Tariq, M.R., Irfan, A., 2020. Development of sustainable magnetic chitosan biosorbent beads for kinetic remediation of arsenic-contaminated water. Int. J. Biol. Macromol. 163, 603–617. https://doi.org/10.1016/ j.ijbiomac.2020.06.287.

Cao, C., Xiao, L., Chen, C., Shi, X., Cao, Q., Gao, L., 2014. In situ preparation of magnetic Fe_3O_4/chitosan nanoparticles via a novel reduction precipitation method and their application in adsorption of reactive azo dye. Powder Technol. 260 (7), 90–97. https://doi.org/10.1016/j.powtec.2014.03.025.

Dodic, J. M., Vucurovic, D. G., Dodic, S. N., Grahovac, J. A., Popov. D., Nedeljkovic, N. M. 2012. Kinetic modelling of batch ethanol production from sugar beet raw juice. Appl Energy 99:192–197. https:// doi. org/ 10. 1016/j. apene rgy. 2012. 05. 016.

El Bakri, A., El Boujaady, H., Ferraa, N., Bennani-Ziatni, M., 2024. The removal of phenol through adsorption onto synthetic calcium phosphates–a study encompassing analyses of kinetics and thermodynamics. Ecological Engineering and Environmental Technology (EEET) 25 (4), 301–315. https://doi.org/10.12912/27197050/184155.

Fan, H.L., Zhou, S.F., Jiao, W.Z., Qi, G.S., Liu, Y.Z., 2017. Removal of heavy metal ions by magnetic chitosan nanoparticles prepared continuously via high-gravity reactive precipitation method. Carbohydr. Polym. 174, 1192–1200. https://doi.org/ 10.1016/j.carbpol.2017.07.050.

Gao, C.H., Cao, H., Cai, P., Sørensen, S.J., 2021. The initial inoculation ratio regulates bacterial coculture interactions and metabolic capacity. The ISME journal, 15(1), pp.29-40. https://doi.org/10.1038/s41396-020-00751-7.

Germec, M., Turhan, I., Karhan, M., Dermirci, A., 2019. Kinetic modeling and techno-economic feasibility of ethanol production from carob extract-based medium in biofilm reactor. Appl Sci 9 (2121):1–19. https:// doi. org/ 10. 3390/ app91 02121.

Gholamipour-Shirazi, A. and Mossige, E.J.L., 2024. Impact of Mixing on Flavor and Aroma Development in Fermented Foods. arXiv preprint arXiv:2412.10190. https://doi.org/10.48550/arXiv.2412.10190.

Guadalupe-Daqui, M. M., Goodrich-Schneider, R. M., Sarnoski, P. J., Carriglio, J. C., Sims, C. A., Pearson, B. J., MacIntosh, A. J., 2023. The effect of CO2 concentration on yeast fermentation: rates, metabolic products, and yeast stress indicators, Journal of Industrial Microbiology and Biotechnology 50 (1): 1-9. https://doi.org/10.1093/jimb/kuad001.

Kheirkhah, T., Neubauer, P. and Junne, S., 2023. Controlling Aspergillus niger morphology in a low shear-force environment in a rocking-motion bioreactor. Biochemical Engineering Journal, 195, p.108905. https://doi.org/10.1016/j.bej.2023.108905.

Liu, L., Zhang, Z., Wang, J., Fan, Y., Shi, W., Liu, X., Shun, Q. 2019. Simultaneous saccharification and co-fermentation of corn stover pretreated by H2O2 oxidative degradation for ethanol production. Energy 2019; 168: 946- 952. https://doi.org/10.1016/j.energy.2018.11.132.

Maryanti, R., Nandiyanto, A.B.D., Manullang, T.I.B., Hufad, A., Sunardi, S., 2020. Adsorption of dye on carbon microparticles: Physicochemical properties during adsorption, adsorption isotherm and education for students with special needs. Sains Malays 49, 2949–2960. https://doi.org/10.17576/jsm-2020-4912-09.

Meena, H.M., Kukreti, S. and Jassal, P.S., 2025. Synthesis of novel Chitosan-Tannic acid adsorbent for removal of Aluminum (III) from wastewater: characterisation, kinetics, equilibrium isotherms and thermodynamic studies. Adsorption, 31(2), p.46. https://doi.org/10.1007/s10450-025-00604-9.

Miah, R., Siddiqa, A., Chakraborty, U., Tuli, J.F., Barman, N.K., Uddin, A., Aziz, T., Sharif, N., Dey, S.K., Yamada, M. and Talukder, A.A., 2022. Development of high-temperature simultaneous saccharification and fermentation by thermosensitive *Saccharomyces cerevisiae*

and *Bacillus amyloliquefaciens*. Scientific Reports, 12(1), p.3630. https://doi.org/10.1038/s41598-022-07589-3.

Nancib, N., Branlant, C., Boudrant, J. 1991. Metabolic roles of peptone and yeast extract for the culture of a recombinant strain of *Escherichia coli*, J. Ind. Microbiol, 8 (3): 165–169, https://doi.org/10.1007/BF01575849.

Nduka, F.O., Onwurah, I.N.E., Obeta, C.J., Nweze, E.J., Nkwocha, C.C., Ujowundu, F.N., Eje, O.E. and Nwigwe, J.O., 2024. Effect of nickel oxide nanoparticles on bioethanol production by *Pichia kudriavzveii* IFM 53048 using banana peel waste substrate. Environmental Technology, 45(16), pp.3283-3302. https://doi.org/10.1080/09593330.2023.2215450.

Petry, F. and Salzig, D., 2021. Impact of bioreactor geometry on mesenchymal stem cell production in stirred‐tank bioreactorS. chemie Ingenieur Technik, 93(10), pp.1537-1554. https://doi.org/10.1002/cite.202100041.

Phukoetphim, N., Salakkam, A., Laopaiboon, P., Laopaiboon, L., 2017. Kinetic models for batch ethanol production from sweet sorghum juice under normal and high gravity fermentations: logistic and modified Gompertz models. J Biotech 243:69–75. https:// doi. org/10. 1016/j. jbiot ec. 2016. 12. 012.

Rorke, D.C.S., Suinyuy, T.N., Gueguim Kana, E.B., 2017. Microwave-assisted chemical pretreatment of waste sorghum leaves: Process optimization and development of an intelligent model for determination of volatile compound fractions. Bioresour. Technol. 224, 590–600. https://doi.org/10.1016/j.biortech.2016.10.048.

Sanusi, A.I., Suinyuy, T.N., Kana, G.E.B., 2021. Impact of nanoparticle inclusion on bioethanol production process kinetic and inhibitor profile. Biotechnol. Rep. 29 (1–12), e00585 https://doi.org/10.1016/j.btre.2021.e00585.

Sarawan, C., Suinyuy, T.N., Sewsynker-Sukai, Y., Gueguim Kana, E.B., 2019. Optimized activated charcoal detoxification of acid-pretreated lignocellulosic substrate and assessment for bioethanol production. Bioresour. Technol. 286, 1–10. https://doi. org/10.1016/j.biortech.2019.121403.

Sathendra-Elumalai R, Ramanujam P, Tawfik MA, Ravichandran P, Gurunathan B., 2023. Optimisation and kinetics modelling for enhancing the bioethanol production from banana

peduncle using *Trichoderma reesei* and *Kluveromyces marxianus* by co-pretreatment methods, Sustainable Energy Technologies and Assessments, 56: 103129. https://doi.org/10.1016/j.seta.2023.103129.

Teoh, Y., Ooi, Z., 2016. Evaluation of unstructured kinetic models for the production of bioethanol from banana and pineapple wastes. Bioresources, 11: 4295–4305. https://doi.org/10.15376/BIORES.11.2.4295-4305.

Yan. S., Chen, X., Wu, J., Wang, P., 2013. Pilot-scale production of fuel ethanol from concentrated food waste hydrolysates using *Saccharomyces cerevisiae* H058. Bioprocess Biosyst Eng 36(7):937– 946. https:// doi. org/ 10. 1007/s00449-012- 0827-9.

Yang, Z., Liu, Y., Liu, P., Yang, L., Zhang, A., Liu, Z., Li, X. and Li, Z., 2024. Study on material structure design, selective adsorption mechanism, and application for adsorption recovery of oil substances in coal chemical wastewater. Chemosphere, 349, 140943. https://doi.org/10.1016/j.chemosphere.2023.140943.

Yang, Z., Liu, Z., Shi, B., Yang, R., Lei, J., Wang, J., Zhang, A. Liu, Y., 2025. Adsorption of phenol on a novel porous nanocomposites prepared from coal gangue: studies on preparation conditions, adsorption characteristics and mechanism. Colloids and Surfaces A: Physicochemical and Engineering Aspects, p.137596. https://doi.org/10.1016/j.colsurfa.2025.137596.

Zhu, J., Jiao, N., Zhang, H., Xu, G., Xu, Y., 2022. Detoxification of lignocellulosic pre-hydrolysate by lignin nanoparticles, prepared from biorefinery biowaste, to enhance ethanol production. Bioprocess Biosyst. Eng. 45, 1011–1018. https://doi.org/ 10.1007/s00449-022-02720-0. https://doi.org/10.1007/s00449-022-02720-0.

CHAPTER 9

Conclusions and recommendations

9.1. Conclusions

The implementation of an efficient bioprocess strategy to enhance bioethanol conversion from lignocellulosic biomass (LCB) will significantly contribute to achieving a carbon-neutral bioeconomy and advancing sustainable biofuel production. However, process bottlenecks, such as the formation of inhibitory compounds during LB pretreatment that hamper efficiency bioethanol production processes. Hence, this research was undertaken to address these limitations, thereby improving bioethanol production efficiency towards viable industrial-scale implementation. Major findings derived from this study are summarized as follows:

9.1.1. Nanoparticle-based detoxification was modelled and optimized for the removal of five (5) fermentation process inhibitors to improve bioethanol productivity. Under optimized conditions (NP concentration [0.021 w/v%], temperature [35.37 °C], contact time [12.74 min], and pH [4.14]), Fe_3O_4 NP adsorbent achieved high removal efficiencies for furfural (1.65-fold), 5-hydroxymethylfurfural (1.21-fold), phenol (1.95-fold), acetic acid (3.25-fold), and formaldehyde (1.55-fold), without sugar loss. The structural and chemical nature of the Fe_3O_4 nanoadsorbent pre- and post-adsorption were revealed with strong suggestion of surface adsorption and complexation as the primary detoxification mechanisms, with pH and initial inhibitor concentration as the principal influencing factors. These results highlight the desirability and the potential of using nano-sized adsorbents in the detoxification of pretreated hydrolysate.

9.1.2. Moreover, the adsorption kinetics, isotherm, and thermodynamics of the detoxification process were evaluated to ascertain the mechanism of Fe_3O_4 nanoparticle adsorbent. Adsorbent dosage, initial inhibitor concentration, temperature, pH, and exposure time were found to strongly influence the adsorption capacity and adsorption efficiency of Fe_3O_4 nanoparticle. In addition, the inhibitory compound removal by Fe_3O_4 NPs can be strongly attributed to diffusion within the absorbent particles, the presence of binding active sites, adsorbate-absorbate interactions, and the impact of the chemisorption process (indicated by the pseudo-second-order kinetics). The potential binding forces involved in the adsorption process are mainly hydrogen bonds, π–π interactions, π-hydrogen bonding, and electrostatic interactions. The adsorption isotherm data for phenol and HMF best fit the Freundlich model, suggesting

heterogeneous multilayer adsorption. Acetic acid and formaldehyde conformed to the Langmuir model, suggesting homogeneous monolayer adsorption, while furfural aligned with the Temkin model, revealing adsorbate-adsorbate interaction and multilayer adsorption onto the Fe_3O_4 NP. These confirmed Fe_3O_4 NP adsorbent multi-site adsorption of the inhibitors. The thermodynamic coefficients (ΔG^0, $\Delta S^{0,}$ and ΔH^0) indicated that the inhibitory compound adsorption onto Fe_3O_4 NPs was predominantly spontaneous and endothermic. This provides additional insights into the potential and adsorption mechanism of Fe_3O_4 nanoadsorbent in removing inhibitory compounds (ICs) from pretreated PPW hydrolysate, thereby improving bioethanol productivity and yield.

9.1.3. In addition, bioethanol fermentation using the optimally detoxified hydrolysate achieved a saccharification efficiency of 88.95% and a bioethanol concentration of 26 g/L. SSF outperformed SHF in terms of overall fermentation efficiency and integration benefits. The kinetics of the bioethanol production by *S. cerevisiae* using optimally detoxified potato peel waste (PPW) hydrolysate revealed the dynamics of cell biomass accumulation, product formation, and substrate utilisation. The non-linear fitting of the logistic function modified Gompertz, Luedeking-Piret, and modified Luedeking-Piret kinetic models, demonstrated a strong correlation with experimental data, highlighting the efficacy of these models in predicting the dynamics of fermentation processes. Evidently, the removal of the inhibitory compound significantly improved the fermentation performance, resulting in high P_m (25.925 g/L) and X_{max} (9.983 g/L). The improved metabolic performance was predominantly growth-associated (α = 3.515 g P/g X and γ = 6.543 g S/g X), with a low cell maintenance coefficient (δ) value (0.0019 g S/g X.h).

9.1.4. Furthermore, efficient bioconversion of the detoxified hydrolysate (which contains xylose alongside abundant glucose) prompted the development of a simultaneous saccharification and co-fermentation (SSCF) model designed to enhance bioethanol yield. The co-fermentation of *S. cerevisiae* and *P. stipitis* demonstrated a synergistic effect, leading to improved bioethanol yields from the detoxified PPW hydrolysate. Optimal fermentation conditions were established at a 10% (w/v) solid loading, with an inoculum ratio of 1:4 (*S. cerevisiae* to *P. stipitis*) and a zero-hour inoculation time. Remarkably, the optimized co-culture approach yielded maximum specific growth rate (μ_{max}) (0.752 h^{-1}), glucose utilisation (99%), bioethanol concentration (48.73 g/L), bioethanol productivity (4.06 g/L/h), and yield (0.505 g/g). The concurrent utilisation of glucose (by *S. cerevisiae* and *P. stipites*) and xylose (by *P.*

stipites) in the co-fermentation system increased bioethanol production by approximately 34% compared to reported processes using only *S. cerevisiae*. This highlights the importance of the SSCF approach in improving bioethanol production efficiency from the detoxified PPW hydrolysate.

9.1.5 Finally, the optimized SSCF system was thereafter implemented in a pilot scale-up. The finding confirms that maintaining a consistent impeller tip speed (V_{tip}) is crucial for achieving high fermentation performance, resulting in a 21% reduction in shear stress and rate on the 10 L scale, which resulted in low cell damage and high cell viability. Likewise, desirable pumping capacity ($V_P = 3.9 \times 10^{-4}$ m^3/**s**) and 10-fold reduction in Power to Volume ratio (P/V_L) 1.2 W/m^3 characterised the 10L-scale bioreactor, indicating a significant improvement in energy efficiency at the larger scale. The suitable and coherent geometric, rheological and hydrodynamic properties of the process ensured the successful translation of the optimized laboratory-scale bioethanol production to a pilot-scale. The obtained fermentation waste effluent exhibited a rich composition of essential elements (Ca, K, Na, P) and a high total organic carbon (78 % g/g), making it a potential feedstock for microalgae cultivation, biofertilizer, and other valuable byproducts.

These findings demonstrate the technical feasibility and practical viability of an optimized co-fermentation process using nano-assisted detoxified hydrolysate for sustainable bioethanol production with scale-up potential. The results also provide valuable insights to inform decision-making in industrial bioprocess development within the framework of a circular economy and integrated biorefinery systems.

9.2. Recommendation for future studies

Building on the significant findings of this study, the following recommendations are proposed for future research to address current limitations and to facilitate the transition towards commercial-scale implementation:

9.2.1. To improve process efficiency and industrial relevance, future research should focus on integrating nanoparticle-assisted detoxification into continuous or fed-batch fermentation systems. Detailed studies are necessary to evaluate the stability and recycling potential of nanoparticles in continuous bioreactor operations.

9.2.2. Future research should also focus on genetic modification of fermenting microbes or metabolic engineering of strains to enhance co-utilisation of sugars, and with potential

for inhibitor resistance. Such improvements are critical for the scalability of lignocellulosic bioethanol production systems.

9.2.3. A detailed techno-economic analysis (TEA) is essential to evaluate the cost implications and economic viability of the nano-assisted detoxification process, co-fermentation configurations, and energy inputs. In parallel, a life cycle assessment (LCA) should be conducted to determine the environmental footprint of the process.

9.2.4. The development of integrated biorefinery systems that valorize fermentation effluents and residual streams through microalgae cultivation, anaerobic digestion, and composting, resulting in environmental sustainability of the overall process, aligning with circular economy and biorefinery principles.